CMBE13

3rd International Conference on Computational & Mathematical Biomedical Engineering

16th – 18th December 2013

City University of Hong Kong, HK SAR

Edited by:

Perumal Nithiarasu
Civil and Computational Engineering Centre
School of Engineering, Swansea University
Swansea, UK

Kim M Liew
College of Science and Engineering
Dept of Civil and Architectural Engineering
City University of Hong Kong, HK SAR

Rainald Löhner
Center for Computational Fluid Dynamics
College of Sciences, George Mason University
Fairfax, Virginia, US

Co-Edited by:

Etienne Boileau
Civil and Computational Engineering Centre
School of Engineering, Swansea University
Swansea, UK

Chenfeng Li
Civil and Computational Engineering Centre
School of Engineering, Swansea University
Swansea, UK

CW Lim
College of Science and Engineering
Dept of Civil and Architectural Engineering
City University of Hong Kong, HK SAR

Raoul van Loon
Civil and Computational Engineering Centre
School of Engineering, Swansea University
Swansea, UK

Igor Sazonov
Civil and Computational Engineering Centre
School of Engineering, Swansea University
Swansea, UK

Xianghua Xie
Department of Computer Science
Swansea University
Swansea, UK

3rd International Conference on Computational & Mathematical Biomedical Engineering, 2013, HK SAR

First edition, December 2013

Printed for CMBE in HK SAR

ISBN: 978-0-9562914-2-4
ISSN: 2227-3085 (print)
ISSN: 2227-9385 (electronic)

PREFACE

It is indeed our pleasure to welcome you to Hong Kong for the 3rd edition of the *International Conference on Computational and Mathematical Biomedical Engineering* (CMBE13).

This event is meant to be an interdisciplinary forum for exchange of knowledge on the latest mathematical, computational and experimental biomedical engineering results. As a sign of its success, the CMBE Proceedings is now a publication series, and it is subject to a strict publishing ethics policy. We hope that the interaction between researchers during the conference leads to translational research and new collaborations.

CMBE13 consists of eight plenary invited lectures, ten organised mini-symposia and several standard sessions. All delegates will be given the Conference Proceedings on a USB flash drive. The CMBE13 Proceedings is also available to download from the conference website at http://www.compbiomed.net. All the participants of CMBE13 are invited to submit an extended version of their paper for possible publication in the '*International Journal for Numerical Methods in Biomedical Engineering*' (http://mc.manuscriptcentral.com/cnm).

We thank CMBE13 sponsors, mini-symposia organisers, the international and local committees, and all reviewers for their support. We wish you a pleasant stay in Hong Kong and we hope you will enjoy the conference programme.

CMBE13 team

SPONSORS & PARTNERS

WILEY

香港城市大學
City University of Hong Kong

Prifysgol Abertawe
Swansea University

Department of
Civil and Architectural Engineering 土木及建築工程系

C2EC

HKIE THE HONG KONG INSTITUTION OF ENGINEERS 香港工程師學會
Mechanical, Marine, Naval Architecture & Chemical Division
機械、輪機、造船及化工分部

HKIE THE HONG KONG INSTITUTION OF ENGINEERS 香港工程師學會
Biomedical Division
生物醫學分部

COMMITTEES

Co Chairs

P. Nithiarasu, Swansea University, UK
K.M. Liew, City University of Hong Kong, HK SAR
R. Löhner, George Mason University, USA

International Advisory Committee

A. Al-Jumaily, Auckland University of Technology, New Zealand
P.J. Blanco, LNCC, Brazil
D. Drikakis, Cranfield University, UK
Y. Fan, Beihang University, China
R. Feijoo, LNCC, Brazil
X.Q. Feng, Tsinghua University, China
C.A. Figueroa, Kings College London, UK
L. Formaggia, Politecnico di Milano, Italy
A.F. Frangi, University of Sheffield, UK
T. Franz, University of Cape Town, South Africa
J.F. Gerbeau, INRIA, France
M. Heil, University of Manchester, UK
G.A. Holzapfel, Graz University of Technology, Austria
G.R. Liu, University of Cincinnati, USA
X. Luo, University of Glasgow, UK
A. Malan, University of Cape Town, South Africa
T. McGloughlin, University of Limerick, Ireland
K. Miller, University of Western Australia, Australia
M. Oshima, University of Tokyo, Japan
J. Peiro, Imperial College London, UK
D. Reddy, University of Cape Town, South Africa
J.N. Reddy, Texas A&M University, USA
A.M. Robertson, University of Pittsburgh, USA
B. Schrefler, University of Padova, Italy
K.N. Seetharamu, IEEE EMBS Section and PES College, India
M. Siebes, University of Amsterdam, The Netherlands
N. Smith, King's College London, UK
T.E. Tezduyar, Rice University, USA
M. Vazquez, BSC-CNS, Spain
A. Veneziani, Emory University, USA
Y. Ventikos, University of Oxford, UK
W.A. Wall, TUM, Germany
T.J. Wang, Xi'an Jiaotong University, China
G. Wei, Michigan State University, USA
Y. Xu, Imperial College London, UK
S.Y. Yeo, Institute of HPC, Singapore

Organising Committee

C.W. Lim, City University of Hong Kong, HK SAR
R.L.T. Bevan, Swansea University, UK
L. Bian, Chinese University of Hong Kong, HK SAR
E. Boileau, Swansea University, UK
D.C.C. Lam, Hong Kong University of Science & Technology, HK SAR
C. Li, Swansea University, UK
Y. Lin, University of Hong Kong, HK SAR
S.B. Lu, City University of Hong Kong, HK SAR
R. van Loon, Swansea University, UK
I. Sazonov, Swansea University, UK
Z.K. Wang, City University of Hong Kong, HK SAR
X. Xie, Swansea University, UK
Y. Yang, City University of Hong Kong, HK SAR
H.M. Yao, The Hong Kong Polytechnic University, HK SAR

CONTENTS

Invited Lectures

MS-A1: Heart Valve Modelling

Organised by Raoul van Loon and Xiaoyu Luo

MS-A2: Multiphysics & Multiscale Models for Simulating Total Heart Function

Organised by Toni Lassila, Alfio Quarteroni and Martin Weiser

MS-A3: Segmentation & Registration for Biomedical Applications

Organised by Xianghua Xie and Majid Mirmehdi

MS-A4: Multiphysics Modelling & Applications of the Cardiovascular System I

Organised by Marek Behr, C.Alberto Figueroa, Luca Formaggia, Jean-Frédéric Gerbeau and Christian Vergara

MS-B1: Aneurysm Modelling: From Basic Science to Clinical Translation I

Organised by Paul N. Watton, Juan R. Cebral and Anne M. Robertson

MS-B2: Numerical Simulation of Cardiovascular Devices & Procedures

Organised by Ferdinando Auricchio, Michele Conti, Simone Morganti, Alessandro Reali and Alessandro Veneziani

SS-B3: Standard Session I

SS-B4: Standard Session II

SS-C1: Standard Session III

MS-C2: Aneurysm Modelling: From Basic Science to Clinical Translation II

Organised by Paul N. Watton, Juan R. Cebral and Anne M. Robertson

MS-C3: Modelling of Pulse Wave Propagation in the Arterial Tree I

Organised by Frans N. van de Vosse and Nikos Stergiopulos

MS-D1: Inverse Problems in Cardiovascular Mathematics

Organised by Luca Bertagna, Huanhuan Yang and Alessandro Veneziani

MS-D2: Numerical Techniques for Computational Surgery

Organised by Elias Cueto, Francisco Chinesta and Marc Garbey

MS-D3: Multiphysics Modelling & Applications of the Cardiovascular System II

Organised by Marek Behr, C.Alberto Figueroa, Luca Formaggia, Jean-Frédéric Gerbeau and Christian Vergara

MS-D4: Towards Clinically Relevant Computational Vascular Mechanics

Organised by C.Alberto Figueroa, T.Christian Gasser, Michael W. Gee and Wolfgang A. Wall

MS-E1: Modelling of Pulse Wave Propagation in the Arterial Tree II

Organised by Frans N. van de Vosse and Nikos Stergiopulos

SS-E2: Standard Session IV

Poster Abstracts

Invited Lectures

3rd International Conference on Computational and Mathematical Biomedical Engineering - CMBE2013
16-18 December 2013, Hong-Kong
P. Nithiarasu and R. Löhner (Eds.)

Experimentally validated computational models of cardiovascular flows towards clinical translation

Ajit P. Yoganathan
Georgia Institute of Technology, Emory University, USA

SUMMARY

The use of *in vitro* experiments and computational modeling for the *a priori* assessment of clinical interventions and planning surgical procedures is a new paradigm in the use of engineering tools to advance the practice of medicine. This aspect has been particularly useful in cardiovascular systems where the dynamics of bio-fluids and structures are crucial in a variety of phenomena across a wide range of length and velocity scales. Over the past three decades, the Cardiovascular Fluid Mechanics Laboratory at Georgia Tech has taken significant strides in this area using both experimental and computational approaches with the ultimate purpose of clinical translation to refine diagnostic measures and disease treatment to improve patient quality of life. This talk will review some of the accomplishments in the areas of cardiovascular medical device design, advancing diagnostic techniques and surgical planning for pediatric heart defects. The assessment of native and prosthetic heart valves using multi-modality in vitro experimental platforms have provided clinicians with improved tools to assess disease severity and helped identify effective treatment options, while simultaneously providing benchmark data for validation of numerical simulations. For the treatment of congenital heart defects, the development of novel computational modeling tools to simulate surgical procedures and the associated hemodynamic outcomes has provided clinicians with new ways to plan treatments for individual patients to improve patient outcome. The specific focus of this presentation is to highlight the importance of validating computational models with high fidelity in vitro experiments for application in predictive models of diseased conditions, clinical interventions and hemodynamic outcomes of complex surgical procedures.

3rd International Conference on Computational and Mathematical Biomedical Engineering - CMBE2013
16-18 December 2013, Hong-Kong
P. Nithiarasu and R. Löhner (Eds.)

Soft tissue mechanics and fluid-structure interaction

Xiaoyu Luo
School of Mathematics and Statistics, University of Glsagow

Abstract

Soft tissue mechanics and fluid-structure interaction are among the most challenging issues in modelling and simulation of physiological systems. This is because one needs to solve momentum equations for the biofluid and soft tissues in two different coordinate systems. In addition, soft tissues present multi-physics, anisotropic and fibre-reinforced constitutive behaviours, and often undergo finite strain, nonlinear and dynamic deformation under physiological and pathological conditions. In this talk, I shall select a few applications involving soft tissue mechanics and fluid-structure interaction that are studied by the Glasgow group. These range from human gallbladder pain, arteries and dissection, mitral valves and multi-scale heart modelling, and are studied using various numerical methods, including the finite element method, the immersed boundary method, and a hybrid immersed-boundary finite-element method, as well as analytical approaches. Material parameters may be estimated based on patient-specific information and experimental data, and numerical simulations provide physical insights into complex physiological systems.

3rd International Conference on Computational and Mathematical Biomedical Engineering - CMBE2013
16-18 December 2013, Hong-Kong
P. Nithiarasu and R. Löhner (Eds.)

Elastic theory of fluid membranes of Helfrich model and its application in other soft matters

Zhong-can Ou-Yang
Institute of Theoretical Physics, Chinese Academy of Sciences, Beijing 100190, China

SUMMARY

Shape problems stemmed from real bio- and abiotic materials in nature initial many nice theories in sciences. The observation of law of constant angle of crystal planes by N. Stensen (1669) leads to G. Wulff construction for convex crystal shape (1901). The beautiful shapes of soap films observed by J. Plateau (1803) emerges a 'golden age' in the study of minimal surface. The investigation on the rise of a liquid in a capillary tube generates T. Young (1805) and P.S. Laplace (1806) theory on a surface of constant mean curvature which predicts liquid bubble to be sphere only (Alexandrov (1950's)). However, a long-standing problem in physiology, why the red blood cells (RBCs) in human bodies are always in a rotationally symmetric and biconcave shape, has puzzled peoples for more than 100 years. It is finally solved by W. Helfrich (1973) who recognized membrane being a liquid crystal (LC) film and derived from curvature elastic theory of LC a free energy of fluid membranes. The variation with the energy leads a generalized Young-Laplace shape equation (Ou-Yang and Helfrich, 1987). In this talk some progress of our study following Helfrich model for 25 years are reported. We found that the shape equation predicts not only the exact solution for RCB shape but also a special kind of torus vesicle which have soon afterwards confirmed by experimental observations. Especially, the Helfrich model was successfully extended to investigate the complex structures in other soft matters such as the formation of focal conic domains in smectic LC, helical carbon nanotubes, the tube to sphere transition in peptide nanostructures, and Icosahedral self-assemblies in virus capsids.

3rd International Conference on Computational and Mathematical Biomedical Engineering - CMBE2013
16-18 December 2013, Hong-Kong
P. Nithiarasu and R. Löhner (Eds.)

Surface wrinkling of soft biological tissues

Xi-Qiao Feng
Department of Engineering Mechanics, Tsinghua University, Beijing 100084, P.R. China

SUMMARY

Surface instability and morphological evolution of such soft materials as hydrogels and biological tissues is a major concern in a wide diversity of fields. In this talk, surface instability of soft materials and biological tissues are discussed within the framework of continuum mechanics. Firstly, a generic method is presented for analyzing the surface stability of a thin film resting on a substrate with arbitrary geometry. Secondly, the growth and buckling of mucosas that commonly line organs and cavities throughout the animal body are analyzed theoretically, numerically and experimentally. Finally, the surface wrinkling of soft core-shell matters induced by swelling or shrinking is investigated. The results demonstrate that the evolution of the sphere may be characterized by a process of smooth surface, buckyball-like wrinkling pattern, and then undergoing a wrinkling-to-fold transition into labyrinth-like folded patterns, in agreement with our experimental observations.

3rd International Conference on Computational and Mathematical Biomedical Engineering – CMBE2013

16-18 December 2013, Hong-Kong

P. Nithiarasu and R. Löhner (eds)

Evaluation of device efficacy for cerebral aneurysm treatment: From deployment to clot development

Y. Ventikos[1], M.N. Ngoepe[2], T.W. Peach[2], K. Spranger[2], D. Zajarias-Fainsod[2]

[1] Department of Mechanical Engineering

University College London (UCL), Torrington Place, London, WC1E 7JE, UK

Email: y.ventikos@ucl.ac.uk

[2]Institute of Biomedical Engineering and Department of Engineering Science

University of Oxford, Parks Road, Oxford, OX1 3PJ, UK

SUMMARY

Cerebral aneurysm treatment outcome is dependent on the specific patient in question. A framework which could be used to predict outcome is presented and is used to compare the efficacy of different treatment methods. This framework accounts for vascular architecture reconstruction, device deployment, computation of local haemodynamics and clot development in the aneurysm sac. The results illustrate that in some cases, device deployment improves the situation and depicts characteristics associated with reduced rupture risk.

Key Words: *cerebral aneurysm, patient-specific, device deployment, haemodynamics, thrombosis.*

1. INTRODUCTION

The treatment of cerebral aneurysms remains a challenge as post-intervention outcome is highly patient-specific: the use of any particular treatment method may be extremely successful in one patient and prove detrimental in another. The ability to predict treatment outcome prior to intervention would therefore be very useful. Such a tool would enable an interventionist to explore different treatment methods for a specific patient and make a selection based on the best possible outcome for that patient [1]. In this work, we compare the efficacy of different cerebral aneurysm treatment devices. This is achieved by using a complete *in silico* workflow which accounts for geometry reconstruction, device deployment, subsequent local haemodynamic changes and clot formation in the aneurysm sac.

2. METHODOLOGY AND OUTCOMES

In order to predict the outcome of cerebral aneurysm treatment, a comprehensive system comprising four key steps is developed and implemented. The first step involves the segmentation and volumetric reconstruction of the vascular geometry, followed by simulation of device deployment in the aneurysm region. The device's effect on local haemodynamics is then examined in a third step. The final step simulates the growth of a clot or thrombus in the aneurysm sac.

Although various methods for segmentation of vascular anatomy have been documented and employed, few produce results with high fidelity. Moreover, these algorithms focus on full automaticity, excluding the clinician from the process. In this study, a new method for segmentation is explored using a semi-automatic algorithm that allows the neuroradiologist to begin segmentation by locating the aneurysm. The architecture of the parent and branching vessels is then resolved by employing a volume-growing technique to provide both robustness and accuracy combined with thresholding techniques and edge detection. Finally, the clinician confirms accuracy and the three-dimensional geometry is used for subsequent simulations.

The placement of a foreign device in the human body has an effect on the organ or vessel in which the device is deployed. Often, altered haemodynamic conditions and alterations to the vessel geometry are observed [2]. For flow diverters, a method which is able to simulate the final position of the device and the subsequent interaction with the vessel wall is presented. Five key steps are accounted for in the deployment algorithm. The first step focuses on the reconstruction of the particular device geometry. At the beginning of the device deployment in the clinical setting, the prosthesis is located inside the delivery system in the crimped configuration. The second step in the deployment simulation, therefore, involves the calculation of this crimped (folded-up) configuration. This can be done by the explicit prescription of the nodal displacements to the device's load-free configuration, under the radial constraint of the delivery

catheter. Thereafter, the crimped device is placed onto the centreline of the vessel, or at any other desired location, for the start of the deployment. In the fourth step, the deployment process is simulated in order to accurately position the prosthesis at the site of the targeted pathology. The expansion process is guided by the internal elastic forces of the device's material, which is typically nitinol. Finally, the contact with the vessel occurs due to the expansion of the device, which can eventually lead to changes in the vessel geometry resulting from the forces that the prosthesis exerts on the vessel wall. Similarly, embolic coiling is simulated using an implicit model of coiling. A core of the aneurysm volume is created, representing the bulk of the coils in the aneurysm sac. The geometry is then classified into three distinct volumes with specific properties: a parent vessel with full flow permeability, an aneurysm perimeter region with anisotropic permeability (reflecting the preferential orientation of the coils along the sac) and an interior aneurysm region with isotropic permeability.

In order to further quantify the overall effect of the prosthesis on a specific patient, it is necessary that haemodynamic computations be carried out for a specific geometry before and after device deployment. Once the geometry has been configured, it is imported into a non-confirming anisotropic Cartesian mesh generator, CFD-Viscart (ESI Group, Paris, France). Appropriate boundary conditions are applied, (for example pulsatile inflow velocity profiles representing the cardiac cycle as inlet). The mesh is then imported to a multiphysics solver, CFD-ACE+ (ESI Group, Paris, France), based on the control volume method, where transient flow simulation is conducted. While blood exhibits non-Newtonian properties, the vessels under consideration are sufficiently large for blood to be considered a Newtonian fluid [3]. A central differencing scheme is used for spatial discretisation and pressure-velocity coupling is accounted for by the SIMPLEC scheme. An algebraic multigrid solver is used for convergence acceleration. Changes in aneurysm flow pattern and inflow are observed and compared across multiple treatment options. Lengthening of residence time and altered washout patterns of blood in the aneurysm dome are also investigated by means of 'virtual contrast injection', which then allows simulations to be validated with the clinical outcome of each patient-specific aneurysm geometry.

The main desirable outcome of device deployment is the development of a clot in the aneurysm sac. Clotting is a patient-specific process which is dependent on local haemodynamics, vessel geometry and biochemical composition. An imbalance in the procoagulant and anticoagulant mechanisms can result in haemophilia if the anticoagulant mechanism is dominant or thrombosis if the procoagulant mechanism is favoured. Complications which arise from the dominance of one of these systems are even more hazardous under pathological conditions. Clot development is computed before and after device deployment. The underlying biochemical network at play is described by the Wagenvoord model [4] and changes in species concentrations are calculated using a stiff equation solver. Propagation of the growing clot and tracking of the clot surface are described by the Level Set method. These equations are solved using the CFD-ACE+ Suite. The clot region assumes different porosity and permeability values to the rest of the fluid region, thus

allowing for three-way interaction between the growing clot, biochemical reactions and the fluid region.

3. CONCLUSIONS

The computations carried out illustrate that in some cases, device deployment reduces the perceived rupture risk. Complex flow is seen to become less vortical after deployment. In addition, a clot which occludes the aneurysm sac without extending into the parent vessel is observed. In other cases, the placement of a device results in even more complex flow and only partial thrombosis, possibly increasing rupture risk. Such outcomes highlight the extent to which the process is patient-specific and the need for case-by-case consideration. While this work presents a computational framework which could be used in a clinical setting in the future, extensive validation of the different stages of the workflow would be necessary prior to such use.

REFERENCES

[1] J. R. Cebral, M. A. Castro, J. E. Burgess, R. S. Pergolizzi, M. J. Sheridan and C. M. Putman, "Characterization of cerebral aneurysms for assessing risk of rupture by using patient-specific computational haemodynamics models," *American Journal of Neuroradiology,* vol. 26, pp. 2550-2559, 2005.

[2] B. Hong, L. Zhang, Q. Huang, Y. Wu, Y. Xu and J. Liu, "Vascular Geometry Change Because of Endovascular Stent Placement for Anterior Communicating Artery Aneurysms," *American Journal of Neuroradiology*, vol. 32, pp. 1721-1725, 2011.

[3] K. Perktold, M. Resch and H. Florian, "Pulsatile non-Newtonian flow characteristics in a three-dimensional human carotid bifurcation model," *Journal of Biomechanical Engineering,* vol. 113, no. 4, pp. 464-475, 1991.

[4] R. Wagenvoord, P. W. Hemker and H. C. Hemker, "The limits of simulation of the clotting system," *Journal of Thrombosis and Haemostasis,* vol. 4, no. 6, pp. 1331-1338, 2006.

3rd International Conference on Computational and Mathematical Biomedical Engineering - CMBE2013
16-18 December 2013, Hong-Kong
P. Nithiarasu and R. Löhner (Eds.)

Numerical investigation of cerebrovascular circulation after carotid artery stenting

Marie Oshima, Masaharu Kobayashi, Kei Fujisawa
Interfaculty Initiative in Information Studies, The University of Tokyo

SUMMARY

When atherosclerosis progresses and carotid artery stenosis becomes sever, the carotid stenting is performed, After the stenting, sometimes cerebral hyperperfusion syndrome is caused. Therefore, it is important to examine the changes in the flow distributions in the cerebrovascular circulation.

The purpose of the paper is to develop a numerical method for one-dimension (1D) and zero-dimension (0D) simulation to predict the flow distribution in the cerebrovascular circulation after carotid stenting by considering the entire circulation. The general circulation is modeled in a manner such that the large main arteries are modeled in 1D and the remaining parts like peripheral arteries, vein and heart are modeled in 0D. The 1-D simulation is conducted for the patient-specific geometry of the arterial circular of Willis combined with 1D-0D simulation of the general circulatory system. The present method is applied to the pre- and post-operative medical images of the patient, who had carotid stenting. The results such as the flow rate and the pressure distributions are compared between pre- and post- operation and the effects of the 1D-0D simulation are investigated.

3rd International Conference on Computational and Mathematical Biomedical Engineering - CMBE2013
16-18 December 2013, Hong-Kong
P. Nithiarasu and R. Löhner (Eds.)

From Simulations to Assimilations: Challenges and Perspectives of Bringing Cardiovascular Mathematics to the Bedside

Alessandro Veneziani⋆
⋆Department of Mathematics & Computer Science, Emory University
400 Dowman Dr, Suite W401, Atlanta (GA) USA 30322
avenez2@emory.edu

Key Words: *Data assimilation, Variational Methods, Cardiovascular Mathematics, Inverse Problems, Model Reduction Techniques*

Mathematical and numerical modeling of cardiovascular problems has experienced a terrific progress in the last years, evolving into a unique tool for patient-specific analysis [1]. *In silico* models are acknowledged to be not only complementary but also sometimes more reliable than animal models in representing specific pathologies [2]. However, the extensive introduction of numerical procedures as a part of an established clinical routine and more in general of a consolidated support to the decision making process of physicians still requires some steps both in terms of infrastructures (to bring computational tools to the operating room or to the bedside) and methods. In particular, the quality of the numerical results needs to be carefully assessed and certified. In this scenario, an important research line quite established in other fields is the integration of numerical simulations and measurements in what is usually called *Data Assimilation*. A rigorous merging of available data (images, measures) and mathematical models is expected to reduce the uncertainty intrinsic in mathematical models featuring parameters that would require a patient-specific quantification; and to improve the overall quality of information provided by measures. However, computational costs of assimilation procedures - and in particular variational approaches - may be quite high, as typically we need to solve inverse problems, dual and possibly backward-in-time equations. For this reason, appropriate *model reduction* techniques are required, to fit assimilation procedures within the timelines and the size of patient cohorts usually needed by medical doctors. In this talk, we will consider some applications of variational data assimilation in vascular and cardiac problems and associated model reduction techniques currently investigated to bring operatively numerical simulations into the clinical routine. *Hierarchical modeling* of the solution of partial differential equations in domains featuring a prevalent mainstream, like arteries will be in particular addressed [3].

The coexistence of the Emory School of Medicine, the Department of Biomedical Engineering of GA Tech and the Department of Mathematics and Computer Science at Emory in Atlanta is a sort of ideal environment for a fast translation of new techniques from prototype benchmarks to clinical practice. Methodological challenges and perspectives relevant to this purpose will be discussed with several examples coming from a daily activity with physicians.

Acknowledgements. This work has been possible thanks to the help of several people, beyond PhD students (L. Bertagna, H. Yang, B. Yang): Dr. W.R. Taylor, Dr. H. Samady, Dr. S. King, Dr. B. Gogas, Dr. F. Tong, Dr. D. Gupta, Dr. M. Piccinelli at the Emory School of Medicine, Dr. T. Passerini at Siemens Princeton, Dr. L. Gryngarten at Emory, Dr. D. Giddens, Dr. L. Timmins, Dr. D. Molony at the Department of Biomedical Engineering of GA Tech, Dr. F. Fenton at the Department of Physics at GA Tech, Dr. A. Quaini, Dr. S. Canic at the Department of Mathemtaics,

University of Houston, Dr. F. Auricchio, Dr. A. Reali, Dr. M. Conti, Dr. S. Morganti at the Department of Civil Engineering of University of Pavia (Italy), Dr. S. Perotto at the Department of Mathematics, Politecnico di Milano (Italy), Dr. P. Blanco at the LNCC, Petropolis (Brazil)..

REFERENCES

[1] A. Veneziani and C. Vergara, *Inverse problems in Cardiovascular Mathematics: towards patient-specific assimilation and optimization* - editorial, Int J Num Meth Biomed Eng, to appear (2013)

[2] I.C. Campbell, D. Weiss, J.D. Suever, R. Virmani, A. Veneziani, R.P. Vito, J.N. Oshinski, W.R. Taylor, *Biomechanical modeling and morphology analysis indicates plaque rupture due to mechanical failure unlikely in atherosclerosis-prone mice*, Am J Physiol Heart Circ Physiol, 304(3), 2013

[3] S. Perotto, A. Ern and A. Veneziani. *Hierarchical local model reduction for elliptic problems: a domain decomposition approach.* SIAM Multiscale Model. Simul., 8 (2010), no. 4, 1102-1127.

3rd International Conference on Computational and Mathematical Biomedical Engineering - CMBE2013
16-18 December 2013, Hong-Kong
P. Nithiarasu and R. Löhner (Eds.)

A comprehensive computational model to obtain clinically relevant insight into the human respiratory system

Wolfgang A. Wall, Mahmoud Ismail, Christian Roth & Lena Yoshihara
Institute for Computational Mechanics, Technische Universität München Boltzmannstr. 15,
85748 Garching b. München, Germany
e-mail: wall@lnm.mw.tum.de, web page: http://www.lnm.mw.tum.de/

SUMMARY

Essential processes in the human lung span a variety of different scales and different fields in a rather complex geometrical setup. This combination of complexities together with the fact that only very few relevant quantities can be measured in patients, is causing a huge lack of knowledge about the detailed functioning of this organ. This is in clear contradiction to the importance of this organ and to how desperately the medical community is looking for a better understanding. For this purpose we are developing a number of different novel computational models and are combining it to a comprehensive model of the respiratory system. Our original motivation was the development of protective ventilation strategies and hence our research was mainly concerned with computational modeling of the respiratory system against the background of acute lung diseases and mechanical ventilation. But meanwhile we also extended it to other scenarios.

In this talk we will give an overview of our comprehensive computational model of the human lung and will provide a deeper focus into a few specific and important theoretical and methodical developments. In this context we will cover different relevant aspects like states of strain, flow and transport in this complex system. Models will include the full range from three-dimensional to 0D models also incorporating some important coupled models. A focus will also be on the interplay between flow and tissue deformation, since this has a special importance in this scenario it is not only defining challenging flow boundary condition information but often is also the actuator of the flow. As a last important aspect of this organ we will also briefly address different transport phenomena and how these can be modeled in such a complex setup.

Heart Valve Modelling

3rd International Conference on Computational and Mathematical Biomedical Engineering – CMBE2013

16-18 December 2013, Hong-Kong

P. Nithiarasu and R. Löhner (eds)

Subject-specific acquisition of normal aortic valve geometry from 3D+t TEE images

Michel R. Labrosse, PhD*, Bahareh Momenan*, Carsten J. Beller, MD, Munir Boodhwani, MD***, Benjamin Sohmer, MD*****

*Department of Mechanical Engineering, University of Ottawa,
161 Louis Pasteur, Ottawa, K1N 6N5 Ontario, Canada,
Michel.Labrosse@uottawa.ca;
**Department of Cardiac Surgery, University of Heidelberg,
INF 326, 69120 Heidelberg, Germany;
***Division of Cardiac Surgery, University of Ottawa Heart Institute,
42 Ruskin Street, Ottawa, K1Y 4W7 Ontario, Canada

SUMMARY

Aortic insufficiency (AI) is a heart valve disease in which the aortic valve (AV) leaflets fail to prevent backflow once blood is ejected by the left ventricle of the heart into the aorta. Despite its potential advantages over AV surgical replacement, AV repair, wherein the AV components are corrected rather than replaced, is not frequently employed due in part to the incomplete understanding of the mechanisms underlying AI. Although transesophageal echocardiography (TEE) is available for 3D+t imaging of cardiac valves, it is still mostly used in 2D which limits the assessment of the complex spatial relationships in AV structure, and thus hinders more widespread use of AV repair. In this abstract are described the steps towards the modeling of normal AVs from 3D+t TEE images using an automated graphical-user interface, AVQ. Measurements using AVQ from ten 3D+t TEE datasets of normal AVs were assessed for inter- and intra-observer variability; in addition, measurements from a 3D TEE dataset of a rapid-prototyped model of a normal AV were compared to their ground-truth counterparts. Given the accuracy and reproducibility of the data obtained, AVQ may be used toward subject-specific finite element modeling of the normal aortic valve biomechanics.

Key Words: *3D+t ultrasound imaging, aortic valve modeling, subject-specific anatomy.*

1 INTRODUCTION

The aortic valve (AV) is normally made of three leaflets that open when the left ventricle of the heart contracts (systole) to eject blood into the aorta. The AV function is to close and prevent

backflow when the left ventricle relaxes (diastole). The AV leaflets are attached inside the aortic root which balloons out around each of the leaflets' attachments, creating the three aortic sinuses. Aortic insufficiency (AI) occurs when the leaflets do not properly seal the valve in diastole, allowing blood to flow in reverse direction. The diseased valves may be replaced or repaired. Although AV repair presents important benefits for AI patients, many AI cases still undergo replacement because of the incomplete understanding of the patho-anatomy and pathophysiology of AI, and lack of predictability in the outcome of the surgical techniques employed. In the past decades, developments in transesophageal echocardiography (TEE) have opened new horizons in reconstructive surgery of the aortic valve (AV), whereby corrections are made to normalize the geometry and function of the valve, and effectively treat leaks. In the following, a new framework is described to extract geometrical information about the AV from 3D+t TEE images.

2 METHODS

The AV anatomy was estimated from images in late diastole extracted from the 3D+t TEE datasets. The AV model consisted of an idealization of the left-ventricular outflow tract (LVOT), the aortic leaflets, the aortic sinuses and the proximal portion of the ascending aorta. The model was parameterized by the positions of 21 anatomical landmarks, 6 of which were used to determine the individual free edge lengths and heights of the aortic leaflets. The landmarks were extracted from the images through a manual process run using an automated graphical-user interface (GUI) dubbed AVQ, which was specially designed for this purpose in MatLab (The MathWorks, MA, USA). The process is described in the following.

Stage 1: Valve alignment and centering: Equally-spaced approximate short-axis views taken from a 3D+t TEE dataset in late diastole are presented in one screen. The user is first prompted to select three views showing the LVOT, the valve center (e.g. where the three leaflets meet), and the ascending aorta, respectively. Then, the user is sequentially asked to approximate a circle around the LVOT contour, select a point at the center of the valve, and approximate a circle around the ascending aorta. Based on this information, AVQ aligns the 3-D dataset such that the short axis views are centered and perpendicular to the AV centerline.

From this stage onward, four sub-screens appear (Fig. 1, left). The bottom right sub-screen provides the user with step-by-step written directions on the use of the GUI. The bottom left sub-screen shows the short-axis view of the valve, while the top left and right sub-screens show orthogonal long-axis views of the valve. The green, red, blue and black cursors allow the user to, respectively, examine the valve from any point of view in the z, θ, r coordinates and at any time in the cardiac cycle. Each of the three views shows only two orthogonal colored lines at a time.

After the user is asked to place a label identifying the right-coronary sinus in the short axis view in order for AVQ to be fully oriented, specialized cross-hairs and labels (namely RC, LC, NC for right-, left- and non- coronary sinuses, respectively) are overlaid on the short-axis view (Fig. 1, left), and manual selection of the anatomical landmarks can begin.

Stage 2: Selection of 15 anatomical landmarks in late diastole: The point in space where the three mutually orthogonal lines meet is uniquely defined by cylindrical coordinates (r, θ, z). Clicking on the Proceed/Grab button saves these coordinates for future use. The anatomical landmarks

successively consist of the hinge point of the right leaflet at the nadir of the leaflet attachment line (*R*0), the apex of the right-coronary sinus (*R*1), and the top of the right-coronary sinus (*R*2). Similarly, landmarks *L*0, *L*1, *L*2 and *N*0, *N*1, *N*2, are acquired for the left- and non-coronary portions of the AV root. Thereafter, the commissures between the right-left, non-right and left-non leaflets are approximated as straight segments described by their two ends: *RL*1, *RL*2; *LN*1, *LN*2, and *NR*1, *NR*2, respectively.

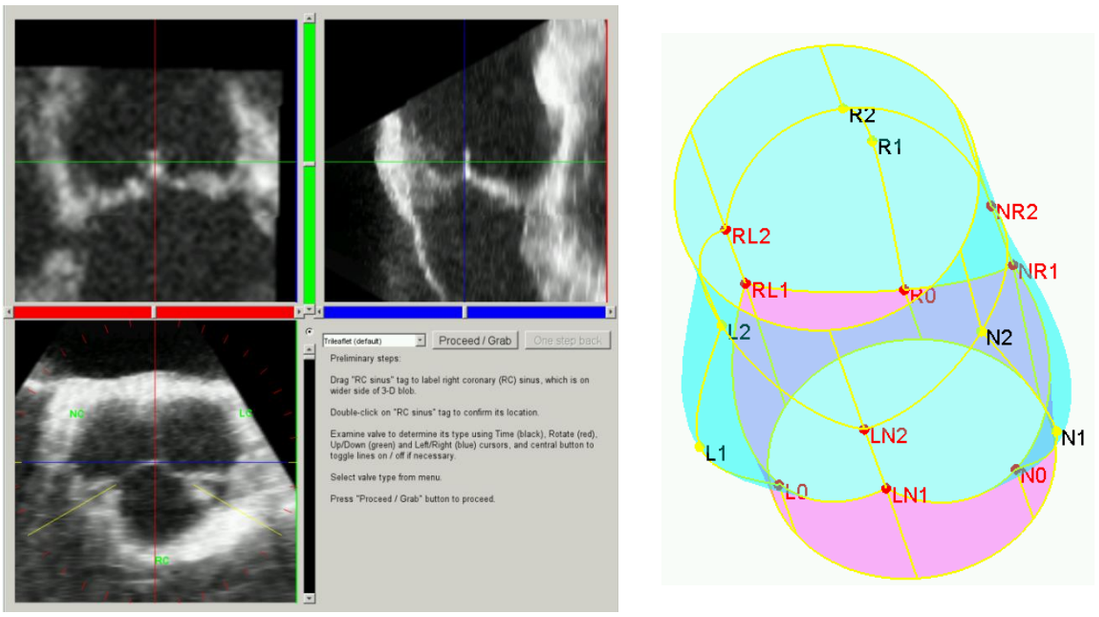

Figure 1: AVQ environment to navigate through the aortic valve and select anatomical landmarks (left); aortic root reconstructed in late diastole (leaflets not shown) (right).

Stage 3: Visual assessment of the positions of the landmarks chosen so far: After selection of the first 15 anatomical landmarks, the 3-D aortic root without leaflets is reconstructed in late diastole (Fig. 1, right), and embedded into the original 3-D gray scale dataset. The anatomical landmarks are labeled for easy identification. Visual inspection is facilitated using mouse-guided rotations and moveable cutting planes controlled by cursors. In addition, a cursor controls the transparency of the model.

Stage 4: Selection of 6 additional anatomical landmarks: Additional landmarks are defined towards the centerline of the valve and describe the bottom and top ends of the central coaptation heights between right- and left-; left- and non-, and non- and right-coronary leaflets. Then, the free edge lengths and heights for the leaflets are calculated by AVQ based on the 3D coordinates of the respective landmarks. Additionally, the leaflet coaptation areas are approximated [1].

After the landmark selection is complete, the user is asked to find the first time step in the 3D+t dataset when the valve is fully open (early systole), and the last time step when the valve is still fully open (late systole). AVQ then displays the valve in mid-systole and prompts the user to

trace the contour of the open leaflets in the short-axis view. The surface area enclosed by the curve represents an estimate of the geometric orifice area (GOA) in mid-systole.

3 RESULTS

Once the processing of a 3D+t dataset is complete, AVQ generates a summary file that contains: the annulus (or LVOT) diameter, the sinotubular junction (STJ) diameter, the valve height, the distance of the sinuses apices with respect to the valve centerline, the sinus heights, the longitudinal distances between the sinuses apices and the plane of the LVOT circle, the angles between the top commissures as viewed from the valve centerline, the leaflet height and free edge lengths, the commissure heights, the central leaflet coaptation heights, the leaflet coaptation areas, and the GOA measured in mid-systole. Measurements using AVQ from ten 3D+t TEE datasets of normal AVs were assessed for inter- and intra-observer variability; in addition, measurements from a 3D TEE dataset of a rapid-prototyped model (Shapeways, NY, USA) of a normal AV in late diastole were compared to their ground-truth counterparts. These tests demonstrated a combined mean measurement error of 0.44 mm for inter- and intra-observer repeatability and for measurements in a physical model.

4 DISCUSSION AND CONCLUSION

The accuracy of the proposed approach compares well with the mean error of 1.34 mm on linear dimensions between measurements from an automated processing system and human experts in 36 CT aortic valve datasets reported in [2]. It also compares well with another method recently proposed in [3] for the 3D parametric reconstruction of the native aortic valve. The authors of [3] report a mean error between their calculated geometry and 3D TEE measurements in one specific valve of 0.78 mm. Importantly, especially in the larger context of AI and aortic valve repair, the leaflet coaptation surface areas obtained with AVQ also correlates well with those determined manually in [1]. The data acquired with AVQ may be used toward subject-specific finite element modeling of the normal aortic valve biomechanics.

REFERENCES

[1] Sohmer B, Hudson C, Atherstone J, Lambert AS, Labrosse M and Boodhwani M, 2012. Measuring aortic valve coaptation surface area using three-dimensional transesophageal echocardiography. *Can J Anaesth* 60(1):24-31.

[2] Ionasec RI, Voigt I, Georgescu B, Wang Y, Houle H, Vega-Higuera F, Navab N and Comaniciu D, 2010. Patient-specific modeling and quantification of the aortic and mitral valves from 4-D cardiac CT and TEE. *IEEE Trans Med Imaging*, 29(9):1636-1651.

[3] Haj-Ali R, Marom, Ben Zekry S, Rosenfeld M and Raanani E, 2012. A general three-dimensional parametric geometry of the native aortic valve and root for biomechanical modeling. *J Biomech* 45:2392–2397.

3rd International Conference on Computational and Mathematical Biomedical Engineering - CMBE2013
16-18 December 2013, Hong-Kong
P. Nithiarasu and R. Löhner (Eds.)

Fluid-structure interaction simulations of tissue heart valves with a calcified leaflet using immersed boundary-finite element method

Iman Borazjani⋆
⋆Mechanical and Aerospace Engineering Department, University at Buffalo, State University of New York, 337 Jarvis Hall, Buffalo, NY 14260, USA, iman@buffalo.edu

SUMMARY

Three-dimensional, fluid-structure interaction (FSI) simulations of tissue heart valves has been carried out using a recently developed immersed boundary-finite element method [Borazjani, Compu Meth in App Mech and Eng, 2013]. In this method a sharp-interface immersed boundary incompressible Navier-Stokes solver for fluids is coupled with a non-linear large deformation finite element method for soft tissue. A Fung-type constitutive law is used for the soft tissue of heart valves that can capture the experimentally observed non-linear anisotropic stress-strain behavior of the heart valve tissue. Two sets of simulations is carried out: one with all leaflets functioning normally, and the other with one of eaflet calcified (fixed and not free to move) to assess the effect of calcification on the hemodynamics of heart valves. Calcification is one the most common complications of heart valves, requiring the patients to undergo valve replacement surgery. The simulations reveal that the heart valves with one fixed leaflet create higher flow asymmetry and pressure loss relative to the normal valves.

Key Words: *heart valves, fluid-structure interaction, immersed boundary, finite element.*

1 INTRODUCTION

Heart valves open and close passively due to the fluid forces on the leaflets. Simulating such a motion is quite challenging due to the non-linear large deformations of the tissue, flow pulsatility, transition to turbulence, and non-linear fluid-structure interaction. Due to large deformation of the leaflets, non-boundary conforming methods such as the immersed boundary method, which do not create highly skewed grid cells, are typically preferred. The pioneering work of Peskin [11]simulated blood flow through the heart valves using the immersed boundary method. The original immersed boundary, however, diffuses the boundary effects over several grid nodes and do not capture the interface as a sharp edge. The diffuse interface methods require excessive resolution near the immersed boundary to accurately resolve the boundary. In addition, these methods cannot accurately provide the wall shear stress, which is an important hemodynamic factor in biomedical applications. Therefore, a series of sharp-interface immersed boundary methods have been proposed [9], such as the one used in this work [6]. Another challenge is that the heart valve tissue exhibits an anisotropic, non-linear stress-strain relationship with large deformations under physiological loads [13], which is accommodated here by the implementation [1] of a finite element formulation for large deformations on unstructured triangular meshes of Taylor et al. [15].

Previous FSI simulations of heart valves were carried out with quadrant symmetry assumption [4, 10, 16, 17, 7]. However, Boarzjani [1] results showed that the flow loses its three-fold symmetry

early in systole, i.e., questioning the accuracy of the symmetry assumption. Furthermore, the quadrant symmetry assumption inherently assumes that all the leaflets are functioning properly and have the same material property. Calcification, which is a major problem for tissue heart valves [12, 14], can affect the one or two leaflets. Here the effect of calcification on the hemodynamics is investigated by making one of the leaflets highly rigid, which does not allow the leaflet to open. We compare this case against a tissue valve with all the leaflet functioning normally.

2 MAIN BODY

2.1 Numerical Method

The simulations here are carried out using the recently developed immersed boundary-finite element method of Borazjani [1]. The flow solver solves the incompressible Navier-Stokes equations over curvilinear grids using a fully staggered discretization [5] with Quick scheme for the convective terms, and central scheme for the viscous terms. The equations are integrated in time using an efficient, second-order accurate fractional step methodology with a Jacobian-free, Newton-Krylov solver for the momentum equations and a GMRES solver enhanced with multigrid as a preconditioner for the Poisson equation [3, 5]. The large deformations of the heart valve tissue is handled using the sharp-interface immersed boundary method, by reconstructing the boundary conditions at the nodes that are exterior to, but adjacent to the immersed-boundary surface using a 2^{nd} order accurate interpolation along the local normal to the boundary [6]. The background nodes at each time step are classified using an efficient ray-tracing algorithm described in detail in Borazjani et al. [3]. The motion of the leaflets are calculated based on large deformation finite element method with Fung-type experimentally-measured properties for heart valve tissue [1] based on the formulation of Ref. [15].

2.2 Results

The FSI simulations with on rigid leaflet are carried out in the same setup and with the same computational details as in [1]. The simulations were carried out on 240 cpus, which took about 3 to 4 days. Fig. 1 compares the flow created by the calcified valve and the normal valve simulated in [1] at four different time instant in the cardiac cycle (one cycle is 860 ms): early systole (t=52 ms), mid systole (t=120 ms), peak systole (t=189 ms), and after peak systole (t=275 ms). It can be observed that at all time instants, there are higher velocities at the orifice of the valve with one rigid because of smaller orifice area relative to the normal valve. At early systole, the higher velocities creates a strong jet that becomes unstable and gets skewed toward the opposite side of the rigid leaflet. At mid systole, the normal valve leaflets are fully open and create vortex shedding. The valve with a rigid leaflet creates a large separation region behind the rigid leaflet and the flow breaks into small vortical structures. At the peak systole, the normal valve flow does not show any vortical structures in the sinus region as they are washed away toward the outlet. However, the flow downstream of the calcified valve remains chaotic with many small vortical structures. After the peak systole, the normal valve flow still does not show any vortical structure in the sinus region as the vortices are washed away. Nevertheless, some structures are observed after the sinus near the walls of the conduit. In the calcified valve, in contrast, the sinus is now filled with small vortical structures. As shown by the previous work, regions of high vorticity are related to high shear stress, which can potentially activate the platelets that initiate blood clot formation.

Comparing the normal tissue valve, the calcified valve, and a mechanical heart valve, it can be observed that the normal tissue valve does not create the chaotic, turbulent-like state with many

small vortical structures, which is observed in mechanical heart valves [3]. However, the calcified valve with one rigid leaflets creates a chaotic, turbulent-like state similar to the mechanical heart valves.

Figure 1: Heart valve simulation: comparison of the flow field with one rigid leaflet and all leaflet functioning at different time steps during the cardiac cycle. The flow is visualized using velocity vectors and out-of-plane vorticity (left columns) and q-criteria (right columns).

3 CONCLUSIONS

The simulations show that the calcification of one leaflet creates a higher pressure gradient across the valve, which increases the load on the left ventricle. In addition, the higher flow asymmetry and smaller eddies has the potential to activate platelets to form blood clots. These simulations were carried out in an *in vitro* setting with an axis-symmetric inflow and outflow. In the future, the immersed boundary-finite element of Borazjani [1] will be combined with the overset-curvilinear immersed boundary method of Borazjani et al. [2] to carry out simulations of heart valves in anatomic geometries. Fig. 2 shows preliminary simulations of a tissue valve driven by the LV

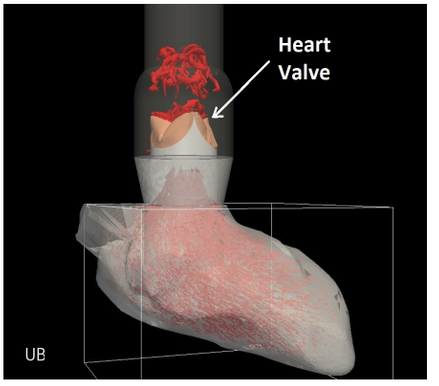

Figure 2: LV-heart valve simulation using [1, 2]: 3D vortical structures in the aorta and velocity vectors in the LV are visualized.

motion based on [8].

REFERENCES

[1] I. Borazjani. Fluid-structure interaction, immersed boundary-finite element method simulations of bio-prosthetic heart valves. *Computer Methods in Applied Mechanics and Engineering*, 257(0):103–116, 2013.

[2] I. Borazjani, L. Ge, T. Le, and F. Sotiropoulos. A parallel overset-curvilinear-immersed boundary framework for simulating complex 3d incompressible flows. *Computers and Fluids*, 77:76–96, 2013.

[3] I. Borazjani, L. Ge, and F. Sotiropoulos. Curvilinear immersed boundary method for simulating fluid structure interaction with complex 3d rigid bodies. *Journal of Computational Physics*, 227(16):7587–7620, 2008.

[4] J. De Hart, G. W. M. Peters, P. J. G. Schreurs, and F. P. T. Baaijens. A three-dimensional computational analysis of fluid–structure interaction in the aortic valve. *Journal of Biomechanics*, 36(1):103–112, 2003.

[5] L. Ge and F. Sotiropoulos. A numerical method for solving the 3d unsteady incompressible navierstokes equations in curvilinear domains with complex immersed boundaries. *Journal of Computational Physics*, 225(2):1782–1809, 2007.

[6] A. Gilmanov and F. Sotiropoulos. A hybrid cartesian/immersed boundary method for simulating flows with 3d, geometrically complex, moving bodies. *Journal of Computational Physics*, 207(2):457–492, 2005.

[7] T. Kaufmann, T. Linde, E. Cuenca-Navalon, C. Schmitz, M. Hormes, T. Schmitz-Rode, and U. Steinseifer. Transient, three-dimensional flow field simulation through a mechanical, trileaflet heart valve prosthesis. *ASAIO Journal*, 57(4):278–282, 2011.

[8] C. Luo, D. Ramachandran, D. L. Ware, T. S. Ma, and J. W. Clark Jr. Modeling left ventricular diastolic dysfunction: classification and key in dicators. *Theoretical Biology and Medical Modelling*, 14(1):1–46, 2011.

[9] R. Mittal and G. Iaccarino. Immersed boundary methods. *Annual Review of Fluid Mechanics*, 37:239–261, 2005.

[10] A. Narracott, C. Zervides, V. Diaz, D. Rafiroiu, P. Lawford, and D. Hose. Analysis of a mechanical heart valve prosthesis and a native venous valve: Two distinct applications of fsi to biomedical applications. *International Journal for Numerical Methods in Biomedical Engineering*, 26(3 4):421–434, 2010.

[11] C. S. Peskin. Flow patterns around heart valves: A numerical method. *Journal of Computational Physics*, 10:252–271, 1972.

[12] K. Pohle, R. Maffert, D. Ropers, W. Moshage, N. Stilianakis, W. G. Daniel, and S. Achenbach. Progression of aortic valve calcification association with coronary atherosclerosis and cardiovascular risk factors. *Circulation*, 104(16):1927–1932, 2001.

[13] M. Sacks and A. Yoganathan. Heart valve function: a biomechanical perspective. *Philosophical Transactions of the Royal Society B: Biological Sciences*, 362(1484):1369–1391, 2007.

[14] F. J. Schoen. Evolving concepts of cardiac valve dynamics. *Circulation*, 118(18):1864–1880, 2008.

[15] R. L. Taylor, E. Onate, and P. Ubach. Finite element analysis of membrane structures. *Textile Composites and Inflatable Structures*, 3:47–68, 2005.

[16] E. Weinberg, D. Shahmirzadi, and M. Mofrad. On the multiscale modeling of heart valve biomechanics in health and disease. *Biomechanics and modeling in mechanobiology*, 9:1–15, 2010.

[17] E. J. Weinberg and M. R. Kaazempur Mofrad. Transient, three-dimensional, multiscale simulations of the human aortic valve. *Cardiovascular Engineering*, 7(4):140–155, 2007.

3rd International Conference on Computational and Mathematical Biomedical Engineering - CMBE2013
16-18 December 2013, Hong-Kong
P. Nithiarasu and R. Löhner (Eds.)

Image-based immersed boundary/finite element model of the human mitral valve

X. S. Ma[⋆], H. Gao[⋆], N. Qi[⋆], C. Berry[⋆⋆], B. E. Griffith[†,‡], and X. Y. Luo[⋆]
[⋆]School of Mathematics and Statistics, University of Glasgow, Glasgow, UK
[⋆⋆]Institute of Cardiovascular and Medical Science, University of Glasgow, Glasgow, UK
[†]Leon H. Charney Division of Cardiology, Department of Medicine, New York University School of Medicine, New York, NY USA
[‡]Department of Mathematics, Courant Institute of Mathematical Sciences, New York University, New York, NY USA
email: xiaoyu.luo@glasgow.ac.uk

SUMMARY

Numerical simulation of mitral valve biomechanics can provide insight into valve function and dysfunction. In this study, we develop a new image-derived mitral valve model reconstructed from clinical magnetic resonance images of a healthy subject. Simulations are performed with this model using an immersed boundary method that incorporates a finite element description of the structural mechanics, enabling us to model fluid-structure interaction while accounting for the nonlinear, anisotropic material response of the mitral valve leaflets using a finite-strain description of the leaflet structure.

Key Words: *mitral valve, immersed boundary method, finite element, fibre-reinforced material*

1 INTRODUCTION

Dysfunction of the mitral valve (MV) causes significant mortality and remains a major medical problem worldwide [1], and improvements in our understanding of human MV biomechanics promise to lead to the development of new therapies and treatment strategies for patients suffering from valvular heart disease. Although there has been significant work on developing computational models of the MV over the past 20 years, because of the difficulties associated with both the finite-strain deformational kinematics and fluid-structure interaction (FSI), most MV models that include realistic anatomical geometries and constitutive models consider only the structural mechanics of the valve [2]. In previous work [3, 4, 5], we developed FSI models of the MV using an immersed boundary (IB) approach in which the elasticity of the MV is described in terms of systems of elastic fibres. In this study, we extend these models by using a hybrid version of the IB method that incorporates finite-strain elasticity models using a finite element (FE) approach [6], and we use this IB/FE method to simulate the dynamics of an imaging-derived MV model that employs an anisotropic fibre-reinforced hyperelastic constitutive model.

2 METHODOLOGY

2.1 MV model construction

A cardiac magnetic resonance (MR) imaging study was performed on a healthy volunteer (male, age 28) using a Siemens (Erlangen, Germany) MAGNETOM Verio 3 T scanner. The study was approved by the ethics committee at the University of Glasgow, and written informed consent was obtained before the scan. Images from twelve slices along the left ventricular outflow tract (LVOT) were acquired to cover the entire mitral valve. Typical parameters were: slice thickness: 3 mm, matrix size: 432 $\times$ 572, in-plane resolution: 0.7 mm $\times$ 0.7 mm, frame rate: 25 phases per cardiac cycle.

The MV was reconstructed at mid-diastole using the following steps:

- *Leaflet Segmentation:* MV leaflets were manually segmented on LVOT views using two separate lines in the anterior and posterior leaflets, respectively [5], assuming a uniform thickness of 1 mm, as shown in fig. 1(a);
- *Geometry:* The segmented leaflets were imported into SolidWorks (Dassault Systèmes SolidWorks Corp., Waltham, MA, USA) geometrical reconstruction using the 'surface loft' method. The final 3D MV model geometry was reconstructed by stitching surfaces together with two solid parts for the anterior and posterior leaflets. A total of 16 evenly distributed marginal chordae were defined based on anatomical descriptions, with 10 associated with the posterior leaflet and six with the anterior leaflet, as shown in fig. 1(b);
- *Mesh Generation:* The MV model geometry was imported into ICEM (ANSYS Inc. PA, USA) for tetrahedral FE mesh generation;
- *fibre Architecture:* fibres oriented in the circumferential direction were constructed to account for the anisotropy of the MV leaflets, as shown in fig. 1(c,d).

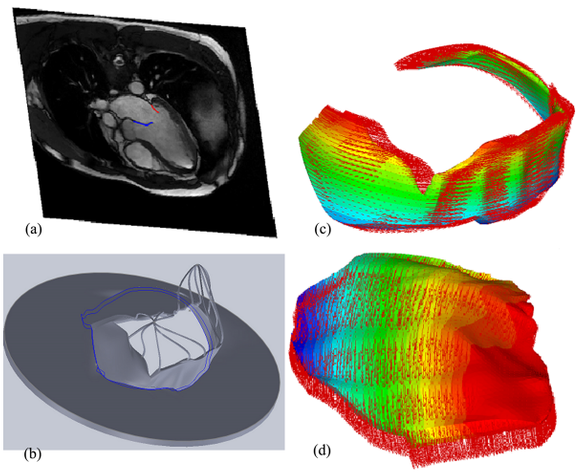

Figure 1: Mitral valve model construction: (a) leaflet segmentation using LVOT images; (b) reconstructed MV model with chordae attached to the anterior and posterior leaflets, with the annulus ring highlighted in blue; (c) the fibre architecture of the posterior leaflet; and (d) the fibre architecture of the anterior leaflet.

2.2 The immersed boundary formulation

Let $\Omega \subset \mathbb{R}^3$ denote the physical domain occupied by the fluid-structure system, and let $U \subset \mathbb{R}^3$ denote the reference coordinate system attached to the mitral valve. Let $\mathbf{x} = (x_1, x_2, x_3) \in \Omega$ denote fixed physical coordinates, let $X = (X_1, X_2, X_3) \in U$ denote material coordinates attached to the structure, let $\boldsymbol{\chi}(\mathbf{X}, t) \in \Omega$ denote the physical position of material point $\mathbf{X}$ at time t, and let $\mathbf{N}(\mathbf{X})$ denote the exterior unit normal to $\mathbf{X} \in \partial U$. The IB form of the equations of motion is:

$$\rho \left(\frac{\partial \mathbf{u}}{\partial t}(\mathbf{x}, t) + \mathbf{u}(\mathbf{x}, t) \cdot \nabla \mathbf{u}(\mathbf{x}, t) \right) = -\nabla p(\mathbf{x}, t) + \mu \nabla^2 \mathbf{u}(\mathbf{x}, t) + \mathbf{f}^{\mathrm{s}}(\mathbf{x}, t), \tag{1}$$

$$\nabla \cdot \mathbf{u}(\mathbf{x}, t) = 0, \tag{2}$$

$$\mathbf{f}^{\mathrm{s}}(\mathbf{x}, t) = \int_U \nabla \cdot \mathbb{P}^{\mathrm{s}}(\mathbf{X}, t)\, \delta(\mathbf{x} - \boldsymbol{\chi}(\mathbf{X}, t))\, \mathrm{d}\mathbf{X} - \int_{\partial U} \mathbb{P}^{\mathrm{s}}(\mathbf{X}, t)\, \mathbf{N}(\mathbf{X})\, \delta(\mathbf{x} - \boldsymbol{\chi}(\mathbf{X}, t))\, \mathrm{d}A(\mathbf{X}), \tag{3}$$

$$\frac{\partial \boldsymbol{\chi}}{\partial t}(\mathbf{X}, t) = \int_\Omega \mathbf{u}(\mathbf{x}, t)\, \delta(\mathbf{x} - \boldsymbol{\chi}(\mathbf{X}, t))\, \mathrm{d}\mathbf{x}, \tag{4}$$

in which ρ is the mass density, μ is the viscosity, $\mathbf{u}(\mathbf{x}, t)$ is the Eulerian velocity field of the fluid-structure system, $p(\mathbf{x}, t)$ is the Eulerian pressure field, $\mathbf{f}^{\mathrm{s}}(\mathbf{x}, t)$ is the Eulerian elastic force density, and $\delta(\mathbf{x}) = \delta(x_1)\, \delta(x_2)\, \delta(x_3)$ is the three-dimensional Dirac delta function. These equations express the conservation of momentum and mass in Eulerian form while using a Lagrangian description of the structural deformations and stresses. Specifically, we use the first Piola-Kirchhoff stress tensor $\mathbb{P}^{\mathrm{s}}$ to describe the stresses generated by the immersed structure. $\mathbb{P}^{\mathrm{s}}$ is related to the Cauchy stress σ^{s} by $\mathbb{P}^{\mathrm{s}} = J\, \sigma^{\mathrm{s}}\, \mathbb{F}^{-T}$ in which $\mathbb{F} = \partial \boldsymbol{\chi} / \partial \mathbf{X}$ is the deformation gradient associated with the structural deformation and $J = \det(\mathbb{F})$. $\mathbb{P}^{\mathrm{s}}$ is determined from the passive hyperelastic properties of the leaflets by a strain energy functional W by $\mathbb{P}^{\mathrm{s}} = \frac{\partial W}{\partial \mathbb{F}}$. The leaflets of the MV are modeled as an incompressible fibre-reinforced material, in which W is a functional of invariants of the right Cauchy-Green deformation tensor $\mathbb{C} = \mathbb{F}^T \mathbb{F}$ that takes the form

$$W = \frac{a}{2b} \exp\left[b(I_1 - 3.0) \right] + \frac{a_{\mathrm{f}}}{2b_{\mathrm{f}}} \exp\left[b_{\mathrm{f}} (I_{4\mathrm{f}} - 1)^2 - 1 \right], \tag{5}$$

in which $I_1 = \mathrm{trace}(\mathbb{C})$ and $I_{4\mathrm{f}} = \mathbf{f}_0 \cdot (\mathbb{C} \mathbf{f}_0)$, with $\mathbf{f}_0$ denoting the unit tangent to the fibre direction field in the reference state. The parameters a, b, a_{f}, and b_{f} are chosen from [2].

2.3 Simulation parameters

In the simulations, the MV structure is immersed in a 10 cm $\times$ 10 cm $\times$ 16 cm fluid box. The valve leaflets are mounted on a housing and outer tube that are approximately fixed in place using a penalty method. Because subject-specific trans-valvular pressure data were not available, a typical physiological pressure profile is used in which the pressure waveform is rescaled to match the peak systolic pressure of 150 mmHg of the subject. The simulations employ the open-source IBAMR software framework (`https://ibamr.googlecode.com`) [7, 8], which provides an adaptive and distributed-memory parallel infrastructure for developing fluid-structure interaction models that use IB method.

3 RESULTS & DISCUSSION

Fig. 2 shows initial results of MV models. Fig. 2(a) shows the fully-open state of the MV with a jet flow in the center of MV orifice, Fig. 2(b) is the time when the MV begins to close because

of the increased downstream pressure, and Fig. 2(c) shows the MV in a nearly completely closed configuration.

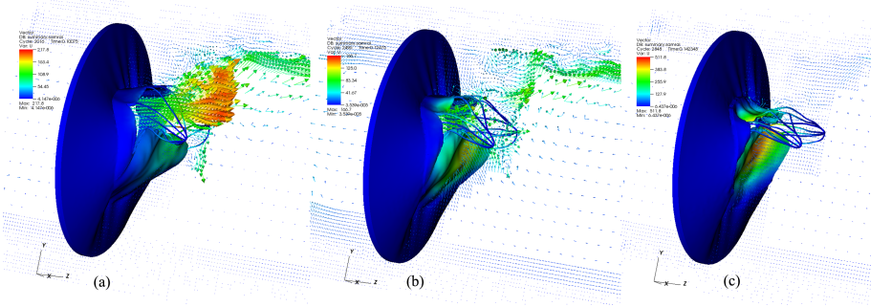

Figure 2: Mitral valve dynamic: (a) fully open; (b) beginning of closing; (c) closing.

4 CONCLUSIONS

In this study, we have described the application of an IB/FE method to the FSI simulation of using an image-derived model of the human MV with an anisotropic hyperelastic model for the structural mechanics of the MV leaflets. Our numerical scheme employs an unstructured FE discretization of structural equations while retainsing a Cartesian grid finite difference scheme for the incompressible Navier-Stokes equations for the fluid. The initial results show that the IB/FE framework has great potential for more complete descriptions of MV dynamics.

5 ACKNOWLEDGMENTS

We are grateful for funding provided by the UK EPSRC (EP/I1029990), the British Heart Foundation (PG/11/2/28474), the Medical Research Scotland, the Royal Society of Edinburgh, and the Royal Academy of Engineering. B.E.G. acknowledges research support from the American Heart Association (AHA award 10SDG4320049) and the National Science Foundation (US NSF awards DMS-1016554 and OCI-1047734).

REFERENCES

[1] Z. G. Turi. Mitral valve disease. Circulation, 109(6):e38–e41, 2004.

[2] Q. Wang and W. Sun. Finite element modeling of mitral valve dynamic deformation using patient-specific multi-slices computed tomography scans. Ann Biomed Eng, 41(1):142–153, 2013.

[3] B. E. Griffith, X. Luo, D. M. McQueen, and C. S. Peskin. Simulating the fluid dynamics of natural and prosthetic heart valves using the immersed boundary method. Int J Appl Mech, 1(1):137–177, 2009.

[4] X. Y. Luo, B. E. Griffith, X. S. Ma, M. Yin, T. J. Wang, C. L. Liang, P. N. Watton, and G. M. Bernacca. Effect of bending rigidity in a dynamic model of a polyurethane prosthetic mitral valve. Biomech Model Mechanobiology, 11(6):815–827, 2012.

[5] X. S. Ma, H. Gao, B. E. Griffith, C. Berry, and X. Y. Luo. Image-based fluid-structure interaction model of the human mitral valve. Comput Fluid, 71:417–425, 2013.

[6] B. E. Griffith and X. Y. Luo. Hybrid finite difference/finite element version of the immersed boundary method. Submitted.

[7] B. E. Griffith, R. D. Hornung, D. M. McQueen, and C. S. Peskin. An adaptive, formally second order accurate version of the immersed boundary method. J Comput Phys, 223(1):10–49, 2007.

[8] B. E. Griffith, R. D. Hornung, D. M. McQueen, and C. S. Peskin. Parallel and adaptive simulation of cardiac fluid dynamics. In M. Parashar and X. Li, editors, Advanced Computational Infrastructures for Parallel and Distributed Adaptive Applications. John Wiley and Sons, Hoboken, NJ, USA, 2009.

3rd International Conference on Computational and Mathematical Biomedical Engineering - CMBE2013
16-18 December 2013, Hong-Kong
P. Nithiarasu and R. Löhner (Eds.)

Simulating the effects of intersubject variability in aortic root compliance by the immersed boundary method

Vittoria Flamini[⋆]**, Abe DeAnda**[⋆⋆]**, and Boyce E. Griffith**[†,‡]
[⋆]Department of Mechanical and Aerospace Engineering, Polytechnic Institute of New York University, Brooklyn, New York, USA
[⋆⋆]Department of Cardiothoracic Surgery, New York University School of Medicine, New York, New York, USA
[†]Leon H. Charney Division of Cardiology, Department of Medicine, New York University School of Medicine, New York, New York, USA
[‡]Department of Mathematics, Courant Institute of Mathematical Sciences, New York University, New York, New York, USA
email: boyce.griffith@nyumc.org

SUMMARY

The aortic root comprises the structures of the aortic valve, including the aortic valve cusps, the sinuses of Valsalva, the aortic annulus, and the sinotubular junction. The aortic root has significant compliance, and although it is well appreciated that this compliance is important in facilitating both coronary perfusion and effective valve closure, there is a growing understanding that aortic root compliance also is important in reducing wear on the native aortic valve cusps during forward flow. In this study, we describe fluid-structure interaction models of the aortic root that employ compliant models of the aortic root that are based on human experimental data. Our simulations use an immersed boundary method with a finite element description of tissue elasticity. We specifically focus on the effects of intersubject differences in compliance on the dynamics of the valve.

Key Words: *aortic valve, fluid-structure interaction, hyperelasticity, finite element method, immersed boundary method.*

1 INTRODUCTION

The aortic root comprises the structures of the aortic valve, including the aortic valve cusps, the sinuses of Valsalva, the aortic annulus, and the sinotubular junction. This portion of the aorta is composed of a mosaic of tissues whose different compliances have a key role in ensuring effective valve closure and avoiding flow regurgitation. Of particular importance to valve closure are the sinuses of Valsalva, which are three bulbous pouches that protrude from the aortic root. The aortic sinuses are positioned directly behind the valve leaflets and act as pockets that stretch and fill with blood during systole only to recoil and release blood during diastole. Towards the end of the systolic phase of the cardiac cycle, vortices within the sinuses exert forces on the valve leaflets that facilitate efficient closure. It is clear that changes in aortic root compliance can effect the dynamics of valve closure. More recently, it has also become clear that aortic root compliance is important for reducing shear stresses on the valve leaflets during systolic ejection.

Cases in which the compliance of the aortic root is dramatically modified are include surgical interventions, diseases, and aging. When ascending aortic diseases are treated surgically, the aortic

root is often replaced by a graft. Aortic root grafts can be pulmonary autografts or woven polymeric implants but they all present a different compliance from the original tissue, thus altering the physiology of the ejection mechanism [1]. Changes due to diseases or aging are more subtle, but nonetheless result in an altered aortic root compliance or blood flow patterns.

In the present work, we aim to assess the effect of aortic root compliance on the physiology of the aortic root using a fluid-structure interaction model based on the immersed boundary method. To account for varying degree of aortic sinuses compliance we use biaxial tensile test data acquired by Azadani et al. [2] from human aortic roots.

2 METHODS AND RESULTS

The immersed boundary formulation of the equations of fluid-structure interaction uses a Lagrangian description of the stresses and deformations of the immersed structures (e.g., the valve leaflets and vessel wall) and an Eulerian description of the momentum, viscosity, and incompressibility of the fluid-structure system. Herein we use a fiber-based model of the aortic valve leaflets, as we have done in earlier studies [3], and we describe the vessel wall as an isotropic, incompressible, hyperelastic solid with a Fung-like strain-energy functional. Let $\mathbf{q} \in U \subset \mathbb{R}^2$ indicate curvilinear coordinates attached to the valve leaflets, with $\mathbf{q} = (q_1, q_2)$, let $\mathbf{X} \in V \subset \mathbb{R}^3$ indicate the material coordinate system of the aortic wall, with $\mathbf{X} = (X_1, X_2, X_3)$, and let $\mathbf{x} \in \Omega$ indicate physical coordinates. The physical position of fiber point $\mathbf{q}$ at time t is given by $\boldsymbol{\phi}(\mathbf{q}, t) \in \Omega$, and the physical position of reference coordinate $\mathbf{X}$ at time t is given by $\boldsymbol{\chi}(\mathbf{X}, t) \in \Omega$. The equations of motion for the coupled fluid-structure system are:

$$\rho\left(\frac{\partial \mathbf{u}}{\partial t}(\mathbf{x},t) + \mathbf{u}(\mathbf{x},t)\cdot\nabla\mathbf{u}(\mathbf{x},t)\right) = -\nabla p(\mathbf{x},t) + \mu\nabla^2\mathbf{u}(\mathbf{x},t) + \mathbf{f}(\mathbf{x},t) + \mathbf{g}(\mathbf{x},t), \quad (1)$$

$$\nabla\cdot\mathbf{u}(\mathbf{x},t) = 0, \quad (2)$$

$$\mathbf{f}(\mathbf{x},t) = \int_U \mathbf{F}(\mathbf{q},t)\,\delta(\mathbf{x}-\boldsymbol{\phi}(\mathbf{q},t))\,\mathrm{d}\mathbf{q}, \quad (3)$$

$$\mathbf{g}(\mathbf{x},t) = \int_V \nabla_{\mathbf{X}}\cdot\mathbb{P}(\mathbf{X},t)\,\delta(\mathbf{x}-\boldsymbol{\chi}(\mathbf{X},t))\,\mathrm{d}\mathbf{X} - \int_{\partial V}\mathbb{P}(\mathbf{X},t)\,\mathbf{N}(\mathbf{X})\,\delta(\mathbf{x}-\boldsymbol{\chi}(\mathbf{X},t))\,\mathrm{d}A(\mathbf{X}), \quad (4)$$

$$\frac{\partial\boldsymbol{\phi}}{\partial t}(\mathbf{q},t) = \int_\Omega \mathbf{u}(\mathbf{x},t)\,\delta(\mathbf{x}-\boldsymbol{\phi}(\mathbf{q},t))\,\mathrm{d}\mathbf{x}, \quad (5)$$

$$\frac{\partial\boldsymbol{\chi}}{\partial t}(\mathbf{X},t) = \int_\Omega \mathbf{u}(\mathbf{x},t)\,\delta(\mathbf{x}-\boldsymbol{\chi}(\mathbf{X},t))\,\mathrm{d}\mathbf{x}, \quad (6)$$

in which ρ is the mass density, μ is the dynamic viscosity, $\mathbf{u}(\mathbf{x},t)$ is the Eulerian velocity field, $p(\mathbf{x},t)$ is the Eulerian pressure field, $\mathbf{f}(\mathbf{x},t)$ is the Eulerian elastic force density generated by deformations to the fiber model of the valve leaflets, $\mathbf{g}(\mathbf{x},t)$ is the Eulerian elastic force density generated by deformations to the solid-body model of the vessel wall, $\mathbf{F}(\mathbf{q},t)$ is the Lagrangian elastic force density of the fiber model, $\mathbb{P}(\mathbf{X},t)$ is the Lagrangian (first Piola-Kirchhoff) elastic stress tensor of the solid model, $\mathbf{N}(\mathbf{X})$ is the outward unit normal along ∂V, and $\delta(\mathbf{x}) = \delta(x_1)\,\delta(x_2)\,\delta(x_3)$ is the three-dimensional Dirac delta function.

In this study, the aortic root geometry is based on the data available in the work by Swanson and Clark [4]. The aortic sinuses and the ascending aorta are modeled as the same material, whereas the left ventricle outflow tract is modeled as semi-rigid. The valve leaflets are modeled as being composed of two families of fibers that run orthogonal to each other. One family of fibers runs

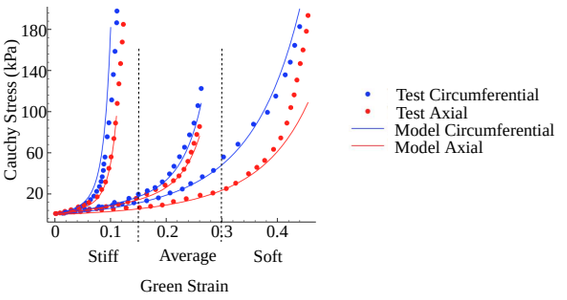

Figure 1: Data from biaxial tensile tests performed on human aortic sinus tissue by Azadani et al. [2] and fits obtained for each curve. Vertical lines are used to highlight the thresholds used to label the cases of interest.

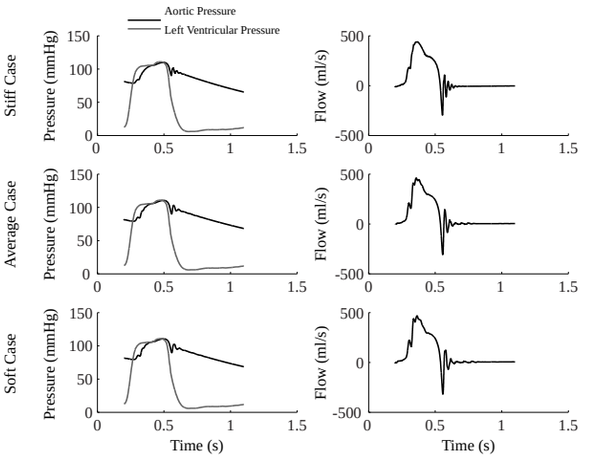

Figure 2: Pressure waveform and flow waveform obtained over a single heartbeat for the three aortic root models.

from commissure to commissure, and the other runs from the aortic annulus to the free edge of the valve leaflet. The physical domain is taken to be a 10 cm $\times$ 10 cm $\times$ 10 cm rectangular box.

For simplicity, the aortic root is modeled as an incompressible hyperelastic material with an isotropic Fung-like strain energy function. Material constants were obtained by least-square fits to experimental curves of Azadani et al. [2], who provide biaxial tensile test data for human aortic sinuses; see Figure 1. Based on the maximum Green strain E and empirical clustering of the experimental curves [2], specimens were labeled as 'stiff' ($E < 0.15$), 'average' ($0.15 < E < 0.3$), and 'soft' ($E > 0.3$). For each group of curves, a representative curve was extracted and analyzed to find the constitutive parameters using a custom routine implemented in MATLAB (The MathWorks, Natik, MA, USA); see Figure 1. To account for the initial strain, i.e., the strain due to the baseline aortic inflation at 80 mmHg, a fixed point iteration routine [5] was implemented in ABAQUS (Simulia, Providence, RI, USA) to recover the zero-pressure geometry of a blood vessel. This procedure was performed for each set of material parameters and resulted in three different zero-pressure geometries.

Spatially adaptive IB simulations were performed using the IBAMR software [6]. Each zero-pressure aortic geometry and the valve leaflets were imported in IBAMR and loaded with a physiological pressure distributions. In each case, a physiological left ventricle pressure waveform provides the inlet driving pressure, and a Windkessel model provides downstream loading conditions at the outlet [3]. Representative results are shown in Figures 2 and 3. Bulk hemodynamic

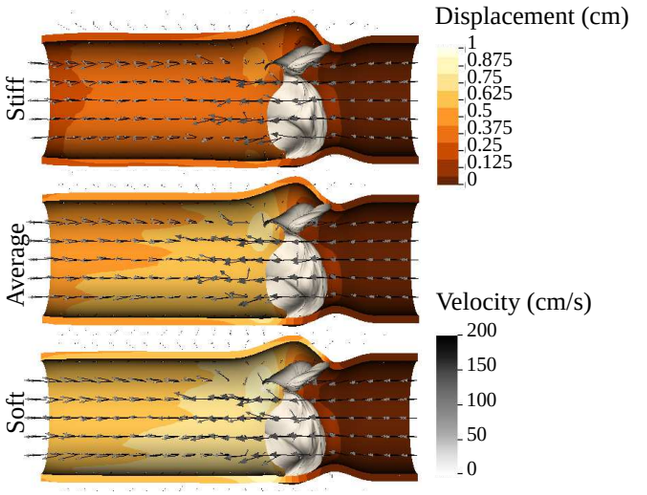

Figure 3: Contour plots of displacements from the zero pressure configuration at the time of peak flow for the three cases considered.

parameters, such as maximum pressure, peak flow rate, and cardiac output, are relatively insensitive to the compliance changes in the aortic root and remain consistent with normal physiological data, but we can observe that there are subtle changes in the computed waveforms.

3 CONCLUSIONS

This work considers the effects of changes in aortic root compliance on the dynamics of the aortic valve. Although we do not observe significant changes in terms of bulk hemodynamic parameters, the present analysis does not consider the effects of these changes on stress distributions, e.g., in the valve leaflets. Such analyses will require more complete structural models of the valve leaflets than are considered in this work, and we are actively working to develop such models. We also aim to incorporate more realistic, fiber-reinforced models of the aortic sinsues and ascending aorta. Further developments of this model could be used to assess the best implant solution for the surgical treatment of aortic root diseases in terms of both design and compliance.

REFERENCES

[1] N. T. Kouchoukos, T. H. Wareing, S. F. Murphy, and J. B. Perrillo. Sixteen-year experience with aortic root replacement. Results of 172 operations, *Annals of Surgery*, 214, 1991.

[2] A. N. Azadani, S. Chitsaz, P. B. Matthews, N. Jaussaud, J. Leung, T. Tsinman, L. Ge, and E. E. Tseng. Comparison of mechanical properties of human ascending aorta and aortic sinuses, *The Annals of Thoracic Surgery*, 93, 2012.

[3] B. E. Griffith, Immersed boundary model of aortic heart valve dynamics with physiological driving and loading conditions.*International Journal for Numerical Methods in Biomedical Engineering* 28, 2012.

[4] W. M. Swanson and R. E. Clark, Dimensions and geometric relationships of the human aortic value as a function of pressure, *Circulation Research* 35, 1974.

[5] J. Bols, J. Degroote, B. Trachet, B. Verhegghe, P. Segers, and J. Vierendeels, A computational method to assess in vivo stresses and unloaded configuration of patient-specific blood vessels, *Journal of Computational and Applied Mathematics* 246, 2013.

[5] `ibamr.googlecode.com`.

3rd International Conference on Computational and Mathematical Biomedical Engineering - CMBE2013
16-18 December 2013, Hong-Kong
P. Nithiarasu and R. Löhner (Eds.)

Parameter estimation of heart, valve and vasculature

Andrew Tappenden*, Adrian Ionescu, Xianghua Xie* and Raoul Van Loon***
*Swansea University, Singleton Park,Swansea,SA2 8PP,Wales, UK
**Cardiac Centre, Morriston Hospital, Morriston Swansea, SA6 6NL
Corresponding Address: R.VanLoon@Swansea.ac.uk

SUMMARY

The purpose of this project is to obtain clinically relevant patient specific information on valvular lesions by estimating the coefficients of a lumped model, which describes the heart, valves and arterial network, in an attempt to aid clinical diagnosis.

Key Words: *Optimisation, Stenosis, Heart valves, Lumped model, Arterial Network*

1 INTRODUCTION

A mathematical lumped model is proposed to investigate the entangled effects of valvular lesions in patients, using coefficients defining the heart, valve and vasculature. Patient data is characterised through the optimisation of the model coefficients. This is performed by minimising the error produced from the output of the governing equations when compared to patient specific input information, and so finding the coefficients that reproduce the original data best. This information is then used for understanding the interactions of combined valvular lesions.

Past research has examined singularly the aspects involved in this project, however, the purpose here is to explore the combining of heart, valve and vasculature models, when subject to valvular diseases. From this viewpoint, pressures of the left ventricle and aorta are used as the outputs for the 0D lumped model proposed.

2 METHODS

The proposed lumped model currently includes the equations for a (stenotic) aortic valve, a heart and the vasculature, and describes the corresponding left ventricular and aortic pressures.

These calculated pressures are used in the objective function of the Modified Cuckoo Search optimisation method, which minimises the error between the input (real or simulated) and the 0D lumped model results, so when the error is minimal, the 0D lumped model pressure curves recreate the input pressure data, and consequently the coefficients that create the input pressures.

1) Heart To capture the relation between the left ventricular pressure and volume, a standard elastance equation is used [1], while the elastance curve is described in [2]. The elastance of the ventricle can be seen to be the left ventricular pressure divided by the ventricular volume (minus the theoretical unstressed volume (*Vo*)), which can be seen in Figure 1, where *Emax* is estimated from the pressures and volumes at end systole (end of ejection). *Vo* and *Emax* represent coefficients of the heart, however, by using the aforementioned elastance curve [2], further heart coefficients, namely m_1, m_2, τ_1 and τ_2 representing the contraction rate constant, relaxation rate constant, and systolic time and diastolic time constants, respectively, are also introduced.

2) Valve Figure 2 and Equation 1 show that, net transvalvular pressure gradient (*TPGnet*) is the net difference of the recovered static pressure of blood when travelling from the left ventricle to the reattachment point of the ascending aorta, having passed through the aortic valve. The maximum *TPG* is located at the vena contracta (VC), defined as the location where the cross sectional area of the ejecting blood jet from the aortic valve is minimal.

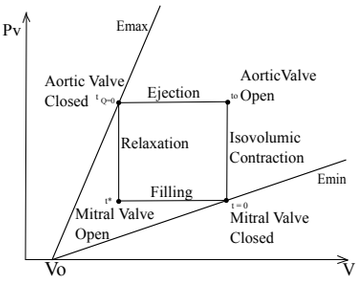

Figure 1: *Pressure Volume representation showing peak and minimum elastance and valve states*

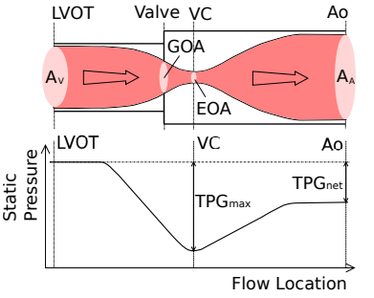

Figure 2: *(top) Representation of blood flow from left ventricular outflow tract (LVOT), through Aortic Valve to ascending Aorta, (Bottom) Transvalvular Pressure Gradient*

TPG_{net} (eq. (1)), uses the Energy loss Coefficient (*ELCo*) of the aortic valve (*AV*), which provides information on the health state of the *AV*. *ELCo* is a function of effective orifice area (*EOA*) and the sinotubular junction area (A_{stj}) of the ascending aorta (Eq. (2)), and so is of significant use in a clinical setting.

$$TPG_{net}(t) = P_V(t) - P_A(t) = \frac{2\pi\rho}{\sqrt{E_L C_O}}\frac{\partial Q(t)}{\partial t} + \frac{\rho}{2}\frac{Q^2(t)}{{E_L C_O}^2} \tag{1}$$

$$ELCo = \frac{EOA.A_{stj}}{A_{stj} - EOA} \tag{2}$$

Considering the range of A_{stj} [3], and the clinical ranges for *EOA* set by the British Heart Foundation shown in Table 1, the range for *ELCo* for aortic valves are shown in Figure 3, which can be used in diagnoses.

Table 1: *British Heart Foundation (BHF) EOA ranges for levels of Aortic Stenosis*

	Normal	Mild	Moderate	Severe
EOA(cm^2)	>2	2-1.5	1.5-1.0	<1.0

3) Vasculature The 3 element Windkessel model detailed in Equation 3, can be represented as an electrical circuit, and is used in combination with Equation 1 and the standard elastance equation used to calculate the aortic pressures for the 0D lumped model. By using the 3 element model instead of the 4 element, the number of optimised coefficients are limited to three, where *C*, *R* and *Zo* are total arterial compliance, total vascular resistance and characteristic impedance.

$$\frac{\partial P_A(t)}{\partial t} + \frac{P_A(t)}{RC} = \frac{Z_0 + R}{RC}Q(t) + Z_0\frac{\partial Q(t)}{\partial t} + \frac{P_{VE}}{RC} \tag{3}$$

4) Optimisation (Modified Cuckoo Search (MCS) To calculate the patient specific coefficients that recreate the original patient data inputs, a gradient free optimisation method i.e. Modified Cuckoo Search (MCS)[4], is used. This gradient free optimisation method is part of the family of genetic algorithm methods, and has been shown to be quite effective because it passes information forward to the following iterations, and due to the strong non-linearity of the problem, the gradient free nature of the optimisation method helps ensure that the solution does not end in local minima.

The coefficients to be optimised are, the representatives of the heart, *Emax*, *Vo*, m_1, m_2, τ_1 and τ_2; the representation of valve state, *ELCo* and the vasculature representations *R*, *C* and *Zo*. With this number of parameter estimations, different combinations could provide satisfactory error fits, but provide incorrect final coefficient values, and so the optimisation objective function is used with restrictions to ensure the results are correct.

The convergence of the method is demonstrated in Figure 4, in which the upper graph shows all of the value combinations for two of the coefficients being run, and at the bottom, how the error reduces as the iterations proceed.

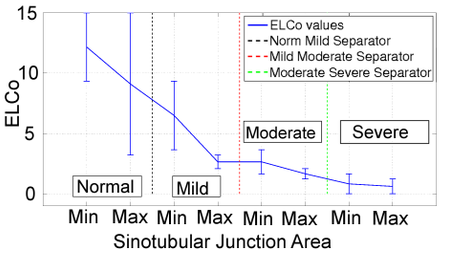

Figure 3: *Energy Loss Coefficient (ELCo) Ranges calculated using max and min Sinotubular Junctuion and EOA Areas for stenoses*

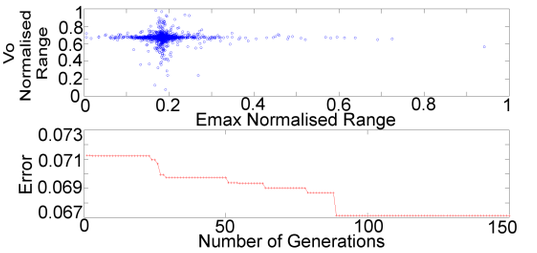

Figure 4: *Modified Cuckoo Search - Search Space for 2 parameters and Reducing Error*

5) Project Data The model requires verification of its accuracy and reproducibility, however, such that 1) the optimised coefficients of the model represent the actual measured information (representing physiology) and 2) the measurements are reproducible for different initialisations. As a first approach, optimisation of a forward run problem was performed with the coefficients taken from literature [5], which demonstrated that the optimisation method functioned with the 0D model well. Secondly, data from a 1D arterial network computer model [6](ANM) is used as a substitute for the measurement data. The ANM can be easily adapted to simulate valvular and vascular diseases which makes it ideally suited for this task.

For the verification analysis, the 1D ANM is run using initial conditions set by the user, and its output "measurements" are used in the objective function. The MCS optimisation then uses a number of restrictions and an objective function which minimises the 0D lumped output wave towards the real "measurements". These restrictions to the simulations decide whether the 0D outputs are "worthy" to go through the objective function, which adds to the computational cost. If the restrictions such as stroke volume tolerance and ejection duration are not similar to the input data, the objective function is bypassed, and a maximum error is passed back to the optimisation.

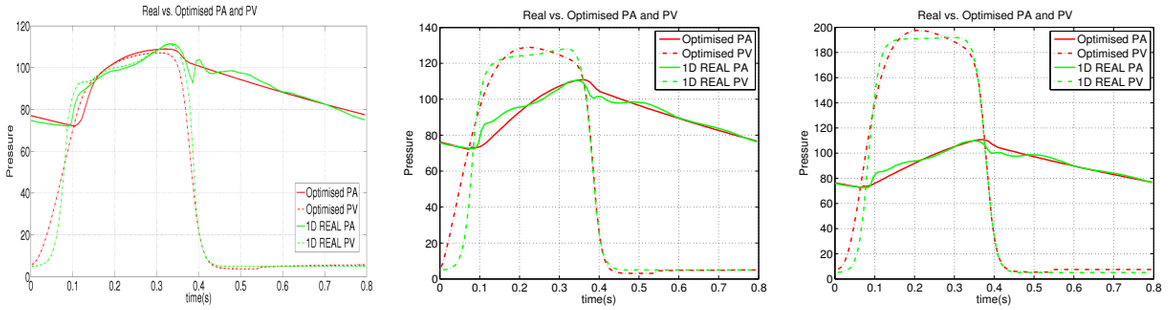

Figure 5: *Pressure Comparisons for (a) Non-Stenosis (M_{st}=1) (b) Moderate-Stenosis (M_{st}=0.2) (c) Severe-Stenosis (M_{st}=0.1)*

3 RESULTS & CONCLUSIONS

The 1D arterial network model has been run for varying cases of aortic valve stenosis, using a coefficient to restrict the maximum valve area (M_{st}). By changing (M_{st}), this alters the *GOA* (geometric orifice area), which highly affects *EOA*, because *EOA* = *GOA***Cc*, where *Cc* is the contraction coefficient (although this *Cc* is affected by shape of the orifice, for this research *Cc*$\approx$ 0.7 [7]). As *EOA* changes, so does *ELCo*, changing the transvalvular pressure gradient (difference).

By running different stenosis levels of the *AV*, it has been determined that the 0D model is highly affected by the permitted ranges of the coefficients, especially *Zo* and *ELCo*, because increasing *Zo* increases the ventricular pressure. If the acceptible range is too large for *Zo* and *ELCo*, viable fitting results of the pressure plots are obtained, however produce incorrect values of *ELCo*, by increasing *Zo*. When several simulation runs of the

same case were completed, a correlation coefficient analysis was performed on the results, and a relatively linear relationship was found between some of the coefficients. Because of this relationship, it was decided to estimate the total arterial compliance of the system [8], ensuring that the other coeffiecients which are linearly linked, would fluctuate less.

The ANM results have been used for the 0D lumped optimisation model and as can be seen in Figure 5, the overall fits for the normal and severly stenotic cases are acceptible given the simplicity of the lumped model.

The reproducibility of the coefficients for the normal and severly stenotic cases show that for repeated simulations, there is little fluctuation in the estimated coefficients (see Figure 6), have reducing *ELCo* values for more severe stenoses, and the optimised results show good agreement with the "measured" data, having a relatively small error tolerance. However, the mild and moderate stenosis cases require more additions to the model to ensure accuracy and consistency.

When the mild and moderate cases are completely accurate and consistent in calculating the correct coefficient values, the next step in the project is to run multiple compliance cases of the 1D ANM to validate the current 0D optimisation model completely, and when verified, mitral regurgitation can be added into the lumped model. When validation for the next stage is finalised, transcatheter aotic valve implantation (TAVI) patient data sets will be used as the model inputs and verified. The coefficients produced from the interactions between these valvular lesions will then be studied and better understood and will be able to provide improved information on timescales and diagnoses for medical intervention.

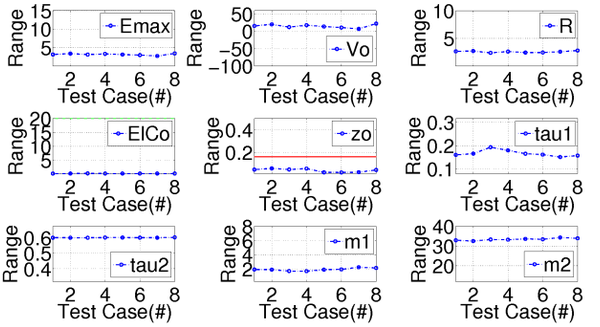

Figure 6: *Coefficient Comparisons for Severe-Stenosis Case (M_{st}=0.1), when re-testing using different initialisation nest locations*

Acknowledgment

This project was generously funded by the National Institute for Social Care and Health Research (NISCHR).

REFERENCES

[1] H. Suga and K. Sagawa, Instantaneous pressure-volume relationships and their ratio in the excised, supported canine left ventricle, *Circulation: Journal of the American Heart Association*, vol. 35, pp. 117 - 126, July 1974.

[2] J. P. Mynard, M. R. Davidson, D. J. Penny, and J. J. Smolich, A simple, versatile valve model for use in lumped parameter and one-dimensional cardiovascular models, *International Journal for Numerical Methods in Biomedical Engineering*, 2011.

[3] H. R. BSC and J. B. C. MD, *Echocardiography: A Practical Guide For Reporting*. Informa healthcare, 2nd edition ed., 2007.

[4] S. Walton, O. Hassan, K. Morgan, and M. Brown, Modified cuckoo search: A new gradient free optimisation algorithm, *Chaos, Solitons & Fractals*, vol. 44, pp. 710 - 718, September 2011.

[5] D. Garcia, P. J. C. Barenbrug, P. Pibarot, A. L. A. J. Dekker, F. H. van der Veen, J. G. Maessen, J. G. Dumesnil, and L.-G. Durand, A ventricular-vascular coupling model in presence of aortic stenosis, *American Journal of Physiology: Heart and Circulatory Physiology,* vol. 288, pp. 1874 - 1884, April 2005.

[6] K.W. Q. LOW, A one-dimensional human arterial network blood flow model with applications to stenoses and aneurysms, mphil, College of Engineering, Swansea University, Singleton Park, Swansea, SA2 8PP, 2012.

[7] D. Garcia, P. Pibarot, C. Landry, A. Allard, B. Chayler, J. G. Dumesnil, and L.-G. Durand, Estimation of aortic valve effective orifice area by doppler echocardiography: Effects of valve inflow shape and flow rate, *Journal of the American Society of Echocardiography,* vol. 17, no. 7, pp. 756 - 765, 2004.

[8] J. Alastruey, T. Passerini, L. Formaggia, and J. Peiro, Physical determining factors of the arterial pulse waveform: theoretical analysis and calculation using the 1-d formulation, *Springerlink*, 2012.

Multiphysics & Multiscale Models for Simulating Total Heart Function

3rd International Conference on Computational and Mathematical Biomedical Engineering - CMBE2013
16-18 December 2013, Hong-Kong
P. Nithiarasu and R. Löhner (Eds.)

Integrated Heart – Coupling multiscale and multiphysics models for simulation of total heart function

Toni Lassila[⋆], Simone Rossi[⋆,†], Ricardo Ruiz-Baier[⋆⋆] and Alfio Quarteroni[⋆,‡]

[⋆]Ecole Polytechnique Fédérale de Lausanne,
Av. Piccard, Station 8, CH-1015 Lausanne, Switzerland,
toni.lassila@epfl.ch, simone.rossi@epfl.ch, ricardo.ruiz@epfl.ch, alfio.quarteroni@epfl.ch

[†]Instituto Superior Técnico, Av. Rovisco Pais 1, 1049-001 Lisbon, Portugal

[⋆⋆]Université de Lausanne, Bâtiment Géopolis, CH-1015 Lausanne, Switzerland

[‡]Politecnico di Milano, P.za Leonardo da Vinci 32, I-20133 Milano, Italy

SUMMARY

We present results on numerical modeling of total heart function focusing on the interaction between models for cardiac electrophysiology, activation mechanisms, fiber contraction, and fluid dynamics inside the ventricles. We discuss in particular the development of robust finite element methods and numerically stable and efficient coupling and solution algorithms tailored for the simulation of the cardiac excitation-contraction mechanism and for ventricular fluid-structure interaction. The implications of different modeling and algorithmic choices into the electromechanic-haemodynamical behavior of the heart are addressed in detail, and we report on several preliminary results with a prototype baseline model, aimed at studying the main aspects of the overall cardiac function.

Key Words: *heart modelling, coupling algorithms, cardiac mechanics, multiscale models.*

1 INTRODUCTION

The physiological process of heart function is intrinsically of multiscale nature and so are the equations that govern each subsystem, ranging from subcell excitation-contraction mechanimsms to fluid dynamics and structural mechanics of the tissue at the organ level. The importance of a multiphysics model is evident when looking at several mechanisms of the healthy and pathological heart function, that are not a consequence of e.g. the mechanical cardiac function alone. Our objective is to construct computational models of total heart function that are able to model at some level the entire tree of cardiac biomechanisms, starting from fundamental cell-level mechanisms and proceeding all the way to simulating and predicting changes in cardiac output induced by specific pathologies in the heart.

Despite the growing literature devoted to experimental and computational research of the different subsystems of heart function to the best of our knowledge the only work proposing and analyzing numerical methods for the successful simulation of total heart function is [1]. We believe the main reason for this is the difficulty of providing stable and computationally efficient coupling algorithms that are able to join together computational models of widely different spatio-temporal

scales in such a way that the solution algorithms scale well up to the large-scale modern supercomputers that are needed to simulate accurately multiphysics phenomena taking place in the heart.

Our aim is to present a baseline multiscale coupling framework in the form of an integrated heart model to study the interaction between four basic fields related to the heart function: the cell-level electrophysiological behavior, the subcellular activation mechanisms, the elastic deformation of the tissue, and the ventricular fluid mechanics. Our philosophy is to use the simplest (possibly phenomenological) model with the minimal number of tunable parameters that is still is able to present relevant physiological response of the total heart. The study of more specific phenomena could then be addressed in specific clinical application by replacing some of these pieces with more accurate and refined models.

The usual choice for multiphysics coupling is to use segregated algorithms, where each subsystem is simulated individually with its own internal time-step using a solver strategy specialized for that particular subproblem, information is exchanged through the coupling interface, and the process iterates until the coupling conditions are satisfied up to some predetermined tolerance. The segregated approach can be computationally and implementationally attractive, but often suffers from instabilities when different subsystems are strongly coupled through the physics, necessitating a large number of coupling iterations before convergence. Its counterpart is the monolithic approach, where all the subproblems are written as one big system that is solved (theoretically) in one go. This leads to the most stable algorithms in strongly coupled multiphysics problems while eliminating the need for coupling iterations, but makes it more difficult to provide robust and computationally efficient solution algorithms because subproblem-specific assumptions are not necessarily valid for the monolithic problem and thus less efficient algorithms may need to be used.

An additional difficulty involving monolithic coupling schemes arises when the two coupled systems exhibit very different time scales. As far as cardiac electromechanics is considered, the choice of the time-step is driven by the dynamics at the cellular level, where complex calcium dynamics may necessitate time steps as small as 10^{-4} ms during the upstroke of the action potential when explicit time-stepping methods are used. On the other hand, the solid mechanics are usually solved using implicit methods and can thus be solved using much larger time steps without sacrificing the accuracy. Different spatial discretization resolutions also need to be considered for the different subproblems. When attempting to accurately capture the depolarization front of the electrophysiology that requires spatial resolutions of 0.1 mm are needed, whereas the resolution needed to simulate cardiac tissue mechanics may be taken an order of magnitude larger. Resolving the complex three-dimensional vortex dynamics inside the left ventricle during diastole again requires either fine meshes or high order approximation spaces. Thus there is a need for the transfer of quantities between approximation spaces of very different and potentially different polynomial orders. All of these issues need to resolved as part of the construction of the model.

2 A MULTISCALE MODEL FOR TOTAL HEART FUNCTION

Our computational model for total heart function is implemented in the open-source finite element library **LifeV** (`http://www.lifev.org`[1]). It is based on parallel solvers for the electrophysiology, solid mechanics and fluid mechanics subproblems. Mesh partitioning is performed with ParMETIS, and the linear problems are solution strategy based on multigrid or algebraic additive Schwarz preconditioners implemented within the Trilinos library (Sandia National Labs).

[1] **LifeV** is managed by a consortium between EPFL, Politecnico di Milano and Emory University.

We choose a segregated and loosely coupled algorithm for the electromechanics, where information between the electrophysiology and the solid mechanics is exchanged only once per time-step. This choice allows different time-steps to be used for the electrophysiology and ventricular mechanics. The electrophysiology problem is solved in the strongly coupled sense but with operator splitting separating the reaction and diffusion parts, and with mass lumping being used in order to reduce numerical instabilities near the front when using medium-sized meshes. The minimal model of Bueno-Orovio et al. [2] is coupled with the monodomain equations, which are efficiently preconditioned through algebraic multigrid techniques. The reaction part is integrated in time using the adaptive third-order linearly implicit Rosenbrock method ROS3P.

To model the electromechanical muscle contraction we use a stretch-dependent activation model based on thermodynamically consistent transversely anisotropic active strain model [3] that is able to capture the correct transmural thickening of the tissue. The passive mechanics model is adapted from the seminal work [4] and includes both fiber and sheet directional orthotropy.

For the ventricular fluid-solid coupling we opt for a monolithic approach as it provides in our experience the best stability and computational efficiency for large displacement fluid-structure interaction problems. In order to take advantage of the specific properties of the different subsystems we use a composed preconditioner for the monolithic fluid-structure interaction problem based on approximate block factorization [5]. This allows us to apply suitable preconditioners for both the fluid and solid subproblems that have been validated to be strongly scalable up to 256 parallel MPI processes.

The fluid solver employs a standard mixed velocity-pressure formulation for the Navier-Stokes equations in an arbitrary Lagrangian-Eulerian frame, supplemented by a variational multiscale stabilization method [6] to simulate the transient flow during peak diastole. To prescribe the ventricular afterload we couple the heart to a geometrical multiscale model [7] consisting of a 1-D network of arteries and lumped parameter Windkessel terminals, where the description of the arterial tree and the parameters are taken from [8].

Different spatial resolutions can be used for each of the three different sub-problems; to accomplish this we use an advanced version of radial basis function interpolation with spatially varying support radius (chosen appropriately to obtain a sparse yet well-conditioned interpolation system) and inverse rescaling of the shape functions in order to interpolate exactly constant fields, which improves the approximation stability.

3 CONCLUSIONS

Fully integrated models of total heart function including also the fluid dynamics inside the ventricle are on the horizon as computational algorithms become more efficient, allowing more comprehensive simulations of cardiovascular pathologies. Due to the multiscale and multiphysics nature of heart activity, a careful consideration between different algorithmic choices (monolithic vs. segregated, strong vs. loose, explicit vs. implicit) has to be made in order to obtain the best compromise between stability and scalability. We have presented a baseline computational model for simulation of total heart function that can act as a starting point for more in-depth studies on cardiac function and dysfunction.

REFERENCES

[1] S. Sugiura, T. Washio, A. Hatano, J. Okada, H. Watanabe and T. Hisada, Multi-scale simulations of cardiac electrophysiology and mechanics using the University of Tokyo heart simulator, *Progr. Biophys. Molecular Biol.*, 110:380–389, 2012.

[2] A. Bueno-Orovio, E.M. Cherry and F.H. Fenton, Minimal model for human ventricular action potential in tissue, *J. Theor. Biol.* 253:544–560, 2008.

[3] S. Rossi, R. Ruiz-Baier, L.F. Pavarino and A. Quarteroni, Orthotropic active strain models for the numerical simulation of cardiac biomechanics, *Int. J. Numer. Methods Biomed. Engr.* 28(6–7):761–788, 2013.

[4] G.A. Holzapfel and R.W. Ogden, Constitutive modelling of passive myocardium: a structurally based framework for material characterization, *Phil. Trans. Royal Soc. London A* 367:3445–3475, 2009.

[5] P. Crosetto, S. Deparis, G. Fourestey and A. Quarteroni, Parallel algorithms for fluid-structure interaction problems in haemodynamics, *SIAM J. Sci. Comput.* 33(4): 1598–1622, 2011.

[6] Y. Bazilevs, V.M. Calo, J.A. Cottrell, T.J.R. Hughes, A. Reali, and G. Scovazzi, Variational multiscale residual-based turbulence modeling for large eddy simulation of incompressible flows, *Comput. Methods Appl. Mech. Enrg.* 197(1):173–201, 2007.

[7] A.C.I. Malossi, Partitioned solution of geometrical multiscale problems for the cardiovascular system: Models, algorithms, and applications, PhD Thesis, Ecole Polytechnique Fédérale de Lausanne, 2012.

[8] P. Reymond, F. Merenda, F. Perren, D. Rüfenacht, N. Stergiopulos, Validation of a one-dimensional model of the systemic arterial tree. *Am. J. Physiol. Heart Circ. Physiol.* 297(1):H208–H222, 2009

3rd International Conference on Computational and Mathematical Biomedical Engineering - CMBE2013
16-18 December 2013, Hong-Kong
P. Nithiarasu and R. Löhner (Eds.)

An effective algorithm for the generation of patient-specific Purkinje networks in computational electrocardiology

S. Palamara*, D. Catanzariti, M. Centonze***, E. Faggiano****, F. Nobile*****, A. Quarteroni****** and C. Vergara*******

*MOX, Dipartimento di Matematica, Politecnico di Milano, Piazza Leonardo da Vinci 32, 20133 Milano, simone.palamara@polimi.it

**Divisione di Cardiologia, Ospedale S. Maria del Carmine, Corso Verona 4, 38068 Rovereto (TN), domenico.catanzariti@apss.tn.it

***Divisione di Radiologia Diagnostica, Presidio Ospedaliero di Borgo Valsugana, Viale Vicenza 9, 38051 Borgo Valsugana (TN), Maurizio.Centonze@apss.tn.it

****MOX, Dipartimento di Matematica, Politecnico di Milano, Piazza Leonardo da Vinci 32, 20133 Milano, elena.faggiano@polimi.it

*****Ecole Polytechnique Fédérale de Lausanne,Av. Piccard, Station 8, CH-1015 Lausanne, Switzerland, fabio.nobile@epfl.ch

******Ecole Polytechnique Fédérale de Lausanne,Av. Piccard, Station 8, CH-1015 Lausanne, Switzerland, alfio.quarteroni@epfl.ch

*******Dipartimento di Ingegneria, Università di Bergamo, viale Marconi 5, 24044 Dalmine (BG), christian.vergara@unibg.it

SUMMARY

In this talk we propose a new methodology for the generation of patient-specific Purkinje networks in computational electrophysiology. This genaration is obtained as a correction of a fractal network driven by clinical measures of the activation times. We present several numerical results, both in ideal and real geometries, highlighting the suitability of our method.

Key Words: *Purkinje fibers, patient-specific electrophysiology, Eikonal equation.*

1 INTRODUCTION

The development of biophysical models of the heart is fundamental to get deep insights in the mechanisms controlling its activity and also, in pathological cases, to give to the clinicians a powerful instrument that could help in the diagnosis and in the design of new therapies.
A key aspect of the heart modeling is the study of electrical activation, that triggers the heart contraction. The electrical activation is regulated by the cardiac conduction system (CCS), responsible for the fast and coordinated distribution of the electrical impulse in the heart.
In particular, in the ventricles, the activation is regulated by the peripheral part of the CCS, the Purkinje fibers (PF), located in the inner ventricular walls of the heart, just beneath the endocardium. The electrical signal spreads rapidly in the PF and it enters the ventricular wall only at certain insertion sites, called Purkinje muscle junctions (PMJ) [1]. From these sites the depolarization wave propagates in the myocardium, allowing the ventricular excitation and contraction thanks to the activation of the cardiac muscle cells [2].
Therefore, since the electrical activation of the ventricle depends strongly on the PF, it is necessary to model the presence of the latter to obtain a realistic activation model.

2 COMPUTATIONAL GENERATION OF A PATIENT-SPECIFIC PURKINJE NETWORK

The focus of our work is to provide a computational algorithm for the generation of a *patient-specific Purkinje network*, driven by clinical measures of the electrical activation in the ventricle. These measures consist of the activation times acquired on the endocardium of the left ventricle, for example before an ablation procedure to burn anomalous propagation sites.
The proposed method for the generation of the patient-specific Purkinje network is based on searching the optimal locations of the PMJ to best fit the clinical measures. In particular, starting from an initial network, generated by means of a fractal law [3,4], our algorithm adjusts this network to the measures by moving, deleting and creating new PMJ, obtaining a patient-specific Purkinje network. Regarding the mathematical models used to compute the activation times in the PF and in the ventricles, we considered the Eikonal equation [5,6], with values of the conduction velocities in the physiological range.
We tested the accuracy and robustness of our method considering both an ideal geometry with synthetically generated data and four patient-specific geometries, with real clinical measures, considering both normal and pathological activations. In particular, as pathological activations, we considered data from two patients, one of them had a case of Wolff-Parkinson-White syndrome (WPW) and the other one had a case of heart failure. We analysed the accuracy of the proposed method with respect to other activation models used so far in the literature.

3 CONCLUSIONS

The numerical results proved the essential role of the Purkinje network, both in modeling the healthy and the pathological activation of the left ventricle. Moreover, we proved the importance of generating a patient-specific Purkinje network to recover an accurate activation, when clinical measures are available.

REFERENCES

[1] Rawling DA., Joyner RW., Overholt ED. Variations in the functional electrical coupling between the subendocardial purkinje and ventricular layers of the canine left ventricle. *Circ Res* 57(2):252-261, (1985).

[2] Anderson RH., Yanni J., Boyett MR., Chandler NJ., Dobrzynski H. The anatomy of the cardiac conduction system. *Clin Anat* 22(1):99-113, (2009).

[3] Abboud S., Berenfeld O., Sadeh D. Simulation of high-resolution qrs complex using a ventricular model with a fractal conduction system. Effects of ischemia on high-frequency qrs potentials. *Circ Res* 68(6):1751-1760, (1991).

[4] Sebastian R., Zimmerman V., Romero D, Frangi A. Construction of a computational anatomical model of the peripheral cardiac conduction system. *IEEE T Biomed Eng* 58(12):3479-3482, (2011).

[5] Colli Franzone P., Guerri L. Spreading excitation in 3-D models of the anisotropic cardiac tissue, I. Validation of the Eikonal Model. *Math Biosci* 113:145-209, (1993).

[6] Keener JP. An eikonal-curvature equation for action potential propagation in myocardium. *J Math Biol* 29(7):629-651, (1991).

3rd International Conference on Computational and Mathematical Biomedical Engineering - CMBE2013
16-18 December 2013, Hong-Kong
P. Nithiarasu and R. Löhner (Eds.)

Parallel multilevel solvers for cardiac electromechanical models

P. Colli Franzone⋆, L. F. Pavarino⋆⋆ and S. Scacchi⋆⋆
⋆Dipartimento di Matematica, Università di Pavia, Via Ferrata, 27100 Pavia, Italy.
colli@imati.cnr.it
⋆⋆Dipartimento di Matematica, Università di Milano, Via Saldini 50, 20133 Milano, Italy.
luca.pavarino@unimi.it, simone.scacchi@unimi.it

SUMMARY

We develop a parallel solver for the coupling of cardiac electromechanical models. The myocardium is modeled as a nearly-incompressible transversely isotropic hyperelastic material, while the spread of the electric impulse in the myocardium is modeled by the Bidomain system with two nonlinear parabolic partial differential equations coupled through the reaction term with a membrane model, a stiff system of ordinary differential equations. The discretization of the whole electromechanical model is performed by Q1 finite elements in space and a semi-implicit finite difference scheme in time. This approximation strategy yields at each time step the solution of a large scale ill-conditioned linear system for the Bidomain model and a nonlinear system for the finite elasticity model. The parallel solver developed solves the linear system with the Conjugate Gradient method, preconditioned by a Multilevel Schwarz preconditioner, and the nonlinear system with a Newton-Krylov-Algebraic Multigrid solver. 3D parallel numerical tests show that the proposed solver is scalable and robust with respect to the cardiac deformations.

Key Words: *Cardiac electromechanics, Bidomain model, Finite Elasticity, Multilevel Schwarz preconditioners, Algebraic Multigrid.*

1 CARDIAC ELECTROMECHANICAL MODELS

Mechanical model. From a mechanical point of view, the cardiac tissue is modeled as a nonlinear elastic material satisfying the quasi-static Cauchy's equation of equilibrium, without body force,

$$\mathrm{Div}(\mathbf{FS}) = \mathbf{0}, \qquad \mathbf{X} \in \hat{\Omega}, \tag{1}$$

where $\mathbf{S} = \{s_{ij}\}$ is the second Piola-Kirchoff stress tensor, $\mathbf{F}(\mathbf{X}, t) = \{F_{ij}\} = \left\{ \frac{\partial x_i}{\partial X_j} \quad i,j = 1,2,3 \right\}$ is the deformation gradient, $\mathbf{X} = (X_1, X_2, X_3)^T$ are the undeformed (material) coordinates of the reference cardiac domain, $\mathbf{x} = (x_1, x_2, x_3)^T$ are the deformed (spatial) coordinates of the deformed domain. The tensor $\mathbf{S}$ is given by the sum of a passive elastic component $\mathbf{S}^{pas}$ and an active biochemically generated component $\mathbf{S}^{act}$, i.e. $\mathbf{S} = \mathbf{S}^{pas} + \mathbf{S}^{act}$, as in many previous studies; see [8] for a comparison with an alternative multiplicative approach. The passive component $\mathbf{S}^{pas}$ is computed from a suitable strain energy function W and the Green-Lagrange strain $\mathbf{E} = \frac{1}{2}(\mathbf{C} - \mathbf{I})$ (where $\mathbf{C} = \mathbf{F}^T\mathbf{F}$ is the Cauchy-Green deformation tensor)

$$S^{pas}_{ij} = \frac{1}{2}\left(\frac{\partial W}{\partial E_{ij}} + \frac{\partial W}{\partial E_{ji}} \right) \quad i,j = 1,2,3.$$

Among the many strain energy functions proposed in the literature, in this paper we choose the exponential strain energy function [12] for transversely isotropic hyperelastic materials

$$W = \frac{1}{2}\, c\, \left(e^{Q} - 1\right), \qquad Q = b_{ll}E_{ll}^2 + b_{tn}(E_{nn}^2 + E_{tt}^2 + 2E_{nt}^2) + 2b_{lt}(E_{lt}^2 + E_{ln}^2),$$

where (l) denotes the fiber direction and (n), (t) two others orthogonal cross fiber directions. We model the myocardium as a nearly-incompressible material, so following [12], we add a bulk modulus K multiplying a volume change penalization term into the strain energy

$$W = \frac{1}{2}c\left(e^{Q} - 1\right) + K\left(\sqrt{\det(C)} - 1\right)^2.$$

We close the quasi-static mechanical model (1) by imposing a prescribed displacement on a Dirichlet boundary and no traction force on a Neumann boundary. The active stress component of the second Piola-Kirchhoff tensor is given by $\mathbf{S}^{act} = J\, T_a \mathbf{F}^{-1}\sigma^{act}\mathbf{F}^{-T}$, where $J = det\mathbf{F}$ and we assume, as in other studies, that the generated active force acts only in the direction of the fiber, hence $\sigma^{act} = T_a \mathbf{a}_l \otimes \mathbf{a}_l$, where $\mathbf{a}_l$ is a unit vector parallel to the local fiber direction and T_a is the active stress related to the deformed domain, given as in Nash and Panfilov [4] by

$$\frac{\partial T_a}{\partial t} = Q(V, T_a) = \epsilon(V)(k_{T_a}V - T_a), \text{ with } \epsilon(V) = \begin{cases} 1 & \text{for } V < 0.05 \\ 10 & \text{for } V \geq 0.05, \end{cases}, \quad k_{T_a} = 47.9\, kPa.$$

Bidomain electrical model. The macroscopic Bidomain representation of the cardiac tissue volume Ω is obtained by considering the superposition of two anisotropic intra- (i) and extra- (e) cellular media, coexisting at every point of the tissue and separated by a distributed continuous cellular membrane; see e.g. [7] for a derivation using homogenization techniques. In order to take into account the mechanical deformation of the tissue, following [4,5,13] we will now introduce the parabolic-parabolic formulation of the Bidomain system on the reference cardiac domain $\hat{\Omega}$. Given an applied extracellular current per unit volume $I_{app}^e : \hat{\Omega} \times (0,T) \to R$, and initial conditions $v_0 : \hat{\Omega} \to R$, $w_0 : \hat{\Omega} \to R^{N_w}$, find the intra- and extracellular potentials $u_{i,e} : \hat{\Omega} \times (0,T) \to R$, the transmembrane potential $v = u_i - u_e : \hat{\Omega} \times (0,T) \to R$, the gating and ionic concentrations variables $(w, c) : \hat{\Omega} \times (0,T) \to R^{N_w} \times R^{N_c}$ such that

$$\begin{cases} c_m \dfrac{\partial v}{\partial t} - J^{-1}\,\mathrm{Div}(J\mathbf{F}^{-1}D_i\mathbf{F}^{-T}\,\mathrm{Grad}\,u_i) + I_{ion}(v,w,c) = 0 & \text{in } \hat{\Omega}\times(0,T) \\ -c_m \dfrac{\partial v}{\partial t} - J^{-1}\,\mathrm{Div}(J\mathbf{F}^{-1}D_e\mathbf{F}^{-T}\,\mathrm{Grad}\,u_i) - I_{ion}(v,w,c) = I_{app}^e & \text{in } \hat{\Omega}\times(0,T) \\ \dfrac{\partial w}{\partial t} - R(v,w) = 0, \quad \dfrac{\partial c}{\partial t} - S(v,w,c) = 0, & \text{in } \hat{\Omega}\times(0,T) \\ \hat{\mathbf{n}}^T\mathbf{F}^{-1}D_{i,e}\mathbf{F}^{-T}\,\mathrm{Grad}\,u_{i,e} = 0 & \text{in } \partial\hat{\Omega}\times(0,T) \\ v(\mathbf{x},0) = v_0(\mathbf{x}), \quad w(\mathbf{x},0) = w_0(\mathbf{x}), \quad c(\mathbf{x},0) = c_0(\mathbf{x}) & \text{in } \hat{\Omega}, \end{cases}$$

where $\mathbf{F}$ is the deformation gradient tensor and we have assumed an insulated cardiac boundary $\partial\hat{\Omega}$. For an applied extracellular current I_{app}^e satisfying the compatibility condition $\int_\Omega I_{app}^e\,\mathrm{dx} = 0$, this system uniquely determines v, while the potentials u_i and u_e are defined only up to the same additive time-dependent constant related to the reference potential, determined here cardiac volume by imposing $\int_\Omega u_e\,\mathrm{dx} = 0$. The nonlinear reaction term I_{ion} and the ODE system for the gating variables w are given by the ionic membrane model, chosen here as the Luo–Rudy I (LR1) model [3]. The conductivity tensors $D_i(\mathbf{x})$ and $D_e(\mathbf{x})$ at any point $\mathbf{x} \in \Omega$ are defined as

$$D_{i,e}(\mathbf{x}) \quad = \sigma_l^{i,e}\,\mathbf{a}_l(\mathbf{x})\mathbf{a}_l^T(\mathbf{x}) + \sigma_t^{i,e}\,\mathbf{a}_t(\mathbf{x})\mathbf{a}_t^T(\mathbf{x}) + \sigma_n^{i,e}\,\mathbf{a}_n(\mathbf{x})\mathbf{a}_n^T(\mathbf{x}).$$

Here $\mathbf{a}_l(\mathbf{x}),\ \mathbf{a}_t(\mathbf{x}),\ \mathbf{a}_n(\mathbf{x})$, is a triplet of orthonormal principal axes with $\mathbf{a}_l(\mathbf{x})$ parallel to the local fiber direction, $\mathbf{a}_t(\mathbf{x})$ and $\mathbf{a}_n(\mathbf{x})$ tangent and orthogonal to the radial laminae, respectively, and both being transversal to the fiber axis. Moreover, $\sigma_l^{i,e},\ \sigma_t^{i,e},\ \sigma_n^{i,e}$ are the conductivity coefficients in the intra- and extracellular media measured along the corresponding directions $\mathbf{a}_l, \mathbf{a}_t, \mathbf{a}_n$. In this work, the electric conduction of the cardiac tissue is model as an *axi-symmetric* anisotropic media with respect to the local finer direction, i.e. $\sigma_n^{i,e} = \sigma_t^{i,e}$.

2 DISCRETIZATION AND NUMERICAL MODELS

The time discretization is performed by a semi-implicit splitting method. At each time step:
1) given v^n, w^n, c^n, T_a^n, solve the ODEs of the membrane model and active force equation with a first order IMEX method to compute the new w^{n+1}, c^{n+1}, T_a^{n+1},
2) given T_a^{n+1} solve the mechanical problem to compute the new deformed coordinates $\mathbf{x}^{n+1}$, providing the new deformation gradient tensor $\mathbf{F}_{n+1}$,
3) given w^{n+1}, c^{n+1}, $\mathbf{F}_{n+1}$, and $J_{n+1} = \det(\mathbf{F}_{n+1})$ solve the Bidomain system with a first order IMEX method computing the new electric potentials u_i^{n+1}, u_e^{n+1}, $v^{n+1} = u_i^{n+1} - u_e^{n+1}$.

For the space discretization, we use structured grids of hexahedral isoparametric Q_1 finite elements in space, for both the nonlinear elasticity system and the Bidomain equations. At each time step, the main computational effort consists of:
a) solving the nonlinear system deriving from the discretization of the mechanical problem. We use the Newton method, with GMRES for the linear Jacobian system, preconditioned by an Algebraic Multigrid preconditioner [2];
b) solving the linear system deriving from the discretization of the Bidomain model. We use the Conjugate Gradient method preconditioned by a Multilevel Hybrid Schwarz preconditioner with L levels (MHS(L)), see [6,9,10] and [11] for a general introduction to these methods. Inexact ILU(0) local solvers are used for the local problems on the subdomains.

3 NUMERICAL RESULTS

In this section, we present the results of parallel numerical experiments performed on the Linux Cluster IBM SP6/5376 of the Cineca Consortium (www.cineca.it). Our FORTRAN-j0 code is based on the parallel library [1], from the Argonne National Laboratory. We perform a weak scaling test on truncated ellipsoidal domains of increasing size, modeling wedges of the ventricular wall. The number of subdomains (and processors) is increased from 8 to 512, so that the local mesh size is kept constant ($16 \cdot 16 \cdot 16$ for the mechanical mesh of size $h = 0.02\ cm$ and $32 \cdot 32 \cdot 32$ for the electrical mesh of size $h = 0.01\ cm$). The global size of the discrete systems increases as indicated in Table 1. The simulation is run for 10 time steps of $0.05\ ms$ during the plateau phase of the cardiac action potential, where the deformation due to the mechanical contraction is stronger. The results regarding the mechanical and Bidomain solvers are reported in Table 1. Both the nonlinear Newton iteration (nit) and linear GMRES iteration (lit) are completely scalable. The scalability of the GMRES iterations is achieved by the use of the AMG preconditioner. Nevertheless, the CPU times are not scalable, because they increase with the number of processors, due to the setup of the AMG preconditioner at each Newton iteration. The MHS(4) Bidomain preconditioner, considering or neglecting ($\mathbf{F} = \mathbf{I}$) the influence of the mechanical tissue deformation on the conductivity tensor, is robust with respect to the domain deformations due to the mechanical contraction. Moreover, the MHS(4) preconditioner is completely scalable, both in terms of the mathematical quantities (condition number and CG iterations) and CPU times.

	Mechanical solver AMG preconditioner				Bidomain solver MHS(4) preconditioner						
						non-deforming			deforming		
procs	dof	nit	lit	time	dof	κ_2	it	time	κ_2	it	time
8	107,811	2	42	12.06	549,250	1.11	3	1.05	1.11	3	1.31
27	352,957	2	42	16.70	1,825,346	1.11	3	1.19	1.12	3	1.17
64	823,875	2	39	23.45	4,293,378	1.12	3	1.23	1.13	3	1.21
125	1,594,323	2	39	30.66	8,346,562	1.13	3	1.31	1.18	4	1.49
216	2,738,019	2	40	49.12	14,378,114	1.18	4	1.55	1.20	4	1.55
343	4,328,691	2	39	92.93	22,781,250	1.15	4	1.62	1.17	4	1.66
512	6,440,067	2	40	75.09	33,949,186	1.14	4	1.96	1.17	4	1.67

Table 1: Weak scaling test. Comparison of mechanical AMG preconditioner and Bidomain MHS(4) preconditioners on deforming and non-deforming ($\mathbf{F} = \mathbf{I}$) domains. Number of processors (procs), Degrees of freedom (dof), Condition number (κ_2), CG iteration counts (it), CPU time in seconds (time).

REFERENCES

[1] S. Balay, K. Buschelman, W. D. Gropp, D. Kaushik, M. Knepley, L. Curfman McInnes, B. F. Smith and H. Zhang. PETSc Users Manual.Tech. Rep. ANL-95/11 - Revision 2.1.5, Argonne National Laboratory, 2002. http://www.mcs.anl.gov/petsc, 2001.

[2] V. E. Henson, U. M. Yang. BoomerAMG: A parallel algebraic multigrid solver and preconditioner. *Appl. Numer. Math.* 41 (1): 155–177, 2002.

[3] C. Luo and Y. Rudy. A model of the ventricular cardiac action potential: depolarization, repolarization, and their interaction. *Circ. Res.*, 68 (6): 1501–1526, 1991.

[4] M. P. Nash and A. V. Panfilov. Electromechanical model of excitable tissue to study reentrant cardiac arrhythmias. *Progr. Biophys. Molec. Biol.*, 85: 501–522, 2004.

[5] P. Pathmanathan and J. P. Whiteley. A numerical method for cardiac mechanoelectric simulations. *Ann. Biomed. Engrg.*, 37 (5): 860–873, 2

[6] L. F. Pavarino and S. Scacchi. Multilevel additive Schwarz preconditioners for the Bidomain reaction-diffusion system. *SIAM J. Sci. Comput.*, 31 (1): 420–443, 2008.

[7] M. Pennacchio, G. Savaré and P. Colli Franzone. Multiscale modeling for the bioelectric activity of the heart. *SIAM J. Math. Anal.*, 37 (4): 1333–1370, 2006.

[8] S. Rossi, R. Ruiz-Baier, L. F. Pavarino and A. Quarteroni. Orthotropic active strain models for the numerical simulation of cardiac biomechanics. *Int. J. Num. Meth. Biomed. Engrg.*, 28: 761–788, 2012.

[9] S. Scacchi. A hybrid multilevel Schwarz method for the bidomain model. *Comp. Meth. Appl. Mech. Engrg.*, 197 (45–48): 4051–4061, 2008.

[10] S. Scacchi. A multilevel hybrid Newton-Krylov-Schwarz method for the Bidomain model of electrocardiology. *Comput. Meth. Appl. Mech. Engrg.*, 200 (5–8): 717–725, 2011.

[11] A. Toselli and O. B. Widlund. *Domain Decomposition Methods: Algorithms and Theory*. Computational Mathematics, Vol. 34. Springer-Verlag, Berlin, 2004.

[12] F. J. Vetter and A. D. McCulloch. Three-dimensional stress and strain in passive rabbit left ventricle: a model study. *Ann. Biomed. Engrg.*, 28: 781–792, 2000.

[13] J. P. Whiteley, M. J. Bishop and D. J. Gavaghan. Soft tissue modelling of cardiac fibres for use in coupled mechano-electric simulations. *Bull. Math. Biol.*, 69: 2199–2225, 2007.

3rd International Conference on Computational and Mathematical Biomedical Engineering - CMBE2013
16-18 December 2013, Hong-Kong
P. Nithiarasu and R. Löhner (Eds.)

Adaptive simulation of electro-mechanical coupling in cardiac simulation with spectral deferred correction methods

Martin Weiser[⋆], Simone Scacchi[⋆⋆] and Bodo Erdmann[⋆]
[⋆]Zuse Institute Berlin, Takustr. 7, 14195 Berlin, Germany, {weiser,erdmann}@zib.de
[⋆⋆] Department of Mathematics, University of Milano, Via Saldini 50, 20133 Milano, Italy, simone.scacchi@unimi.it

SUMMARY

Electro-mechanical coupling exhibits features of very different spatial and temporal scales. Spatio-temporal adaptivity is a promising way to reduce the computational complexity, but numerical experience shows that the induced overhead essentially kills the performance gain. In this talk we investigate the use of spectral deferred correction methods as a means to reduce this overhead while retaining most of the performance advantage. The properties of the resulting method are discussed at some numerical examples.

Key Words: *electro-mechanical coupling, mesh adaptivity, spectral deferrred corrections.*

1 INTRODUCTION

Simulations of electro-mechanical coupling of cardiac excitation cover very different spatial and temporal scales. A reasonable approximation of the depolarization front requires mesh sizes of less than 1mm and time steps of not more than 1 ms, which leads to a high computational effort for whole-organ simulations of relevant duration. The elastic deformation usually exhibits much less local features, for which reason it is often computed on a coarser but nested grid.

Further reduction of computational complexity can be expected from spatio-temporal adaptivity, as away from the depolarization front coarser meshes and longer time steps are sufficient. Numerical experience with standard methods of adaptivity, however, indicates that any performance gain can easily be killed by the overhead of adaptivity, such as error estimation and repeated reassembly on mesh refinement or coarsening.

In this paper we take a step towards a computationally efficient, adaptive method for electro-mechanic cardiac simulations. In particular, we aim at amortizing the overhead of spatial adaptivity over longer time steps, at re-using data computed before mesh refinement or step size reduction, and multi-rate time stepping. A promising class of time stepping schemes that can be tweaked into these directions are spectral deferred correction methods [1].

2 ELECTRO-MECHANICAL SIMULATION WITH SPECTRAL DEFERRED CORECTION METHODS

2.1 Electro-mechanical coupling

For the two-way coupling of electrical excitation and mechanical deformation we employ the simple model from [3]. The excitation part is described by a monodomain two-variable FitzHugh-Nagumo type model. Active stress generation along the fiber direction is derived from the transmembrane voltage by a linear ODE. The quasi-static deformation is given as the minimizer of a hyperelastic stored energy. This results in a coupled system of four PDEs for the transmembrane voltage u, the gating variable v, the active tensile stress a, and the displacement y:

$$\begin{aligned}
\dot{u} &= -\operatorname{div}(D(y_x)\nabla u) - 8u(u-0.1)(u-1) + uv + I_s \\
\dot{v} &= 0.25(0.01 + 0.07v/(u+0.3))(-v - 8u(u-1.1)) \\
\dot{a} &= \epsilon(u)(47.9u - 0.1) \\
0 &= \frac{\partial W}{\partial y}
\end{aligned}$$

For simplicity, the fiber direction is assumed to be the x_1 direction, hence the conductivity D depends on the displacement derivative y_x due to

$$D = 10^{-3} F^{-1} \begin{bmatrix} 2 & 0 \\ 0 & 1 \end{bmatrix} F^{-T}, \quad F = I + y_x.$$

I_s denotes the stimulation current. The jump function

$$\epsilon(u) = \begin{cases} 1, & u < 0.05 \\ 10, & u \geq 0.05 \end{cases}$$

induces a delay in stress development. Finally, the stored energy function W is formulated in terms of the Green-Lagrange strain tensor $E = \frac{1}{2}(y_x + y_x^T + y_x^T y_x)$ and $Q = b_{ij} E_{ij}^2$ as

$$W = 3e^Q + aE_{11} + 200b(\det(I + y_x)), \quad b(x) = x - \log x.$$

2.2 Spatially adaptive SDC-DIRK methods

Spectral deferred correction methods are fixed point iterations for collocation equation systems. The attractive feature is that one iteration consists of a sweep of n simpler time steps, e.g., implicit Euler steps, going through the n collocation nodes one at a time, such that an implementation can be a thin wrapper around a simple Euler scheme. The drawback is that, on non-equidistant collocation grids, e.g. Radau points suitable for stiff equations, the contraction rate can be quite close to one. With a slight modification of the right hand sides and the coefficients of the Euler scheme, one sweep can be interpreted as a specialized diagonally implicit Runge-Kutta method and restores reasonably fast convergence also on non-equidistant grids, see Fig. 1 left. For details, we refer to [4].

For the electro-mechanical cardiac model, we use second order finite elements for the transmembrane voltage and linear finite elements for the smoother gating variable, active stress, and displacement. An SDC integrator is used for the three dynamic variables, and Newton's method on each collocation point for the stationary hyperelastic equation. During each sweep, the variables are integrated independently of each other. Their coupling is realized only through the SDC iteration, which could be exploited for parallelization.

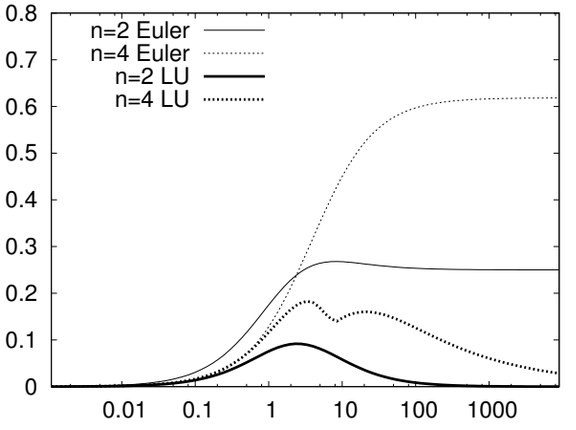

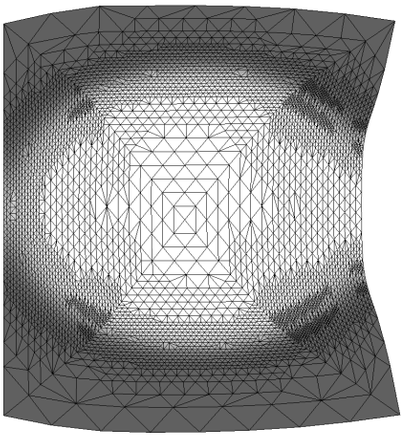

Figure 1: Left: Contraction rates of SDC methods for the Dahlquist equation on $n = 2, 4$ Radau collocation points. Euler sweeps vs. specialized DIRK sweeps. Right: Excitation front propagating through deformed tissue after 7.5 ms.

After each sweep, an embedded hierarchical error estimator is employed for estimating the spatial discretization error of the transmembrane voltage. If the required accuracy is not reached, the grid is refined as needed and the current SDC iterates are prolongated to the finer mesh. After this, another sweep is performed on the new mesh. With this approach, the effort of adaptivity (error estimation, reassembly) can be amortized over more stages and longer time steps than with, e.g., a Rosenbrock method, and the results obtained on the coarser mesh are reused as valid SDC iterates.

Once a whole SDC step is accepted, the mesh is coarsened wherever the mesh resolution is finer than required for representing the solution at the end of the step up to the requested accuracy.

2.3 Numerical example

The method outlined above has been implemented in the C++ finite element toolbox Kaskade 7 [2] and tested on a 2D unit square example, with Dirichlet boundary conditions for the displacement on the left edge of the square. The stimulation current was applied in $[0.5, 0.55]^2$ for 2 ms. With a fixed time step size of 1.5 ms, three Radau points, and at least three SDC sweeps, reasonable results were obtained (see Fig. 1 right). The most crucial issue is the convergence of Newton's method for the hyperelastic material. A stepsize damping is necessary in order not to limit the time step.

3 CONCLUSIONS

The electro-mechanical coupling of cardiac simulations can effectively be solved by SDC methods. The preliminary implementation does not yet exploit the whole potential flexibility of the SDC approach, but already works reasonably well. Including advanced features such as local and multi-rate time stepping, adaptive sweep count and step size selection, and parallelization within the SDC sweeps appears to be a promising way towards a very efficient simulation method.

REFERENCES

[1] A. Dutt, L. Greengard, and V. Rokhlin. Spectral deferred correction methods for ordinary differential equations. *BIT*, 40(2):241–266, 2000.

[2] S. Götschel, M. Weiser, and A. Schiela. Solving optimal control problems with the Kaskade 7 finite element toolbox. In A. Dedner, B. Flemisch, and R. Klöfkorn, editors, *Advances in DUNE*, pages 101–112. Springer, 2012.

[3] M.P. Nash and A.V. Panfilov. Electromechanical model of excitable tissue to study reentrant cardiac arrhythmias. *Progr. Biophys. Mol. Biol.*, 85:501–522, 2004.

[4] M. Weiser. On goal-oriented adaptivity for elliptic optimal control problems. *Optim. Meth. Softw.*, 28(13):969–992, 2013.

3rd International Conference on Computational and Mathematical Biomedical Engineering - CMBE2013
16-18 December 2013, Hong-Kong
P. Nithiarasu and R. Löhner (Eds.)

Towards a scalable numerical framework for multiscale-multiphysics models of cardiac function

Gernot Plank[⋆], Aurel Neic[⋆⋆], Manfred Liebmann[⋆⋆], Thomas E. Fastl[⋆], Anton J. Prassl[⋆], Gundolf Haase[⋆⋆] and Christoph M. Augustin[⋆]
[⋆]Medical University of Graz, Institute of Biophysics, Harrachgasse 21/4, A-8010 Graz, Austria, gernot.plank@medunigraz.at
[⋆⋆]University of Graz, Institute of Mathematics and Scientific Computing, Heinrichstrasse 36, A-8010 Graz, Austria

SUMMARY

The heart is a highly complex multiphysics organ whose main function is to propel blood around the circulatory system, thus providing oxygen and metabolites to the organs. Integrated models of cardiac function are vital to gain better insight into the complex interplay of biological processes across different spatial and temporal scales as well as between the different physics involved. However, developing efficient frameworks for such multiscale-multiphysics simulations of cardiac function remains to be a challenging task due to the vast computational costs and the numerical complexities involved in coupling different physics which are governed by different spatio-temporal scales. In this study we report on a novel methodological approach to strongly coupled models of cardiac electromechanics. Methods are designed with the main objective to achieve good strong scaling characteristics, thus allowing to use a large number of compute cores to keep simulations tractable.

Key Words: *bidomain equation, nonlinear elasticity, strong scaling, accelerators.*

1 INTRODUCTION

The physiological function of the heart is regulated by a cascade of processes in which a propagating electrical wavefront controls mechanical contraction and relaxation. Any disturbance in this highly ordered sequence of events may trigger severe malfunctions, either with immediately lethal consequences such as the formation of reentrant activation patterns which precede sudden cardiac death, or, by initiating a progressive degradation of pumping efficiency which, eventually, leads to severe morbidity and mortality, as it is common with pathologies such as heart failure.

Integrated models of cardiac function are playing a vital role in gaining better insight into the complex interplay of biological processes taking place across different spatial and temporal scales as well as between the different physics involved which are electrical activation and repolarization (bidomain equations), mechanical contraction and relaxation (nonlinear deformation equations), interaction of cardiac and vascular walls with the fluid they comprise (fluid structure interaction), and the flow of fluids within the cavities of the heart and the cardiovascular system (Navier-Stokes equations).

In this study we focus on numerical aspects of developing a strongly coupled model of ventricular electromechanics. Owing to the vastly different spatio-temporal scales which

govern electrical and deformation equations, and the significant computational burden imposed by solving both the bidomain as well as the nonlinear deformation equations, the development of a suitable numerical framework is a challenging task. The resulting discretized systems of equations are large, with several millions of unknowns, and are solved by making consequent use of parallelization techniques [1].

The Cardiac Arrhythmia Research Package (CARP) [2], a multiphysics solver framework developed in our group, is routinely used for solving i) the bidomain equations linked to a topologically realistic Purkinje system [3], ii) the interstitial diffusion equation and iii) the adjoint equations arising in optimal control problems applied to the cardiac monodomain equation. Additionally, standard post-processing problems such as iv) optical fluorescence mapping, as modeled by the photon diffusion equation [4], v) computations of the electrocardiogram (ECG) based on a pseudo-bidomain approach or extracellular potential recovery [5] or vi) the magnetocardiogram (MCG) can be solved. Building on these previous developments we extended our numerical framework to allow simulations of cardiac electromechanics, in which mechanical deformation is solved on the same high resolution grid as the bidomain equations. While this alleviates the data transfer problem between overlapping unstructured grids of different spatial resolution, it entails a significant increase in computational cost. This additional cost is addressed by developing and implementing a custom-tailored multigrid preconditioner for an iterative conjugate gradient solver for both CPU and GPU execution which shows good strong scaling characteristics, thus allowing to use a large number of compute cores to keep simulations tractable.

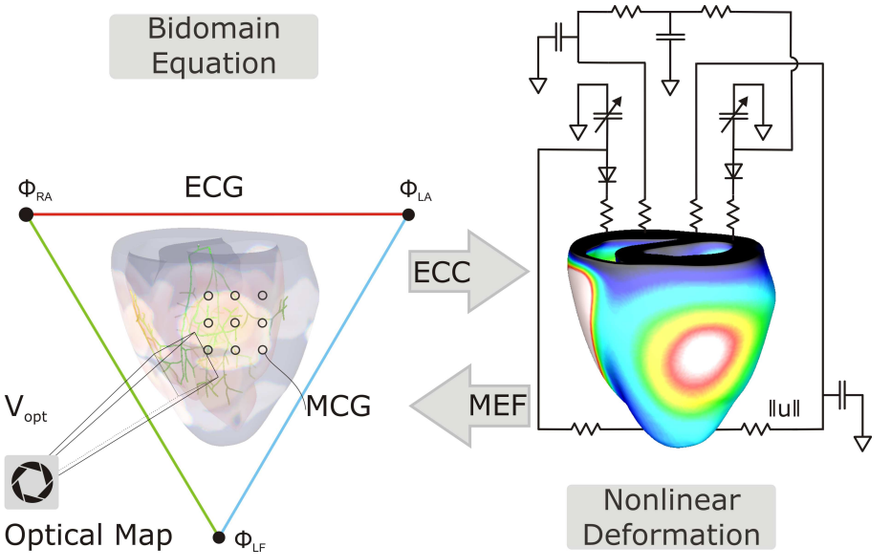

Figure 1: Illustration of CARP multiphysics modeling framework: A cardiac electrophysiology model, based on the bidomain equations including a realistic Purkinje system, is bidirectionally linked through excitation contraction coupling (ECC) and mechanoelectric feedback (MEF) to nonlinear mechanics. A lumped model of the cardiovascular system is used to regulate pressure-volume relations during ejection and filling phase. Electrocardiograms (ECG), magnetocardiograms (MCG) and optical fluorescence maps (V_{opt}) are computed or evaluated as a post-processing option.

2 METHODS

2.1 Model generation

Segmented medical image stacks of rabbit ventricles were fed into the image-based unstructured mesh generation software Tarantula (CAE Software Solutions, Eggenburg, Austria) which builds fully unstructured, boundary fitted, locally refined, hex-dominant hybrid tessellations [6]. Hybrid meshes were tessellated into tetrahedral elements and each finite element in the mesh was tagged either as electrically and mechanically active myocardium or as electrically and mechanically passive connective tissue. Orthotropic tissue properties were assigned using a rule-based approach [7]. Two rabbit ventricular models of different complexity were generated for running strong scaling benchmarks, an anatomically stylized model discretized at an average resolution of 250 μm (5 082 272 elements, 862 515 nodes), and an anatomically detailed model which resolves the ventricular geometry at a paracellular resolution of 100 μm (40 992 163 elements, 6 901 583 nodes). Both models were equipped with a topologically realistic model of the endocardial Purkinje system [3], where the latter model also accounted for the free-running Purkinje system which traverses the ventricular cavities.

2.2 Governing equations

The set of equations governing cardiac electromechanics is given by

$$\nabla \cdot (\boldsymbol{\sigma}_\mathrm{i} + \boldsymbol{\sigma}_\mathrm{e}) \nabla \phi_\mathrm{e} = -\nabla \cdot \boldsymbol{\sigma}_\mathrm{i} \nabla V_\mathrm{m}, \quad (1)$$

$$\nabla \cdot \boldsymbol{\sigma}_\mathrm{i} \nabla V_\mathrm{m} = -\nabla \cdot \boldsymbol{\sigma}_\mathrm{i} \nabla \phi_\mathrm{e} + \beta I_\mathrm{m}, \quad (2)$$

$$I_\mathrm{m} = C_\mathrm{m} \frac{\partial V_\mathrm{m}}{\partial t} + I_\mathrm{ion}(V_\mathrm{m}, \boldsymbol{\eta}), \quad (3)$$

$$V_\mathrm{m} = \phi_\mathrm{i} - \phi_\mathrm{e}, \quad (4)$$

$$\frac{\partial \boldsymbol{\eta}}{\partial t} = f(\boldsymbol{\eta}, V_\mathrm{m}, \sigma_\mathrm{a}), \quad (5)$$

$$-\operatorname{div} \boldsymbol{\sigma}(\mathbf{u}) = \mathbf{b}, \quad (6)$$

$$\boldsymbol{\sigma} = \boldsymbol{\sigma}_\mathrm{p} + \boldsymbol{\sigma}_\mathrm{a}, \quad (7)$$

$$\boldsymbol{\sigma}_\mathrm{p} = 2J^{-1}\mathbf{F}\frac{\partial \Psi(\mathbf{C})}{\partial \mathbf{C}}\mathbf{F}^\mathrm{T}, \quad (8)$$

$$\boldsymbol{\sigma}_\mathrm{a} = \sigma_\mathrm{a}\left(\hat{\mathbf{f}} \otimes \hat{\mathbf{f}}\right), \quad (9)$$

$$\sigma_\mathrm{a} = h(V_\mathrm{m}, \boldsymbol{\eta}, \lambda, \dot{\lambda}). \quad (10)$$

In the bidomain equations (1)-(5) describing electrophysiology, ϕ_i and ϕ_e are the intracellular and extracellular potentials, respectively, $V_\mathrm{m} = \phi_\mathrm{i} - \phi_\mathrm{e}$ is the transmembrane voltage, $\boldsymbol{\sigma}_\mathrm{i}$ and $\boldsymbol{\sigma}_\mathrm{e}$ are the intracellular and extracellular conductivity tensors, respectively, β is the membrane surface to volume ratio, I_m is the transmembrane current density, C_m is the membrane capacitance per unit area, and I_ion is the membrane ionic current density which depends on V_m and a set of state variables, $\boldsymbol{\eta}$. Deformation is governed by (6)-(9) with (9) linking electrics and mechanics.

The deformation is governed by the equilibrium equation (6) with unknown displacement field $\mathbf{u}$. The stress tensor $\boldsymbol{\sigma}$ consists of a passive (8) and an active contribution (9), while the latter depends on the normalized myocyte orientation $\hat{\mathbf{f}}$. Here, $\mathbf{F}$ is the deformation gradient, $\mathbf{C} = \mathbf{F}^\mathrm{T}\mathbf{F}$ is the right Cauchy-Green tensor, and Ψ is a function which describes the strain energy density of the specific material. Using a particular cell model, indicated by the function $h(\bullet)$, the scalar-valued active stress term σ_a is computed (10), thus providing the link for ECC. To specify prescribed displacements or tractions, e.g., pressure, additional boundary conditions are incorporated into the external time-dependent load vector $\mathbf{b}$, for which a state machine is used to account for different loading conditions during the four phases of a full cardiac cycle, i.e., isovolumetric contraction, ejection, isovolumetric relaxation and filling phase.

3 RESULTS

The computation times were obtained using a monodomain model for the electrics and an orthotropic myocardium model for the mechanics. The benchmarks were performed over 100 time steps (approx. 5 Newton steps for each mechanics step) using 16 to 640 CPU cores running on the PRACE high performance computing facility CURIE. Results of a strong scaling benchmark for both geometries, see Sect. 2.1, are summarized in Fig. 2.

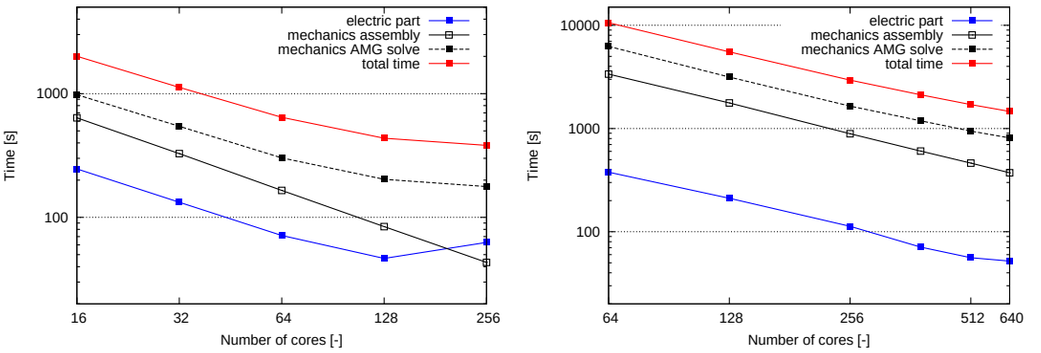

Figure 2: For the coarser model (left panel) we have strong scaling up to 128 cores for the electric part and up to 256 cores for the mechanics solve. For a higher amount of cores the number of degrees of freedom per subdomain gets too small and the increasing MPI communcation impedes better scaling properties. For the more detailed model (right panel) both the electric part and the mechanics solve scale up to 640 cores. In both test cases the assembling of the stiffness matrices (black lines) scales almost perfectly since here the communication costs are negligible.

4 CONCLUSIONS

Strong scaling benchmarks suggest that strongly coupled simulations of ventricular electromechanics are becoming feasible. Computational costs for electromechanical monodomain simulations are comparable to pure electrophysiology simulations using a full bidomain model.

REFERENCES

[1] S. Niederer, L. Mitchell, N. Smith, and G. Plank, Simulating human cardiac electrophysiology on clinical time-scales. *Front Physiol*, 2, p. 14, 2011.

[2] E. J. Vigmond, R. Weber dos Santos, A. J. Prassl, M. Deo, and G. Plank, Solvers for the cardiac bidomain equations. *Prog Biophys Mol Biol*, 96(1-3), pp. 3-18, 2008.

[3] E. J. Vigmond, C. Clements, Construction of a computer model to investigate sawtooth effects in the purkinje system. *IEEE Trans Biomed Eng*, 54(3), pp. 389-399, 2007.

[4] M. J. Bishop et al., The role of photon scattering in voltage-calcium fluorescent recordings of ventricular fibrillation. *Biophys J*, 101(2), pp. 307-318, 2011.

[5] M. J. Bishop and G. Plank, Representing cardiac bidomain bath-loading effects by an augmented monodomain approach: application to complex ventricular models. *IEEE Trans Biomed Eng*, 58(4), pp. 1066-1075, 2011.

[6] A. J. Prassl et al., Automatically generated, anatomically accurate meshes for cardiac electrophysiology problems. *IEEE Trans Biomed Eng*, 56(5), pp. 1318-1330, 2009.

[7] J. D. Bayer et al., A novel rule-based algorithm for assigning myocardial fiber orientation to computational heart models. *Ann Biomed Eng*, 40(10), pp. 2243-2254, 2012.

3rd International Conference on Computational and Mathematical Biomedical Engineering - CMBE2013
16-18 December 2013, Hong-Kong
P. Nithiarasu and R. Löhner (Eds.)

Complex modeling and estimation of cardiac tissue anisotropy

A. Nagler, C. Bertoglio and W.A. Wall
Institute for Computational Mechanics, Technische Universität München, Germany
nagler,bertoglio,wall@lnm.mw.tum.de

SUMMARY

In cardiac modeling, after the geometry segmentation and mesh generation, the next crucial step is to represent the myocardium histology, namely the intricate distribution and orientation of muscle fibers, whose coordinated contraction results in the systole of the heart [11, 6]. Most fiber representations to date employ rule-based models (RBM). These models are often oversimplified as regards the representation of the actual fiber histology, see e.g. [9, 13, 2]. In this work we specify how we estimate, through the solution of an inverse problem, the degrees of freedom of a RBM of high complexity, namely, the degrees-of-freedom of the fiber angle distribution on the epi- and endocardial surfaces, from noisy fiber direction measurements coming from magnetic-resonance imaging (MRI) - the so called Diffusion Tensor MRI [1, 10, 3]. This strategy allows to: (a) reconstruct the fiber (or generally diffusion tensor) in the whole heart geometry from *in vivo*-like multislice measurements and (b) to reuse the estimated parameters in new geometries where the subject-specific fiber data is not available.

Key Words: *cardiac fiber architechture, difusion tensor imaging, heart biomechanics*

1 METHODS

The rule-based fiber model. The first step in the construction of our generic RBM for the fibers is to define a surface patch from heart-specific surface coordinates (axial ξ and circumferential η, see Figure 1). Then, at each vertex of the patch we define a set of degrees-of-freedom Θ_i, $i = 1, \dots, p$ which we use in the construction of a bilinear field $\theta(x) = \sum_{i=1}^{p} N_i(\xi(x), \eta(x))\Theta_i$ on the heart surface. In our context, $\theta(x)$ corresponds to the angle of the fiber vector on the surface with respect to the circumferential and long axis directions. This surface fiber vectors and then lifted to the heart volume using Poisson interpolation as done in [13]. Hence, choosing different values for Θ_i we can obtain complex representations for the surfacic and then volumetric fibers fields, see examples in the next section.

The estimation algorithm. In order to get realistic fiber distributions we aim to estimate the degrees-of-freedom Θ_i from measured patient data. For this purpose we adopt the Reduced-Order Unscented Kalman Filter (ROUKF) [7] (but assuming only one measurement snapshot), inspired from [4, 5]. It does not require any tangent operator and allows to run the estimation with a computational cost of the same order of the forward problem since it is highly parallelizable.

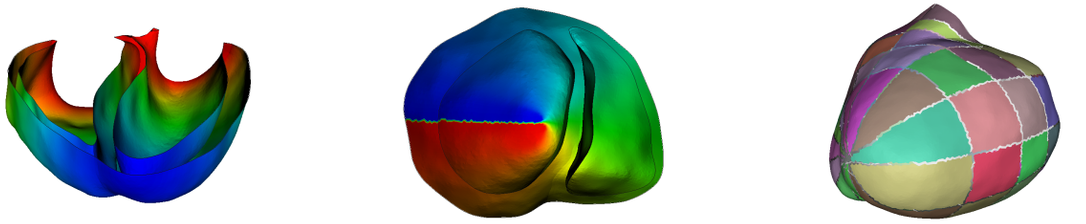

(a) Long-axial coordinate ξ (b) Circumferential coordinate η (c) Sample epicardium patch

Figure 1: Example for the construction of the surface patches.

2 RESULTS

Estimation from 3D-DTMRI. In Figure 2 we show compare three different fiber organizations: a RBM with constant surface angle, i.e. $\theta = 60^o$, a fiber set obtained from 3D-DTMRI [1], and the RBM estimated from the same 3D-DTMRI using the ROUKF with $p = 144$. We also illustrate the contraction patterns arising from different fiber organizations. Notice that we do constraint nowhere the heart in order to highlight the effect of the fiber orientations in the contraction pattern. Since the estimated fibers are in good agreement with DT-MRI data in the left ventricle, the contraction pattern too, but using the RBM we obtain a smooth stress distribution.

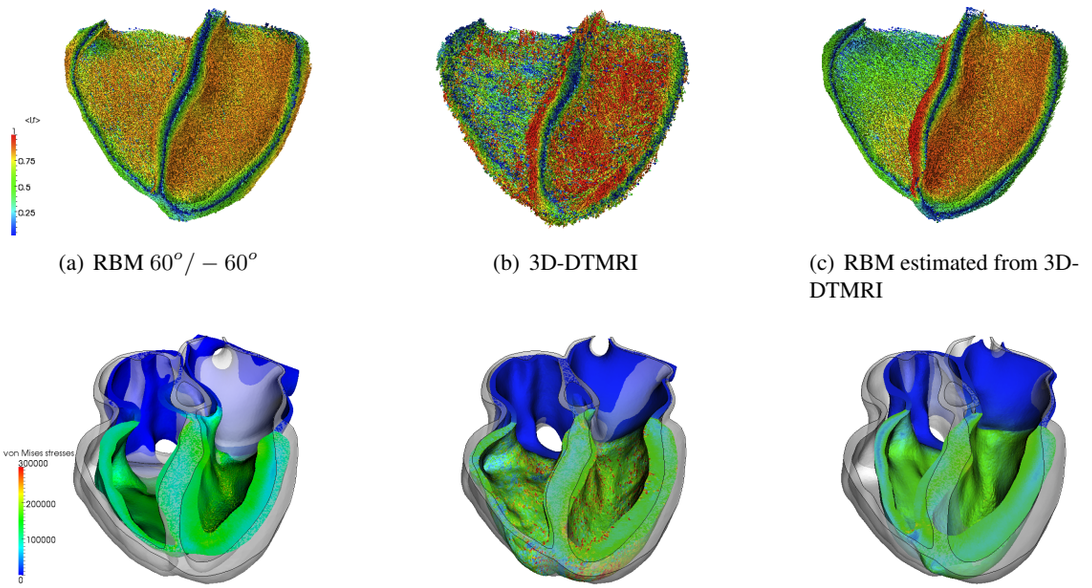

(a) RBM $60^o/-60^o$ (b) 3D-DTMRI (c) RBM estimated from 3D-DTMRI

(d) RBM $60^o/-60^o$ (e) DTMRI (f) Estimated from DTMRI

Figure 2: Top: Ventricular fiber organization, colored by the magnitude of long-axis component. Bottom: Snapshots of the contraction simulation, superposed with the initial geometry (grey).

Estimation from multislice DTMRI. Even though the estimated RBM from 3D-DTMRI provides a valuable tool for more realistic heart biomechanical analysis, this type of data is still far from being able to be acquired in vivo. However, the same framework can be applied by using

[1] Openly available on http://gforge.icm.jhu.edu/gf/project/dtmri_data_sets/

multislice (MS-)DTMRI (i.e., fiber data acquired on few slices). Hence, we undersampled the 3D-DTMRI data into the MS-DTMRI type of data in order to get the resolution typically obtained to date, see e.g. [12] and references therein. The results are presented in Figure 3.

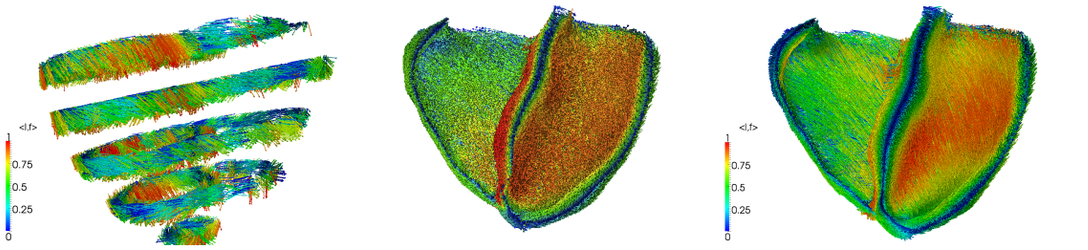

(a) MS-DTMRI (b) RBM estimated from 3D-DTMRI (c) RBM estimated from MS-DTMRI

Figure 3: Multislice fiber measurements and estimated ventricular fiber organizations.

3 CONCLUSIONS

We introduced an extension of the methodology, introduced in [8], for estimating the degrees-of-freedom of a Ruled Based Model (RBM) for cardiac fiber architecture from DT-MRI data. We first detailed the mathematical fiber RBM. Then, we outlined the estimation algorithm, namely a reduced-order Unscented Kalman Filter (ROUKF), in order to minimize the discrepancy between measured and model fiber distribution by optimizing the degrees-of-freedom of the RBM. We show tests using 3D-DTMRI and multislice DTMRI.

We are also currently extending the general fiber model for the whole Difusion Tensor. Doing so, the three principal directions of the model can be simultaneously estimated from the diffusion weighted images directly. Hence, if the probability distribution function of the noise in the diffusion weighted images is known (are reasonably assumed), this would allow to compute reliable confidence intervals of the estimated degrees-of-freedom and on the measurement noise in a bayesian estimation framework.

ACKNOWLEDGEMENT

The results presented in this article are part of the *Advanced Cardiac Mechanics Emulator*, an initiative supported by the Institute for Advanced Study (TU München) and one of its fellow Prof. Michael Ortiz (Caltech), whom we sincerely thank. We also thank to Radomír Chabiniok (King's College London) for the valuable discussions. Finally to Drs. Patrick A. Helm and Raimond L. Winslow at the Center for Cardiovascular Bioinformatics and Modeling and Dr. Elliot McVeigh at the National Institute of Health for provision of data.

References

[1] P.J. Basser, J. Mattiello, and D. Lebihan. Estimation of the effective self-diffusion tensor from the nmr spin echo. *Journal of Magnetic Resonance, Series B*, 103(3):247 – 254, 1994.

[2] J.D. Bayer, R.C. Blake, G. Plank, and N.A. Trayanova. A novel rule-based algorithm for assigning myocardial fiber orientation to computational heart models. *Annals of Biomedical Engineering*, 40:2243–2254, 2012.

[3] Urs Gamper, Peter Boesiger, and Sebastian Kozerke. Diffusion imaging of the in vivo heart using spin echoesconsiderations on bulk motion sensitivity. *Magnetic Resonance in Medicine*, 57(2):331–337, 2007.

[4] S. Julier, J. Uhlmann, and H.F. Durrant-Whyte. A new approach for filtering nonlinear systems. In *American Control Conference*, pages 1628–1632, 1995.

[5] S. Julier, J. Uhlmann, and H.F. Durrant-Whyte. A new method for the nonlinear transformation of means and covariances in filters and estimators. *Automatic Control, IEEE Transactions on*, 45(3):477–482, 2000.

[6] I. J. LeGrice, B. H. Smaill, L. Z. Chai, S. G. Edgar, J. B. Gavin, and P. J. Hunter. Laminar structure of the heart: ventricular myocyte arrangement and connective tissue architecture in the dog. *American Journal of Physiology - Heart and Circulatory Physiology*, 269(2):H571–H582, 1995.

[7] P. Moireau and D. Chapelle. Reduced-order Unscented Kalman Filtering with application to parameter identification in large-dimensional systems. *COCV*, 17:380–405, 2011. doi:10.1051/cocv/2010006.

[8] A. Nagler, C. Bertoglio, M. Gee, and W. Wall. Personalization of cardiac fiber orientations from image data using the Unscented Kalman Filter. *LNCS 7945*, pages 132–140, 2013.

[9] M. Potse, B. Dube, J. Richer, A. Vinet, and R.M. Gulrajani. A comparison of monodomain and bidomain reaction-diffusion models for action potential propagation in the human heart. *IEEE Trans. Biomed. Eng.*, 53:2425–2435, 2006.

[10] D. F. Scollan, Alex Holmes, Raimond Winslow, and John Forder. Histological validation of myocardial microstructure obtained from diffusion tensor magnetic resonance imaging. *American Journal of Physiology - Heart and Circulatory Physiology*, 275(6):H2308–H2318, 1998.

[11] Daniel D. Streeter, Henry M. Spotnitz, Dali P. Patel, John Ross, and Edmund H. Sonnenblick. Fiber orientation in the canine left ventricle during diastole and systole. *Circulation Research*, 24(3):339–347, 1969.

[12] Nicolas Toussaint, Maxime Sermesant, ChristianT. Stoeck, Sebastian Kozerke, and PhilipG. Batchelor. In vivo human 3D cardiac fibre architecture: Reconstruction using curvilinear interpolation of diffusion tensor images. In Tianzi Jiang, Nassir Navab, JosienP.W. Pluim, and MaxA. Viergever, editors, *Medical Image Computing and Computer-Assisted Intervention MICCAI 2010*, volume 6361 of *Lecture Notes in Computer Science*, pages 418–425. Springer Berlin Heidelberg, 2010.

[13] Jonathan Wong and Ellen Kuhl. Generating fibre orientation maps in human heart models using poisson interpolation. *Computer Methods in Biomechanics and Biomedical Engineering*, pages 1–10, 2012. PMID: 23210529.

Segmentation & Registration for Biomedical Applications

3rd International Conference on Computational and Mathematical Biomedical Engineering – CMBE2013
16-18 December 2013, Hong-Kong
P. Nithiarasu and R. Löhner (eds)

Tracing vocal-fold vibrations using level-set segmentation method

Tailong Shi, Grace Ling and Yuling Yan*

Department of Bioengineering
Santa Clara University
500 El Camino Real, Santa Clara
*Address all correspondence to this author: yyan1@scu.edu

SUMMARY

High-speed digital imaging (HSDI) of the larynx can provide important information on the vocal fold kinematics. This information is useful for better understanding the mechanism of phonation and assisting clinical assessment of voice disorders. Automatic tracing of the vocal fold vibration is a key step for meaningful analysis and subsequent characterization of vocal fold vibrations, which are known to correlate with voice quality and health condition. We introduce a new approach that combines the use of level-set segmentation method and motion cue to exact vocal fold displacements. This approach is applied to videokymogram (VKG)-form image, obtained from a sequence of laryngeal images captured by the HSDI. To utilize the motion cue for more effective level-set based segmentation on the VKG, we construct a so-called STD (standard deviation) image by mapping the pixel-based measure of temporal intensity dispersion from the initial HSDI sequence. The STD image maps the extent of vocal fold motion, and followed by threshold operation, a region of interest (ROI) that encloses vocal fold motion, or glottis region, is identified. The performance of the proposed approach is evaluated using clinical datasets representing both normal and pathological voice conditions.

Key Words: *High-speed laryngeal imaging, videokymogram, level set image segmentation, vocal fold motion, region of interest*

1 INTRODUCTION

High-speed digital imaging (HSDI) of the larynx, also referred to as high-speed laryngeal imaging, or high-speed videoendoscopy, has now become a clinical reality. The HSDI systems typically record images of the vibrating vocal folds at 2000 ~ 4000 frames per second, fast enough to resolve a specific, sustained phonatory vocal fold oscillation (100~400 Hz in speaking voice) [1].

Vocal-fold vibration is the key dynamic event responsible for voice production, and the vibratory characteristics of the vocal folds correlate closely with voice quality and voice condition. However, credible analysis and characterization of the vocal fold vibration requires accurate and effective exaction of the vocal fold displacements from the sequence of glottis images captured by the HSDI. One way to exact vocal fold motion is to segment the glottis image frame-by-frame using threshold, region-grow [2], snake-based or the active contour methods [3-5]. After the glottis contours are delineated from sequential segmentation process, both glottis area waveform and vocal fold displacements at specific location can be obtained.

Videokymography is an alternative laryngeal imaging modality [6] in which each vibratory glottis cycle is documented in terms of a sequence of several images, and can be acquired directly from a single-line camera, or extracted from a sequence of images captured by the HSDI system [7]. In this paper, we use single images in form of VKG that are constructed using a sequence of HSDI images for viewing glottal cycles and local vocal-fold motions. The level set segmentation method is applied to individual VKG image to exact the bilateral vocal fold displacements at specific location across the vocal folds.

2 METHODOLOGY

While applying the level set method for the segmentation of VKG image, we need to address two issues: 1), where to set the initial contour for the level set iteration, and 2), how to eliminate the interference of the background (outside of the glottis region). Here we introduce the so-called STD (standard deviation) image, derived from the vocal fold motion cue. The STD image provides a map of the vocal fold motion based on which a region of interest (ROI) can be identified, and subsequently, the segmentation process can be performed within the ROI applied to the VGK image. The proposed general approach is illustrated in the flow chart (Fig. 1).

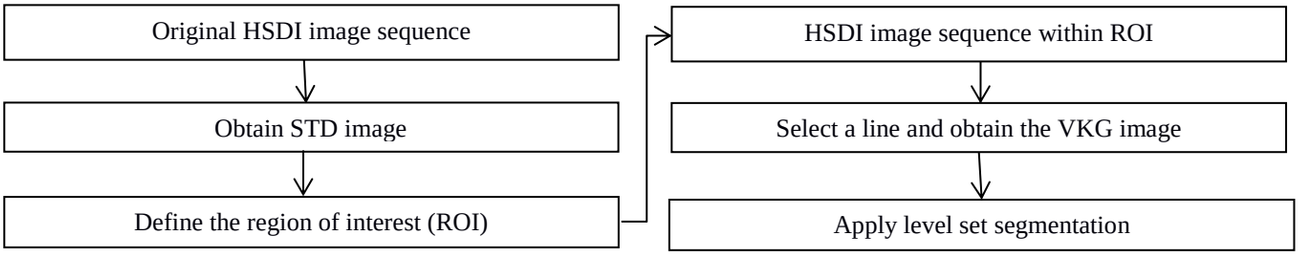

Fig. 1. The flow chart of the proposed approach

2.1 VKG image

To generate the VKG, we select an image frame and a measuring line position (left, Fig. 2), and then generate a composite image by arranging the selected line images from a sequence of successive image frames in the HSDI recording in vertical axis representing frame number or time; the time between two successive image frames is 0.5 msec (with an acquisition rate of 2000 frames per second). The resultant composite image, known as videokymogram, or VKG, is a unique and at-a-glance display of multiple glottis cycles (right, Fig. 2). VKG allows visualization of key features of vocal fold vibrations e.g. aperiodic vibration and left-right asymmetry among other important characteristics within a single image.

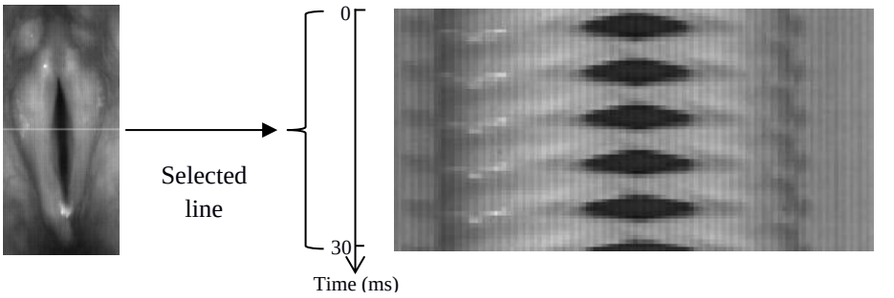

Fig. 2. The VKG image extracted from HSDI dataset. Left: one frame of the HSDI sequence; Right: the resultant VKG image. The white line on the left image indicates the scanning position for the videokymogram.

2.2 Glottis segmentation using level set method

Active contour models implemented via level set methods [8,9] have been proposed to solve numerous image segmentation problems [10-13]. The basic idea is that a contour C in a domain Ω can be represented by the zero level set of a higher level embedding function $\Phi: \Omega \rightarrow \mathbb{R}$. Rather than directly evolving the contour C, one evolves the level set function Φ. The embedding function Φ is defined as the signed distance function (SDF) with $\Phi > 0$ inside the shape, $\Phi < 0$ outside the shape and $|\nabla \Phi| = 1$ almost everywhere. The evolution of the level set function Φ is governed by a partial differential equation (PDE). Consider the following curve evolution equation:

$$\frac{dC}{dt} = F\vec{N} \tag{1}$$

which evolves the curve C according to the speed field F in the normal direction $\vec{N}$. This evolution is achieved by numerically solving the following PDE on the regular grid

$$\frac{d\Phi}{dt} + F|\nabla \Phi| = 0 \tag{2}$$

Fig. 3 (b) shows the VKG after edge contour detection using level set method. Although the original VKG image, as shown in Fig.2 (a), is embedded in strong noise (a number of vertical stripes are observed in the original VKG image), we still achieved a reasonably accurate contour detection using the level set method. Compared with the result using Otsu method [14], as shown in Fig. 3 (c), it is clear that the level set method is more effective and robust in a noisy background.

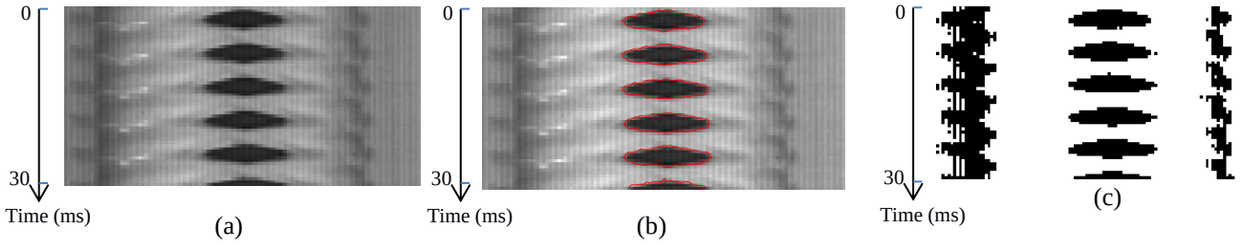

Fig. 3. VKG images. (a) Before segmentation, (b) After the segmentation using level set method. (c) After Otsu threshold segmentation.

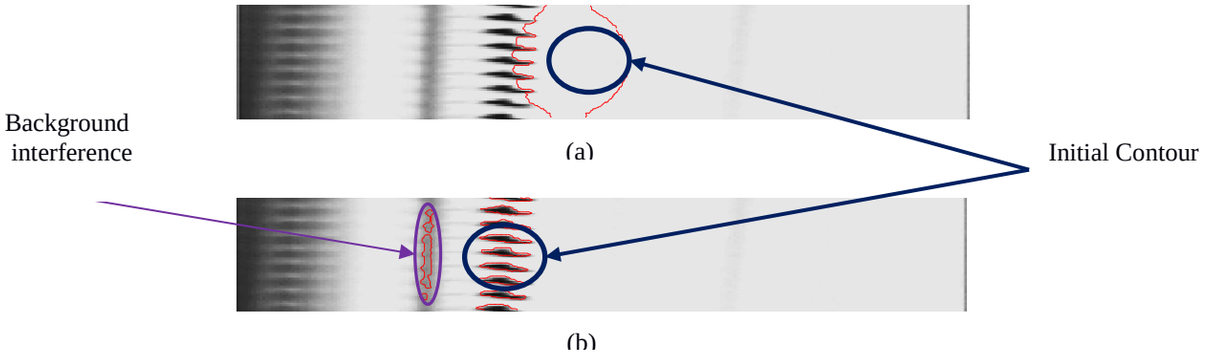

Fig. 4. Results of segmentation using level set method. (a) Initial contour centered at the middle. (b) Manually adjusted initial contour.

However, two problems were encountered when the level set method was applied to more VKG images. One is the automatic selection of the initial contour position in level set method. Fig.4 shows the results of segmentation with different choices of initial contour position. Although the results are significantly improved after manually adjust the position of the initial contour, as shown in the image at right, an automatic selection is desired, for example, to place the initial contour at the center of the image. The other problem is the interference from the background. Fig.4 (b) shows an example of erroneous contour detection owing to the background.

To address the above-mentioned problems, we define a region of interest (ROI) to restrict the segmentation within the ROI. The ROI is constructed using a so-called STD image as introduced in the following section.

2.3 Define ROI using STD image

In normal voicing, the vibrating vocal folds open and close quasi-periodically, thus causing a change in gray-scale brightness level within the glottis region, or region of the vocal-fold opening. In contrast, there is little change in gray level values outside of the glottis region. This motion cue can be effectively used to improve the accuracy and efficiency of the VKG segmentation. The STD image is constructed based on the intensity variation in sequential glottis images at corresponding spatial location. The STD(x, y) value for each pixel location (x, y) of the STD image is calculated as follows:

$$Std(x,y) = \frac{1}{N}\sum_{i=1}^{N}\sqrt{(I_i - \bar{I})^2} \tag{3}$$

where, N is the number of image frames used to construct the STD image, I_i represents the pixel intensity value in the sequential images at the same location (x, y), and $\bar{I}$ is the average value of I_i. It is clear that the STD (x, y) value indicates the extent of the intensity variation at each pixel location (x, y) over the glottis cycles.

We used a sequence of 60 images (approximately 5 glottis cycles) to construct the STD image (displayed in pseudo color in Fig. 5). This image is used to identify a region enclosing motion of the vocal folds. A brighter pixel in the STD image refers to a greater value of STD(x, y) calculated from the intensity profile of the pixel. Fig. 5 (b) shows the intensity profile of a bright pixel location labeled 1 in Fig. 5 (a), in contrast, the black pixel at a location labeled 2 has a smaller STD value as calculated from its intensity profile as shown in Fig. 5 (c). We can observe that the bright region in the STD image represents the region of interest where the vocal fold motion occurs, while the darker region represents the background.

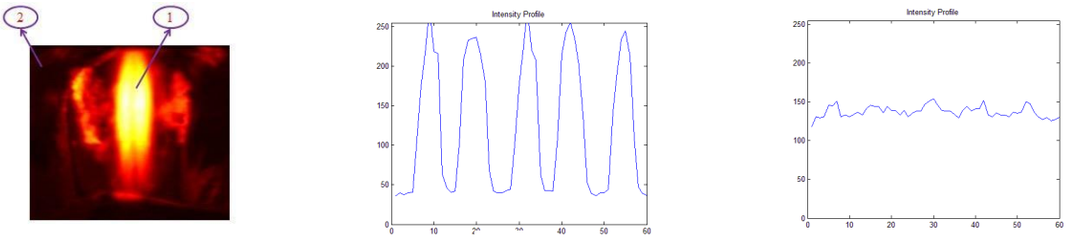

(a) (b) (c)

Fig. 5. (a) STD image. (b) Intensity profile of point 1 in the STD image. (c) Intensity profile of point 2 in the STD image.

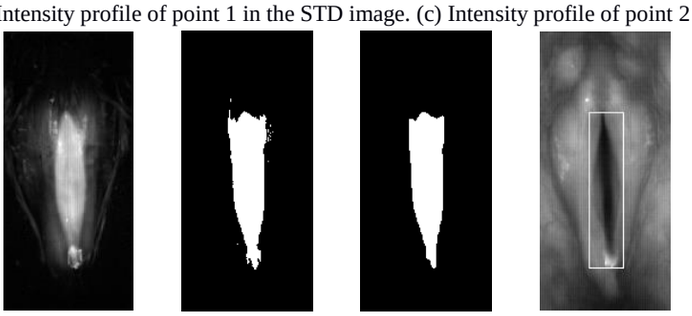

(a) (b) (c) (d)

Fig. 6. (a) STD image. (b) Binary image obtained from STD image. (c) Binary image after morphological operation. (d) The rectangle representing the ROI is overlaid onto the initial glottis image.

To define the boundary of maximum glottis region, first we obtain the binary image by performing Otsu threshold segmentation to the STD image and then morphological operation is applied to remove the isolated areas. This is followed by defining the boundary of the remaining region of the binary image to serve as ROI. The results are shown in Fig. 6 where the outline of the region of maximum motion is delineated (Fig. 6 (d)). Since the ROI encloses entire or part of the glottis where vocal fold motion occurs, it can help solve the two problems mentioned above.

3 EXPERIMENTAL RESULTS

After restricting the sequence of HSDI images to the ROI, we obtain a truncated VKG image. This resultant new VKG image eliminates the unwanted background while encloses the region of vocal fold motions. Fig.7 shows the VKG image extracted from a sequence of 60 images within the ROI. With the VKG image restricted within the ROI, we can automatically select the center of the

image to position the initial contour, thus address the problem encountered in the contour detection using level set method. Furthermore, since the background is now minimized the accuracy in segmentation is significantly improved.

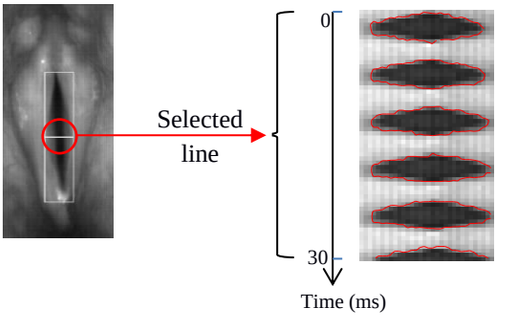

Fig.7. VKG image extracted from a sequence of 60 HSDI images within ROI. Left: one image frame in the sequence - the rectangle indicates the ROI, and the mid-line indicates the line position for the VKG; Right: the resultant VKG.

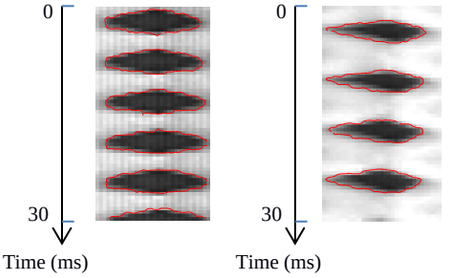

Fig. 8. VKG image after segmentation. Left: normal voice condition; Right: vocal pathology.

Fig. 8 shows two VKG images representing normal voice condition (left) and vocal pathology (right) respectively. After restricting the ROI area on the HSDI image sequence, the level set method successfully detected the edge contour of the VKG images. It is observed from the VKG that left-right asymmetry existed in the patient's bilateral vocal fold vibrations, while the vibrations are almost symmetric in the left and right folds in the normal subject.

4 CONCLUSION

Tracing vocal fold motion is a key step towards quantitative analysis of vocal fold vibrations and assessment of voice disorders. A new approach is proposed that combines level-set segmentation method and motion cue to exact bilateral vocal fold displacements from VKG image generated from the sequence of images captured by HSDI. Prior to applying level set algorithm, the vocal fold motion cue is used to improve the accuracy and efficiency of the segmentation. In particular, the STD image is constructed based upon the measure of temporal intensity variation (std value) at each pixel location. Following simple threshold and morphological operations, the ROI is defined, within which a restricted segmentation is performed on the VKG image. We have shown that this approach generated much improved segmentation results.

5 ACKNOWLEDGEMENT

We would like to thank Dr. Krzysztof Izdebski for his help with the acquisition of clinical HSDI data that were used in this work.

REFERENCES

[1] Y. Yan, K. Ahmad, M. Kunduk, and D. Bless, Analysis of vocal fold vibrations from high-speed laryngeal images using Hilbert transform-based methodology, *J.Voice*, Vol. 19, No. 2, 161-175, 2005

[2] Y. Yan, X. Chen, and D. Bless, Automatic tracing of vocal-fold motion from high-speed digital images, *IEEE Trans. Biomed. Engr*., Vol. 53, No.7, 1394-1400, 2006

[3] Y. Yan, G. Du, C. Zhu and G. Marriott, Snake based automatic tracing of vocal-fold motion from high-speed digital images, *IEEE Int. Conf. on Acoustics, Speech and Signal Processing*, 593-596, Mar. 2012.

[4] S.Z. Karakozoglou, N. Henrich, C. d'Alessandro, and Y. Stylianou, Automatic glottal segmentation using local-based active contours and application to glottovibrography, *Speech Comm*., Vol. 54(5), 641–654, June 2012.

[5] C.Manfredi, L. Bocchi, N. Migali, G. Cantarella, Objective vocal fold vibration assessment from videokymographic images, *Biomedical Signal Processing and Control*, 1, 129-136, 2006.

[6] J.G. Svec, H.K. Schutte, Videokymography: high-speed line scanning of vocal fold vibration, *J. Voice*, 10, 201–205, 1996.

[7] H.Larsson, S. Hertegard, P.-A. Lindestad, B. Hammarberg, Vocal fold vibrations: high-speed imaging, kymography and acoustic analysis, *Laryngoscope*, 110, 2117–2122, 2000.

[8] J. Sethian, Level Set Methods and Fast Marching Methods: Evolving Interfaces in Computational Geometry, Fluid Mechanics, Computer Vision, and Materials Science. Cambridge, U.K.*: Cambridge Univ. Press*, 1999.

[9] S.Osher and R. Fedkiw, Level Set Methods and Dynamic Implicit Surfaces. New York: *Springer Verlag*, 2002.

[10] A. Skalski, T. Zielinski, D. Deliyski, Analysis of vocal folds movement in high speed videoendoscopy based on level set segmentation and image registration, *Int. Conf. on Signals and Electronic Systems*, 223-226, 2008.

[11] S. Kichenassamy, A. Kumar, P. Olver, A. Tannenbaum, and A. Yezzi, Gradient flows and geometric active contour models, in *Proc. ICCV*, Boston, MA, 810–815,1995.

[12] M. Bertalmio, G. Sapiro, and G. Randall, Morphing active contours: A geometric approach to topology-independent image segmentation and tracking, *Proc. Int. Conf. Image Processing*, Vol. 3, 318–322, 1998.

[13] T. Chan and L. Vese, Active contours without edges, *IEEE Trans. Image Process*., Vol. 10, No. 2, 266–277, Feb. 2001.

[14] N. Otsu, A threshold selection method from gray-level histograms, *IEEE Trans. Sys., Man and Cyber.*, Vol. 9, No. 1, 62-66, 1979

3rd International Conference on Computational and Mathematical Biomedical Engineering - CMBE2013
16-18 December 2013, Hong-Kong
P. Nithiarasu and R. Löhner (Eds.)

Interactive segmentation of media-adventitia border in OCT

Jonathan-Lee Jones*, Ehab Essa, Xianghua Xie*** and James Cotton******
*Department of Computer Science, Swansea University, UK, csjj@swansea.ac.uk
**Department of Computer Science, Swansea University, UK, csehab@swansea.ac.uk
***Department of Computer Science, Swansea University, UK,x.xie@swansea.ac.uk
****The Royal Wolverhampton NHS Trust, jamescotton@nhs.net

SUMMARY

In this paper, we present an approach for user assisted segmentation of media-adventitia border in OCT images. This interactive segmentation is performed by a combination of point based soft constraint on object boundary and stroke based regional constraint. The edge based boundary constraint is imposed through searching the shortest path in a three-dimensional graph, derived from a multi-layer image representation. The user points act as attraction points and are treated as soft constraints, rather than hard constraints that the segmented boundary has to pass through the user specified points. User can also use strokes to specify foreground (region of interest). The probabilities of region of interest for each pixel are then calculated and their discontinuity is used to indicate object boundary. This combined approach is formulated as an energy minimization problem that is solved using a shortest path search algorithm.

Key Words: *Image segmentation, graph segmentation, Dijkstra shortest path, OCT segmentation, media-adventitia border.*

1 INTRODUCTION

Optical Coherence Tomography (OCT) imaging technique is a catheter based technology, used in cardiology diagnosis. This catheter based approach is widely used to assess the severity of any stenosis present and to categorize their morphology. It also allows for the measurement of vessel diameter the location of any lesions, as well as many other clinical and therapeutic studies. In most OCT images, a cross-section of the arterial wall is proceeded, with three regions: the lumen, the vessel (made up of the intima and media layers), and the adventitia surrounding the vessel wall. The media-adventitia border is the dividing layer representing the outer arterial wall.

There have been many different approaches to the problem of segmenting medical images, such as IVUS images, e.g. [12, 11, 6, 5, 7, 15, 2, 10, 9]. These can be broadly categorized into fully automatic methods, or methods that allow user interactions, which can act as a basis for segmenting the similar images produced by OCT. Methods incorporating user prior knowledge into segmentation hence is often necessary and has been shown to be an effective approach [3, 7]. For instance, in [7] Ehab *et al.* incorporated a shape prior into graph cut construction to regularize segmentation of media-adventitia border. However, these approaches generally require significant amount of training data and model re-training is often necessary in order to adapt to new dataset. User initialization is an alternative approach to transfer expert knowledge into segmentation, e.g. [1, 13, 14, 16, 4, 8, 17, 18, 19, 20]. However, most user interactions are limited to either boundary

based landmark placement or strokes indicating foreground and background regions. in this work, we propose an approach to combine these two different types of user interactions, i.e. boudary based and region based, to segment media-adventitia border in OCT. The user points, are treated as soft constraint, instead of hard constraint in most interactive segmentation methods. We show that this soft user constraint allows effective combination of boundary and region based features. The method is compared on an OCT dataset with manually labelled "ground-truth" and compared against state-of-the-art techniques.

2 METHOD AND RESULTS

The proposed method involves the user selecting a series of points on the image and in order to enhance the image segmentation, the user can also select areas for foreground using strokes. These then form the basis of the energy function.

By assuming the user points are in a sequential order, we construct a multi-layer graph with each layer encapsulating a single individual user point. The segmentation problem is then transformed into searching the shortest path in this layered graph.

Conventionally, user input to segmentation is focused on foreground and background specification [1, 13, 14, 16]. For example, in [13], the user interaction consists of dragging a rectangle around the object of interest and in doing so the user specifies a region of background that is modeled in separating the foreground object. Several other methods require user to specify points on the object boundaries instead [4, 8, 17]. However, more often than not, these boundary based user points are treated as anchor points and the segmentation path has to go through them. This kind of hard constraint is not always desirable. It does not allow imprecise user input, and it can lead to difficulties in combining region based and boundary based approaches as discrepancy between different object descriptions is generally expected. Notably, in [17] the authors introduced soft constraint user point by embedding the user constraint in distance functions. The segmentation result is considered to be the shortest path to loosely connect the user points. In this work, we follow this approach to treat boundary based user points. However, we also allow user to place region based strokes. These strokes are used to model foreground probability, and the discontinuity in foreground probability indicates the presence of object boundary. We combine these two types user input with image features in an energy functional which is then optimized using graph partitioning through finding the shortest path from the first to last user points.

We construct a layered graph from the set of user points. The user points are assumed to be placed in a sequential order, which reduces the complexity from NP-hard to polynomial time.

For each user point, $X_i, i \in \{1, 2, ..., n\}$, we create a layer of directed graph. In that way we have a series of layers equal to the number of user points n, plus an additional layer to ensure a closed curve. This results in a multi-layer directed graph, $G = (V, E)$. For each pixel p, there exits an edge e to each of its neighboring 8 pixels on the same layer. Therefore, a pair of neighboring pixels $(p, q) \in N$ with a corresponding edge $e = (v_p, v_q)$ also have an edge to the corresponding point on the superseding layer $e = (v_{p_n}, v_{p_{n+1}})$. For each edge, we assign a weight w to build a weighted graph (G, w). These weights are calculated based on whether the edge is internal to a layer (w_i) or trans-layer (w_x). By creating the graph in this way, an order is established with the user points.

The edges on the directed layered graph are categorized as internal edges w_i within individual layers and interlayer edges w_x. The weighting for these two types edges is assigned differently.

The internal edges are assigned with two types of weights, i.e. boundary based edge weights and region based edge weights. The boundary based edge weights are calculated based on the

magnitude of image gradients. The region based edge weights are computed from foreground probabilities, obtained from the user strokes and the attraction force imposed by user points and is materialized through the interlayer edge weights w_x.

The attraction force imposed by user points is materialized through the interlayer edge weights w_x.

Therefore, the energy function for any curve C in our method is a combination of three terms, i.e.

$$\mathcal{E}(C, s_1, ..., s_n) = \alpha \sum_{i=1}^{n} ||C(s_i) - X_i|| + \beta \int_0^{L(C)} g(C(s))ds + \int_0^{L(C)} g_f(C(s))ds, \quad s.t. s_i < s_j, \forall i < j. \tag{1}$$

The first term is used to enforce the soft constraint by the user points, and it penalizes the path further away from the user points. The second term is the boundary based data term that prefers the path passing through strong edges, while the last term is the region based data term which prefers path traveling through abrupt changes in foreground probability. By using the layered graph construction, the minimization of the energy functional is achieved by finding the shortest path from the start point r to the end point t. The Dijkstra's algorithm is used to calculate the shortest path in the layered directed graph.

We compare our method on example images against the recent star graph-cut method [16] which utilizes user input and a generic shape prior as a constraint. This star shape constraint requires the object boundary does not occlude itself from the center of the object, star point, which is very appropriate for OCT segmentation. We also show performance of the proposed method with user points alone, i.e. without user strokes. Fig. 1 shows our preliminary results.

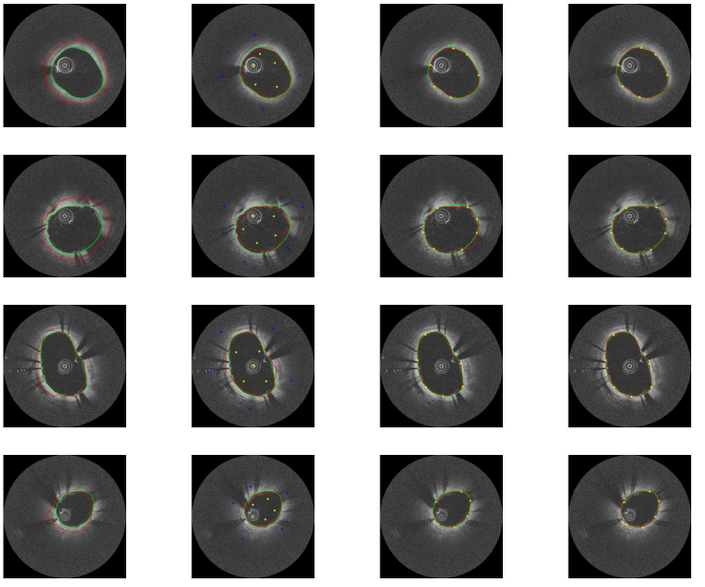

Figure 1: Comparison between groundtruth (green) and (from left to right) Star Graph Cut, Seeded Star Graph Cut, Single Method (no regional constraints), Proposed Method (red).

3 CONCLUSION

We present an interactive segmentation technique which combines boundary based and region based object representations, adopting a layered graph representation to simplify computation.

The proposed method was compared against a very recent graph cut technique that uses both implicit shape prior and user initialization, and shows very favourable results in the preliminary data.

REFERENCES

[1] Boykov, Y., Jolly, M.P.: Interactive organ segmentation using graph cuts. In: MICCAI. pp. 276–286 (2000)

[2] Brathwaite, P.A., Chandran, K.B., McPherson, D.D., Dove, E.L.: Lumen detection in human IVUS images using region-growing. In: Computers in Cardiology. pp. 37–40 (1996)

[3] Chiverton, J., Xie, X., Mirmehdi, M.: Probabilistic sequential segmentation and simultaneous on-line shape learning of multi-dimensional medical imaging data. In: Probablistic Models for Medical Image Analysis, A MICCAI Workshop (2009)

[4] Cohen, L., Kimmel, R.: Global minimum for active contour models: A minimal path approach. IJCV 24(1), 57–78 (1997)

[5] Essa, E., Xie, X., Sazonov, I., Nithiarasu, P.: Automatic ivus media-adventitia border extraction using double interface graph cut segmentation. In: ICIP. pp. 69–72 (2011)

[6] Essa, E., Xie, X., Sazonov, I., Nithiarasu, P., Smith, D.: Graph-based segmentation of optimal ivus media-adventitia border using shape prior. In: Medical Image Understanding and Analysis. pp. 143–149 (2012)

[7] Essa, E., Xie, X., Sazonov, I., Nithiarasu, P., Smith, D.: Shape prior model for media-adventitia border segmentation in ivus using graph cut. In: MICCAI Workshop on Medical Computer Vision. pp. 114–123 (2013)

[8] Falcao, A.X., Udupa, J.K., Samarasekera, S., Sharma, S., Hirsch, B.E., de A. Lotufo, R.: User-steered image segmentation paradigms: Live wire and live lane. Graphical Models and Image Processing 60(4), 233 – 260 (1998)

[9] Jones, J.L., Essa, E., Xie, X., Smith, D.: Interactive segmentation of media-adventitia border in ivus. In: Computer Analysis of Images and Patterns. pp. 466–474 (2013)

[10] Katouzian, A., Angelini, E.D., Carlier, S.G., Suri, J.S., Navab, N., Laine, A.F.: A state-of-the-art review on segmentation algorithms in intravascular ultrasound (IVUS) images. IEEE Trans. Info. Tech. in Biomed. 16(5), 823–834 (2012)

[11] Katouzian, A., Angelini, E.D., Sturm, B., Laine, A.F.: Automatic detection of luminal borders in ivus images by magnitude-phase histograms of complex brushlet coefficients. In: EMBC. pp. 3072–3076 (2010)

[12] Luo, Z., Wang, Y., Wang, W.: Estimating coronary artery lumen area with optimization-based contour detection. T-MI 22(4), 564–566 (2003)

[13] Rother, C., Kolmogorov, V., Blake, A.: Grabcut: interactive foreground extraction using iterated graph cuts. ACM Transactions on Graphics 23(3), 309–314 (2004)

[14] Sinop, A.K., Grady, L.: A seeded image segmentation framework unifying graph cuts and random walker which yields a new algorithm. In: ICCV. pp. 1–8 (2007)

[15] Sonka, M., Zhang, X., Siebes, M., Bissing, M.S., DeJong, S.C., Collins, S.M., McKay, C.R.: Segmentation of intravascular ultrasound images: A knowledge-based approach. T-MI 14(4), 719–732 (1995)

[16] Veksler, O.: Star shape prior for graph-cut image segmentation. In: ECCV. pp. 454–467 (2008)

[17] Windheuser, T., Schoenemann, T., Cremers, D.: Beyond connecting the dots: A polynomial-time algorithm for segmentation and boundary estimation with imprecise user input. In: ICCV. pp. 717–722 (2009)

[18] Xie, X., Mirmehdi, M.: Level-set based geometric colour snake with region support. In: ICIP. vol. 2 (2003)

[19] Xie, X., Mirmehdi, M.: Magnetostatic field for the active contour model: A study in convergence. In: BMVC. pp. 127–136 (2006)

[20] Zhang, H., Essa, E., Xie, X.: Graph based segmentation with minimal user interaction. In: ICIP. pp. 4074–4078 (2013)

3rd International Conference on Computational and Mathematical Biomedical Engineering – CMBE2013
16-18 December 2013, Hong-Kong
P. Nithiarasu and R. Löhner (eds)

Computational biomechanics of the brain brings real benefits in the operating theatre

Revanth R. Garlapati*, Adam Wittek*, Ahmed Mostayed*, Aditi Roy*, Grand R. Joldes*, Neville Knuckey**
Simon K. Warfield*, Ron Kikinis**** and Karol Miller***

*Intelligent Systems for Medicine Laboratory, The University of Western Australia, Perth, Australia, revanth@mech.uwa.edu.au, adam.wittek@uwa.edu.au, mostayed@mech.uwa.edu.au, aroy@mech.uwa.edu.au, grand.joldes@uwa.edu.au, karol.miller@uwa.edu.au

**Centre for Neuromuscular and Neurological Disorders, The University of Western Australia, Perth, Australia, neville.knuckey@uwa.edu.au

***Computational Radiology Laboratory, Children's Hospital, Harvard Medical School, Boston, MA, USA, simon.warfield@childrens.harvard.edu

****Surgical Planning Laboratory, Brigham & Women's Hospital, Harvard Medical School, Boston, MA, USA, kikinis@bwh.harvard.edu

SUMMARY

Neurosurgical planning is done using high-quality magnetic resonance images (MRIs) of the brain acquired before surgery. However, the brain deforms during surgery, which necessitates updating (registration) of such images to the current (i.e. intra-operative) brain geometry using either rigid body or deformable (e.g. using BSpline) image transforms. The registration process typically involves cumbersome and expensive acquisition of intra-operative MRIs to provide target images for the registration. In our previous studies, we proposed to predict the intra-operative deformation field within the brain using patient-specific non-linear biomechanical (finite element) models that require only very sparse information about the intra-operative brain geometry as an alternative to intra-operative acquisition of the entire brain MRI. In this contribution, we present our evaluation of accuracy of the registration conducted by warping the pre-operative MRIs using the predicted deformations. The results suggest that, despite requiring much less intra-operative data, the accuracy of our biomechanics-based registration is at least as high as that of non-rigid registration using BSpline and higher than the accuracy of rigid registration, which remains a method of choice in commercial image-guided surgery systems.

Key Words: *brain, Non-rigid registration, biomechanics, Hausdorff distance.*

1. INTRODUCTION

Complete (or nearly-complete) surgical removal of a tumour is desirable from the perspective of medical outcomes [1]. Such removal requires precise neuro-navigation, which is further complicated by the brain deformation (known as a brain shift) induced by craniotomy (surgical opening of the skull) [1]. The brain shift distorts the pre-operative anatomy and diminishes the utility of high-quality images acquired pre-operatively. This necessitates fusing high-resolution pre-operative imaging data with the intra-operative configuration of the patient's brain. Such fusing can be achieved by updating the pre-operative image to the current intra-operative configuration of the brain through registration [1]. The current commercial image-guided navigation systems use rigid registration. However, we are starting to see a shift towards non-rigid registration (such as those using BSpline interpolation between the pre-operative and intra-operative images [2]) that accounts for the brain tissue deformations during neurosurgery.

Vast majority of rigid and non-rigid registration methods require acquisition of the whole brain intra-operative images, which are used as the target for image registration. However, intra-operative MRI scanners are very expensive and often cumbersome. Hardware limitations of these scanners make them infeasible for frequent acquisition of the whole brain images during surgery. Therefore, recent research efforts for non-rigid neuro-image registration employ sparse information about the intra-operative brain geometry and non-linear biomechanical models to predict deformations within the brain due to craniotomy-induced brain shift [1].

In our previous studies, we developed fully non-linear finite element algorithms for real-time computation of soft tissue deformations on commodity hardware [3] and evaluated the accuracy of prediction of intra-operative brain deformations using the biomechanical brain models implemented by means of such algorithms [1]. In this contribution, we focus on comparison of the accuracy of neuro-image registration using our biomechanical models with that of non-rigid BSpline and rigid registration.

2. METHODOLOGY AND RESULTS

We analysed 33 craniotomy cases for patients with cerebral gliomas (tumours) [1].

2.1 Pre-operative to intra-operative registration using BSpline algorithm and image rigid-body transformation

We applied widely-used BSpline-based free form deformation (FFD) [2] and rigid registration algorithms implemented in 3D Slicer medical image processing software (http://www.slicer.org). These algorithms use an intra-operative image as a target image.

2.2 Registration using biomechanical modelling

In the biomechanics-based neuro-image registration, the deformation fields predicted using a numerical brain model were applied to warp the pre-operative images to the intra-operative brain configuration [3]. As explained in [3], sparse information about the intra-operative brain configuration is needed to drive the computation of brain deformations, but unlike in BSpline and rigid registrations, the process does not require acquisition of intra-operative images of the whole brain [1, 2].

Construction of patient-specific finite element meshes: As described in detail in [3], we obtained the geometry for mesh construction through segmentation of the pre-operative MRIs. In segmentation, we sub-divided the brain into healthy parenchyma, tumour and ventricles. As shown in Figure 1, we used mixed meshes consisting of hexahedral and non-locking tetrahedral elements [3]. For our cohort, accurate representation of the brain geometry necessitated meshes consisting of an order of 30000 elements and 20000 nodes .

Loading and boundary conditions: We defined the loading by prescribing deformations on the exposed brain surface in the craniotomy area. A frictionless contact is defined at the brain-skull interface to prevent the brain surface from penetrating the skull and allow sliding at the interface [3].

Constitutive properties for the brain models: As in our previous studies [3], we employed a nearly incompressible (Poisson' ratio of 0.49) neo-Hookean hyper-elastic model for the brain tissues. For the brain parenchyma, we used the Young's modulus of 3000 Pa, and for the tumour — the Young's modulus of 3000 Pa. The ventricles were assigned properties of a very soft compressible elastic solid with a Young's modulus of 10 Pa and Poisson's ratio of 0.1[3].

Solution algorithm: We used the previously developed fully non-linear finite element procedures that utilises Total Lagrangian formulation with explicit time-stepping and dynamic relaxation [3]. To achieve the real-time computation on commodity hardware (a desktop PC), these procedures were implemented on Graphics Processing Unit (GPU) [3].

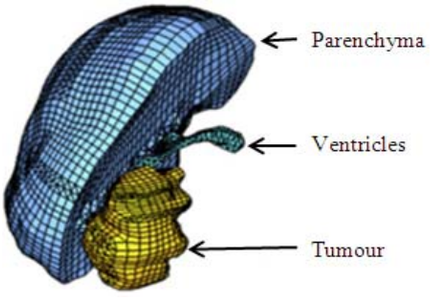

Figure 1: An example of patient-specific brain mesh used in this study. The mesh shown in this figure consists of 30574 elements and 15433 nodes. It takes less than 60 s of computation on a standard personal computer (Intel E6850 dual-core 3.00 GHz processor, 4 GB of internal memory, Windows XP operating system) to predict the brain deformations using our specialised finite element algorithms [3].

2.3 Results

To evaluate the registration accuracy, we determined an edge-based Hausdorff distance (HD) [1] between registered images (i.e. warped pre-operative MRIs) and whole brain images acquired during surgery. HD is a commonly used measure of the differences between two images [1]. As shown in Figure 2, the biomechanics-based registration is at least as accurate as that using BSpline despite the fact that it requires only very sparse intra-operative information (about deformation of the brain surface exposed during the craniotomy).

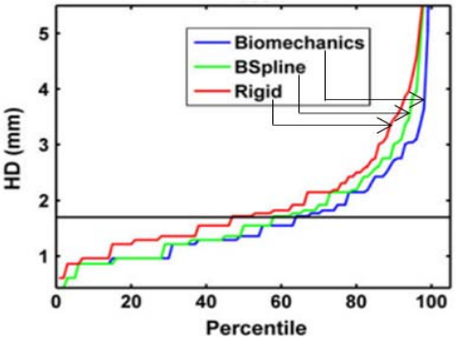

Figure 2: Typical plot of percentile edge-based Hausdorff distance between registered pre-operative and intra-operative images against the corresponding percentile of edges obtained showing relative accuracy of biomechanical, BSpline and rigid registration. At almost all percentiles, the registration error for biomechanics-based method is lower than that of BSpline and rigid registration.

For large brain deformations (exceeding 10 mm), the biomechanics-based registration is more accurate than the rigid registration [1]. This observation is further confirmed by the results of a statistical test for difference in proportions conducted to evaluate the null hypothesis that the proportion of patients for whom improved neuro-navigation can be achieved, is the same for rigid and biomechanics-based registration [1]. The null hypothesis was confidently rejected (p-value$<10^{-4}$) [1]. Even the modified hypothesis that less than 25% of patients would benefit from the use of biomechanics-based registration was rejected at a significance level of 5% (p-value = 0.02). The biomechanics-based method proved particularly effective for cases experiencing large craniotomy-induced brain deformations [1].

3. CONCLUSIONS

The results presented in this study suggest that neuro-image registration relying on sparse information about the intra-operative brain geometry and non-linear biomechanical models for predicting the intra-operative deformations within the brain is at least as accurate as the widely used non-rigid BSpline registration that requires intra-operative acquisition of the whole brain MRI. The results also indicate that biomechanical registration provides improved neuro-navigation data for a larger proportion of patients, compared to the rigid registration methods that are traditionally used in commercial neuro-navigation systems. This allows us to state that the use of comprehensive biomechanical computations for predicting the intra-operative organ deformations in the operating theatre may present a viable and economical alternative to intra-operative MRI.

4. ACKNOWLEDGEMENTS

The financial support of National Health and Medical Research Council (Grant No. APP1006031) is gratefully acknowledged. This investigation was also supported in part by NIH grants R01 EB008015 and R01 LM010033, and by a research grant from the Children's Hospital Boston Translational Research Program. The authors also gratefully acknowledge the financial support of Neuroimage Analysis Center (NIH P41 EB015902), National Center for Image Guided Therapy (NIH U41RR019703) and the National Alliance for Medical Image Computing (NAMIC) funded by the National Institutes of Health through the NIH Roadmap for Medical Research, Grant U54 EB005149.

REFERENCES

[1] R.R. Garlapati, A. Roy, G.R. Joldes, A. Wittek, A. Mostayed, B. Doyle, S.K. Warfield, R. Kikinis, N. Knuckey, S. Bunt, K. Miller. Biomechanical modelling provides more accurate data for neuronavigation than rigid registration, *Journal of Neurosurgery*, (submitted).

[2] D. Rueckert, L.I. Sonoda, C. Hayes, D.L. Hill, M.O. Leach, D.J. Hawkes. Nonrigid registration using free-form deformations: application to breast MR images, *IEEE Transactions on Medical Imaging*, 18, 712-721, 1999.

[3] K. Miller, *Biomechanics of the Brain*, 1st Edition, Springer, 2011.

3rd International Conference on Computational and Mathematical Biomedical Engineering - CMBE2013
16-18 December 2013, Hong-Kong
P. Nithiarasu and R. Löhner (Eds.)

Modification of the GPF method for efficient segmentation of high dimensional medical scans

Igor Sazonov⋆, Xianghua Xie⋆ and Perumal Nithiarasu⋆
⋆Swansea University, Singleton Park, Swansea, U.K., SA2 8PP, i.sazonov@swansea.ac.uk

SUMMARY

Compared with standard segmentation methods, the GPF (geometric potential force) method proposed in [1] has advantages in processing low quality, noisy scans. But its main drawback is: it requires too much memory to allocate all necessary intermediate arrays. In this work, we propose a memory economic modification of the GPF method. Numerical studies show that the proposed method looks very promising for biomedical applications based on 3D and 4D scans.

Key Words: *image segmentation, active surface methods, level set methods.*

1 INTRODUCTION

Gradient based deformable modelling is a popular approach in medical image segmentation as it allows segmenting objects of complicated geometrical shape [2,3]. Convenient techniques suffer from weak edge, image noise and also convergence issues. Therefore, attempts to improve of the performance of these methods are described in numerous works on image segmentation.

In [1], Yeo *et al.* have proposed a deformable model that is based on a hypothetical non-physical interaction between the image gradient vector and active level set surface. It is shown that this method, called the geometrical potential force (GPF) method, is robust towards noise interference, weak edges, and exhibits invariant some convergence capabilities.

Let $I(\mathbf{x})$ be a given n-dimensional greyscale image defined in domain Ω with $\mathbf{x} = [x_1, x_2, ..., x_n]^T \in \Omega$ be the vector of coordinates of the image grid-points (voxel centres). The segmentation process of image I by the GPF method comprises two stages. At the first stage, the geometrical potential $G(\mathbf{x})$ is computed as a convolution of the image gradient $\nabla I(\mathbf{x})$ and the special kernel $\mathbf{K}(\mathbf{x})$:

$$G(\mathbf{x}) = \sum_{\mathbf{x}' \in \Omega} \nabla I(\mathbf{x}') \cdot \mathbf{K}(\mathbf{x} - \mathbf{x}'), \qquad \mathbf{K}(\mathbf{x}) = \begin{cases} \mathbf{x} / \|\mathbf{x}\|^{n+1}, & \mathbf{x} \neq \mathbf{0} \\ \mathbf{0}, & \mathbf{x} = \mathbf{0} \end{cases} \tag{1}$$

where dot stands for the dot product. The image gradient ∇I is computed by central differences.

At the second stage, the once computed geometrical potential (GP) is used in the conventional PDE (e.g. [4]) with respect to the levels set function $\Phi(t, \mathbf{x})$

$$\partial\Phi/\partial t = \alpha\, g\kappa \|\nabla\Phi\| - (1-\alpha)\, \mathbf{F}\nabla\Phi. \tag{2}$$

Here $g(\mathbf{x}) = 1/(1+\|\nabla I\|^2)$ is the stopping function; $\kappa(t, \mathbf{x}) = \nabla\hat{\mathbf{n}}$ is the curvature of isosurfaces of Φ; $\hat{\mathbf{n}}(t, \mathbf{x})$ is the unit vector normal to isosurfaces of Φ; $\mathbf{F}(t, \mathbf{x}) = G\hat{\mathbf{n}}$ is the GPF that acts as the external force; $\alpha \in [0, 1]$ is a weighting parameter. Deformable contour/surface/hypersurface is defined as $S(t) = \{\mathbf{x}, \Phi(t, \mathbf{x}) = 0\}$.

Direct calculation of the geometrical potential G in 3D and 4D is computationally expensive. A natural approach to calculate convolution (1) is to apply the fast Fourier transform (FFT). This approach described in [1] has a significant drawback: it requires too much of computer memory. We have to compute and store n components of the image gradient ∇I and twice more for the real and imaginary part of their Fourier image, also n components of the kernel $\mathbf{K}$ and twice more for the Fourier image. For example, for a 3D image, it requires about 20 fold memory size of the initial image. Therefore becomes inefficient for a typical 3D scan size of 512^3 on a standard computers with, say, 4G memory. That's why a memory economic and computationally efficient method to evaluate the GP is so desirable.

In this work, we propose several modifications of computing algorithm for GP allowing us to decrease essentially the memory requirement. The proposed methods are valuated on both numerical examples and real world 3D data.

2 MATHEMATICAL DERIVATIONS

To start mathematical manipulating with Eq. (1) in order to obtain a more appropriate computational equations we write down the continuous analogue of (1)

$$G(\mathbf{x}) = \int \nabla I(\mathbf{x}') \cdot \mathbf{K}(\mathbf{x} - \mathbf{x}') \, \mathrm{d}^n \mathbf{x}', \qquad \mathbf{K}(\mathbf{x}) = P.V. \frac{\mathbf{x}}{\|\mathbf{x}\|^{n+1}}. \tag{3}$$

Here P.V. means that function $\mathbf{K}(\mathbf{x})$ should be regarded as a distribution (generalized function), and an integral with it should be considered in terms of the *principal value* (see, e.g. [5]).

One of the possible approaches to reduce memory usage is to derive an analytical formula for the kernel spatial spectrum and use it in computations. This is less time ans memory consuming than computing the kernel in the x-space via (1) and after that evaluating its spectrum via the FFT. Performing the Fourier transform we can obtain

$$\tilde{\mathbf{K}}(\mathbf{k}) = \int \mathbf{K}(\mathbf{x}) e^{\mathrm{i}\mathbf{k}\mathbf{x}} \, \mathrm{d}^n \mathbf{x} = \mathrm{i} B_n \frac{\mathbf{k}}{\|\mathbf{k}\|} \tag{4}$$

where $\mathrm{i} = \sqrt{-1}$, factor B_n depends on the image dimension: $B_2 = \pi, B_3 = \pi^2, B_4 = \frac{4}{3}\pi^2$, etc.

Alternatively, we rearrange the intergrand in (3) as a product of a scalar function and a scalar kernel instead of a dot product between vectors. Applying sort of integration by part we convert (3) into

$$G(\mathbf{x}) = \int I(\mathbf{x}') \nabla \mathbf{K}(\mathbf{x} - \mathbf{x}') \, \mathrm{d}^3 \mathbf{x}' = \int I(\mathbf{x}') \mathcal{K}(\mathbf{x} - \mathbf{x}') \, \mathrm{d}^3 \mathbf{x}'. \tag{5}$$

Thus, we only have to deal with the scalar kernel $\mathcal{K} = \nabla \mathbf{K}$. It is also a distribution but it has a higher order singularity than the initial kernel $\mathbf{K}$.

The both modifications can be combined together as the Fourier image of the scalar kernel can be easily calculated:

$$\tilde{\mathcal{K}} = \mathrm{i}\mathbf{k}\tilde{\mathbf{K}} = -B_n \|\mathbf{k}\| . \tag{6}$$

To distinguish all these approaches we refer to the direct computation of the convolution in (1) as to method 0. Then we refer to the approach described in [1] and based on the use of the FFT for computation the convolution (1) as to method 1 . The approach based on the use of formula (4): the analytical computation of the vector kernel, will be called method 2. The approach based on the use of scalar kernel (5) will be called method 3. The combined approach based on use of (5) and (6) will be called method 4.

To compute the GP with the use of method 4, we need to store only the real and imaginary parts of the image's spatial spectrum. Then we can multiply them element-by element by the scalar kernel spectrum computed for every element of the arrays directly. So we have to allocate only 4 arrays of the same size as the initial image: the initial image, its spectrum (two arrays) and the output array—GP. The number of arithmetic operations is reduced as well.

The CPU time and memory requirement for computation GP of a 3D image size of 256^3 for all the methods is presented in the Table below.

	method 0	method 1	method 2	method 3	method 4
CPU time	$\sim$ 7days	91s	55s	42s	30s
Memory required	0.6G	1.8G	1.0G	0.6G	0.4G

The computation is made in Linux, Intel(R) Xeon 3.00GHz, RAM 4G. The higher the number of the method, the more effectively it can economize the memory. The 512^3 image (typical 3D medical scan) can be processed only by method 4: it requires 7 min of the CPU time and 3G of memory. Thus the numerical results confirm effectiveness of the algorithms.

3 REDUCING THE NOISE SENSITIVITY

GP computed on the base of methods 2,3,4 works well for segmentation of artificial smooth images without noise. But being applied to a noisy image or a real medical scan, they give GP with more oscillating behaviour as seen in Fig. 1(left) that decreases the quality of the segmentation. This is because the GP computed by methods 2,3,4 occurs to be more sensitive to the noise, especially to the delta-correlated noise. The matter is: deriving Eqs. (4)–(6) we neglect the finiteness of the domain and its discreetness to simplify the mathematical manipulation.

The analytical spectrum (4) is not decaying when $\|\mathbf{k}\|$ grows whereas the spectrum computed numerically does decay towards maximal $\|\mathbf{k}\|$ that makes method 1 to be less sensitive to the noise. To improve the performance of the method 2 we can multiply $\tilde{\mathbf{K}}$ by a decaying function $f(\mathbf{k})$ which plays role of a low-pass filter. An example of such function is

$$f(\mathbf{k}) = 1 - \|\mathbf{k}'\| + \frac{(\xi\,\|\mathbf{k}'\| - 1)^2}{(\xi + \xi\,\|\mathbf{k}'\| - 2)\,\xi}, \quad \mathbf{k}' = \left[\frac{k_1}{k_{1,\max}}, \frac{k_2}{k_{2,\max}}, \frac{k_3}{k_{3,\max}}\right]^T, \quad \xi = \max_{i=1,2,3} |k'_i|. \tag{7}$$

To improve performance of method 3 we can compute the vector kernel $\mathbf{K}(\mathbf{x})$ by Eq. (1) first and then to calculate its divergence $\mathcal{K} = \nabla\mathbf{K}$ numerically by the central differences.

In method 4, when computing ∇I, the central differences are substituted by derivatives computed through the FFT, i.e. through the multiplication by i$\mathbf{k}$ which makes the result more sensitive to the delta-correlated noise. Note that the central differences operator in the $\mathbf{k}$-space is equivalent to the multiplication by function i$\mathbf{g}$:

$$\mathbf{g}(\mathbf{k}, \mathbf{h}) = \left[\frac{\sin k_1 h_1}{h_1}, \frac{\sin k_2 h_2}{h_2}, \ldots, \frac{\sin k_n h_n}{h_n}\right]^T \tag{8}$$

where $\mathbf{h} = [h_1, h_2, \ldots, h_n]^T$ is the vector of voxel sizes. Therefore the best way to compute $\tilde{\mathcal{K}}$ in method 4 is

$$\tilde{\mathcal{K}}(\mathbf{k}) = -B_n \frac{\mathbf{k} \cdot \mathbf{g}}{\|\mathbf{k}\|} f(\mathbf{k}). \tag{9}$$

Right plot in Fig. 1 indicates that the GP computed by methods 2,3,4 with the noise reduction correction is very close to that computed via methods 0,1. Example of blood vessel segmentation by the GPF approach when the GP is calculated by method 4 is shown in Fig. 2

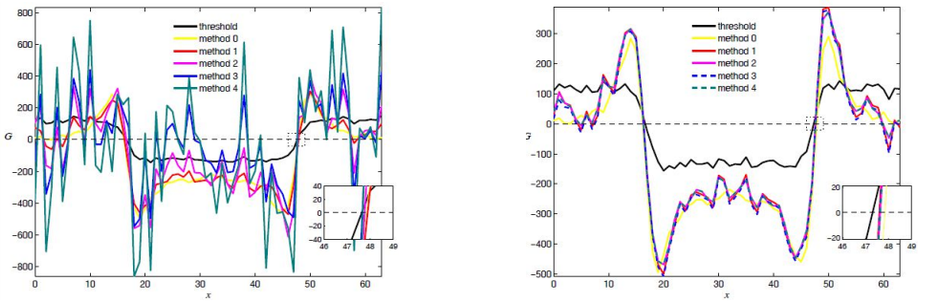

Figure 1: A 1D cut of a 3D GP: left—without the noise reduction correction, right—with it.

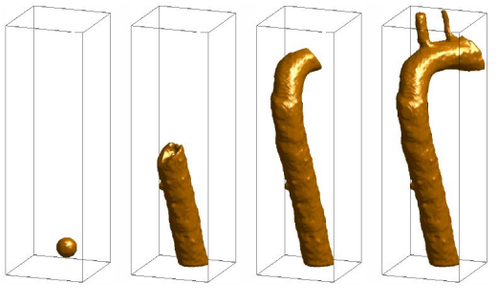

Figure 2: Stages of the automatic segmentation of thoracic aorta.

4 CONCLUSIONS

We proposed several modifications for algorithm of computation the geometrical potential in the GPF model and tested them. The approach which combines analytical kernel spectrum and scalar kernel conversion is the most computationally efficient and memory economic one. The methods were evaluated on 3D and 4D synthetic datasets, as well as 3D real world data. This preliminary work provided promising results which suggest that the proposed method has a great potential in efficient deformable modelling in high dimensional space without decomposing the space into a sequential order.

REFERENCES

[1] S. Yeo, X. Xie, I. Sazonov and P. Nithiarasu, Geometrically Induced Force Interaction for Three-Dimensional Deformable Models, *IEEE Transactions on Image Processing*, 20(5), 1373–1387, 2011.

[2] R. Malladi, J. A. Sethian, B. C. Vemuri, Shape modelling with front propagation: A level set approach, *IEEE Transactions on Image Processing*, 17(2), 158-175, 1995.

[3] R. Whitaker, Modeling deformable surfaces with level sets. *IEEE Computer Graphics and App.*, 24(5), 6-9, 2004.

[4] V. Caselles, R. Kimmel, G. Sapiro, Geodesic active contour, *International Journal of Computer Vision*, 22(1), 6179, 1997.

[5] V. S. Vladimirov, *Methods of the Theory of Generalized Functions*. Taylor & Francis, 2002.

3rd International Conference on Computational and Mathematical Biomedical Engineering - CMBE2013
16-18 December 2013, Hong-Kong
P. Nithiarasu and R. Löhner (Eds.)

Bone segmentation by clustering

G. Espinosa[a], N. Moreno[b], P. Vignal[c], F. Ramirez[a],T. Amin[d], I. Chikalov[d], M. Moshkov[d], and V. M. Calo[d,e]

[a]Universidad de los Andes, Bogota, Colombia, g-espino@uniandes.edu.co
[b]Environmental Science and Engineering, Kingdom of Saudi Arabia, nicolas.morenochaparro@kaust.edu.sa
[c]Material Science and Engineering, King Abdullah University of Science and Technology, Kingdom of Saudi Arabia
[d]Mathematical and Computer Sciences & Engineering Division, King Abdullah University of Science and Technology, Kingdom of Saudi Arabia
[e]Center of Numerical Porous Media and Earth Science and Engineering Department, King Abdullah University of Science and Technology, Kingdom of Saudi Arabia

SUMMARY

Patient-specific geometric models from imaging data is an important issue in biomechanical simulation-based medical planning. Generating a mesh requires an initial segmentation of a morphological image to identify the specific cloud of points that conform a particular bone [6]. This stage can be particularly challenging in many applications, such as in the modelling of the trapeziometacarpal joint, due to the physiological structure of the bones and resolution limitations of the image. In this paper we present a new method for morphological image segmentation based on a clustering approach, typically used for crystallographic analysis [5]. The proposed approach is specifically applied to the segmentation of the metacarpus cortical bone, from input data stemming from a computed medical tomography (CT). The extracted information is then used to construct a solid non-uniform rational B-splines (NURBS) mesh, for patient-specific models of geometry which are then suitable for isogeometric analysis, a finite element analysis framework.

Key Words: *bone segmentation, clustering, mesh generation.*

1 INTRODUCTION

Medical image segmentation is the first stage in computational modelling of human “organs”. Even though the procedure can be performed manually, it is often tedious, time consuming and lacks robustness [2]. Therefore, many automatic and semi-automatic (user driven) segmentation methodologies have been proposed to solve the problem, such as thresholding, edge detection, neural networks and shape analysis [6]. Nonetheless, experience indicates that combining human expertise with computational intelligence improves the accuracy of the segmentation, as well as its efficiency [3].
Solving biomechanical models of the trapeziometacarpal and metacarpophalangeal joints, requires two preprocessing steps. A bone segmentation to identify the joints is done first, followed by mesh generation from the cloud of points associated to each bone. These tasks are cumbersome for two reasons:

- the identification of the joints from medical images is patient specific. Diseases such as arthritis can make the visualisation even harder, as the separation between bones is reduced.
- the saddle shape geometry is hard to model.

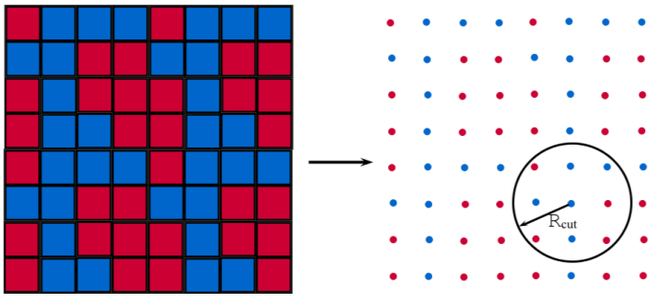

Figure 1: Clustering methodology using a particle-like representation of the data set. The only free parameter in our clustering approach is the maximum cutoff radius R_{cut}, where only nearest-neighbour particles can be considered part of the same cluster.

In order to make the bone identification accurate, fast, and robust, we propose in this paper an automatic clustering-based segmentation procedure. Clustering techniques have been widely developed for crystallographic analysis in molecular dynamics (MD) modelling [4], which allows for processing of large data sets with highly parallelizable algorithms. Taking advantage of the existing tools for MD, we successfully processed a CT data set, and were able to get segmentations of the phanlangeal, metacarpal and carpal sections of the studied sample. The complex geometrical modelling can be handled using a Non-Uniform Rational B-Spline (NURBS) reconstruction. NURBS is widely used due to their accurate shape modelling capabilities [1].

2 BONE SEGMENTATION

SEGMENTATION DETAILS

CT medical imaging data for hand bony structures are set with 80 tomography transects, with a separation of 0.625mm between them. Preprocessing image techniques, such as contrast enhancement, filtering, and Bi-level thresholding segmentation, are applied to the image data to differentiate the bone region. The data is then fitted in a three dimensional grid and based on the centroid of each voxel, a particle representation is constructed as seen in Figure 1. The data set generated is composed of one million particles.
Three consecutive clustering stages are applied using different cutoff distances. During the first stage, no-bony artefacts are identified and removed; the second stage is applied to detect high contrast bones. To detect bones with a low contrast, common neighbour analysis is used to identify the coordination number for every particle (voxel) and contour particles are removed. The last clustering step is then applied, in which bones that were artificially merged, are identified and separated. Contours and skeleton of the identified bone clusters are extracted and used to construct solid NURBS meshes. The meshes generated can later be taken as domains to perform Isogeometric Analysis.

Table 1: Number of clusters detected for different cutoff radii. Due to the regular distribution of the particle representation, an optimal cutoff radius of 1.5 is identified, suitable for the different clustering stages. Lower R_{cut} result in splits of clusters that should be together (artificial split of bones), while greater values produces merging of bones that are physically disjoined.

Number of clusters	Cutoff radius (R_{cut})
1070478	0.90
146431	1.00
49	1.01
49	1.40
40	1.50
30	2.00

3 RESULTS

Starting from the CT data, and applying different steps of clustering it was possible to extract the topological information of phalangeal, metacarpal and carpal regions. Low contrast bones were separated by removing contour particles. Once the bones are completely identified, the whole data set is used to generate the mesh. The workflow of the proposed methodology is presented in Figure 2, where we start with CT data and finish with the segmented bony structure. Bone detection can be enhanced by a multistage clustering-coordination thresholding procedure, as seen in Figures 2.b - 2.c. The optimal clustering cutoff radius was identified based on geometrical constraints since all the particles are spaced equidistantly. Values smaller or greater than $R_{cut}^{optimal}$ in this case produce either an artificial bone splitting or a merging, as shown in Table 1.

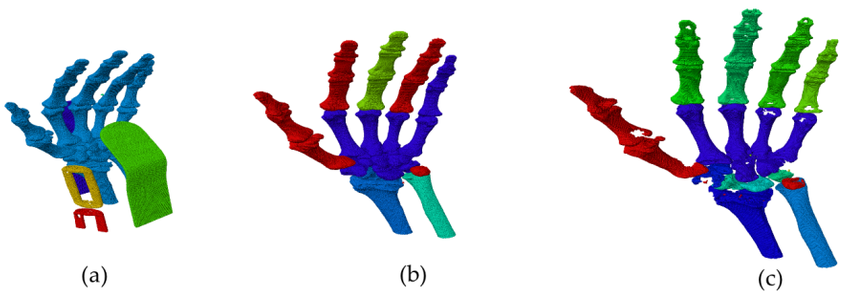

Figure 2: Sequential segmentation by multiple clustering stages. The first segmentation stage, where noise is removed from the image ($R_{cut} = 5d_{min}$) is shown in (2.a), and the second segmentation stage where the primary, high-contrast bones are identified is shown in (2.b), with $R_{cut} = 1.5d_{min}$. The third segmentation stage, (2.c), identifies the low-contrast bones after contour voxel elimination, with an $R_{cut} = 1.5d_{min}$.

The coordination analysis prior to the final clustering stage is required to increase the contrast between bones detected as a single cluster in the previous steps. This procedure takes advantage of the difference in number of neighbors between inner and outer bone voxels. The outer (or contour) voxels have a smaller coordination number and can be easily removed by thresholding, as seen in Figure 3. In it, the multistage coordination thresholding - clustering procedure is presented.

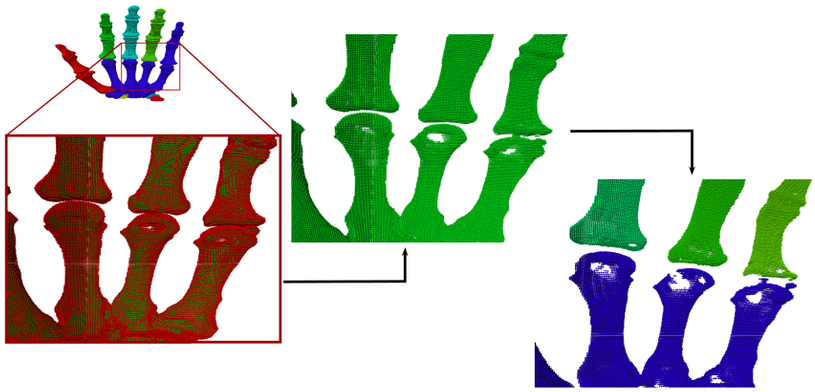

Figure 3: Coordination thresholding for low resolution bone identification.

4 CONCLUSIONS

An automatic segmentation methodology was proposed to efficiently identify bone morphologies using clustering techniques. With the identified domains, $3D$ NURBS solid meshes for patient-specific bones can be constructed. Our study stands as a basis for developing patient-specific biomechanical simulations of bone structures and joints.
The proposed methodology is well suited for either $2D$ or $3D$ morphology images, and can be readily used in other applications such as tissue volume measurement, disease diagnosis and localization of tumors. Density based clustering may improve the limitations of the nearest-neighbour based clustering to identify low contrast bones without contour refinement.

REFERENCES

[1] G. Espinosa and R. Fernando. Isogeometric analysis for biomechanical simulation in metacarpus bone. *10th Word Congress on Computational Mechanics*, 2012.

[2] V. Martin and M. Thonnat. A Cognitive Vision Approach for Image Segmentation Thresholding Images of Historical Documents with Back-to-Front Interference. 1:480–487, Oct. 2007.

[3] K. McGuinness and N. E. OConnor. A comparative evaluation of interactive segmentation algorithms. *Pattern Recognition*, 43:434 – 444, 2010.

[4] A. Stukowski. Structure identification methods for atomistic simulations of crystalline materials. *Modelling and Simulation in Materials Science and Engineering*, 20(4):045021, June 2012.

[5] J. Urban. Crystallography of Clusters. *Crystal Research and Technology*, 33(7-8):1009–1024, Oct. 1998.

[6] F. Zhao and X. Xie. An Overview on Interactive Medical Image Segmentation. *Annals of the British Machine Vision Association (BMVA)*, 2013(7):1–22, 2013.

Multiphysics Modelling & Applications of the Cardiovascular System I

3rd International Conference on Computational and Mathematical Biomedical Engineering - CMBE2013
16-18 December 2013, Hong-Kong
P. Nithiarasu and R. Löhner (Eds.)

A continuum model for platelet plug formation and growth under flow

Francesca Storti, Thomas H.S. van Kempen and Frans N. van de Vosse
Biomedical Engineering, Eindhoven University of Technology, Eindhoven, The Netherlands,
{F.Storti,T.H.S.v.Kempen,F.N.v.d.Vosse}@tue.nl

SUMMARY

When the wall of a blood vessel is damaged, the immediate response of the body to prevent blood loss is the creation of a platelet plug. The process is both chemical (platelets are chemically activated to adhere to the injured wall) and mechanical (platelets are convected by blood flow, which interacts with the forming plug). A continuum model for platelet plug formation and growth is presented in this work, which allows to study the interaction between platelet plug morphology and local haemodynamics. The framework consists of two parts: a biochemical model [5] and a platelet plug growth model. Results for different cases are shown, together with a comparison between the sole biochemical model and the complete model which includes plug growth. The model opens the way to the development of continuum models for full blod clot formation and growth in physiologically relevant configurations.

Key Words: *platelet plug formation, platelet plug growth, haemodynamics, continuum model, numerical model.*

1 INTRODUCTION

Haemostasis is the complex process which prevents blood loss [1]. Under physiological conditions, it keeps the blood in a fluidic state and it constantly repairs the walls of veins and arteries by forming and destroying solid blood clots. When the wall of a blood vessel is damaged, primary and secondary haemostasis leads to the creation of a patch around it. Primary haemostasis consists of chemical and mechanical activation of platelets, which adhere to the rip forming a platelet plug. Secondary haemostasis ensures the formation of fibrin fibers, which stabilize the platelet plug leading to the formation of a blood clot. When the rip is completely sealed, the clot dissolves.
In recent years, a number of numerical models for studying primary haemostasis, secondary haemostasis and clot stabilization and retraction has been proposed [2],[3],[4]. However, so far clot growth and fluid structure interaction between blood flow and clot has not been deeply investigated. Such knowledge would be of importance for general insight in the blood clot formation process.
We focus in this work on primary haemostasis, i.e. on platelet plug formation and growth and its interaction with the blood flow around. We propose a general framework for modelling the process. It consists of two main parts:

1. a biochemical model for platelet plug formation [5],
2. a platelet plug growth model.

2 MATHEMATICAL FRAMEWORK

In a first stage we propose a two-dimensional framework. Assuming symmetry in the vertical direction, only the lower half of a blood vessel is considered. A part of the lower wall is described as injured (see Fig. 1).

Figure 1: Schematic representation of a 2D vessel for the simulations: the reactive wall is a part of the lower wall. Symmetry of the geometry is assumed.

Biochemical model. The biochemical model has to describe the platelet plug formation process, through the dynamics of platelets and chemical species involved in the process. The model we present is based on the one presented in [5]. It consists of a system of convection-diffusion-reaction equations, which general form is the following

$$\frac{\partial c_i}{\partial t} + (\mathbf{u} \cdot \nabla) c_i = D_i \Delta c_i + S_i(c_j), \quad j = 1, \ldots, N, \tag{1}$$

where c_i is the concentration of species i, $\mathbf{u}$ is the local blood flow velocity (computed with Navier-Stokes equations), D_i is the diffusion coefficient of species i and $S_i(c_j)$ is the source term of species i which can depend on all species j (N is the total number of species). The reaction term $S_i(c_j)$ describes the production/consumption of each species, possibly depending on the dynamics of the others. $N = 7$ in our case and the species are the following: unactivated and activated platelets, adenosine diphosphate, thromboxane, prothrombin, thrombin and antithrombin.
Interaction with the damaged wall is described through a flux. A positive flux means efflux from the domain, so adhesion of the species to the wall, while a negative flux means influx into the domain, so release at the wall. Therefore a Robin boundary condition is prescribed for each species i on the damaged wall

$$D_i \frac{\partial c_i}{\partial n} = R_i(c_j), \quad j = 1, \ldots, N, \tag{2}$$

where $R_i(c_j)$ is the specific adhesion or release term for each species i which can depend on species j.
The main outcome of the biochemical model is the flux of deposited bounded platelets j_{bp} on the injured part of the wall.

Platelet plug growth. The platelet plug growth law is based on the flux of depositing platelets on the injured wall j_{bp}. The displacement of the plug interface $\mathbf{d}_{bp}$ can be defined as

$$\mathbf{d}_{bp} = j_{bp} \cdot (1 + \alpha) \cdot V_p \cdot \Delta t \cdot \mathbf{n}\,, \tag{3}$$

where α indicates the void fraction between platelets, V_p the volume of a single activated platelet, Δt the time step and we assume the growth to happen in normal direction $\mathbf{n}$ with respect to the platelet plug interface.
From a numerical point of view, the plug interface has to be moved at every time step. This results in a mesh update. An ALE (arbitrary Lagrangian Eulerian) method is chosen to redistribute the nodal points.

Model implementation. All equations are solved through the finite element method. Taylor-Hood triangular elements are chosen to discretize the 2D domain. An implicit Euler time discretization is used with a time step $\Delta t = 1$ s. Final simulation time is set to 10 minutes, i.e. $T = 600$ s. When mesh update is not enough to prevent nodes overlap and too large elements deformation, remeshing is performed [6].

3 RESULTS

The framework can be applied to different configurations. By changing the parameters of the model (diffusion coefficients, inlet distributions for platelets and inlet velocity profile), different cases are investigated: full blood, platelet enriched plasma and/or different haemodynamic conditions. We show results for the full blood case combined with a skewed inlet platelet concentration for a low (100 s^{-1}) and a high shear rate (1000 s^{-1}).

Platelet plug formation and growth over time is shown in Fig. 2 (top). The central part of the vessel only, where the injury occurs, is depicted. When the shear rate is low the plug shape is skewed to the frontal part of the injury and platelet deposition reaches about one third of the half vessel. When the shear rate is high total platelet deposition is much higher (it reaches about three quarters of the vessel half height) and the plug shape is completely different. It starts growing skewed to the distal part of the injury to reach a relatevely flat but irregular shape at the end of the simulation.

It is interesting to compare platelet deposition results when the sole biochemical model (Fig. 2, bottom, black line □) or the complete growth model (Fig. 2, bottom, red line ○) is considered. If for low shear rate the results are comparable, final platelet distribution for high shear rate shows some differences. In the no-growth case the concentration of bounded platelets reaches the peak at the front of the reactive part, to gradually decrease till its end. In the growth case the peak is at the end of the injured part and total platelet distribution shows an irregular profile.

4 CONCLUSIONS

Based on the existing biochemical model of platelet deposition [5] a continuum model for platelet plug formation and growth has been developed that allows to study the interaction between platelet plug morphology and local haemodynamics. By changing the parameters of the model, many different configurations can be investigated. In general, to predict correct platelet plug size and shape, it is not possible to neglect the effect of plug growth on the local flow phenomena. The interaction between growing plug and blood flow determines plug shape and size.

The model opens the way to the development of continuum models for full blod clot formation and growth in physiologically relevant configurations. In particular, different constitutive relations for the platelet plug could be investigated ranging from an elastic solid to a poroviscoelastic solid. This would imply the implementation of a fluid structure interaction coupling between the solid plug and the blood flow.

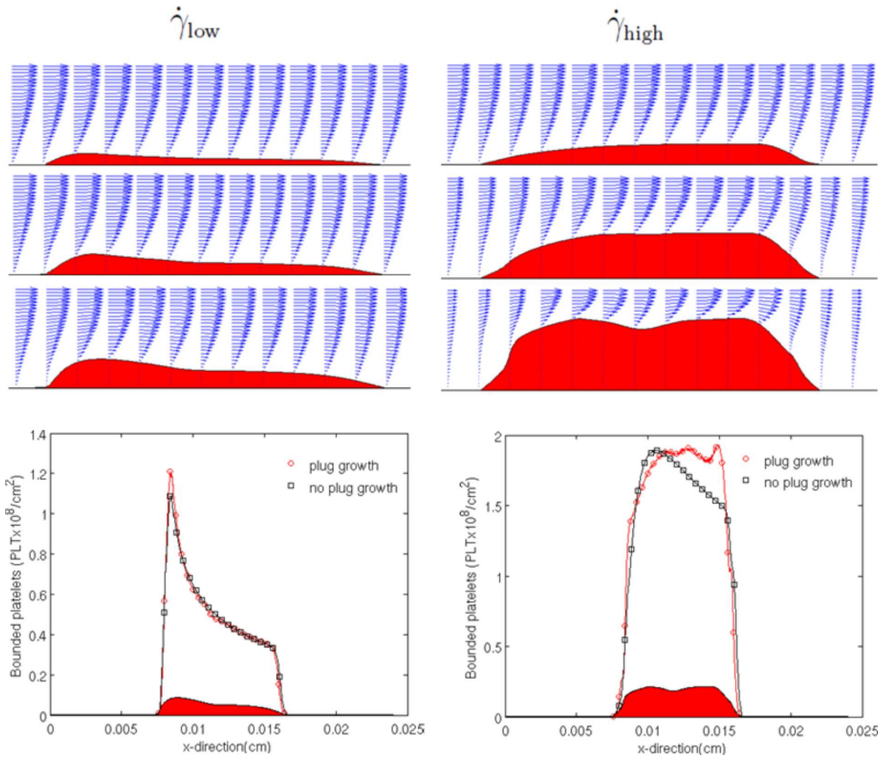

Figure 2: Top: 2D visualization of platelet plug growth in time at the injury site; from top to bottom: $t = 200$ s, $t = 400$ s, $t = 600$ s. Bottom: distribution of bounded platelets at the lower wall of the vessel in case of plug growth (red lines, $\circ$) or no plug growth (black lines, $\square$) at final time $T = 600$ s. Note that maximum values on y axis are different for the two pictures.

REFERENCES

[1] A.C. Guyton and J.E. Hall. *Textbook of medical physiology*, 10th. Edition, W.B. Saunders company, 2000.

[2] Z. Xu, O. Kim, M.M. Kamocka and M. Alber, Multiscale models of thrombogenesis, *Wiley Interdisciplinary Reviews Systems Biology and Medicine*, 4(3), 237-246, 2012.

[3] G. Moiseyev and P.Z. Bar-Yoseph, Computational modeling of thrombosis as a tool in the design and optimization of vascular implants, *Journal of Biomechanics*, 46, 248-252, 2013.

[4] M.H. Flamm and S.L. Diamond, Multiscale systems biology and physics of thrombosis under flow, *Annals of Biomedical Engineering*, 40, 2355-2364, 2012.

[5] E.N. Sorensen, G.W. Burgreen, W.R. Wagner and J.F. Antaki, Computational simulation of platelet deposition and activation: I. Model development and properties, *Annals of Biomedical Engineering*, 27, 436-448, 1999.

[6] C. Geuzaine and J.F. Remacle, Gmsh: A 3-D finite element mesh generator with builtin pre- and post-processing facilities, *International Journal for Numerical Methods in Engineering*, 79, 1309-1331, 2009.

3rd International Conference on Computational and Mathematical Biomedical Engineering - CMBE2013
16-18 December 2013, Hong-Kong
P. Nithiarasu and R. Löhner (Eds.)

Intra-cardiac turbulence in a realistic human left heart

Franck Nicoud⋆, Christophe Chnafa⋆⋆ and Simon Mendez⋆⋆
⋆University Montpellier 2, CNRS 5149 I3M , 34095 Montpellier, France,
franck.nicoud@univ-montp2.fr
⋆⋆ CNRS 5149 I3M , 34095 Montpellier, France

SUMMARY

A numerical framework designed to compute the blood flow in patient-specific human hearts is presented. The geometry of the heart cavities and associated wall motion are extracted from ECG gated 3D medical images while the valves of the heart are accounted for thanks to low order geometrical models. The resulting blood flow equations are solved using a fourth-order low-dissipative finite-volume scheme and a mixed Arbitrary Lagrangian-Eulerian / Immersed Boundary framework. On top of retrieving the main fluid flow phenomena commonly observed in the left heart, the methodology allows studying the heart flow dynamics, including the turbulence characteristics and cycle-to-cycle variations.

Key Words: *blood flow, left heart, turbulence.*

1 INTRODUCTION

Phase-contrast magnetic resonance imaging (PC-MRI) is nowadays able to provide 3D in-vivo images of the haemodynamics in heart chambers in a non-invasive way [1]. Nevertheless, accuracy of the velocity field is questionable in disturbed flows [2]. In addition, flow quantities such as wall shear stresses and pressure, which constitute relevant clinical information, cannot be measured directly with the PC-MRI method. Computational fluid dynamics (CFD) constitutes a possible, yet challenging, alternative for patient-specific non-invasive flow characterization. The blood flow domain variations over the cardiac cycle can theoretically be computed by solving an appropriate fluid-structure-bioelectric interaction problem. However, the mechanical/electrical properties of the heart muscle are patient specific and can hardly be assessed in practice; besides, the outer boundary conditions for such coupled problem stem from the interactions between the heart and its environment and are thus virtually unknown. An alternative consists in using dynamic medical images (4D) for the computation of the heart deformations. In this view, endocardium movements are extracted from morphological medical images and prescribed as boundary conditions of the fluid problem, thus avoiding solving a coupled multiphysics problem [3]. The present work describes a CFD framework based on this principle and its application to an actual patient left heart.

2 METHOD

The YALES2BIO solver (http://www.math.univ-montp2.fr/ yales2bio/) used in this study is a fully explicit 3D CFD in-house code dedicated to the resolution of microscopic and macroscopic cardiovascular flows. It relies heavily on the YALES2 solver widely validated for complex engineering

applications [4]. It is based on fourth-order finite-volume approximation and an explicit fourth-order Runge-Kutta scheme for time integration. Due to the expected transitional nature of the flow, large eddy simulations are performed to represent turbulence, using advanced subgrid scale models able to handle transitional wall bounded flows in complex geometries [5-6].

The numerical domain is extracted from a set of 10 computed tomography (CT) images available along the cardiac cycle of an actual patient. One native cardiac phase is first selected among the available phases; the corresponding volumetric data is imported into an image processing software (ScanIP; Simpleware Ltd., Exeter, UK). The region of interest is isolated and segmentation process is made by the thresholding method. The extracted geometry is imported in a commercial mesh generator (Gambit, ANSYS) to generate the finite volumes mesh of the native numerical domain. As shown in Fig. 1, the computational domain includes the left atrium (LA), left ventricle (LV), the aortic root (AO) and the pulmonary veins. Note that the papillary muscles were not accounted for to ease the ventricle desciption, although they could influence the vortex breakdown during the diastole. Smaller geometrical elements like the aortic valve (AV) and the mitral valve (MV) are handled by an immersed boundary method [7]. Their exact shape and dynamics are approximated using the partial information contained in the medical images. The AV which has a moderate impact on the ventricular flow is modeled as a planar region being alternatively permeable and impermeable depending on the phase in the cardiac cycle. Its location can be easily determined thanks to the aortic valve annulus, visible in the medical images. The MV is modelled by a more realistic geometry based on measurements (open surface, leaflets lengths) extracted from the medical images. Moreover, the AV and MV are assumed to be alternatively closed/opened in phase opposition during the cardiac cycle: MV open-AV closed during diastole (LV volume increasing) and MV closed-AV open during systole (LV volume decreasing). The flow waveform imposed to the four inlet conditions of the computational domain can then be calculated by applying the mass conservation principle to the time evolving LV/LA volumes. The resulting inlet velocity is periodic and displayed in Fig. 1A. A nearly isotropic grid with spatial resolution close to 0.8 mm and approx. three-million tetrahedral elements is used. In order to make the computational grid follow the physiological heart deformations over time, fields of deformations between the native image and the other images taken at different phases of the cardiac cycle are first computed by a non-linear image registration algorithm [3]. Applied to the native mesh, these deformations allow generating a time evolving mesh consistent with the 4D medical images and whose connectivity remains unchanged over the cardiac cycle. This enables to use the Arbitrary Lagrangian-Eulerian methodology to account for the grid motion when solving the fluid flow equations. The simulation time step is fixed by a CFL condition consistent with the explicit time integration used in YALES2BIO and leading to $\Delta t \approx 10^{-4}$ s in the present case. Blood is modeled as an incompressible Newtonian fluid with kinematic viscosity 4×10^{-6} m^{2}s^{-1} and density close to 1000 kg m^{-3}.

3 RESULTS

The peak Reynolds numbers based on flow rate and cross sections mean diameters are indicated in Fig. 1B at different locations within the computational domain; the computed values are in the range 2000-5000 and clearly correspond to transitional flow regime where turbulent effects are expected to occur. This is an a posteriori justification of the choice made to use an appropriate LES framework (low dissipative, high order scheme [4], advanced sub-grid scale model [5-6]) to account for the turbulence activity within the heart flow.

Due to the transitional nature of this complex cyclic flow, the velocity pattern changes from one cycle to the other. 20 cardiac cycles were computed and phase averages were gathered over the

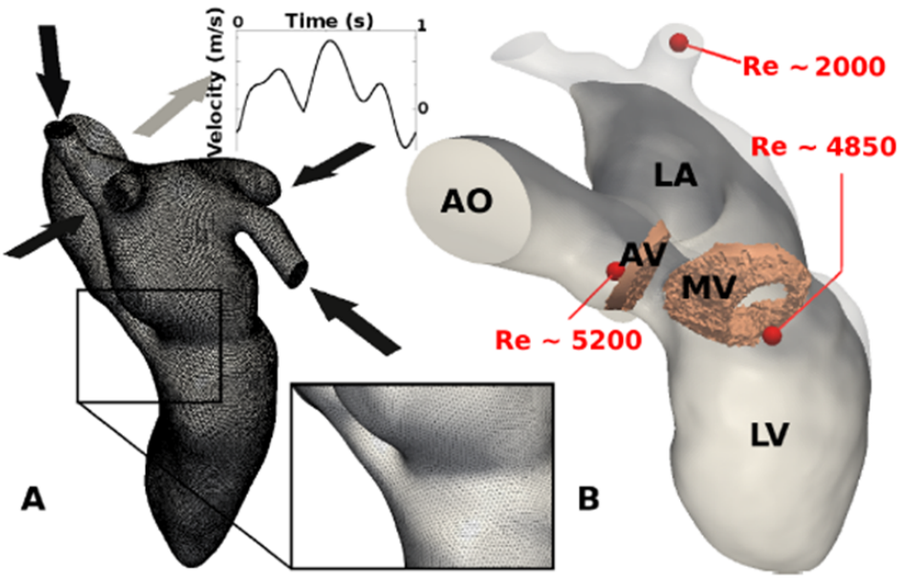

Figure 1: A: computational mesh of the luminal surface of the left heart and zoom on the grid. The inlets (pulmonary veins) are indicated by black arrows, the outlet (aorta) by the gray arrow. The inlet waveform is sketched. B: AV and MV modeled valves are visible by transparency. Peak Reynolds numbers at different locations are indicated.

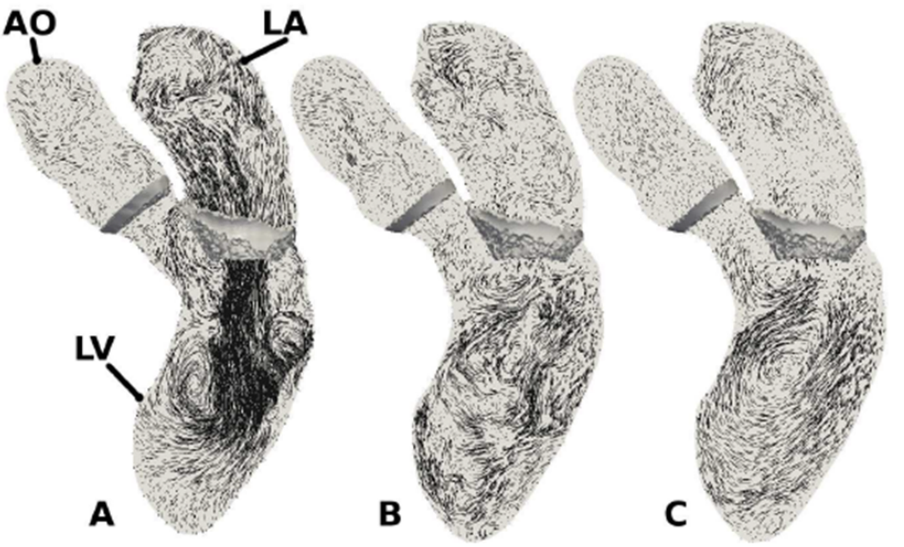

Figure 2: Slices of the left heart simulation. Velocity vectors are represented during the entering of the jet through the MV at time t = 530 ms (A) and during the late diastole phase, t = 690 ms, (B,C). (B) is an instantaneous view of the flow while (C) is the phase-averaged flow.

last 15 cycles. Cycle-to-cycle variations are not observed during the whole cycle. During flow acceleration, the jet formed at the mitral valve is very stable (Fig. 2A). On the contrary, during phases of deceleration, the instantaneous velocity (Fig. 2B) and phase-averaged velocity (Fig. 2C) are clearly different. While a highly disturbed flow is seen for the instantaneous view of the velocity field in the LV, a large recirculation cell and two others smaller recirculation zones (below the AV and next to the apex) are visible in the phase-averaged view. Interestingly, phase-averaged velocity flow fields are very similar to recent PC-MRI measurement of the flow in a left heart [1]. In the common description of the LV, the large recirculation cell is characteristic of late diastole. The present results show that this description is true only in the phase-averaged sense, while instantaneous velocity fields reflect the turbulent nature of the intra-cardiac blood flow.

Fields of turbulent kinetic energy $(u_{\mathrm{rms}}^2 + v_{\mathrm{rms}}^2 + w_{\mathrm{rms}}^2)/2$ (the fluctuations are defined with respect to the phase averaged velocity fields) extracted from the simulations (not shown) show that the turbulence intensity can be as high as 20 % during the late diastole while the flow is virtually laminar during the ventricle filling.The intra-cardiac turbulence is thus highly intermittent and should only be represented by large-eddy simulations techniques rather than classical Reynolds-Averaged Navier-Stokes (RANS) turbulence models (e.g.: k-ϵ; k-ω among many others) designed to handle fully developed, ergodic turbulent flows.

4 CONCLUSIONS

A numerical method developed for the computations of the flow in patient-specific human hearts has been exposed and applied to an actual human left heart. The motions of the ventricle, atrium and ascending aorta were deduced from medical images while a rough model of the mitral valve was used, with only two possible states (open or closed). Still, the flow obtained is consistent with the current knowledge regarding the intra-cardiac blood flow. In addition, cycle-to-cycle variations are observed, demonstrating that averaged information as provided by MRI only partially describes the flow structure in the left heart.

REFERENCES

[1] M. Markl, P. Kilner and T. Ebbers, Comprehensive 4D velocity mapping of the heart and great vessels by cardiovascular magnetic resonance. *Journal of Cardiovascular Magnetic Resonance* 13 (1), 7, 2011.

[2] D. Hollnagel, P. Summers, D. Poulikakos and S. Kollias, Comparative velocity investigations in cerebral arteries and aneurysms: 3D phase-contrast MR angiography, laser doppler velocimetry and computational fluid dynamics. *NMR Biomed.* 22, 795808, 2009.

[3] M. Midulla, R. Moreno, A. Baali, M. Chau, A. Negre-Salvayre, F. Nicoud, J.P. Pruvo, S. Haulon, S. and H. Rousseau, Haemodynamic imaging of thoracic stent-grafts by computational fluid dynamics (CFD): presentation of a patient-specific method combining magnetic resonance imaging and numerical simulations. *European Radiology* 22, 20942102, 2012

[4] V. Moureau, P. Domingo and L. Vervisch, Design of a massively parallel CFD code for complex geometries. Comptes Rendus Mécanique de l'Académie des Sciences 339 (23), 141 148, 2011

[5] M. Germano, U. Piomelli, P. Moin and W. Cabot A dynamic subgrid-scale eddy viscosity model. *Phys. Fluids* 3, 17601765, 1991

[6] F. Nicoud, H. Baya Toda, O. Cabrit, S. Bose and J. Lee, Using singular values to build a subgrid-scale model for Large Eddy Simulations. *Phys. Fluids* 23, 085106, 2011

[7] R. Verzicco, J. Mohd-Yusof, P. Orlandi and D. Haworth, Large eddy simulation in complex geometric configurations using boundary body forces *AIAA J.*, 38, 427-433, 2000

3rd International Conference on Computational and Mathematical Biomedical Engineering - CMBE2013
16-18 December 2013, Hong-Kong
P. Nithiarasu and R. Löhner (Eds.)

Numerical modeling of blood flow in right coronary arteries.

Ming-Jyh Chern[⋆], Ming-Ting Wu[⋆⋆], Ya-Lin Lau[⋆], Yu-Hsiung Hsiao[⋆] and Hong-Da Hsiao[⋆⋆⋆]

[⋆]National Taiwan University of Science and Technology, Taipei 10607 Taiwan, mjchern@mail.ntust.edu.tw

[⋆⋆]Kaohsiung Veterans General Hospital, Kaohsiung 81362 Taiwan, wu.mingting@gmail.com

[⋆⋆⋆]National Center for High-performance Computing, Hsinchu 30076 Taiwan, c0074300@nchc.org.tw

SUMMARY

In order to investigate the effect of atherosclerosis on hemodynamics of coronary arteries, computational models based on CT images of coronary arteries were established. CAD models were obtained from CT images first. Subsequently, tetrahedral cell were used to discretized the flow domain. Computational fluid dynamics based on finite volume method was used to simulate blood flow in coronary arteries with plaques. Velocity, pressure, and wall shear stress were predicted in the numerical model. Results were presented in a cardiac cycle. The numerical prediction of blood flow in coronary arteries with atherosclerosis would be useful for medical doctors to understand the pathological phenomena.

Key Words: *blood flow, wall shear stress, coronary artery, atherosclerosis.*

1 INTRODUCTION

Atherosclerosis in coronary arteries is one of the main causes of morbidity and mortality in the world. Although some of risk factors causing atherosclerosis in coronary arteries are known, e.g. improper diet habit, smoking, hypertension, and diabetes, the inception and development of atherosclerosis are still unclear. According to available literature, it may be associated with blood flow in coronary arteries as well. Therefore, understanding hemodynamics in arteries plays a vital role in prediction and cure of atherosclerosis. Coronary arteries originate from the beginning of the aorta that deliver oxygen-rich blood to myocardium. There are two main coronary arteries called left coronary artery (LCA) and right coronary artery (RCA), respectively. The present study focus on hemodynamics in a right coronary artery.

Atherosclerosis is a common cardiovascular disease affecting arterial blood vessels. Endothelium plays a key player in atherogenesis. Furchgott and Zawadzki [1] performed an $in\ vitro$ study on rabbit arteries to investigate the role of endothelium in atherogenesis. It was found that arteries with endothelium became vasodilation when some acetylcholine were added. Nevertheless, when endothelium was removed from arteries, the arteries became constricted under the same condition. In terms of that, they explained that the endothelium is the critical role to maintain the balance between vasodilator and constrictor of arteries. Provided that the balance is broken, many problems of regulatory process will come out. Subsequently, the endothelium-derived relaxing

factor (EDRF) NO found by Ignarro [2] becomes more important. NO is synthesized in endothelial cells by endothelial NO synthase (eNOS). Given the expression of eNOS is decreased, it may result in endothelial dysfunction.

Blood flow in an artery is a crucial factor in the pathology of atherosclerosis. In general, flow variations can be either measured in experiments or predicted using numerical simulations. Due to the fast progress of computational technology, applications of computational fluid dynamics (CFD) to hemodynamics in an artery have receiving more and more attentions. Numerical simulations for hemodynamics in a right coronary artery were investigated by several researchers. For example, Myers *et al.* [3] performed steady flow simulations with three different inlet velocity profiles in a right coronary artery. Furthermore, the effects of physiologically realistic cardiac-induced motion on hemodynamics in a right coronary artery have been explored by Zeng *et al.* [4]. Simulations were carried out with steady and pulsatile inflow conditions in both fixed and moving RCA models in their study. According to available literature, it is found that the influences of the periphery of RCA on the flow variation, the distribution of AWSS is not clear. For example, the curvature of the major bend in the proximal part and the angle of the bifurcations of RCA. Hence, this study aims to investigate the effects by simulations in reconstructed RCA models from CT images.

2 MATHEMATICAL FORMULAE AND NUMERICAL MODEL

2.1 Governing Equations

Blood is the working fluid in an artery and should obey conservation principles of mass and momentum. In this study, blood is assumed to be incompressible, so the equations of motion are denoted as
continuity equation

$$\nabla \cdot \ \mathbf{u} = 0 \quad , \tag{1}$$

and momentum equation

$$\frac{\partial(\rho \mathbf{u})}{\partial t} + \nabla \cdot (\rho \mathbf{u}\mathbf{u}) = -\nabla P + \nabla \cdot \tau \quad , \tag{2}$$

where $\mathbf{u}$ represents a velocity vector of flow, P is pressure, t is time, ρ is density of blood, τ is shear stress tensor. The density of blood ρ is set as 1060 $\mathrm{kg} \cdot \mathrm{m}^{-3}$. Since blood is a non-Newtonian fluid, so the shear stress of blood is determined by the experimental results of Walbum and Schneck [5].

2.2 Numerical Methods and Parameters Setting

In this study, the finite volume method is used to solve the equations of motion, and the equation of mass transfer with boundary conditions. As a result, flow patterns and wall shear stress distribution in RCA can be predicted. The commercial software CFD-ACE+ which is based a finite volume method and the SIMPLEC algorithm is employed to conduct numerical simulations for flows in RCA.

2.2.1 CT Images and Grid Generation

In order to establish a numerical model of the right coronary artery, CT images are utilized. Sliced images of the right artery are obtained from CT images based on DICOM formats. Those sliced

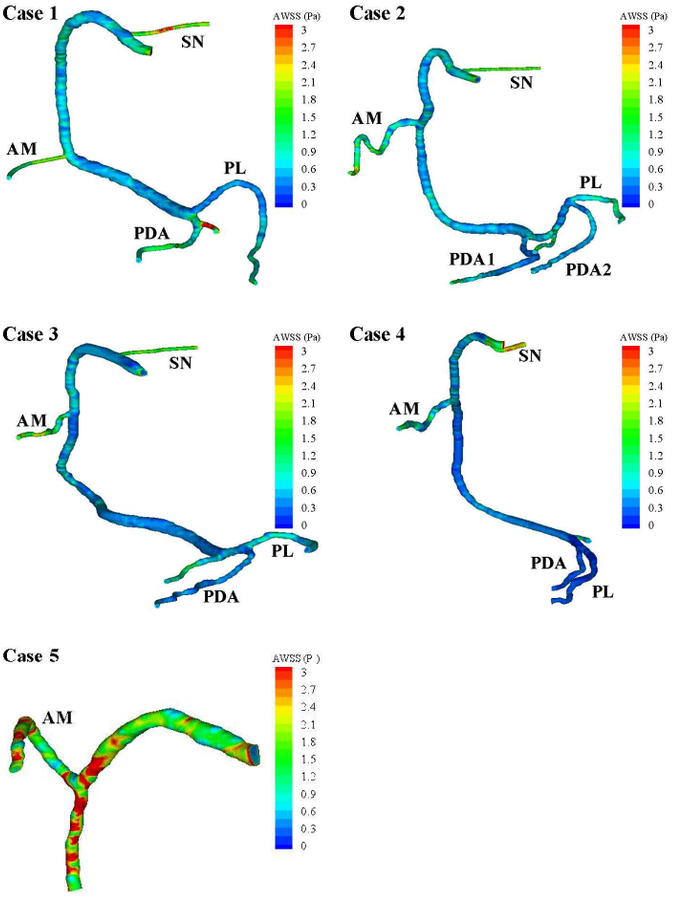

Figure 1: Distributions of AWSS of five cases.

images of the right artery are saved in TIF format. Those sliced TIF images are connected together. As a result, a computer aided design (CAD) file in STL format is given. Subsequently, computational cells are generated inside the CAD model. Since the geometry of RCA is too complicated to generate structured cells, unstructured grid is used to generate computational cells. Once computational cell generation is finish, the computational cells are utilized in the flow solver. In this study, CFD-ACE+ is employed as the flow solver to simulate blood flows in the right coronary artery.

3 RESULTS AND DISCUSSION

According to Knight *et al.* [6], the inception of atherosclerosis relates to the parameter low average wall shear stress (AWSS), although there are a group of similar parameters to estimate the influences of wall shear stress on atherosclerosis, e.g. oscillatory shear index (OSI). They demonstrated that AWSS had a higher sensitivity for the prediction of location of a plaque than other parameters. Therefore, the distribution of AWSS on an arterial wall can provide the information where atherosclerosis may occur in an artery. Fig. 1 shows distributions of AWSS on walls of all RCA models. It is found that the distribution of Case 5 changes more seriously than other cases. Also, AWSS of Case 5 is higher than other cases as well. In general, all AWSS values in Case 5 are higher than 1 Pa and the maximum values are around 3 Pa. However, AWSS values in other

cases are less 1 Pa. It seems that AWSS in a short RCA is higher than a long one. According to the available literature mentioned in Introduction, atherosclerosis may occur in a low wall shear stress region, so Cases 1-4 may be more possible for the inception of atherosclerosis.

4 CONCLUSIONS

We reconstructed 3-D right coronary artery (RCA) models based on computer tomography (CT) images and use those models to simulate blood flows. Meanwhile, the distribution of average wall shear stress (AWSS) in RCA was undertaken in this study because they are related to atherogenesis. Five RCAs are considered to investigate the flow variations due to peripheries of models and the distributions of AWSS due to those flow variations. The Dean flow is observed in the proximal part of RCA. AWSS along the inner wall of RCA is generally lower than those along the outer wall. In terms of predicted results, it turns out that a longer RCA has low AWSS than a short one. In general, those regions where AWSS is low may have more possibilities for atherosclerosis in RCA. Prediction of distributions of AWSS may provide useful information to estimate the location where atherosclerosis may happen.

ACKNOWLEDGEMENTS

The authors would like to express their gratitudes for the financial support from National Science Council Taiwan under the grant NSC 102-2221-E-011-042.

REFERENCES

[1] R. Furchgott and J. Zawadzki, The obligatory role of endothelial cells in the relaxation of arterial smooth muscle by acetylcholine. *Journal of the American Medical Association*, 288, 373-379, 1980.

[2] L.J. Ignarro, Nitric oxide: a unique endogenous signaling molecule in vascular biology. *Nobel Lecture*, 178-198, 1998.

[3] J.G. Myers, J.A. Moore, M. Ojha, K.W. Johnston, and C.R. Ethier, Factors influencing blood flow patterns in the human right coronary artery. *Annals of Biomedical Engineering*, 29, 109-120, 2001.

[4] D. Zeng, Z. Ding, M.H. Friedman, and C.R. Ethier, C.R., Effects of cardiac motion on right coronary artery hemodynamics. *Annals of Biomedical Engineering*, 31, 420-429, 2003.

[5] F.J. Walburn and D.J. Schneck, A constitutie equation for whole human blood. *Biorheology*, 13, 201-210, 1976.

[6] J. Knight, U. Olgac, S.C. Saur, D. Poulikakos, W. Jr Marshall, P.C. Cattin, H. Alkadhi and V. Kurtcuoglu, Choosing the optimal wall shear parameter for the prediction of plaque location-A patient-specific computational study in human right coronary arteries. *Atherosclerosis*, 210, 578-581, 2010.

3rd International Conference on Computational and Mathematical Biomedical Engineering - CMBE2013
16-18 December 2013, Hong-Kong
P. Nithiarasu and R. Löhner (Eds.)

Aortic hemodynamics post Thoracic Endovascular Repair (TEVAR): a focus on *birdbeak* drawback

M. Conti[⋆], F. Auricchio[⋆], A. Lefieux[⋆], A. Reali[⋆], T. Passerini[⋆⋆], A. Veneziani[⋆⋆], S. Trimarchi[⋆⋆⋆], G. van Bogerijen[⋆⋆⋆]

[⋆]Dept. of Civil Engineering and Architecture (DICAr), Pavia University, Pavia, Italy.
[⋆⋆]Department of Mathematics and Computer Science, Emory University, Atlanta, GA, USA.
[⋆⋆⋆]IRCCS Policlinico San Donato, Thoracic Aortic Research Center, Milan, Italy.

SUMMARY

The study addresses a patient-specific Computational Fluid Dynamics (CFD) analysis of endograft implant to treat aortic dissection. We evaluate the hemodynamics of three scenarios for the same patient: i) pre-operative; ii) as-is post-operative; iii) post-operative where a distal stenosis of the lumen was virtually removed.

Key Words: *CFD, endograftng, patient-specific modeling.*

1 INTRODUCTION

Thoracic endovascular aortic repair (TEVAR) is a treatment modality for thoracic aortic disease, such as dissections or aneurysms, rapidly implemented into clinical practice. However, TEVAR has proved to be more challenging than endovascular repair of the abdominal aorta, having a greater frequency and variety of device-related complications, such as device compression, invagination, misaligned deployment, retrograde type A dissection, kinks and aortic perforation. All these issues call for engineering tools aimed at supporting procedure planning; for this reason in the present study we quantitatively evaluate the impact of TEVAR on aortic hemodynamics with a focus on bird-beak drawback, i.e., the graft protrusion into the aortic lumen at the level of the arch.

2 METHODS

The study is based on the accurate analysis of a real a clinical case where TEVAR was performed to treat a significative thoracic dissection. Such an analysis combines dedicated medical image elaboration of the pre- and post-operative Computed Tomography Angiography (CTA) datasets and computational fluid-dynamics (CFD) aimed at assessing a patient-specific investigation of the pre- post-operative hemodynamic conditions.

Medical image analysis. According to the approach proposed in [**?**], we perform the image segmentation of the two CTA datasets using the open-source software ITK-Snap.

CFD analyses. The post-operative lumen configuration suggests us to assess the aortic hemodynamics in three specific aortic regions: i) the inner part of aortic arch where the *bird-beak* drawback is evident; ii) the partially covered entry of the left subclavian, and iii) the distal part of the thoracic aorta characterized by a significant lumen narrowing. At the same time, we have exploited

the capability of computer-based simulations to explore *what-if scenarios*; thus, our study is based on the three different CFD analyses, each of them based on a specific aortic lumen configuration: *case A*, as-is post-operative lumen; *case B*, pre-operative lumen; *case C*, post-operative lumen without *stenosis* of the distal thoracic aorta.

3 RESULTS

A global view of the streamlines of blood velocities, at the selected time instant for each of the investigated cases, is depicted in Figure 1.

Case A: as-is post-operative lumen

The streamline path for this case highlights three peculiar effects in the regions of interest, contoured by a red box in Figure 1: (i) the stent-graft produces two bluffs: one at the location of the bird-beak and the second at the end of the aortic arch. Such bluffs induce *boundary-layer flow separations*, resulting in a disturbed flow in the arch; (ii) the graft protrusion into the arterial lumen al the level of the aortic arch produces also a significant occlusion of the left subclavian artery, resulting in a *backward facing step* geometry of the lumen profile, producing disturbance in the flow, clearly not present in the other two supra-aortic branches (i.e., brachiocephalic trunk and in the left common carotid artery); (iii) the stenosis of the distal thoracic aorta due to the compression of the true lumen by the false lumen, unfortunately not enlarged by the graft apposition, has an evident effect on the blood flow; in fact, as highlighted by Figure 1, a strong velocity increase and flow disturbance are also present. Consequently, a first observation deriving from these results is that the disturbance induced by the stenosis to the aortic flow appears more evident than the one induced by the bird-beak.

Case B: pre-operative lumen

Clearly, the pre-operative aortic arch shows a sharper angle than in the post-operative case, leading to more pronounced disturbance in the flow. Actually, for this specific cases, the stent-graft reduced the sharpness in the geometry of the aortic arch, thus reducing the disturbance of the flow.

Case C: post-operative lumen without stenosis

The path of streamlines in this case suggests that the stenosis of the distal thoracic aorta, which was virtually enlarged for this analysis, has no effect on the arch hemodynamics. At the same time, it is evident that the recovery of a smooth, physiological lumen profile eliminates the flow disturbance in this region highlighted by the results of the case A.

4 CONCLUSIONS

Our findings underline the value of proposed simulations; in fact, CFD analyses allow to observe important flow effects resulting from the specificities of patient vessel geometries. Consequently, our results are reinforcing the potential impact of the knowledge translation from computational biomechanics to clinical practice and viceversa.

REFERENCES

[1] F. Auricchio, M. Conti, S. Marconi, A. Reali, J. L. Tolenaar, S. Trimarchi, Patient-specific aortic endografting simulation: From diagnosis to prediction, *Computers in Biology and Medicine*, 43(4), 386-394, 2013.

Figures.

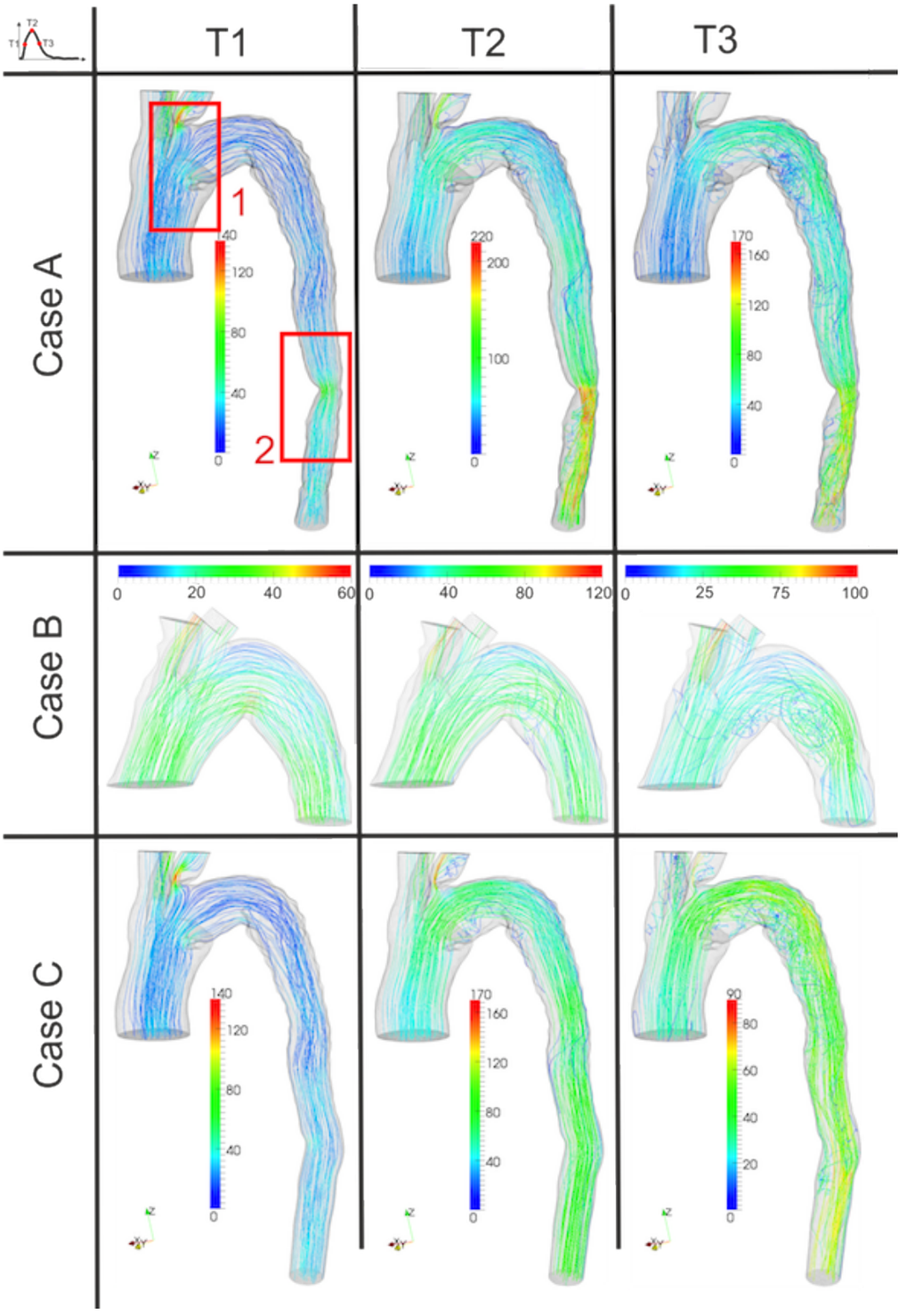

Figure 1: Velocity streamlines for each investigated cases. The corresponding velocity magnitude [cm/s] is used to color each streamline.

3rd International Conference on Computational and Mathematical Biomedical Engineering - CMBE2013
16-18 December 2013, Hong-Kong
P. Nithiarasu and R. Löhner (Eds.)

Numerical simulation of blood flow in the vascular network with pathologies or implants

Tatiana K. Dobroserdova[⋆], Yuri V. Vassilevski[⋆⋆], Sergey S. Simakov[⋆⋆⋆], Maxim A. Olshanskii[⋆†], Yuri A. Ivanov[⋆⋆], Vasiliy K. Kramarenko[⋆⋆⋆]
[⋆]Lomonosov Moscow State University, 119991, Leninskie Gory, Moscow, Russia, DobroserdovaTK@gmail.com
[⋆⋆]RAS Institute of Numerical Mathematics, 119333, Gubkina St. 8, Moscow, Russia, vasilevs@dodo.inm.ras.ru
[⋆⋆⋆]Moscow Institute of Physics and Technology, 141700, Institutski Lane 9, Dolgoprudny, Russia,simakov@crec.mipt.ru
[†]University of Houston,4800 Calhoun Rd. Houston, TX 77204-3008, United States of America

SUMMARY

Hemodynamics can be calculated by 1D model of global blood circulation. We present two methods to take into consideration influence of endovascular implants or pathologies on the blood flow by such model. The first way is to recover the state equation of the model. This equation describes elastic properties of the vessel wall. Modification takes place via the elastic fiber or fiber-spring model. The second way is to use 3D model of the blood flow in the region of interest. 3D model should be coupled with the 1D model of global blood circulation.

Key Words: *blood flow, multiscale modeling, boundary conditions, atherosclerosis, endovascular implants, vessel wall.*

1 INTRODUCTION

We use 1D model of global blood circulation [1-3] to describe hemodynamics in the vascular network. The model is based on the mass and momentum conservation laws. The third equation of this model, so-called the state equation, represents the dependence between transmural pressure and the area of vessel cross section. We propose two ways to take into consideration influence of endovascular implants or pathologies by the model of global blood circulation. The first method is based on modification of the state equation. The second method is multiscale: 3D model and 1D models of blood flow are coupled.

2 MODIFICATION OF THE STATE EQUATION BY THE ELASTIC FIBER OR FIBER-SPRING MODEL

The state equation is an empirical function for healthy arteries and veins. Endovascular implants or pathologies change elastic properties of the vessel wall. The state equation for such vessels changes too. We suggest to modify it using fiber or fiber-spring model of the elastic vessel wall [4,5].

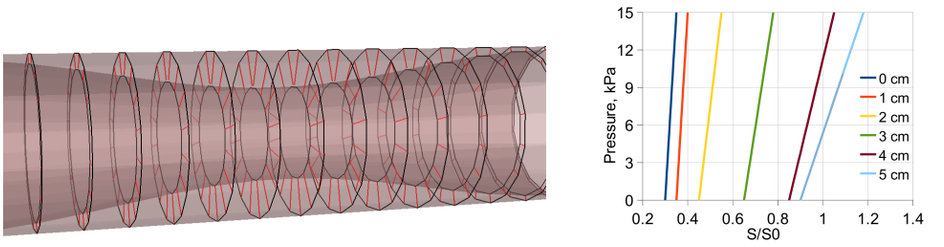

Figure 1: Left: Geometry of the atherosclerotic plaque. The minimal lumen is 30%. Right: The state equation for such atherosclerotic artery. The index of each curve corresponds to the distance (in cm) to the minimal cross section.

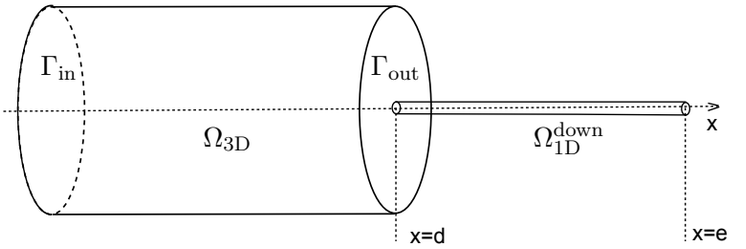

Figure 2: The schematic coupling of Ω_{3D} and $\Omega_{1D}^{\text{down}}$ domains.

The vessel wall is represented by a set of fibers. Every fiber has own parameters and corresponds to one of three types: elastic, smooth muscle or collagenous. This model allows us to calculate reaction of the vessel wall to the deformation. Deformation can be caused by the transmural pressure or the impact of implant.

The wall of the artery with atherosclerotic plaque is modeled as a three-layer shell (see fig.1 left). Three layers correspond to fibrous cap, lipid pool and vessel wall. The fibrous cap and the vessel wall have the same structure. They are represented by a set of fibers. The lipid pool is modeled by a set of radial springs. Such three-layer structure describes deformation of the atherosclerotic vessel wall under transmural pressure and allows to calculate the state equation for such artery (see fig.1 right). The new state equation also depends on x-coordinate. Some numerical results with blood flow simulations in the atherosclerotic networks are presented in [4].

3 COUPLING OF 3D AND 1D MODELS OF BLOOD FLOW

The region with pathology or implant is considered to be 3D. The Navier-Stokes equations are solved in 3D domain. Hemodynamics in other parts of vascular system is calculated by the 1D model of global blood circulation. 3D and 1D models should be coupled. For the 3D-1D domain, shown in fig. 2, we consider various types of coupling.

One common choice is to impose the continuity of the normal stress and the flux on the downstream boundary of 3D domain Γ_{out} coupled with 1D domain $\Omega_{1D}^{\text{down}}$ in point $x = d$. The cumulative energy of the coupled model is inconsistent in this case. It is not clear if cumulative energy is dissipated, as it holds for the full 3D Navier-Stokes equations and 1D model[6]. In [7] it was suggested to impose the continuity of flux and so-called total stress. In this case the cumulative energy

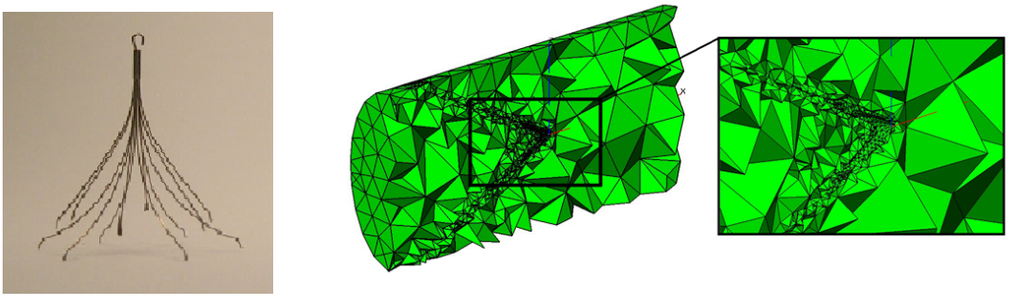

Figure 3: The visualization of the adaptive mesh for the flow over a model cava-filter problem: the left picture shows the cava-filter; the right shows the zoom of the mesh in the neighborhood of the filter's 'head'.

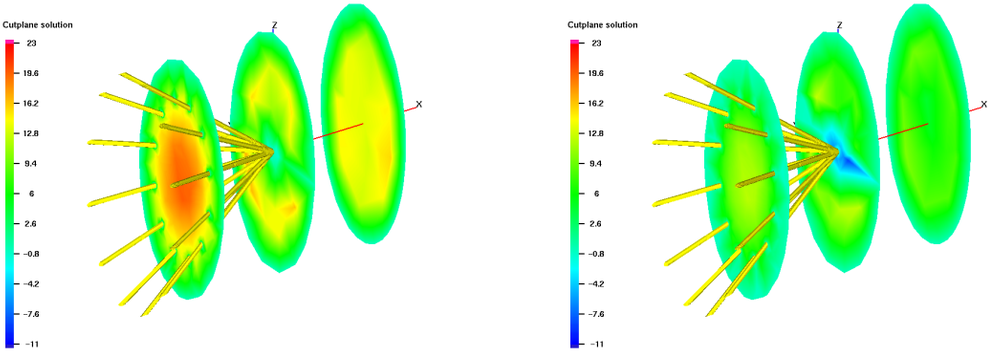

Figure 4: The visualization of the velocity x-component in several cutplanes orthogonal to x-axis for two times.

of the model dissipates. But the continuity of total stress is the natural boundary condition for the rotation form of the Navier-Stokes equations. Solving Navier-Stokes equations in such form is not a standard option in the existing software. Using the common convection or conservation forms leads to non-linear coupling conditions and often requires iterative treatment.

To describe the blood flow in Ω_{3D}, we use the standard convection form of the Navier-Stokes equations. To provide correct energy balance of the coupled model we offer to use new boundary condition. It demands the continuity of the linear combination of the fluid flux and the energy flux [6]:

$$\bar{p} \int\limits_{\Gamma_{out}} \mathbf{u} \cdot \mathbf{n} \mathbf{ds} + \frac{\rho}{2} \int\limits_{\Gamma_{out}} |\mathbf{u}|^2 (\mathbf{u} \cdot \mathbf{n}) \mathbf{ds} = (\bar{p} S \bar{u} + \frac{\rho}{2} S \bar{u}^3)|_{x=d}, \tag{1}$$

$\mathbf{u}$ is the velocity of blood in Ω_{3D}; $\bar{u}, S, \bar{p}$ are the velocity, the area of cross section and the pressure in Ω_{1D}; ρ is the density of blood. The condition (1) should be combined with the continuity of flux. The correct energy balance is valid for coupled model with such boundary conditions. The problem can be easily decoupled with splitting methods into the separate 1D problem and the 3D problem with usual inflow-outflow boundary conditions on every time step. The inequalities $\mathbf{u} \cdot \mathbf{n} < 0$ or $\mathbf{u} \cdot \mathbf{n} > 0$ are *not* necessarily pointwise satisfied on Γ_{in} or Γ_{out}, respectively ($\mathbf{n}$ is the outward normal vector). This is very important for modeling of blood flow in veins, where the values of x-component of velocity can be negative.

The geometry of 3D domain may be complex. It can model different types of pathologies, such as

aneurisms, stenosis, or different implants. We performed numerical simulation of the blood flow in the vein with cava-filter. 3D domain has strongly anisotropic inclusion. The adaptive mesh (see fig.3) and all 3D calculations were produced by the software package Ani3D [8]. This 3D domain is coupled with 1D model at the inflow and outflow boundaries.

Periodic velocity was prescribed. We visualize the computed solutions in fig. 4 by showing the values of the x-component of the velocity in several cutplanes orthogonal to x-axis. Behind the filter the velocity x-component eventually has negative values, indicating the occurrence of circulation zones and 'returning' flows. Numerical experiment allows us to calculate such important statistics as the drag force experienced by a filter during cardiac cycle. The waveforms in the 1D domains coupled to upstream and downstream boundaries of Ω_{3D} are very close. This suggests that the coupling conditions are efficient in conserving averaged flow quantities such as mean flux.

4 CONCLUSIONS

Two approaches for blood flow simulation in the vessel network with pathologies or implants have been developed. Both methods allow us to study the impact of local changes of wall properties or the implantation of endovascular filters to global hemodynamics. Results of numerical experiments conform to medical data.

ACKNOWLEDGEMENTS

This work was partially supported by RFBR grants 11-01-00971, 12-01-00283, 12-01-31223, 11-01-00767, 12-01-33084, 11-01-00855, MK 2719.2012.9.

REFERENCES

[1] S.S. Simakov and A.S. Kholodov. Computational study of oxygen concentration in human blood under low frequency disturbances. *Mathematical Models and Computer Simulations*, 1(2), 283–295, 2009.

[2] A. Quarteroni, L. Formaggia. Mathematical Modelling and Numerical Simulation of the Cardiovascular System. *Chapter in Modelling of Living Systems, Handbook of Numerical Analysis Series, P.G Ciarlet et J.L. Lions Eds.* Amsterdam: Elsevier, 2004.

[3] S.J. Sherwin, V. Franke, J. Peiro, K. Parker. One-dimensional modeling of vascular network in space-time variables. *J. of Engineering Mathematics*, 47, 217-250, 2003.

[4] Y. Vassilevski, S. Simakov, V. Salamatova, Y. Ivanov, T. Dobroserdova. Vessel wall models for simulation of atherosclerotic vascular networks. *Mathematical Modelling of Natural Phenomena*, 6(7), 82–99, 2011.

[5] Y.V. Vassilevski, S.S. Simakov, S.A. Kapranov. A multi-model approach to intravenous filter optimization. *International Journal for Numerical Methods in Biomedical Engineering*, 26, 915–925, 2010.

[6] T. Dobroserdova, M. Olshanskii. A finite element solver and energy stable coupling for 3D and 1D fluid models. *Computer Methods in Applied Mechanics and Engineering*, 259, 166 – 176, 2013.

[7] L. Formaggia, A. Moura, F. Nobile. On the stability of the coupling of 3D and 1D fluid-structure interaction models for blood flow simulations. *ESAIM: Mathematical Modelling and Numerical Analysis*, 41 (4), 743–769,2007.

[8] ANI3D: Advanced Numerical Instruments. http://sourceforge.net/projects/ani3d

Aneurysm Modelling: From Basic Science to Clinical Translation I

3rd International Conference on Computational and Mathematical Biomedical Engineering - CMBE2013
16-18 December 2013, Hong-Kong
P. Nithiarasu and R. Löhner (Eds.)

Clinical relevance of mechano-biological transduction in intracranial aneurysms: the mediating role of thrombus formation and inflammatory response expressing as aneurysm shape

Sven Hirsch⋆, Julien Egger⋆⋆, Isabelle Wanke⋆⋆⋆&⋆⋆⋆⋆, Zsolt Kulcsar⋆⋆⋆⋆ and Daniel A. Rüfenacht⋆⋆⋆⋆

⋆ZHAW, Zurich University of Applied Sciences, CH-8820 Wädenswil, sven.hirsch@zhaw.ch
⋆⋆ETH, Dept. of Electrical Engineering, CH-8092 Zurich, julien.egger@vision.ee.ethz.ch
⋆⋆⋆Dept. of Radiology, University of Essen, D-45122 Essen, isabel.wanke@uni-due.de
⋆⋆⋆⋆SwissNeuroInstitute, Dept. of Neuroradiology, Hirslanden Clinic, CH-8032 Zurich, [zsolt.kulcsar,daniel.rufenacht]@hirslanden.ch

SUMMARY

We present a clinical perspective, supported by biological findings, reflecting the potential of computational tools to understand and treat intracranial aneurysms. Thrombus formation and chronic inflammation are integral to disease progression, driven by blood flow energy. The interplay between flow energy, blood clotting and remodeling of the tissue is key to an enhanced disease understanding, to improve patient counseling and ultimately endovascular treatment planning. Current concepts suggest that blood governs wall remodeling by multiple biological steps. The process starts with flow induced thrombus adhesion (atherothrombosis) to the wall that secondarily leads to the release of biological mediators of inflammation entertaining destructive remodeling. Destructive wall remodeling jeopardizes the mechanical wall integrity with ensuing circumscribed softening and expansion of the aneurysm shape. The shape of an aneurysm is the visible result of these complex pathological processes and characterizes its disease status. Wall adherent thrombus formation, inflammatory reactions and the driving force of blood flow cause lumen shape changes. Here, shape irregularity is a distinctive sign of focal wall weakening. The integration of shape-analysis, vascular biology and phenotypical information will allow for personalized characterization of aneurysmal vascular disease and help to identify and establish shape as an image-based biomarker. Future translational efforts should aim at providing adequate IT tools and contributing to validation and disease understanding. Ensuing results will have a high likelihood to impact significantly on current clinical disease management.

Key Words: *blood flow, thrombus, aneurysm, remodeling, endovascular treatment.*

1 THE INTRACRANIAL ANEURYSM

An aneurysms is a pathological condition of the arterial wall, mostly circumscribed (focal), leading to the development of a saccular expansion. Less often, with involvement of the arterial circumference (segmental disease) it shows a fusiform appearance of the pathological arterial expansion. Combinations of both conditions are often observed. A variety of initial damages may weaken the vessel wall and prepare for aneurysm development, involving one or more of the three constituents of the vessel wall: elastic fibers, collagenous fibers or smooth muscle cells. In bifurcations, already a sustained period of localized shear stress increase is capable of mechanically disrupting

the subintimal elastic membrane. This mechanism is today considered the most frequent likely cause of aneurysm inception at bifurcations. Other mechanisms, like e.g. septic emboli stopped at a bifurcation may also lead to weakening of the adjacent vascular wall and facilitate initiation of an aneurysm development after infection and induction of wall fragility. This latter type of lesion is observed typically in more peripheral bifurcations of the cerebral arterial tree. Other known conditions leading to localized, focal or more extensive, segmental vessel wall damage include arteriosclerosis, infectious vasculitis, inflammatory vasculitis, sharp or blunt trauma, high blood pressure peaks or sustained hypertension and pathological vessel structures that may exist in the context of tumor or genetic predisposition, or a combination of any of the aforementioned pathologies. Basically, any type of damage to one or more of the three constituents of the vessel wall may lead to weakening and ensuing aneurysm development, becoming visible in diagnostic imaging with undue dilation of the arterial lumen. Epidemiological data tell us that the vessel wall will regularly find biological responses to compensate for induced weakness and even in case of further aneurysm evolution continue to function well without rupturing. Indeed, intracranial aneurysm disease presents with a low but risky incidence of hemorrhage (10/100'000/y) due to rupture. Still, there is a high prevalence of silent lesions (approx. 3/100), most of them being localized at arterial bifurcations. Currently, main indicators for rupture risk, size, location and shape have been identified in large clinical trials [1].

2 MECHANO-BIOLOGICAL TRANSDUCTION

Mechano-biological transduction in the context of aneurysms conceptually embraces the influence of physical blood flow energy on biology and subsequently, of biology on physical tissue properties of the aneurysm wall. Depending on the background of the scientific community, there is an accentuated focus on physical aspects, or alternatively, on biological aspects. The interface of both aspects is key to an integral understanding mechano-biological transduction.

The biological aspects of the transduction from blood flow energy to aneurysm wall reaction are often looked at as being quite direct and following rules similar to what is known for the interaction of blood flow with a healthy arterial wall. Increased flow would normally entail enlargement of a vessel lumen and increased pressure would lead to thickening of the vessel wall – all reactions that are triggered in the wall tissue after being sensed through complex cellular transduction mechanisms. These are mainly sensitive to changing forces of shear stress and pressure. A healthy endothelial layer picks up the flow dependent shear signal and cells of the arterial wall are capable of sensing the pulsatile pressure changes. The conditions for aneurysms are somewhat different, since these sensors become increasingly absent and other mechanisms prevail.

Current concepts suggest that the fluid-wall interaction is governed by intermediate biological steps initiated and mediated by wall adherent thrombus deposits that lead through release of biological mediators to inflammatory, destructive wall remodeling. In this case the energy of flow would act mainly through biological events related to such blood deposits (atherothrombosis) on the biology of wall (inflammatory reaction), and by this secondarily on the biomechanics of the wall (circumscribed softening and expansion of the aneurysm shape) – these are the critical steps of the mechano-biological transduction chain in aneurysm disease, as is understood today [2]. Decoding such mechanisms in detail will allow for further evolved concepts, including on how flow energy acts indirectly through production of areas of flow stagnation, on how subsequent thrombus forms, on how adjacent wall inflammation and ensuing regional softening of the vessel wall prone to undergo expansion under pressure (aneurysm growth) occur, and possibly, on how these steps prepare for rupture: a complex, complicating event in this chain of destructive aneurysm wall degradation. Blood is the main actor in the lifecycle of the aneurysm: flowing blood at

the same time provides mechanical energy and regulates the biological processes in the vessel. Simulations of the aneurysm for long concentrated on blood flow and wall shear stress only, to mechanistically understand the disease with established engineering tools. In turn, clot formation has been simulated with experimental simulation code since the early 90s [3], but only in recent years thrombosis is reflected in computational aneurysm studies [e.g.4]. Although integrating flow mechanics and vessel biology is highly desirable, it is today far from being solved. This shortcoming is mainly due to the lack of appropriate simulation methodologies that go beyond even the most sophisticated approaches of computational fluid dynamics. Secondly, due to the high complexity and biological variability it is dauntingly difficult to gauge and validate models with actual experiments.

3 THE BIOLOGY ON ENDOVASCULAR TREATMENT

Endovascular treatment (EVT) offers novel options to induce healing by flow corrections with specific implants. The approach is undergoing further rapid evolution and understanding biological mechanisms is fundamental to safeguard a successful outcome with new design. Flow diversion was the term coined with the advent of finely braided stents, exhibiting a reduced porosity and designed to slowing down the blood flow in pathologically expanded, aneurysmal vascular segments external to the implant. A flow diverter is by its presence primarily reconstructing the vessel lumen, where the low porosity surface provides a scaffold to the formation of endothelial layer. Somewhat similar to a covered stent-graft, however, distinctly different: a flow diverter is just another implant helping to induce thrombus that is supposed to progressively turn into a reliable scar repair and to be resorbed stepwise along the processes of reverse remodeling of the vessel wall. With early clinical use of flow diverters interventionists were taught a surprising lesson, unseen in preclinical evaluation, but already well studied in its basic biological principle [2]: Rapid formation of a large thrombus could lead to an overwhelming inflammatory response of the aneurysm wall with ensuing decomposition and possible secondary rupture [5]. The different EVT techniques and implants will produce variable biological reactions, where thrombus formation in our mind always gears towards stable reverse remodeling. Unfortunately, this has not always been the case and still cannot be reliably achieved. The principle of flow diversion has steadily improved the power of EVT, but with current devices also increased the potential of complications, mainly due to yet difficult delivery and risks given by increased device thrombogenicity. Here clinicians envision further improvements:

- Improved delivery, with easier and more precise deployment, including the capability of adding implants in the aneurysmal lumen for the purpose of initiating controlled building of stable thrombus and with the goal of facilitating a timely and lasting reverse remodeling.
- Flow diversion focused to the area of interest that maintains flow in branching vessels.
- Reduced short- and long-term thrombogenicity on device surface to avoid continuous, high-dose intake of antiaggregants, applied to reduce periprocedural overshooting clot formation and to avoid formation of delayed thrombosis on stent-covered branches.
- Improved apposition to vessel wall to avoid unwanted thrombus formation.
- Avoid uncontrolled and overshooting build-up of implant material or device kinking along inner curves of sharp arterial bends, such as may be observed in the carotid siphon.
- Improve lumen visibility in post treatment MR by reducing magnetic field disturbances.

Further, since we have accepted the fact that aneurysm biology is influenced by thrombus and ensuing inflammation, the flow as driver of thrombus formation is recognized and could be increasingly heralded by endovascular means – a fact that brings forward the interest of using computational flow dynamics, when it comes to designing new devices and to choose the best device for a given condition.

4 SHAPE AS SURROGATE FOR THE DISEASE STATE

Due to the high quality of current medical imaging silent aneurysms are increasingly being found incidentally. By flow-based and contrast-agent enhanced visualization of the circulating blood, all currently used medical imaging evaluation methods for aneurysms can, after adequate reconstruction, provide a digital 3D replica of the vascular lumen. The wall of an aneurysm being too thin to be visualized directly by such imaging, the characterization of its quality, however, remains a matter of indirect assessment. Once detected, prediction of disease evolution and possibly treatment planning are clinically of utmost interest. Such predictions are issue of personalized assessment. The shape of an aneurysm is the result of the complex processes described above and carries information about its biological history. In pathological situations, as is the case in aneurysms, rules of mechano-biological transduction may differ from rules in normal conditions. Flow dependent thrombus apposition will entertain inflammation, which by enzymatic reaction softens the vascular matrix. Depending on this process, the wall may locally bulge and express irregular shape features representing a variable degree of instability. In this notion, shape reflects the disease status and shape features may therefore serve as imaging biomarkers for disease state. Mathematical shape analysis to uniquely characterize aneurysms can then provide the basis to characterize aneurysms according to identified risk patterns. With the advent of automated mathematical shape analysis (e.g. Zernike moments [6]), able to represent any individual aneurysm 3D shape in a reproducible code of numbers, the computational aneurysm assessment has become the most promising, reproducible instrument for characterizing image-based information on intracranial aneurysms.

5 ACKNOWLEDGEMENTS

We are grateful for the support of this project (CR32I3 127008) by the Swiss National Science Foundation.

REFERENCES

[1] Morita, A., et al. The Natural Course of Unruptured Cerebral Aneurysms in a Japanese Cohort, *New England Journal of Medicine*, 366(26), 2474-2482, 2012.

[2] J. Frosen, et al. Saccular intracranial aneurysm: pathology and mechanisms, *Acta neuropathologica*, 123(6), 773-786, 2012.

[3] A.L. Fogelson. Continuum Models of Platelet-Aggregation – Formulation and Mechanical-Properties, *Siam Journal on Applied Mathematics*, 52(4), 1089-1110, 1992.

[4] G. Moiseyev and P.Z. Bar-Yoseph. Computational modeling of thrombosis as a tool in the design and optimization of vascular implants, *Journal of Biomechanics*, 46(2), 248-252, 2013.

[5] Z. Kulcsar et al. Intra-aneurysmal thrombosis as a possible cause of delayed aneurysm rupture after flow-diversion treatment, *American Journal of Neuroradiology*, 32(1), 20-25, 2011.

[6] J.M. Pozo, M.C. Villa-Uriol and A.F. Frangi. Efficient 3D geometric and Zernike moments computation from unstructured surface meshes. *IEEE Transactions on Pattern Analysis and Machine Intelligence*, 33(3), 471-484, 2011.

3rd International Conference on Computational and Mathematical Biomedical Engineering - CMBE2013
16-18 December 2013, Hong-Kong
P. Nithiarasu and R. Löhner (Eds.)

A novel chemo-mechano-biological mathematical model of intracranial aneurysm evolution.

Emilie C. Dickinson*, Aikaterina Mandaltsi* and Paul N. Watton,*****
*Institute of Biomedical Engineering, Department of Engineering Science, University of Oxford, emilie.c.dickinson@gmail.com
**Department of Computer Science, University of Sheffield, p.watton@sheffield.ac.uk
*** INSIGNEO Institute for in silico Medicine, University of Sheffield

SUMMARY

We present a novel coupled flow-solid-growth-transport (FSGT) mathematical model of aneurysm evolution. The aim of this model is to establish the effect of thrombus on the delivery of oxygen to an arterial wall and the consequential influence on the growth and remodelling of the collagenous constituents therein. In this aim, the conceptual cylindrical model of IA evolution presented by Watton et al. [1] is extended to additionally *(i)* model dynamic thrombus formation; *(ii)* compute mass transport of oxygen through a propagating thrombus and thinning wall; *(iii)* link growth and remodelling (G&R) to local oxygen levels. In this conceptual model, we observe that impedance to wall oxygenation may arise as a result of thrombus propagation. Furthermore, the coupling of oxygen deficiency to fibroblast functionality made the difference between a stable and an enlarging aneurysm. This model demonstrates a starting point for multi-scale, multi-physics modelling of IA evolution which accounts for the biochemical, mechanobiological and haemodynamic processes involved in aneurysm pathophysiology.

Key Words: *aneurysm, growth and remodelling, thrombus, oxygen mass transport.*

1 INTRODUCTION

Five percent of strokes are caused by subarachnoid haemorrhages (SAHs), of which an estimated 85% are secondary to the rupture of an intracranial aneurysm (IA), a localised, blood-filled dilation of the artery wall. In spite of the advancements in neurosurgical and endovascular therapies, fatality due to an aneurysmal SAH remains between 40 and 50%. Nevertheless, the prevalance of ruptured IAs is far lower than their overall occurrence; an estimated 9 to 20 per 100 000 aneurysmal SAHs per year compared to the 3-6% observed during prospective autopsies and angiographic studies. In terms of patient care, this has accentuated the importance of assessing the risk of preventative treatment versus the potential that an IA will stay asymptomatic, whereby it stabilises and never ruptures. Interventional treatment by the means of implanting endovascular devices aims to reduce intrasaccular flow and eventually trigger the formation of a stable thrombus, thus removing the IA from circulation. However, regardless of high occlusion rates, there are still reports of initial or further haemorrhaging following treatment. This has brought into question the possible deleterious effects of thrombus formation on wall viability, in particular the limitation of oxygen supply to the aneurysmal wall. Chronic hypoxia can lead to endothelial dysfunction, smooth muscle cell (SMC) and fibroblast apoptosis, excessive production of proteases, reduced

collagen deposition and the accumulation of inflammatory cells: a culmination of which are hypothesised to lead to ultimate IA rupture. Thus, although the widely reported haemodynamic and mechanical benefits of thrombus formation have been the basis for choosing endovascular therapy, a broader understanding of the possibly detrimental biochemical impact of thrombus is vital to ensure optimum patient care. On this basis, we propose an innovative fluid-solid-growth-transport (FSGT) mathematical model based on the 1D conceptual cylindrical model developped by Watton et al [1] to explore the biochemical role of thrombus on the evolution of an IA.

2 METHODS

The conceptual model presented is a 1D, single layer, non-linear cylindrical membrane which is subjected to a constant axial pre-stretch λ_z, and a circumferential stretch λ due to the inflation by a constant internal pressure P acting normal to the membrane. The gross mechanical response of the artery is shown to be defined by the following governing force balance equation:

$$P = \frac{H}{R\lambda}\frac{1}{\lambda\lambda_z}\sum_{J=E,C} m_J \sigma_J(\lambda), \tag{1}$$

whereby the overall elastic potential is an additive split of the elastinous (i.e. ground substance, elastin fibres and passive SMCs) and collagenous contributions of the membrane. R and H are the arterial radius and wall thickness in the unloaded configuration respectively. m_J is the mass concentration of either elastin $(J = E)$ or collagen $(J = C)$. Similarly $\sigma_J(\lambda)$ is the azimuthal Cauchy stress derived from the strain energy function of each constituent J. The Cauchy stress of elastin may be defined in terms of the potential energy stored per unit volume $\hat{\Psi}_E$ which characterises the isotropic behaviour of elastin as a neo-Hookean material:

$$\sigma_E(\lambda) = \lambda\frac{\mathrm{d}\hat{\Psi}_E}{\mathrm{d}\lambda} = K_E\lambda^2\left(1 - \frac{1}{\lambda_z^2\lambda^4}\right). \tag{2}$$

K_E is the material parameter of elastin. The azimuthal Cauchy stress due to contributions from collagen fibres of pitch ϕ is defined in terms of the potential energy stored per unit volume $\hat{\Psi}_C$, which is set to a simple nonlinear polynomial function:

$$\sigma_C\left(\lambda_C^\phi\right) = \lambda_C^\phi\frac{\mathrm{d}\hat{\Psi}_C}{\mathrm{d}\lambda_C^\phi}\cos^2\phi = K_C\left(\lambda_C^\phi\right)^2\left(\frac{\left(\lambda_C^\phi\right)^2 - 1}{\left(\lambda_C^{AT}\right)^2 - 1}\right)^5\cos^2\phi, \qquad \lambda_C^\phi > 1. \tag{3}$$

Collagen fibres are inactive under low loads, hence $\hat{\Psi}_C = 0$ when $\lambda_C^\phi < 1$. K_C is the material parameter of collagen. The stretch in collagen is defined as $\lambda_C^\phi = \lambda^\phi/\lambda_R^\phi$, whereby λ^ϕ is the stretch in elastin resolved in the direction of collagen fibres and the recruitment stretch, λ_R^ϕ, is stretch of the elastin in the direction of the collagen as it becomes load bearing. Fibroblasts attach and configure the collagen fibres in a state of stretch. It is postulated that this 'attachment' stretch (λ_C^{AT}) remains constant regardless of the altered configuration as collagen remodels under strain.

In order to mimic histological observations of slow degradation of elastin over time: $m_E(t) = 0.01^{t/5}$ for $0 \leq t \leq 5$years, after which $m_E(t) = 0$. The collagen fabric is assumed to adapt (i.e. remodel and grow/atrophy) in order to compensate for the loss of load bearing elastin. It is hypothesised that new homeostasis is achieved by restoring the stretch in collagen towards to the fixed attachment stretch, λ_{AT}^C. For this model this is accomplished by individually modelling two different functionalities of fibroblasts: (i) remodelling of the recruitment stretch in the aim to reduce the stretch at which collagen is recruited to bear load (eq. 4) and (ii) up(down)regulation of collagen synthesis in reponse to variations in stretch (eq. 5).

$$\frac{\mathrm{d}\lambda_R}{\mathrm{d}t} = \alpha \left(\frac{\left(\lambda_C^{\phi}\right)^2 - \left(\lambda_C^{AT}\right)^2}{\left(\lambda_C^{AT}\right)^2 - 1} \right) \quad (4) \qquad \frac{\mathrm{d}m_C}{\mathrm{d}t} = \beta m_C \left(\frac{\left(\lambda_C^{\phi}\right)^2 - \left(\lambda_C^{AT}\right)^2}{\left(\lambda_C^{AT}\right)^2 - 1} \right) \quad (5)$$

The remodelling parameter α relates to the fibre turnover rate (i.e. collagen half-life), and the growth parameter β phenomenologically relates to the rate at which fibroblasts synthesis collagen. It has been observed that platelet aggregation and adhesion during the formation of thrombus is intrinsically linked to local wall shear rates ($\dot{\gamma}$) and hence it is hypothesised that thrombus propagation velocity, V_{th} is inversely proportional to ($\dot{\gamma}$) at the lumen/wall interface [2]: $V_{th} = \zeta \pi r_i^3 / 4Q$, whereby the flow rate through the artery Q is maintained constant and r_i is the inner radius of the artery in contact with the flow. The rate of thrombus growth is regulated by the constant ζ. It is assumed that thrombus growth halts when the shear rate has reached homeostatic values: $V_{th} = 0$ when $|\dot{\gamma}| \leq |\dot{\gamma}_0|$.

The steady-state oxygen distribution through the thrombus and wall layers of the 1D model are deemed to be through diffusion-only transport,

$$\mathscr{D}_L \frac{\mathrm{d}}{\mathrm{d}r} \left(\frac{\mathrm{d}\mathscr{C}_L}{\mathrm{d}r} \right) = -r\dot{q_L}. \qquad L = w, th \quad (6)$$

Whereby $\mathscr{C}$ and $\mathscr{D}$ are the concentration and the diffusivity of oxygen respectively for the thrombus ($L = th$) and wall layers ($L = w$). The O_2 consumption by cellular components within the thrombus layer is deemed negligible: i.e. $\dot{q_{th}} = 0$. The consumption rate within the wall, $\dot{q_w}$, is a function of the mass density of SMCs and fibroblasts, as well as the normalised average oxygen tension within the wall ($\overline{\mathscr{C}_w}$) to take into account adjustment to cellular energy demand required for aerobic energy production through adaptive responses to hypoxia. The rate at which reduced oxygen levels affects fibroblast functionality is explored by implementing the following:

$$\beta = \beta_0 + (\beta_{min} - \beta_0) \left[\frac{\left(\overline{\mathscr{C}_w}\right)^i - \left(\overline{\mathscr{C}_w}\right)_0^i}{\left(\overline{\mathscr{C}_w}\right)_{min}^i - \left(\overline{\mathscr{C}_w}\right)_0^i} \right] \qquad \overline{\mathscr{C}_w} > 2\%. \quad (7)$$

The exponential index i allows for a variation in the rate at which β decreases with $\overline{\mathscr{C}_w}$. The '0' subscript denotes initial values as $t = 0$. Fibroblasts are assumed to remain functional even in extreme hypoxic conditions: $\beta_{min} = 0.04\beta_0$ for $\forall \overline{\mathscr{C}_w} \leq 2\%$.

The following four growth functions (GF) are explored to establish the impact of both the thrombus propagation rate ζ and the rate at which oxygen levels reduce fibroblast functionality β (by means of varying the exponential index i) on membrane expansion:

- GF1: $i = 1/16$, $\zeta = 2e^{-4}$;
- GF2: $i = 1/4$, $\zeta = 2e^{-4}$;
- GF3: $i = 1/4$, $\zeta = 5e^{-4}$;
- GF4: $i = 1$, $\zeta = 2e^{-4}$;

3 RESULTS AND DISCUSSION

Figure 1 presents the results of this novel FSGT model. Overall, all four GFs proposed resulted in the continual expansion of the membrane over the 30 year time frame. The mass density of collagen is limited by the gradually hypoxic conditions within the wall as a result of the growing thrombus layer. If the collagen fibre density does not increase at a sufficient rate, the existing fibres undergo a greater stretch in order to maintain mechanical equilibrium: i.e λ_{ϕ}^{C} diverges away from λ_{AT}^{C}, resulting in an unstable evolving membrane over time.

The work presented here demonstrates the potential for modelling the possible detrimental effects of thrombus on IA progression. Nonetheless, this conceptual 1D-cylindrical FSGT model has its

limitations which can only be improved upon so as to gradually step closer to a fully multi-scale, multi-physics model of IA evolution. Current work involves extending this to a two-layer (adventitia and media) 1D model which implements shear-regulated elastin degradation, the passive and active mechanical responses of SMCs, as well as the possible effect of oxygen tension on SMC apoptosis. This sophisticated framework and numerical investigation will be presented.

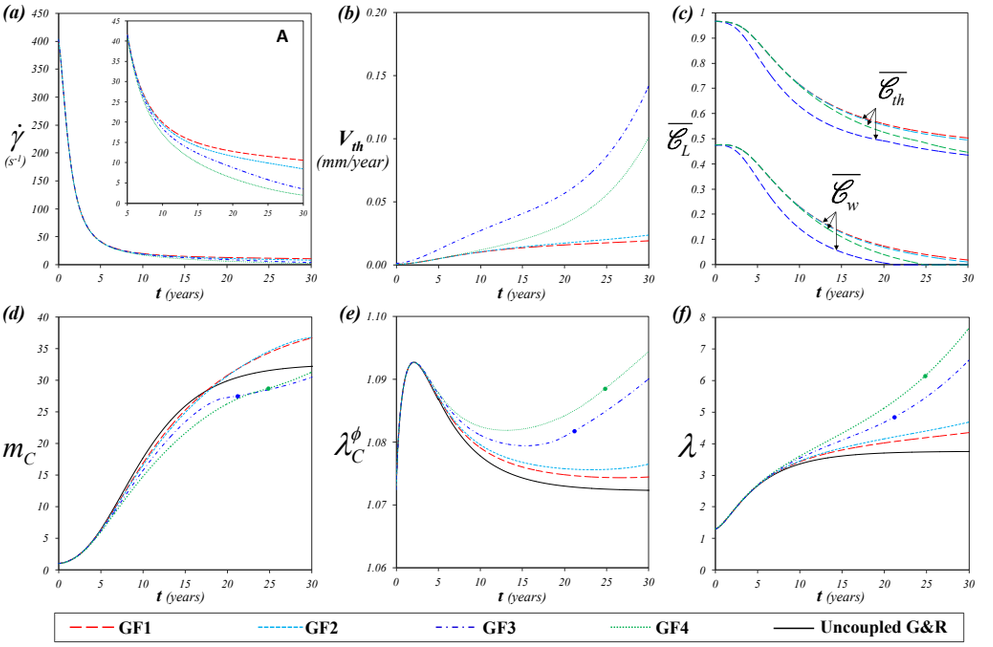

Figure 1: Results for all four growth functions (GFs) for the coupled FSGT model compared to the uncoupled G&R model of a cylindrical membrane: *(a)* decrease in shear rate ($\dot{\gamma}$) at the inner radius (r_i) as the cylinder expands due to onset of elastin degradation, inset **A** is a closer inspection of first 5 years; *(b)* resulting shear-regulated thrombus propagation velocity V_{th}; *(c)* normalised average oxygen concentration through the thickening thrombus ($\overline{\mathscr{C}_{th}}$) and thinning arterial wall ($\overline{\mathscr{C}_w}$); *(d)* variations in collagen mass density as a result of thrombus-induced oxygen tension decline within the wall, *(e)* resulting stretch in collagen fibres; *(f)* overall increase of circumferential stretch with time. Blue and green dots highlight temporal time points at which $\overline{\mathscr{C}_w} = 0$ for GF3 and GF4.

4 CONCLUSIONS

A novel FSGT mathematical model is conceived to explore the biochemical impact of thrombus on IA evolution. The shear-regulated propagation of a thrombus layer during membrane expansion leads to the gradual decrease in oxygen tension within the wall. Moreover, as a consequence of coupling this oxygen deficiency to fibroblast functionality, the collagen fibre mass density was shown to increase at an insufficient rate to compensate for the transfer in load from the degrading elastinous consitituents to the collagenous constituents, thus resulting in the increased stretch of collagen fibres in order to maintain mechanical equilibrium. Moreover this over-expansion results in the gradual unstable evolution of the membrane.

REFERENCES

[1] P.N. Watton, Y. Ventikos and G.A. Holzapfel, Modelling the growth and stabilisation of cerebral aneurysms, *Mathematical Medicine and Biology*, 26(2), 133-64, 2009.

[2] T. Bowker. *A computational model for thrombus prediction*, PhD Thesis, University of Oxford, 2010.

3rd International Conference on Computational and Mathematical Biomedical Engineering - CMBE2013
16-18 December 2013, Hong-Kong
P. Nithiarasu and R. Löhner (Eds.)

A novel mathematical model for the microstructural adaption of the collagen fabric during aneurysm evolution

H. Chen[1], A. M. Robertson[2], P. N. Watton[3,4]
[1]Department of Engineering Science, University of Oxford, Oxford, UK
[2]Department of Mechanical Engineering and Materials Science, University of Pittsburgh, USA
[3]Department of Computer Science, University of Sheffield, Sheffield, UK
[4]INSIGNEO Institute for *in silico* Medicine, University of Sheffield, UK
haoyu.chen@eng.ox.ac.uk, rbertson@pitt.edu, p.watton@sheffield.ac.uk

SUMMARY

We propose a novel model of intracranial aneurysm (IA) evolution. The arterial wall is modelled as a non-linear elastic cylindrical membrane subject to an axial stretch and internal pressure. Following previous models, we assume that collagen fibres are configured to the arterial wall in a state of stretch in the loaded configuration. However, we now simulate that they are configured with a distribution of attachment stretches. Each layer of the artery is modelled as a fibre-reinforced composite consisting of elastin and a population of collagen fibres with varying undulation relative to the unloaded configuration. Initially, in the *in vivo* configuration, we assume that the media bears all the load whilst the adventitia acts solely as a protective sheath. To simulate IA evolution, we prescribe a loss of the medial layer and allow the adventitia to adapt to take on a load bearing role: this is achieved by remodelling the distribution of fibre attachment stretches. We observe that remodelling of the collagen fibre attachment stretch distribution is necessary to accurately simulate the evolving wall thickness of an IA.

Key Words: *aneurysm, growth and remodelling, collagen fibres, attachment stretch.*

1 INTRODUCTION

An intracranial aneurysm (IA) is a balloon-like out-pouching fo the arterial wall. The prevalence rate is estimated between 0.4% and 6%. The fatality rate can be as high as 50% if rupture occurs; however, most cases remain asymptomatic. Mathematical models of aneurysm evolution may help understand the aetiology of the disease. A common approach for such models is to assume that collagen fibres are configured to the artery in a state of stretch relative to the loaded configuration. We refer to this as the attachment stretch. In most previous studies, the attachment stretch has been assumed to be a constant. However, experimental observations demonstrate that collagen fibres are physiologically distributed with a range of waviness relative to unloaded tissue: this implies that there must be a distribution of attachment stretches. We propose a novel collagen remodelling methodology which simulates an attachment stretch distribution and its adaption during IA evolution.

2 METHODOLOGY

We model the artery as non-linear elastic cylindrical membrane. Deformation of the artery under internal pressure is governed by the principle of virtual displacement. It can be derived that the gross mechanical response of the artery can be expressed as:

$$p = \frac{1}{R\lambda}\frac{1}{\lambda\lambda_Z}\sum_{L=M,A}\sum_{J=E,C} H_L m_{J_L}\sigma_{J_L}(\lambda) \tag{1}$$

where p is the blood pressure and R is the radius in the unloaded configuration. L can take either M or A, indicating the media or adventitia layer. H_L is the thickness of layer L layer in the unloaded configuration. λ_Z is the axial pre-stretch. m_{J_L} is the normalised mass-density of elastin ($J = E$) or collagen ($J = C$) in layer L. $\sigma_{J_L}(\lambda)$ is the azimuthal Cauchy stress of J constituent in the L layer derived directly from the strain energy functions (SEF) of these constituents. Arterial elastin is modelled using a Neo-Hookean constitutive model. We also assume that each individual collagen fibre is neo-Hookean and that gradual fibre recruitment gives rise to the nonlinearity of the collagen response. Fibres are gradually recruited for load bearing in a statistical manner represented by a probability distribution function (pdf) of recruitment stretches $P(\lambda_{R_L})$ [2, 3]. We follow Martufi et al.'s approach and utilise a triangular pdf for simplicity [3]. Fig. 1 shows an example of the collagen recruitment stretch distribution $P(\lambda_{R_L})$, in which $\lambda_{R_L}^{min}$ relates to the recruitment stretch at which the first collagen fibre is recruited, $\lambda_{R_L}^{max}$ relates to the recruitment stretch at which the last collagen fibre is recruited and $\lambda_{R_L}^{mod}$ relates to the recruitment stretch at which most collagen fibres are recruited.

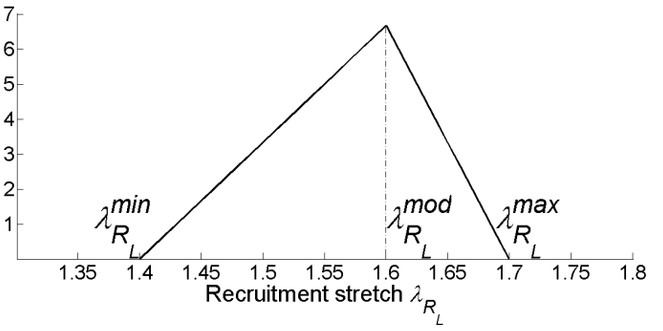

Figure 1: An example of the collagen recruitment stretch distribution $P(\lambda_{R_L})$. $\lambda_{R_L}^{min}$: recruitment stretch at which the first collagen fibre is recruited. $\lambda_{R_L}^{max}$: recruitment stretch at which the last collagen fibre is recruited. $\lambda_{R_L}^{mod}$: recruitment stretch at which most collagen fibres are recruited.

The Cauchy stress $\sigma_{C_L}(\lambda)$ of unit volume collagen is computed by the gradual recruitment of single fibres within the volume during load bearing:

$$\sigma_{C_L}(\lambda) = \lambda\frac{\mathrm{d}\widehat{\Psi}_{C_L}}{\mathrm{d}\lambda} = \lambda\frac{\mathrm{d}}{\mathrm{d}\lambda}\int_1^{\lambda}\Psi^*_{C_L}P\left(\lambda_{R_L}\right)\mathrm{d}\lambda_{R_L} \tag{2}$$

where $\Psi^*_{C_L}$ and $\widehat{\Psi}_{C_L}$ are the strain energy stored in a single collagen fibre and unit volume respectively.

IA growth is often characterised by the loss of media layer. Consequently, the adventitia must adapt to become the main load bearer. We assume fibres are configured with a distribution of attachment stretches, i.e. $P\left(\lambda_{AT_L}\right)$. Collagen fibres with maximum attachment stretch $\lambda_{AT_L}^{max}$ are the

first to be recruited, having the minimum recruitment stretch $\lambda_{R_L}^{min}$. Contrarily, collagens with minimum attachment stretch $\lambda_{AT_L}^{min}$ are the last to be recruited, having maximum recruitment stretch $\lambda_{R_L}^{max}$. Hence the distribution of recruitment stretches $P\left(\lambda_{R_L}\right)$ (as measured in experiments) is a natural consequence of a distribution of the attachment stretches. The remodelling of collagen fibres is simulated through modelling the adaption of recruitment stretch distribution $P\left(\lambda_{R_L}\right)$, which is determined by three variables: $\lambda_{R_L}^{min}$, $\lambda_{R_L}^{max}$ and $\lambda_{R_L}^{mod}$. The increase of minimum attachment stretch $\lambda_{R_L}^{min}$ pushes $P\left(\lambda_{R_L}\right)$ to shift rightwards, and is modelled through Eqn. 4, where α is a remodelling rate parameter which relates to the collagen fibre turnover rate, with greater value indicating faster turnover and $\lambda_{C_L}^{max}$ is the maximum collagen stretch during the cardiac cycle; fibre growth is modelled using a first order ODE, i.e. Eqn. 3, where β is a growth-rate parameter.

$$\frac{\mathrm{d}m_{C_A}}{\mathrm{d}t} = \beta m_{C_A}\left(\frac{\lambda_{C_A}^{max} - \lambda_{AT_A}^{max}}{\lambda_{AT_A}^{max}}\right) \quad (3) \qquad \frac{\mathrm{d}\lambda_{R_L}^{min}}{\mathrm{d}t} = \alpha\left(\frac{\lambda_{C_L}^{max} - \lambda_{AT_L}^{max}}{\lambda_{AT_L}^{max}}\right) \quad (4)$$

For medial collagen, the minimum and maximum attachment stretches, $\lambda_{AT_M}^{min}$ and $\lambda_{AT_M}^{max}$, are set to be 0.9 and 1.1 throughout the simulation. For adventitia, initial values of $\lambda_{AT_A}^{min}$ and $\lambda_{AT_A}^{max}$ are set to be 0.8 and 1.0. Initially, we assume that all the load in borne by the medial layer. We simulate the degradation of the medial layer and the adaption of the adventitia to take on a load bearing role in the homeostatic configuration. This is achieved by increasing the maximum attachment stretch $\lambda_{AT_A}^{max}$ of adventitial collagen fibres; for illustration the minimum attachment stretch $\lambda_{AT_A}^{min}$ is taken to be $\lambda_{AT_A}^{min} = \lambda_{AT_A}^{max} - 0.2$.

3 RESULTS

Figure 2a illustrates the prescribed degradation of the media and Fig. 2b depicts the evolution of adventitia collagen concentration: notice that the greater the value of $\lambda_{A_{AT}}^{max}(t = T)$, the lower the value of m_{C_A} when the IA stabilises. Fig. 2c shows the evolution of stretch with different $\lambda_{A_{AT}}^{max}(t = T)$. Fig. 2d shows evolution of collagen stretches with $\lambda_{A_{AT}}^{max}(t = T) = 1.12$. Fig. 2e illustrates the evolution of the wall thickness for different values of $\lambda_{A_{AT}}^{max}(t = T)$. Notice that the larger $\lambda_{A_{AT}}^{max}(t = T)$ is, the smaller the final wall thickness will be. Lastly, Fig. 2f illustrates the evolution of the thickness to radius ratio.

4 CONCLUSION

A novel mathematical model is proposed to represent a distribution of collagen fibre attachment stretches and their remodelling during aneurysm evolution. This sophistication enables the adaption of the load bearing role of the adventitia in the homeostatic configuration to be modelled. Moreover, it yields predictions for the evolution of the aneurysm wall thickness consistent with in vivo observations.

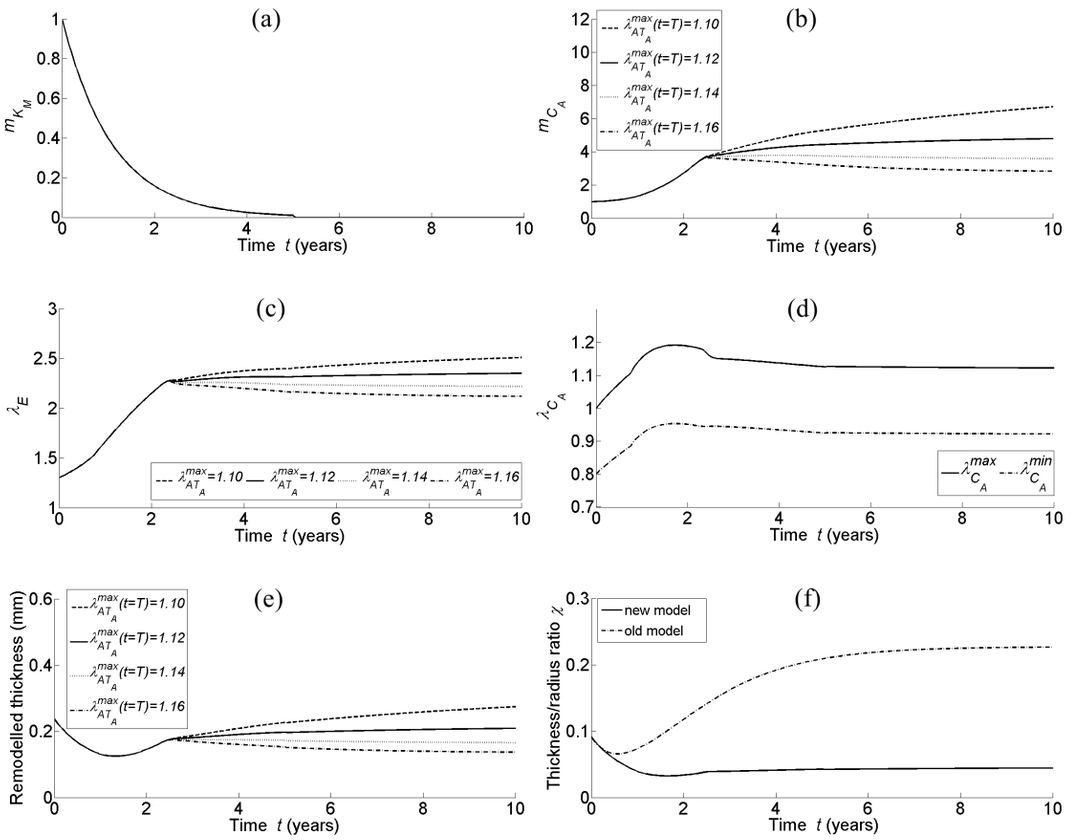

Figure 2: Results illustration: (a) Medial fibre degradation (K can take either E for elastin or C for collagen). (b) Adventitia collagen growth. The higher value $\lambda_{AT_A}^{max}$ stabilises at, the smaller m_{C_A} is. T: duration of the simulation. (c) Elastin stretch evolution. (d) Evolution of adventitia collagen stretch $\lambda_{C_A}^{max}$ and $\lambda_{C_A}^{min}$ with $\lambda_{AT_A}^{max}$ stabilising at 1.12. (e) Evolution of total remodelled wall thickness. (f) Comparison of remodelled thickness to evolving radius ratio between old model and new model with $\lambda_{A_{AT}}^{max}(t = T) = 1.12$.

REFERENCES

[1] P. N. Watton et al., Modelling the growth and stabilization of cerebral aneurysms. *Mathematical medicine and biology*, 26, 133-164, 2009.

[2] M. R. Hill et al., A theoretical and non-destructive experimental approach for direct inclusion of measured collagen orientation and recruitment into mechanical models of the artery wall. *Journal of Biomechanics*, 45, 762-71, 2012.

[3] G. Martufi and T. C. Gasser, A constitutive model for vascular tissue that integrates fibril, fiber and continuum levels with application to the isotropic and passive properties of the infrarenal aorta. *Journal of Biomechanics*, 44, 2544-2550, 2011.

ACKNOWLEDGMENT: Haoyu Chen is funded by the Qualcomm scholarship provided by Qualcomm Inc. (Qualcomm Inc., San Diego, CA). This support is gratefully acknowledged.

3rd International Conference on Computational and Mathematical Biomedical Engineering - CMBE2013
16-18 December 2013, Hong-Kong
P. Nithiarasu and R. Löhner (Eds.)

A computational model of arterial wall degeneration: Coupling signalling pathways to vascular mechanobiology

P. Aparício[⋆], M.S. Thompson[⋆⋆] and P.N. Watton[⋆⋆⋆,⋆⋆⋆⋆]
[⋆]Systems Biology Doctoral Training Centre, University of Oxford, Oxford, UK,
pedro.aparicio@dtc.ox.ac.uk
[⋆⋆]IBME, Department of Engineering Science, University of Oxford, Oxford, UK
[⋆⋆⋆]Department of Computer Science, University of Sheffield, Sheffield, UK
[⋆⋆⋆⋆]INSIGNEO Institute of *in silico* Medicine, University of Sheffield, Sheffield, UK

SUMMARY

Degeneration and maladaptation of the arterial wall is on the basis of many widelly spread vascular diseases such as arterial aneurysms. Existing computational models make use of phenomenological terms to link disturbed wall mechanics to pathologic Growth and Remodelling (G&R) processes, without capturing the underlying biological mechanisms. A computational model coupling signalling pathways to arterial wall biomechanics is proposed here. The network of interactions between infiltrating leukocytes, arterial wall cells, growth factors (TGF-β1), proteolytic enzymes and blood vessel structural elements (elastin, collagen) is explicitly modelled. Fluid–domain mechanical variables are linked to vascular endothelium permeability and inflammatory cell infiltration, while solid domain mechanical variables are coupled to the evolution of arterial structural components, capturing fibroblast mechanotransduction. The proposed model is regarded as the first step towards a biologically–meaningful description of degeneration of the arterial wall.

Key Words: *inflammation, mechanobiology, fibroblast, collagen, TGF-beta, MMP, aneurysm*

1 INTRODUCTION

Degeneration and maladaptation of the arterial wall underlies many highly prevalent vascular diseases such as aneurysms. Accurately modelling the progression of vessel wall degradation would have a significant clinical impact, however it is highly challenging. The normal blood vessel is a dynamic, continuously remodelling structure where mural cells (endothelial cells (EC), fibroblasts, smooth muscle cells (SMC)) mediate the turnover of vessel wall constituents (collagen, elastin) in response to their surrounding mechanical and biochemical environment. The coupling between mechanical and biochemical transduction is particularly significant in arterial wall inflammation, where many cell types and molecular effectors take part in multiple coupled feedback loops determining vascular cell phenotype and arterial wall structural condition [1].

Existing computational models of aneurysm development generally prescribe an initial insult to the arterial wall, and then allow for Growth and Remodelling (G&R) to drive aneurysm enlargement [2]. Some models attempt to address the progression of the inflammatory reaction and EC/SMC dysfunction by including a phenomenological term linking some measure of blood shearing (e.g. Wall Shear Stress (WSS)) to the rate of elastin degradation [3]. However, a biologically–meaningful description of aneurysm inception and development integrating mechanobiological processes with regulatory signalling pathways is still lacking.

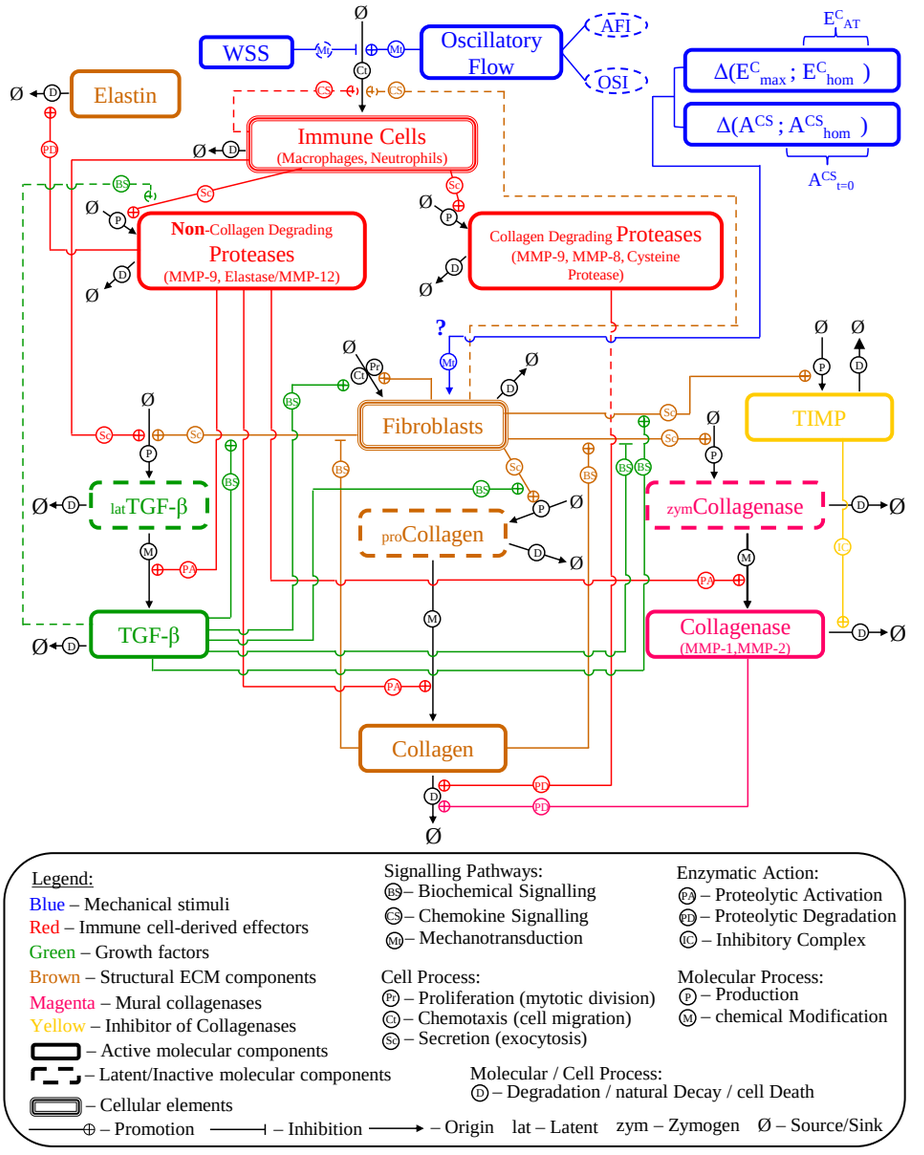

Figure 1: Diagram representation of the model proposed, coupling haemodynamic and arterial wall mechanical stimuli to inflammatory and signalling pathways.

2 MODEL FORMULATION

The model proposed here integrates transduction of mechanical stimuli with biochemical signalling by vascular cells, c.f. Figure 1. The mechanical state of the arterial wall is determined by its content in the load–bearing fibres elastin (**e**) and collagen (**c**). Fibroblasts (**f**) are cells responsible for the production of both collagen, collagenases (**ca**), the proteolytic enzymes responsible for its degradation, and Tissue Inhibitors of MMPs (TIMPs, $\mathbf{I_{ca}}$), molecular species which bind to proteases and permanently suppress their action [4]. The balance between collagen, collagenases and their inhibitors' secretion rates determines net collagen turnover and thus arterial mechanical condition, and it is regulated in response to the cells' local microenvironment. Biochemically, the concentration of signalling molecules such as the Transforming Growth Factor(TGF)-β1 ($\boldsymbol{\beta}$) influences Extra–Cellular Matrix (ECM) turnover: high TGF-β1 concentrations promote ECM

production by stimulating collagen secretion and inhibiting collagenase production.

Mechanical Factors are other key determinants of ECM turnover. If the artery is treated in first approximation as an idealised 1D composite multilayered cylindrical membrane, the force–balance equation governing its overall mechanical response is computed by summing the contributions of each constituent J (elastin, collagen) in each arterial layer L (media, adventitia) [5]:

$$p = \frac{1}{R\,\lambda_z\,\lambda^2} \sum_L \sum_J H_L m_{J_L} \sigma_{J_L}(\lambda) \tag{1}$$

where p: internal pressure, R: radius of unloaded artery, λ_z: axial pre-stretch, λ: circumferential (i.e. azimuthal, hoop) stretch, H_L: thickness of layer L and m_{J_L}, $\sigma_{J_L}(\lambda)$: concentration and circumferential Cauchy stress of constituent J in layer L, resp. Using the previous equation and prescribing specific constitutive relations for elastin and collagen (e.g. derived from hyperelastic strain energy functions), the stretch ratios (or equivalently the Green–Lagrange strains, $E = ((\lambda)^2 - 1)/2$) of the collagen fibres can be computed for particular (systolic, diastolic) values of p. The deformation of the arterial wall is assumed to influence fibroblast population dynamics and their secretion of molecular species (procollagen, zymogenic collagenase and collagenase inhibitors), whose rates are taken to be proportional to the deviation between the current matrix strain $\mathbf{E^C}$ and the homeostatic reference strain $\mathbf{E^C_{hom}}$ of fibroblasts and collagen fibres [5]. The precise mechanotransduction mechanism is unknown (**?** sign in Figure 1), however the model allows for several coupling modes to be implemented.

When inflammatory processes are present the above network is changed. The proteases produced by Immune Cells (IC, **i**) infiltrating the arterial wall have two main actions: non-collagen degrading proteases ($\mathbf{p_{NCD}}$) degrade elastin and proteolytically activate latent forms of mural molecular species (latent TGF-β1 (β_l), procollagen ($\mathbf{c_p}$) and zymogenic collagenase ($\mathbf{ca_z}$)), while collagen degrading proteases ($\mathbf{p_{CD}}$) increase collagen degradation rate. **Mechanical Factors** related to the haemodynamical environment determine immune cell infiltration and inflammatory response, modelling the published links between aneurysm inception and oscillatory flows, and aneurysm growth and low WSS [2]. Computational Fluid Dynamics (CFD) simulations using adequate boundary conditions and blood rheology would allow for the computation of the **WSS** distribution in the idealised cylindrical arterial geometry previously mentioned. If a time–dependent flow profile (e.g. mimicking peripheral blood flow over cardiac cycle) is prescribed, measures of flow oscillation such as the Aneurysm Formation Index (**AFI**) or the Oscillatory Shear Index (**OSI**) can be computed and inputted to the signalling pathways model.

The network of pathways in Figure 1 provides a quantitative description by means of a system of 12 coupled ODEs with constant rates, which governs the evolution of 12 system variables (i, f, e, c, c_p, β_l, β, ca_z, ca, p_{NCD}, p_{CD}, I_{ca}) describing the levels of cellular and molecular species.

3 DISCUSSION

In the present study a computational model of arterial wall degeneration and maladaptation integrating vascular mechanobiology and signalling pathways was developed. The biochemical network of interactions between immune and mural cells, growth factors, proteolytic enzymes and arterial wall structural elements is explicitly modelled, and coupling to fluid and solid–domain mechanical variables is included. Several simplifications were made to reduce the biological complexity of the problem and allow for mathematical tractability without compromising meaningfulness of results: (i) describing all immune cells (macrophages, neutrophils, lymphocytes [1]) and collagen types (I,III) jointly; (ii) modelling only TGF-β1 isoform, a potent ECM regulator; (iii)

grouping over 30 MMPs and other proteases [1] into 3 classes, ca, p_{NCD} and p_{CD}, according to their major actions [1]; (iv) considering spatial homogeneity. Guidance from experimental work will be crucial to decide on the validity of these assumptions and guide future model refinement.

Integration of this model with mechanical simulation algorithms using idealised radially–symmetric geometries is straightforward, allowing for the computation of the straining level of arterial collagen fibres (E^C) luminal wall shear stress (WSS). Simulation results should prove the ability of the model to capture two characteristic behaviours: (i) continuous domain enlargement, and (ii) convergence towards a steady state; such behaviours correspond to the clinical observation that some aneurysms stabilise while others continuously grow until rupture [3]. The following step will consist in integrating this network model in Fluid–Solid–Growth (FSG) Framework previously developed [6], see Figure 2. Structural Analysis (SA) (i) and CFD (ii) simulations are run to compute the haemodynamic and structural environment experienced by mural cells (iii), which is then fed to the model presented here to compute an updated estimate of the arterial wall structural constituents (iv); the resulting concentrations and stretch variables are then used to update the arterial geometry, on which new SA and CFD simulations run again, iteratively. This framework allows for the usage of realistic patient-specific 3D arterial geometries, where more involved mechanical quantities (e.g. Areal Cyclic Stretch A^{CS} [3]) can be computed.

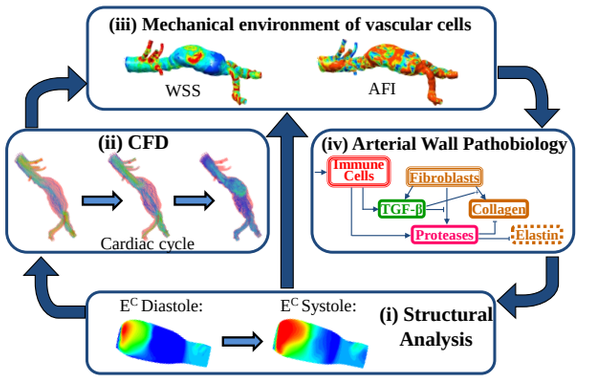

Figure 2: FSG framework for modelling of vascular pathobiology [3, 6]. Simulation of Abdominal Aortic Aneurysm is illustrated, but framework is general.

This model is regarded as a component of the recently proposed "Systems Biology approach" to vascular pathobiology [7]. It integrates processes of different nature spanning a range of spatio–temporal scales, and addresses the identified need to incorporate a more detailed description of the mechanobiology underlaying aneurysm development [8] by directly linking mechanical factors to inflammatory and signalling pathways resulting in arterial wall degradation. Both theoretical vascular biology research and clinical patient management are envisaged to benefit from multi–scale models such as the one proposed here.

ACKNOWLEDGEMENTS

P.N. Watton holds a University Research Lectureship funded by the Centre of Excellence in Personalized Healthcare (funded by the Wellcome Trust and EPSRC, grant number WT 088877/Z/09/Z). P. Aparício holds a EPSRC Studentship. The support is greatly acknowledged.

REFERENCES

[1] K. Rizas et al, "Immune cells and molecular mediators in the pathogenesis of the abdominal aortic aneurysm," *Cardiol Rev*, vol. 17, pp. 201–210, 2009.

[2] D. Sforza et al, "Computational fluid dynamics in brain aneurysms," *Int J Numer Method Biomed Eng*, 2011.

[3] P. Watton et al, "Modelling Cerebral Aneurysm Evolution," in *Biomechanics and Mechanobiology of Aneurysms* (T. McGloughlin, ed.), ch. 12, pp. 307–322, Heidelberg: Springer-Verlag, 2011.

[4] K. Brew, D. Dinakarpandian, and H. Nagase, "Tissue inhibitors of metalloproteinases: evolution, structure and function.," *Biochimica et biophysica acta*, vol. 1477, pp. 267–83, Mar. 2000.

[5] P. Watton et al, "Modelling the growth and stabilization of cerebral aneurysms," *Math Med Biol*, vol. 26, pp. 133–164, 2009.

[6] P. Aparicio et al, "Modelling the influence of endothelial heterogeneity on abdominal aortic aneurysm evolution." Int J Numer Method Biomed Eng (accepted), 2013.

[7] H. Ho et al, "Multiscale modeling of intracraneal aneurysms: Cell signalling, hemodynamics, and remodeling," *IEEE Trans Biomed Eng*, vol. 58, no. 10, pp. 2974–2977, 2011.

[8] J. Humphrey and G. Holzapfel, "Mechanics, mechanobiology, and modeling of human abdominal aorta and aneurysms," *J Biomech*, vol. 45, no. 5, pp. 805 – 814, 2012.

3rd International Conference on Computational and Mathematical Biomedical Engineering - CMBE2013
16-18 December 2013, Hong-Kong
P. Nithiarasu and R. Löhner (Eds.)

Volumetric growth and remodelling of a fibre composite

Thomas S.E. Eriksson⋆, Paul N. Watton⋆⋆, Xiaoyu Luo⋆⋆⋆ and Yiannis Ventikos⋆⋆⋆⋆
⋆Department of Engineering Science, University of Oxford, UK, thomas.eriksson@eng.ox.ac.uk
⋆⋆Department of Computer Science, University of Sheffield, UK, and
INSIGNEO Institute for in silico Medicine, University of Sheffield, UK,
p.watton@sheffield.ac.uk
⋆⋆⋆Department of Mathematics and Statics, University of Glasgow, UK,
xiaoyu.luo@glasgow.ac.uk
⋆⋆⋆⋆Department of Mechanical Engineering, University College London, UK,
y.ventikos@ucl.ac.uk

SUMMARY

We propose a framework for volumetric growth of a fibre reinforced composite, suitable for modelling the evolution of an Abdominal Aortic Aneurysm (AAA). We investigate two underlying assumptions on how material is deposited/degraded, namely through Constant Individual Density (CID) or Constant Individual Volume (CIV) and we determine the effect these assumptions have in a AAA evolution simulation. We show that the framework is suitable to model AAA evolution, including volumetric growth, and conclude that it may be advantageous to assume CIV for elastin and CID for collagen.

Key Words: *fiber-reinforced composite material, volumetric growth, aneurysm.*

1 INTRODUCTION

In this presentation we show the implementation of a thick-walled growth and remodelling (G&R) framework for fibre reinforced composite materials such as arteries in a finite element (FE) setting. We show the framework by modelling the evolution of an abdominal aortic aneurysm (AAA). The AAA develops as a fusiform dilation of the abdominal aorta and is associated with an increased risk for rupture. The healthy abdominal artery is a thick-walled composite that is composed of mainly elastin and collagen. Elastin fibres are randomly distributed and is the main contributor to load bearing at lower physiological loads. The collagen fibres, however, are aligned forming fibre families that are arranged in a helical pathway. In an unloaded state, collagen fibres are wavy but straighten and contribute to load bearing at higher physiological loads [1]. Collagen fibres are also in a continuous state of deposition and degradation with a half-life of 3-90 days and they respond to changes in the physiological conditions in which they live. The development of a AAA is associated with a significant loss of elastin and a weakening of the arterial wall together with the remodelling of collagen fibres. Watton et al. [2], developed a model for AAA evolution by prescribing the degradation of elastin, assuming elastin atrophy to be responsible for driving G&R of AAA. In this communication, we extend this model, which treated the arterial wall as a membrane, to a thick-walled formulation. We incorporate non-volume changing (isochoric) measures that occurs at a short time scale, i.e. seconds, as well as volume changing measures that occurs over longer time scales, i.e. months or years.

2 MATERIAL AND METHODS

Following the work by Schmid et al. [3], who developed a volumetric growth formulation for an isotropic cube, we define the normalised mass, density and volume changes $\hat{m} = m(\tau)/m(\tau_0)$, $\hat{\rho} = \rho(\tau)/\rho(\tau_0)$ and $\hat{v} = \mathrm{d}V(\tau)/\mathrm{d}V(\tau_0)$, respectively, as the difference between its reference value at time τ_0 and its current value at time τ. For a material with $\zeta = 1, \ldots, N$ constituents, the partial density, ρ_ζ, and the individual density, ϱ_ζ, of constituent ζ are defined as $\rho_\zeta = m_\zeta/\mathrm{d}V$ and $\varrho_\zeta = m_\zeta/\mathrm{d}V_\zeta$, where m_ζ is the partial mass of constituent ζ, $\mathrm{d}V$ is the partial volume of the material and $\mathrm{d}V_\zeta$ is the partial volume of constituent ζ. We assume that when a material either deposits or degrades a constituent, that constituent follows one of two assumptions; Constant Individual Density (CID) or Constant Individual Volume (CIV). The meaning of these assumptions are that either the individual density, ϱ_ζ, of the constituent is constant, while the individual volume of the constituent changes, thus leading to CID, or the individual volume of the constituent, $\hat{v}_\zeta$, stays the same, while the individual density of the constituent changes, thus leading to CIV. The total normalised volume change due to growht, $\hat{v}(\tau)$, is determined by which assumption CID or CIV that is used. Naturally, there can be a mix of which assumption, CID or CIV, the constituents in a material follow. Using a volumetric-isochoric split of the deformation gradient $\mathbf{F}$, originating from Flory [4], i.e. $\mathbf{F} = J^{1/3}\mathbf{I}\overline{\mathbf{F}}$ were $\overline{\mathbf{F}} = J^{-1/3}\mathbf{F}$ and $J = \det(\mathbf{F})$, we define isochoric invariants suitable for an anisotropic material with 2 fibre families ($i = 1, 2$) in the direction $\mathbf{a}_{0i}$, as $\bar{I}_1 = \overline{\mathbf{C}} : \mathbf{I}$ and $\bar{I}_{4,i} = \overline{\mathbf{C}} : \mathbf{A}_{0i}$, see [1]. Here $\mathbf{I}$ is the second order identity tensor, $\overline{\mathbf{C}} = \overline{\mathbf{F}}^{\mathrm{T}}\overline{\mathbf{F}} = J^{-2/3}\mathbf{C}$ and $\mathbf{A}_{0i} = \mathbf{a}_{0i} \otimes \mathbf{a}_{0i}$. We further define an isochoric recruitment stretch variable as $\bar{I}_{4\mathrm{rec}_i} > 1$. This variable adapt to changes in the mechanical environment and is used to adjust the point when collagen fibres start to bear load. This variable is therefore used to determine the collagen stretch, $\bar{I}_{4\mathrm{c}_i}$, by

$$\bar{I}_{4\mathrm{c}_i} = \begin{cases} 1, & \text{if} \quad \bar{I}_{4,i} < \bar{I}_{4\mathrm{rec}_i} \\ \bar{I}_{4,i}/\bar{I}_{4\mathrm{rec}_i} & \text{else.} \end{cases} \tag{1}$$

Now we consider an artery with two layers, the media (M) and the adventitia (A), which we denote $\gamma = \{\mathrm{M}, \mathrm{A}\}$. An isotropic ground matrix (g) and two collagen fibre families (c_i) are present in both layers. In the media layer elastin fibres, (e), are also present. These have an isotropic contribution as the elastin fibres are evenly distributed. The strain-energy function for the artery is $\Psi = U(J, \hat{v}) + \sum_{\gamma=\mathrm{M,A}} \overline{\Psi}^{\gamma}$ and we define the strain-energy function for each layer as

$$\overline{\Psi}^{\gamma} = H(\gamma)\hat{\rho}_{\mathrm{e}}\overline{\Psi}_{\mathrm{e}}(\bar{I}_1) + \hat{\rho}^{\gamma}_{\mathrm{g}}\overline{\Psi}_{\mathrm{g}}(\bar{I}_1) + \sum_{i=1,2} \hat{\rho}^{\gamma}_{\mathrm{c}_i}\overline{\Psi}^{\gamma}_{\mathrm{c}_i}(\bar{I}_{4\mathrm{c}_i}), \tag{2}$$

where we use the Heaviside function to include the elastin constituent in the media, i.e. $H(\mathrm{M}) = 1$ and $H(\mathrm{A}) = 0$. A modified Neo-Hookean model for the isochoric and isotropic strain-energy function is used for the ground matrix and the elastin, i.e.

$$\overline{\Psi}_{\mathrm{g}} = \frac{\mu_{\mathrm{g}}}{2}(\bar{I}_1 - 3), \qquad \text{and} \qquad \overline{\Psi}_{\mathrm{e}} = \frac{\mu_{\mathrm{e}}}{2}(\bar{I}_1 - 3), \tag{3}$$

where μ_{g} and μ_{e} are material parameters related to the shear modulus of an isotropic material. The collagen fibre family with Lagrangian direction $\mathbf{a}_{0i}$ is modelled using

$$\overline{\Psi}^{\gamma}_{\mathrm{c}_i} = \frac{k^{\gamma}_1}{2k^{\gamma}_2}\{\exp[k^{\gamma}_2(\bar{I}_{4\mathrm{c}_i} - 1)^2] - 1\} \tag{4}$$

where k^{γ}_1 and k^{γ}_2 are material parameters for collagen. The isochoric deformation occur over a short time scale, t, in seconds. Due to changes in mass over a longer time, τ, in months or

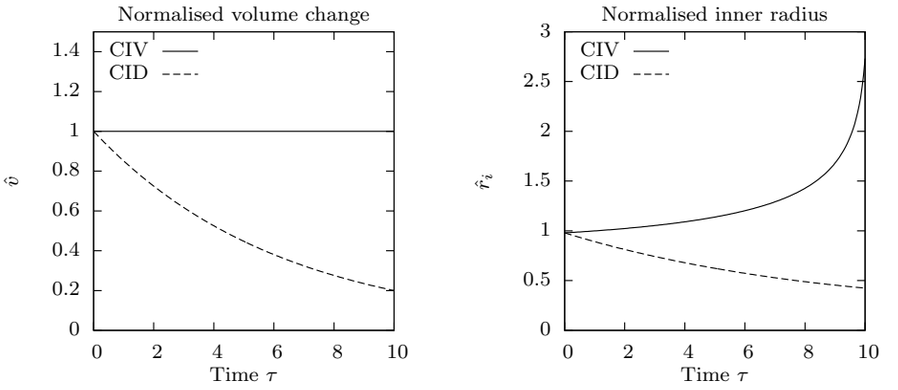

Figure 1: Response in a pressurised arterial segment over time when degrading elastin. Left: normalised volume change; Right: normalised inner radius. The values are normalised against the reference configuration.

years, the tissue does change in volume. We use the normalised volume change, determined by the mixture of constituents following CID or CIV, to govern the volumetric function, $U(J, \hat{v})$, according to

$$U(J, \hat{v}) = \frac{\mu_\kappa}{2}[J(t) - \hat{v}(\tau)]^2, \tag{5}$$

where μ_κ is a user specified penalty parameter enforcing the volume change as $J(t) \rightarrow \hat{v}(\tau)$. We investigate two cases; an arterial segment which we assume consists only of elastin, and an artery that include two layers corresponding to the media and adventitia, where the media is the innermost layer. The artery is stretched axially and inflated with a constant pressure in both cases. In the first case, we assume a homogeneous atrophy of elastin and investigate the radial dilations when elastin follows the assumptions CID or CIV. In the second case, we prescribe elastin atrophy in a manner that leads to the evolution of a AAA. The adventitia follows the assumption of CID, while the media follows the assumption of CIV.

3 RESULTS

Figure 1 shows the volume and inner radius change with only the elastin constituent present in the artery, when using either CID or CIV. When using CIV, the volume is constant and the inner radius is increased as expected. Using CID instead, leads to a reduced volume which is to be expected, but in addition, a reduced inner radius. This phenomenon is similar to what was observed by Valentín et al. [5] and can be explained by force balance equations. It is not likely, however, that this phenomenon is reasonable for elastin from a physiological perspective. More likely is that the elastin constituent follows the assumption of CIV, leading to a constant volume, and that the reduced density of elastin i replaced by proteoglycans, which can be modelled as an increase in the density of the ground matrix by $\hat{\rho}_\mathrm{g} = 2 - \hat{\rho}_\mathrm{e}$, where $\hat{\rho}_\mathrm{g} = 1$ in the reference configuration (and before G&R starts). In the second case, we therefore assume that elastin follows CIV, while the collagen, which will increase in mass, follows CID and the ground matrix respond to the reduced elastin content. The resulting normalised mass, density and volume changes are seen in Fig. 2. We see that the density changes for collagen are much lower than the mass changes. It is also clear that the largest volume increase occurs at the apex of the aneurysm which is also where the stretches are highest and where the increases of $\hat{m}_\mathrm{c}$ and $\hat{\rho}_\mathrm{c}$ are largest.

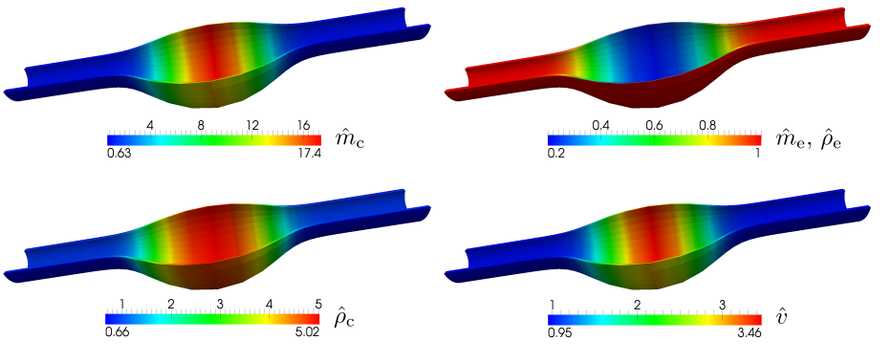

Figure 2: Normalised mass, density and volume changes in a AAA at time $\tau = 10$ years using CID–CIV for the collagen and elastin, respectively.

4 CONCLUSIONS

We show a formulation for volumetric G&R of a fibre composite, suitable for modelling the evolution of a AAA by using and extending the works by [2, 3, 6], among others. We investigate the framework and modelling assumptions by two examples. The first show that when modelling the atrophy of elastin, assumptions of CID may lead to unexpected results. It may therefore be advantageous to model the elastin using CIV and instead increase the density of the ground matrix in response to the loss of elastin mass. The second example, albeit still simple, shows the evolution of a AAA using a more complex form of the elastin degradation. We show that there are quite large differences in mass and density changes of collagen and that the framework is suitable to capture AAA evolution. Even though we have used stylised geometries in these examples, the framework is general and may advantageously be used on complex patient-specific computational models as well as in cases beyond vascular G&R.

REFERENCES

[1] G. A. Holzapfel, T. C. Gasser, and R. W. Ogden. A new constitutive framework for arterial wall mechanics and a comparative study of material models. *J. Elasticity*, 61:1–48, 2000.

[2] P. N. Watton, N. A. Hill, and M. Heil. A mathematical model for the growth of the abdominal aortic aneurysm. *Biomech. Model. Mechanobiol.*, 3:98–113, 2004.

[3] H. Schmid, L. Pauli, A. Paulus, E. Kuhl, and M. Itskov. Consistent formulation of the growth process at the kinematic and constitutive level for soft tissues composed of multiple constituents. *Comput. Methods Biomech. Biomed. Engin.*, 15:547–561, 2012.

[4] P. J. Flory. Thermodynamic relations for highly elastic materials. *Trans. Faraday Soc.*, 57:829–838, 1961.

[5] A. Valentín, J. D. Humphrey, and G. A. Holzapfel. A finite element based constrained mixture implementation for arterial growth, remodeling, and adaptation: Theory and numerical verification. *Int. J. Numer. Meth. Biomed. Engng.*, in press, 2013.

[6] P. N. Watton and N. A. Hill. Evolving mechanical properties of a model of abdominal aortic aneurysm. *Biomech. Model. Mechanobiol.*, 8:25–42, 2009.

3rd International Conference on Computational and Mathematical Biomedical Engineering – CMBE2013
16-18 December 2013, Hong-Kong
P. Nithiarasu and R. Löhner (eds)

Modeling rupture of growing aneurysms

Kirill Balakhovsky[1], Mahmood Jabareen[1] and Konstantin Volokh[1, 2]

[1] Faculty of Civil and Environmental Engineering, Technion-I.I.T, Israel,
volokh@cv.technion.ac.il
[2] Department of Structural Engineering, Ben-Gurion University of the Negev, Israel
volokhk@bgu.ac.il

SUMMARY

Growth and rupture of aneurysms are driven by micro-structural alterations of the arterial wall yet precise mechanisms underlying the process remain to be uncovered. In the present work we examine a scenario when the aneurysm evolution is dominated by turnover of collagen fibers. In the latter case it is natural to hypothesize that rupture of individual fibers (or their bonds) causes the overall aneurysm rupture. We examine this hypothesis in computer simulations of growing aneurysms in which constitutive equations describe both collagen evolution and failure. Failure is enforced in constitutive equations by limiting strain energy that can be accumulated in a fiber. Within the proposed theoretical framework we find a range of parameters that lead to the aneurysm rupture. We conclude in a qualitative agreement with clinical observations that some aneurysms will rupture while others will not. Besides, we suggest based on the obtained results that aneurysm rupture is triggered by disintegration of the collagen net rather than failure of individual fibers.

Key Words: *aneurysm, rupture, modeling, growth.*

1 INTRODUCTION

Aneurysms are abnormal dilatations of vessels in the vascular system, and they exist in two major forms: fusiform and saccular. Fusiform aneurysms are found in the human abdominal aorta. Saccular aneurysms are found in cerebral blood vessels. Fully developed aneurysms have the characteristic geometry of a thin-walled, balloon-like structure. Starting with the pioneering work by Watton et al [1] various mathematical theories of aneurysm growth and remodeling (G&R) have been developed with emphasis on the intracranial (saccular) and abdominal aortic (fusiform) aneurysms [2–4]. Though biomechanical features of intracranial and abdominal aortic aneurysms have differences [4] the mathematical grounds of the G&R description can be common in both cases. Most mentioned theories consider turnover of collagen fibers as the main scenario of the

aneurysm evolution. Despite the success in describing growth and remodeling all mentioned theories were short of a failure description that should be a natural component of the theory. Volokh and Vorp [5] proposed a new paradigm of Growth-Remodeling-Failure (G&R&F) by enforcing failure in a description of growth and remodeling. A failure description was enforced with the help of the *energy limiter* constant which provided a saturation value for the strain energy function [6–7]. The new constant controlled material failure and it could be interpreted as an average energy of molecular bonds from the microstructural standpoint. Work [5] used a purely phenomenological approach and was not guided by micro-structural considerations. Such considerations are taken into account in the present work in which we hypothesize that rupture of individual fibers (or their bonds) causes the aneurysm overall rupture.

2 METHODS

Most models of aneurysm growth and remodeling use fiber-based microstructural approaches. Any of these models can be enhanced with a failure description in the way it is done in the present paper. We assume that the aneurysm can be modeled as a membrane composed of collagen layers with the strain energy of the i^{th} layer prescribed in the form

$$\psi_i(t) = \int_{-\infty}^{t} g(t, t_{dp}) \dot{m}_i(t_{dp})\, f_i(t, t_{dp}) dt_{dp},$$

where $\dot{m}_i$ is the rate of the collagen fiber production; f_i is the strain energy of the deposited fiber; t_{dp} is the time of the fiber deposition; and the life cycle function $g(t, t_{dp})$ is defined by the fiber life time t_{lf} with the help of the Heaviside step functions H as follows $g(t, t_{dp}) = H(t - t_{dp}) - H(t - t_{dp} - t_{lf})$. In order to define constitutive laws for the rate of the fiber production and the fiber energy we have, first, to define kinematics of a fiber.

We assume that $\mathbf{M}$ is a unit vector in the initial configuration at time $t = -\infty$ which defines direction of fiber deposition in the *i*th layer. Then, at time $t = t_{dp}$ a new fiber is deposited in direction $\mathbf{M}_{dp} = \mathbf{F}(t_{dp})\mathbf{M}$, where $\mathbf{F}(t_{dp})$ is the deformation gradient mapping the initial configuration at time $t = -\infty$ to the configuration at time $t = t_{dp}$. The deposited unit fiber $\mathbf{M}_{dp} / |\mathbf{M}_{dp}|$ is further mapped into $\mathbf{m} = |\mathbf{M}_{dp}|^{-1} \mathbf{F}_{dp} \mathbf{M}_{dp} = |\mathbf{M}_{dp}|^{-1} \mathbf{F}(t)\mathbf{M}$, where $\mathbf{F}_{dp} = \mathbf{F}(t)\mathbf{F}^{-1}(t_{dp})$ is the deformation gradient mapping material configuration at the time of the fiber deposition $t = t_{dp}$ to the current configuration at time t.

We prescribe a specific form of the fiber strain energy function in the i^{th} layer that enforces a failure description

$$f_i(t,t_{dp}) = \frac{1}{10}\Phi_i\left\{\Gamma\left[\frac{1}{10},0\right] - \Gamma\left[0.1,\left(\frac{W_i(t,t_{dp})}{\Phi_i}\right)^{10}\right]\right\},$$

$$W_i(t,t_{dp}) = \mu(\lambda_{pre}^2|\mathbf{m}|^2 - 1)^3,\ \dot{m}_i(t_{dp}) = \beta\left|\mathbf{M}_{dp}\right|^{2\alpha},$$

where $\Gamma[s,x] = \int_x^\infty t^{s-1}\exp(-t)\,dt$ is the upper incomplete gamma function; Φ_i is the energy limiter for fiber in the i^{th} layer; W_i is the strain energy of intact (without failure) fiber in the i^{th} layer; μ is a fiber stiffness parameter; λ_{pre} is a pre-stretch of the deposited fiber; β and α are the growth constants.

The figure below shows the stress-stretch curve for individual fiber ($\mu = 1\cdot 10^7$[Pa]) based on the proposed constitutive model. The limit points corresponding to various critical stretches designate the onset of fiber failure.

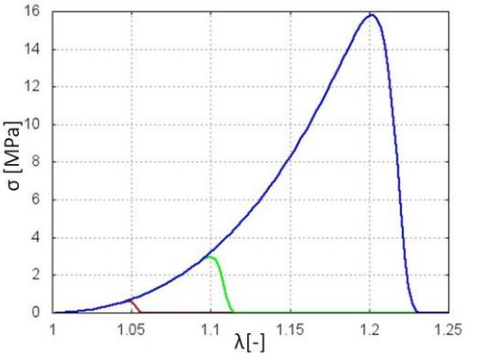

We applied the described constitutive model to simulations of evolving saccular and fusiform aneurysms. The former were modeled as circular axisymmetric membranes while the latter as the cylindrical axisymmetric ones. In the absence of reliable patient-specific data we performed parametric studies by varying the fiber stiffness, critical rupture stretch, deposition rate and lifetime. We tracked the singularity of the Hessian (the global tangent stiffness matrix) of the total potential. The singularity indicated the onset of the rupture process (crack formation and propagation), which was not tracked, however. We found a range of parameters within which aneurysms stay intact or rupture.

3 CONCLUSIONS

We found that some aneurysms rupture while others do not. It is interesting that according to the considered model rupture occurs very quickly if it occurs at all. On the contrary, clinical observations show that aneurysms can live long before rupture. This discrepancy between theory and observations is a consequence of the assumption of constant energy limiters used in simulations. Indeed, the accumulated energy of the intact (no energy limiters) material reaches its peak very quickly and it gradually declines with the aneurysm development and stabilization. If the energy limiter is constant then rupture is expected when the accumulated energy reaches its peak as happens in simulations.

Thus, the energy limiter should gradually alternate with time to allow the aneurysm to enlarge without rupture. Collagen fibers deposited during the aneurysm evolution should lose their strength with time. The latter conclusion might sound controversial if the strength is defined as a property of the fiber itself. It is probably more reasonable to interpret the fiber strength as the strength of the inter-fiber bond or, nicer said, a measure of the tissue integrity. We mean that tissue loses its strength because collagen fibers disintegrate rather than isolated fibers weaken. The collagen turnover is not accompanied by proper reproduction of bonds composing fiber nets. Without such bonds mechanical response becomes stiffer because collagen dominates the micro-structure. At the same time strength weakens because collagen fibers are poorer integrated in a net. The described situation is actually in a well qualitative correspondence with the known histopathological data which can be found in the works listed in References.

In view of the obtained results it will be necessary to modify theoretical models by incorporating evolution of the strength in them (cf. [5]). Moreover, the strength should be interpreted as a property of bonds rather than collagen fibers themselves. There is no doubt that experimental assessment of the micro-structure of the ruptured aneurysm could essentially guide the development of the macroscopic mathematical framework.

REFERENCES

[1] Watton, P. N., Hill, N. A., Heil, M., 2004. A mathematical model for the growth of the abdominal aortic aneurysm. *Biomech. Model. Mechanobiology* 3, 98–113.

[2] Kroon, M. and Holzapfel, G.A., 2007. A model of saccular cerebral aneurysm growth by collagen fiber remodeling. *J. Theor. Biology* 247, 775-787.

[3] Baek, S., Rajagopal, K.R., Humphrey, J.D., 2006. A theoretical model of enlarging intracranial fusiform aneurysms. *J. Biomech. Engng.* 128, 142-149.

[4] Humphrey, J.D., and Taylor, C.A., 2008. Intracranial and abdominal aortic aneurysms: similarities, differences, and need for a new class of computational models. *Annu. Rev. Biomed. Eng.* 10, 221-46.

[5] Volokh, K.Y. and Vorp, D.A., 2008. A model of growth and rupture of abdominal aortic aneurysm. *J. Biomech.* 41, 1015-1021.

[6] Volokh, K.Y., 2011. Modeling failure of soft anisotropic materials with application to arteries. *J. Mech. Behav. Biomed. Materials* 4, 1582-1594.

[7] Volokh, K.Y., 2013. Review of the energy limiters approach to modeling failure of rubber. *Rubber Chem. Technology*, in press.

Numerical Simulation of Cardiovascular Devices & Procedures

3rd International Conference on Computational and Mathematical Biomedical Engineering – CMBE2013

16-18 December 2013, Hong-Kong

P. Nithiarasu and R. Löhner (eds)

Fluid-dynamics in ascending aorta in presence of a bicuspid aortic valve

C. Vergara*, D. Bonomi, E. Faggiano***, and G.B. Luciani******

*Dipartimento di Ingegneria, Università di Bergamo, Viale Marconi 5, 24044, Dalmine (BG), Italy, christian.vergara @unibg.it

** MOX, Dipartimento di Matematica, Politecnico di Milano, Piazza Leonardo da Vinci 32, 20133 Milano, Italy, diddi_89@hotmail.it

*** MOX, Dipartimento di Matematica, Politecnico di Milano, Piazza Leonardo da Vinci 32, 20133 Milano, Italy, elena.faggiano@gmail.com

**** Cardiosurgery Division, P.le A. Stefani 1, 37126, Verona, Italy, giovannibattista.luciani@univr.it

SUMMARY

We performed a computational parametric study in the ascending aorta of real patients with bicuspid aortic valve, highlighting the differences with the tricuspid configuration also in the case of a normally functioning valve.

Key Words: *blood flow, bicuspid aortic valve, ascending aorta, helical flow.*

1. INTRODUCTION

Bicuspid aortic valve (BAV), the most common congenital heart disease, is related to an increased prevalence of ascending aortic dilatation and aneurysm in normally functioning valvular regime when compared to tricuspid aortic valve (TAV). These complications seem to be correlated with the abnormal fluid-dynamics experienced in this subjects in the ascending aorta. In particular, three peculiar phenomena have been recognized so far from radiological images: high wall shear stresses (WSS) in the region of dilatation [1], asymmetry of the sistolic jet entering in aorta [2], helical systolic flow in the ascending aorta [3].

2. MAIN BODY

In this work, we studied the fluid-dynamics of blood in ascending aorta to understand which are the differences between a normally functioning BAV and the classical TAV configurations. To do this, we considered the assumption of rigid walls and we solved the incompressible Navier-Stokes equations in real geometries of patients with BAV considering physiological inlet conditions. To do a comparison, we drew on the same geometry the TAV configuration and different BAV configurations so to compare different scenarios. The numerical results were obtained with the finite element library LIFEV (www.lifev.org).

In the first set of simulations, we considered no leaflets modeled. Surprisingly, we found that the three phenomena described above characterizing BAV configurations were recovered by our simulations, highlighting big differences with respect to the TAV case [4,5]. This suggested that the particular orifice of BAV configurations is responsible for the abnormal fluid-dynamics in ascending aorta. To understand if also the presence of the leaflets contributes in creating such phenomena, we included the leaflets in our simulations. In this case we found that the presence of high WSS, the asymmetry of the jet and the formation of systolic vortices were emphasized by the presence of the leaflets, suggesting that both the shape of the orifice and the leaflets contribute in the formation of abnormal fluid-dynamic patterns in BAV (see Figure).

We also performed several parametric studies, by varying the area of the orifice, its orientation to account for the two principal BAV orientations (antero-posterior and latero-lateral), the inlet flow rate, the dimension of the aorta.

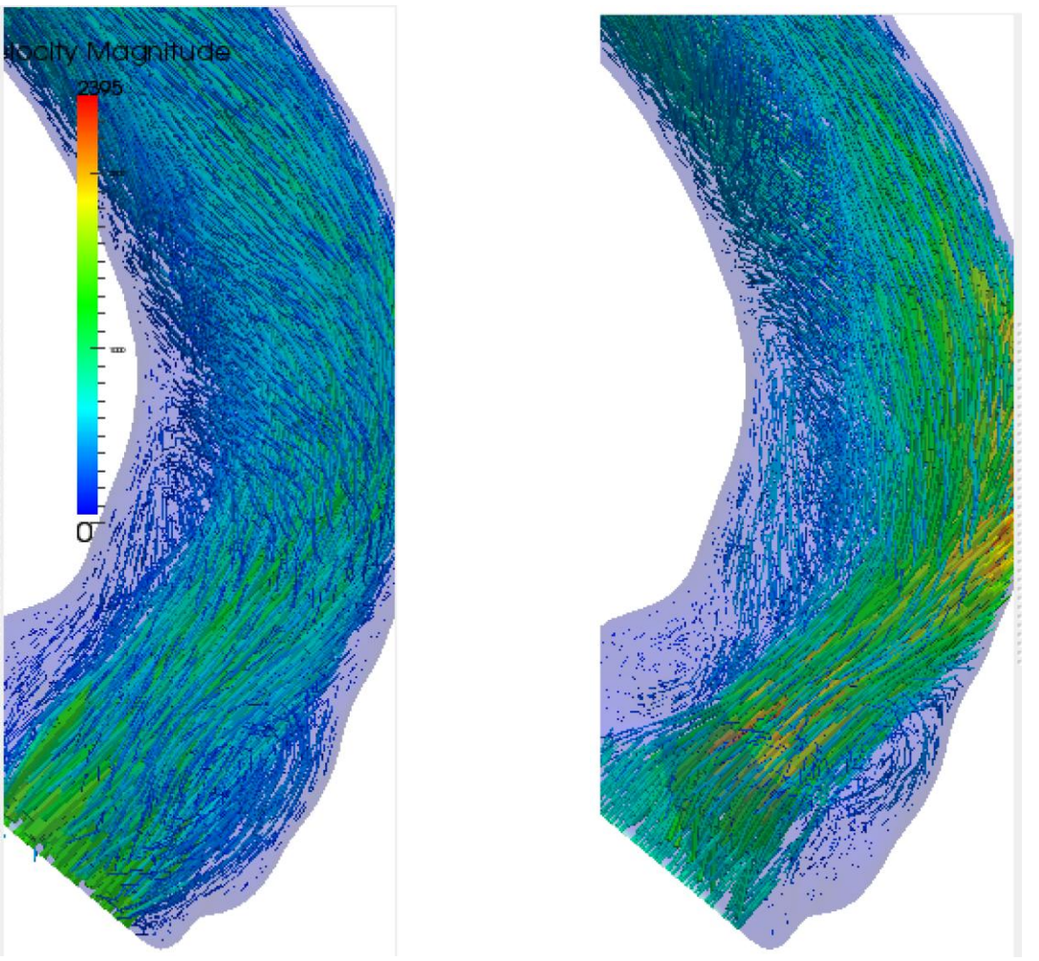

Figure: Fluid-dynamics in a BAV patient without (left) and with (right) leaflets modeled.

3. CONCLUSIONS

In this study, we found that the computational tools are suitable to reproduce the abnormal fluid-dynamics in the ascending aorta in presence of BAV configurations. The next steps in this work will be the inclusion of the fluid-structure interaction problem to model both the interaction between blood and the aortic vessel, and the movement of the leaflets.

REFERENCES

[1] Weigang E, Kari FA, Beyersdorf F, et al. Flow sensitive four dimensional magnetic resonance imaging: flow patterns in ascending aortic aneurysms, *Eur J Cardiothorac Surg*, 34, 11–16, 2008.

[2] Barker AJ, Markl M, Bürk J, Lorenz R, Bock J, Bauer S, Schulz-Menger J, von Knobelsdorff-Brenkenhoff F, Bicuspid aortic valve is associated with altered wall shear stress in the ascending aorta. Clinical perspective, *Circ Cardiovasc Imaging*, 5(4):457–466, 2012.

[3] Hope M, Hope T, Meadows A, Ordovas K, Urbania T, Alley M, HigginsC, Bicuspid aortic valve: four-dimensional mr evaluation of ascending aortic systolic flow patterns, *Radiology*, 255(1): 53–61, 2010.

[4] Vergara C, Viscardi F, Antiga L, Luciani GB, Influence of bicuspid valve geometry on ascending aortic fluid dynamics: a parametric study. *Artif Organs*, 36(4):368–378, 2011.

[5] Faggiano E, Antiga L, Puppini G, Quarteroni A, Luciani GB, Vergara C, Helical Flows and Asymmetry of Blood Jet in Dilated Ascending Aorta with Normally Functioning Bicuspid Valve, *Biomechanics and Modeling in Mechanobiology,* 12(4), 801-813, 2013.

[6] D. Bonomi, Numerical study of the influence of aortic valve leaflets in the fluid-dynamics in ascending aorta , MSc in Mathematical Engineering, Politecnico di Milano, Accademic year '12-'13

3rd International Conference on Computational and Mathematical Biomedical Engineering - CMBE2013
16-18 December 2013, Hong-Kong
P. Nithiarasu and R. Löhner (Eds.)

Patient-specific finite element analysis of TAVI: evaluation of paravalvular leakage and prosthesis post-operative configuration

S. Morganti*, F. Auricchio, , M. Conti** and A. Reali****
*Dip. di Ingegneria Industriale e dell'Informazione, University of Pavia, Via Ferrata 3, 27100 Pavia, Italy
**Dip. di Ingegneria Civile e Architettura, University of Pavia, Via Ferrata 3, 27100 Pavia, Italy

SUMMARY

A finite-element analysis strategy to realistically model transcatheter aortic valve implantation (TAVI) is proposed and investigated in two different cases. Patient-specific models of the entire aortic root including calcium deposits are considered. Paravalvular leakage and stresses on the native aortic root are quantitatively evaluated.

Key Words: *TAVI, patient-specific modelling, FEA.*

1 INTRODUCTION

Calcific aortic stenosis is a common aortic valve disorder [6], especially in elder patients, inducing a narrowing of the aortic valve opening. The impact of such a cardiovascular disease is constantly increasing due to higher life expectancy and population average age [7].
In the last decade, a minimally-invasive therapeutic option, called TAVI, has become a valuable alternative to open-heart surgery for the treatment of aortic stenosis [3, 4]. It consists in the delivery and positioning of an aortic valve prosthesis, made of a biological valve sewn into a metallic frame, over the stenotic native valve.
As for other minimally-invasive procedures, the clinical outcomes are strictly related to patient selection, operator skills, and dedicated pre-procedural planning based on accurate medical imaging and analysis [5].
Moving from such considerations, the present work proposes an approach to realistically simulate TAVI, tailored to the clinical practice; in particular, we propose a study, based on the analysis of pre-operative medical images of two real patients who underwent TAVI, with the final aim of predicting the post-operative performance of the prosthesis depending on to the specific anatomical features. The present work represents a step forward with respect to the current state of the art, addressing novel issues and considering the following innovative aspects: i) the aortic valve model is complete of both the aortic sinuses and the native valve leaflets, ii) the calcific plaque is also included within the model on the basis of imaging data, iii) the geometry of the prosthetic stent is very accurate, being obtained from micro-CT reconstruction.

2 MAIN BODY

Two patients are recruited for the present study, both with severe symptomatic aortic stenosis. In both cases, the preoperative planning is based on CT examinations performed using a dual-source

computed tomography scanner. For both patients the Edwards SAPIEN XT size 26 has been selected by physicians as the optimal device for implantation.

2.1 Modeling of the native aortic valve

The CT data sets are processed using OsiriX software [**?**]. In particular, the aortic lumen data can be extracted as STL file and elaborated to obtain a suitable mesh for finite element analysis. Native leaflets can be then geometrically reconstructed within the obtained aortic root anatomy by integrating CT information of the attachment lines and ultrasound measurements of the leaflet free margins. Finally, calcifications extracted from CT data are considered and included in the model (see Figure 1).

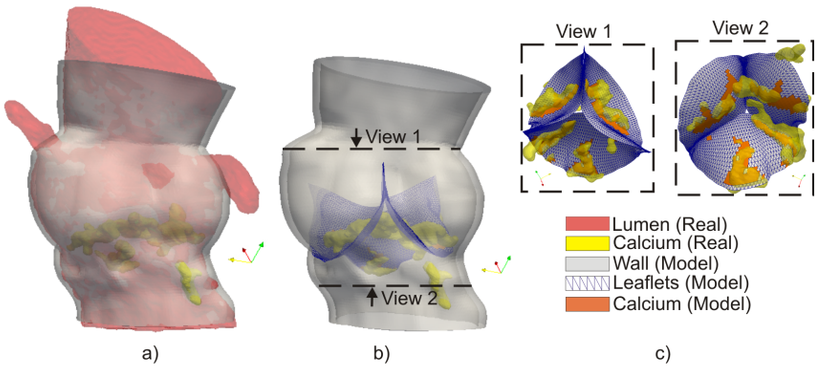

Figure 1: Rendering of the STL file vs aortic model created for simulations: a) the real aortic root lumen (red) and calcifications (yellow) are overlapped to the aortic wall model (grey); b) the closed native leaflets (blue mesh) of our model are perfectly matching with real calcifications obtained by processing CT images; c) top and bottom views are shown.

The aortic wall model of *Patient 1* is meshed using 265976 tetrahedral elements for the healthy region and 2936 for the calcific part while the leaflets are discretized using 3212 shell elements with reduced integration for the healthy tissue and 427 for the calcific region.
The aortic wall model of *Patient 2* is completely calcium-free because all the calcifications are localized in the leaflets. The model is meshed using 135558 tetrahedral elements; the healthy tissue of the leaflets is discretized using 3258 shell elements with reduced integration (S4R) while for the calcific plaque 342 elements are used. For the sake of simplicity, all material models are assumed to be isotropic and homogenous [8, 1, 2].

2.2 Modeling of the Edwards SAPIEN prosthesis

As previously stated, both patients were treated with an Edwards Lifesciences SAPIEN XT size 26. A faithful geometrical model of this device is based on a high-resolution micro-CT scan of a real device sample, extracted during a failed surgical procedure. The obtained stent model is meshed using 84435 solid elements with reduced integration. A Von Mises plasticity model with an isotropic hardening is adopted for the stent material [1].

2.3 Finite element simulations

The simulation strategy we propose consists in the following two main steps:

a. stent crimping and deployment: in this step, the prosthesis stent model is crimped to achieve the catheter diameter which, for a transapical approach, is usually 24 French (8 mm); then, the prosthetic stent is expanded within the patient-specific aortic root to reproduce the implantation due to balloon expansion;

b. valve mapping and closure: the prosthetic leaflets are mapped onto the implanted stent and a physiological pressure of 0.01 MPa is applied to virtually recreate the diastolic behavior of the SAPIEN device, as already discussed in [1].

All the analyses are performed using Abaqus/Explicit v6.10 (Simulia, Dassáult Systems, Providence, RI, USA). In Figure 2 the main procedural steps of TAVI simulation are shown.

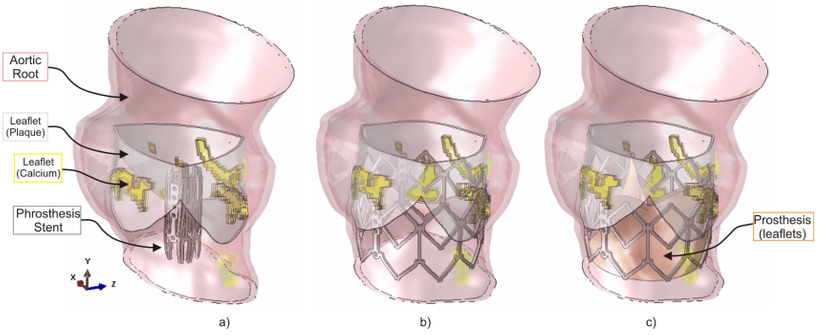

Figure 2: Procedural steps of TAVI reproduced through a simulation strategy: a) the crimped stent is properly placed inside the aortic root model; b) the stent is expanded within the patient-specific aortic root; c) prosthetic leaflet closure is reproduced to evaluate postoperative performance.

3 Results

The simulation of stent crimping and deployment allows the computation of the aortic root configuration change induced by prosthesis apposition and the associated stress distribution; through the second stage of simulation (i.e., valve mapping and closure), we may evaluate the competence of the prosthesis leaflets. In this manner, we have a computer-based tool able to quantitatively provide clinically relevant patient-specific information of the TAVI performance. In particular, we can evaluate: i) diameter variation of the aortic virtual ring; ii) distribution of aortic wall stress during the prosthesis deployment; iii) risk of paravalvular leakage (see Figure 3); iv) coaptation of the prosthetic leaflets.

4 CONCLUSIONS

We believe that, with the present study, a step forward in the direction of creating a computational tool able to support TAVI preoperative planning has been addressed. Patient-specific finite element analyses including native leaflets and calcifications and considering realistic prosthetic models may give useful clinical information to guide the surgeon towards an optimal operation choice.

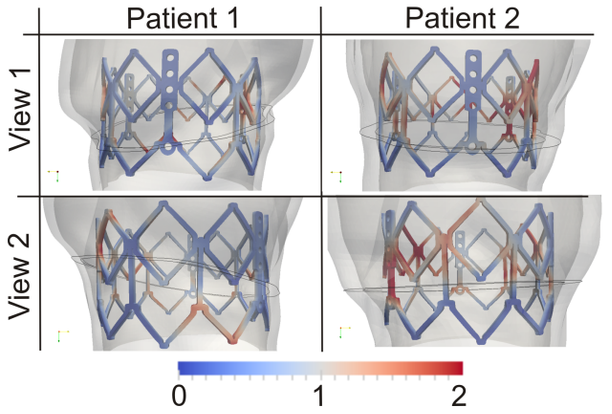

Figure 3: Evaluation of the degree of apposition between the prosthesis stent and the patient-specific root anatomy: a contour plot of the distance [mm] between the aortic wall and the prosthetic stent is represented.

ACKNOWLEDGEMENT

This work is partially funded by Cariplo Foundation through the Project no. 2009.2822 and partially by the European Research Council through the Project no. 259229 entitled 'ISOBIO: Isogeometric Methods for Biomechanics'. The authors would acknowledge Dr. M. Aiello of IRCCS Policlinico San Matteo, Pavia, Italy, for for his support on medical aspects related to the present work, Dr. A. Valentini of IRCCS Policlinico San Matteo, Pavia, Italy, for support to the imaging aspects of the present work, and Eng. Anna Paola Parrilli, Istituto Ortopedico Rizzoli (IOR), Bologna, Italy, for providing the prosthetic stent reconstruction.

References

[1] F. Auricchio, M. Conti, S. Morganti, and A. Reali. Simulation of transcatheter aortic valve implantation: a patient-specific finite element approach. *Computer Methods in Biomechanics and Biomedical Engineering*, page accepted for Publication, 2012.

[2] C. Capelli, M. Bosi, E. Cerri, J. Nordmeyer, T. Odenwald, P. Bonhoeffer, F Migliavacca, and S. Taylor, A.M.and Schievano. Patient-specific simulations of transcatheter aortic valve stent implantation. *Medical and Biological Engineering and Computing*, 368:183–192, 2012.

[3] A. Cribier, H. Eltchaninoff, A. Bash, N. Borenstein, C. Tron, F. Bauer, G. Derumeaux, F. Anselme, F. Laborde, and M.B. Leon. Percutaneous transcatheter implantation of an aortic valve prosthesis for calcific aortic stenosis: First human case description. *Circulation*, 106:3006–3008, 2002.

[4] E. Grube, J.C. Laborde, U. Gerckens, T. Felderhoff, B. Sauren, L. Buellesfeld, R. Mueller, M. Menichelli, T. Schmidt, B. Zickmann, S. Iversen, and G.W. Stone. Percutaneous implantation of the corevalve self-expanding valve prosthesis in high-risk patients with aortic valve disease: The siegburg first-in-man study. *Circulation*, 114:1616–1624, 2006.

[5] R. Gurvitch, E.L. Tay, N. Wijesinghe, J. Ye, F. Nietlispach, D.A. Wood, S. Lichtenstein, A. Cheung, and J.G. Webb. Transcatheter aortic valve implantation: Lessons from the learning curve of the first 270 high-risk patients. *Catheterization and Cardiovascular Interventions*, 78:977–984, 2011.

[6] William C. Roberts and Jong M. Ko. Frequency by decades of unicuspid, bicuspid, and tricuspid aortic valves in adults having isolated aortic valve replacement for aortic stenosis, with or without associated aortic regurgitation. *Circulation*, 111(7):920–925, 2005.

[7] Vronique L. Roger, Alan S. Go, Donald M. Lloyd-Jones, Robert J. Adams, and Jarett D. et al. Berry. Heart disease and stroke statistics2011 update. *Circulation*, 123(4):e18–e209, 2011.

[8] F.L. Xiong, W.A. Goetz, C.K. Chong, Y.L. Chua, S. Pfeifer, E. Wintermantel, and J.H. Yeo. Finite element investigation of stentless pericardial aortic valves: Relevance of leaflet geometry. *Annals of Biomedical Engineering*, 38:1908–1918, 2010.

[9] P.A. Yushkevich, J. Piven, H.C. Hazlett, R.G. Smith, S. Ho, J.C. Gee, and G. Gerig. User-guided 3D active contour segmentation of anatomical structures: Significantly improved efficiency and reliability. *Neuroimage*, 31(3):1116:1128, 2006.

3rd International Conference on Computational and Mathematical Biomedical Engineering - CMBE2013
16-18 December 2013, Hong-Kong
P. Nithiarasu and R. Löhner (Eds.)

Patient specific application of a structural beam model for biomechanical analysis of transcatheter aortic valve implantation

Michael Gessat*, Raoul Hopf, Christoph Russ***, Simon H. Sündermann****, Edoardo Mazza** and Volkmar Falk****

*University of Zurich, Hybrid Laboratory for Cardiovascular Technologies, Rämistrasse 100, 8091 Zürich, Switzerland, michael.gessat@usz.ch

**Swiss Federal Institute of Technology (ETH) Zurich, Institute of Mechanical Systems, Tannenstrasse 3, 8092 Zurich, Switzerland, hopf/mazza@imes.mavt.ethz.ch

***Swiss Federal Institute of Technology (ETH) Zurich, Computer Vision Laboratory, Sternwartstrasse 14, 8092 Zürich, Switzerland, russc@ethz.ch

****UniversityHospital Zurich, Division of Cardiovascular Surgery, Rämistrasse 100, 8091 Zürich, Switzerland, simon.suendermann@usz.ch; volkmar.falk@usz.ch

SUMMARY

A beam model of a nitinol stent and a shell model of the aortic root anatomy are proposed as a means for accurate, numerically stable, and computationally efficient simulation of transcatheter aortic valve implantation (TAVI). Experimental validation of the stent model and image-based validation of the virtual stent implantation are presented. In a clinical setting, the model can be used to predict stent shape and force distribution after TAVI, which allows for estimating transvalvular flow conditions and paravalvular leakage.

Key Words: *structural mechanics, stent, aortic valve, beam model.*

1 INTRODUCTION

In Transcatheter Aortic Valve Implantation (TAVI), the selection of the optimal approach and prosthesis type as well as the determination of an optimal landing zone for the device have been identified to be crucial in order assure good treatment outcome [1].

The current gold standard in treatment planning for TAVI is geometric assessment of the aortic root and the vasculature along the route of access in terms of diameters, distances and grade of calcification in preoperative CT images [2]. With our work, we aim at laying the scientific foundation for the next generation of TAVI planning procedures, where biomechanical analysis is included into the workflow, allowing for prediction and, through that, optimization of treatment outcomes.

In the presented work, we focus on analysing the relationship between the radial force after implantation of a stented aortic valve through a transcatheter approach and the two most frequent complications after TAVI: aortic insufficiency (AI) through paravalvular leaks and pacemaker requirement due to impairment of the atrioventricular (AV) node or the left bundle branch (LBB). We propose a computationally very efficient and stable model of the aortic root based on two-dimensional shell elements of the Medtronic CoreValve prosthesis based on one-dimensional beam elements.

2 MAIN BODY

Stent Modelling
Most work found on stent modelling uses solid elements, such a tetrahedrons or hexahedrons, for constructing the stent. In 2006, Hall and Kasper [3] investigated the numerical stability, the accuracy, and the computational complexity of different modelling techniques for stents and concluded that linear beam-elements are the optimal choice for such tasks. Following their recommendation, we chose the linear Timoshenko Beam element (B31 in Abaqus) for building a model of the self-expanding Medtronic CoreValve stent.

The geometry (see Fig. 1, left) of the model was derived from microCT images. The whole stent consists of 30 strings, which are running in s-curves from the proximal to the distal end of the stent. Cubic Hermite Bezier spline curves were used to describe the centrelines of these strings. For each of the struts connecting the 165 intersection points of the stent, a third-order Bezier spline was defined in a manner that ensures c2-continuity over the whole stent.

Since our focus lies not on accurately depicting the whole process of stent crimping and release, we chose a linear-elastic material model ($E = 60\,GPa,\ = 0.33$), which is valid to describe the low-strain regime in which the stent will find itself at the end of the deployment process. This selection further added to the stability and further reduced the computational complexity compared to the standard approach to modelling Nitinol stents with a complex, non-linear material model.

Aortic Root Modelling
Preoperative contrast enhanced computer tomography (CTA) images of the patients chest acquired at diastole were the basis for defining a patient-specific morphologic model of the aortic root and left ventricle. The main reason for this choice was the fact, that these images are routinely acquired for TAVI patients, giving us access to patient data without the need to change the clinical workflow.

The HeartNavigator software (Philips Healthcare, Best, The Netherlands) was used to extract surface models of the ascending aorta, aortic valve, and left ventricle from the CTA images. In addition, a self-made programme was employed for extracting surface models of the calcifications at the aortic valve, since this was not offered by the HeartNavigator version we had access to. The triangular surfaces exported from both tools are optimized for rendering purposes and therefore do not satisfy any of the usual mesh requirements for finite element analysis.

To overcome these issues, NURBS surfaces were used to define a parametric shell model of the aortic root, aortic valve, and left ventricle, ensuring a high degree of regularity in the mesh with

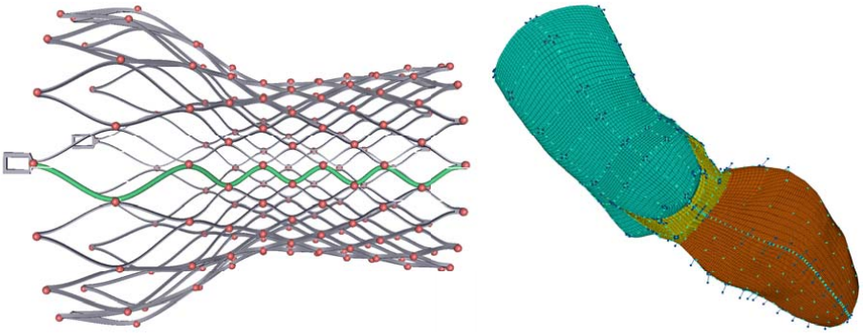

Figure 1: Left: Model of the Medtronic CoreValve stent. The red balls indicate the 165 *intersection points, the blue curve represents of the* 30 *strings. Right: patient-specific multi-material shell model of the aortic root and left ventricle.*

respect to aspect ratio of each element, compatibility of neighbouring structures, and overall mesh resolution. The parameters of this generic model can be tuned to adapt the mesh derived from it to the geometry defined by the surface models segmented from the CTA images for each patient. Non-linear material models were assigned to the different regions of this model according to the literature [4].

Simulation

For virtual deployment of the stent model in the anatomical model, the explicit solver of Abaqus was used. To handle a large variety of general impact cases within the simulation, a penalty contact method was used in combination with the augmented Lagrange method for improved accuracy. The stent is virtually crimped and positioned inside the aortic root model. A very rigid cylinder shell model is used to simulate the sheath, which holds the stent in the crimped state before deployment. The sheath is retracted to simulate the slow release of the stent (see Fig. 2).

Validation Methodology

To verify our modelling approach of the stent, a solid-model consisting of first order hexahedral elements with a reduced integration scheme (C3D8R in Abaqus) was created. Convergence analysis was employed to find the required resolution of such a model.

Two-point tensile tests were employed for experimental validation of the stent model. For each test, a pair of intersection points of the stent was selected. The stent was clamped at these points and a standard tensile test was performed. The same experiment was set up in Abaqus and the characteristic curves measured in vitro and simulated in silico were compared.

For validation of the virtual stent deployment, postoperative CT-images were acquired from six patients. The actual shape of the deployed stents were extracted from these images (see [5] for details) and compared to the geometry of the virtually implanted stent models. An error metric was defined based on the local circumference: In both models, the circumference of the stent was computed at different levels along the stents centre lines.

Validation Results

At a level of $300k$ hexahedral elements, the solid model showed convergence, no relevant differences were found compared to a 600 model when running several standard loading cases. A beam-model with $7,560$ beam elemts was as accurate as the $300k$ solid model. The computation time for the solid model exceeded for the beam model by one to two orders of magnitude. The experimental validation of both, the solid and the beam model showed a good agreement between the simulated

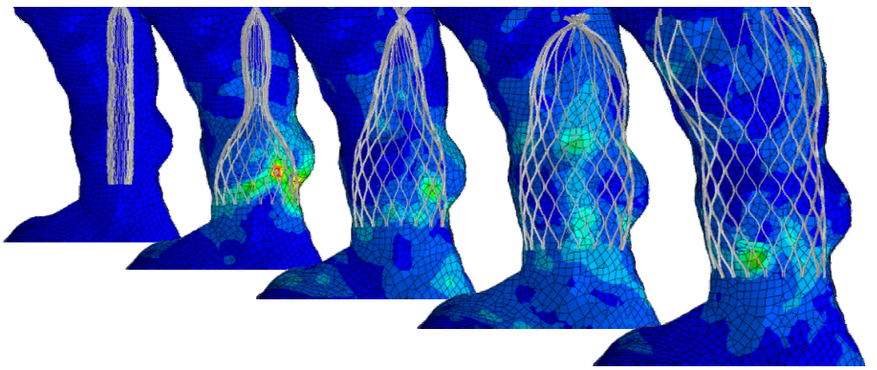

Figure 2: Virtual CoreValve stent deployment in patient-specific multi-material antomcial model.

and the measured characteristic curves for deflections up to $1.5\ mm$ (see Fig. 3). The mean circumferential error of the simulation was between $2.9\ \%$ and $6.3\ \%$, the latter being the case in a patient with severe aortic calcifications which were at the point not considered by the simulation.

3 CONCLUSIONS

Timoshenko Beam elements are a very efficient and numerically stable means of modelling the behaviour of the CoreValve. The model outperforms a classical solid-modelling approach in terms of computational complexity without losing accuracy. A biomechanical shell-element model of the aortic root can be generated fully automatically based on CTA images. In order to improve the accuracy of the presented simulation approach, the impact of calcium need to be considered in the simulation.

REFERENCES

[1] N. Piazza, R. Lange, G. Martucci, P.W. Serruys, Patient selection for transcatheter aortic valve implantation: patient risk profile and anatomical selection criteria, *Arch Cardiovasc Dis*, 105(3), 65-73, 2012.

[2] R. Zhang, Y. Song, Y. Zhou, L. Sun, Comparison of aortic annulus diameter measurement between multi-detector computed tomography and echocardiography: a meta-analysis, *PLoS One*, 8(3), e58729, 2013.

[3] G. J. Hall and E. P. Kasper, Comparison of element technologies for modelling stent expansion, *Journal of Biomechanical Engineering*, 128(5), 751-756, 2006.

[4] N. D. Ferreira, D. Caeiro, L. Ado, M. Oliveira, H. Gonalves, J. Ribeiro, M. Teixeira, A. Albuquerque, J. Primo, P. Braga, L. Simes, V. G. Ribeiro, Incidence and predictors of permanent pacemaker requirement after transcatheter aortic valve implantation with a self-expanding bioprosthesis, *Pacing Clin Electrophysiol.*, 33(11):1364-72 (2010).

[5] M. Gessat, R. Hopf, T. Pollok, C. Russ, T. Frauenfelder, S.H. Sündermann, S. Hirsch, E. Mazza, G. Székely, V. Falk, Image-Based Mechanical Analysis of Stent Deformation. Concept and Exemplary Implementation for TAVI Stents, *Biomedical Engineering, IEEE Transactions on*, published online ahead of print: http://dx.doi.org/10.1109/TBME.2013.2273496

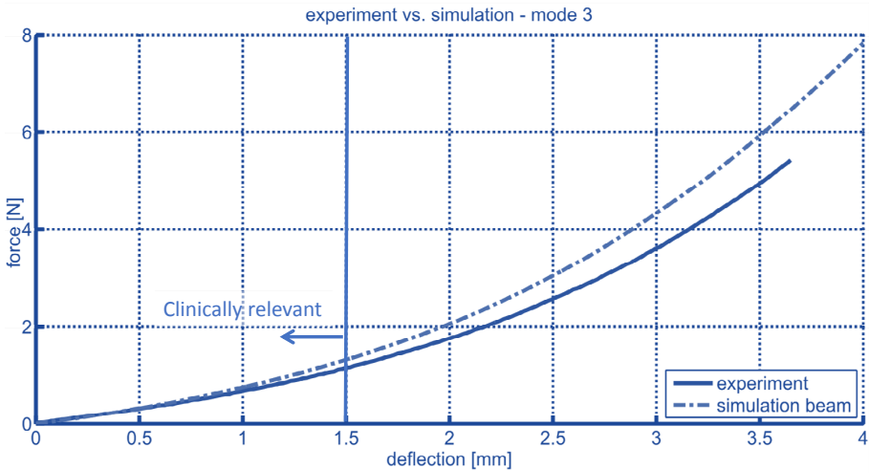

Figure 3: Validation of the stent model in tensile test. Up to a deflection of $1.5\ mm$*, the experiment matches well with the simulation.*

3rd International Conference on Computational and Mathematical Biomedical Engineering – CMBE2013
16-18 December 2013, Hong-Kong
P. Nithiarasu and R. Löhner (eds)

Image-based computational simulations for patient-specific surgery planning in congenital heart defects

Maria Restrepo[*], Elaine Tang[**], Christopher M. Haggerty[*], Mark Luffel[***], Kirk R. Kanter[****], Timothy C. Slesnick[*****], Jarek Rossignac[***], Thomas L. Spray[******], Mark A. Fogel[*******], Ajit P. Yoganathan[*]

[*]Wallace H. Coulter Department of Biomedical Engineering, Georgia Institute of Technology and Emory University, Atlanta, GA USA

[**]School of Chemical and Biomolecular Engineering, [***]College of Computing, Georgia Institute of Technology, Atlanta, GA USA

[****]Division of Cardiothoracic Surgery, [*****]Division of Pediatric Cardiology; Department of Pediatrics, Emory University school of Medicine and Children's Healthcare of Atlanta Atlanta, GA USA

[******]Division of Cardiothoracic Surgery, [*******]Division of Cardiology; Children's Hospital of Philadelphia, Philadelphia, PA USA

Key Words: *computational fluid dynamics, congenital heart diseases, patient-specific surgical planning*

1 INTRODUCTION

Image-based computational modeling provides a novel means to pre-operatively evaluate blood flow characteristics and tailor the surgery to the patient-specific anatomy. This framework has been applied to the total cavopulmonary connection (TCPC) design in single ventricle patients[1]. We have aimed to provide the clinical team with a series of options that seek to optimize the naturally adverse hemodynamics in the connection. Additionally, the paradigm is now being extended to other congenital heart diseases such as double outlet right ventricle (DORV).

2 METHODS

Cardiac magnetic resonance (CMR) images are segmented to create patient-specific vascular models (i.e., bi-directional Glenn or existing TCPC connections, and ventricular volumes)[2, 3] and reconstruct flow information[4], if available. Then, a specially designed virtual surgery environment is used to mimic the procedure of interest: baffle placement in Fontan patients[5], and patch location for biventricular repair in DORV. Blood flow simulations using computational fluid dynamics[6] are performed to characterize hemodynamic metrics (i.e., power loss and hepatic flow distribution) to compare theoretical connection performances and provide input to surgical decision-making. Geometrical measurements such as volume computations are also acquired to assess the

quality of the option proposed in DORV patients. A schematic of the image-based surgery planning approach is outlined in Figure 1.

3 RESULTS

Computer-based surgical planning has been prospectively used for 30 Fontan patients, including 8 with a 'failed' existing connection. The primary indication for most cases was pulmonary arteriovenous malformations, which are believed to form in the absence of hepatic factor in the blood reaching pulmonary arterial segments. Thus, the modeling objective was to optimally distribute hepatic blood flow to the lungs. Short-term follow-up has shown favorable clinical outcomes and consistency between model predictions and operative results.

For the DORV patients, we have now performed 8 prospective surgical planning cases in which we have provided the clinical team an evaluation of the ventricular volumes based on the patches designed in the surgical planning environment.

4 CONCLUSIONS

Computer-based surgery planning is an exciting new paradigm for patients with congenital heart defects, and has the potential to deliver patient-specific benefit. In addition, surgical planning can help in the evaluation of more complex surgical options in order to assess the benefits of pursuing it.

REFERENCES

1. Sundareswaran K, de Zélicourt D, Sharma S, Kanter K, Spray T, Rossignac JR, Sotiropoulos F, Fogel M, Yoganathan AP. Correction of pulmonary arteriovenous malformation using image based surgical planning. *JACC Imaging*. 2009;2:1024-1030
2. Frakes DH, Conrad CP, Healy TM, Monaco JW, Fogel M, Sharma S, Smith MJ, Yoganathan AP. Application of an adaptive control grid interpolation technique to morphological vascular reconstruction. *IEEE Trans Biomed Eng*. 2003;50:197-206
3. Frakes DH, Smith MJ, Parks J, Sharma S, Fogel M, Yoganathan AP. New techniques for the reconstruction of complex vascular anatomies from mri images. *J Cardiovasc Magn Reson*. 2005;7:425-432
4. Sundareswaran K, Frakes D, Fogel M, Soerensen D, Oshinski JN, Yoganathan A. Optimum fuzzy filters for phase-contrast magnetic resonance imaging segmentation. *Journal of Magnetic Resonance Imaging*. 2009;29:155-165
5. Pekkan K, Whited B, Kanter K, Sharma S, de Zelicourt D, Sundareswaran K, Frakes D, Rossignac J, Yoganathan AP. Patient-specific surgical planning and hemodynamic computational fluid dynamics optimization through free-form haptic anatomy editing tool (surgem). *Med Biol Eng Comput*. 2008;46:1139-1152
6. de Zélicourt D, Ge L, Wang C, Sotiropoulos F, Gilmanov A, Yoganathan A. Flow simulations in arbitrarily complex cardiovascular anatomies - an unstructured cartesian grid approach. *Comput Fluids*. 2009;38:1749-1762

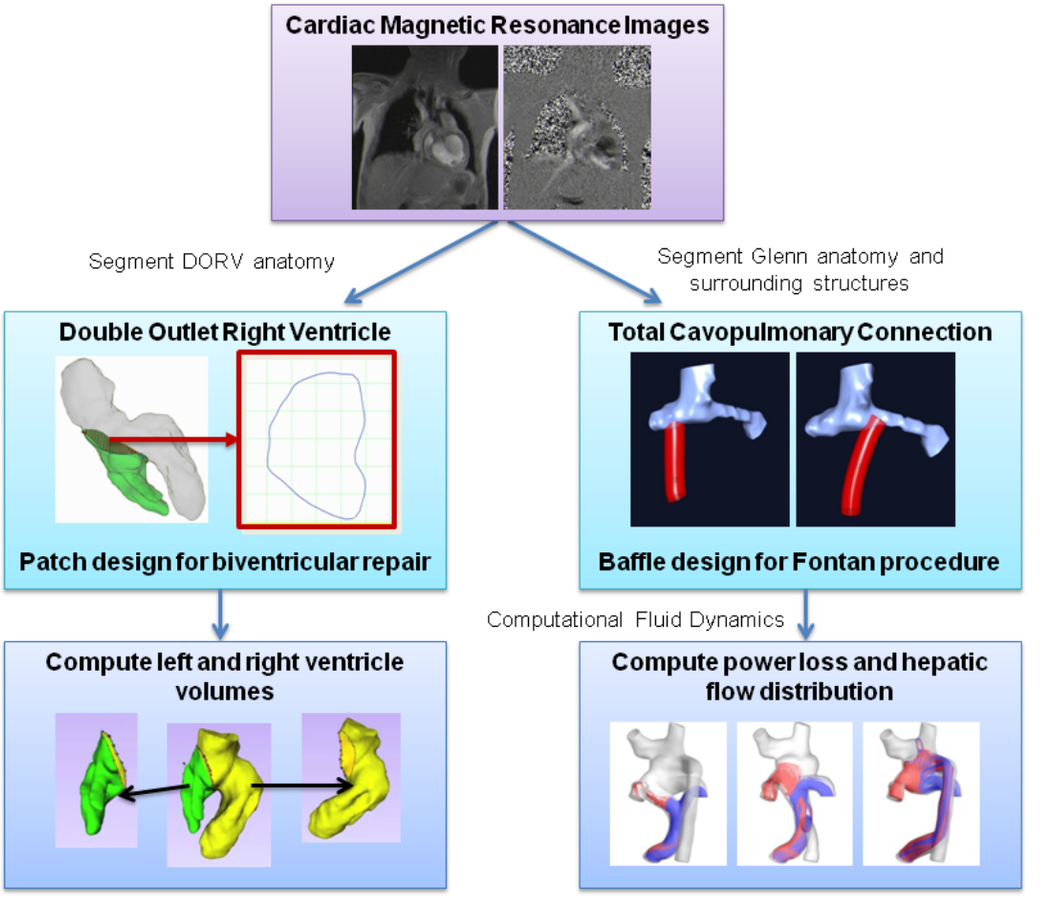

Figure 1. Schematic of the image-based simulation of patient-specific surgery planning for DORV and Fontan patients

3rd International Conference on Mathematical and Computational Biomedical Engineering – CMBE2013
16-18 December 2013, Hong-Kong
P. Nithiarasu and R. Löhner (eds)

Biomechanical analyses of the thoracic aorta: Could wall stress and 3D geometry help identify patients at risk of acute aortic dissection?

Barry J. Doyle,[*,] Peter R. Hoskins,[**,***] Karol Miller,[*] David E. Newby[****] and Marc R. Dweck[****]**

* Intelligent Systems for Medicine Laboratory, The University of Western Australia, Australia. Barry.Doyle@ul.ie

** Centre for Cardiovascular Science, The University of Edinburgh, UK. p.r.hoskins@ed.ac.uk

*** Department of Mechanical, Aeronautical and Biomedical Engineering, University of Limerick, Ireland.

**** Clinical Research Imaging Centre, The University of Edinburgh, UK. mdweck@ed.ac.uk; d.e.newby@ed.ac.uk

SUMMARY

Aortic dissection is an often fatal clinical condition which is challenging to accurately diagnose and if untreated, further progression of the dissection is inevitable. The aim of this study was to biomechanically investigate a cohort of patient-specific thoracic aortas to determine potential factors that may contribute to aortic dissection. Fifty patients were included in the study. Patient-specific finite element analysis was performed to estimate the in vivo wall stresses. Geometric parameters were measured and statistical analysis was used to identify any significant correlations. Ascending aortic diameter, arch radius and tortuosity were all significantly related to wall stresses. Arch type, gender and smoking status had no significance influence on wall stresses. Maximum wall stress was located in the ascending aorta or the aortic arch in the majority of cases (>90%), which coincides with the locations of clinical intimal entry tears in acute Type A dissection. Geometry influences wall stress and regions of elevated wall stresses appear to coincide with the location of acute Type A aortic dissection intimal entry tears. Computational modeling and three dimensional geometric analyses may potentially improve the diagnosis of aortic dissection. However, this work needs to be extended to include a group of known aortic dissection cases to verify any clinically-relevant parameters.

Key Words: *aortic dissection, wall stress, geometry.*

1. INTRODUCTION

Aortic dissection is characterized by the separation of the layers of the aorta, usually the intima-media layers, causing blood to flow within. The flow of blood into this false lumen causes further propagation and dissection of the layers, resulting in a lethal condition. Aortic dissection is currently the most common cause of aortic emergency requiring surgical repair [1]. Incidence rate is approximately 2.9 - 3.5 per 100,000 person-years; however, reports suggest that this may be increasing, most likely due to improvements in medical imaging and an aging population. The condition has a very high mortality rate, with one study reporting that 68% of cases died within 48 hours of hospital admission. This high rate is partly attributed to the failure to accurately recognize aortic dissection. Nevertheless, even when properly diagnosed and treated, the in-hospital mortality is still 25%. Additionally, autopsy reports suggest thoracic aortic dissection and rupture accounts for twice the number of deaths per year as abdominal aortic aneurysm (AAA) rupture, even though AAA incidence rates are much higher. Over recent years, biomechanical modeling has been employed to better understand the role of in vivo stresses acting on the thoracic aortic wall. The aim of this present study is to examine the wall stress and geometry of the thoracic aorta, in a cohort of elderly patients, with the aim of identifying geometric parameters that correlate with wall stress, and thus, which may encourage acute aortic dissection.

2. METHODS

Study Group

Patients were selected from a recent clinical trial (NCT01358513) [2], whereby all cases were > 50 years with no known aortic dissection. Patients had varying levels of aortic valve disease which was not accounted for in this study. Ethical approval was granted by the local research ethics committee and all computed tomography (CT) was performed as part of Dweck et al. [2]. All patients underwent full clinical assessment at baseline which included recording of their blood pressure and routine clinical parameters at the time of imaging.

3D Reconstruction, Mesh and Stress Analysis

CT datasets were imported into Mimics v15 (Materialise, Belgium). Segmentation of the aorta began at the sinotubular junction (STJ) and ended at the diaphragm level of the descending thoracic aorta. The surface of each model was then conservatively smoothed. Each 3D model was then imported into 3-matic v6 (Materialise, Belgium) and as the exact wall thickness cannot be determined from conventional CT, a uniformly thick aortic wall (2.32 mm) was created.

The models were then discretized into 3D 10-node tetrahedral solid stress finite elements and exported for analyses with the non-linear large deformation solver in ABAQUS/Standard (Dassault Systemes, USA). Each model was simulated using three mesh densities, with each mesh size approximately doubling in number. Models were deemed independent of mesh size when the change in the 99th-percentile of peak von Mises wall stress was < 2%. The aortic wall was modeled as a hyperelastic isotropic material using data determined from non-aneurysmal thoracic aortas. Each model was rigidly constrained at the aortic root and the distal region of the descending aorta to simulate tethering to the heart and the abdominal aorta. We also examined the role of aortic root motion. For each analysis, the 99th-percentile of von Mises, circumferential and longitudinal stress was calculated, and the location of each maximum stress recorded. Location of peak stresses were compared to the clinical locations of intimal tearing in Type A aortic dissection [3].

Geometry Measurements

3D models were used to determine several geometric measurements within Mimics. Firstly, the centerline of the each model was created and the total tortuosity measured. The centerline was then divided into two sections using the apex of the aortic arch, with tortuosity of the ascending and descending aorta determined. The arch angle was measured from the right lateral view along the inner surface of the arch. The radius of the arch was measured by inscribing a circle to the inner curvature of the arch centerline and recording the maximum radius. Finally, the best-fit ascending aortic diameter was quantified using the centerline and the outer aortic wall. A schematic of these measurements is shown on an example geometry in Figure 1.

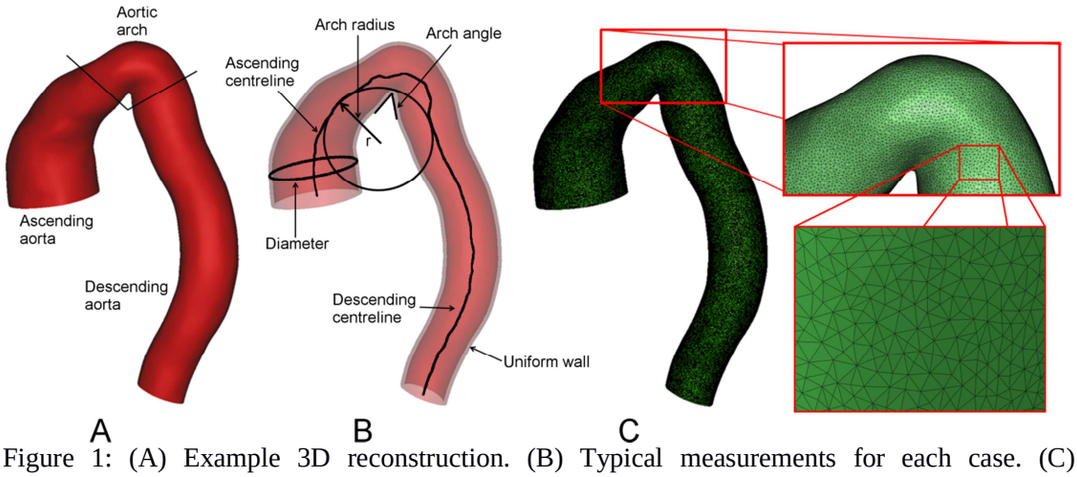

Figure 1: (A) Example 3D reconstruction. (B) Typical measurements for each case. (C) Discretized geometry showing typical mesh-independent element size (inserts).

3. RESULTS

Patient Characteristics and Geometries

The mean age of the cohort was 73.8 ± 8.2 (54 - 90) years, with an even gender distribution (male = 27, female = 23). Mean blood pressure was 146 ± 18 (109 - 193) mmHg and body mass index (BMI) was 26.8 ± 3.7 (19.9 - 40.0). The maximum best-fit ascending aortic diameter was 36.1 ± 4.8 (28.1 - 56.6) mm. Total centerline tortuosity was 0.53 ± 0.06 (0.43 - 0.67), ascending aortic tortuosity was 0.12 ± 0.04 (0.06 - 0.23) and descending aortic tortuosity was 0.15 ± 0.04 (0.07 - 0.27). The mean arch angle was 113 ± 16° (45 - 151°) and arch radius was 46.8 ± 6.3 (34.9 - 62.3) mm. The cohort consisted of 23 Type I and 27 Type II aortic arches.

Wall Stresses and Locations

Mesh size was dependent on diameter ($p<10e^{-5}$) and arch angle ($p<10e^{-6}$). The mean von Mises wall stress was 0.16 ± 0.02 (0.11 - 0.25) MPa, circumferential wall stress was 0.13 ± 0.02 (0.09 - 0.21) MPa and the longitudinal wall stress was 0.11 ± 0.01 (0.08 - 0.16) MPa. The ascending aorta experienced high von Mises, circumferential and longitudinal wall stress, in particular along the inner and outer curvatures. The location of maximum stresses for the entire cohort are presented in Figure 2 and compared to the location of clinical intimal tears in 17 patients detected with 64-slice CT [3]. Peak wall stress was observed in the ascending aorta or aortic arch in the majority of cases (94% of von Mises stress; 90% of circumferential stress; 96% of longitudinal stress).

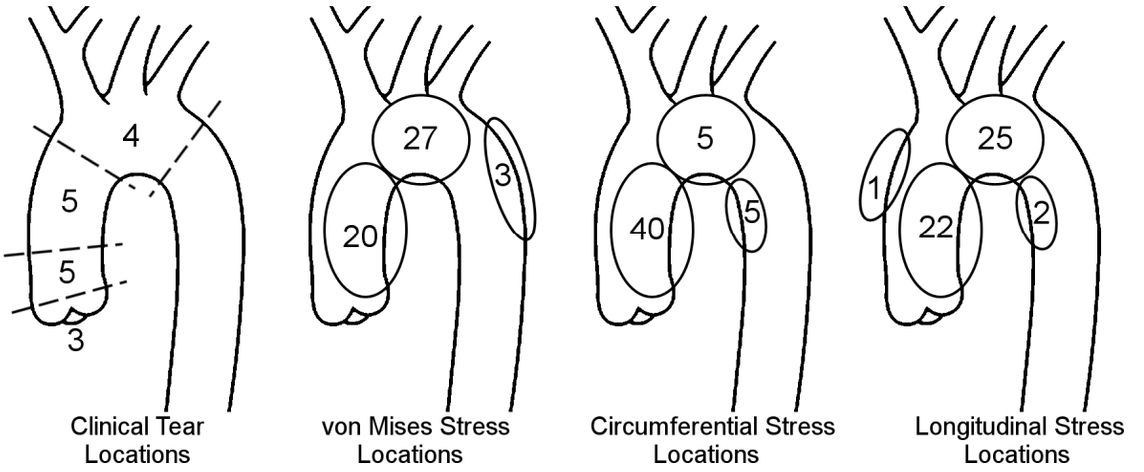

Figure 2: Illustration showing locations of maximum von Mises, circumferential and longitudinal stresses for the entire cohort, compared to the location of clinical intimal entry tears observed in 17 patients [3].

4. CONCLUSIONS

In this cohort of human thoracic aortas, peak wall stresses were found in the ascending aorta and aortic arch, which coincide with regions where the majority (>80%) of intimal entry tears occur in acute aortic dissection. The geometry of the aorta, but not necessarily the arch type (i.e. Type I or II), was observed to be a significant factor in wall stress. Ascending aorta best-fit diameter was the most influential on von Mises ($p<10e^{-7}$), circumferential ($p<10e^{-7}$) and longitudinal ($p<10e^{-7}$) wall stresses. It would appear that the diameter of the ascending aorta is a good indicator of potential pathologies that may develop as a result of elevated thoracic wall stresses. Arch radius also significantly correlated with von Mises ($p<10e^{-6}$), circumferential ($p<10e^{-5}$) and longitudinal ($p<10e^{-5}$) wall stresses. It was found that the total tortuosity of the aortic centerline influenced both von Mises ($p=0.044$) and circumferential ($p=0.045$) wall stresses, whereas the tortuosity of the descending aorta correlated with both the von Mises ($p=0.011$) and longitudinal ($p=0.009$) wall stresses. Best-fit diameter, arch radius and tortuosity can all be quantified from 3D reconstructions and may be useful clinical parameters in the risk assessment of aortic dissection, and potentially used independent of wall stress analysis. Next, we aim to extend this study to a group of pre and post aortic dissection cases to verify any clinically-relevant parameters. Future studies building on the data presented here may help establish the role of patient-specific modeling as a diagnostic tool in the assessment of aortic dissection.

REFERENCES

[1] B.K. Khandheria, Aortic dissection. The last frontier, Circulation, 87, 1765-1768, 1993.

[2] M.R. Dweck, et al. Assessment of valvular calcification and inflammation by positron emission tomography in patients with aortic stenosis, *Circulation,* 125, 76-86, 2012. N.

[3] N. Jassaud, et al. Acute type A aortic dissection intimal tears by 64-slice computed tomography: a role for endovascular stent-grafting? *Journal of Cardiovascular Surgery (Torino),* 54, 373-381, 2013.

Standard Session I

3rd International Conference on Computational and Mathematical Biomedical Engineering – CMBE2013
16-18 December 2013, Hong-Kong
P. Nithiarasu and R. Löhner (Eds.)

Computational study of bone tissue cryo-freezing incorporating nanoparticles

K.J. Chua* and S.K. Chou**
*****Department of Mechanical Engineering, 9 Engineering Drive 1 Singapore 117576, mpeckje@nus.edu.sg
******Department of Mechanical Engineering, 9 Engineering Drive 1 Singapore 117576, mpecsk@nus.edu.sg

SUMMARY

Cryosurgery appears to be a particularly attractive option for treating solid tumors locked in skeletal masses and cavities as it allows the affected part to be removed while preserving the natural anatomy of the skeleton. In this work, an experimentally validated nanocryosurgical bone model is presented to simulate nano-assisted cryo-freezing in a femur bone. Comparisons made with experiments demonstrated good agreement with a maximum discrepancy of 8.6%. We evaluated the impact of judiciously introducing nano-particles to the bone tissue before cryo-freezing. Simulated results with lamb femur bones indicated that the rate of freezing was enhanced by injecting nano-particles. Specifically, nano-diamond and nano-magnetite intensified cryo-freezing and shorten the duration for the bone-tissue to achieve lethal ablation temperature by 79% and 73.4%, respectively.

Key Words: *computational model, nanocryosurgery, bone tissue, nanoparticles.*

1 INTRODUCTION

In nano-cryosurgery, the introduction of a heterogeneous solution of nano-particle suspension into the target tissues can potentially promote thermal tissue conductivity in the tissue. This will lead to an enhanced freezing effect and an increased number of cell deaths due to the higher likelihood of intracellular ice formation. In addition, the nano-particles in the tissue act as preferred nucleation sites for ice formation. Due to the presence of such preferential sites, the frequency of such ice nucleation increases. The effective surface energy is lower at these sites, thus requiring less energy than homogeneous nucleation to occur under the same conditions.

Thus far, there exist little or no work on the development of a nano-cryo freezing model specifically dedicated to bone tumor ablation. Furthermore, the developed model has to be accurate and highly versatile to study the impact of nano-particles freezing on the efficacy of cryo-ablation bone tumors.

2 MODEL DEVELOPMENT

The detailed model for this work has been presented in two earlier publications [1,2]. Only the gist of the model will be presented here.

The numerical modeling of a cryosurgery problem requires the prediction of the position and form of a freezing front propagating in an unfrozen domain, Ω (bone tissue). The computational domain is an 80mm diameter region. From a mathematical standpoint, it consists of solving a bio-heat conduction equation in the domain Ω with a domain demarcated by frozen, mushy, and unfrozen phases.

Heat transfer by conduction has been assumed to be the only heat transfer mode during cryosurgery. This is a reasonable assumption since the cryoprobe operates at an extremely low temperature such that the effect of other heat transfer mechanisms may be nullified and considered negligible. The fundamental Pennes heat transfer equation has been adopted in the formulation of the mathematical model:

$$(\rho c)_t \frac{\partial T(X,t)}{\partial t} = \nabla \cdot k_t \nabla T(X,t) + (\rho c)_b \omega_a (T_a - T(X,t)) + Q_m \quad \text{where} \quad X \in \Pi(t) \qquad (1)$$

In our approach, the mushy zone is treated explicitly as one of the sub-domains of the entire computational domain. The mushy region is defined at the temperature region between solidus and liquidus region.

By applying eq. (1) to the various freezing zones, as shown in Fig. 3, and employing Cartesian geometry, the following governing equations may be written:

(a) In the frozen region, due to the absence of blood perfusion and metabolic rate, the heat balance equation may be expressed as

$$\rho_s c_s \frac{\partial T_s(X,t)}{\partial t} = \nabla \cdot k_s \nabla T_s(X,t) \quad \text{where} \quad X \in \Pi(t) \qquad (2)$$

(b) In the mushy region, we can write

$$\rho_i c_i \frac{\partial T_i(X,t)}{\partial t} = \nabla \cdot k_i \nabla T_i(X,t) + \omega_b \rho_b c_b [T_b - T_i(X,t)] + Q_m + \rho_i h_L \frac{df_s}{dt} \quad \text{where} \quad X \in \Pi(t) \qquad (3)$$

where f_s , the solid fraction during phase change, may be written as:

$$f_s = \begin{cases} 0 & if \quad T_i(X,t) = T_{liquidus} \\ 1 & if \quad T_i(X,t) = T_{solidus} \\ \dfrac{T_i(X,t) - T_{liquidus}}{T_{solidus} - T_{liquidus}} & if \quad T_{solidus} < T < T_{liquidus} \end{cases} \quad \text{where} \quad X \in \Pi(t) \qquad (4)$$

(c) In the unfrozen region, we have

$$\rho_L c_L \frac{\partial T_L(X,t)}{\partial t} = \nabla \cdot k_L \nabla T(X,t) + \omega_b \rho_b c_b [T_b - T_L(X,t)] + Q_m \quad \text{where} \quad X \in \Pi(t) \qquad (5)$$

The thermal tissue properties of the tumor are expected to change when the nanoparticles are injected to the tumor. Two key properties that need specific attention are the thermal conductivity and the specific properties of the tissue when nanoparticles are introduced. [3]. These thermal properties are quantified using the classical Hamilton-Crosser thermal conductivity model to account for the change in conductivity once nanoparticles are introduced and are presented as follows:

$$k_t = k_{ft}\frac{k_p + 2k_{ft} - 2\eta\left(k_{ft} - k_p\right)}{k_p + 2k_{ft} + \eta\left(k_{ft} - k_p\right)} \quad 6(a)\,; \qquad k_u = k_{ut}\frac{k_p + 2k_{ut} - 2\eta\left(k_{ut} - k_p\right)}{k_p + 2k_{ut} + \eta\left(k_{ut} - k_p\right)} \quad 6(b)$$

With regards to the thermal capacities, taking in account the energy equation for a two-component biomaterial system (biological part and induced nanoparticle part), Yan and Liu [3] presented them to be as follows:

$$c_f = c_{ft}\cdot\left(1-\eta\right) + c_p\cdot\eta \quad 7(a)\,; \qquad c_u = c_{ut}\cdot\left(1-\eta\right) + c_p\cdot\eta \quad 7(b)$$

where subscripts f and u represent frozen and unfrozen mixture, respectively while subscripts *ft* and *ut* denote frozen and unfrozen tissue, respectively. Subscript *p* stands for loaded nanoparticles. The respective thermal conductivities are 0.56 W/mK for unfrozen tissue, 2.0 W/mK for frozen tissue, 7.1 W/mK for nano-magnetite (Fe_3O_4) and 2000 W/mK for nano-diamond. And the respective C_p values for unfrozen tissue (C_{ut}) and frozen (C_{ft}) are $3.6X10^6$ J/m^{3o}C and $2.0X10^6$ J/m^{3o}C, respectively. And C_p values are $3.6X10^6$ J/m^{3o}C for nano-magnetite (Fe_3O_4) and $1.4X10^6$ J/m^{3o}C for nano-diamond.

The developed model has been validated with experimental data in the radial direction of the ice-ball. The maximum percentage difference between experiments and simulated results from the model was obtained to be 8.6% as illustrated in Figure 1b.

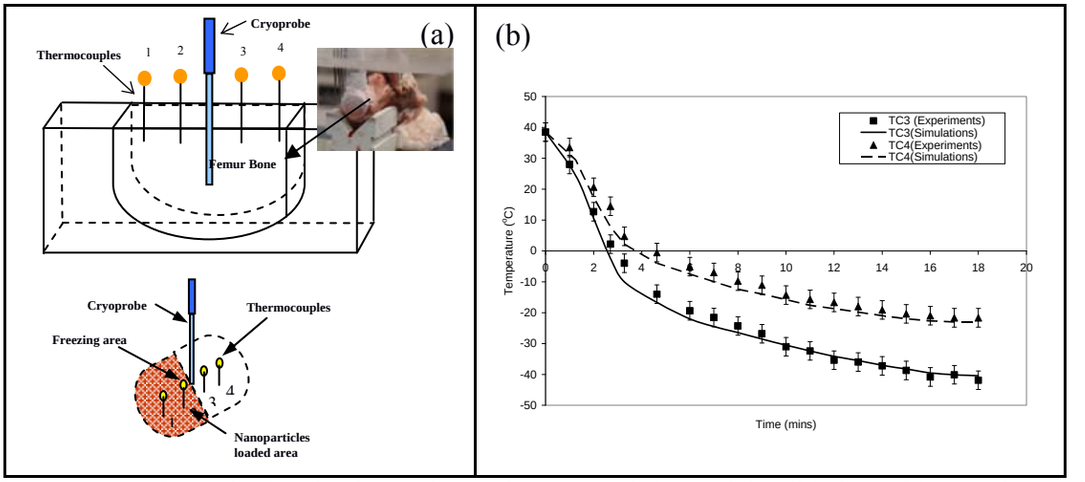

Figure 1. (a) Schematic sketch of experimental setup; and (b) model validation with experimental data obtained for bone tissue during cryo-freezing process.

3 RESULTS AND DISCUSSION

According to Gage and Baust (1998), experiments conducted with diverse animal tissues have set the lethal cell destructive temperature to be -40^{o}C and below [4].

The effect of incorporating nano-magnetite to the cryo-freezing of bone is shown in Figure 2. From the experimental results, data have shown that using nano-diamond will allow the tissue to reach lethal temperature faster with reduction in freezing time of about 79%. The model was re-simulated then computed, this time using nano-magnitite particles and results are shown in Figure 2. From the experimental results, the experimental results show that the percentage of time saved using nano-magnetite is 73.4% for the tissue to reach the lethal temperature of -40^{o}C.

We can infer that nano-particles markedly promotes freezing during bone cryosurgery. Results indicated that nano-diamond achieved the most desirable results in terms allowing tissue to achieve lethal temperature earlier. Injecting nano-diamonds and nano-magnetite allowed tissue to shorten freezing time by 79% and 73.4%, respectively.

Other known advantages of introduction of nanoparticles during cryosugery include better localization and control of the ice-ball growth, thus being able to reach small cavities of the bone or the edges of irregular tumors and reducing the number of cryoprobes used for large complex solid tumors.

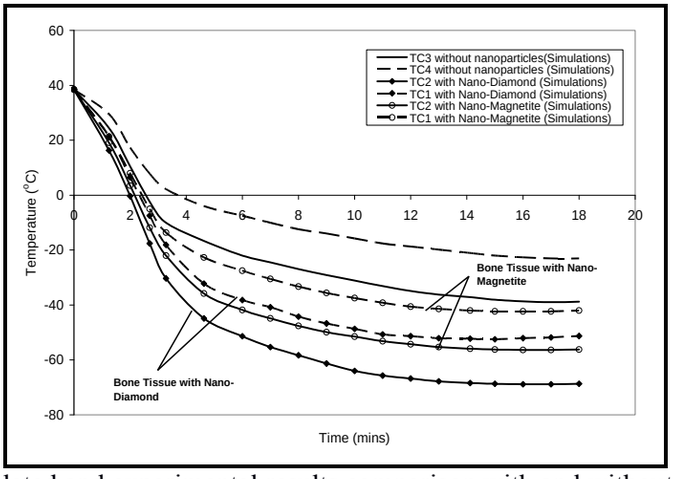

Figure 2. Simulated and experimental results comparison with and without nanoparticles.

4 CONCLUSIONS

Through an experimentally validated model, computational results have shown that the introduction of nano-particles, namely nano-diamond and nano-magnetite, led to acceleration of freezing rates. Accordingly, bone tissue is able to achieve the lethal temperature of -40°C much earlier. Incorporating nano-diamonds and nano-magnetite led to enhanced tissue thermal conductivity, resulting in significant increase in freeze rate with all other variables being held the same. Comparatively, nano-diamond had a major influence on the enhancing the thermal conductivity of the tissue and thus had a greater impact on promoting bone tissue freezing.

REFERENCES

[1] K.J. Chua, S.K. Chou and J.C. Ho. An analytical study on the thermal effects of cryosurgery on selective cell destruction. *Journal of Biomechanics,* 40(1), 100-116, 2007.

[2] K.J. Chua. Computer simulations on multiprobe freezing of irregularly shaped tumors. *Computer Biology and Medicine,* 41(7), 493-505, 2011.

[3] J.F. Yan and J. Liu. Nano-cryosurgery and its mechanisms for enhancing freezing efficiency of tumor tissue. *Nanomedicine: Nanotechnology, Biology, and Medicine*, 4, 79-87, 2008.

[4] A.A. Gage and Baust J. Mechanisms of tissue injury in cryosurgery. *Cryobiology*, 37, 171-186, 1998.

3rd International Conference on Computational and Mathematical Biomedical Engineering - CMBE2013
16-18 December 2013, Hong-Kong
P. Nithiarasu and R. Löhner (Eds.)

Thermal microenvironment of keratinocytes and fibroblasts during cauterisation by laser devices

Elisa Budyn*, Sagar Bhogle, Steve Lacey***, Jim Radosevich** and Mike Colvard****

*Ecole Nationale Supérieure de Cachan, 61 Avenue du Président Wilson, 94235 Cachan, France, e-budyn@alumni.northwestern.edu

**University of Illinois at Chicago, 801 South Paulina Street, Chicago, IL 60612, USA, sbhogl2@uic.edu, jrados@uic.edu, colvard@uic.edu

***Indiana University Fairbanks School of Public Health, 714 North Senate Ave, Indianapolis, IN 46202, USA, selacey@iupui.edu

SUMMARY

Skin is the outer layer of the body of mammals and is a protective layer against the aggressions of the environment. Skin is also preserves the body internal temperature and water and is a storage layer for water and lipids. Skin contains specific mechanical and nervous receptors that sense heat and cold, touch, pressure, vibration and pain. Any surgical procedure therefore causes a dramatic reaction in response to the inflicted damage. Thermal damage applied to porcine skin is imaged and modelled to identify the thermal thresholds of the observed modifications of the epidermal and dermal ECM tissues by histology and estimate the depth of burns produced by laser devices during cauterisation.

Key Words: *skin, laser, keratinocyte, fibroblast, cauterisation.*

1 INTRODUCTION

Skin is composed of the protective epidermis and dermis that are first cut in any emergency surgery. To prevent excessive bleeding, laser cauterisation of the wound edges burns the skin over a usually unknown thickness that we propose to identify to assess the healing prognosis.

2 HIERARCHICAL MULTI-SCALE THERMAL MODEL

In the epidermis four strata (corneum, granulosum, spinosum and germinativum), keratinocyte stem cells germinate to undergo differentiation until cornification into corneocytes attached by corneo-desmosomes. Beneath, the two strata of the dermis (papillare and reticulare) are composed of collagen-elastin fibrous connective tissues produced by fibroblasts immersed in the hydrous ground substance containing proteins and proteoglycans. The reticulare stratum contains hair follicles, sweat glands, sebaceous glands, apocrine glands, nerves, Parcinian and Meissner corpuscles, lymphatic vessels and blood vessels. The hypodermis below produced by adipocytes is attached to the muscles and bones. Besides its mechano-sensing function of touch, pressure, pain and heat, skin is part of the adaptive immune system and contributes to the body temperature regulation. The method proposes a Bio-heat hierarchical multi-scale numerical model of the

porcine skin ran in parallel with laser surgeries.

$$\rho_{skin} c_{skin} V \frac{\partial T}{\partial t} = V\nabla(k_{skin}\nabla T) + h_{air/skin} A_{conv}(T_{surface} - T_{air}) + V Q_m^v + A_e Q_{laser}^{se} + A_d Q_{laser}^{sd} \quad (1)$$

where ρ_{skin} is the skin density. c_{skin} is the specific heat. k_{skin} is the skin conductivity and V is the sample volume. The skin medium is decomposed into a series of observed constituents immersed in a collagen fibrous matrix. The values of the densities and the thermal properties of the constituents and the epidermis and dermis sublayers are calculated by a hierarchical multi-scale approach. The properties are calculated from the macro-molecular level to the single cell immersed in its ECM level. The fibrous collagenous ECM of the dermis is distinguished into loose and dense regions [1,2]. The laser surface heat flux, Q_{laser}^s, in the dermis and the epidermis depend on the heat power and laser wave length that are measured experimentally.

The model is fed by information obtained from samples along the wound edges treated by histological methods based on the loss of antigenicity.

The results give the thermal conductivities and specific heats of the skin layers at the cell and organ scales. The model identifies the temperature field, damage depth and temperature thresholds of different burn damages generated by a series of continuous or pulsed laser devices. The results are validated by histology as shown in Figure 1.

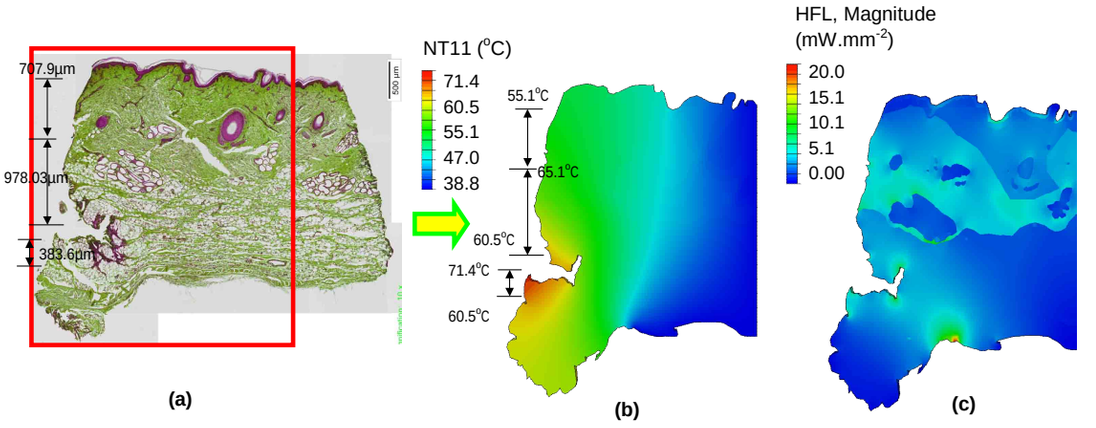

Figure 1: Identification of the temperature threshold in the damage areas in Surgery 4BF under steady-state conditions: (a) histology, (b) temperature field, (c) heat flux

3 CONCLUSIONS

Figures 2 shows the thermal fields in two finite element models that either uses epidermal and dermal properties from the literature (a) or properties calculated by the previously described hierarchical approach. In both surgeries the hierarchical model shows a larger temperature span and a higher temperature region of dimensions resembling the microscopic observations.

The model offers successfully assessment laser thermal damage and promising results for further thermo-chemical studies of laser treatments.

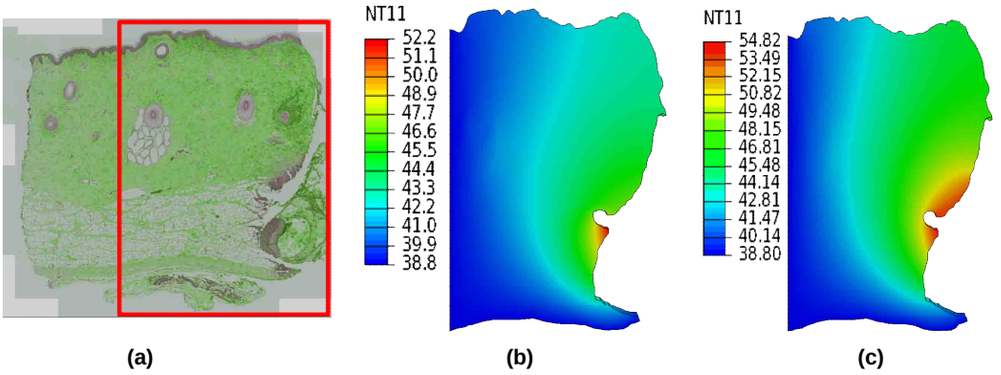

Figure 2: Porcine skin sample for Surgery 5: (a) antibody staining observation, temperature fields (b) when calculated using epidermal and dermal property values from the literature and (c) when calculated using hierarchical models for the epidermal and dermal tissues.

REFERENCES

[1] J. W. Y. Jor, M. P. Nash, P. M. F. Nielsen, and P. J. Hunter, Estimating material parameters of a structurally based constitutive relation for skin mechanics, *Biomechanical Modeling in Mechanobiology*, 10, 767-778, 2011.

[2] J. W. Y. Jor, P. M. F. Nielsen, M. P. Nash, and P. J. Hunter, Modelling collagen fibre orientation in porcine skin based upon confocal laser scanning microscopy, *Skin Research and Technology*, 17, 149-159, 2011.

3rd International Conference on Mathematical and Computational Biomedical Engineering – CMBE2013

16-18 December 2013, Hong-Kong

P. Nithiarasu and R. Löhner (eds)

Structural modelling of the annulus fibrosus - an anisotropic hyperelastic model approach at the lamellar level

Marlene Mengoni, Vithanage N. Wijayathunga, Alison C. Jones
Ruth C. Wilcox

Institute of Medical and Biological Engineering, University of Leeds, Leeds LS2 9JT, UK, m.mengoni@leeds.ac.uk

SUMMARY

This work was aimed at developing a first approach to produce structural models of the Annulus Fibrosus, i.e. constitutive models of individual lamellae. Parameters of Holzapfel's model were fitted using literature data on the behaviour of tissue components. Used on sample-specific or simplified geometries, the effect on the whole annulus deformation of the fibre angles, inter-lamellar behaviour, and incompressibility was analysed to assess their role in the disc mechanics.

Key Words: *annulus fibrosus lamellae, anisotropic hyperelasticity, finite element analysis.*

1 INTRODUCTION

The annulus fibrosus is the fibrous avascular outer part of the intervertebral disc (IVD). It is composed of a series of circumferential layers called the lamellae [1]. Each lamella is composed of collagen fibre bundles embedded into a ground matrix. Secondary structures such as bridges across the lamellae or surrounding elastin walls are also present. In each lamella, the fibres are quasi-uniformly oriented in one direction at an angle of 20° to 50° with the transverse plane. This angle alternates between adjacent lamellae. The inner part of the IVD, surrounded by the annulus, is a gel-like substance called the nucleus pulposus.

The IVD is a permanently loaded environment. It acts as a joint between two adjacent vertebrae and gives the spine its flexibility. It is subjected to compressive loads, bending and shear. In particular, the annulus withstands internal pressure due to the nucleus hydrostatic compressive stress. As the annulus bulges, the tissue is extended, making tension an important mode of loading for the annulus fibrosus [1]. A realistic virtual model of the IVD can give insight into the significance of deformation patterns and is a help for the design of novel treatment approaches.

As such the understanding of the mechanical properties of the different constituent tissues and their role in the IVD mechanics is of greater importance. In the last decade, many constitutive models of the annulus fibrosus have been proposed, most of these considering an annulus constituted of two sets of fibres with different orientations and an isotropic elastic matrix [2,3], with some accounting for the cross-links between adjacent lamellae [4]. To our knowledge no previous model has accounted for fibres and matrix of individual lamella, the inter-lamellar behaviour and the cross-bridges. This study took the first step towards such a model. The approach was focused on the structural aspects and did not account for viscous or damage effects.

2 METHODS

Considering the nonlinear behaviour of the collagen fibres and the structural aspect the model has to represent, an anisotropic hyperelastic model was chosen for the lamellar behaviour. Such a model allows consideration of separate energy density functions for the matrix and the fibres, including their specific orientation. It also allows the consideration of incompressibility for the lamellae. In particular, Holzapfel's constitutive model [5], developed mainly for arterial walls, was used in this work. It assumes a linear shear behaviour of the ground matrix (neo-Hookean model) and a non-linear exponential behaviour of oriented fibres, that bear load only in tension.

First, 1D analytical stress-strain curves for each component of Holzapfel's model were fitted against experimental data for a single lamellae extracted from the literature. Details of mechanical tests on lamellar samples prepared in such a way that the fibres would not bear loads, and thus representative of the matrix behaviour, are available in [6]. Data from shear tests were used to characterise the ground matrix mechanical behaviour. Single lamellar tension tests performed along the fibre direction [3,7,8] were used to characterise the fibre behaviour.

The constitutive model with the fitted parameters was then used in a sample-specific finite element (FE) model. The geometry was acquired from a micrograph of a sample cut through the annulus width in the radial direction [9]. Segmentation and tetrahedral mesh generation were performed using ScanIP 5.1 (Simpleware Ltd). This FE model was used to assess the relevance of an anisotropic hyperelastic model versus a neo-Hookean model with equivalent shear stiffness.

Finally, the constitutive model was used in a finite element model of the whole annulus fibrosus represented as a simplified cylindrical geometry. This model consisted of 12 concentric perfectly circular lamellae subjected to internal pressure. It was used to analyse the effect of inter-lamellar behaviour on the annulus bulge as well as the effect of the site-dependency of the fibrous behaviour, the fibre orientation, and the incompressibility.

All finite element analyses were performed using the implicit finite element software Abaqus 6.12 (Dassault Systèmes) with linear tetrahedral or hexahedral elements.

3 RESULTS

Data available in [6] clearly shows the ground matrix shear behaviour is non-linear. However a linear model that characterises the shear behaviour of the neo-Hookean model can be fitted (r^2=0.982) up to 30% shear strains (Figure 1, left). The non-linear behaviour of the fibres depends on the fibre location around the annulus (Figure 1, right - dots). An exponential behaviour as in Holzapfel's model can be fitted (Figure 1, right - lines) for each experimental test (r^2 between 0.986 and 0.999) over the whole available stretch range.

The longitudinal force (radial in terms of the IVD geometry) needed to stretch a radial cut through the annulus, for two material models (Holzapfel's model or a neo-Hookean model), is shown on Figure 2 (right). As the elongation is perpendicular to the fibre stretch, the neo-Hookean model, being isotropic, necessitates a higher force (20% greater at 20% strain).

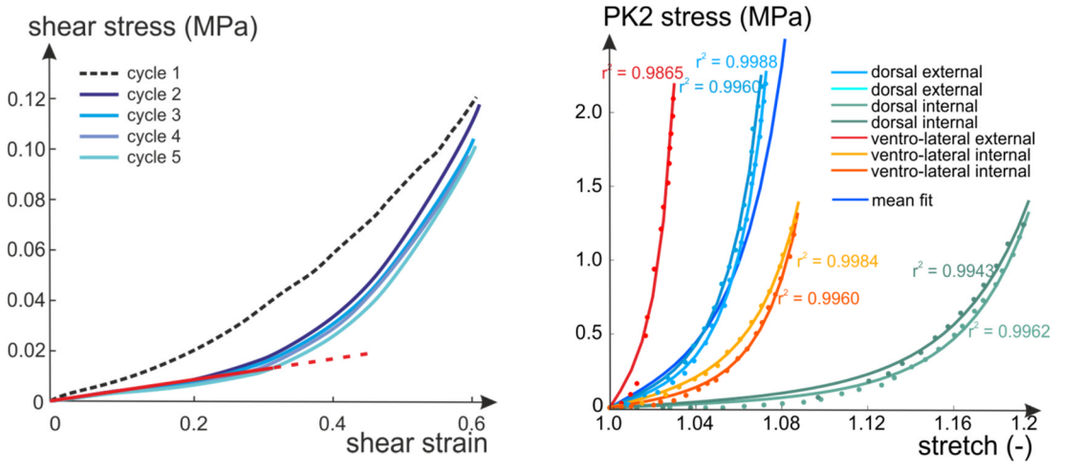

Figure 1- Results of a parameter fit: Left: a neo-Hookean model of the ground matrix (exp. data from [6], linear fit in red); Right: an exponential behaviour of the collagen fibres (exp. data from [7,8]).

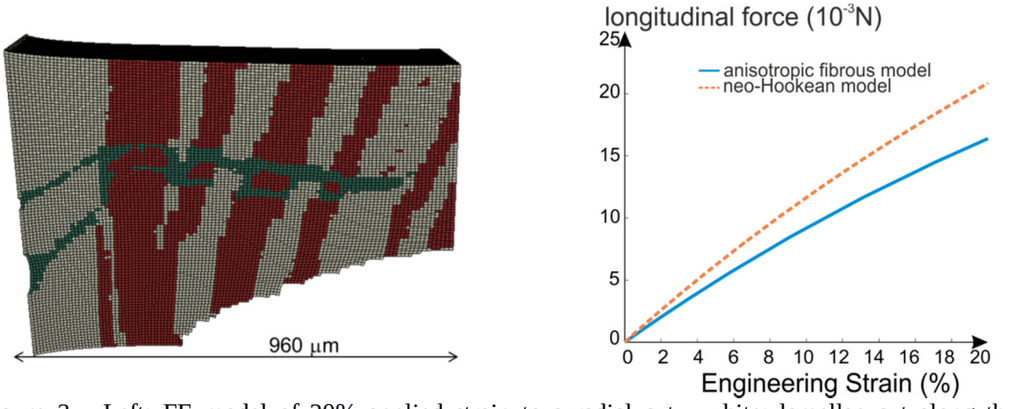

Figure 2 – Left: FE model of 20% applied strain to a radial cut - white: lamellae cut along the fibre direction, red lamellae with sectioned fibres, green: cross-bridges; Right: Force vs. strain for a neo-Hookean model (in orange) and a Holzapfel one (in blue).

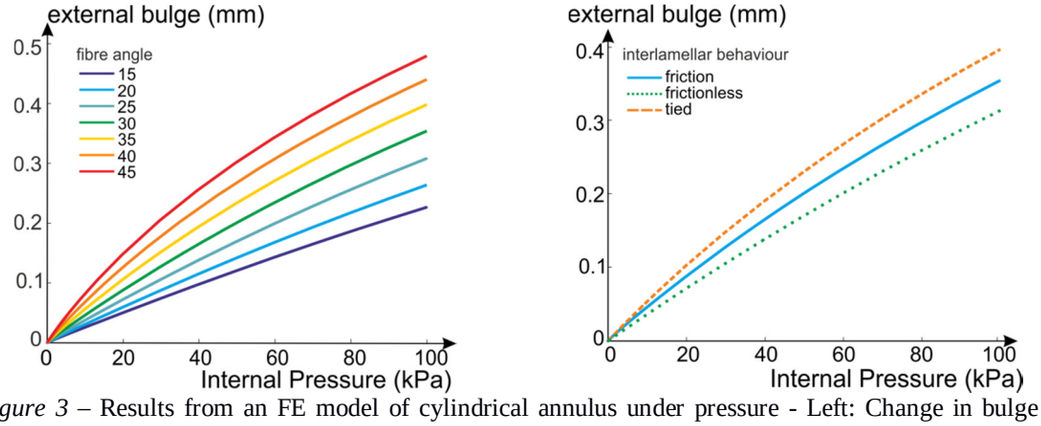

Figure 3 – Results from an FE model of cylindrical annulus under pressure - Left: Change in bulge vs. internal pressure as a function of the fibre angle. Right: Change in bulge vs. internal pressure as a function of the inter-lamellar interaction model.

Finally, the bulge of a cylindrical annulus under pressure is presented in Figure 3. It shows a dependence on the assumed fibre angle (adjacent lamellae have supplementary angles from the transverse plane). It also shows a strong dependence on the assumed inter-lamellar behaviour.

4 DISCUSION/CONCLUSIONS

This work, focussing on a structural model of the annulus fibrosus, showed that the use of Holzapfel's constitutive model with one fibre orientation to represent each lamellae shows promising results. The exponential model of the fibre mechanics is adequate on the whole tested range available in the literature. The linear model of the matrix gives relevant results up to 30% shear strains. This is a limitation at very large strain but not essentially for clinically relevant deformations. A radial stretching model of an actual sample showed that using an anisotropic law rather than a neo-Hookean law is worth the extra-computational cost. When used on a cylindrical representation of the annulus, the model shows not only a sensitivity to the fibre angle but also to the assumed inter-lamellar behaviour. Future work will propose experimental tests to further validate the model of the lamellar components, including the incompressibility and the possible pre-stress. The use of a validated lamellar constitutive model in conjunction with whole annulus experimental data could give insight to the inter-lamellar behaviour.

Acknowledgment

This work was funded through WELMEC, a Centre of Excellence in Medical Engineering funded by the Wellcome Trust and EPSRC, under grant number 088908/Z/09/Z

REFERENCES

[1] J.J. Cassidy, A. Hiltner & E. Baer, Hierarchical structure of the intervertebral-disc, *Connect Tissue Res*, 23, 75-88, 1989

[2] D.M. Elliott & L.A. Setton, A Linear Material Model for Fiber-Induced Anisotropy of the Anulus Fibrosus, *J Biomech Eng*, 122, 173-179, 2000

[3] R. Eberlein, G.A. Holzapfel & C.A.J. Schulze-Bauer, An Anisotropic Model for Annulus Tissue and Enhanced Finite Element Analyses of Intact Lumbar Disc Bodies, *CMBBE*, 4, 209-229, 2001

[4] H.L. Guerin & D.M. Elliott, Quantifying the Contributions of Structure to Annulus Fibrosus Mechanical Function Using a Nonlinear, Anisotropic, Hyperelastic Model, *J. of Orthopaedic Research*, 25, 508-516, 2007

[5] G.A. Holzapfel, T.C. Gasser & R.W. Ogden, A New Constitutive Framework for Arterial Wall Mechanics and a Comparative Study of Material Models, *J Elasticity* 61, 1-48, 2000

[6] J.P. Little, M.J. Pearcy, G. Tevelen, J.H. Evans, G. Pettet & C.J. Adam, The mechanical response of the ovine lumbar anulus fibrosus to uniaxial, biaxial and shear loads, *J Mech Behav Biomed Mater*, 3, 146-157, 2010

[7] G.A. Holzapfel, C.A.J. Schulze-Bauer, G. Feigl & P. Regitnig, Single lamellar mechanics of the human lumbar anulus fibrosus, *Biomech Model Mechanobiol*, 3, 125-40, 2005

[8] D.L. Skaggs, M. Weidenbaum, J.C. Iatridis, A. Ratcliffe & V.C,. Mow Regional Variation in Tensile Properties and Biochemical Composition of the Human Anulus Fibrosus, *Spine*, 19, 1310-1319, 1994

[9] B.J. Luxmoore, Computational Simulation of the Intervertebral Disc, PhD Thesis, University of Leeds, School of Mechanical Engineering, 2013

3rd International Conference on Computational and Mathematical Biomedical Engineering – CMBE2013

16-18 December 2013, Hong-Kong

P. Nithiarasu and R. Löhner (eds)

A non-linear heterogeneous finite element model of vertebral trabecular bone using greyscale-based material properties

D. J. Rollins*, A. C. Jones*, R. K. Wilcox* and D. C. Barton*

*University of Leeds, IMBE - Institute of Medical and Biological Engineering, Leeds, United Kingdom – mndjr@leeds.ac.uk

SUMMARY

A methodology is presented for generating high resolution finite element models of trabecular bone with both homogeneous and greyscale-based material properties. Also presented are their effects on the apparent mechanical response at varying threshold values. The results indicate that greyscale-based models are less sensitive to variations in threshold value than homogenous based models. This work also presents initial results for non-linear models and the effects of different material property definitions on the distribution of local yield in the trabecular structure.

Key Words: *Finite element modeling, trabecular bone, non-linear, heterogeneity.*

1. INTRODUCTION

High resolution models of subsections of trabecular bone have been used to explore the mechanisms of failure at the micro-mechanical level [1]. These models are often created from micro-Computed Tomography (μCT) images of real bone samples so that anisotropic morphology of the trabecular bone is represented in the model and so that they can be validated experimentally. However it is often assumed that the material properties are homogenous and constant throughout specimens.

While the effects of the variations in the trabecular structure on the apparent mechanical properties are well explored [1], the intra-specimen variations of tissue material properties have been somewhat neglected. Nano-indentation tests on ovine trabecular bone show that the tissue modulus varies from 8.2 GPa in the centre of a trabecular strut to 4 GPa at the surface [2]. It has also been shown that both the apparent mechanical properties and local stresses and strains vary significantly with tissue modulus distribution [3]. Using greyscale-based material properties, local property variations can be represented in the model and highlight areas of weakness in the trabecular bone due to the material properties as opposed to just the trabecular bone morphology.

Any image-based model has a volume and topology dependent on the image segmentation process. In the case of μCT-based trabecular model, a lower threshold value will result in a larger segmented volume and increased connectivity. The correct choice of threshold value is not easily determined and this aspect of the model development remains a challenge.

This study shows how using greyscale-based material properties can mitigate segmentation errors by making the elements involved in the resulting volume change less critical to the load bearing behavior of the sample. This development is a step towards a robust process for developing finite element models from µCT data, which is an essential prerequisite for advances in non-linear finite failure modeling.

2. METHODS

Five 8 mm trabecular bone cores were taken from the centre of the vertebral bodies of a 3 year old ovine vertebra. The samples were cut to a length of 12mm and the marrow was broken down in an ultrasonication bath of monosodium citrate solution and removed using a water pick. Each sample was scanned in a µCT Scanner (µCT100, ScanCo Medical AG, Switzerland) at a resolution of 22 µm. The µCT images were imported into ScanIP V6.0 (Simpleware Ltd., United Kingdom) and segmented by selecting all voxels with greyscale values over a single threshold before being flood filled to remove unconnected parts from the mask. The mask was then converted into a tetrahedral volume mesh with minimum target element edge length of 25 µm and a maximum target of 50 µm which equate to ¼ of the approximate lower and upper boundaries of trabecular thickness 100-200 µm [4]. Additional models with varying bone volume/total volume (BV/TV) were created using different threshold values, as shown in Table 1.

Table 1 - Table showing the variation of sample data with different threshold values.

Threshold Value	BV/TV		Mean Greyscale ($\boldsymbol{GS_\mu}$)		Standard Deviation ($\boldsymbol{GS_\sigma}$)	
27	0.353	+/- 0.015	56.88	+/- 0.75	18.00	+/- 0.41
29	0.340	+/- 0.014	58.06	+/- 0.73	17.38	+/- 0.40
31	0.327	+/- 0.013	59.14	+/- 0.75	16.74	+/- 0.44
33	0.315	+/- 0.013	60.20	+/- 0.71	16.14	+/- 0.44
35	0.303	+/- 0.012	61.26	+/- 0.71	15.56	+/- 0.41

For the homogeneous tissue properties an initial value of 5 GPa was taken as it is within the range of values for ovine trabecular bone [3]. The greyscale conversion factor (E_{GS}) is then calculated from the homogeneous tissue modulus (E_H) and used to determine the tissue modulus per-element.

$$E_{element} = E_{GS} \cdot GS^{\gamma}$$

Where E_{GS} is the greyscale conversion factor, GS [0,255] is the greyscale value of the element and γ is a power factor to allow for exponential scaling. A higher exponent will widen the range in Young's Modulus between upper and lower limits of greyscale values. The greyscale conversion factor is calculated from the homogeneous material properties using the equation:

$$E_{GS} = \frac{E_H}{0.5 \cdot [(GS_\mu - GS_\sigma)^{\gamma} + (GS_\mu + GS_\sigma)^{\gamma}]}$$

Where GS_μ and GS_σ are the mean and standard deviation of the greyscale value of the bone tissue. This equation scales the greyscale conversion factor with respect to γ so that the average modulus throughout all elements in the model is constant for all values ofγ.

For non-linear models, the yield strength was set to 2.5% of the Young's modulus. All models were run in Abaqus/Standard 6.11-1(Dassault Systèmes S.A., France). For the non-linear models, NLGEOM was enabled accounting for geometric non-linearities caused by large deformations.

Figure 1 shows a cross section of a typical sample with homogeneous (i) and greyscale-based (ii) material properties. It can be seen that the thick sections in model contain significantly more detail when greyscale-based material properties are used. Additionally, it can be seen that the centre of the trabecular struts are a higher tissue modulus than the edges.

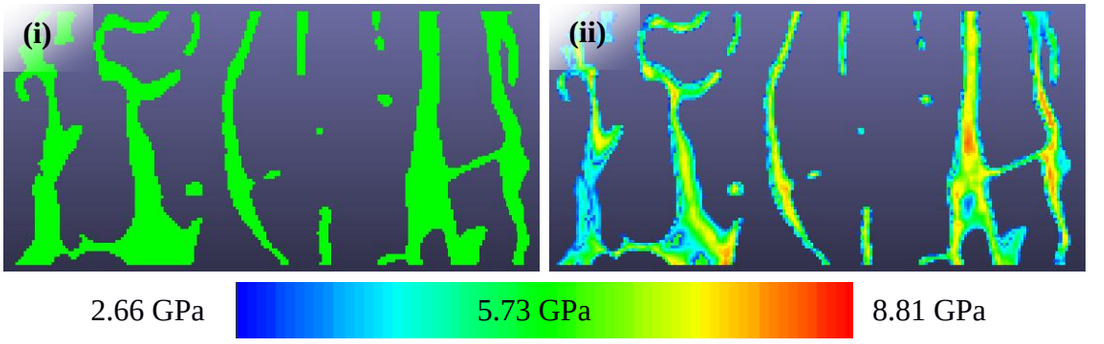

Figure 1 – Masks representing bone selected during the threshold operation. The colour map represents Young's Modulus. (i) homogeneous material properties and (ii) greyscale-based material properties [γ=1.0].

2. RESULTS & DISCUSSION

Figure 2 shows the variation of apparent modulus of a sample with bone volume/total volume (BV/TV) for 3 different tissue property definitions. These results show that the variation of apparent modulus with BV/TV is non-linear, with thinner structures showing larger apparent stiffness changes with added material than those that are already relatively thick. However, using greyscale-based material properties reduces this variation by ~40% for linear distribution and >50% for exponential distribution (γ=1.5). This reduction is due to the edges of the trabeculae having a lower greyscale value, and therefore Young's Modulus, so they contribute less to the load carrying of the structure.

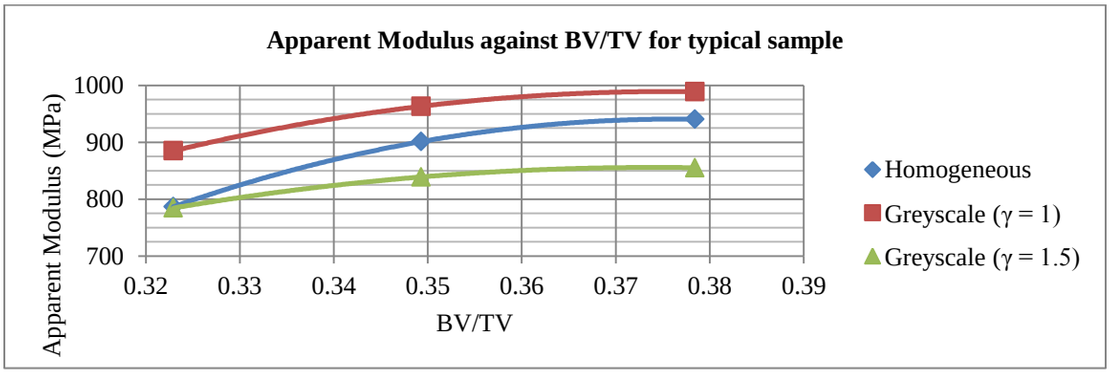

Figure 2 - Graph showing how variation of Apparent Modulus with BV/TV for a single sample using homogeneous and greyscale-based material properties.

Figure 3 shows the failed elements of a typical sample under 2 mm compression. The three different material property definitions show differences in percentage of yielded elements under the same loading conditions. The failed elements occur in more regions throughout the models with greyscale-based material properties than in the models with homogeneous material properties, this is likely due to areas of low material density deforming more than they would under homogenous material properties.

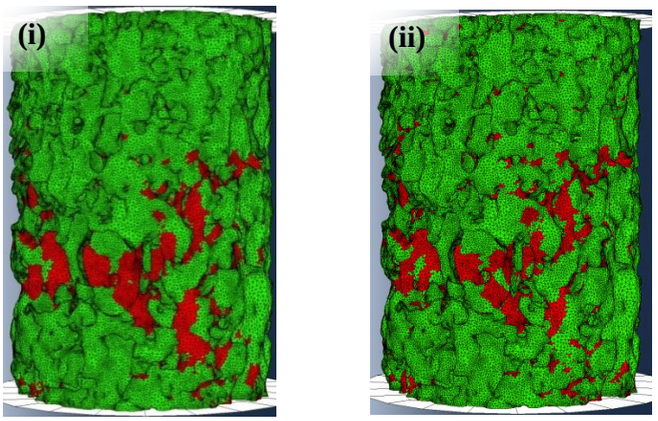

Figure 3- Finite element model of a typical sample under 2mm displacement for a) homogeneous material properties and b) greyscale-based material properties. Percentage yielded elements at 2mm displacement: H = 3.71%, GS1 = 4.53% and GS1.5 = 5.16%.

3. CONCLUSIONS

A robust methodology for the development of micro-mechanical finite element model of trabecular bone is presented. The study shows that using greyscale-based material properties over homogenous material properties, renders the results less sensitive to BV/TV and therefore to segmentation errors. Initial non-linear finite element models show that the distribution of yielded elements is larger for greyscale-based material properties suggesting that some regions of the bone are weaker as a result of the material properties rather than the structure. Material properties specific to these models are still need to be determined before they can be validated against experimental data and CT scans of the sample under load.

REFERENCES

[1] Tony M. Keaveny, Elise F. Morgan, Glen L. Niebur, and Oscar C. Yeh, Biomechanics of Trabecular Bone, *Annual Review of Biomedical Engineering*, Vol. 3: 307-333, 2001.

[2] Noel M. Harrison, Pat F. McDonnell, Denis C. O'Mahoney, Oran D. Kennedy, Fergal L. O'Brien and Peter E. McHugh, Heterogeneous linear elastic trabecular bone modelling using micro-CT attenuation data and experimentally measured heterogeneous tissue properties, *Journal of Biomechanics*, Vol. 41, Issue 11, 2589–2596, 2008.

[3] Michael J. Jaasma, Harun H. Bayraktar, Glen L. Niebur, Tony M. Keaveny, Biomechanical effects of intraspecimen variations in tissue modulus for trabecular bone, *Journal of Biomechanics*, Vol 35, issue 2, 237-246, 2002.

[4] M.J. Silva and L. J. Gibson, Microstructural model of vertebral trabecular bone, *Bone*, Vol. 21, No. 2,191-199, 1997.

3rd International Conference on Computational and Mathematical Biomedical Engineering - CMBE2013
16-18 December 2013, Hong-Kong
P. Nithiarasu and R. Löhner (Eds.)

Stochastic modeling of cortical bone: Application to ultrasound axial transmission measurements

Salah Naili ⋆, Vu-Hieu Nguyen ⋆, Mai-Ba Vu ⋆, Christophe Desceliers ⋆⋆, Christian Soize ⋆⋆
Université Paris Est,
Laboratoire Modélisation et Simulation Multi-Echelle (MSME UMR 8208 CNRS),
⋆ 61 avenue du Général de Gaulle 94010 Créil, France
⋆⋆ 5, boulevard Descartes, 77454 Marne-la-Vallée, France

SUMMARY

This paper aims to study the effects of the random fluctuation of mechanical properties of cortical bone on its ultrasonic responses. The numerical results focused on studying the FAS (First Arriving Signal) velocity will be presented, allowing to consider dependence of this quantity on the dispersion induced by statistical fluctuations of bone's elasticity.

Key Words: *stochastic modeling, cortical bone, ultrasound.*

1 INTRODUCTION

Ultrasound axial transmission technique (ATT) technique plays an important role among experimental methods used for the diagnostic of long bones. This technique measures the travel time and attenuation of the wave propagating along bone's longitudinal direction to evaluate mechanical as well as geometrical characteristics of the bone. In the literature, the simulation of ATT often considers cortical long bone as a homogeneous or functionally graded medium [2]. Moreover, most of parametric studies of wave propagation in bone are limited to deterministic media which may not be suitable to reflect the fact that cortical bone is a heterogeneous and random medium at the vascular scale due to the fluctuation of pore distribution and physical properties of mineralization of bone tissues. Some studies have recently been carried out to investigate the influence of random properties of cortical bone in the context of ultrasound characterization. A probabilistic model based on the maximum entropy principle has been constructed for considering cortical bone plate as homogeneous or multi-layered media [3,4] to simulate the *in vivo* measurements in the statistical sense. However, only material inhomogeneities in the direction of the bone's cross section's have been considered. In this paper, we present a more realistic stochastic model to consider the random fluctuation of material properties in both radial and longitudinal directions in a cortical bone plate.

2 METHOD

The system of cortical long bone coupled with soft tissues is modeled as an random anisotropic elastic plate immersed deterministic idealized fluids. Parametric probabilistic models are built by modeling the local physical properties of the medium. In this work, the elasticity tensor $\mathbb{C}(\mathbf{x})$, of which the mean value is defined by $\mathbb{c}(\mathbf{x})$, will be considered as a random matrix. In practice,

it is not easy to collect a sufficient large set of experimental data on bone material, to estimate the probability distribution of the random elasticity tensor. Moreover, the random spatial variation of the elastic property should be considered. Here, we use Soize's model [5] whereby the probability distribution is built by full-filling the maximum entropy principle. Using this principle, the stochastic elasticity tensor $\mathbb{C}(\mathbf{x})$ may be parameterized by *its mean values* $\mathbb{c}(\mathbf{x})$ *via* its matrix representation, and by a *minimal set of essential parameters* which consists of only 4 parameters: one scalar dispersion level δ and one vector $\boldsymbol{\lambda}$ that contains three spatial correlation lengths.

The time domain finite-difference method is employed to solve the wave propagation problem . For this work, an explicit scheme, which is based on a staggered grid formulation for the velocity and stress components, has been implemented. The scheme is second-order in time and fourth-order in space. In order to avoid any effect of the wave reflected by the boundaries of the domain Ω on all recorded radio-frequency signals, the PML (Perfectly Matched Layer) technique has been is used.

3 RESULTS

We will some results on studying an ultrasound wave (with a central frequency 1MHz) propagating through a random 4mm-thickness cortical bone layer. In this study, the mean property of the bone is taken from the work of Dong *et al* [6] who measured the homogenized bone properties by performing tensile and torsional tests with a mechanical testing system on 18 different human femoral bone specimens. In the menstioned paper, mean values of 4 elastic constants were provided: the longitudinal Young's modulus $E_L = 16.6$ GPa, and the transverse Young's modulus $E_T = 9.5$ GPa), the longitudinal shear modulus $G_L = 4.7$ GPa and longitudinal Poisson's ratio $\nu_L = 0.37$.

Fig. 1 (left) presents the $\mathrm{V_{FAS}}$ obtained for all of 800 Monte-Carlo realizations. Two levels of dispersion $\delta = 0.1$ and $\delta = 0.3$ have been considered. It can be seen that when $\delta = 0.1$, the values of $\mathrm{V_{FAS}}$ oscillate around the one corresponding to the mean model which is shown as the red continuous line ($\mathrm{V_{FAS}^{mean}} = 3606\ \mathrm{m.s^{-1}}$). When the dispersion is higher ($\delta = 0.3$), the measured values of $\mathrm{V_{FAS}}$ are globally decrease. It may be explained by the fact that when the heterogeneity of the medium is greater, the scattering phenomenon becomes more significant and may modify the global wave velocity in the domain. In addition, we obtained a greater dispersion of $\mathrm{V_{FAS}}$ is more important in the case $\delta = 0.3$ than the one in the case $\delta = 0.1$. In Fig. 1 (right), the probability density functions (PDF)of $\mathrm{V_{FAS}}$ are computed for both cases. The dependency of the PDF of the FAS shows that in the practice, neglecting the uncertain heterogeneity in bone may lead to a poor prediction of the mean value of mechanical properties by using $\mathrm{V_{FAS}}$ as a index.

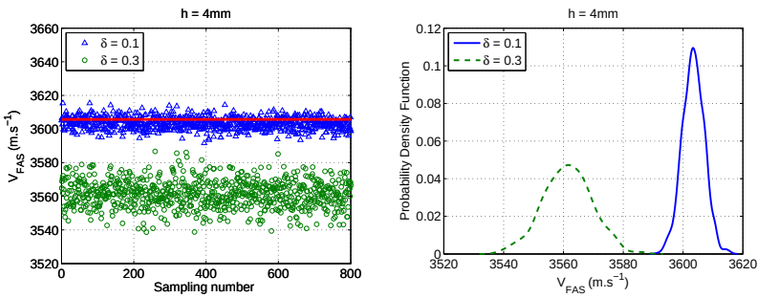

Figure 1: (left) Values of $\mathrm{V_{FAS}}$ evaluated at each realization; the solid line is obtained for the homogeneous material properties; (right) probability density functions of $\mathrm{V_{FAS}}$

4 CONCLUSION

Because the statistical data on real bone material is hardly found, a parametric probabilistic method, which is based on the maximum entropy principle, has been used to generate an optimal probabilistic model for taking into account the uncertainties of bone elasticity. A explicit FDTD solver has been developed for simulating the wave propagation in a transversely isotropic heterogeneous medium in the time domain. Due to the limited scope of this paper, we only presented a preliminary result on V_{FAS} which shown that this quantity is very sensitive to dispersion of the bone's elasticity tensor in statistic sense.

REFERENCES

[1] Lowet, G. and Van der Perre, G., Ultrasound velocity measurements in long bones: measurement method and simulation of ultrasound wave propagation, *J. Biomech.*, 29,1255–1262, 1996.

[2] Naili, S., Vu, M.-B., Grimal, Q., Talmant, M., Desceliers, C., Soize, C., and Haiat, G., Influence of viscoelastic and viscous absorption on ultrasonic wave propagation in cortical bone: Application to axial transmission. *J. Acoust. Soc. Am.*, 127(4):2622–2634, 2010.

[3] Macocco, K., Grimal, Q., Naili, S., and Soize, C., Elastoacoustic model with uncertain mechanical properties for ultrasonic wave velocity prediction; application to cortical bone evaluation. *J. Acoust. Soc. Am.*, 119(2):729–740, 2006.

[4] Desceliers, C., Soize, C., Naili, S., and Haiat, G., Probabilistic model of the human cortical bone with mechanical alterations in ultrasonic range. *Mech. Sys. and Sig. Proc.*, 32:170–177, 2012

[5] Soize, C., Non-Gaussian positive-definite matrix-valued random fields for elliptic stochastic partial differential operators. *Comput. Methods Appl. Mech. Eng.*, 195:26–64, 2006

[6] Dong, X. N. and Guo, X. E., The dependence of transversely isotropic elasticity of human femoral cortical bone on porosity. *J. Biomech.*, 37(8):1281–1287, 2004.

3rd International Conference on Computational and Mathematical Biomedical Engineering – CMBE2013
16-18 December 2013, Hong-Kong
P. Nithiarasu and R. Löhner (eds)

Inverse dynamics simulation in patients with developmental dysplasia of the hip and effect biomechanical of hip with use abduction splint

[*] Carlos Andrés Pérez A., [**] Gabriel Fernando Fletscher C., [***] Angelica María Ramírez M. and [****] Diego Alexander Garzón A.

[*] Msc. Researcher Biomedical Engineering Manuela Beltran University, Bogotá, COLOMBIA, Postal Address 110911, carlos.perez@docentes.umb.edu.co

[**] MD Resident Orthopedics and Traumatology National University, Bogotá, COLOMBIA

[***] Phd Eng. Researcher Mechanical Engineering Central University, Bogotá, COLOMBIA

[****] Phd Eng. Researcher Mechanical Engineering National University, Bogotá, COLOMBIA

SUMMARY

Currently there is debate on leave to walk or not children with abduction orthesis, when diagnosis is developmental dysplasia of the hip. First the gait involves a increased biomechanical demands in hip, and second have not been evaluated biomechanical changes caused by the use of a hip abduction orthosis while performing the walking [1]. Available studies regarding the use of abduction splint are clear that the therapeutic effect of these measures in the context of child and effects on the acetabulum still not well understood. Several studies to evaluate the effect of combined abduction orthosis with walking, have shown an increase in the proportion of reluxations, however these have been poor and lacking at suitable experimental groups for your comparison[2]. Some clinical observations recommend use the splint during the gait, some report no data that contraindicate its use and others suggest a beneficial effect.

Key Words: *Developmental Dysplasia of the Hip, abduction splint, Inverse Dynamic,.coxofemoral joint*

1 INTRODUCTION

Developmental Dysplasia of the Hip a progressive disorder of this joint, with presentation at any time during the process of maturation of the hip joint in which the bone of the joint components, acetabulum and proximal femur and soft tissue, capsule articular muscles and ligaments are altered. The term is used for grouping broad spectrum of diseases that have in common biomechanical deficiencies for hip joint leading to a progressive deterioration of the same. It has been demonstrated mathematically that in the presence of short or deficient acetabulum, be determined by an index or a high acetabular coverage of the femoral head deficient (Wiberg edge center), there is an abnormal distribution of loads within the hip joint that take even stress peak lateral rim of the acetabulum, and their subsequent and labral chondral degeneration and finally eventually to osteoarthritis [3].

It is now recognized the vital role that has the early diagnosis of the disease and secondary intervention in the first six months of life, where the results with orthosis hip abduction, the most common in our setting, "Milgram splint" . However, this therapeutic intervention takes place in a period of development of the child important where neuronal maturation of both the brain and spinal progressively going allowing development of walking patterns [1].

Figure 1. Capture patient with orthosis hip abduction

Available studies regarding the use of abduction splint are clear that the effect of these therapeutic measures in the context of child walker and the effects on the acetabulum still not well understood. Prospective studies approach in order to evaluate the effect of combined abduction orthosis with ambulation, have shown an increase in the proportion of reluxaciones methodological design however has been poor and lacking of suitable groups for comparison. Secondary clinical observations counter some doctors consider the use of the splint during the walking, some report no data that contraindicate its use and others suggest a beneficial effect.

The aim of this study is to assess the changes occurring in the gait pattern in patients with splint Milgram walkers using laboratory movement. The determination of these, allow computationally using inverse dynamics model, the behavior of loads and forces acting on the hip when the child begins to walk with this splint.

2 MAIN BODY

The population for the study included fifteen patients between 13 to 20 months of age with a diagnosis of Developmental Dysplasia of the Hip, prior informed consent of their parents, were evaluated by video recording techniques (gait lab) analysis was performed on sagittal plane kinematics, coronal and front of the joints of the hip, knee and ankle.

The graphs extracted during operation correspond to functional data. Its behavior is recorded on a time series of coordinates between angle and cycle percentage. These curves do not have a logical order. For modeling periodic data opted for Functional Principal Component Analysis (FPCA). All this modeling is performed in the R language, a free tool for statistical analysis and functional data graphic.

Figure 2. Methodology for inverse dynamic model using statistical modeling tool R and Opensim

To evaluate the changes that occur in the gait pattern in patients with splint Milgram walkers in the motion analysis laboratory, was found significant changes in the behavior of flexion-extension and abd-adduction of the hip and knee joint mainly. The determination of these allow computationally modeling in OpenSim ® platform using inverse dynamics model to evaluate the behavior of loads and forces acting on the hip when the child begins to walk with this splint.

The determination of these allow computationally modeling in OpenSim ® platform using inverse dynamics model to evaluate the behavior of loads and forces acting on the hip when the child begins to walk with this splint.

But local forces will determine the appearance of the secondary ossification centers are there published information currently not clear the consequences of using abduction brace or stand or during single-leg stance, and impact that occurs at the hip joint relative to the cartilage and bone maturation secondary to altered kinetics and kinematics during walking with abduction brace (orthosis Milgram).

3 CONCLUSIONS

During the analysis of the results, the more relevant question is the relation of patient vs splint, finding differences between older and younger children, was evident in the observations than in older children (18-20 months) in which the splint allows greater freedom in relation to the smallest no decrease abduction and hip flexion during stance. It was also observed decrease in external rotation during the displacement movement and decrease pelvic extension.

The findings described given the joint position during movement evidenced the emergence of a vector of ground reaction that face forward on his knees and hips, moving the center of gravity, which is offset by the hyperextension of the back, causing biomechanical changes in all extremity joints and the column level. Additionally, it is clear that the use of abduction orthosis (splint Milgram) while walking, causes changes in all phases of gait pattern in relation to own up to the age and relative to normal gait pattern.

The present study demonstrates the modification of the kinematic variables assessed and the consequent alteration of the biomechanics of the normal age for causing a disturbance of local forces in the hip and knee, unable to get to know the impact mechanobiological they can have to short or long term.

REFERENCES

[1] Mubarak et al. Pitfalls in the use of the Pavlik harness for treatment of congenital dysplasia, subluxation, and dislocation of the hip. J Bone Joint Surg Am. 1981

[2] Maquet. Biomechanics of Hip Dysplasia 1999

[3] Hu Z, Xu Y, Liang J, Effect of abducens orthosis combined with walker on developmental dysplasia of the hip 2009 Journal Cent South University Jul;34(7):667-71

Standard Session II

3rd International Conference on Computational and Mathematical Biomedical Engineering – CMBE2013

16-18 December 2013, Hong-Kong

P. Nithiarasu and R. Löhner (Eds.)

Computational fluid dynamics analysis of thoracic aortic dissection

D. Dillon-Murphy[1], A. Noorani[1], D. A. Nordsletten[1], R. E. Clough[1, 3], P. R. Taylor[2, 3], C. A. Figueroa [1*]

Departments of [1]Biomedical Engineering and [2] Cardiovascular Imaging,
King's College London, London SE1 7EH, UK

[3] Vascular Surgery, Guy's and St Thomas' NHS Foundation Trust, London SE1 7EH

*Corresponding Author:
C. Alberto Figueroa
3rd Floor Lambeth Wing, St Thomas' Hospital
King's College London, London SE1 7EH, UK

Telephone: +44 20 7188 7188 ext. 53224
Fax: +44 188 5442
e-mail: alberto.figueroa@kcl.ac.uk

Submitted for inclusion in Mini Symposium 13

SUMMARY

The objective of this research is, using multiple imaging and segmentation techniques, to develop a non-invasive, image-based modelling protocol to characterise pressure and flow in true and false lumens of aortic dissection patients.

Key Words: *Aortic dissection, patient specific modelling, computational fluid dynamics*

1. INTRODUCTION

Aortic dissection is characterised by the delamination of the aortic intima and the creation of a true and false lumen. The disease is associated with a high incidence of mortality. The typical treatment strategy aims to occlude the entry tear to the false lumen, stagnating blood flow and invoking thrombus formation. Morphology can vary significantly between patients. It has been observed that patients with similar morphology exhibit different outcomes: some present a stable patent false lumen for many months or even years, others exhibit stable full thrombus formation, and lastly a third group exhibits partial thrombus which has been associated with high morbidity relative to no thrombus formation (Tsai et al. 2007). The haemodynamic conditions which lead to these outcomes still remain a subject of debate.

Computational modelling techniques allow simulation of haemodynamics indices, such as pressure, velocity and wall shear stress in a non-invasive manner. In this work we combine advanced imaging techniques (CT, 2D PC-MRI and 4D PC-MRI Flow) and

modelling techniques to characterise hemodynamics in a subject specific model of aortic dissection.

2. METHODS

Image Acquisition and model building: A non-gated contrast enhanced CT scan with voxel size of 0.55×0.55×2.5mm was acquired in a 59 year old male patient exhibiting an acute DeBakey Type IIIa, Stanford type B aortic dissection. The first goal of this work was to create a patient specific CAD segmentation that faithfully captured the complex anatomy of the aortic dissection. Several segmentation methods were examined. Direct 3D methods, while allowing a relatively fast segmentation, were found to be insufficient to accurately capture the dissection flap. A 2D segmentation approach was eventually used to create a patient specific 3D CAD representation of the dissection (Wilson et al. 2005). While more labour intensive than direct 3D automatic segmentation techniques, this method allowed a greater degree of user control in the segmentation process and ultimately a more accurate representation of the thin dissection flap.

Three different CAD models were produced. The first model, labelled as "maximal tears", includes nineteen communicating tears. The quality of the image data however makes it such that several of these tears may actually correspond to image artefacts. To investigate this uncertainty, a second model, labelled as "minimal tears", was produced by only including the clearly identifiable entry and exit tears. The third and final model represents a healthy aorta, generated by virtually removing the flap from the diseased model.

Mesh Generation: Finite element meshes were created for each CAD model using boundary layers and local refinement. Hessian-driven mesh adaptation techniques were used to produce the final computational meshes for each of the three models. The meshes comprised 9-13.5 million elements and 1.7-2.4 million nodes and exhibited a high degree of local refinement in areas of highly complex flow such as those observed in the region of the connecting tears or around branching vessels and bifurcations.

Analysis: Analyses were run using a time step size of 125 μs to 250 μs on 256 cores of a 640 core SGI Altix-UV HPC with Nehalem-EX architecture. Residual control was set to 1×10^{-3}. Each cardiac cycle took approximately 12 hours to run. Between 4 to 7 cardiac cycles were run until periodicity in the model was achieved. In each analysis, the outflows of the model were coupled to a three-element Windkessel model to represent the impact of the distal vasculature.

3. RESULTS

Figure 1 shows the computed velocity streamlines at peak systole for the "maximal tears" and "minimal tears" case and compares them to the 4D PC-MRI velocity data. This data provides an averaged representation of the complex velocity field acquired via the method described in (Clough et al. 2012). Note that the simulation and 4D PC-MRI data are plotted in the same velocity scale. The figure demonstrates a good qualitative comparison between simulation and image data. Furthermore, it is observed that the "maximal tears" model exhibits more complex velocity patterns in the true and false lumen, particularly in the vicinity of the communicating tears, than the "minimal tears" case.

Figure 2 shows a comparison between computed and 2D PC-MRI flows in the true and false lumens at two locations in the descending aorta for the "maximal tears" and "minimal tears" cases. This comparison shows that while flow in the "minimal tears" case matches better the 2D PC-MRI data in the proximal section of the aorta, the results of the "maximal tears" case produce a superior comparison in the distal sections. This suggests that at least some of the communicating tears in the descending aorta do have a significant influence on the haemodynamics. Therefore, one could argue that a hybrid model excluding some of the proximal tears of the "maximal tears" model may produce a better representation of the measured haemodynamics.

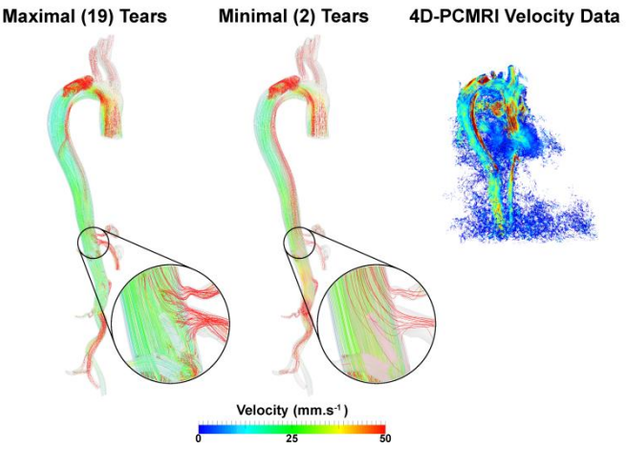

Figure 1: Peak systolic velocity streamlines and corresponding 4D PC-MRI data

One last study was performed to understand the impact of the dissection flap on the workload of the heart (Figure *3*). Here, a heart lumped parameter model (Lau and Figueroa 2013) was tuned to produce equivalent peak and mean flows to those measured with 2D PC-MRI. PV loops were obtained and a 26% increase in workload of the heart was calculated for the dissection model relative to the healthy model.

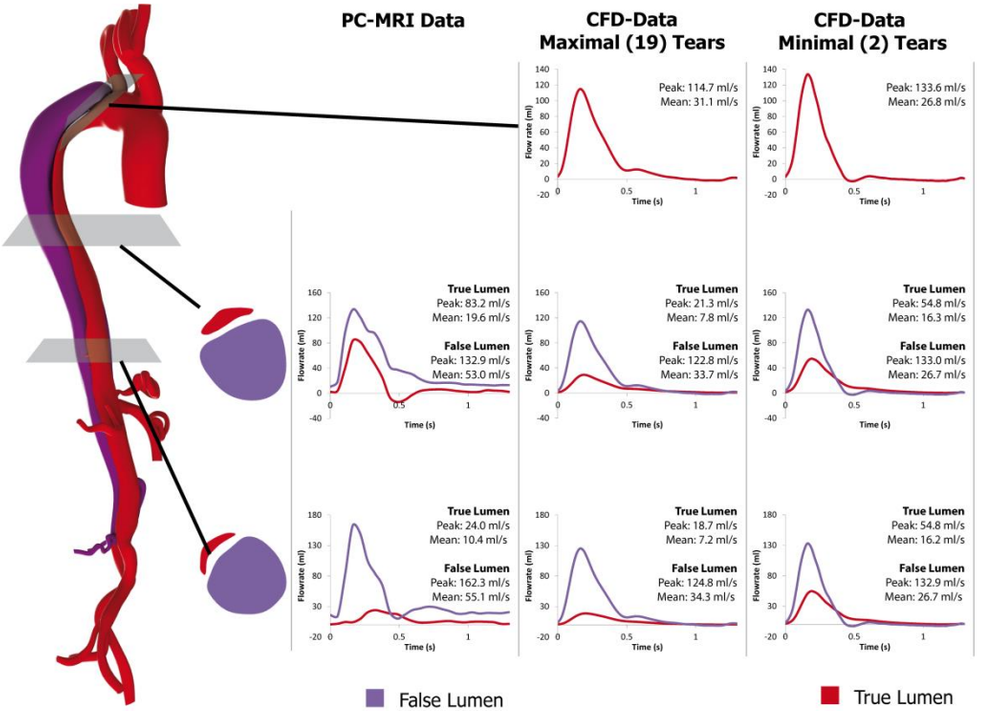

Figure 2: Comparison of flow data acquired from 2D-PCMRI and CFD analysis for the maximal and minimal tears models

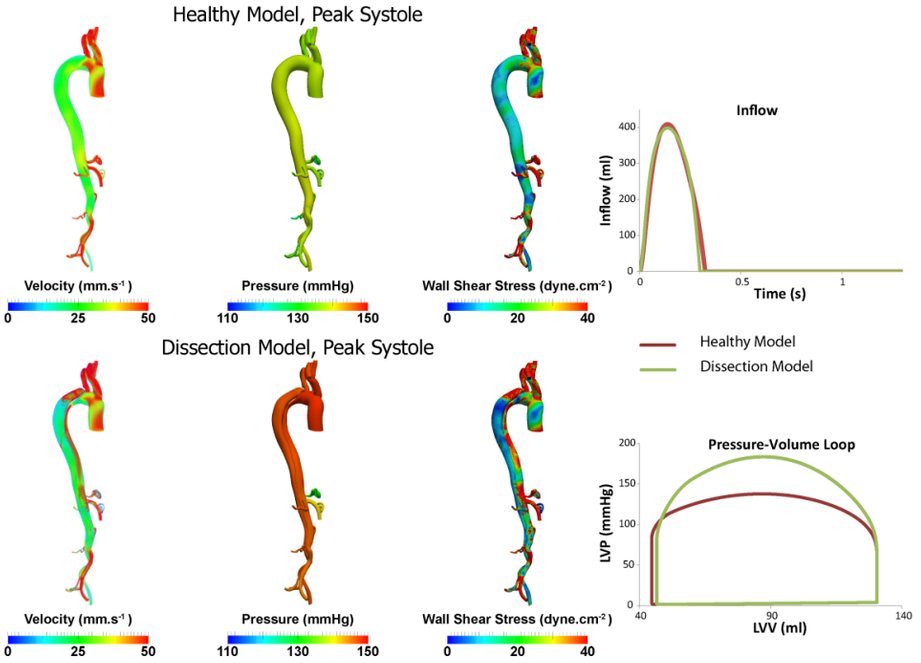

Figure 3: Velocity Streamline at Peak Systole and corresponding 4D PC-MRI data

5. CONCLUSIONS

The results of this study provide a detailed description of the haemodynamics in a human dissected aorta. Computational methods may offer insight into the detrimental effects introduced by the dissection flap on heart workload, tissue perfusion, false lumen pressure and thrombus formation, etc. An improved understanding of these haemodynamics will ultimately provide a non-invasive method for patient risk stratification.

REFERENCES

[1] Clough et al., A new imaging method for assessment of aortic dissection using four-dimensional phase contrast magnetic resonance imaging, *J Vasc Surg*., 55(4), 914-23, 2012.

[2] Lau and Figueroa., A three-dimensional formulation for short-term pressure regulation in the systemic circulation, *In Submission*.

[3] Tsai et al., Partial thrombosis of the false lumen in patients with acute type B aortic dissection, *N Engl J Med*., 357(4), 349-59, 2007.

[4] Wilson et al., Predicting changes in blood flow in patient-specific operative plans for treating aortoiliac occlusive disease, *Comput Aided Surg*., 10(4), 257-77, 2005.

We gratefully acknowledge support from the European Research Council under the European Union's Seventh Framework Programme (FP/2007-2013) / ERC Grant Agreement n. 307532, and the United Kingdom Department of Health via the National Institute for Health Research (NIHR) comprehensive Biomedical Research Centre award to Guy's & St Thomas' NHS Foundation Trust in partnership with King's College London and King's College Hospital NHS Foundation Trust.

3rd International Conference on Computational and Mathematical Biomedical Engineering - CMBE2013
16-18 December 2013, Hong-Kong
P. Nithiarasu and R. Löhner (Eds.)

Fluid flow patterns within porous scaffolds: influence of porosity and permeability

Ginu U. Unnikrishnan*, Vinu U. Unnikrishnan and J. N. Reddy***
*Department of Mechanical Engineering, Texas A&M University, College Station, TX - 77843
**Department of Aerospace Engineering and Mechanics, The University of Alabama, Tuscaloosa, AL - 35487

SUMMARY

Bioreactors provide an important link in the development of viable substitutes for tissues through tissue engineering. Optimal performance of the bioreactors can be achieved by varying the material properties of scaffolds. In this work, a 3D computational model is implemented to study the influence of the scaffold material properties, like porosity and permeability, on the fluid flow behavior within the bioreactor. The computational model can accurately determine the mechanical environment within the bioreactor and thereby provide a unique understanding of the mechanics of tissue formation.

Key Words: *theory of mixtures, finite element method, tissue engineering, bioreactors*

1 INTRODUCTION

Tissue engineering aims to repair and restore living tissues using biomaterials, cells and engineering principles, individually or in combination. Tissue engineering has emerged as an alternative promising strategy for the development of viable substitutes for tissues. Bioreactors play a very important role in tissue engineering as they provide the necessary physiological and mechanical environment for the development of scaffolds [1]. Among other physiological and mechanical factors, fluid flow patterns within the bioreactors have been observed to play a major role in the development of tissue substitutes [2]. The flow is affected, in addition to the inlet velocity conditions, by the material properties like porosity and permeability of the scaffolds, which are often varied to arrive at the optimal designs of bioreactors. In this work, computational model previously developed by the authors [3] is extended to capture the 3D flow behavior in a bioreactor made of porous scaffold.

2 FINITE ELEMENT MODEL

2.1 Governing Equations

Considering a spatial position x at time *t* occupied simultaneously by particles of each constituents (solid and fluid phases), a reference configuration $\mathbf{X}_\alpha$ is assigned to each constituent. The motion is prescribed in a rectangular Cartesian system as [4]

$$\mathbf{x} = \boldsymbol{\chi}_\alpha \left(\mathbf{X}_\alpha, t \right) \tag{1}$$

Assuming the domain is composed of components that are chemically inert, the governing equations are derived in the following manner a domain having a boundary with the total volume V with fluid volume and solid volume fraction. The fluid is assumed to be viscous and incompressible, while the solid is assumed to be linearly elastic. With the volume fractions for the fluid and solid phases represented as ϕ^f and ϕ^s, respectively, which are defined as $\phi^\alpha = \frac{V^\alpha}{V}$, where $\alpha = s, f$ such that $\phi^s + \phi^f = 1$, the velocity for the fluid and solid phases represented as v^f and v^s, the continuity equation for the fluid is given as

$$\nabla . \left(\varphi^s \mathrm{v}^s + \varphi^f \mathrm{v}^f \right) = 0 \tag{2}$$

Neglecting the inertia and body forces, conservation of linear momentum of the solid and fluid phases yields:

$$\begin{aligned} \nabla . \boldsymbol{\sigma}^s - p \nabla \varphi^f + K \, \mathrm{I} . \left(\boldsymbol{v}^f - \boldsymbol{v}^s \right) = 0 \\ \nabla . \boldsymbol{\sigma}^f + p \nabla \varphi^f - K \, \mathrm{I} . \left(\boldsymbol{v}^f - \boldsymbol{v}^s \right) = 0 \end{aligned} \tag{3}$$

where p is the apparent pressure, $\boldsymbol{\sigma}^\alpha$ is the Cauchy stress tensor, $\boldsymbol{v}^\alpha$ is the velocity field vector for $\alpha = s, f$ phases and K is the diffusive drag coefficient. Constitutive relations for solid and fluid phase are introduced at this stage to capture the individual properties of the mixtures.

The bioreactor can be divided into fluid only domain and of porous scaffold domains. Using the theory of mixtures approach, the fluid flow in the fluid-only domain and the porous scaffold can be assumed to be governed by similar equations with change in numeric value of the interaction term. The finite element model is therefore developed for the entire fluid and porous domains and the interface is allowed to lie across the inter-element boundary [3, 5]. The advantage of this method is that the interface between the fluid and porous domains need not be specified explicitly and no additional boundary condition needs to be prescribed for the problem.

2.2 Numerical Solution

A simplified model of the scaffold (Figure 1) with interconnected fluid chambers was considered to study the influence of material properties of the scaffold on the fluid flow patterns within the bioreactor and to evaluate the 3D computational model. The scaffold was taken to be 2.0 mm in length and 1.0 mm in width and 1.0 mm in height. The fluid chambers within the scaffold were arranged in parallel and perpendicular to the direction of fluid flow. The entire domain was meshed using linear, hexahedral elements [6]. The elements in the scaffold and the fluid domain were identified and assigned corresponding material properties. Fluid velocity was prescribed at the right side of the domain and on the left side - free flow boundary conditions were prescribed. The bottom of the scaffold was assumed to be rigidly fixed to an impermeable substrate. No boundary condition was prescribed at the fluid-scaffold interface. In the first case, the entire solid phase was assumed to be a rigid, impervious material. The solid and fluid velocity at each node within the scaffold was constrained in all directions. In the second case, the scaffold was assumed to be rigid, but porous in nature (solid volume fraction of 0.2). Under this condition, the solid velocity was set to zero.

The fluid flow distribution within the scaffolds was shown to be significantly affected by the nature of the material properties of the scaffold. As expected, the magnitude and distribution of fluid velocity through the scaffold was different for a rigid, impervious medium when compared to that of a rigid, porous scaffold (Figure 2), which shows the influence of porosity of the scaffold on the mechanical environment within the biroeactor. The void volume fraction (Figure 3) and also the permeability (Figure 4) was observed to influence the fluid velocity within the scaffold.

3 CONCLUSIONS

In this study, the fluid flow within a porous scaffold was analyzed. The study showed that the material properties of the scaffold influences the flow patterns. The results highlight the limitations of assuming a rigid and impervious scaffold. The model developed in this study will be able to assess the mechanical forces and fluid flow behavior within the porous and fluid regions of the bioreactor simultaneously and can also analyze its influence on the development of scaffolds. The computational tools developed in this work would also help in fine-tuning the current investigation procedures in tissue engineering, bone healing, and stem cell research.

REFERENCES

[1] I. Martin, D. Wendt, M. Heberer, The role of bioreactors in tissue engineering, Trends in Biotechnology 22 (2004) 80–86.

[2] K. A. Williams, W. Saini, T. M. Wick, Computational fluid dynamics modeling of steady-state momentum and mass transport in a bioreactor for culture tissue engineering, Biotecnol Prog 18 (2002) 951–963.

[3] G. U. Unnikrishnan, V. U. Unnikrishnan, J. N. Reddy, Finite element model for nutrient distribution analysis of a hollow fiber membrane bioreactor, International Journal for Numerical Methods in Biomedical Engineering 28 (2) (2012) 229–238.

[4] J. N. Reddy, An Introduction to Continuum Mechanics, 2nd Edition, Cambridge University Press, New York, 2013.

[5] G. U. Unnikrishnan, V. U. Unnikrishnan, J. N. Reddy, Tissue-fluid interface analysis using biphasic finite element method, Computer Methods in Biomechanics and Biomedical Engineering 12 (2) (2009) 165–172.

[6] J. N. Reddy, An Introduction to the Finite Element Method, 3rd Edition, Engineering Series, McGraw-Hill, New York, 2006.

FIGURES

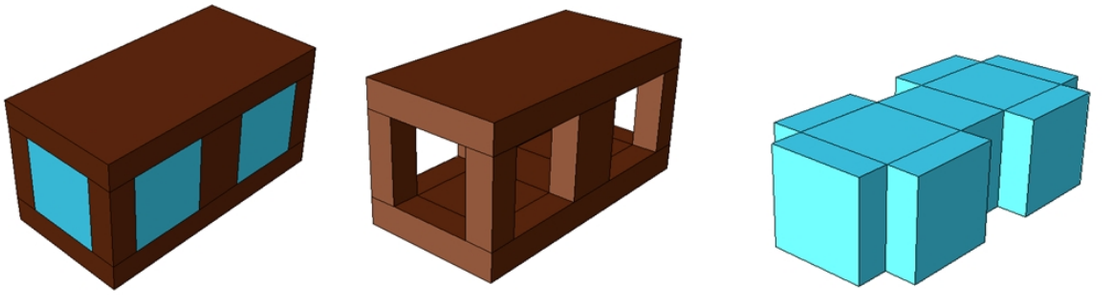

Figure 1: Geometry considered for the finite element analysis of the scaffold-fluid models. The domain consists of rectangular channels of fluid chamber connecting the scaffold regions.

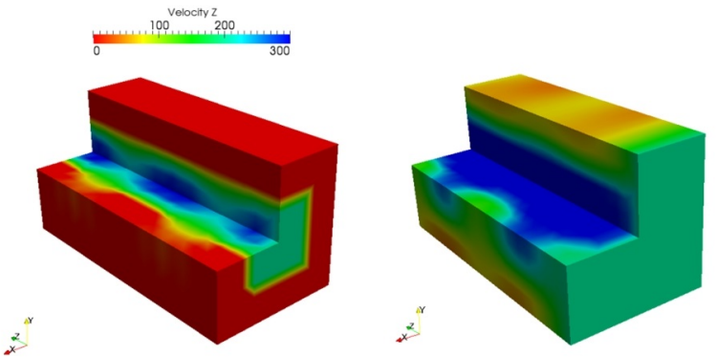

Figure 2: Distribution of fluid velocity (μm/s) along the axial direction for (a) rigid, impervious scaffold, and (b) rigid, porous scaffold.

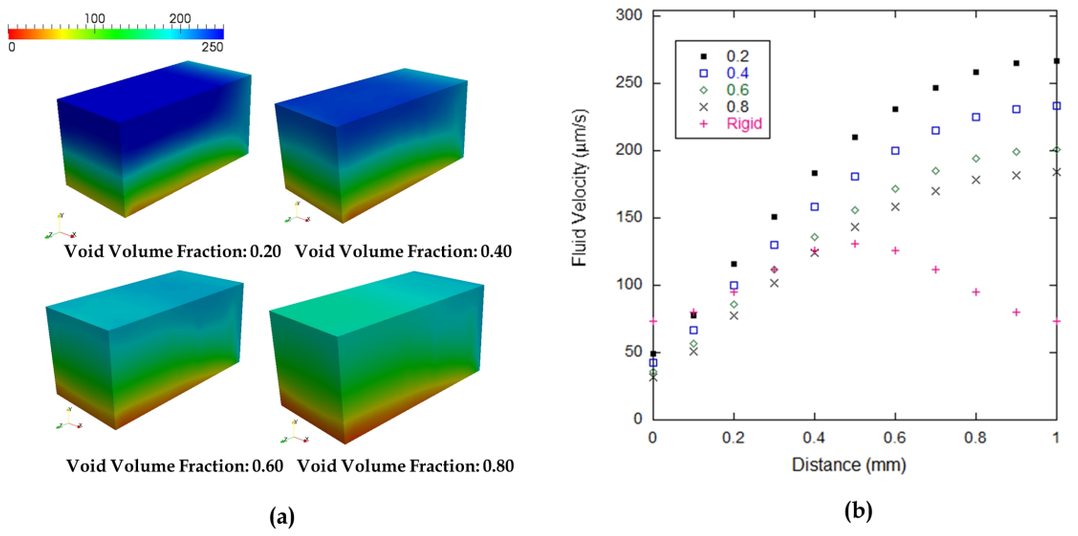

Figure 3: Axial velocity of fluid (μm/s) in the porous and fluid domains for the prescribed inlet velocity with changes in the void fraction of scaffold.

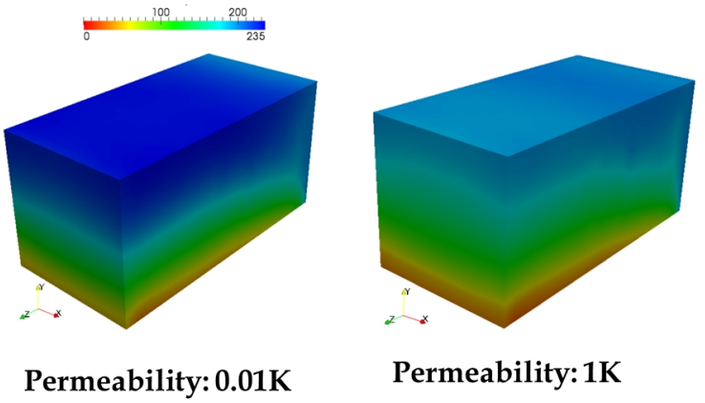

Figure 4: Velocity of fluid (μm/s) in the porous and fluid domains with the prescribed inlet velocity for changes in the permeability of scaffold.

3rd International Conference on Computational and Mathematical Biomedical Engineering - CMBE2013
16-18 December 2013, Hong-Kong
P. Nithiarasu and R. Löhner (Eds.)

Blood flow simulations in the cerebral venous network

Olivia MIRAUCOURT⋆, Stéphanie SALMON⋆, Marcela SZOPOS⋆⋆ and Marc THIRIET†
⋆Laboratoire de Mathématiques EA 4535, FR CNRS ARC 3399, Université de Reims Champagne-Ardenne, Campus Moulin de la Housse - BP 1039, 51687 REIMS cedex 2, FRANCE, olivia.miraucourt, stephanie.salmon@univ-reims.fr
⋆⋆Institut de Recherche Mathématique Avancée, UMR 7501 CNRS/Université de Strasbourg, 7, rue René Descartes, 67084 STRASBOURG Cedex, FRANCE, szopos@unistra.fr
† Laboratoire Jacques-Louis Lions, Université Pierre et Marie Curie, Boîte courrier 187, 4, place Jussieu, 75252 PARIS cedex 05, FRANCE, marc.thiriet@inria.fr

SUMMARY

The present work aims at carrying out a model of blood flow in the cerebral venous network visible by medical imaging. Once the 3D reconstruction from MRA data is obtained, a suitable computational mesh is constructed. The flow of an incompressible Newtonian blood in rigid veins is then computed using adequate values of the flow governing parameters and boundary conditions, demonstrating that the whole chain is achievable.

Key Words: *blood flow, cerebral venous network, computational meshes.*

1 INTRODUCTION

This work is part of the VIVABRAIN project [1], whose final purpose is to compute virtual cerebral angiography images. We aim at reconstructing the total arterial and/or venous cerebral network from medical images, transforming the vascular model obtained in a computational mesh and computing the blood flow in the entire network. The final step asks for simulating the physical mechanisms of acquisition of the images to compute virtual angiographies (see also [1] for a similar approach). We focus in the present article on the simulation of cerebral venous blood flow.

The cerebral vasculature is a complex network, whose role is to maintain a stable perfusion of blood in the brain. The arterial cerebral vasculature is characterized by a relatively stable anatomic pattern (see [2], [3]) and several works have been devoted in the current literature to the modeling and simulation of blood flow in arteries (see, for instance [4] and the references therein). However, there is still a lack of work in blood flow simulation in veins, as their bio-mechanical behavior is still not fully understood. Several difficulties are to be considered: the asymmetric and considerably more various pattern of the venous network compared to the arterial one [3], the highly individual variations of the venous outflow [2].

The anatomical description of the venous system of the brain mainly represents the central venous system and the extracranial draining pathways (see Fig. 1). The central venous system is constituted of dural sinuses and of cerebral veins. The venous outflow from the superior sagittal sinus and deep cerebral veins is then directed via the confluence of sinuses toward the lateral sinuses and the jugular veins (see [3] and the references therein).

[1] http://vivabrain.fr. The research leading to these results has received funding from the French Agence Nationale de la Recherche (Grant Agreement ANR-12-MONU-0010).

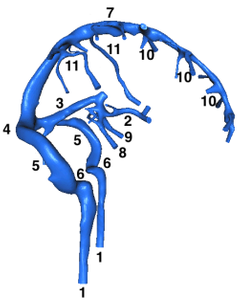

Figure 1: Cerebral venous network.
1, internal jugular veins. 2, vein of Galen. 3, straight sinus. 4, confluence of sinuses. 5, lateral sinus (transverse portion). 6, lateral sinus (sigmoid portion). 7, superior sagittal sinus. 8, internal cerebral vein. 9, basilar vein. 10, superior cerebral veins. 11, superior anastomotic veins.

2 DESCRIPTION OF THE METHODOLOGY

Bio-mechanical modeling In this part, we focus on deriving an appropriate model for flow in large and medium-sized cerebral veins. We start by adopting the following standard assumptions: (i) the blood density is constant; (ii) the flow is assumed to be incompressible and isothermal; (iii) the Newtonian model is used for blood flow. The latter assumption, which consists in neglecting shear thinning and viscoelastic effects, is suitable in large and medium-sized vessels [4], [5], as those considered in the present work. It should be noted that recent available results [6] assessing the sensitivity of hemodynamic simulations of cerebral aneurysms with respect to blood rheology observed differences in solutions of the order of 5% with respect to the rheological model.

Another important issue is the relevance of using either a complex fluid-structure interaction model (which is a particularly challenging task from the numerical point of view) or a fluid model (hence neglected the interaction with the vessel wall). In adults, the cranium is considered as a rigid closed box, and the brain tissue and cerebrospinal fluid contain mainly water, hence constitute an incompressible tissue. Thus, the cerebral venous network (major sinuses and intracerebral veins) is quite constrained in the brain, and we suppose in the present work (at least as a first step) that vessel walls are rigid. Nevertheless, future investigations are needed in this direction, especially when taking into account jugular veins, since recent studies show that the extracranial compartment of the venous drainage system has a higher elasticity than the intracranial one (see [2]).

Let us consider the Navier-Stokes equations for modeling the blood flow dynamics that read as follows :

$$\left\{\begin{array}{rcll} \rho(\partial_t \mathbf{u} + (\mathbf{u}\cdot\nabla)\mathbf{u}) - \mu\Delta\mathbf{u} + \nabla p &=& \mathbf{f} & \text{in } \Omega\times[0,T] \\ \text{div}\,\mathbf{u} &=& 0 & \text{in } \Omega\times[0,T] \\ \mathbf{u}|_{t=0} &=& \mathbf{u_0} & \text{in } \Omega \end{array}\right. \tag{1}$$

where $\mathbf{u} = (u_1, u_2, u_3)$ is the fluid velocity, p its pressure, ρ the density of the fluid, μ its viscosity, $\mathbf{f}$ is an applied body force and $\mathbf{u_0}$ an initial velocity field. System (1) needs to be completed with suitable boundary conditions that will be discussed in the sequel. After having chosen proper characteristic scales and obtained the dimensionless Navier-Stokes equations, using values from [2], we compute governing parameters (Reynold, Stokes and Strouhal numbers) corresponding to blood flow in the jugular veins and the superior sagittal sinus. We then deduce that an appropriate model for computing venous blood flow is either the steady or unsteady Navier-Stokes equations according to the predominant force type taken into account (either convective inertial forces or viscous ones).

We also need to prescribe the initial status of the fluid velocity, $\mathbf{u_0}$. We recall that $\mathbf{u_0}$ can not be arbitrary, since it has to be divergence-free to be admissible. Moreover, in hemodynamic computations usually $\mathbf{u_0}$ is unknown, hence chosen equal to the solution of a steady Stokes problem (see the last section of this article).

Concerning boundary conditions, we prescribe a steady profile (constant velocity of small magnitude) at the inflow, since blood comes from the microcirculation (modeled by a quasi-steady / steady Stokes flow). Then, as we have assumed the walls to be rigid, the no-slip condition is imposed on the wall boundary. Finally, for the outflow boundary conditions should take into account the position (see [7]). To mimic the supine position we have chosen the free traction boundary condition (better than $p = 0$, but takes into account the fact that we are not far from the atrium, where $p \equiv 0$). and or the upright position, we use a 0D resistive model (since it seems that blood flows through small vessels and not through the jugular vein, as in the previous case, [2]).

Computational mesh We describe here how the cerebral network is reconstructed from MRA images acquired by our collaborators (IMIS team, ICube, Strasbourg University). By segmentation techniques and discrete image analysis, a vascular model is obtained (see Fig. 2, left panel) constituted of blocks of voxels representing the vessels [8] (voxels = volume elements). These models allow to obtain a surface mesh which has to be pre-processed in order to obtain the three-dimensional mesh suitable for computation. For example, we need to label the inlets and outlets to be able to impose the necessary boundary conditions for the mathematical model. This step, from vascular models to computational meshes, is realized by an in-house code, called "Cutmesh" developed by one of our collaborators O. Génevaux (Strasbourg University) and some open source softwares as [10] to smooth the surface triangulation. Then, the three-dimensional mesh is achieved by a software tetrahedral generator (see Fig. 2, middle panel, for the entire mesh and Fig. 2, right panel, for a zoom of a part of this image, which shows the mesh in detail).

Figure 2: One example of a vascular model (left), of the 3D corresponding tetrahedral mesh of 237438 elements (middle), magnified view of the mesh (right).

3 NUMERICAL EXPERIMENTS AND OUTLOOK

In this section, we present blood flow computations performed using a code based on the finite element library FreeFem++[2]. We first verify with an analytical solution of the 3D steady Stokes problem proposed in [11] that we obtain the theoretically predicted convergence rates. We test the prescribed solution in the cube $[0, 1]^3$ with mixed boundary conditions on the velocity. More precisely, let $\Omega \subset \mathbb{R}^3$ be the bounded domain and Γ its boundary and $[0, T]$ a finite time interval. Suppose that Γ consists of two measurable parts Γ_D, where Dirichlet boundary conditions are imposed, and Γ_N, where Neumann boundary conditions are prescribed. Let also $\mathbf{n}$ be the unit outward normal vector to Ω on its boundary Γ. As previously derived in the first section, we consider the Navier-Stokes problem (1) with the following mixed boundary conditions:

$$\left\{ \begin{array}{rcll} \mathbf{u} & = & \mathbf{u_b} & \text{on } \Gamma_D \times [0,T], \\ \nu \dfrac{\partial \mathbf{u}}{\partial \mathbf{n}} - p\mathbf{n} & = & \mathbf{g} & \text{on } \Gamma_N \times [0,T]. \end{array} \right. \tag{2}$$

[2]http://www.freefem.org

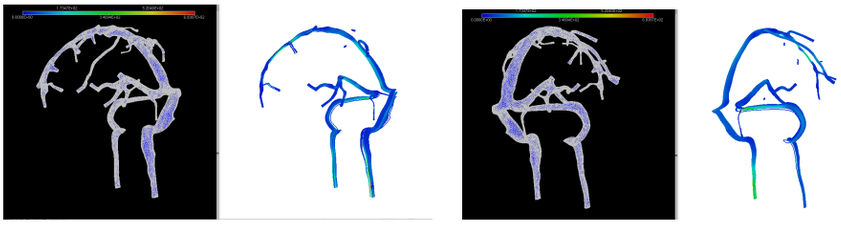

Figure 3: Pressure and streamlines on the venous network mesh.

Using $\mathbb{P}^2 - \mathbb{P}^1$ finite elements for the velocity-pressure discretisation, the L^2 errors slopes (about 3.45 for the velocity and 1.99 for the pressure) correspond to the theory (3 for the velocity and 2 for the pressure). The slope of the velocity H^1 error, about 2.36, is also in accordance with the second-order convergence expected.

We present the results of the first computations on the realistic mesh performed with FreeFem++ installed on CLOVIS (Computing center of the Region Champagne-Ardenne[3]). These preliminary calculations, steady Stokes problem with $\mathbb{P}^2 - \mathbb{P}^1$ finite elements, are important as the first step (the initial guess) for initializing the unsteady problem. We impose a constant flow at the 29 inlets and the last 2 branches are considered outlets (Fig. 3); fluid in the middle artery comes mostly for the right branch, confirming the possible asymmetric pattern of venous blood flow. Moreover, the simulation demonstrates that the whole chain we propose, from images to computation is achievable. Ongoing work includes the study of the effects of posture and gravity, with direct consequences on the choice of boundary conditions, in order to obtain more realistic results.

REFERENCES

[1] M.D. Ford, G.R. Stuhne, H.N. Nikolov, D.F. Habets, S.P. Lownie, D.W. Holdsworth, D.A. Steinman. Virtual angiography for visualization and validation of computational models of aneurysm hemodynamics., *IEEE Trans Med Imaging*, 24(12),1586-1592, 2005.

[2] S. Stoquart-El Sankari, P. Lehmann, A. Villette, M. Czosnyka, M.-E. Meyer, H. Deramond, O. Balédent. A phase-contrast MRI study of physiologic cerebral venous flow. *J Cereb Blood Flow Metab*, 29, 1208-1215, 2009.

[3] B. Schaller. Physiology of cerebral venous blood flow: From experimental data in animals to normal function in humans. *Brain Res Rev*, 46, 243-260, 2004.

[4] L. Formaggia, K. Perktold, A. Quarteroni. Basic mathematical models and motivations. In *Cardiovascular Mathematics. Modeling and Simulation of the Circulatory System*, Formaggia L., Quarteroni A., Veneziani A. (eds), Series: MS&A Vol. **1**, Springer, 2009.

[5] M. Thiriet. Cell and tissue organization in the circulatory and ventilatory systems. *Biomathematical and Biomechanical Modeling of the Circulatory and Ventilatory Systems*, Vol. **1**, Springer, 2011.

[6] A. Gambaruto, J. Janela, A. Moura, A. Sequeira. Sensitivity of haemodynamics in patient specific cerebral aneurysms to vascular geometry and blood rheology. *Mathematical Biosciences and Engineering*, 8, 409-423, 2011.

[7] J. Gisolf, J.J. Van Lieshout, K. Van Heusden, F. Pott, W. J. Stok, J.M. Karemaker. Human cerebral venous outflow pathway depends on posture and central venous pressure, *J Physiol*, 560, 317-327, 2004.

[8] N. Passat, C. Ronse, J. Baruthio, J.-P. Armspach, C. Maillot. Magnetic resonance angiography: From anatomical knowledge modeling to vessel segmentation, *Medical Image Analysis*, 10(2):259-274, 2006.

[10] P. Frey. A fully automatic adaptive isotropic surface remeshing procedure, INRIA RT0252, 2001.

[11] C. Ross Ethier, D. A. Steinman. Exact fully 3D Navier-Stokes solutions for benchmarking, *International Journal for Numerical Methods in Fluids*, 19(5), 369-375,1994.

[3] www.romeo2.fr/

3rd International Conference on Computational and Mathematical Biomedical Engineering – CMBE2013

16-18 December 2013, Hong-Kong

P. Nithiarasu and R. Löhner (eds)

A computational fluid dynamics approach to magnetic drug targeting

M. Kelly[*], A. Lee[*] and G.H. Yeoh[*,]**

[*]School of Mechanical and Manufacturing Engineering, University of New South Wales, Sydney NSW 2052, Australia, g.yeoh@unsw.edu.au

[**]Australian Nuclear Science and Technology Organisation (ANSTO), Locked Bag 2001, Kirrawee DC, NSW 2232, Australia, guan.yeoh@ansto.gov.au

SUMMARY

Magnetic drug targeting is continuing to draw attention as a potential technique for cancer and tumour treatment. This paper focused on the development of computational fluid dynamic models for magnetic drug targeting. Magnetic particle capture was simulated in a 90 degree bend for a range of different particle diameters. The magnetic field is produced by a current carrying wire. It was found that increasing the diameter of magnetic particles increases the capture of particles. Extensions were made on the model to include the effects of non-Newtonian fluid and the pulsating nature of blood flow. These extensions improved the basic model by simulating a more physiologically accurate application of magnetic drug targeting.

Key Words: *computational fluid dynamics, magnetic drug targeting, blood flow*

1. INTRODUCTION

There has been a growing interest in the specific and clinical application of magnetic drug carrier particles as magnetic drug targeting vehicles. Magnetic drug targeting, which is based on the drug being encapsulated in or conjugated on the surface of the magnetic micro-spheres or nano-spheres, aims to resolve the problem by magnetically guiding the drug to the disease site. When administered intravenously, accumulation of the drug occurs in the area to which the magnetic field is applied. They could be then activated by an enzyme, pH, temperature, or magnetic trigger (Alexiou et al., 2000, Derfus et al., 2007, Hu et al., 2007, Kim et al., 2008). Nevertheless, treatment via magnetic drug targeting poses many challenges, partly because of the dynamics of magnetic particles in blood are poorly understood. Also, the efficiency of particle capture is influenced by parameters such as particle size, surface characteristic, field strength, blood flow

rate, and the length of time the particles are exposed to the external magnet. All of these parameters need to be carefully selected in order to aptly optimize the target action.

The main objective in this current study is to present the feasibility of adopting the computational fluid dynamics approach to magnetic drug targeting. Firstly, the model developed is validated by comparing the results produced by Haverkort et al. (2009). Secondly, the model is expanded to investigate more realistic flow conditions for large human arteries: (i) applying a Non-Newtonian viscosity model for the rheology of blood, and (ii) modelling the pulsating flow of blood.

2. NUMERICAL MODEL

For validation purpose, the three-dimensional tube has a circular cross-section of radius R = 3.5 *mm* such as depicted in Figure 1(a). This geometry represents a physiologically high curvature case similar to the coronary artery bend (Haverkort et al., 2009). The fluid is taken to be Newtonian and incompressible with a dynamic viscosity of 3.5×10^{-3} *Pa.s* and density of 1000 kg/m^3. The average velocity at the inlet is taken to be 0.1 m/s. A velocity profile for fully developed flow will be set through the user defined function (UDF) which is incorporated into ANSYS Fluent 14.5. The velocity function is given by $V_x = 2 \times 0.1(1 - r^2/R^2)$ where r is the radial distance from the inlet center. The Reynolds number of the flow is calculated to be approximately 200; a laminar flow is thus analyzed.

Particle motion is modeled via the disperse particle model (DPM). Forces acting on the particles are due to particle drag and external magnetic field (Kelvin force). The non–uniform magnetic field is modeled as an infinitely long straight wire carrying a current I. The wire goes "into the page" (in the z direction). Two wire locations are analyzed. These locations are shown in Figure 1. For both cases, the wire is located 10 *mm* away from the centerline of the tube. The Kelvin force is given by $F_m = \frac{\mu_o x D^3 I^2}{24\pi r^3}\begin{pmatrix} x-a \\ y-b \\ 0 \end{pmatrix}$. Iron has been chosen due to its favorable magnetic properties. The particles are a combination of 67.5% iron and 32.5% carbon, and have a density of 6450 kg/m^3. The particle is modeled with a magnetic susceptibility of x = 3. A magnetic field strength of $B = \mu_o H = 2T$ at the centerline is modeled. This required a current of $I = 10^5$ *A*. A UDF is written and implemented into ANSYS Fluent 14.5 to model the magnetization forces on the particles.

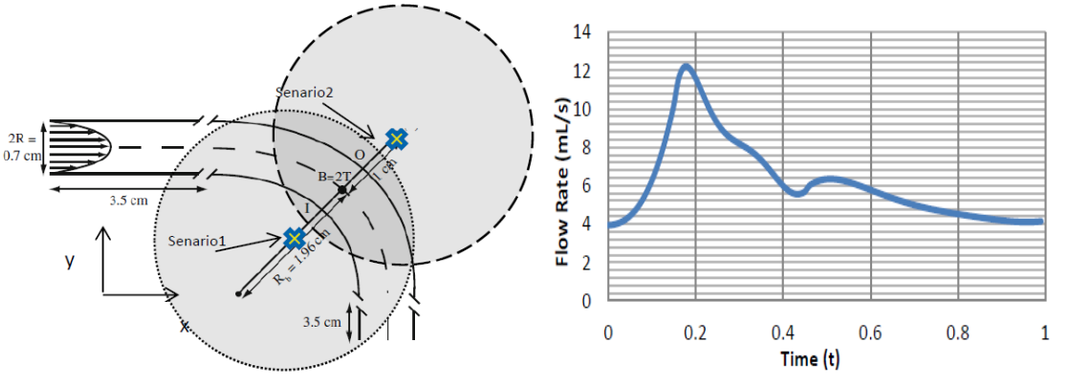

Figure 1 (a) A 90^o bend circular tube for magnetic particle capture with two locations of electromagnetic wires and (b) Pulsating profile of blood flow imposed at the inlet.

In a separate model, the Non-Newtonian viscosity of blood is based on the generalized power law adapted from Ballyk et al. (1994). A piecewise function representing the pulsating nature of the blood flow is shown in Figure 1(b). Both the Non-Newtonian viscosity and pulsating flow models are employed in attempts to more accurately model the real situation.

3. RESULTS AND DISCUSSION

Based on a grid independent mesh of 437,000 elements, particle deposition subject to external magnetic field in blood flow was validated by the measure of particle capture efficiency. Figure 2 compares the results from current model predictions and those of Haverkort et al. (2009). The predicted capture efficiency for Simulation 2 – the wire being on the outside of the bend – was found to agree very well with the numerical results of Haverkort et al. (2009). For Simulation 1, the model predictions followed the same trend as those of Haverkort et al. (2009). The departure of current model predictions was found to exhibit the greatest different for particles less than $0.5\mu m$. One plausible explanation was the way the particles were injected at the inlet, which could lead to the differences in results. Overall, these results served as a strong case for verification of the model proposed by this paper.

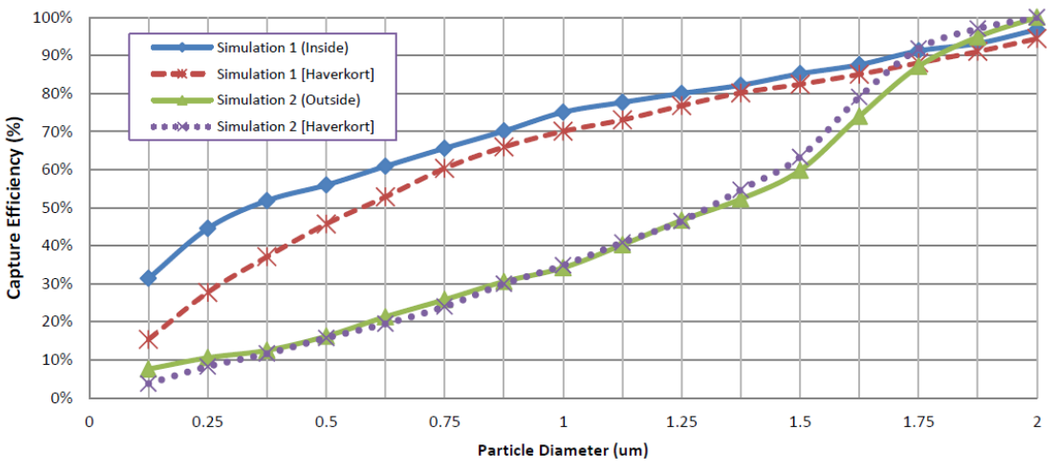

Figure 2 Particle capture efficiency against different particle sizes.

Figure 3 depicts the disposition of particles at different stages in time after injection at inlet. Apparently, majority of trapped particles were captured within the first second. Figure 3(e) shows the particle disposition at three seconds (T = 3 *s*); where most of the particles have either been trapped or passed through the bend. This is in contrast to the case where there was no magnetic field applied (see Figure 3(f)). It can be clearly demonstrated that the applied external magnetic field effectively trapped the particles against the wall of the circular tube.

For the model with a Non-Newtonian viscosity of blood, the fluid has a maximum viscosity of 3.38×10^{-2} *Pa.s* in areas of high flow strain, and a minimum viscosity of 3.52×10^{-3} *Pa.s*. It has been found that a more viscous flow led to a decrease in the capture efficiency due to the increase of the particle drag force. This theory was supported by the CFD results; the particle capture efficiency decreased from to when the wire was located on the inside of the bend.

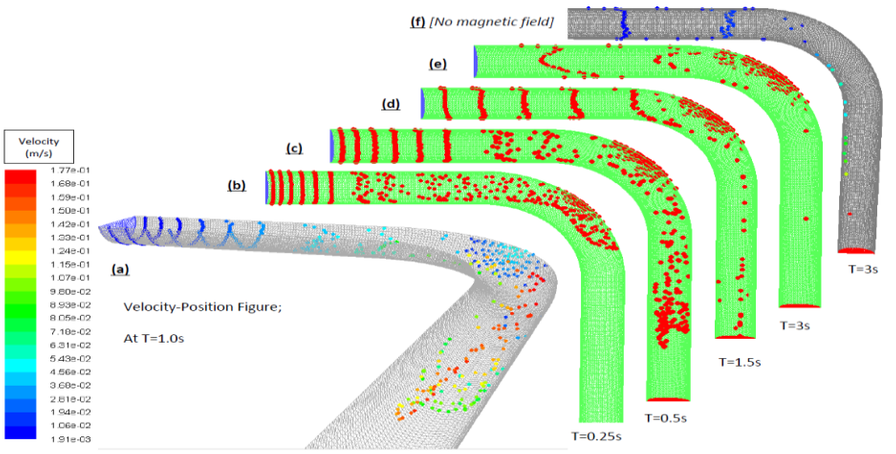

Figure 3 Transient motion of particles in blood flow: (a) T = 1 *s*, (b) T = 0.25 *s*, (c) T = 0.5 *s*, (d) T = 1.5 *s*, (e) T = 3 *s* and (f) T = 3 *s* (without magnetic field).

4. CONCLUSIONS

A computational fluid dynamics model has been developed for magnetic drug targeting. Through performing analysis on a 90^o bend circular tube geometry, the current model has been found to successfully replicate the results of Haverkort et al. (2009). This provided confidence in the development and implementation of the physical models used to capture the interaction between magnetic fields and iron particles. Results show that increasing particle diameter size led to improved capture efficiency. It was also ascertained that location of the magnetic field source and the nature of the fluid flow were important factors influencing the particle capture efficiency. Through including the effects of non-Newtonian blood viscosity it was found that particle capture efficiency decreased when compared to the standard model. Initial steps were also made to analyze the effects of pulsating flow on particle capture efficiency.

REFERENCES

[1] C. Alexiou, W. Arnold, R.J. Klein, F.G. Parak, P. Hulin, C. Bergemann, W. Erhardt, S. Wagenpfeil and A.S. Lubbe. Locoregional cancer treatment with magnetic drug targeting, *Cancer Research*, 60, 6641-6648, 2000.

[2] A.M. Derfus, G. von Maltzahn, T.J. Harris, T. Duza , K.S. Vecchio, E. Ruoslahti and S.N. Bhati..Remotely triggered release from magnetic nanoparticles, *Advanced Materials*, 19, 3932-3936, 2007.

[3] S.H. Hu, T.-Y. Liu, D.-M. Liu and S.-Y. Chen. Controlled pulsatile drus release from a ferrogel by a high-frequency magnetic field, *Macromolecules*, 40, 6786-6788, 2007.

[4] D.H. Kim, D.E. Nikles, D.T. Johnson and C.S. Brazel. Heat generation of aqueously dispersed CoFe2O4 nanoparticles as heating agents for magnetically activated drug delivery and hyperthermia, *Journal of Magnetism and Magnetic Materials*, 320, 2390-2396, 2008.

[5] J.W. Haverkort, S. Kenjeres and C.R. Kleijn. Computational simulations of magnetic particle capture in arterial flows, *Annals of Biomedical Engineering*, 37, 2436–2448, 2009.

3rd International Conference on Mathematical and Computational Biomedical Engineering – CMBE2013
16-18 December 2013, Hong-Kong
P. Nithiarasu and R. Löhner (eds)

Physical modeling of the heart with the atrioventricular plane as a piston unit

Elira Maksuti*, Jonas Johnson*, Anna Bjällmark*, and Michael Broomé*,***,****

*Department of Medical Engineering, School of Technology and Health, KTH Royal Institute of Technology, Stockholm, Sweden. elira.maksuti@sth.kth.se

**Department of Molecular Medicine and Surgery, Karolinska Institute, Stockholm, Sweden

***ECMO Department, Karolinska University Hospital, Stockholm, Sweden

****Department of Physiology and Pharmacology, Karolinska Institutet, Stockholm, Sweden

SUMMARY

Cardiac models do not often take the atrioventricular (AV) interaction into account, even though medical imaging and clinical studies have shown that the heart pumps with minor outer volume changes throughout the cardiac cycle and with back and forth longitudinal movements in the AV region. We present a novel cardiac model based on physical modeling of the heart with the AV-plane as a piston unit. Model simulations generated realistic outputs for pressures and flows as well as AV-piston velocity, emphasizing the relevance of myocardial longitudinal movements in cardiac function.

Key Words: *cardiac function, AV-plane, physical modeling, bond graphs, Dymola.*

1. INTRODUCTION

Cardiac function is commonly explained by a radial squeezing motion, where the heart pumps and regulates blood flow with a considerable change in outer volume. In contrast to this view, it was suggested that the heart can be described as a displacement pump with the atrioventricular (AV)-plane acting like a piston unit [1]. This unit pumps with back and forth longitudinal movements, i.e. in the base-apex direction, generating volume displacements during ventricular contraction (the stroke volume of the heart) and ventricular diastole (filling volume). Subsequently, this theory was supported by cardiac imaging showing an approximately fixed apex, distinct movement of the AV-plane (hereafter referred to as the AV-piston) and minor outer volume changes in healthy individuals [2]. In 0-D cardiac modeling, the most widely used approach is the time-varying elastance function [3], which is based on system identification using experimental measurements and thus gives limited physical insights into cardiac function. Furthermore, complex 3D models of the left ventricle do not take the AV interaction into account [4]. The aim of this study was to develop a novel cardiac model based on physical modeling of the AV-piston displacement in a nearly fixed outer volume, in order to deepen the understanding of cardiac systolic contraction and diastolic filling.

2. MAIN BODY

The proposed model of the left side of the heart (Fig. 1a) is composed of an upper chamber (the atrium), a lower chamber (the ventricle) and a piston unit. One-way valves are located between the atrium and the ventricle (mitral valve) and between the ventricle and the artery model (aortic valve). Since the atrial cross-section in the heart is smaller than the ventricular ($A_1<A_2$, Fig. 1b), the piston unit in the model is constructed with different areas towards the atrium and the ventricle. During the ejection phase, an external input force is applied to push down the piston unit (ventricular systole) causing the opening of the aortic valve as well as the closing of the mitral valve. During the relaxation phase (ventricular diastole), the input force ceases, the aortic valve closes due to reversal of the pressure gradient, the mitral valve opens and the piston unit returns to its initial position. This backwards movement of the piston is mainly caused by a hydraulic return due to similar pressures acting on the two different areas. The model was successively converted to the bond graph formalism (Fig. 2c), which allowed for a unified representation of all physical domains [5]. The cardiac model was connected to a closed-loop vascular model constituted by three resistive elements, two elastic elements and an inertial element. The model was implemented and simulated in Dymola (Dassault Systèmes, France), based on the object-oriented programming language Modelica. For simulation, the input to the model (Se, Fig. 1c) was a trapezoidal function force (amplitude = 6800 mmHg·cm2, total duration = 0.35 s, rising = 0.1 s, falling = 0.01 s, period = 0.95 s) applied only during the contraction phase. This implies that during the relaxation phase, the model behavior was not dependent on any external input. A similar input force was applied during atrial contraction in the opposite direction (amplitude = -1500 mmHg·cm2, total duration = 0.2 s, rising/falling = 0.1 s each), causing the rising of the AV-piston and an additional redistribution of blood from the atrium into the ventricle. See text in Fig. 1 for other model parameters. In order to evaluate how magnitude of piston areas affects ventricular filling, the model was simulated with different values of ventricular area (A_2 = 40, 50 and 60 cm^2), while keeping all other parameters constant.

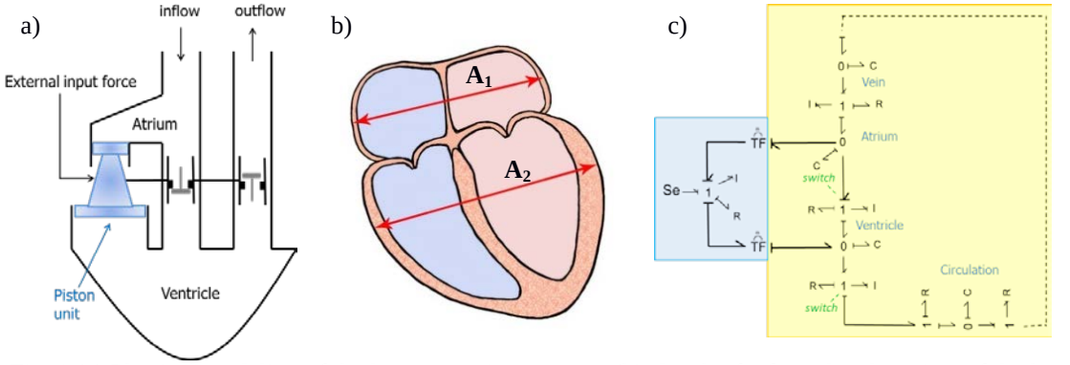

Fig. 1 (a) Physical modeling of the heart as a piston pump; (b) sketch of a four chamber view of the heart where the different diameters in the atria and in the venticles can be seen; (c) equivalent bond graph model: hydraulic domain (yellow) and mechanical domain (blue). Parameters for the hydraulic domain: atrium and ventricle (C=0.3), mitral valve (R=0.008, I=0.0002), aortic valve (R=0.045, I=0.00002), circulation (R=0.08, C=1.01, R=1.28), vein (C=500, I=0.0001, R=0.01). Units: I [mmHg·s^2/ml], R [mmHg·s/ml] and C [ml/mmHg]. Parameters for the mechanical domain: I=30 mmHg·cm·s^2, R=300 mmHg·cm·s, upper TF (A_1=25 cm^2), lower TF (A_2=50 cm^2).

Simulation results are shown in Fig. 2 and 3. Figure 2a shows the comparison between piston velocity obtained from simulation and the velocity profile of a healthy individual measured in proximity to the AV-plane using the ultrasound technique Tissue Velocity Imaging (TVI). As can be seen, the model can reproduce the direction of the main systolic and diastolic movements (peak systolic velocity S', peak early diastolic velocity E' and peak late diastolic velocity A'), with realistic velocity magnitude; whereas it does not reproduce biphasic, rapid movements occurring during the isovolumentric phases. These physiological features are involved in the process of pre and post systolic ventricular reshaping and vary among individuals. Since the present model does not include the cardiac muscle, these phases cannot be reproduced. Despite using a linear model with few constant parameters, simulations of left ventricular and aortic pressures as well as flows through the valves are realistic during ventricular contraction and filling, matching profiles shown in standard physiology textbooks (Fig. 2b-c). Furthermore, utilizing the bond graphs formalism, the abstraction of equivalent electrical circuits was avoided.

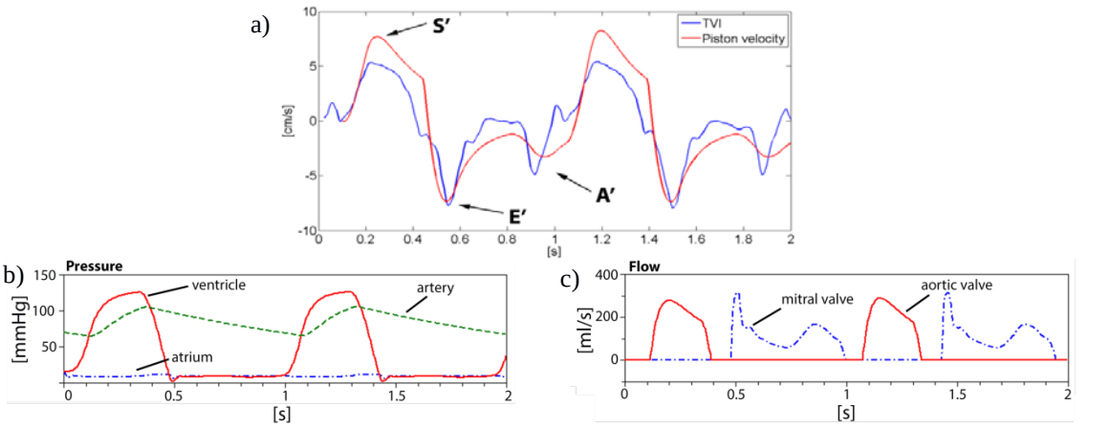

Fig. 2 (a) Simulation of the AV-piston velocity (red) compared to a TVI curve in the proximity of the AV-plane (blue) ; (b) simulation of atrial, ventricular and arterial pressure; (c) simulation of mitral and aortic flow.

Figure 3 shows how the parameter A_2 influences aortic and mitral flow. It can be noted that ventricular filling increases with increased A_2 value, as larger difference in area between ventricular and atrial side will cause a hydraulic return of higher velocity and larger displacement. In humans, the size of A_2 varies with left ventricular compliance and the duration of the diastasis. Since the piston unit is moving, there can be flow through the valve even if the blood itself is not in motion, i.e. it is the valve moving with respect to the blood. This should be kept in mind when comparing the valve flows in Fig. 2c and Fig. 3 with the flows measured in clinical practice by ultrasound Doppler, since the Doppler signal represents the relative movement of the blood with respect to the ultrasound transducer and not to the valve leaflets.

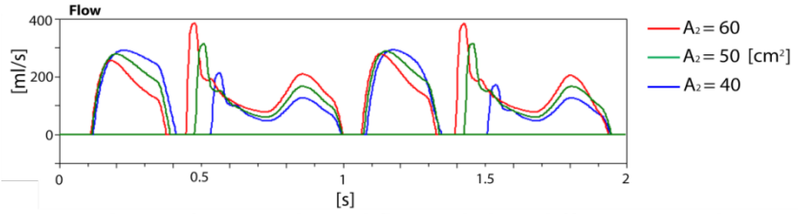

Fig. 3 Simulation of aortic and mitral flow with three different ventricular areas.

Parameters estimation is a complex task in cardiovascular modeling due to interpersonal variability and the fact that direct measurement is often not achievable. This problem was encountered when estimating parameters related to the AV-piston, such as inertia (mass of the AV-piston) and resistance (viscosity). The model in its present form is able to reproduce direction of changes in AV-piston velocity, but not exact magnitude. Better parameter estimation would probably have resulted in less magnitude errors. Further comparison of model output with clinical data could help parameter optimization and is part of future work.

The pumping and regulating function of the heart has been a longstanding debate. Over the last decades there has increased interest in the longitudinal motion of the heart, as this motion has been shown to strongly correlate with left ventricular function [6]. Furthermore, the ability of the heart to pump blood with small outer changes and an internal redistribution of blood between atria and ventricles - as with a longitudinal piston motion - makes the entire process energy efficient since pushing and pulling of surrounding tissues are avoided. The agreement between simulation and normal physiology supports the theory of the heart as a piston pump, where its hydraulic return is an important contribution during diastolic ventricular filling.

4. CONCLUSIONS

This study presents a new approach to cardiac modeling based on the AV interaction. In addition to common model output such as pressure and flow curves, the model can also generate AV-piston velocity profile, providing physical insights that could help understanding the main features of cardiac pumping function. The cardiac model generates realistic output for pressures and flows as well as for AV-piston velocity, supporting the concept of the heart as a displacement pump with a piston unit pumping with back and forth longitudinal movements. Moreover, the ventricular filling pattern is influenced by the difference between ventricular and atrial cross-section.

REFERENCES

[1] S. Lundback, "Cardiac pumping and function of the ventricular septum," *Acta physiologica Scandinavica. Supplementum,* vol. 550, pp. 1-101, 1986.

[2] M. Carlsson, P. Cain, C. Holmqvist, F. Stahlberg, S. Lundback, and H. Arheden, "Total heart volume variation throughout the cardiac cycle in humans," *American journal of physiology. Heart and circulatory physiology,* vol. 287, pp. H243-50, Jul 2004.

[3] Y. Shi, P. Lawford, and R. Hose, "Review of zero-D and 1-D models of blood flow in the cardiovascular system," *Biomedical engineering online,* vol. 10, p. 33, 2011.

[4] P. J. Hunter, A. J. Pullan, and B. H. Smaill, "Modeling total heart function," *Annual review of biomedical engineering,* vol. 5, pp. 147-77, 2003.

[5] V. Le Rolle, A. I. Hernandez, P. Y. Richard, J. Buisson, and G. Carrault, "A bond graph model of the cardiovascular system," *Acta Biotheoretica,* vol. 53, pp. 295-312, Dec 2005.

[6] J. S. Simonson and N. B. Schiller, "Descent of the base of the left ventricle: an echocardiographic index of left ventricular function," *Journal of the American Society of Echocardiography : official publication of the American Society of Echocardiography,* vol. 2, pp. 25-35, Jan-Feb 1989.

3rd International Conference on Computational and Mathematical Biomedical Engineering – CMBE2013

16-18 December 2013, Hong-Kong

P. Nithiarasu and R. Löhner (Eds.)

On Human Gut Microbial Ecosystem: *In Vitro* Experiment and Mathematical Modelling

L. Jiang[*], S. Plummer[**], C.F. Li[*,†] and D.R.J. Owen[*]

[*] College of Engineering, Swansea University, Swansea, SA2 8PP, UK

[**] Obsidian Research Ltd., Baglan Industrial Park, Port Talbot, SA12 7BZ, UK

[†] Corresponding Author, c.f.li@swansea.ac.uk

SUMMARY

The human gut microbiota is considered to be a highly specialized organ providing nourishment, regulating epithelial cell development, modulating innate immune responses and colonization resistances, and it significantly impacts human health and disease. Although this topic has been extensively studied for several decades, the functionality of the microbiota colonization in the human gastrointestinal tract and the mechanisms of the interactions between the host and bacteria are still poorly understood. This research of human gut microbial ecosystem follows a novel and unique approach, which combines the complementary strengths of in vitro experiment and mathematical modelling. The first part of this research conducted a number of carefully planned in vitro experiments to investigate the growth and competition of a specific set of probiotic strains under different culture conditions. Performed on a specially designed anaerobic fermentation platform, these in vitro experiments improved the understanding for the growth behaviour of the specific probiotic strains. The second part of this research focused on the development of mathematical and computational models of human gut microbial ecosystem. The outcome from this part of the research includes a new bacterial growth model, a versatile computational framework to simulate in vitro fermentation experiments, and a comprehensive mathematical model for human gut and gut microbiota.

Key Words: *gut microbiota, microbial competition, fermentation, metabolite, computational modelling*

1 INTRODUCTION

The large bowel consisting of the proximal colon, the transverse colon and the distal colon forms the last part of the human GI tract, as shown in Figure 1. For a long time, the main function of the large bowel was thought to be water and ion absorption. However, it is now clear that the large intestine plays far more important roles than just absorbing water and ions. It contributes significantly to carbohydrate and protein metabolism, provides essential protection against pathogen invasion, and stimulates and modulates the immune system. These critical physiological functions are not so much associated with the anatomical structure of the large intestine, and instead they are accomplished by the microorganisms living in the large bowel. The large intestine of a healthy adult houses hundreds of microbial species (most of them are beneficial to man), and they form a stable and active microbial ecosystem with over 10^{14} microbial cells, which is ten times larger than the total somatic and germ cells of human. The metabolic activity of gut microorganisms has also been found associated with obesity, malnutrition, neurological disorders, inflammatory bowel disease and cancer (large bowel is the third largest cancer killer in the UK) etc. The gut microbiota could be considered as a "new organ" inside the human body.

The human colon is one of the most complex ecosystems on the planet, whose normal microbial community is determined by a number of factors, including host genomics, diet, age, immune function and health status etc. There have been marked progresses in our understanding of the micro ecology of the GI tract in recent years. However, we are still at the very beginning of understanding the functional relationships between the microbiota and the host, in health and disease. Many fundamental questions remain outstanding: what is a healthy intestinal microbiota composition, which microbial groups and activities are involved in health and disease, what are the benefits of specific probiotic and prebiotic, is it possible and if so how to favorably manipulate the gut microbiota to improve human health and prevent and treat disease etc.

The main challenges of researching gut microbial ecosystem arise from two aspects.

• The intrinsic complexity of the system. It is estimated that the gut microbiota of a healthy individual comprises around 400-1000 bacteria species, whose total cell count outnumbers the somatic and germ cells of man by ten times. A great variation also exists between individuals such that the profile of gut microbiota has been recognized as a microbial "fingerprint" of humans. Compared with the great diversity of the gut microbiota, their metabolic and immune functions and interaction mechanisms with the host are even more complex.

• The lack of direct measuring or monitoring approaches. Due to technical and ethical restrictions, it is very difficult to obtain accurate in vivo data of gut microbiota from human, and the limited data are often fragmented and corrupted with errors. Animal trials can help to some extent, but it is well known that the gut microbiota in animals have very different physiological functions and totally different population structures compared with human. In vitro studies have therefore become a very popular approach for studying the gut microbiota. But its complexity is highly limited. It is very difficult, if not impossible, to simulate in vitro even a small portion of the whole gut microbial community because a large number of microbial species in the human colon are not cultivatable with known culture media.

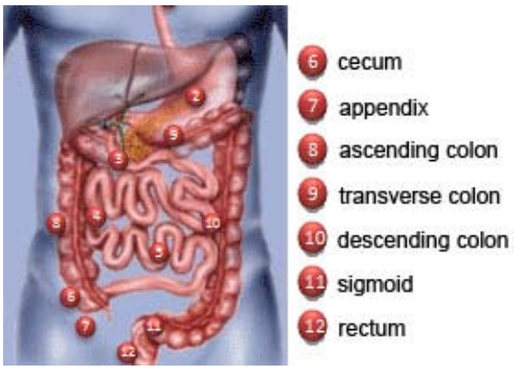

Figure 1 The gastrointestinal tract of human

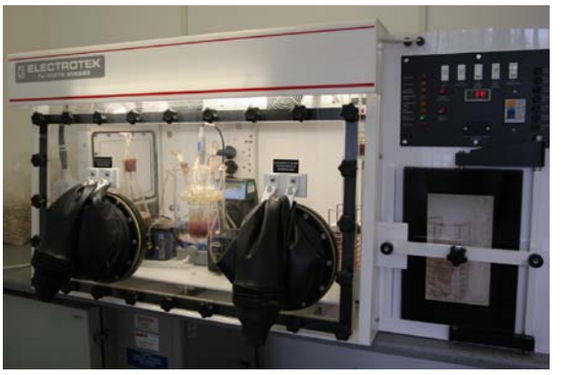

Figure 2 The *in vitro* fermentation model

2 *IN VITRO* EXPERIMENT

As shown in Figure 2, a reliable and flexible anaerobic multistage continuous fermentation platform has been developed, and it can facilitate various in vitro anaerobic fermentation experiments to investigate the human gut microbial ecosystem. Using this new system, a series of general testing has been performed to study the interaction of commercial probiotics and typical microorganisms found in the human GI tract. A snapshot of the experimental results is shown in Figure 3.

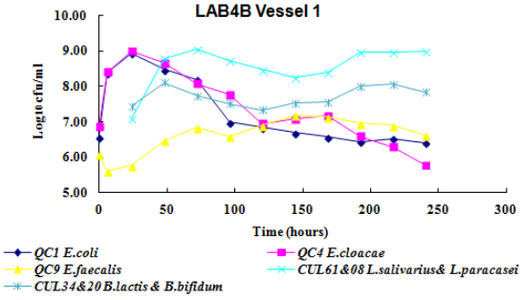

(a) Microbial competition with pH5.5

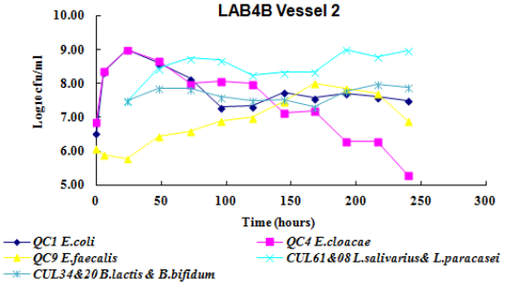

(b) Microbial competition with pH6.5

Figure 3 Two-stage continuous flow fermentation

3 MATHEMATICAL MODELLING

We developed a comprehensive mathematical model for the human gut and the gut microbial ecosystem. The new model correctly recognizes the fluid flow in the gut as Stokes flow, takes into account the deformation of the gut and its dynamic interaction with the gut media flow, and captures the anaerobic fermentation performed by various colonic microorganisms. The model is derived from reliable knowledge of the human gut and gut microbiota, principles in physics (mass and momentum conservations), rigorous mathematical formulations, and appropriate approximations. Eqns. (1-5) summarize the mathematical, and an example of the simulation results is given in Figure 4.

$$\frac{\partial}{\partial t}(a_i r_i A)+\frac{\partial}{\partial x}(a_i r_i A u_i)=F_i^L+G_i^L+H_i \quad i=1,2,\ldots,N, \tag{1}$$

$$\sum_{i=1}^{N} a_i = 1, \tag{2}$$

$$\frac{\partial}{\partial t}\left(a_i r_i A^M\right)=F_i^M+G_i^M-H_i \quad i=N+1,N+2,\ldots,2N, \tag{3}$$

$$\frac{\partial p_i}{\partial x}=\frac{k m_i u_i}{A} \quad i=1,2,\ldots,N, \tag{4}$$

$$p_i = p_0+\frac{\sqrt{\pi}Eh\left(\sqrt{A}-\sqrt{A_0}\right)}{A_0\left(1-\nu^2\right)} \quad i=1,2,\ldots,N. \tag{5}$$

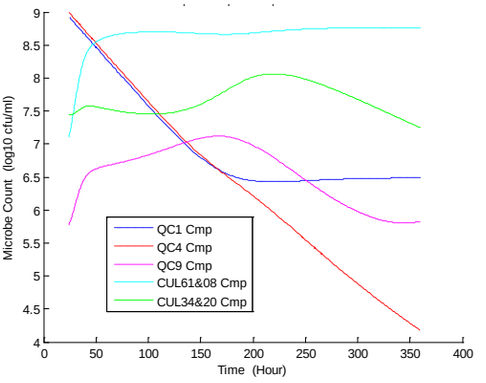

(a) Microbial population

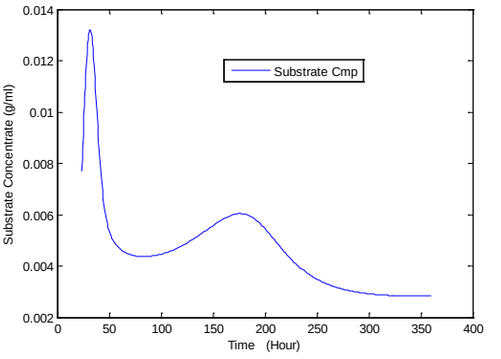

(b) Substrate concentration

Figure 4 Computer simulation of a two-stage fermentation

4 CONCLUSIONS

This research investigated the microbial ecosystem in the human gut. A novel and unique research strategy has been adopted, which combines the strengths of in vitro experiments and mathematical modelling. To the best of our knowledge, this is the first mathematical model that represents the anatomy, physiology and metabolism of the human gut and gut microbial ecosystem as one uniform system.

REFERENCES

[1] L. Jiang, On Human Gut Microbial Ecosystem: *In Vitro* Experiment, *In Vivo* Study and Mathematical Modelling, PhD Thesis, Swansea University, 2013.

Standard Session III

3rd International Conference on Computational and Mathematical Biomedical Engineering - CMBE2013
16-18 December 2013, Hong-Kong
P. Nithiarasu and R. Löhner (Eds.)

Detection and localisation of prostate abnormalities

Andrik Rampun⋆, Zhili Chen⋆, Paul Malcolm⋆⋆ and Reyer Zwiggelaar⋆
⋆Department of Computer Science, Aberystwyth University, Aberystwyth SY23 3DB, UK,
yar,zzc09,rrz@aber.ac.uk
⋆⋆Department of Radiology, Norfolk Norwich University Hospital, Norwich NR4 7UY, UK,
paul.malcolm@nnuh.nhs.uk

SUMMARY

We propose a new methodology for prostate cancer detection and localisation within the peripheral zone based on combining multiple segmentations. We extract four features using Gabor and median filters. Subsequently, we use each feature separately to generate binary segmentations taking the feature space and intensity values into account. We perform erosion on each of the segmentations to remove false positive regions. Finally, we take the intersection of all four binary segmentations, taking a model of the peripheral zone into account. The initial evaluation of this method is based on 66 MRI images from 19 patients and 84.85% of the cases were classified correctly.

Key Words: *Prostate Segmentation, Prostate Cancer Detection, Prostate Cancer Localisation.*

1 INTRODUCTION

Prostate cancer affects millions of men every year [1]. Although several clinical diagnostic tests such as prostate-specific-antiagen (PSA) level, digital rectal examanation (DRE), transrectal ultrasound (TRUS) and biopsy test are widely used, prostate cancer too often goes undetected due to flaws in diagnostic procedures [1]. Prostate magnetic resonance (MR) can provide a non-invasive imaging and in combination with computer technology can provide a detection tool which has the potential to improve the accuracy of clinical diagnostic tests [2]. We introduce a method for prostate abnormality detection and localisation based on the intersection of multiple segmentations of the prostate within the peripheral zone. The proposed method uses a small number of features to discriminate malignant and benign regions within the prostate.

2 METHODOLOGY

The overview of the proposed methodology is illustrated in Figure 1. Firstly, we extract two features using Gabor and median filters. For the Gabor feature (G_1), we use the following parameters: $\sigma_x = 2$, $\sigma_y = 4$, $\omega = 6$ and $\theta = 45°$. The parameters' selection is based on [6,7,8]. According to [6,7] there is little difference in the selection of θ, while Jain and Farrokhnia [8] used $45°$ for an optimal texture segmentation. On the other hand, Weldon et al. [7] indicated that the value σ_y is twice the value of σ_x and small ω values (such as $1\sqrt{2}$ and $2\sqrt{2}$) are not recommended because they capture spatial variations that are too large to correspond to texture [8]. We performed median filtering on the original image to obtain the median feature (M_1), for which we used a

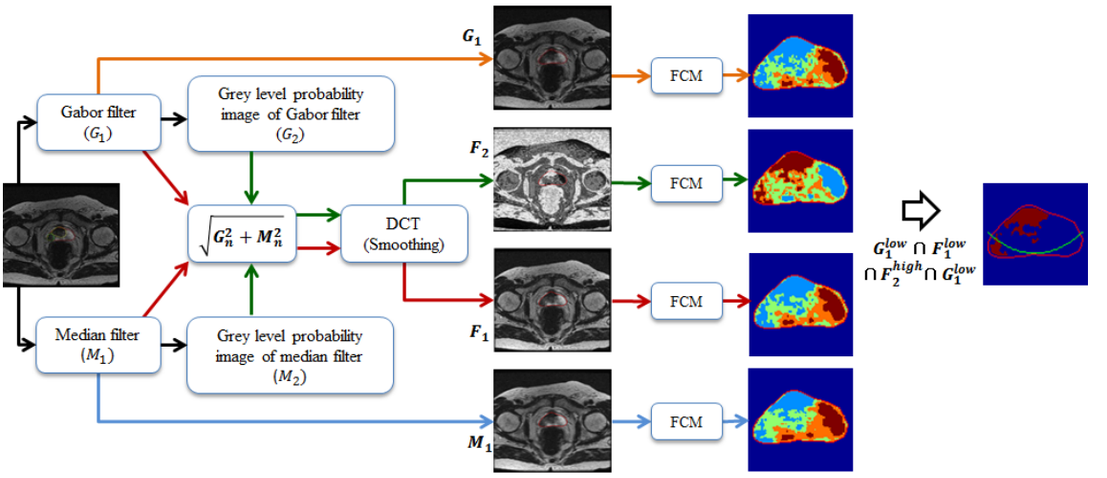

Figure 1: Overview of the proposed algorithm. From the lowest to highest intensity value represents in blue, green, amber and red colours.

3×3 neighbourhood. We extract a probability image from each G_1 and M_1 using equation (1) before we obtain the third feature (F_1) which is calculated using equation (2). This means, each element in F_1 is the sum vector of each component from G_1 and M_1. On the other hand, the fourth feature (F_2) is sum vector of probability images from G_1 and M_1. We calculate the probability images using equation (1) and calculate the vector sum using equation (2). For an $f(i,j)$ image, the probability value for the k^{th} intensity level is calculated using:

$$P(i,j) = \frac{\#(f(i,j) = k)}{M \times N} \tag{1}$$

where $\#(f(i,j) = k)$ is the number of pixels at the k^{th} intensity level in an $M \times N$ image, and as such each element in P is the probability value for a particular intensity level.

$$I_n(i,j) = \sqrt{G_n^2(i,j) + M_n^2(i,j)} \ \ , n = 1 \ or \ 2 \tag{2}$$

At the end of feature extraction, four features are extracted, namely the Gabor feature (G_1), the median feature (M_1), the sum vector of Gabor and median features (F_1) and the sum vector of probability image of Gabor and median features (F_2). Before image segmentation is performed, we applied noise reduction for F_1 and F_2 to smooth the features. The method is based on discrete cosine transform (DCT) which was developed by Gracia [3]. Subsequently, image segmentation is performed using Fuzzy C-Means (FCM) into four classes for each of the extracted features. We chose four classes based on the number of tissue categories in the prostate: normal (non-neoplastic) prostatic tissue (NNT), benign prostatic hyperplasia, high-grade prostatic intraepithelial neoplasia (PIN), and prostatic adenocarcinoma (PCA). Since most malignant regions contain lower intensities, cancerous regions could be detected within the prostate by taking the segmented regions which correspond to the first two lowest average intensity values (indicated by the superscript 'low'). However, malignant regions in F_2 are represented by higher average intensity values.

$$R = G_1^{low} \cap M_1^{low} \cap F_1^{low} \cap F_2^{high} \tag{3}$$

Where 'low' and '$high$' are low and high intensity represented in the segmented region within the prostate. After the region of interest is selected we perform erosion to remove noisy pixels. The number of pixels removed from the objects in an image depends on the size and shape of the structuring element used. In the proposed method we used a 'disk' shape structuring element with

size either 1 or 2. The size selection of the structuring element depends on the size of segmented region within the peripheral zone. If the size of the segmented region within the peripheral zone covers $\geq 20\%$ of the size of the peripheral zone, the size of the structuring element is 2 otherwise 1. This ensures that every segmented region is not over eroded or under eroded during the process. Finally, we combine all four segmented results by taking the intersection of four segmentation results (as shown in equation 3). The prostate gland is divided into peripheral (PZ), transition (TZ) and central (CZ) zones. We define the prostate's PZ using the quadratic equation of $y = ax^2 + bx + c$ based on three crucial coordinate points of the prostate which are v_1, v_2 and v_3 (see Figure 2). They are determined by the outmost x and y coordinates of the prostate boundary which are $x_{min}, x_{max}, y_{min}, y_{max}$ (see Figure 2).

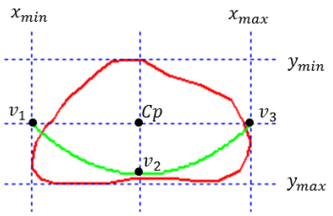

Figure 2: Prostate gland (red) and we define the PZ below $y = ax^2 + bx + c$ (green) which goes through v_1, v_2 and v_3.

$$C_p = ((x_{min} + x_{max})/2, (y_{min} + y_{max})/2) \tag{4}$$

$$v_1 = (x_{min}, (y_{min} + y_{max})/2) \tag{5}$$

$$v_2 = ((x_{min} + x_{max})/2, y_{min} + ((y_{max} - y_{min}) \times \frac{7}{8})) \tag{6}$$

$$v_3 = (x_{max}, (y_{min} + y_{max})/2) \tag{7}$$

Where C_p is the central point of the prostate, v_1,v_2 and v_3 are vertex points which are used to determine the parameters (a, b, c) for the quadratic equation $y = ax^2 + bx + c$. If there are segmented areas under $y = ax^2 + bx + c$ (green line in Figure 2) we assume that the prostate contains is malignant regions.

3 EXPERIMENTAL RESULTS AND CONCLUSIONS

We evaluated the proposed method based on 66 randomly selected (34 cancer and 32 normal slices) prostate MRI images (512×512) from 19 different cases aged 54 to 74. Each case has 3 to 5 slices through the central part of the prostate. The prostates, cancer and central zones were delineated by an expert radiologist on each of the MRI images. Data was analysed and classified as to whether the prostate contains cancer. The detection of cancer occurs when there are any retained segmented regions $(G_1^{low} \cap M_1^{low} \cap F_1^{low} \cap F_2^{high})$ within the peripheral zone. Subsequently, we compared the result with the ground truth whether the prostate contains cancer regions or not. For localisation, we compare the position of the segmented region based on $(G_1^{low} \cap M_1^{low} \cap F_1^{low} \cap F_2^{high}) \subseteq M_r$, where M_r is a cancer region within the peripheral zone. We achieved 84.85% accuracy (56 samples data are classified correctly) and 10 samples data are misclassified with 9.09% (six samples) and 6.06% (four samples) false negative and false positive results, respectively. Erosion with flexible size of structuring element and regions intersection $(G_1^{low} \cap M_1^{low} \cap F_1^{low} \cap F_2^{high})$ reduce the number of false positive and false negative results by $\approx 20\%$. The proposed method

achieved higher accuracy than some of the existing methods in the literature such as [5] (80%) and [6] (83.9%). Nevertheless, the method failed to produce accurate results in two cases: a) when the prostate's peripheral zone is almost non-existent, and b) when the prostate's shape does not conform to the shape of our prostate model. Figure 3 shows the results for three different cases.

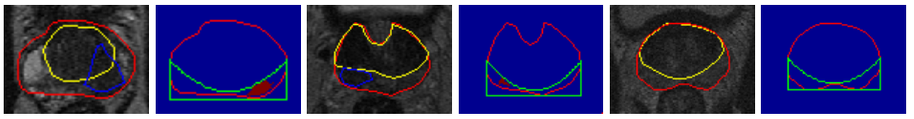

Figure 3: Ground truth: prostate (red), cancer (blue), CZ (yellow), PZ (green). The first four images are prostates containing cancer and their segmentation results (alternately). The last two images represent a prostate with no cancer and its segmentation result.

In summary, the proposed method uses the following features: a) G_1 and F_1 are extracted from Gabor and median filters, and b) F_1 and F_2 are the probability image of G_1 and M_1. The classification of malignant prostate and localisation are defined based on $G_1^{low} \cap M_1^{low} \cap F_1^{low} \cap F_2^{high}$ and $(G_1^{low} \cap M_1^{low} \cap F_1^{low} \cap F_2^{high}) \subseteq M_r$, respectively within the peripheral zone. Erosion and regions intersections are applied to reduce false positve and false negative results. We achieved reasonable high accuracy of abnormality detection (84.85%) with 9.09% and 6.06% false negative and false positive results, respectively. In conclusion, Gabor and median filters together with probability image information show promising potential to be effective texture descriptors to identify cancer regions within the peripheral region. Our idea which is based on regions intersection and flexible size of erosion's structuring element suggest a good prospective to reduce false positive and false negative results in the proposed method.

REFERENCES

[1] Sirovich, B. E., Schwartz, L. M., and Woloshin, S. Screening men for prostate and colorectal cancer in the United States. JAMA: *The Journal of the American Medical Association*, 289(11), 1414-1420, 2003.

[2] Vos, P. C., Barentsz, J. O., Karssemeijer, N., and Huisman, H. J. Automatic computer-aided detection of prostate cancer based on multiparametric magnetic resonance image analysis. *Physics in Medicine and Biology*, 57(6):1527 -1542, 2012.

[3] Garcia, D. Robust smoothing of gridded data in one and higher dimensions with missing values. *Computational Statistics and Data Analysis*,54(4):1167-1178, 2010.

[4] Chan, I., Wells, W., Mulkern, R. V., Haker, S., Zhang, J., Zou, H.K., Maier,S.E., and Tempany, C.M.C. Detection of prostate cancer by integration of line-scan diffusion, T2-mapping and T2-weighted magnetic resonance imaging; a multichannel statistical classifier. *Medical Physics*, 30:2390-2398, 2003.

[5] Castaneda, B., An, L., Wu, S., Baxter, L.L., Yao, J.L., Joseph, J.V., Hoyt.K., Strang, J., Rubens, D.J., Parker,K,J. Prostate cancer detection using crawling wave sonoelastography. Proc. SPIE 7265, *Medical Imaging* 2009: *Ultrasonic Imaging and Signal Processing*, 726513; doi:10.1117/12.811720.

[6] Sandler, R., and Lindenbaum, M. Optimizing Gabor Filter Design for Texture Edge Detection and Classification. *International Journal of Computer Vision*, 84(3):308-324, 2009.

[7] Weldon, T. P., Higgins, W. E., and Dunn, D. F. Efficient Gabor filter design for texture segmentation. *Pattern Recognition*, 29(12): 2005-2015, 1996.

[8] Jain, A. K., and Farrokhnia, F. Unsupervised texture segmentation using gabor filters. *Pattern Recognition*, 24(12):1167-1186, 1991.

3rd International Conference on Computational and Mathematical Biomedical Engineering – CMBE2013

16-18 December 2013, Hong-Kong

P. Nithiarasu and R. Löhner (eds)

Sensitivity analysis of heamodynamics to pre-processing medical images: reducing the geometry definition uncertainty

Ana J. João*, Alberto M. Gambaruto* and Adélia Sequeira*

*CEMAT, Departamento de Matemática, Insituto Superior Técnico,ana.joao@ist.utl.pt

SUMMARY

Mechanical properties of blood flow are common correlators to a wide variety of cardiovascular diseases. In this work variables to analyse and characterise the flow field and its relation with diseases are discussed in the context of cerebral aneurysms, reconstructed from in vivo medical imaging. Medical images are susceptible to different sources of error and artefacts, which lead to image quality degradation and diminishes resolution. Image processing techniques are able to restore many of these downfalls and improve the post-processing and analysis. In this work anisotropic diffusion-filtering methods based on PDEs, and commonly used contrast enhancement methods are used to facilitate the segmentation of the vessel in the case of clinically acquired CTA images and reduce possible geometry reconstruction errors and its propagations to the computational haemodynamics. Results from simulations of Newtonian and non-Newtonian unsteady flow are performed using OpenFOAM, in anatomically accurate cerebral aneurysm geometries and a set of mechanical measures that can be related to diseased state, such as wall shear stress and derived measures, residence times and region of flow impingement, will be analyses and presented.

Key Words: *blood flow, image processing, aneurysm.*

1 INTRODUCTION

There are several studies over the past decades that indicate that cardiovascular diseases such as aneurysms and atherosclerosis are directly related with the heamodynamic properties of the lumen wall (Caro et al, 1971). These are typically the wall shear stress (Caro et al, 1971), the gradient oscillatory number (Shimogonya et al, 2008), oscillatory shear index (Ku et al, 1985) and near-wall residence time. The reasons why fluid parameters on the vessel wall are related with disease sites are mainly the evidence that endothelial cells respond to signaling forces from fluids as well as considerations of transport and diffusion, hence interaction with the vessel and surroundings. Despite of the significance of heamodynamics parameters on the vessel lumen wall in the analysis of the disease, there has been relatively little study on the pre-processing of the medical images used to reconstruct the geometry for computational models, that subject to

uncertainty due to limited imaging resolution and random noise, can result in noticeable differences in the reconstructed vessel surface definition and hence the computed flow field.
The data set in this study represent a configuration of the aorto iliac and comprises of 266 images in the axial plane with resolution parameters: 512×512 pixels of 0.78×0.78mm size, 2.0mm slice thickness and 1.0mm slice spacing (Figure 1). The images presented here (Figure 2 and Figure 3) are a cropped region of interest on slice 154. It is the aim of this work to illustrate the need for care in medical image filtering and enhancement in the reconstruction procedure prior to the numerical simulations of the haemodynamics.

Figure 1. Configuration of the aorto iliac; (left) Image in Study; (center) Respective gradient; (right) Region of Interest

2 METHODS

2.1 Filtering Methods

Improved adaptive complex diffusion despeckling method (NCDF)

The non-linear anisotropic diffusion process, proposed by Perona and Malik, looks for the solution of

$$\frac{\partial}{\partial t} I(x,y,t) = \nabla \cdot [\mathrm{c(x,y,t)} \nabla \mathrm{I(x,y,t)}] \tag{1}$$

Combining findings that show that using linear scale spaces in complex domain and that by replacing $d(\|\nabla I\|^2)$ by $d(\|\nabla(G_\sigma * I)\|^2)$, where * represents the convolution operation, the stability of Eq. 1 is improved during the backward diffusion phase, (Salinas et al., Gilboa et al.), Bernardes et al. implemented a method that aims to improve the process of speckle noise reduction and improve preservation of the edges and important image features.

This is a filter usually applied to Optical coherence tomography data from the human eye (Bernards et al.). Contrary to the majority of non linear diffusion processes, which use a constant adaptive time step (Δt), this method uses an adaptive time step. The reason behind this approach relies on the fact that the diffusion coefficient depends on the gradient of the image, and due to the noise, this gradient is high during the initial steps of the diffusion process (Bernardes et al.), hence more emphasis has to be given to small image features during the initial iteration steps. The diffusion coefficient used here is a function of the Laplacian of the image and not of its gradient. The coefficient $c(x,y,t)$ is approximated by:

$$\mathrm{c(x,y,t)} = \frac{1}{1 + \left(\Delta \mathrm{I}/\beta\right)^2} \tag{2}$$

with β being adapted locally. The adaptive time step is given by:

$$\Delta t = \frac{1}{\alpha}\left[a + b\exp\left\{\frac{\partial I}{\partial t}\Big/_{I}\right\}\right] \quad (3),$$

where $\frac{\partial I}{\partial t}\Big/_{I}$ is the fraction of change of the image at a certain iteration step and *a, b* are constants and control the time step.

(a)

(b)

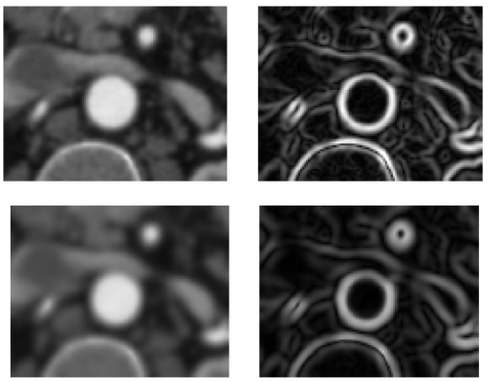

Figure 2. Filtering with NCDF; (a) 7 iterations (b) 20 iterations

Regularisation of backward and forward anisotropic diffusion (RBAF)

Several methods have been proposed for the well-posedness of the Perona-Malik non-linear equation 1, through appropriate choice of the diffusion coefficients and different regularisation approaches. In Guidotti et al. and references therein, a set of different methods are put forwards and studied in depth, based on equation 1, which include fractional derivatives, use of diffusion coefficients as functions of the image Laplacian or gradient magnitude, or also as a function of a convolved image and smooth Gaussian kernel. A more simple choice is following:

$$c(x,y,t) = \frac{1}{1 + |\nabla I|^2} + \delta \quad (4)$$

Several pointers also found in Guidotti et al., on appropriate interpretation of the coefficient $c(x,y,t)$ and are recommended.

(a)

(b)

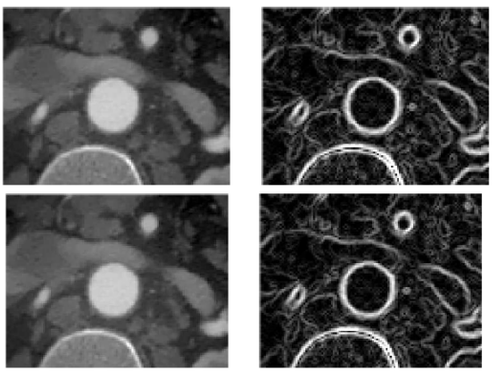

Figure 3. Filtering with RBAF; (a) 15 iterations (b) 20 iterations

2.2Numerical Simulations of the Heamodynamics

The computations were performed using OpenFOAM software package to solve the Navier-Stokes equations, which relies on the finite volume method. The simulations were run for steady and unsteady state. These were chosen in order to be able to both compare accurately the differences between the filtering methods clearly with steady-state, as well as demonstrate the relevance in more physiological scenario with the unsteady simulations. The schemes used are the well known SIMPLE method for the steady state and PISO for the unsteady state. Convergence criterion was set to be 10^{-8} on the residual.

3 CONCLUSIONS

Results indicate that image processing and especially preprocessing can substantially alter the quality of the image to improve desired object extraction. This removes a certain level of uncertainty in the segmentation process. Nevertheless, care must be taken to choose appropriate and robust schemes.
In this work, a survey of different filtering and contrast enhancement methods is undertaken and both geometry and CFD variations are analysed.

REFERENCES

[1] R. Bernardes, C. Maduro, P- Serralho, A. Araujo, S. Barbeiro, J. Cunha-Vaz,. *Improved adaptive complex diffusion despeckling filter*, OPTICS EXPRESS 18:23, p. 24048-24059, 2010.

[2] C.G. Caro, J.M. Fitz-Gerald, R.C Schoreter, *Atheroma and arterial wall shear: observations, correlation and proposal of a shear dependent mass transfer mechanism for atherogenesis*. Proc. R. Soc. London B177, pp. 109-159, 1971..

[3] G. Gilboa, N.Sochen, and Y.Y. Zeevi, *Image enhancement and denoising by complex diffusion processes*. Pattern Analysis and Machine Intelligence, IEEE Transactions, 26:8 1020 – 1036, 2004.

[4] P. Guidotti, *A family of nonlinear diffusions connecting Perona-Malik to standard diffusion.* Discrete and Continuous Dynamical Systems - Series *S(DCDS-S)*, 5(3):581-590, 2012.

[5] P. Perona and J. Malik, *Scale-space, edge detection using anisotropic diffusion.* IEEE Transactions on Pattern Analysis and Machine Intelligence. 12(7):629-639, 1990.

[6] H.M. Salinas and D.C. Fernandez *Comparison of PDE-based non- linear diffusion approaches for image enhancement and denoising in optical coherence tomography*. Medical Imaging, IEEE Transactions on 26 (6), 761 –771, 2007.

3rd International Conference on Computational and Mathematical Biomedical Engineering - CMBE2013
16-18 December 2013, Hong-Kong
P. Nithiarasu and R. Löhner (Eds.)

Shape descriptors to predict diabetic foot deformity: a feasibility study

Moi Hoon Yap*, Choon-Ching Ng*, Andrew J.M. Boulton, Frank L. Bowling** and Neil D. Reeves***

*Manchester Metropolitan University, Faculty of Science & Engineering, Manchester, UK, m.yap@mmu.ac.uk

**University of Manchester, Faculty of Medical & Human Sciences, UK

SUMMARY

The purpose of this study was to investigate the potential of using shape descriptors to predict the deformity of diabetic feet. Photographs were taken of the sole of the feet from 10 patients with diabetes and 10 healthy non-diabetic volunteers (control group). The foot area was automatically segmented by combining the skin segmentation algorithm and k-means segmentation algorithm. Then the shape descriptors of the segmented foot region were extracted. Finally, the machine learning algorithm (Support Vector Machine) was implemented to classify the diabetic foot from the normal foot. With the accuracy of 90%, sensitivity of 100%, specificity of 80%, and Receiver Operating Curve (ROC) area of 0.9, we conclude that shape descriptors have great potential for foot ulcer prediction. In future, the analysis from computer vision will be used to indicate the early sign and the suspected region of a diabetic foot ulcer.

Key Words: *diabetes, foot ulcers, k-means segmentation, shape descriptors.*

1 INTRODUCTION

People with diabetes commonly experience foot deformities associated with peripheral neuropathy (nerve damage). Diabetic peripheral neuropathy affects both sensory and motor nerves. Sensory nerve damage leads to a loss of feeling in the feet. Motor nerve damage leads to foot muscle wasting associated with many different types of foot deformities [1]. Diabetic foot deformities together with the lack of sensory perception in the feet are major risk factors leading to the development of foot ulcers. In particular, foot deformities create high-pressure areas on the foot that become at very high risk of developing an ulcer. A diabetic foot ulcer represents a serious clinical problem for the diabetic patient with a high risk of infection and subsequent limb amputation [2]. Various computational methods and algorithms have been developed to analyze and quantify biomedical data. Some active foot research includes Agic et al. [3], who investigated the relationship between foot anthropometrical and biomechanical descriptors; Acharya et al. [4] proposed an automated identification method of diabetic Type 2 subjects with and without neuropathy using the discrete wavelet transform (DWT) on foot images; and Goulermas et al. [5] proposed a robust discriminant analysis classifier for foot pressure lesions using kinematic data. In this paper, we proposed a novel computer technique to predict diabetic foot deformity.

2 METHOD

Figure 1 shows the modular block diagram of the foot region segmentation and classification.

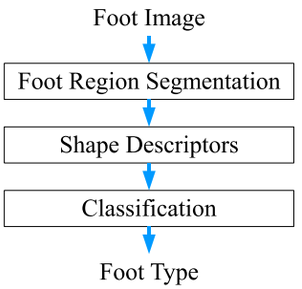

Figure 1: Overview of the methodology

2.1 Dataset

The photographs of foot image were collected from 20 volunteers, 10 patients with diabetes and 10 healthy control volunteers without diabetes. The view of the images for this experiment is the sole of the foot, as illustrated in Figure 2. Figure 2(a) and Figure 2(b) illustrate the images taken of a diabetic foot while Figure 2(c) and Figure 2(d) illustrate the images of a healthy control foot.

2.2 Foot region segmentation

Skin segmentation plays an important role in a wide range of image processing applications [4]. The choice of colour space can be considered as the primary step in skin-color classification. The RGB color space is the default color space for most available image formats. It has been observed that skin colours differ more in intensity than in chrominance [5]. *K*-means clustering is one of the simplest, and has been widely used in segmentation [6]. The *k*-means method aims to minimize the sum of squared distances between all points and the cluster centre. The final clustering will depend on the initial cluster centre chosen and on the value of *k*. To identify the foot region, first the skin segmentation algorithm is implemented. Due to the limitation in skin segmentation algorithm (variation in skin colours), the k-means clusters which overlap with the skin segment are combined and recognized as the foot region.

2.3 Shape descriptors

Shape analysis has been widely utilised in computer vision and has been intensively developed over the past decades in both theoretical and applied domains [7]. Due to the fact that the foot ulcers will alter the shape of the sole view of the foot, we proposed to use the shape descriptors for foot classification. The shape descriptors include *Area to Perimeter ratio* (*AP*), *Solidity*, *Eccentricity*, *Elongation*, *Extent*, *Orientation*, *Aspect ratio of major axis and minor axis* (*AR*), *Compactness*, *Roundness*, and *Form Factor*. The detail explanation of the above shape descriptors can be found at [8].

2.4 Classification

The support vector machines (SVMs) were introduced by Vapnik [9] and are based on statistical learning theory. The benefits of SVMs include rapid classification capability and the ability to generalize in high dimensional spaces. Hence it is widely accepted as an excellent choice in classification. This paper implements Platt's [10] sequential minimal optimization (SMO) algorithm for training a support vector classifier, with 10-fold cross-validation, The classification stage is experimented by

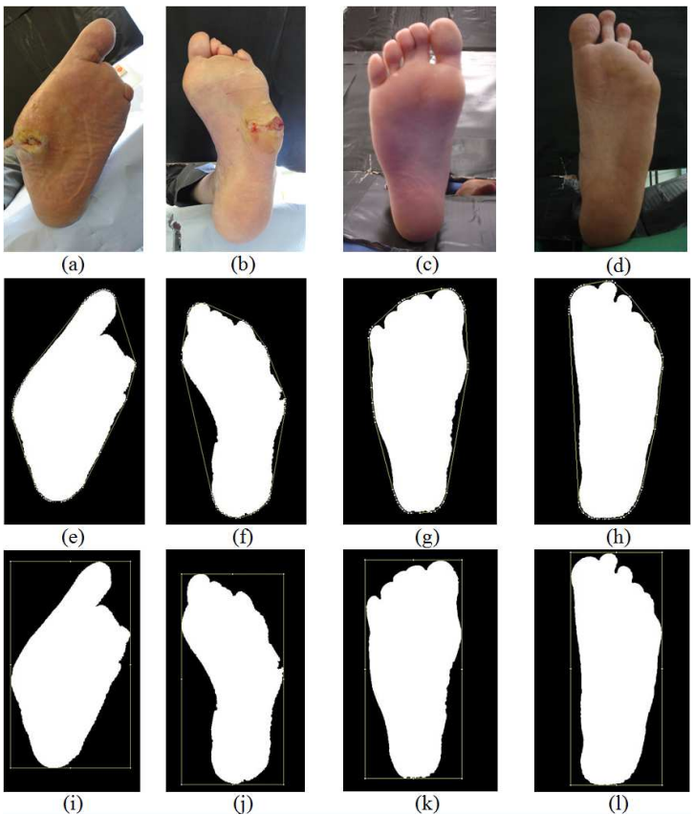

Figure 2: (a) and (b) illustrate original diabetes foot images, (c) and (d) illustrate original healthy foot images; (e), (f), (g), (h) illustrate the segmented region (white area) and convex area (line) of the images in (a), (b), (c), (d) respectively; (i), (j), (k), (l) illustrate the bounding rectangle (line) of the images in (a), (b), (c), (d) respectively

Table 1: Confusion matrix on foot type classification

Actual / Predicted	Foot with ulcer	Normal foot
Foot with deformity & ulceration	10	0
Normal foot	2	8

using WEKA (The Waikato Environment for Knowledge Analysis) [11], the popular, open source, Java based data mining tool. WEKA produces the accuracy, sensitivity, specificity and ROC area.

3 RESULT AND DISCUSSION

Figure 2 illustrate the result of foot region segmentation and some implementation of shape descriptors extraction, such as convex area and the bounding rectangle of the foot images. The classification result is shown in Table 1. The confusion matrix shows that SVM detected 10 True Positive (Foot with ulcer), 0 False Negative (miss-classified foot with ulcer as normal foot), 2 False Positive (miss-classified normal foot as foot with ulcer), and 8 True Negative (Normal foot). The overall accuracy is 90%, the sensitivity is 100%, the specificity is 80%, and the ROC area is 0.9. This result shows shape descriptors are very useful in discriminating different foot shapes. However, a larger sample is needed for future studies.

4 CONCLUSIONS

A feasibility study in the potential use of shape descriptors to predict diabetic foot deformity was carried out. We evaluated the shape descriptors and fed to SVM classifier for classification. The result shows an accuracy of 90%, sensitivity of 100%, specificity of 80% and with 0.9 ROC areas in discriminating the diabetic foot with deformity from normal healthy foot. This promising result shows that there is a great potential in using computer techniques to predict the early sign of a diabetic foot ulcer, and its location. Currently we are recruiting more participants to improve the reliability and accuracy of our method. Future work will be aimed towards a specific detection of foot ulcers in diabetic patients with or without deformity.

ACKNOWLEDGEMENT

The authors would like to thank Adrian Davison for his help in data collection and the volunteers for their participation.

REFERENCES

[1] A. J. Boulton, A. I. Vinik, J. C. Arezzo, V. Bril, E. L. Feldman, R. Freeman, R. A. Malik, R. E. Maser, J. M. Sosenko and D. Ziegler, Diabetic neuropathies a statement by the American Diabetes Association, *Diabetes care*, vol. 28, no. 4, pp. 956-962, 2005.

[2] A. J. Boulton, L. Vileikyte, G. Ragnarson-Tennvall and J. Apelqvist, The global burden of diabetic foot disease, *The Lancet*, vol. 366, no. 9498, pp. 1719-1724, 2005.

[3] A. Agi, V. Nikoli and B. Mijovi, Foot Anthropometry and Morphology Phenomena, *Collegium antropologicum*, vol. 30, no. 4, pp. 815-821, 2006.

[4] R. Acharya, P. H. Tan, T. Subramaniam, T. Tamura, K. C. Chua, S. C. E. Goh, C. M. Lim, S. Y. D. Goh, K. R. C. Chung and C. Law, Automated identification of diabetic type 2 subjects with and without neuropathy using wavelet transform on pedobarograph, *Journal of medical systems*, vol. 32, no. 1, pp. 21-29, 2008.

[5] J. Y. Goulermas, A. H. Findlow, C. J. Nester, D. Howard and P. Bowker, Automated design of robust discriminant analysis classifier for foot pressure lesions using kinematic data, *IEEE Transactions on Biomedical Engineering*, vol. 52, no. 9, pp. 1549-1562, 2005.

[6] P. Kakumanu, S. Makrogiannis and N. Bourbakis, A survey of skin-color modeling and detection methods, *Pattern recognition*, vol. 40, no. 3, pp. 1106-1122, 2007.

[7] J. C. Russ, *The image processing handbook*, 5 ed., CRC press, 2007.

[8] M. H. Yap, E. Edirisinghe and H. Bez, Computer Aided Detection and Recognition of Lesions in Ultrasound Breast Images, *International Journal of Computational Models and Algorithms in Medicine (IJCMAM)*, vol. 1, no. 2, pp. 53-81, 2010.

[9] V. Vapnik, *The Nature of Statistical Learning Theory*, SpringerVerlag, 1995.

[10] J. Platt, Fast training of support vector machines using sequential minimal optimization, in *Advances in Kernel Methods - Support Vector Learning*, B. Schoelkopf, C. Burges, and A. Smola, Eds., MIT Press, 1998.

[11] I. H. Witten and E. Frank, *Data Mining: Practical machine learning tools and techniques*, Morgan Kaufmann, 2005.

3rd International Conference on Computational and Mathematical Biomedical Engineering - CMBE2013
16-18 December 2013, Hong-Kong
P. Nithiarasu and R. Löhner (Eds.)

Integral approach to atlas-based whole-body segmentation with application to small-animal PET-CT

Fabian Gigengack*, Robin Sobanski*, Lars Ruthotto, Xiaoyi Jiang* and Klaus P. Schäfers*****

*Department of Mathematics and Computer Science & European Institute for Molecular Imaging, University of Münster, Germany, {gigengack, robinsobanski, xjiang}@uni-muenster.de

**Department of Earth, Ocean and Atmospheric Sciences, University of British Columbia, Vancouver, Canada, lruthotto@eos.ubc.ca

***European Institute for Molecular Imaging, University of Münster, Germany, schafkl@uni-muenster.de

SUMMARY

Whole-body organ segmentation is required for many medical applications. Particularly for biodistribution studies or partial volume correction in positron emission tomography (PET). In this work we propose a fully-automated whole-body segmentation approach with high accuracy. The proposed pipeline consists of an initial alignment to correct major anatomical differences. A subsequent refinement step is performed to obtain highly accurate and organ-specific contours using improved passive contour segmentation. The integral approach is evaluated in a study of 13 PET-CT data sets of mice and is quantitatively compared to manually drawn VOIs.

Key Words: *segmentation, registration, passive contour, atlas, PET-CT, whole-body.*

1 INTRODUCTION

Adequate whole-body organ segmentation is required to access individual organ concentration for biodistribution studies or to perform partial volume correction in positron emission tomography (PET). In this work we propose an atlas-based two-step segmentation procedure based on a pair of spatially aligned PET and CT images of the same subject.

The approach divides into two steps. The goal of the first step is to achieve a good estimation of major anatomical differences. We chose the hierarchical bone registration of Baiker et al. [1], which pursues exactly this goal. The contours of inner organs without proximity to bones are further improved in a subsequent refinement step. Tailored atlas-based segmentation, based on an extended version of the passive contours approach proposed in our previous work [5], was used for this purpose.

In related work, Yezzi et al. [7] present an active contours segmentation framework with a simultaneous registration of features. The method is, however, inapplicable for multiple organ segmentation tasks as treated in this work.

Small-animal PET segmentation based on a statistical shape model was proposed by Wang et al. [6]. The registration is guided by high uptake organs and provides adequate estimates for low uptake organs as well. However, a drawback is the need of a manual labeling of organs.

2 METHODS

2.1 Atlas-based segmentation according to Baiker et al.

In order to achieve a good initial alignment of the atlas and real data, the hierarchical atlas segmentation method of Baiker et al. [1] is applied. The method consists of a skeleton and skin registration exclusively on the CT data.

The skeleton is extracted from the real CT data with a threshold segmentation and each individual bone of the atlas is aligned to the skeleton in a hierarchical manner. The individual bone alignment is performed with the iterative closest point (ICP) [2] algorithm due to its low computational costs and at the same time high accuracy. The less rigid structures, i.e., spine and skin, are treated individually with a non-linear registration.

A thin-plate-spline (TPS) transformation can be obtained from the estimated corresponding points between the real and atlas data. Application to the atlas gives a first approximation of the whole-body segmentation. Particularly the bones and organs close to the skeleton show already a high spatial correspondence. For more details about the exact procedure we refer to [1].

2.2 Joint Passive Contour Segmentation and Registration

The result of the Baiker segmentation serves as the input for a refined passive contour segmentation [5], operating simultaneously on CT and PET data. The aim of this tailored segmentation is to further improve the segmentation accuracy, particularly of inner organs. Four distance terms drive the passive contour registration:

1. Distance $\mathcal{D}^{\text{SSD}}$ of the atlas CT $\mathcal{R}_{CT} : \Omega \to \mathbb{R}$ and real CT $\mathcal{T}_{CT} : \Omega \to \mathbb{R}$
2. Distance $\mathcal{D}^{\text{SSD}}$ of the atlas PET $\mathcal{R}_{PET} : \Omega \to \mathbb{R}$ and real PET $\mathcal{T}_{PET} : \Omega \to \mathbb{R}$
3. Passive contour segmentation distance $\mathcal{D}_{PC}$ of the real CT
4. Passive contour segmentation distance $\mathcal{D}_{PC}$ of the real PET

The functional $\mathcal{D}^{\text{SSD}}$ is thereby the sum of squared differences (SSD) distance. Instead of matching a contour to the data, the passive contour distance $\mathcal{D}_{PC}$ is used to optimize for the transformation that aligns the data best to the (passive) atlas contours.

The passive contour segmentation in this work is an extended version of [5]. The passive contour distance $\mathcal{D}_{PC}$ is not only applied to the PET data, but additionally to the CT data. This leads to an increased segmentation accuracy at the expense of an additional weighting factor in Equation (1).

To find the transformation $y : \mathbb{R}^3 \to \mathbb{R}^3$, representing point-to-point correspondences between the atlas and the real data, the following functional has to be minimized

$$\begin{aligned} \min_{y} \{ & \alpha_{CT} \cdot \mathcal{D}^{\text{SSD}}(\mathcal{T}_{CT} \circ y,\ \mathcal{R}_{CT}) + \alpha_{PET} \cdot \mathcal{D}^{\text{SSD}}(\mathcal{T}_{PET} \circ y,\ \mathcal{R}_{PET}) \\ & + \alpha_{CT}^{PC} \cdot \mathcal{D}_{PC}(\mathcal{T}_{CT} \circ y,\ A) + \alpha_{PET}^{PC} \cdot \mathcal{D}_{PC}(\mathcal{T}_{PET} \circ y,\ A) + \alpha_{\mathcal{S}} \cdot \mathcal{S}(y) \} , \end{aligned} \quad (1)$$

where $\alpha_{CT}, \alpha_{PET}, \alpha_{CT}^{PC}, \alpha_{PET}^{PC}, \alpha_{\mathcal{S}} \in \mathbb{R}^+$ are weighting factors for the individual data terms and the regularization functional $\mathcal{S}$. The delineation of the atlas organs is represented by A according to [5].

To guarantee diffeomorphic transformations and to be highly robust against noise, we utilize hyperelastic regularization [3]. In addition, an identity penalty energy is applied to the bone structures already aligned with Baiker's method, penalizing deviations from the identity transformation.

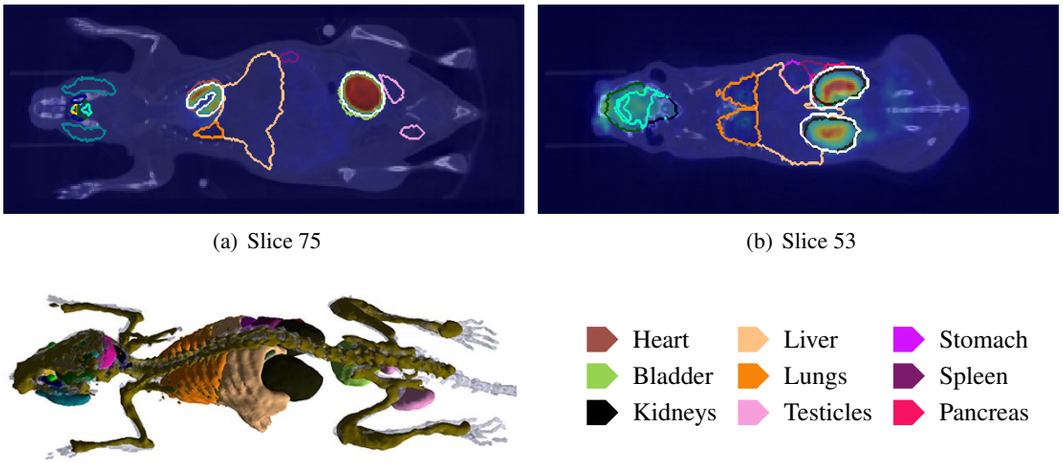

(a) Slice 75 (b) Slice 53

(c) Rendering

Figure 1: (a)-(b) Overlay of slices of the 3D CT and PET data and organ contours. The ground-truth segmentation of the (a) left ventricle, bladder and (b) kidneys is plotted with white contours. The estimated segmentations are shown with colored contours. (c) Rendering of the real CT skeleton (gray) with surface plots of the estimated bone and organ contours. Color codes for exemplary organs are depicted at the bottom right.

Table 1: Proposed method: Dice coefficients for the skeleton, heart, bladder and kidneys.

Mouse	**1**	**2**	**3**	**4**	**5**	**6**	**7**	**8**	**9**	**10**	**11**	**12**	**13**	**Avg.**	**Std.**
Skeleton	0.44	0.46	0.41	0.44	0.48	0.45	0.45	0.42	0.43	0.47	0.45	0.38	0.43	0.44	0.02
Heart	0.84	0.83	0.74	0.83	0.86	0.81	0.82	0.85	0.76	0.80	0.70	0.76	0.81	0.80	0.05
Bladder	0.82	0.86	0.92	0.85	0.94	0.94	0.89	0.82	0.89	0.89	0.93	0.82	0.78	0.87	0.05
Kidneys	0.83	0.77	0.82	0.80	0.80	0.81	0.79	0.80	0.80	0.86	0.82	0.80	0.81	0.81	0.02

3 EXPERIMENTAL RESULTS

^{18}F-FDG-PET/CT data of 13 healthy adult C57/Bl6 mice (without any intervention) are used for the evaluation and represent the most widely used radiotracer and mouse strain in preclinical PET studies. The Digimouse software phantom [4] serves as an atlas. For more details about the real and atlas data we refer to [5].

An exhaustive parameter search is performed for the proposed method based on Equation (1) and the PET and CT data of a randomly selected mouse. For each parameter combination the Dice coefficient of the estimated segmentation and the manual ground-truth segmentation is calculated. For two sets X and Y the Dice coefficient is defined as $D(X,Y) = \frac{2|X \cap Y|}{|X|+|Y|}$. We found the following optimal parameter set for the proposed method: $\alpha_{CT} = 1$, $\alpha_{PET} = 1.5$, $\alpha_{CT}^{PC} = 234$, $\alpha_{PET}^{PC} = 560$. For the hyperelastic regularization we found an optimal weighting of $\alpha_{\mathcal{S}} = 1000$.

The estimated segmentation for one mouse is exemplified in Fig. 1. The Dice coefficients of the proposed method for all analyzed organs and mice can be found in Tab. 1. Results of the proposed method in comparison with the pure Baiker approach and the pure passive contour approach are given in Tab. 2.

Table 2: Comparison: Average Dice coefficients (and standard deviation) for different methods using the same mice as in Tab. 1. The results of the pure Baiker approach were obtained with our own implementation and are in the same range as published in [1]. Results of the pure passive contour approach are taken from our previous publication [5] (note that no Dice coefficient was determined for the skeleton in [5]).

Method	**Baiker**	**Passive Contour**	**Proposed method**
Skeleton	0.44 ± 0.02	–	0.44 ± 0.02
Heart	0.43 ± 0.07	0.73 ± 0.10	0.80 ± 0.05
Bladder	0.29 ± 0.16	0.88 ± 0.05	0.87 ± 0.05
Kidneys	0.62 ± 0.04	0.76 ± 0.07	0.81 ± 0.02

4 CONCLUSIONS

An integral approach to whole-body segmentation of PET data is presented in this work. Based on an accurate initial alignment of bone structures and the skin, an enhanced registration of individual organs is the objective of a subsequent passive contour segmentation. A clear improvement (based on a Dice coefficient evaluation) of the integral approach could be observed compared to the application of the individual approaches alone, cf. Tab. 2.

The primary goal is to apply our method to additional data in future work. Data from other modalities, human data and dynamic PET data (activity over time carries important information for segmentation) are of particular interest. In addition, we will extend this work by analyzing a larger number of data sets with a larger number of volumes of interest (VOIs). In this context it is also planned to analyze the applicability of the proposed method to subjects with tumors.

Acknowledgment: This work was partly funded by the Deutsche Forschungsgemeinschaft, SFB 656 MoBil (projects B2 and B3).

REFERENCES

[1] M. Baiker, J. Milles, J. Dijkstra, T. Henning, A. Weber, I. Que, E. Kaijzel, C. Löwik, J. Reiber, and B. Lelieveldt. Atlas-based whole-body segmentation of mice from low-contrast Micro-CT data. *Med Image Anal*, 14(6):723–737, 2010.

[2] P. Besl and N. McKay. A method for registration of 3-D shapes. *IEEE Transactions on Pattern Analysis and Machine Intelligence*, 14(2):239–256, 1992.

[3] M. Burger, J. Modersitzki, and L. Ruthotto. A hyperelastic regularization energy for image registration. *SIAM Journal on Scientific Computing*, 35(1):B132–B148, 2013.

[4] B. Dogdas, D. Stout, A.F. Chatziioannou, and R.M. Leahy. Digimouse: a 3D whole body mouse atlas from CT and cryosection data. *Physics Med Biol*, 52(3):577, 2007.

[5] F. Gigengack, L. Ruthotto, X. Jiang, J. Modersitzki, M. Burger, S. Hermann, and K.P. Schäfers. Atlas-based whole-body PET-CT segmentation using a passive contour distance. In *Medical Computer Vision*, pages 82–92. Springer, 2013.

[6] H. Wang, T. Olafsen, D.B. Stout, and A.F. Chatziioannou. Quantification of organ uptake from small animal PET images via registration with a statistical mouse atlas. In *MICCAI Workshop Proceedings*, 2011.

[7] A. Yezzi, L. Zöllei, and T. Kapur. A variational framework for integrating segmentation and registration through active contours. *Med Image Anal*, 7(2):171–85, 2003.

3rd International Conference on Computational and Mathematical Biomedical Engineering - CMBE2013
16-18 December 2013, Hong-Kong
P. Nithiarasu and R. Löhner (Eds.)

High resolution human body computational model for bioelectrical impedance analysis

Alexander Danilov⋆, Vasily Kramarenko⋆⋆ and Alexandra Yurova⋆⋆⋆
⋆Institute of Numerical Mathematics, Russian Academy of Sciences, Gubkina 8, Moscow, Russia, a.a.danilov@gmail.com
⋆⋆Moscow Institute of Physics and Technology, Institutskiy pereulok 9, Dolgoprudny, Russia, kramarenko.vasiliy@gmail.com
⋆⋆⋆Lomonosov Moscow State University, Leninskie Gory 1, Moscow, Russia, alexandra.yurova@gmail.com

SUMMARY

An adaptive unstructured tetrahedral mesh generation technology is presented. This technique is applied to simulation of segmental bioelectrical impedance measurements using high-resolution whole body model of the Visible Human Project. Sensitivity field distributions for a conventional tetrapolar, as well as eight- and ten-electrode measurement configurations are obtained.

Key Words: *segmentation, tetrahedral mesh, finite element method, bioelectrical impedance.*

1 INTRODUCTION

Bioelectrical impedance analysis (BIA) is commonly used for body composition and abdominal adiposity assessment in clinical medicine, dietology and sports medicine. BIA is also used in monitoring of body fluids redistribution under various physiological and pathological conditions, e.g. in intensive care. The computational analysis of the existing measurement schemes is essential for accurate data interpretation and the development of new efficient electrode schemes. One of approaches is based on calculation of relative tissues and organs contribution to the result of bioimpedance measurements of the particular body segment. In our work we aimed at computational analysis of segmental BIA, which is used for body composition assessment. We developed a numerical model for computation of the human body bioelectrical impedance for low frequency electric signals. We propose techniques for construction and visualization of sensitivity field distributions for segmental BIA using anatomically accurate 3D model of the human body from Visible Human Project (VHP) [1].

As described in [2], the electrical fields generated during bioimpedance measurements are governed by the equation

$$\mathrm{div}(\mathbf{C}\nabla U) = 0 \quad \text{in} \quad \Omega \tag{1}$$

with the boundary conditions

$$(\mathbf{J}, \mathbf{n}) = I_0/S_\pm \quad \text{on} \quad \Gamma_\pm \tag{2}$$

$$(\mathbf{J}, \mathbf{n}) = 0 \quad \text{on} \quad \partial\Omega\backslash\Gamma_\pm \tag{3}$$

$$U(x_0, y_0, z_0) = 0 \tag{4}$$

$$\mathbf{J} = \mathbf{C}\nabla U \tag{5}$$

where Ω is the computational domain, $\partial\Omega$ is its boundary, $\Gamma_\pm$ are electrode contact surfaces, **n** is an external unit normal vector, U is an electric potential, **C** is a conductivity tensor, **J** is a current density, I_0 is an electric current, $S_\pm$ are areas of the electrode contacts. Equation (1) determines the distribution of electric field in the domain with heterogeneous conductivity **C**. Equation (2) sets a constant current density on the electrode contact surfaces. Equation (3) defines the no-flow condition on the boundary. Uniqueness of the solution is guaranteed by the equation (4), where (x_0, y_0, z_0) is some point in the domain Ω.

Discretization of these equations was obtained using finite element scheme with piecewise linear elements P_1 from Ani3D package [3]. An unstructured tetrahedral mesh was created using CGAL-Mesh library [4] and Ani3D package.

2 SEGMENTATION AND MESH GENERATION

Our high resolution human body geometrical model was constructed in two steps. First, the geometrical model of the human torso was created for Visible Human man data. The data were clipped and downscaled to an array of $567\times305\times843$ colored voxels with the resolution $1\times1\times1$ mm. The initial segmented model of the VHP human torso was kindly provided by the Voxel-Man group [5]. This model has been produced primarily for visualization purposes, contained a significant amount of unclassified tissue and, thus, was not entirely suited for numerical purposes. Therefore, a further processing of the segmented model was needed. It was performed semi-automatically using ITK-SNAP segmentation software program [6]. At the final stage, we used several post-processing algorithms for filling remaining gaps between tissues and final segmented data smoothing. Our segmented model of the human torso contains 26 labels and describes major organs and tissues.

Several meshing techniques were tested for the mesh generation of segmented data. In our work we opted for the Delaunay triangulation algorithm from the CGAL-Mesh library [4]. This algorithm enables defining a specific mesh size for each model material. In order to preserve geometrical features of the segmented model while keeping a feasible number of vertices, we assigned a smaller mesh size to blood vessels and a larger mesh size to fat and muscle tissues. After initial mesh generation we applied mesh cosmetics from Ani3D package. This essential step reduces discretization errors and the condition number of the resulted systems of linear equations. The segmented model and the generated mesh with 413 508 vertices and 2 315 329 tetrahedra are presented in Fig. 1. This mesh retains most anatomical features of the human torso.

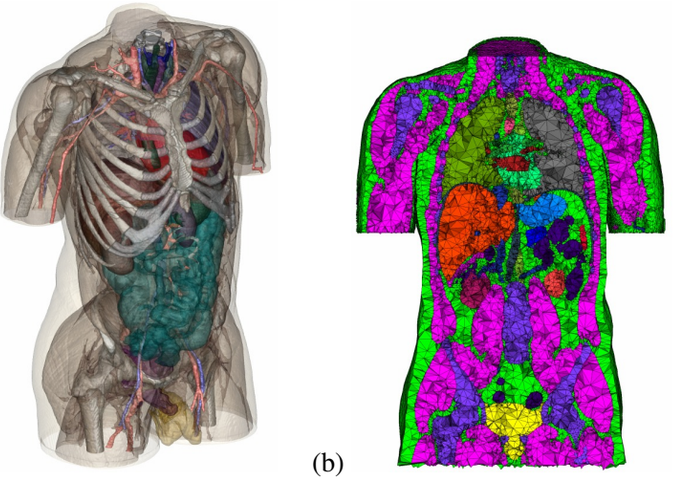

(a) (b)

Figure 1: Geometrical model of the segmented image (a) and unstructured tetrahedral mesh (b).

The whole body segmented model is based on the torso model. Missing parts were segmented using ITK-SNAP software. The final model is a $575\times333\times1878$ voxels array with the resolution $1\times1\times1$ mm segmented in 30 materials.

We used the proposed techniques to construct the computational mesh for the whole body model based on VHP data. The related segmented model and generated mesh containing 574 128 vertices and 3 300 481 tetrahedrons are shown in Fig. 2.

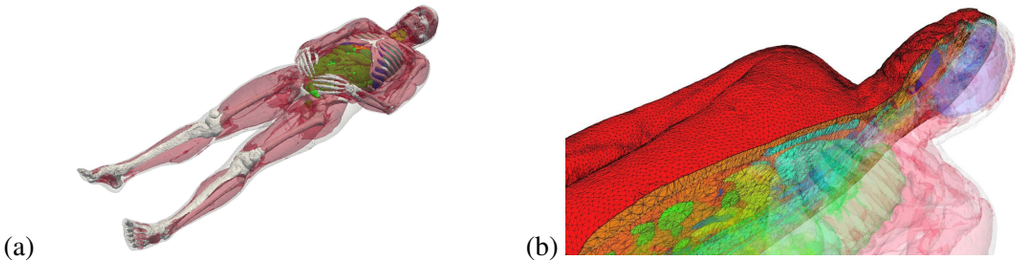

(a) (b)

Figure 2: Segmented whole body model of the Visible Human Man (a) and a part of generated mesh (b).

After mesh generation, we added a skin layer and multilayered electrodes to the surface of the constructed mesh. Boundary triangulation was used to create a prismatic mesh on the surface, and then each prism was split into three tetrahedrons resulting in a conformal mesh.

Along with conventional tetrapolar wrist-to-ankle measurement configuration, two schemes of segmental BIA were considered: an eight-electrode one with the placement of current and potential electrodes 5 cm apart on the back surfaces of the wrists and ankles, and also ten-electrode scheme with an additional electrode pair located on the forehead. Accordingly, five pairs of thin bilayer square objects 23×23 mm in size simulating electrode properties were added on the forehead and distal parts of arms and legs of the segmented model.

3 RESULTS

We simulated BIA measurements at the electrical current frequency 50 kHz using FEM. The electrical conductivity parameters for labeled tissues were taken from [7]. Sensitivity field distributions were obtained according to Geselowitz formula [8].

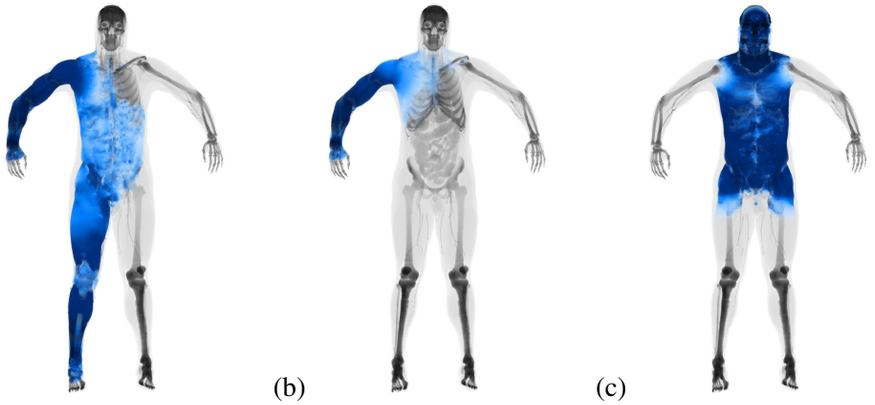

(a) (b) (c)

Figure 3: High sensitivity areas for conventional tetrapolar scheme (a), right arm with 8 electrode scheme (b), head with 10 electrode scheme (c).

Current density fields were calculated from the finite-element model, and the corresponding sensitivity field distributions were obtained for various configurations of electrode sites. Fig. 3 shows the high sensitivity body regions for various schemes of electrodes placement: a conventional tetrapolar scheme (a) and some of those provided by the eight- (b) and ten-electrode configurations (c).

4 CONCLUSIONS

In this study we presented the segmentation and mesh generation technology for human body bioelectrical impedance modeling. We created a tetrahedral mesh and obtained the sensitivity field distributions for the conventional tetrapolar measurement scheme as well as for the segmental BIA as represented by the eight- and ten-electrode configurations. Our data provide accurate interpretation of the results of segmental BIA. The advanced mesh generation approach along with numerical modeling procedure can serve as a valuable tool for evidence-based approach to the development and validation of novel BIA techniques and measurement schemes.

5 ACKNOWLEDGMENTS

This work has been supported in part by RFBR (grants no. 11-01-00971, 12-01-31223), the Federal Program "Academic and pedagogical staff of innovative Russia", and by the Russian President grant MK-3675.2013.1.

REFERENCES

[1] The Visible Human Project, `http://www.nlm.nih.gov/research/visible/`.

[2] S. Grimnes, O. G. Martinsen. *Bioimpedance and bioelectricity basics*, Elsevier, Amsterdam, 2008.

[3] Advanced Numerical Instruments 3D, `http://sourceforge.net/projects/ani3d`.

[4] L. Rineau, M. Yvinec, A generic software design for Delaunay refinement meshing, *Comp. Geom. Theory Appl.*, 38 (1-2), 100-110, 2007.

[5] K. H. Höhne, B. Pflesser, A. Pommert et al., A realistic model of human structure from the Visible Human data, *Meth. Inform. Med.*, 40 (2), 83-89, 2001.

[6] P. A. Yushkevich, J. Piven, H. C. Hazlett et al. User-guided 3D active contour segmentation of anatomical structures: Significantly improved efficiency and reliability, *Neuroimage*, 31 (3), 1116-1128, 2006.

[7] C. Gabriel, A. Peyman, E. Grant, Electrical conductivity of tissues at frequencies below 1 MHz, *Phys. Med. Biol.*, 54 (16), 4863-4878, 2009.

[8] D. B. Geselowitz, An application of electrocardiographic lead theory to impedance plethysmography, *IEEE Trans. Biomed. Eng.*, 18 (1), 38-41, 1971.

3rd International Conference on Computational and Mathematical Biomedical Engineering - CMBE2013
16-18 December 2013, Hong-Kong
P. Nithiarasu and R. Löhner (Eds.)

Continuum elasticity with atomic rigidity

Guo-Wei Wei[⋆,⋆⋆,⋆⋆⋆], **Kelin Xia** [⋆] **and Kristopher Opron**[⋆⋆]
[⋆] Department of Mathematics Michigan State University, MI 48824, USA, wei@math.msu.edu
[⋆⋆] Department of Biochemistry and Molecular Biology Michigan State University, MI 48824, USA
[⋆⋆⋆]Department of Electrical and Computer Engineering, Michigan State University, MI 48824, USA

SUMMARY

This work introduces the multiscale theory of continuum elasticity with atomic rigidity (CEWAR) for macromolecular analysis. The essential idea of CEWAR is to formulate bulk and shear moduli as continuous functions of atomic information. CEWAR allows the separation of the dynamics complexity of a macromolecular system from its static complexity such that the more time-consuming dynamics is described by continuum elasticity theory, while the less expensive static analysis is treated with atomic approaches. A flexibility-rigidity index (FRI) is introduced to analyze macromolecular flexibility and rigidity in atomic detail. The FRI reflects the topological connectivity of macromolecular atoms or residues and characterizes the geometric compactness of the macromolecule. The proposed methods are applied to the analysis of structural proteins.

Key Words: *continuum elasticity with atomic rigidity, flexibility-rigidity index, B-factor, Tissues.*

1 INTRODUCTION

Recent advances in biotechnologies have irreversibly changed traditional life science disciplines such as physiology, plant biology, neuroscience, etc., from macroscopic phenomenological ones into molecular based biosciences. In parallel with this development, a major feature of life sciences in the 21st Century is their profound transition from phenomenological and descriptive disciplines to quantitative and predictive ones. Ample opportunities have emerged for theoretically and computationally driven advances in biological research. Experimental explorations of self-organizing molecular biological systems, such as HIV viruses, molecular motors, DNA and RNA polymerases, and proteins associated with Alzheimer's disease, are dominating driving forces in scientific discovery and innovation in the past few decades. However, the emergence of excessive complexity in self-organizing biological systems poses fundamental challenges to their quantitative analysis and description, because of their excessively high dimensionality. Multiscale modeling, intrinsic manifold extraction and dimensionality reduction, are developed to reduce the computational cost of biomolecular systems while maintaining an essential and adequate description of the biomolecular observables of interest.

The objective of the present work is to develop a new multiscale model, continuum elasticity with atomic rigidity (CEWAR), for describing excessively large biomolecular complexes. The essential ingredient of the CEWAR is to utilize the continuum mechanics for describing macromolecular conformational changes while treating the shear modulus or rigidity with atomic information. In

conjugation with the CEWAR, we propose a flexibility-rigidity index (FRI) approach for protein rigidity and flexibility analysis. The FRI provides an accurate measure of geometric compactness and topological connectivity of a protein at each atom or residue. Stated differently, the FRI reflects the local interaction strength. As such, it gives rise to accurate prediction of protein B-factors.

2 THEORY AND RESULTS

Note that in the present work, the bulk modulus $\lambda = \lambda(\mathbf{r})$ and rigidity $\mu = \mu(\mathbf{r})$ are taken as continuous function with atomic rigidity information. Considering such a position dependence, the governing equation for the elastic dynamics of a macromolecule can be expressed as

$$\rho\ddot{\mathbf{w}} = [\nabla(\lambda+\mu)\nabla\cdot\mathbf{w} + \nabla\cdot\mu\nabla\mathbf{w}] + \mathbf{f}. \tag{1}$$

where ρ is the density of the macromolecules, $\mathbf{w}$ is the displacement, $\mathbf{f} = \mathbf{f}_{\rm FSI} + \mathbf{f}_{\rm RF} + \mathbf{f}_{\rm HG}$ is the total force due to fluid-structure interaction (FSI), reaction field (RF) and heterogeneity (HG) of the biomolecules [1]. With the stress tensor of the elastic molecule $\mathbb{T}_{ij} = \lambda\sigma_{ii}\delta_{ij} + 2\mu\sigma_{ij}$, Eq. (1) can be written as

$$\rho\ddot{\mathbf{w}} = \nabla\cdot\mathbb{T} + \mathbf{f}. \tag{2}$$

The elastostatic state is given by $\nabla\cdot\mathbb{T}+\mathbf{f} = 0$, which describes the shape of an elastic biomolecule at the balance of internal friction and external force. It is meaningful for the equilibrium state but may also be used for a non-equilibrium conformation. Assume that the elastic dynamics of biomolecules admits a time-harmonic solution, we have the following eigenvalue equation

$$\nabla\cdot\mathbb{T} + \mathbf{f} = -\rho\omega^2\mathbf{w}, \tag{3}$$

where ω is the angular frequency. Therefore, the diagonalization of operator $\nabla\cdot\mathbb{T} + \mathbf{f}$ in Eq. (3) for macromolecules produces eigenvalues and eigenvectors. The latter can be used to analyze and visualize the collective motion of macromolecules.

Consider a protein of N atoms with a conformation vector $(\mathbf{r}_1, \mathbf{r}_2, \cdots, \mathbf{r}_j, \cdots, \mathbf{r}_N) \in \mathbb{R}^{3N}$, where $\mathbf{r}_j \in \mathbb{R}^3$ is the position of jth atom. Let us denote $\|\mathbf{r}_i - \mathbf{r}_j\|$ the Euclidean distance between ith atom and the atom. We assume that the correlation between ith particle and the jth particle decays with respective to their Euclidean distance. We define an atomic rigidity index μ_i as

$$\mu_i = \sum_{j\neq i}^{N} w_{ij}\Phi(\|\mathbf{r}_i - \mathbf{r}_j\|; \eta_{ij}), \quad i \neq j,, \quad \forall i = 1, 2, \cdots, N \tag{4}$$

where η_{ij} are characteristic distances between particles, w_{ij} are particle-type related weights and $\Phi(\|\mathbf{r}_i - \mathbf{r}_j\|; \eta_{ij})$ is a real-valued monotonically decreasing correlation kernel. Typically, decaying radial basis functions can be used for the correlation kernel. The atomic rigidity index μ_i measures the rigidity or stiffness at ith atom or particle. The bulk modulus is correlated to the molecular rigidity, $\sum_i^N \mu_i$. A continuous atomic rigidity function is given by

$$\mu(\mathbf{r}) \quad = \quad \sum_j \mu_j \Psi(\|\mathbf{r} - \mathbf{r}_j\|), \quad \mathbf{r} \in \Omega_E, \tag{5}$$

where $\Psi(\|\mathbf{r} - \mathbf{r_j}\|)$ is a general interpolation kernel for scattered data [2].

For polyatomic molecules, one has $\mu_i > 0$. Therefore, we can define an atomic flexibility index

$$f_i = \frac{1}{\mu_i} \quad \forall i = 1, 2, \cdots, N. \tag{6}$$

Physically, atomic flexibility indices of a macromolecule must directly proportion to its B-factor $\{B_i\}$, the latter can be predicted by a standard linear regression [2].

The human body has three major types of proteins including globular proteins, fibrous proteins, and membrane proteins. It is well known that 65-90% of human cell mass is water. Structural proteins provide stiffness and rigidity to prevent biological material from flowing around. Most structural proteins are fibrous proteins including keratin, elastin and collagen. Keratin is found in human hairs and nails. Elastin enables the restoration of tissues after deformation. Collagen is a critical component of connective tissue such as knee cartilage. Some soluble globular proteins can play the role of structural proteins after polymerization. For example, some cytoskeletons are made up of polymerized actin or tubulin.

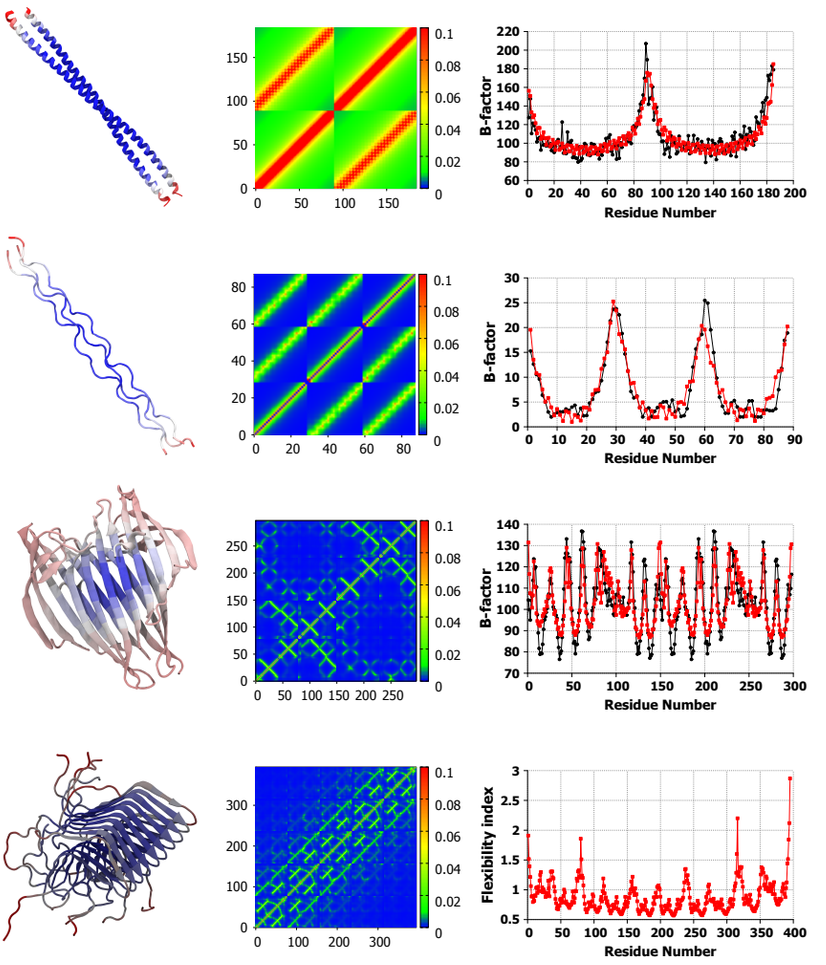

Figure 1: FRI analysis of structural proteins. The secondary structures are illustrated in the left column, from top to bottom: keratin (3NTU), collagen (1CAG), fibroin (3UA0) and amyloid fibrils (2RNM). Flexibility is analyzed by FRI with red for flexible and blue for rigid. The correlation maps computed by using the FRI are given in the middle column, generated with υ=2.0. The FRI prediction of B-factors (dots) are presented in the right column, and compared with B-factors from X-ray crystallography (squares) when they are available. B-factor prediction is calculated with optimal υ values of 1.0, 0.3 and 2.1 for 3NTU, 1CAG and 3UA0. Correlation coefficients for B-factor prediction for 3NTU, 1CAG and 3UA0 are 0.862 0.930 and 0.790. The last structure, 2RNM, is obtained by solid-state NMR and does not have experimental B-factors. All data is calculated by using υ=2.0 for this structure.

We consider a few structural proteins, i.e., keratin (3NTU), collagen (1CAG), fibroin (3UA0) and amyloid fibrils (2RNM) to illustrate our CEWAR model and FRI algorithm. Amyloid fibrils are associated with various neurodegenerative disorders, including Alzheimer's disease, due to their specific structural traits, e.g., aggregated misfolded beta sheets. We use the power-law correlation kernel

$$\Phi(\|\mathbf{r}_i - \mathbf{r}_j\|; \eta_{ij}) = \frac{1}{\|\mathbf{r}_i - \mathbf{r}_j\|^{\upsilon}}$$

in our simulations. Figure 1 depicts the secondary structures, correlation maps, and B-factors of the above-mentioned proteins in a coarse-grained representation. Correlation maps characterize the residue interactions. The predicted B-factors match the experimental data very well.

In Fig. 2, continuous atomic rigidity functions are projected onto the molecular surfaces of four structural proteins. Indeed, the rigidity varies dramatically from residue to residue, indicating the atomic dependence of the proposed elastic dynamics and elastostatic behavior.

3 CONCLUSIONS

We propose continuum elasticity with atomic rigidity (CEWAR) as a new multiscale elastic theory for theoretical modeling and computational analysis of excessively large macromolecules. The atomic rigidity information is obtained from a flexibility-rigidity index (FRI), which manifests the atomic topological connectivity in a macromolecule. We demonstrate capability of the FRI for correlation map analysis and B-factor prediction of a few structural proteins, which are particularly important to human body. The FRI is of $\mathcal{O}(N^2)$ in computational complexity and does not require matrix decomposition. Additionally, the continuous atomic rigidity functions of four structural proteins are constructed for being used in the CEWAR.

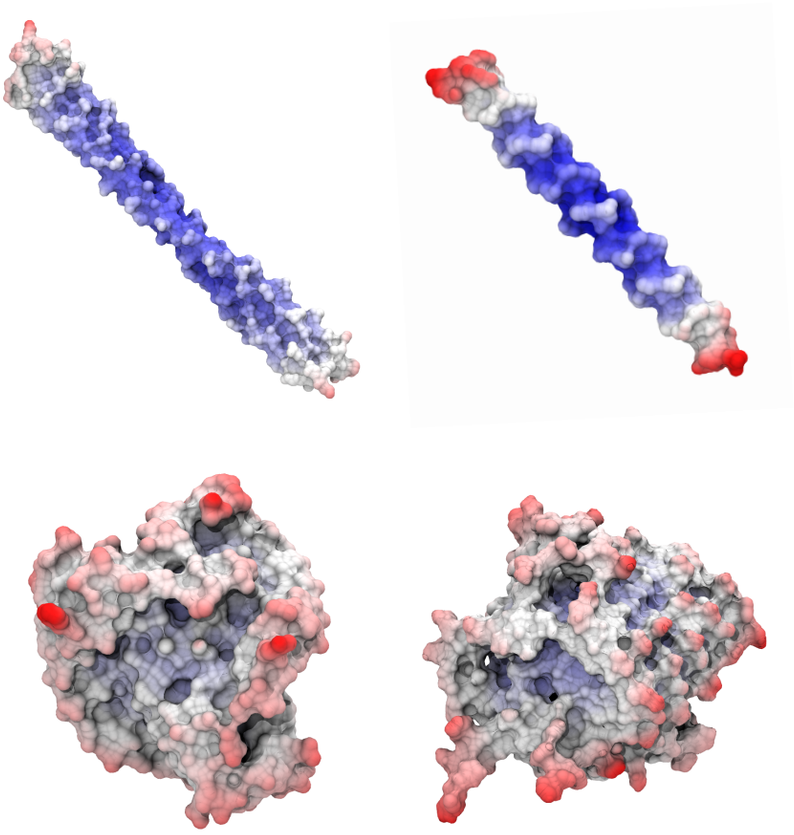

Figure 2: Atomic rigidity functions projected on the molecular surfaces of four structural proteins with red color for flexible regions and blue color for rigid regions. Proteins in the display are, from left to right and top to bottom, keratin (3NTU), collagen (1CAG), fibroin (3UA0) and amyloid fibrils (2RNM). The atomic rigidity functions are calculated using the power-law kernel with υ=1.0, 0.3, 2.1 and 2.0 for 3NTU, 1CAG, 3UA0 and 2RNM.

REFERENCES

[1] Guo-Wei Wei, Multiscale, multiphysics and multidomain models I: Basic theory, *Journal of Theoretical and Computational Chemistry*, 12(8), 1341006, 2013.

[2] K. L. Xia, K. Opron, and G. W. Wei. Multiscale multiphysics and multidomain models Flexibility and rigidity, *Journal of Chemical Physics*, submitted, 2013.

Aneurysm Modelling: From Basic Science to Clinical Translation II

3rd International Conference on Computational and Mathematical Biomedical Engineering – CMBE2013

16-18 December 2013, Hong-Kong

P. Nithiarasu and R. Löhner (eds)

A Method for Automated Flow Analysis in Intracranial Aneurysms

Jingfeng Jiang*, Kristin Flickinger*,

Michael Loecher, Patrick Turski** and Charles Strother****

*BME Department, Michigan Tech University, Houghton, MI, US, jjiang1@mtu.edu

** School of Medicine and Public Health, University of Wisconsin, Madison, WI, US

SUMMARY

We are developing methods for analysing and visualizing aneurysmal flow. Time-resolved three-dimensional (3D) velocity data in and around the intracranial aneurysm (IA) can be obtained from either phase-contrast Magnetic Resonance Angiography (PC-MRA) or "patient-specific" computational fluid dynamic (CFD) simulations. Custom software estimates hemodynamic parameters such as vortex core volume and kinetic energy. These relevant hemodynamic parameters will provide quantitative assessments of intra-aneurysmal hemodynamics, thereby potentially allowing improved clinical management of IAs. This report will summarize our recent progress and experience in data analysis and visualization of intra-aneurysmal flow.

Key Words: *blood flow, segmentation, intracranial aneurysm*

1. INTRODUCTION

An intracranial aneurysm (IA; also known as a cerebral aneurysm) is a pathological dilation at the vessel wall in the brain. The severe consequences of aneurysm rupture, the common occurrence of aneurysms in the adult population (4-7%), the frequent detection of aneurysms in asymptomatic people, the low statistical risk of aneurysm rupture (1% or less per year), the lack of reliable parameters predictive of the risk of aneurysm rupture, and the cost and risk of

aneurysm treatment combine to motivate the continued search for a method which would differentiate aneurysms likely to rupture from ones that have a low risk of rupture.

Recently, there has been significant interest in using PC-MRA techniques [1] and "image-based" CFD [2] to characterize intra-aneurysmal blood flow with the primary goal of searching for correlations between local hemodynamics and the risk of aneurysm rupture. However, visual assessment of 4D flow characteristics through pattern recognition using hundreds of cross-sectional images from multiple cardiac phases may impose an extensive burden on reviewing physicians. Extracting complex quantitative information will make this daunting task even more difficult to clinicians. To this end, the main objective of this study is to explore the feasibility of quantitative and automated assessments of intra-aneurysmal hemodynamics both for measured and simulated velocity data, thereby facilitating clinical utility of CFD and PC-MRA techniques.

2. Methods and Results

2.1 Implementation

As shown in Figure 1, the proposed automated flow analysis in IAs leverages on an open source platform (Vascular Modeling TookKit[3]) and involves multiple steps. These, along with our preliminary results, are briefly presented below.

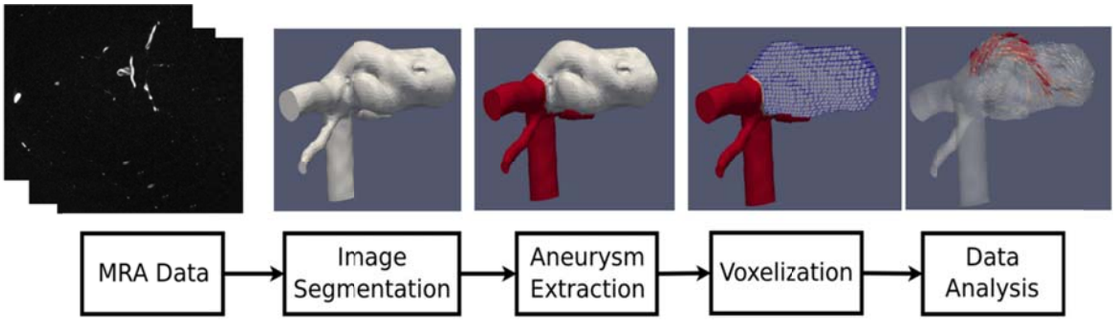

Figure 1 An illustration of five steps in the proposed approach.

As shown in Figure 1, given readily available three-dimensional medical imaging data, a 3D surface representation of the vessel was first generated using one of several imaging segmentation methods [4]. Then, a published method [5] was used to automatically isolate and extract the aneurysm sac (white color in the middle plot). In the fourth step, the isolated aneurysm sac was sealed at the orifice and converted to a binary mask that is spatially-registered with volumetric velocity data. The mask allowed us to analyze intra-aneurysmal velocity data in the fifth step. Of note, CFD-simulated velocity data typically located onto a unstructured grid. Therefore, resampling of CFD-simulated velocity data onto a rectilinear grid was performed.

Once the intra-aneurysmal velocity data were obtained, the classic Lambda2 method [6] was used to identify the vortex core region, *i.e*. a location containing a negative Lambda2 value belongs to a vortex core region. Therefore, for each and every voxel within the aneurysm sac, one

Lambda2 value was calculated. Based on a small negative threshold (*e.g.* 12.5% among all negative Lambda2 values), each voxel was categorized either inside or outside of the vortex core. A simple Marching-Cube algorithm was used to segment out the vortex core regions. It is worth noting that small islands among the segmented vortex cores were removed to improve the visualization and to simplify data analysis. Calculation of the kinetic energy within the aneurysm sac and the vortex core region(s) is straightforward.

2.2 Preliminary Results

The method has been successfully applied to 11 aneurysms (six experimental canine aneurysms [7] and 5 human subjects) selected from our internal database. PC-MRA data acquisition has been described in our previous publication [8]. Figure 2 shows two Basilar Artery tip terminal aneurysms, namely Aneurysms A and B, respectively. Both aneurysms are similar in shape and location as illustrated in Table 1. However, given the calculated kinetic energy values (with respect to the size), the flow was active in Aneurysm A, whereas the intra-aneurysmal flow was slow in Aneurysm B. Complete analysis of flow conditions will be presented in the conference.

While comparing the vortex core structures in Aneurysm A between ones obtained from a steady state CFD simulation and a cardiac-cycle average PC-MRA velocity field, we found that the extracted vortex cores exhibit quite different characteristics. Detailed analyses of this discrepancy are beyond the scope of this paper. Nevertheless, comparing the vortex core structure may offer an alternative way to compare intra-aneurysmal hemodynamics obtained from these two different methods.

Aneurysm	Kinetic Energy within Sac (millijoules)	Kinetic Energy within Vortex Core(s) (millijoules)	# of Vortex Core	Sac Volume (mm^3)	Volume of Vortex Cores (mm^3)
A	6.4	0.8	2	234.6	41.8
B	4.2	0.4	1	399.5	72.8

Table 1: Estimated hemodynamic and geometric parameters of two terminal BA-tip aneurysms.

3. CONCLUSIONS AND FUTURE WORK

We presented a technique for automated analysis of intra-aneurysmal flow. Based on this technique, different hemodynamic parameters derived from either simulated or measured velocity data as well as geometric parameters of the sac can be assessed. Although this technique probably only represents an alternative to other plausible approaches, it does, in our opinion, represents a feasible path to make intra-aneurysmal hemodynamic assessments more quantitative, thereby enabling studies and comparisons of large populations both initially and over time. Perhaps, more importantly, combination of geometric and hemodynamic information may further improve

predictions for rupture risk of IAs. This preliminary result is encouraging and we believe that the method warrants further clinical studies to explore its full clinical utility and significance.

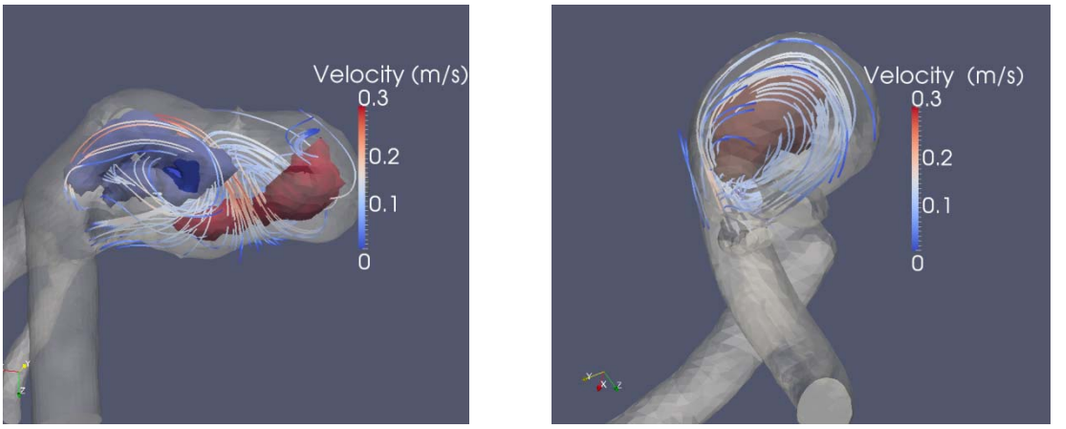

(a) (b)

Figure 2. Plots of streamlines of cardiac-cycle average velocity vectors in (a) Aneurysms A and (b) B, respectively. Streamlines were overlaid with extracted vortex cores: (a) blue and red colored, and (b) brown colored regions.

REFERENCES

[1] S. Meckel, A. F. Stalder, F. Santini, E. W. Radu, D. A. Rufenacht, M. Markl, and S. G. Wetzel, "In vivo visualization and analysis of 3-D hemodynamics in cerebral aneurysms with flow-sensitized 4-D MR imaging at 3 T," *Neuroradiology*, vol. 50, pp. 473-84, Jun 2008.

[2] J. R. Cebral, M. A. Castro, J. E. Burgess, R. S. Pergolizzi, M. J. Sheridan, and C. M. Putman, "Characterization of cerebral aneurysms for assessing risk of rupture by using patient-specific computational hemodynamics models," *AJNR Am J Neuroradiol*, vol. 26, pp. 2550-9, Nov-Dec 2005.

[3] L. Antiga and D. A. Steinman, "Robust and objective decomposition and mapping of bifurcating vessels," *IEEE Trans Med Imaging*, vol. 23, pp. 704-13, Jun 2004.

[4] D. L. Pham, C. Xu, and J. L. Prince, "Current methods in medical image segmentation," *Annu Rev Biomed Eng*, vol. 2, pp. 315-37, 2000.

[5] J. Jiang and C. M. Strother, "Interactive decomposition and mapping of saccular cerebral aneurysms using harmonic functions: its first application with "patient-specific" computational fluid dynamics (CFD) simulations," *IEEE Trans Med Imaging*, vol. 32, pp. 153-64, Feb 2013.

[6] J. Jeong and F. Hussain, "On the identification of a vortex," *Journal of Fluid Mechanics*, vol. 285, pp. 69-94, 1995.

[7] C. M. Strother, V. B. Graves, and A. Rappe, "Aneurysm hemodynamics: an experimental study," *AJNR Am J Neuroradiol*, vol. 13, pp. 1089-95, Jul-Aug 1992.

[8] S. Kecskemeti, K. Johnson, Y. Wu, C. Mistretta, P. Turski, and O. Wieben, "High resolution three-dimensional cine phase contrast MRI of small intracranial aneurysms using a stack of stars k-space trajectory," *J Magn Reson Imaging*, vol. 35, pp. 518-27, Mar 2012.

3rd International Conference on Computational and Mathematical Biomedical Engineering – CMBE2013
16-18 December 2013, Hong-Kong
P. Nithiarasu and R. Löhner (eds)

CFD assessment of small-sized cerebral aneurysm rupture risk: case-control study

R. Ouared*, O. Brina, P. Bouillot*, K.O. Lovblad**, V.M. Pereira****
*University of Geneva, 7 route de Drize CH-1227 Carouge, rafik.ouared@unige.ch
**Hospital of Geneva, Gabriel-Perret-Gentil 4 1205 Geneva,
olivier.brina@hcuge.ch, vitor.mendespereira@hcuge.ch

SUMMARY

Since decades, endeavors were made to signing out the pre-rupture state of the cerebral aneurysms. Several potential geometry and hemodynamic predictors have been defined and studied worldwide, but no one could be used so far by the medical practitioners for effective patient care management. Such a pitfall was hard to avoid, because most of the studies were suffering from the lack of predictive power, statistics, arbitrariness and oversimplification of predictor definitions, along with the hardly ever imaging of pre-rupture aneurysm forms. In this work, we report the preliminary CFD results on aneurysm tear risk assessment based on a case-control study involving 4 cases and 20 controls in 4 different cerebral locations. The aneurysm pre-rupture forms of the cases were all imaged. The size of the ruptured aneurysms was unexpectedly found to be less than 5mm. Unlike in previous studies, single scalar threshold-based metrics have all failed to significantly sign tear in our sample. Therefore, we defined and fitted a wall shear stress (WSS) empirical cumulative distribution function (WSScdf) to compute the set of aneurysm wall shear stress percentiles. Independantly of their locations and hemodynamic regimes, cases were all showing a common balanced figure of their WSS percentiles. Such result suggests the existence of a "rupture-specific" WSS distribution that may precursively sign the likelihood of aneurysm tear, unlike the more unbalanced running low or high WSS distribution hypothesis. Unlike WSS, neither tear signature was observed for relative WSS, WSS gradient and OSI cdfs.

Key Words: *blood flow, wall shear stress (WSS), aneurysm. WSS percentiles, WSS cumulative distribution function (WSScdf). Logistic regression analysis, WSS gradient, OSI, relative WSS.*

1 INTRODUCTION

Rupture risk assessment is essentially based upon factors identified through epidemiological studies, including aneurysm size, site and previous family SAH history. In particular, it is suggested to treat conservatively the aneurysms that are smaller than 7mm on anterior circulation. In our aneurysm clinic, four patients harboring small saccular aneurysms (size less than 5mm) ruptured while being monitored for conservative treatment. Since these aneurysms' shapes were documented with 3D imaging acquired before SAH, a case-control study was designed to evaluate the rupture odds of such small aneurysms and a novel predictor related to wall shear

stress (WSS) percentiles function was explored.

2 MAIN BODY

The cases were patients with small saccular IAs (less than 5mm) who ruptured during follow up. The controls included patients with unruptured saccular IAs. The aneurysms were located, respectively, at the middle cerebral artery (MCA), at the basilar tip (BAT), on the posterior inferior cerebellar artery (PICA) and on the anterior communicating artery (AcomA) (figure 1, left column). For each case, we selected randomly a set of 5 control patients (figure 1, right columns) harboring unruptured IAs who were monitored for a year. The four aneurysm locations in Figure 1. are, sketched from top to bottom: MCA, BAT, PICA and AcomA. Colors represent the logarithmic scale of WSS between 1.0 and 10 Pa.

Figure 1: aneurysm geomety models

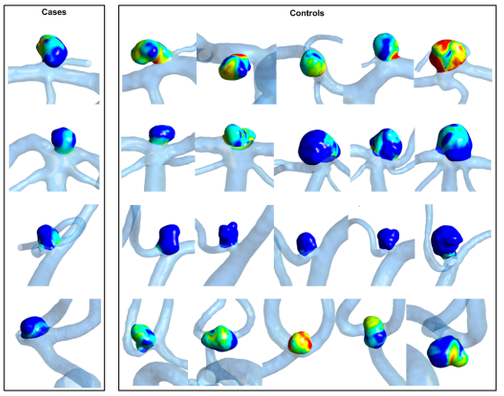

The triangulated surfaces of the patient-specific vessels were reconstructed from the 3-dimensional rotational angiography images (Allura FD20, Philips Healthcare, Best the Netherlands) using Aneufuse toolkit. Then, ANSYS ICEM was used to produce a high-resolution computational unstructured mesh. The mesh element number ranged between 3.3 and 5.6 million, with mesh density larger than 2000 elements/mm^3. The ANSYS CFX commercial solver was used to simulate blood flow as a Newtonian fluid on the computational mesh. We used generic 1D pulsatile boundary conditions. The modeling parameters were the following: a/density: 1066 kg/m3, b/ viscosity: 0.0035 Pa.s, c/ Reynolds number: 350-520, d/ Womersley number: 1.8-2.6, e/ cycle: 0.8s, f/ number of cycles: 2.

Since none of the geometry and hemodynamic factors could predict the thrombosis issues of our cases and control [1,2,3], we evaluated at every spatial element of the aneurysm the WSS averaged over a cycle, and fitted the wall shear stress cumulative distribution function (WSScdf) in the aneurysm with a set of 18 ordered WSS percentiles. Then, we determined the "prone-to-rupture" range by fitting for cases, the optimal WSS empirical cumulative distribution function along with the related 95% confidence interval (CI) with the following power function model:

$$f(x) = \frac{1}{1 + \exp\left[-a\left(x^b - c\right)\right]}$$

where x represents the WSS percentile and f(x) represents WSScdf. The three parameters a, b, c are required to take into account the saturation, the raising edge and the median level of the function, respectively. Cases are expected to have their WSScdf representation curve largely within the prone-to-rupture zone, unlike the controls. Since the fraction of WSScdf curve in the risky zone is directly correlated to rupture odds, a variable Np was set to count the number of WSScdf cutoff points intersecting with this zone. Case-control rupture odds were evaluated with univariate logistic regression analysis based on variable Np.

Figure 2 shows in red, the "prone-to-rupture" 95% CI ($p<0.07$) fitted WSScdf corresponding to the model with parameters: a=15.3, b=0.07, and c=0.93 [5]. Thus, the related average percentiles are in ascending order: 30% for WSS<=0.2Pa, 50% for WSS<=0.4Pa, 70% for WSS<=0.8Pa, 80% for WSS<=1.2Pa, 85% for WSS<=2.0Pa, 90% for WSS<=3Pa, and slow uniform incremental increase for WSS larger than 3 Pa up to local WSS maximum. The circles show the controls all spread out the risky range. Univariate logistic regression analysis based on variable Np resulted in log odds ratio equal to b0=-8.13+-1.95 and b1=0.62+-0.16 (mean+-SD), respectively. The statistical significance of likelihood change of rupture was p=0.047. Case-control odds ratio was evaluated at Np=13.9 to be larger than 24+-7 (mean+-SD) passed the median risk line. Np threshold suggests that rupture becomes certain if ~70% of the whole WSScdf curve intersects with the "prone-to-rupture" range. The test performance is: sensitivity=0.90 [63.7%,100%], specificity=0.97 [81.8%,100%], accuracy: ~0..92, positive predictive value: ~75%, and negative predictive value: ~97%.

Figure 2: the WSScdf for cases and controls.

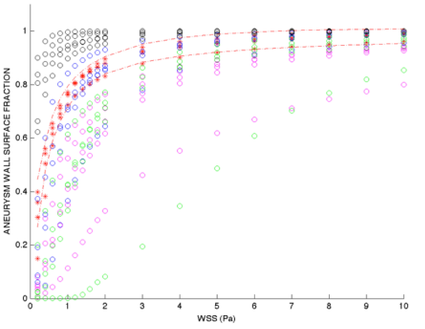

3 CONCLUSIONS

This case-control designed study shows that WSScdf would potentially sign small-sized aneurysm tear with high positive and negative predictive values. This result matches rather well with Goubergrits et al [4] finding who evoked the possibility of high and low WSS cohabitation with large areas of steep WSS transition that might enhance degenerative changes at the wall [5]. In this case, the 50% percentile would correspond to WSS smaller than 0.4Pa. It is foreseeable that the challenge for CFD in the coming years would be to detect an increasing number of potentially dangerous small-size lesions that may rupture despite being resumably of low risk according to epidemiological studies. Indeed, large aneurysms are rarely followed conservatively because their estimated rupture risk is not questionable and the therapeutic decision can be taken without any ambiguity.

REFERENCES

[1] J.R. Cebral, F. Mut, J. Weir and C. Putman, Quantitative characterization of the hemodynamic environment in ruptured and unruptured brain aneurysms, *American Journal of Neuroradiology*, **32**, 145-151, 2011.

[2] H. Takao, Y. Murayama, S. Otsuka, Y. Qian, A. Mohamed, S. Masuda, M. Yamamoto and T. Abe, Hemodynamic differences between unruptured and ruptured intracranial aneurysms during observation, *Stroke, a journal of cerebral circulation*, **43**, 1436-1439, 2012.

[3] S. Dhar, M. Tremmel, J. Mocco, M. Kim, J. Yamamoto, A.H. Siddiqui, L.N. Hopkins and H. Meng, Morphology parameters for intracranial aneurysm rupture risk assessment, *Neurosurgery*, **63**, 185-197, 2008.

[4] L. Goubergrits, J. Schaller, U. Kertzscher, N. van den Bruck, K. Poethkow, C. Petz, H.C. Hege and A. Spuler, Statistical wall shear stress maps of ruptured and unruptured middle cerebral artery aneurysms, *Journal of the Royal Society*, **9**, 677-688, 2012.

[5] V.M. Pereira et al, Wall shear stress distribution of small aneurysms prone to rupture: a case-control study, Submitted to *Medical Journal*, 2013.

3rd International Conference on Computational and Mathematical Biomedical Engineering – CMBE2013
16-18 December 2013, Hong-Kong
P. Nithiarasu and R. Löhner (eds)

In vivo validation of CFD simulations

C. Doenitz*, C. Palm, J. Platz° , V. Seifert° and A. Brawanski***

* University Medical Center Regensburg, Department of Neurosurgery, Franz-Josef-Strauss-Allee 11, 93051 Regensburg, Germany, christian.doenitz@ukr.de

** Regensburg University of Applied Sciences, Regensburg - Medical Image Computing (Re-MIC), Regensburg, Germany

° Johann Wolfgang Goethe-University Frankfurt, Department of Neurosurgery, Frankfurt am Main, Germany

SUMMARY

Intraoperative indocyanine green video angiographies of aneurysms show distinct flow patterns that confirm the results of computational fluid dynamics and contribute to the value of virtual flow simulations.

Key Words: *blood flow, computational fluid dynamics, intracranial aneurysm, indocyanine green video angiography*

1. INTRODUCTION

Computational fluid dynamics (CFD) is increasingly being used for modelling hemodynamics in intracranial aneurysms. These simulations are used to study the formation, growth and rupture of cerebral aneurysms and may contribute to assess the risk of rupture and to improve the treatment.[1,2]
While CFD techniques are well established, the need for validation of simulated results remains. We used intraoperative indocyanine green video angiography (ICG) in aneurysm surgery to directly visualize flow patterns and compared them to the CFD results of these aneurysms.

2. METHODS

Indocyanine green video angiography (ICG):

Indocyanine green is a fluorescent agent. ICG video angiography is a useful method for monitoring blood flow in the exposed vessels during open neurosurgery [3]. A microscope with a special filter and infrared excitation light to illuminate the operating field was used. The intravascular fluorescence was imaged with a video camera attached to the microscope. Videos from ICG video angiography during surgery of middle cerebral aneurysms were screened for visible flow patterns. Images of these sequences were extracted frame-by-frame using conventional video capture software. The frames were analyzed with the ImageJ software v 1.47 (http://rsbweb.nih.gov/ij/). To visualize the flow patterns we used colour-coded point of time of maximum gradient using the HSV colour model.

Computational fluid dynamics (CFD):

3D models of the middle cerebral aneurysms were reconstructed from preoperative 3D angiography using the current version of AneuFuse software v 2.2 (Supercomputing Solutions, Bologna, Italy). The software, which was developed within the @neurIST project, was used to reconstruct the vessel surfaces, create the model and set up the hemodynamic analysis. The solvers used within AneuFuse to solve the fundamental equations describing the blood flow behaviour were ANSYS-ICEM and ANSYS-CFX v 14.5 (Ansys, Inc., Canonsburg, PA, USA). For post-processing visualization of the results and comparison to the ICG-video analyses we used Avizo Wind 3D analysis software v 7.1.1 (Visualization Sciences Group SAS, USA).

3. RESULTS

ICG video angiography revealed meaningful flow patterns in five of eight cases. These flow patterns could be visualized in a single image by analyzing the maximum gradient of brightness in all of these five cases.
The streamline patterns of the CFD simulations correlated well with the flow seen in the ICG video angiography in all cases. The main streamlines, vortices and impingement points could be identified depending on the intraoperative angle of view.

The example (Fig. 1) shows a reconstructed 3D model of a middle cerebral artery aneurysm from 3D angiography (A). The analyzed ICG video angiography image

(B) shows the main flow patterns. Anatomical overlay of model and intraoperative video image (C) reveals the correlation between observed and simulated flow patterns (D).

Fig. 1

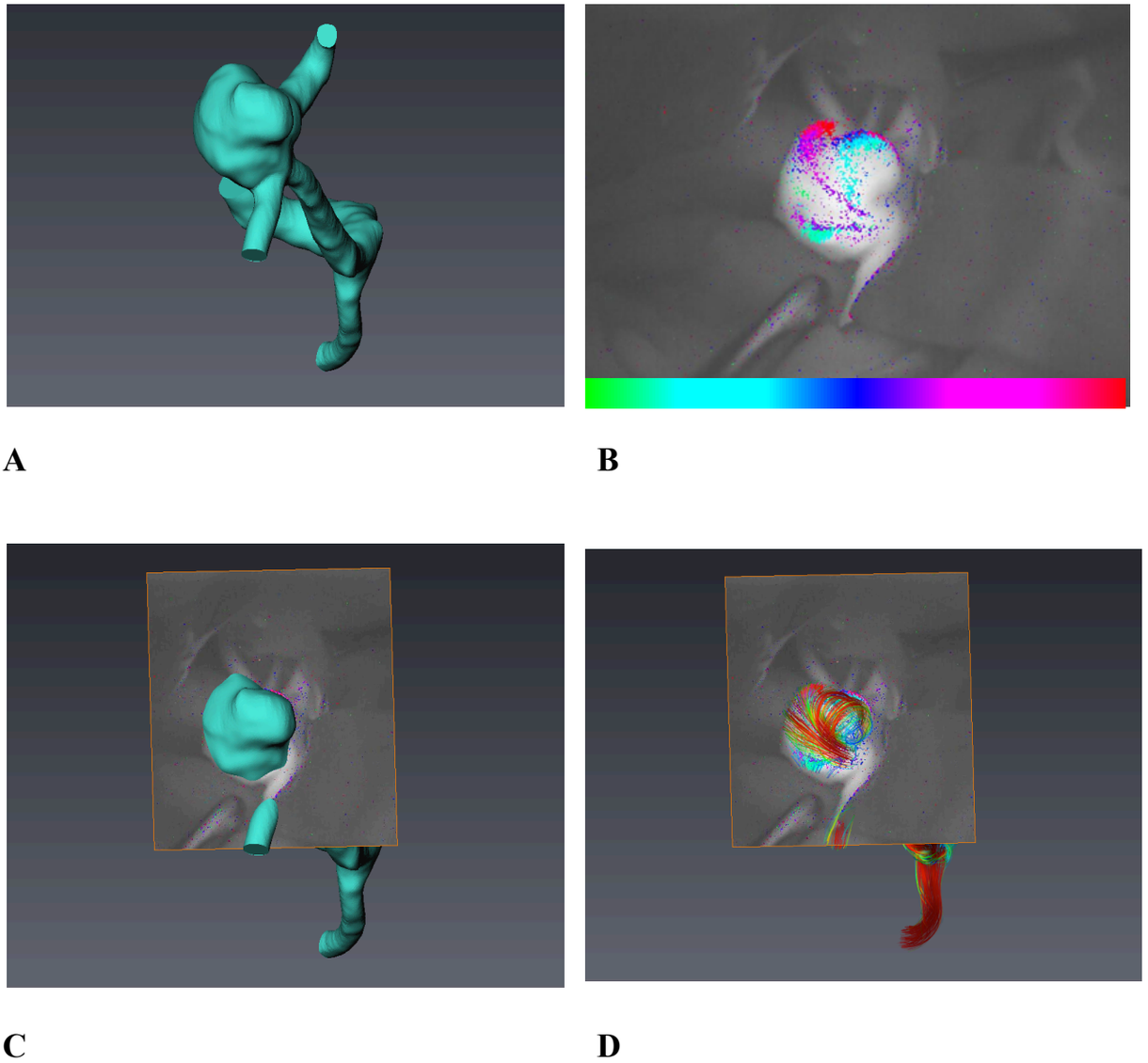

A **B**

C **D**

4. CONCLUSIONS

Validation of computational fluid dynamics is crucial for the scientific value and acceptance of flow simulations. We present a new tool for direct observation of in vivo flow patterns that can help to understand and confirm the influence of various variables on CFD simulations.

REFERENCES

[1] Byrne G, Mut F, Cebral J. Quantifying the Large-Scale Hemodynamics of Intracranial Aneurysms. *AJNR Am J Neuroradiol. 2013 Aug 8.*

[2] Russell JH, Kelson N, Barry M, Pearcy M, Fletcher DF, Winter CD. Computational Fluid Dynamic Analysis of Intracranial Aneurysmal Bleb Formation. *Neurosurgery. 2013 Aug 13*

[3] Oda J, Kato Y, Chen SF, Sodhiya P, Watabe T, Imizu S, Oguri D, Sano H, Hirose Y. Intraoperative near-infrared indocyanine green-videoangiography (ICG-VA) and graphic analysis of fluorescence intensity in cerebral aneurysm surgery. *J Clin Neurosci. 2011 Aug;18(8):1097-100*

3rd International Conference on Computational and Mathematical Biomedical Engineering – CMBE2013
16-18 December 2013, Hong-Kong
P. Nithiarasu and R. Löhner (eds)

Hemodynamic and clinical study of Y-stents for treatment of cerebral aneurysms

Kenichi Kono and Tomoaki Terada
Department of Neurosurgery, Wakayama Rosai Hospital
93-1 Kinomoto, Wakayama, 640-8505, Japan
E-mail (Kenichi Kono): vyr01450@gmail.com

SUMMARY

Y-stent-assisted coil embolization has been performed for wide-necked bifurcation aneurysms. There are two types of intracranial stents: open-cell and closed-cell stents. Y-stent with double closed-cell stents causes narrowed structure. In clinical fields, there is controversy whether narrowed structure is beneficial or harmful. To address this issue, we perform computational fluid dynamics (CFD) simulations using a patient-specific silicone model and Y-stent geometry obtained by micro-computed tomography. In addition, we reviewed four Y-stent cases among 40 consecutive aneurysms treated with stent-assisted coil embolization in our hospital. Results showed that hemodynamic effects in Y-stents may reduce recanalization rates but may increase risk of thromboembolic complications. We believe that this type of research with combinations of CFD and clinical study will become more important to make CFD simulations clinically useful.

Key Words: *Y-stent-assisted coil embolization, closed-cell stent, open-cell stent, computational fluid dynamic simulations, hemodynamics, recanalization, thromboembolic complication.*

1 INTRODUCTION

Y-stent-assisted coil embolization has been performed for complex bifurcation aneurysms [1]. There are two types of stents: open-cell and closed-cell stents. In most Y-stent cases, the second stent is deployed through the interstices of the first stent (crossing Y-stent). Use of double closed-cell stents causes narrowing of the second stent through the interstices of the first stent, while using an open-cell stent as the first stent can avoid this effect of narrowing. In our neurosurgical field, there is controversy whether narrowed structure of Y-stents with closed-cell stents is beneficial or harmful. To address this issue, we preformed CFD simulations and reviewed our Y-stent cases.

2 METHODS

2.1. CFD simulations

A rigid silicone block model of a bifurcation aneurysm was created based on an asymmetric basilar tip aneurysm in a patient with a maximum diameter of 8 mm (Fig. 1). We deployed closed-cell stents, Enterprise (Cordis Neurovascular, Miami, FL, USA), in the silicone model in the following 7 different configurations: single stent placement

from the basilar artery to the right or left posterior communicating artery (PCA), non-overlapping Y-stent, horizontal stent, kissing Y-stent (double stent placement in a parallel fashion), and 2 different crossing Y-stents with a narrowed structure. In one crossing Y-stent, "crossing-Y (R to L)", the first stent was deployed into the right PCA and the second stent was placed into the left PCA through the interstices of the first stent. In another crossing Y-stent, "crossing-Y (L to R)", the order of stent placement was the opposite. Selected configurations of stents are shown in Figure 1.

Stents in the silicone model were scanned by micro-CT. Using an engineering design software, 3-matic (Materialise NV, Leuven, Belgium), we constructed 9 models, including no stent and 8 different configurations of stents (7 stents plus 1 virtual stent): "no-stent", "R-stent", "L-stent", "non-overlapping Y", "virtual-Y", "horizontal", "kissing-Y", "crossing-Y (R to L)", and "crossing-Y (L to R)". We created the "virtual-Y" stent by fusion of 2 single stents, "R-stent" and "L-stent". The "virtual-Y" stent did not have a narrowed structure.

We performed pulsatile CFD simulations in a similar manner as we described previously using ANSYS CFX (ANSYS Inc., Canonsburg, PA, USA) [2]. The fluid domains were meshed to create finite volume tetrahedral elements. The number of elements in each model ranged from approximately 1,800,000 to 2,500,000, which was confirmed to be adequate to calculate the velocity and WSS by creating meshes of finer grid densities.

2.2. Clinical cases of Y-stents in our hospital

Between July 2010 and October 2012, we treated 40 consecutive aneurysms with stent-assisted coil embolization using Enterprise closed-cell stents in our hospital. There were 36 unruptured aneurysms, four chronic or delayed ruptured aneurysms, and no acute ruptured aneurysms. There were four patients with crossing Y-stent cases that were all treated for basilar tip aneurysms. The rest of the 36 patients were treated with a single stent. Patients were divided into two groups: the single stent group (n=36) and the Y-stent group (n=4).

In the single stent group, patients were pretreated with double antiplatelet agents, 100 mg aspirin and 75 mg clopidogrel, 1 week before the procedure, or were loaded with 300 mg aspirin and 300 mg clopidogrel 4 days before the procedure. In the Y-stent group, patients were pretreated with triple antiplatelet agents, 100 mg aspirin, 75 mg clopidogrel, and 200 mg cilostazol, 1 week before the procedure.

We assessed the following factors for statistical analysis: age, sex, aneurysm location (anterior or posterior circulation), aneurysm shape (saccular or fusiform), aneurysm size, neck size, and maximum and minimum size of parent vessels covered by a stent. Statistical analysis was performed using SPSS version 20 (IBM Corp., Armonk, NY, USA). Fisher's exact test or the Mann–Whitney U test was used. Each hypothesis was tested with a two-tailed analysis. The level of significance was set at $P<0.05$.

3 RESULTS

3.1. CFD simulations

Cycle-averaged velocity and WSS in the aneurysm were reduced because of stent placement in the following order: single stent (19% reduction in cycle-averaged velocity) < non-overlapping Y-stent (29%) < virtual Y-stent (32%) < horizontal stent (39%) <

kissing Y-stent (48%) < crossing Y-stent (54%). Comparing with virtual-Y without narrowed structures, crossing Y-stents with narrowed structures redirected impingement flow into the distal vessels because of lowered porosity of stents (data not shown).

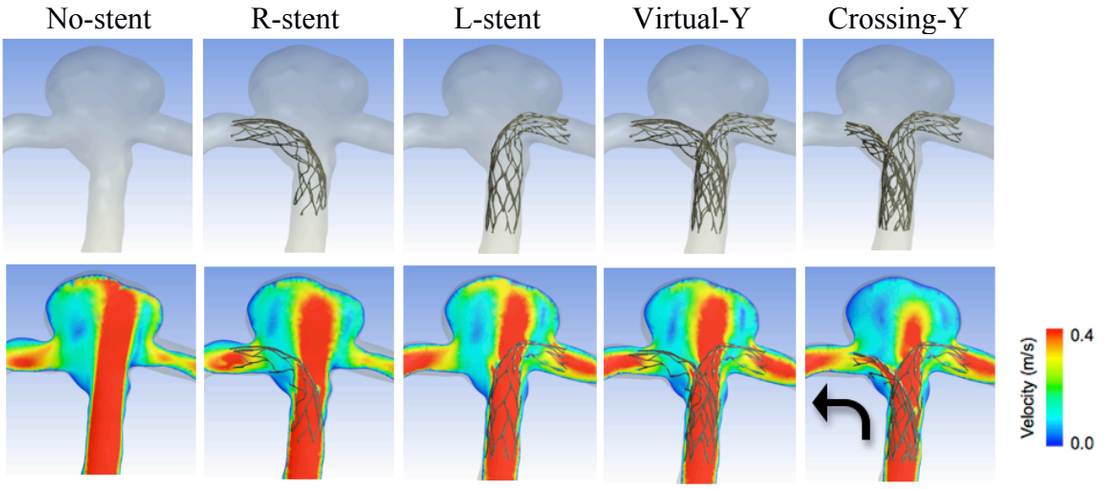

Figure 1. Contours of flow velocity on coronal sections.

3.2. Clinical cases of Y-stents in our hospital

There were two cases of symptomatic complications (2/40, 5%) during the peri-procedural and follow-up period: one transient ischemic attacks and one infarction in two patients. Both thromboembolic complications occurred in the Y-stent group, and a Y-stent was the only significant factor for symptomatic or thromboembolic complications (P=0.008; Fisher's exact test) (Table 1). Despite of these complications, the two patients recovered and were discharged without any neurological deficits. All 40 patients were neurologically intact at the mean follow-up periods of 31 months.

Table 1. Thromboembolic complications

	Thromboembolic complications		
	Negative (n=38)	Positive (n=2)	*P*
Age (years)	61±10	62, 70	0.437
Female sex (%)	23 (61)	2 (100)	0.519
Aneurysm location	13/25		0.550
Anterior circulation (%)	13 (34)	0 (0)	
Posterior circulation (%)	25 (66)	2 (100)	
Aneurysm shape			0.533
Saccular (%)	24 (63)	2 (100)	
Fusiform (%)	14 (37)	0 (0)	
Aneurysm size (mm)	10.4±5.3	7.4, 12.3	0.950
Neck size (mm)	8.6±4.5	8.3, 11.9	0.306
Maximum size of parent vessels (mm)	3.7±0.9	2.9, 3.1	0.162
Minimum size of parent vessels (mm)	3.1±0.9	1.4, 2.0	0.181
Stent configurations			**0.008**
Single stent (%)	36 (95)	0 (0)	
Y-stent (%)	2 (5)	2 (100)	

4 DISCUSSION

In the hemodynamic study, while we used vascular-specific conformed stent geometry obtained by micro-CT, in most of the previous studies, stents were virtually conformed to fit into a parent vessel lumen and deployed across an aneurysm neck. Because the geometry and porosity of stents change by the vascular geometry and radius of vessels, virtual deployment is not appropriate for reproducing the real geometry of stents deployed in vessels. Our study shows that changes in porosity of stents are important for hemodynamics due to stent placement. Among the 8 different configurations used in our study, crossing Y-stents showed the strongest reduction in flow because of the narrowed structures, which lowered porosity of stents and redirected flow. The narrowed structures are unique to closed-cell stents. It seems that Y-stents with closed-cell stents may be desirable treatments because it may reduce recanalization rates. However, the CFD simulations provided us only hemodynamic aspects of Y-stents. In clinical cases, we need to consider other aspects such as ease of stent delivery, wall apposition of stents, patient conditions, possible complications, and so on.

In Y-stent cases in our hospital, we experienced significantly higher thromboembolic complication rates even though we used triple antiplatelet agents. This suggests that strong hemodynamic effects of Y-stents with closed-cell stents may increase thromboembolic complications owing to the narrowed structures. Therefore, we cannot simply conclude that Y-stent-assisted coil embolization with closed-cell stents can be the first-line treatment for bifurcation aneurysms from our CFD study. Although, one large-scale study of Y-stent cases (n=183) showed 2.7% peri-procedural complication rates [3], at the moment, we consider that Y-stents with closed-cell stents may be limited to complex or recanalized aneurysms under appropriate use of antiplatelet agents.

5 CONCLUSIONS

In hemodynamic study by CFD simulations, narrowed structure with closed-cell stents in Y-stents lowered porosity of the stent, which redirected impingement flow into distal vessels. This may be a desirable reconstruction of flow hemodynamics and may decrease recanalization rates. In our clinical Y-stent cases, thromboembolic complications occurred significantly higher than single-stent cases. This may be because of stronger hemodynamic effects. Thromboembolic complication may be reduced with appropriate use of antiplatelet agents. From both CFD and clinical study, we conclude that Y-stent-assisted coil embolization may be an optional treatment for selected cases such as complex or recanalized aneurysms.

REFERENCES

[1] Fargen KM, Mocco J, Neal D, et al. A Multicenter Study of Stent-assisted Coiling of Cerebral Aneurysms Using a Y-configuration. Neurosurgery. 2013 Jun 14. DOI: 10.1227/NEU.0000000000000015

[2] Kono K, Fujimoto T, Shintani A, Terada T. Hemodynamic characteristics at the rupture site of cerebral aneurysms: a case study. *Neurosurgery.* 71, E1202-1209, 2012

[3] Yavuz K, Geyik S, Cekirge S, Saatci I. Double Stent-Assisted Coil Embolization Treatment for Bifurcation Aneurysms: Immediate Treatment Results and Long-Term Angiographic Outcome. *AJNR Am J Neuroradiol.* 2013 May 16.

3rd International Conference on Computational and Mathematical Biomedical Engineering - CMBE2013
16-18 December 2013, Hong-Kong
P. Nithiarasu and R. Löhner (Eds.)

Hemodynamic comparison for a giant cerebral aneurysm treated by coils embolization and flow diverter implantation

Shengzhang Wang*, Xinjian Yang, Xiangkun Liu*****
*Department of Mechanics and Engineering Science, Fudan University, Shanghai 200433, China, szwang@fudan.edu.cn
**Department of Interventional Neuroradiology, Tiantan Hospital, Beijing 100050, China
***Shanghai MicroPort Medical (Group) Co., Ltd., Shanghai 201203, China

SUMMARY

Coils embolization and flow diverter implantation are two options to treat a giant cerebral aneurysm, but there exists controversy for treating the giant aneurysm with interventional ways. The models of a giant cerebral aneurysm treated virtually by coils embolization or flow diverter implantation are constructed and the blood flow in the treated aneurysms is simulated numerically. By analyzing the variations of the hemodynamics factors related to rupture and recanalization of the treated aneurysm, the conclusions are drawn that the giant aneurysm treated by flow diverter has higher rupture risk and treated by coil embolization has higher recanalization risk.

Key Words: *giant cerebral aneurysm, hemodynamics, numerical simulation, flow diverter.*

1 INTRODUCTION

Cerebral aneurysms are pathologic dilations of the cerebral arteries generally occurred in the anterior and posterior regions of the circle of Willis. Rupture of a cerebral aneurysm causes subarachnoid hemorrhage with an associated high mortality and morbidity rate. The mechanisms responsible for the initiation, evolution and rupture of cerebral aneurysms are not well understood until now. However, it is widely accepted that hemodynamic characteristics play an important role in the progression of aneurysms [1].

A giant cerebral aneurysm is defined as one larger than 25 mm in diameter. Giant aneurysms are thought to represent about 5-8% of all cerebral aneurysms, and they are considered to have higher rupture risk than the aneurysms smaller than 25 mm in diameter and need to be treated in clinic when they are recognized [2].

Both coils embolization and flow diverter implantation are interventional treatments to occlude the aneurysms. But there still exists controversy for treating the giant aneurysm with interventional ways because the giant aneurysm with coils embolization has higher recanalization risk or the giant aneurysm with flow diverter implantation has higher rupture risk.

In this study, the models of a giant cerebral aneurysm treated by coils of flow diverter were constructed, the blood flow in the treated aneurysms were simulated and the variations of the hemodynamic factors related to the recanalization or rupture of the treated giant aneurysm were analyzed, and the rupture risk and the recanalization risk for the treated giant aneurysm were compared.

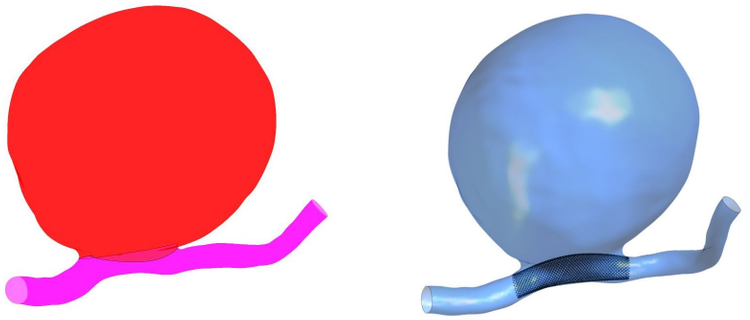

Figure 1: A giant aneurys located at internal carotid artery and the size of the aneurysm is height 27.5mm and width 27.8 mm. The left is the aneurysm model treated by coils embolization, and the right is the model treated by flow diverter implantation.

2 MATERIALS AND METHODS

A giant aneurysm located at the internal carotid artery was treated virtually by coils embolization and flow diverter implantation. The giant aneurysm treated by coils was modeled as a porous media [3], and the flow diverter (Tubridge, produced by Shanghai MicroPort Medical Co., Ltd.)was implanted into the giant aneurysm by finite element method [4] as showed in Figure 1. Assumed that the flow diverter implantation and coils embolization had the same effect to prevent the blood flow into the giant aneurismal sac and the treated aneurysms had the same cross-neck flow rate. The parameters of the porous media for the coiled aneurysm were pack density 0.21 and the permeability coefficient 0.00088 m^2.

The computational grids of three aneurysm models (untreated, treated by coils and treated by flow diverter) were generated by Ansys ICEM-CFD, and the meshes composed by tetra elements were specified in terms of the size as follows: 0.2mm was set to the max element of the aneurysm, 0.02mm was set to the max element near the metal wire of the flow diverter, and the element number of per cubic millimeter in the three model was more than 1800.

The vessel wall was assumed to be rigid and without deformation. The pulsatile velocity profile imposed at the inlet were represented by Fourier series. The boundary condition was traction-free at the outlets and was no-slip on the wall of the vessel and struts of the flow diverter. The blood flow in the three models was simulated by the commercial computational fluid dynamics software Ansys CFX 12.1 and the results were processed and visualized by Ansys CFD-Post.

3 RESULTS AND DISCUSSION

After numerical simulation, the flow pattern and the hemodynamic factors such as time average wall shear stress (TAWSS), oscillatory shear index (OSI), pressure pulse, energy loss in the two models of the giant aneurysm were calculated.

Figure 2 shows the streamlines and the velocity contours in the axial cross section of the two models, and it is observed that the flow pattern in the giant aneurysm treated by flow diverter is more complex than treated by coils.

Figure 3 shows TAWSS and OSI on the two models. The distributions of TAWSS on the two models are similar, and the maximum TAWSS of the two models locates at the aneurysmal neck and

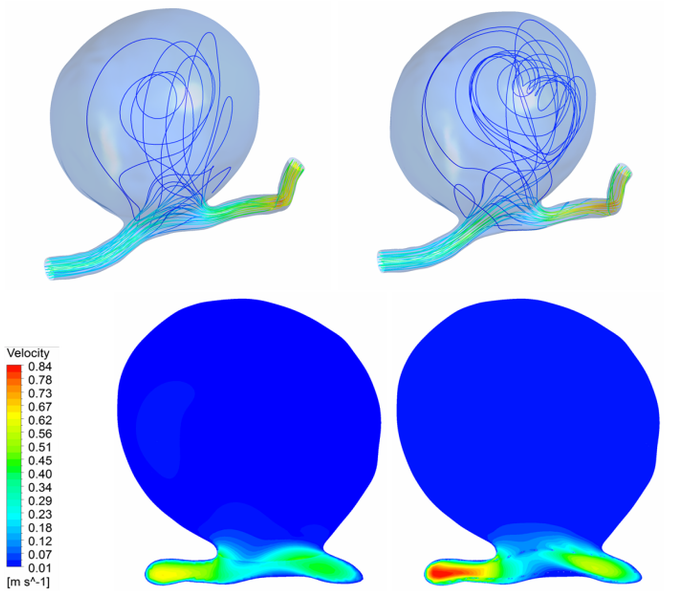

Figure 2: Streamlines and velocity contours in the axial cross sections at systolic peak. The left column is the aneurysm treated by coils embolization and the right column is the aneurysm treated by flow diverter implantation.

Table 1: Pressure pulse and energy loss of the treated aneurysm by coils or flow diverter

	Coils	Flow Diverter
Pressure Pulse (Pa)	837	634
Energy Loss (mw)	20.7	17.6

the values are 10.2 Pa and 4.8 Pa for the aneurysm treated by coils and flow diverter, respectively. The distributions of OSI on the two models are very similar, the maximum values are very close and they are 0.44 and 0.49 in the treated model by coils and flow diverter, respectively.

Table 1 presents pressure pulse and energy loss of the two treated aneurysm in a cardiac cycle. The pressure pulse and energy are 634 Pa and 17.6 mw in the aneurysm treated by coils, and they are 837 Pa and 20.7 mw in the aneurysm treated by flow diverter.

4 CONCLUSIONS

Juvela proposed that the aneurysm with higher pressure pulse has higher rupture risk [5] and Takao et al. believed that higher energy loss in the aneurismal sac during a cardiac cycle has higher rupture risk [6]. On the other side, high TAWSS is considered to be related to the recanalization of the coiled aneurysm [7]. When the giant aneurysm is treated by coils embolization or flow diverter implantation, the maximum TAWSS near the aneurysmal neck is higher but the pressure pulse and energy loss is less in the aneurysm treated by coils than by flow diverter. Therefore, the giant aneurysm treated by flow diverter has higher rupture risk and treated by coil embolization has higher recanalization risk.

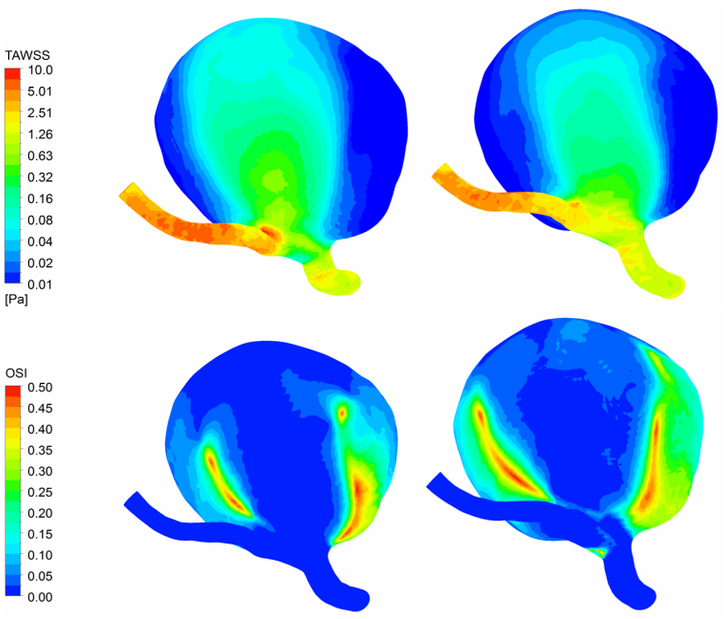

Figure 3: TAWSS contours and OSI contours on the treated aneurysms. The left column is the aneurysm treated by coils embolization and the right column is the aneurysm treated by flow diverter implantation.

ACKNOWLEDGEMENTS

This work is supported by the National Natural Science Foundation of China (No. 11102042).

REFERENCES

[1] D. M. Sforza, C. M. Putman, and J. R. Cebral, Hemodynamics of cerebral aneurysms, *Annual Review of Fluid Mechanics*, 41: 91-107, 2009.

[2] B. Seibert, R. P. Tummala, R. Chow, A. Faridar, S. A. Mousavi and A. A. Divani, Intracranial Aneurysms: Review of Current Treatment Options and Outcomes , *Front Neurol*, 2:1-10, 2011.

[3] A. P. Mitsos, N. M. P. Kakalis, Y. P. Ventikos, J. V. Byren, Haemodynamic simulation of aneurysm coiling in an anatomically accurate computational fluid dynamics model: technical note, *Neuroradiology*, 50:341-347, 2008.

[4] W. Wu, M. Qi, X. P. Liu, D. Z. Yang, W. Q. Wang, Delivery and Release of Nitinol Stent in Carotid Artery and their Interactions: a Finite Element Analysis, *J Biomech*, 40: 3034-40, 2007.

[5] S. Juvela, Prehemorrhage Risk Factors for Fatal Intracranial Aneurysm Rupture, *Stroke*, 34: 1852-1857, 2003.

[6] H. Takao, Y. Murayama, S. Otsuka, Y. Qian, A. Mohamed, S. Masuda, M. Yamamoto, T. Abe, Hemodynamic differences between unruptured and ruptured intracranial aneurysms during observation, *stroke*, 43:1436-1439, 2012.

[7] B. Luo, X. Yang X, S. Wang, H. Li, J. Chen, H. Yu, Y. Zhang, S. Mu, Z. Liu and G. Ding, High shear stress and flow velocity in partially occluded aneurysms prone to recanalization, *Stroke*, 42:745-753, 2011.

3rd International Conference on Computational and Mathematical Biomedical Engineering – CMBE2013
16-18 December 2013, Hong-Kong
P. Nithiarasu and R. Löhner (eds)

Stagnant blood flow in intracranial aneurysms: A possible association with atherosclerosis

Shin-ichiro Sugiyama*, Akira Takahashi**
*Department of Neuroanesthesia, Kohnan Hospital, 4-20-1 Nagamachi-minami, Taihaku-ku, Sendai 982-8523, Japan, sushi@kohnan-sendai.or.jp
**Department of Neuroendovascular Therapy, Tohoku University Graduate School of Medicine, 1-1 Seiryo-cho, Aoba-ku, Sendai 850-8574, Japan, akirat@ivns.med.tohoku.ac.jp

SUMMARY

Intracranial aneurysms can have atherosclerotic wall properties that may be important in predicting aneurysm history. This study aimed to investigate hemodynamic characteristics of atherosclerotic legions in intracranial aneurysms. We conducted computational fluid dynamic analyses of 30 aneurysms using patient-derived geometries and inlet flow rates. Among 30 aneurysms, seven atherosclerotic lesions with remarkable yellow lipid deposition were identified in five aneurysms. All seven atherosclerotic lesions were spatially agreed with the area exposed to stagnant blood flow. Univariate analysis revealed that male (P = 0.031), cigarette smoking (P = 0.047) and the exposure to stagnant blood flow (P = 0.024) are significantly related to atherosclerotic lesion formation on the aneurysmal wall. Of those variables that influenced atherogenesis, the variable male (P = 0.0046) and the exposure to stagnant flow (P = 0.0037) remained significant in the multivariate regression model. In conclusion, male sex and stagnant blood flow inside aneurysms were independent risk factors for atherosclerosis in intracranial aneurysms

Key Words: *cerebral aneurysm, hemodynamics, wall shear stress,*

1 INTRODUCTION

Recently, potentials of computational fluid dynamic (CFD) simulation in predicting natural history of intracranial aneurysms have been reported.[1] However, little work has been done on the atherogenesis in intracranial aneurysms. The purpose of this study was to investigate hemodynamic characteristics of atherosclerotic legions in intracranial aneurysms.

We conducted CFD analysis of 30 unruptured middle cerebral artery (MCA) aneurysms and investigated the relation between the spatial distribution of atherosclerotic lesions on the aneurysm wall and hemodynamic wall parameters including wall shear stress (WSS), oscillatory shear index (OSI), and relative residence time (RRT). WSS is the tangential frictional stress caused by blood flow on the vascular wall. OSI is a dimensionless measure of directional changes in WSS, and used as a marker of oscillatory nature of WSS.[2] RRT demonstrates the residence time of particles near the wall,[3] and was used as a marker of stagnant blood flow in this study.

2 METHODS

This study was granted approval from the ethical committee in Kohnan Hospital. We conducted CFD analysis of 30 MCA aneurysms with atherosclerosis. Data sets of 3D rotational angiography were used to reconstruct accurate geometries of the aneurysms and adjacent arteries. Following the conventions of CFD in large vessels, blood flow was treated as an incompressible Newtonian fluid, vessel walls were assumed rigid and no-slip boundary conditions were applied at the walls.[4] A finite-volume package, ANSYS 12.1 (ANSYS Inc.; Lebanon, NH) was used to solve the governing equations: 3D unsteady Navier-Stokes equations and equation of continuity. The patient-specific pulsatile flow condition measured by magnetic resonance velocimetry was prescribed at the inlet boundary.[5] Traction free conditions were applied to outlets. Three pulsatile cycles were simulated to ensure that numeric stability has been reached, and the results from the third cycle were used for analysis.

Wall shear stress refers to the tangential frictional stress caused by the action of blood flow on the vessel wall. For pulsatile flow, the time-averaged wall shear stress was calculated by integrating WSS magnitude over a cardiac cycle for each tetrahedral element:

$$WSS = \frac{1}{T}\int_0^T |\vec{\tau}_w| dt \quad (1)$$

where $\vec{\tau}$ is the instantaneous wall shear stress vector and T is the duration of the cycle.

To describe the temporal disturbance of intra-aneurysm flow, oscillatory shear index (OSI), a dimensionless measure of directional changes in WSS, was calculated using the formula reported by He and Ku: [2]

$$OSI = \frac{1}{2}\left[1 - \frac{\left|\int_0^T \vec{\tau}_w dt\right|}{\int_0^T |\vec{\tau}_w| dt}\right] \quad (2)$$

Note that $0 \leq OSI < 0.5$, with 0 being completely unidirectional shear and 0.5 being completely oscillatory.

Himburg et al showed that the residence time of particles near the wall is inversely proportional to a combination of WSS and OSI.[3]

$$RRT = \frac{1}{(1 - 2 \times OSI) \times WSS} = \frac{1}{\frac{1}{T}\left|\int_0^T \vec{\tau}_i \, dt\right|} \quad (3)$$

Himburg proposed RRT as a robust marker of disturbed blood flow with low and/or oscillatory WSS.[3] However, RRT may serve as a marker of stagnant blood flow, as the prolongation of RRT means the long residence time of particles near the wall.

In addition to conventional contour maps of WSS, OSI, and RRT, 3D streamlines and WSS vector plots were displayed to examine the temporal variation of wall shear stress vectors.

3 RESULTS

Intra-operative video recordings were examined for all 30 cases. Seven atherosclerotic lesions on five aneurysms (5/30, 16.7%) were distinguished by remarkable yellow lipid deposition. All five patients had several vascular atherosclerosis risk factors such as male sex, old age, obesity, smoking history, hypertension, diabetes mellitus, or dyslipidemia.

Among the three hemodynamic variables examined in the current study, only RRT demonstrated qualitative agreement with the spatial distribution of atherosclerosis in all seven lesions as a single metric. The five lesions on the dome were exposed to low and oscillatory WSS at the center of vortex flow (Figure 1, 2).

To evaluate the risk factor of atherosclerotic change of the intracranial aneurysms,

statistical analyses were performed . Univariate analysis revealed that male (P = 0.031), cigarette smoking (P = 0.047) and maximum RRT (P = 0.024) are significantly related to atherosclerotic lesion on the intracranial aneurysmal wall. Of those variables that influenced atherosclerotic lesion of the intracranial aneurysmal wall, the variable male (P = 0.0046) and maximum RRT (P = 0.0037) remained significant in the multivariate regression model ($R2$ = 0.52).

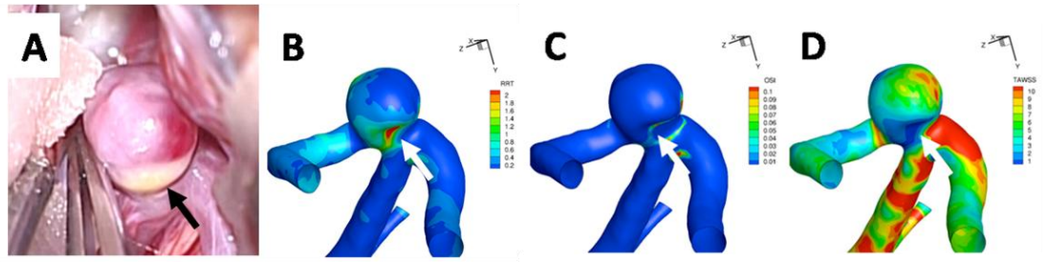

Figure 1. Intraoperative photograph and contour maps of three hemodynamic wall parameters.

A, Intraoperative photograph showed yellowish atherosclerotic legion on the aneurysm wall (black arrow). **B**, Contour maps of relative residence time (RRT) showed qualitative agreement of the prolonged RRT (white arrow) with the spatial distribution of atherosclerosis shown in A.

C, D, Contour maps of oscillatory shear index (OSI, **C**) and time-averaged wall shear stress (WSS, **D**) from the same viewing angle. The area with prolonged RRT had high OSI value and low WSS magnitude (white arrow).

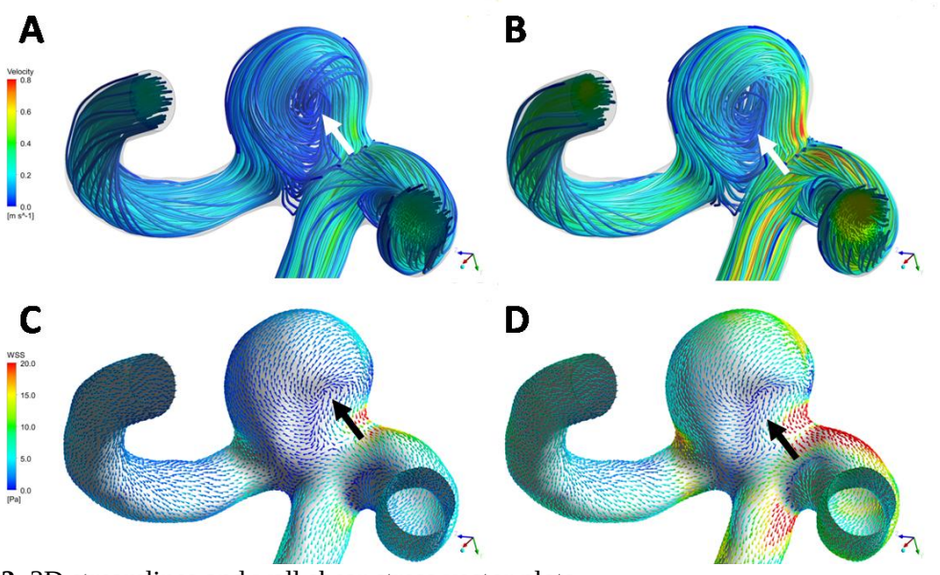

Figure 2. 3D streamlines and wall shear stress vector plots.

A, B, Snapshots of the flow field (3D streamlines) captured at end diastole (**A**) and peak systole (**B**) revealed intra-aneurysm vortex flow moving around over cardiac cycle (white arrow).

C, D, Snapshots of WSS vector plots captured at end diastole (**C**) and peak systole (**D**) showed that WSS vectors were arranged whirl-likely around the vortex center (black arrow) which was correspond to the area with RRT prolongation shown in Figure 1.

4 DISCUSSION

Many hemodynamic studies of intracranial aneurysms have reported that low WSS is involved in aneurysm rupture,[1,6] and speculated that low WSS can induce degenerative vascular wall remodeling in intracranial aneurysms that may lead to thinning or rupture of the aneurysm wall. However, the results of our study raise the possibility that an aneurysm wall exposed to low WSS can progress to atherosclerotic remodeling. We consider that low WSS is a risk for aneurysm rupture.[6] However, aneurysms with low WSS accompanied by the stagnation of blood flow indicated by prolonged RRT may be stabilized by atherosclerotic remodeling process. Stagnant blood flow prolongs residence time of atherogenic particles in the blood near aneurysmal wall, thus inducing lipid exchange and recruitment of macrophages, and promoting atherosclerosis.

5 CONCLUSIONS

The area exposed to stagnant blood flow indicated by prolonged RRT co-localized with atherosclerotic lesions on the aneurysm wall. Male and local stagnant flow were independent risk factors for atherosclerosis in intracranial aneurysms.

REFERENCES

[1] Xiang J, Natarajan SK, Tremmel M, Ma D, Mocco J, Hopkins LN, Siddiqui AH, Levy EI, Meng H. Hemodynamic-morphologic discriminants for intracranial aneurysm rupture. *Stroke*, 42, 144-152, 2011

[2] He X, Ku DN. Pulsatile flow in the human left coronary artery bifurcation: average conditions. *J Biomech Eng*, 118, 74-82, 1996

[3] Himburg HA, Grzybowski DM, Hazel AL, LaMack JA, Li XM, Friedman MH. Spatial comparison between wall shear stress measures and porcine arterial endothelial permeability. *Am J Physiol Heart Circ Physiol*, 286, H1916-1922, 2004

[4] Cebral JR, Mut F, Weir J, Putman C. Quantitative characterization of the hemodynamic environment in ruptured and unruptured brain aneurysms. *AJNR Am J Neuroradiol*, 32, 145-151, 2011

[5] Sugiyama SI, Meng H, Funamoto K, Inoue T, Fujimura M, Nakayama T, Omodaka S, Shimizu H, Takahashi A, Tominaga T. Hemodynamic analysis of growing intracranial aneurysms arising from a posterior inferior cerebellar artery. *World Neurosurg*, 78, 462-468, 2012

[6] Omodaka S, Sugiyama SI, Inoue T, Funamoto K, Fujimura M, Shimizu H, Hayase T, Takahashi A, Tominaga T. Local hemodynamics at the rupture point of cerebral aneurysms determined by computational fluid dynamics analysis. *Cerebrovasc Dis*, 34, 121-129, 2012

Modelling of Pulse Wave Propagation in the Arterial Tree I

3rd International Conference on Computational and Mathematical Biomedical Engineering - CMBE2013
16-18 December 2013, Hong-Kong
P. Nithiarasu and R. Löhner (Eds.)

A comprehensive one-dimensional model of the cardiovascular system

Jonathan P. Mynard, Daniel J. Penny and Joseph J. Smolich
Heart Research Group, Murdoch Childrens Research Institute, and
Department of Paediatrics, University of Melbourne, Parkville, VIC 3052, Australia;
jonathan.mynard@mcri.edu.au

SUMMARY

We present a model of the entire cardiovascular system that accounts for wave propagation in systemic (including coronary and cerebral) arteries and veins, pulmonary arteries and veins, and portal veins. A lumped parameter (0D) heart model incorporates time-varying elastance, source resistance, septal interactions and pericardial constraint. A non-linear windkessel compartment represents vascular beds, while specialised 0D models are employed for the hepatic and coronary vascular beds. The magnitude of forward and backward wave intensity throughout the circulation is characterised for the first time. The model will be useful for studying the mechanics underlying pressure/flow waveforms throughout the circulation and haemodynamic interactions between the heart and all vascular districts under normal and pathological conditions.

Key Words: *wave intensity, arteries, veins, cerebral, coronary, portal, systemic, pulmonary*

1 INTRODUCTION

One-dimensional (1D) blood flow models have played a crucial role in haemodynamics research because they can reproduce, and therefore help explain, the phasic features of blood pressure and flow waveforms. Past 1D models have mainly focused on the systemic arterial circulation (e.g. [3,5]), either neglecting the venous, pulmonary and portal circulations altogether or representing these vascular districts with lumped parameter compartments that do not account for wave propagation effects. In the current study, we present a fully integrated closed-loop circulatory model that accounts for wave propagation effects in all major conduit blood vessels. The 1D vascular networks are coupled to 0D heart and vascular bed models that include a range of phenomena that are important for studying normal and pathological cardiovascular interactions. In this paper, the model is described, an example validation of simulated pressure, flow and wave intensity signals is presented, and the intensity of forward and backward waves throughout the circulation is characterised.

2 MAIN BODY

Methods. The 1D equations governing velocity (u), cross-sectional area (A) and pressure (p) are:

$$\frac{\partial A}{\partial t}+\frac{\partial Au}{\partial x}=0, \qquad \frac{\partial u}{\partial t}+u\frac{\partial u}{\partial x}+\frac{1}{\rho}\frac{\partial p}{\partial x}=-\frac{22\pi\mu}{\rho}\frac{u}{A} \tag{1}$$

where μ and ρ are blood viscosity and density. The chosen wall law is:

$$p(A) - p_{\text{ext}} = \frac{2\rho c_0^2}{b}\left[\left(\frac{A}{A_0}\right)^{\frac{b}{2}} - 1\right] + \gamma\frac{1}{A\sqrt{A}}\frac{dA}{dt} + P_0 \tag{2}$$

where the first and second terms on the right-hand side are the elastic and viscous components respectively, b governs the elastic non-linearity, γ relates to wall viscosity [1], p_{ext} is external pressure and A_0, P_0 and c_0 are reference area, pressure and wave speed. The equations are solved as in [3] with an operator splitting technique for the viscoelastic wall law [1]. At bifurcations, flow conservation and continuity of total pressure (arteries) or static pressure (veins) are enforced.

The 1D vascular networks are shown in Figure 1. Geometry of the large systemic arteries and cerebral arteries is based on prior studies [2,5]. The coronary arterial network is a reduced version of that in [4]. Venous networks are based on anatomical atlases and other published data, with unavailable data estimated via an artery-to-vein diameter ratio of 1.25 or Murray's law (for diameters) and by aligning with arterial geometry (for lengths). The pulmonary veins and left/right pulmonary arteries are equivalent vessels whose lengths are approximated to achieve physiological return time of reflected waves. Wave speed is estimated from vessel radius via empirical relations specific to each vascular district.

Atria and ventricles are represented with a time-varying elastance (E_{A}, E_{V}) and source resistance (R_{A}, R_{V}), while heart valves are modelled as in [2] (Fig. 2A). Septal interactions and pericardial constraint are accounted for [2]. A mirrored windkessel with a pressure-dependent resistance is used for all vascular beds (Fig. 2B), with two exceptions. First, the hepatic vascular bed model incorporates an additional resistance-compliance compartment (R_{art}, C_{art}) that lies between the high pressure hepatic artery and the low pressure portal veins and lobar microvasculature (Fig. 2C, see [2] for full details). Second, the coronary microvascular model accounts for the unequal distribution of lumped vascular properties in the subepicardium, midwall and subendocardium [6], along with the intramyocardial pressure (p_{im}) generated by 1) transmission of ventricular cavity pressure into the heart wall and 2) the shortening-induced thickening of myocytes [4] (Fig. 2D).

Results. Simulated pressure and flow waveforms throughout the circulation were representative of reported waveforms in the literature. For example, Fig. 3A&B compares simulated and in-vivo pressure/flow waveforms and wave intensity profiles from the common carotid artery. Although no data fitting was employed, it can be seen that the simulated waveforms and wave intensity profiles contain all of the phasic features present in-vivo.

Fig. 3C compares overall peak forward and backward wave intensity throughout the circulation, where 'forward' is defined as the direction of mean flow. Noting the use of a logarithmic scale, it can be seen that the intensity of waves differs by approximately six orders of magnitude in different vascular districts. A number of other important observations may be made. First, backward waves in the ascending aorta are smaller than in all other systemic arterial sites, consistent with the principle that systemic arteries are well-matched in the forward but not backward direction. Second, coronary arterial backward waves are relatively large compared with most other systemic arterial sites, due to these waves arising not only from passive reflection of forward waves, but actively via intramyocardial pressure variations. Third, there is a pattern of lower wave intensity in vascular districts with lower operating pressures. Fourth, backward waves in the systemic/pulmonary veins are substantially larger than the forward waves, implying that venous pressure/flow waveforms are mainly governed by atrial contraction/relaxation and suggesting that the venous vascular networks are relatively well-matched in the backward direction, just as arteries are well-matched in the forward direction. Fifth, forward waves are larger than backward waves in portal veins, in contrast to other veins; this implies that portal venous pulsatility, whose origin has been debated, arises mainly from transmission of systemic arterial pulsatility through the gastrointestinal organs rather than transmission of atrial pulsations through the highly compliant hepatic vascular bed.

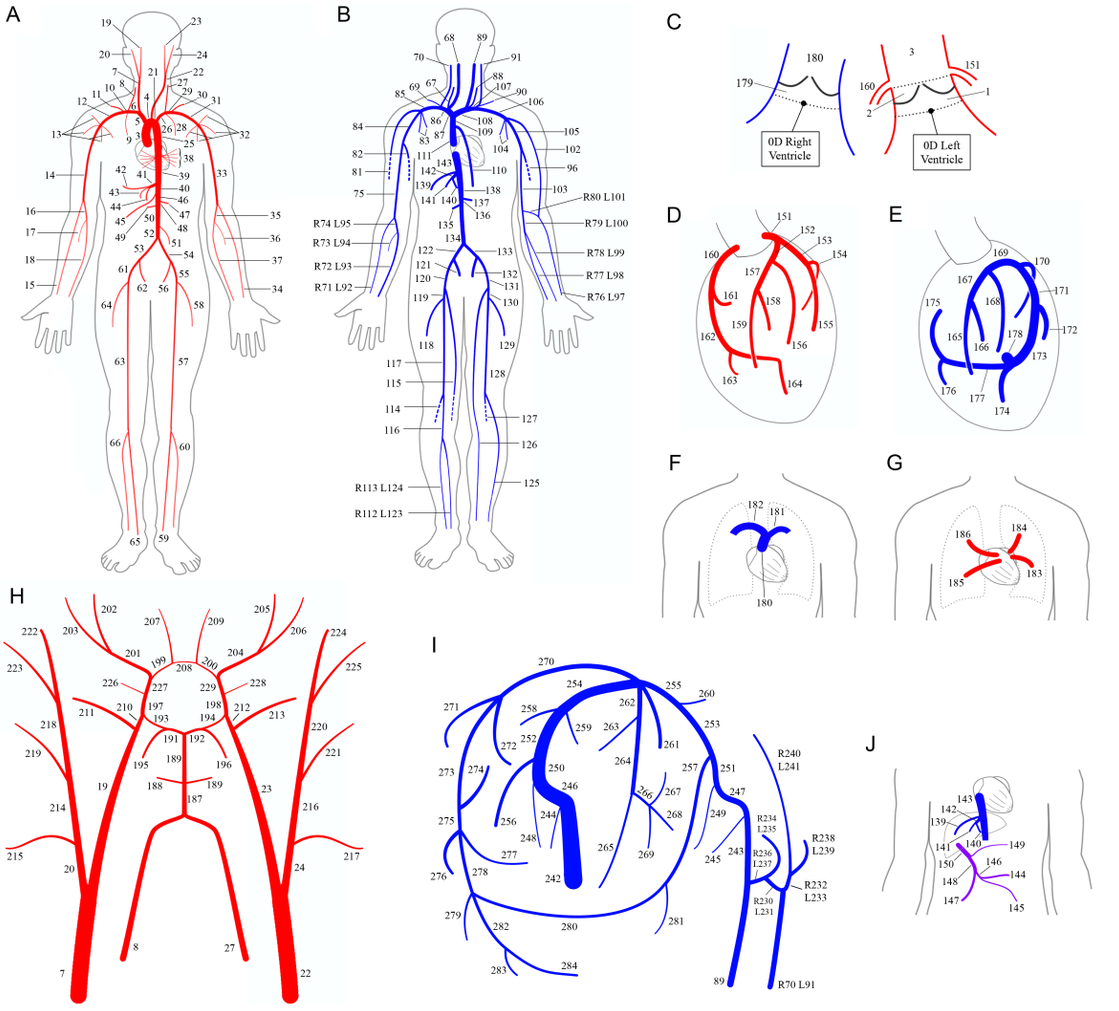

Figure 1: One-dimensional vascular networks of the (A) large systemic arteries, (B) large systemic veins, (C) ventricular outflow tract region, (D) coronary arteries, (E) coronary veins, (F) pulmonary arteries, (G) pulmonary veins, (H) cerebral arteries, (I) cerebral veins, and (J) portal veins. For orientation, segments 7 and 22 are the common carotid arteries, 243 and 244 are the distal internal jugular veins, 150 is the common portal vein, 178 is the coronary sinus.

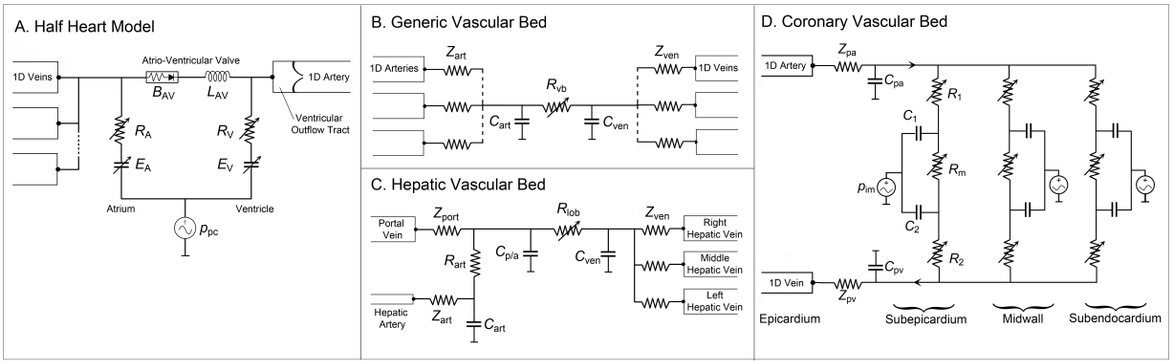

Figure 2: Lumped parameter models of (A) a half-heart, i.e. atrium-valve-ventricle-valve, (B) generic vascular bed, (C) hepatic vascular bed, and (D) coronary vascular bed.

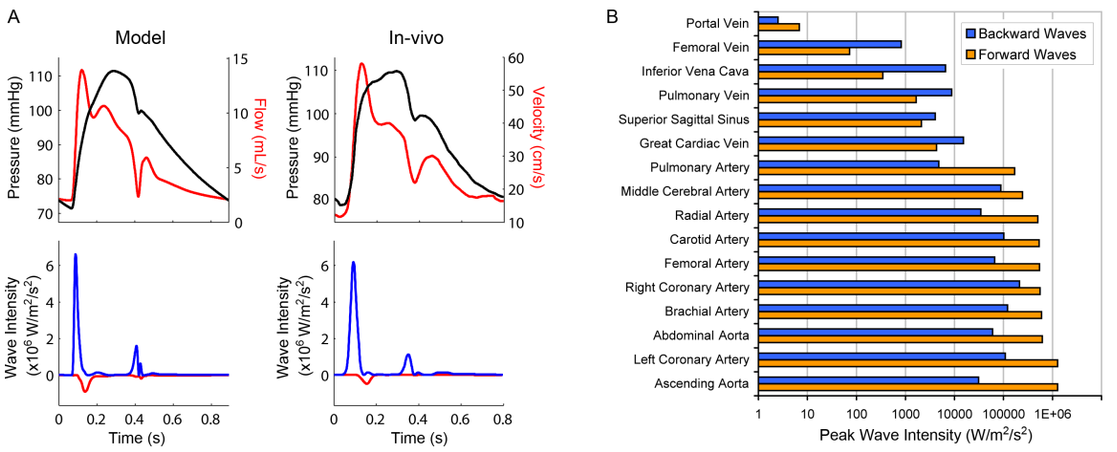

Figure 3: (A) Carotid arterial pressure, flow and wave intensity from the model. (B) Carotid arterial pressure, velocity and wave intensity from a human subject [7]. (C) Peak forward and backward wave intensity magnitude throughout the circulation. Note the logarithmic scale.

3 CONCLUSIONS

A comprehensive 1D model of the cardiovascular system has been presented that includes anatomically-based 1D networks in all vascular districts and physiologically-relevant heart and vascular bed 0D models. Forward/backward wave intensity magnitude throughout the circulation was characterised. The model is likely to be useful for investigating physiological mechanisms underlying pressure-flow waveforms in normal and pathological conditions.

REFERENCES

[1] A. C. I. Malossi, P. J. Blanco, and S. Deparis. A two-level time step technique for the partitioned solution of one-dimensional arterial networks. *Comput Meth Appl Mech Eng*, 237-240, 212-226, 2012.

[2] J. P. Mynard. Computer modelling and wave intensity analysis of perinatal cardiovascular function and dysfunction. PhD Thesis, University of Melbourne, 2011 (http://repository.unimelb.edu.au/10187/10250).

[3] J. P. Mynard and P. Nithiarasu. A 1D arterial blood flow model incorporating ventricular pressure, aortic valve and regional coronary flow using the locally conservative Galerkin (LCG) method. *Comm Num Meth Eng*, 24, 367-417, 2008.

[4] J. P. Mynard, D. J. Penny, and J. J. Smolich. Validation of a multi-scale model of the coronary circulation in adult sheep and newborn lambs. *Proceedings of the 35th Ann Int Conf IEEE Eng Med Biol Soc*, Osaka, Japan, 2013.

[5] P. Reymond, F. Merenda, F. Perren, D. Rufenacht, and N. Stergiopulos. Validation of a one-dimensional model of the systemic arterial tree. *Am J Physiol Heart Circ Physiol*, 297, H208-222, 2009.

[6] J. A. E. Spaan, A. J. M. Cornelissen, C. Chan, J. Dankelman, and F. C. P. Yin. Dynamics of flow, resistance, and intramural vascular volume in canine coronary circulation. *Am J Physiol Heart Circ Physiol*, 278, H383-403, 2000.

[7] A. Zambanini, S. L. Cunningham, K. H. Parker, A. W. Khir, S. A. McG. Thom, and A. D. Hughes, Wave-energy patterns in carotid, brachial, and radial arteries: a noninvasive approach using wave-intensity analysis. *Am J Physiol Heart Circ Physiol*, 289, H270-H276, 2005.

3rd International Conference on Computational and Mathematical Biomedical Engineering - CMBE2013
16-18 December 2013, Hong-Kong
P. Nithiarasu and R. Löhner (Eds.)

An extended pulse wave propagation model to predict (patho-)physiological coronary pressure and flow patterns

Frans N. van de Vosse*, Arjen van der Horst*, and Marcel C.M. Rutten*
*Eindhoven University of Technology, P.O. Box 513, 5600 MB, Eindhoven, The Netherlands,
f.n.v.d.vosse@tue.nl

SUMMARY

A patient-specific model describing the primary relations between the cardiac muscle contraction and coronary circulation might be useful for interpreting coronary hemodynamics and deciding on medical treatment in case multiple types of coronary circulatory disease are present. For this purpose we present the use of a microstructure-based heart contraction model and a micro-structure based fiber reinforced arterial wall model as the basis of a 1D wave propagation model to describe coronary pressure and flow waves. We conclude that this extended pulse wave propagation model adequately can predict coronary hemodynamics in both normal and diseased state based on patient-specific clinical data.

Key Words: *myocardial wall mechanics, coronary wall mechanics, coronary pressure, coronary flow, pulse wave propagation.*

1 INTRODUCTION

Diagnosis of coronary circulatory disease based on coronary pressure and/or flow has been shown to improve the clinical outcome of treatment [1,2]. The direct measurement of coronary hemodynamics, however, is still limited to the large epicardial vessels, which means that microvascular disease can only be determined from proximal measurements using an appropriate model of the vessels and their interaction with the cardiac muscle. Due to the location of the coronary arteries, being embedded into the myocardium, the contraction of the heart influences coronary hemodynamics. Therefor we developed a model of the human cardiovascular system in which clinical data can be incorporated, to enable patient-specific modeling of coronary hemodynamics. The different submodels were chosen such that the model complexity remains minimal, while still enabling the incorporation of both normal and diseased physiologic and geometric clinical data. To represent the heart, the single-fiber contraction model as described by Bovendeerd et. al [3] was chosen. This model is based on microstructural material and macrostructural geometrical properties, allowing the simulation of cardiac disease with geometry-based parameter changes. The large vessels are modeled one-dimensionally [4,5,6] to enable easy implementation of the geometry of the vessels, whereas the small vessels are represented by lumped elements. In a previous study by van den Broek et al. [7], it was shown that using a generic material parameter set, with average morphologic parameters, the mechanical behavior of different porcine coronary arteries could accurately be described. Therefore, the thick-walled, 1D, single-layered, fiber-reinforced model as proposed in that study, was also used here. The only information needed then is a radius measurement at physiological loading and the corresponding pressure. The cardiac muscle contractiom model and the 1D coronary circulation model where coupled using a distributed lumped parameter model of the cardiac microcirculation.

2 METHODS

The model (see Figure 1) consists of three main elements: a heart contraction model represented by a left ventricle (LV), with the mitral (M_v) and aortic valve (A_v), a wave propagation model for the large arteries represented by the aorta and its main side branches and the main arteries in the coronary circulation, and lumped elements to model the coronary and systemic microcirculation. The left main coronary artery (LMCA) has a lengt of 5 mm and splits into the LAD and the LCx, with a length 7.5 cm and 6 cm, respectively. Side branches are modeled at intervals of 1.5 cm. Each coronary segment is represented by the characters a-f. The radius of segment a is 1 mm and Murrays law is used to determine the radius of segments b-f. All a-segments are connected to a three-element windkessel model representing the coronary microvessels. The intramyocardial pressure (p_{im}) acts on the three capacitors that represent the vessel compliance. When a stenosis is modeled, it is incorporated into the c-segment of the LAD. The main elements of the model will be described in more detail below.

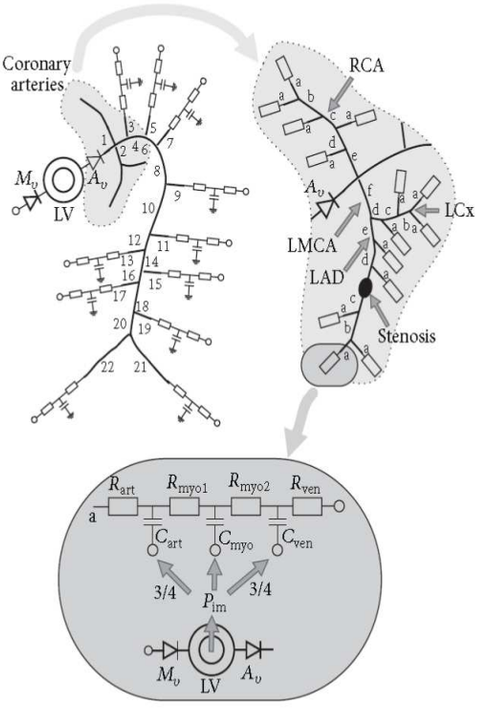

Figure 1: *Schematic of the extended model*

Myocard contraction The cardiac muscle contraction is based on the model proposed by Bovendeerd et al. [3]. In this model the macroscopic pressure in a spherical left ventricle is related to the microstructural stress in the myocardial fibers, a characteristic radial wall stress, and the ratio between the volumes of the left ventricular wall and cavity. The wall stress consists of an orthotropic non-linear passive part superimposed to a Hill-type active part in fiber direction depending on the characteristic length of the sarcomeres, a time dependent activation function, and the sarcomere shortening velocity. A mean intramyocardial pressure then can be derived from the mean wall stress in radial direction and the left ventricular pressure. The system is closed with a geometry determined relation between fiber stretch and the left ventricular wall and cavity volumes.

The valves In the model the atrial contraction has been neglected and only the mitral and aortic valves are relevant. The mitral valve has been represented by a pressure gradient defined as the product of the mitral flow and a non-linear resistance depending on the sign of the pressure gradient, representing the opened and closed position. In the aortic valve the pressure gradient is defined in a similar way but an inertia term is added. The non-linear resistance has been made dependend on the sign of the aortic flow.

Wave propagation The pressure and flow in the larger arteries (i.e. the aorta and the main coronary arteries) are modeled using the wave propagation model as proposed by Bessems et al. [4]. Integration of the mass en momentum equations over the cross-sectional area of the arteries and assuming a velocity profile that depends on the local viscous Stokes layer, results in a generic non-linear equation for pressure and flow waves in which non-linear stationary inertia and viscous

wall shear rate are approximated for the entire range of artery dimensions. The solution of the resulting 1D equations are approximated using a finite element spatial discretisation method and a backward differencing time integration. The pressure drop that results from an arterial stenosis is approximated using a non-linear pressure flow relation based on the work of Bessems et al. [5].

Arterial wall In the wave propagation model the macroscopic wall compliance that needs to be defined has been based on a microstructural fiber reinforced constitutive model for coronary arteries developed by van den Broek et al. [7]. To this end a pressure dependend compliance according to

$$C = C_0 + \frac{C_1}{1 + ((p - p_m)/p_w)^2}$$

has been fitted to the fiber reinforced model. By fixing more or less generic parameters such as the moduli and the fiber and opening angles to population averages a relatively simple model that only requires patient-specific geometrical parameters (i.e. radius and wall thickness) was obtained.

Peripheral vasculature Peripheral vasculature and the myocardial impedances were approximated using three-element windkessel models with parameters determined from predifined flow distributions. The transmural pressure in the myocardial impedance is determined by the intramyocardial pressure derived from the myocard contraction model [3].

3 RESULTS

Coronary stenoses Dynamic pressure measurements proximal and distal to a stenosis (70% diameter, length 7.48 mm), performed at the catheterization laboratory of the Catharina Hospital (Eindhoven, The Netherlands), are used to verify the stenosis model. Since the pressure measurements are performed during hyperaemia, the flow in the model was increased five-fold, by decreasing the coronary microvascular resistances (see figure 2).

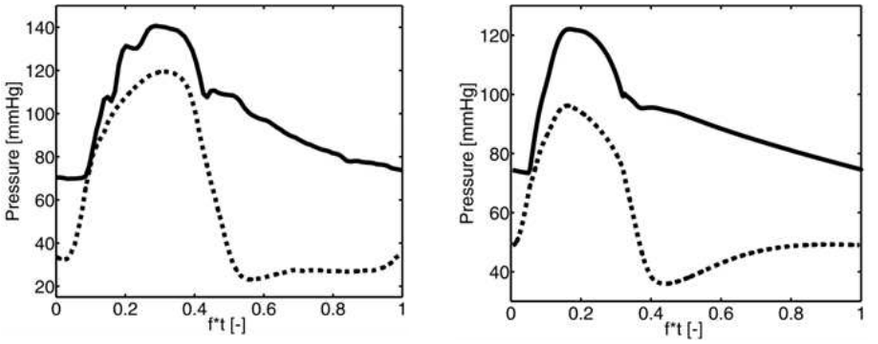

Figure 2: *The pressure proximal (solid) and distal (broken) to a 70% stenosis in the LAD as measured in a human coronary artery (left) and predicted by the model (right).*

The pressures determined with the model showed the same behaviour as the measurements, with the largest pressure gradient in diastole. The FFR value (pressure ratio distal/proximal to stenosis) determined with the measurements was 0.57 whereas the FFR determined with the model was 0.61.

Left ventricular hypertrophy The ability of the model to describe coronary hemodynamics when LVH due to an aortic valve stenosis (AVS) is present is verified with clinical measurements performed by Hildick-Smith and Shapiro [2].

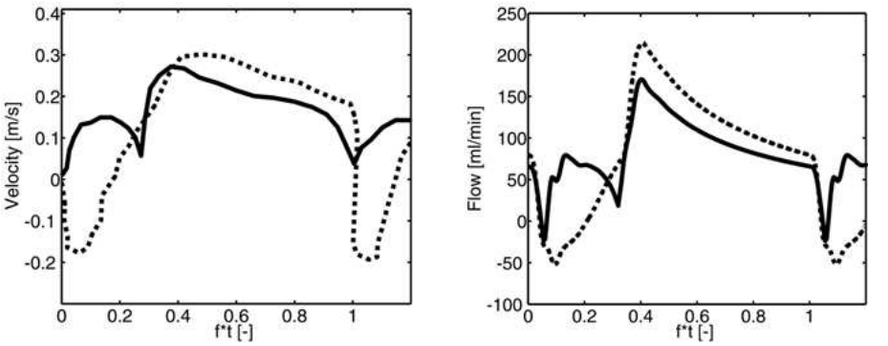

Figure 3: *Flow in the LAD of a LVH-AVS patient befor (broken) and after (solid) AVR measured in a human LAD (left) and predicted by the model (right).*

The normal characteristic flow dynamics, with a low positive systolic and high diastole component, was found after aortic valve replacement (AVR), in both the measurements and the simulations. Before the AVR, so when the LVH-AVS is present, the measurements reveal that the positive systolic flow component was replaced by a period of negative flow. These features were also captured by the model, demonstrating the influence of the increased intramyocardial pressure on the coronary flow dynamics.

4 CONCLUSIONS

We conclude that the proposed extended pulse wave propagation model adequately can predict coronary hemodynamics in both normal and diseased state based on patient-specific clinical data.

REFERENCES

[1] M.J. Kern, A. Lerman, J.W. Bech et al., Physiological assessment of coronary artery disease in the cardiac catheterization laboratory: a scientific statement from the American Heart Association Committee on diagnostic and interventional cardiac catheterization, council on clinical cardiology, *Circulation*, **vol. 114**, 12, 1321-1341, 2006.

[2] D.J.R. Hildick-Smith and L.M.Shapiro, Coronary flow reserve improves after aortic valve replacement for aortic stenosis: an adenosine transthoracic echocardiography study, *Journal of the American College of Cardiology*, **vol. 36**, 6, 1889-1896, 2000.

[3] P.H.M. Bovendeerd, P. Borsje, T. Arts, and F.N. van de Vosse, Dependence of intramyocardial pressure and coronary flow on ventricular loading and contractility: a model study, *Annals of Biomedical Engineering*, **vol. 34**, 12, 1833-1845, 2006.

[4] D. Bessems, M.C.M. Rutten, and F.N. van de Vosse, A wave propagation model of blood flow in large vessels using an approximate velocity profile function, *Journal of Fluid Mechanics*, **vol. 580**, 145-168, 2007.

[5] D. Bessems, *On the propagation of pressure and flow waves through the patient-specific arterial system* [Thesis/dissertation], Eindhoven University of Technology, 2007.

[6] F.N. van de Vosse and N. Stergiopulos, Pulse wave propagation in the arterial tree, *Annual Review of Fluid Mechanics*, **vol. 43**, 467-499, 2011.

[7] C.N. van den Broek, A. van der Horst, M.C.M. Rutten, and F.N. van de Vosse, A generic constitutive model for the passive porcine coronary artery, *Biomechanics and Modeling in Mechanobiology*, **vol. 10**, 2, 249-258, 2011.

3rd International Conference on Computational and Mathematical Biomedical Engineering - CMBE2013
16-18 December 2013, Hong-Kong
P. Nithiarasu and R. Löhner (Eds.)

On the coupling between 3D-FSI and 1D models.

L. Formaggia*, S. Deparis* and C.A.Malossi***,C. Vergara****
*MOX, Dipartimento di Matematica, Politecnico di Milano, Milan, Italy.
luca.formaggia@polimi.it
**Dipartimento di Ingegneria dell'Informazione e Metodi Matematici, Università degli Studi Bergamo, Italy. christian.vergara@unibg.it
***CMCS, Mathematics Institute of Computational Science and Engineering (MATHICSE), Ecole Polytechnique Fèdèrale de Lausanne (EPFL), Switzerland. simone.deparis@epfl.ch, cristiano.malossi@epfl.ch

SUMMARY

We discuss the reliability of the coupling among three-dimensional (3D-FSI) and one-dimensional (1D) models that describe blood flowing into the circulatory tree. We outline some results obtained within the MathCard project (www.mathcard.eu) concerning coupling schemes, energy balance, model consistency.

Key Words: *blood flow, reduced modes, fluid-structure interaction.*

1 INTRODUCTION

Since the preliminary work in [6] the idea of developing numerical simulators for the cardiovascular system by coupling models of different geometrical complexity has gained a wide acceptance among computational scientists as well as bio-engineers.

Many issues however arise when coupling differential models, often of different characteristics, both at the physical and at the numerical level. We will present here a flexible coupling framework developed within the lifev (www.lifev.org) library. We will also discuss the importance of energy satisfying boundary and coupling conditions and of a correct set-up the reduced model.

2 COUPLING HETEROGENEOUS MODELS

The cardiovascular system is a complex network of vessels where local and global phenomena influence each other. Modeling with different degree of detail is therefore mandatory to obtain physiological and patient-specific results. Since the pioneering works in [6, 12] the coupling of heterogeneous models, characterized by different spatial dimension, has become rather common in the simulation of the cardiovascular system[4, 11, 9, 13, 14, 2, 10, 8, 7]. A three-dimensional (3D) accurate description is used in the specific area of interest, yet embedding it in a net of one-dimensional (1D) and/or lumped-parameter (0D) models, which accounts for the rest of the circulatory tree and provides suitable boundary conditions to the 3D model. We will here limit ourselves to the 3D-1D coupling.

It is reasonable to ask whether the 1D model can reproduce physiological results with reasonable accuracy, when used as an approximation of a 3D model of a real vessel geometry with a thick wall. We refer to this topic as *physical consistency* of the 1D model with respect to a 3D-FSI one. Of course, the fulfillment (in a suitable sense) of the physical consistency is a major issue to obtain reliable results when one considers a 3D-1D coupled system. Another important aspect is the existence of energy stable couplings, addressed for instance in [5] and later in [3].

From the numerical point of view, handling complex 1D networks and the coupling with the 3D model in a computationally efficient way requires a careful implementation [7]. We formalize the geometrical multiscale problem in an abstract setting, introduce new coupling algorithms, describe their implementation, and investigate the possible numerical reflections that may occur at the interface between the heterogeneous models.

3 CONCLUSIONS

The coupling of heterogeneous models is nowadays becoming common practice when simulating blood flow in the cardiovascular system. Taking as reference the results in [5, 1, 7] we assess the physical consistency of reduced models and illustrate efficient algorithms for the coupling.

REFERENCES

[1] P.J. Blanco, S. Deparis, and A.C.I. Malossi. On the continuity of mean total normal stress in geometrical multiscale cardiovascular problems. *Journal of Computational Physics*, 251:136–155, 2013.

[2] P.J. Blanco, R.A. Feijòo, and S.A. Urquiza. A unified variational approach for coupling 3d-1d models and its blood flow applications. *Computer Methods in Applied Mechanics and Engineering*, 196:4391–4410, 2007.

[3] TK Dobroserdova and MA Olshanskii. A finite element solver and energy stable coupling for 3D and 1D fluid models. *Computer Methods in Applied Mechanics and Engineering*, 259:166–176, 2013.

[4] L. Formaggia, F. Nobile, A. Quarteroni, and A. Veneziani. Multiscale modelling of the circulatory system: a preliminary analysis. *Comput and Visual in Science*, 2:75–83, 1999.

[5] L. Formaggia, A. Quarteroni, and C. Vergara. On the physical consistency between three-dimensional and one-dimensional models in haemodynamics. *Journal of Computational Physics*, 244:97112, 2012.

[6] L. Formaggia, F. Nobile, A. Quarteroni, and A. Veneziani. Multiscale modelling of the circulatory system: a preliminary analysis. *Computing and Visualization in Science*, 2(2-3):75–83, 1999.

[7] A.C.I Malossi, P.J. Blanco, P. Crosetto, S. Deparis, and A. Quarteroni. Implicit coupling of one-dimensional and three dimensional blood flow models with compliant vessels. *Multiscale Model. Simul.*, 11 (2):474–506, 2013.

[8] C. Malossi, P.J. Blanco, S. Deparis, and A. Quarteroni. Algorithms for the partitioned solution of weakly coupled fluid models for cardiovascular flows. *Int J Num Meth Biomed Eng,*, 27:2035–2057, 2011.

[9] F. Migliavacca, R. Balossino, G. Pennati, G. Dubini, T.Y. Hsia, M.R. de Leval, and E.L. Bove. Multiscale modelling in biofluidynamics: application to reconstructive paediatric cardiac surgery. *J Biomech*, 39:1010–1020, 2006.

[10] T. Passerini, M. de Luca, L. Formaggia, A. Quarteroni, and A. Veneziani. A 3d/1d geometrical multiscale model of cerebral vasculature. *Journal of Engineering Mathematics*, 64(4):319–330, 2009.

[11] A. Quarteroni, M. Tuveri, and A. Veneziani. Computational vascular fluid dynamics: Problems, models and methods. *Computing and Visualisation in Science*, 2:163–197, 2000.

[12] A. Quarteroni and A. Veneziani. Modeling and simulation of blood flow problems. In *Computational Science for the 21st Century*, pages 369–379. J. Periaux et al. eds, J. Wiley and Sons, 1997.

[13] A. Quarteroni and A. Veneziani. Analysis of a geometrical multiscale model based on the coupling of ODE and PDE for blood flow simulations. *Multiscale Model. Simul.*, 1(2):173–195, 2003.

[14] I. Vignon-Clementel, C.A. Figueroa, K. Jansen, and C. Taylor. Outflow boundary conditions for three-dimensional finite element modeling of blood flow and pressure waves in arteries. *Computer Methods in Applied Mechanics and Engineering*, 195:3776–3996, 2006.

3rd International Conference on Computational and Mathematical Biomedical Engineering - CMBE2013
16-18 December 2013, Hong-Kong
P. Nithiarasu and R. Löhner (Eds.)

Coupling of a pulse wave propagation model to a lumped parameter regulation model based on physiological mechanisms

Wouter P. Donders*, Wouter Huberts*, Frans N. van de Vosse and Tammo Delhaas***
*Dept. Biomedical Engineering, Faculty of Health, Medicine & Life Sciences, Maastricht University P.O. Box 616, 6200 MD Maastricht, The Netherlands.
**Cardiovascular Biomechanics, dept. Biomedical Engineering, Eindhoven University of Technology, P.O. Box 513, 5600 MB Eindhoven, The Netherlands

Corresponding author: Wouter P. Donders, w.donders@maastrichtuniversity.nl

SUMMARY

We present a combination of a pulse wave propagation model with an extensive lumped parameter cerebral regulation model. Multiple physiological mechanisms contributing to autoregulation and neurovascular coupling lead to variable impedances in a finite 0-D element that is coupled to the cerebral outlets of 1-D wave propagation network. A simulation of global hemodynamics responding to clamping of an upstream vessel is demonstrated.

Key Words: *cerebral blood flow, pulse wave propagation, blood flow regulation, autoregulation*

1 INTRODUCTION

Distributed models of pulse waves of pressure and flow (or velocity) in the cerebral vasculature have been reported by various researchers [1–3]. For example, Alastruey *et al.* investigated the effects of the anastomotic network made up by the circle of Willis and the anatomical variations thereof on cerebral wave patterns in a computationally inexpensive way [1]. Cerebral wave patterns are also influenced by cerebral blood flow regulation. Many lumped parameter models of cerebral blood flow regulation have been reported in the literature [4–7]. However, combination of these types of models has been limited (e.g. [8]). Such a combination combines the local cerebral blood flow regulation with the global cerebral blood supply. For example, it can provide insights into cerebral hemodynamics during manipulation of supra-aortic vessels that can result in challenges to the cerebral regulation system. Also, the interplay of compensation via the primary collateral architecture of the circle of Willis and the effects of regulation at different basal cerebral vessels can be investigated. Furthermore, local regulation effects can be translated to global wave patterns in more upstream vessels, which are more easily accessible for measurements.

We present a combination of a pulse wave propagation model with an extensive regulation model by Spronck *et al.* [7]. This regulation model can capture both autoregulation and neurovascular coupling by describing neurogenic, metabolic, myogenic and endothelial mechanisms that interactively influence arteriolar smooth muscle tone. The combined model leads to variable outlet impedances at multiple locations in the cerebral vasculature's periphery.

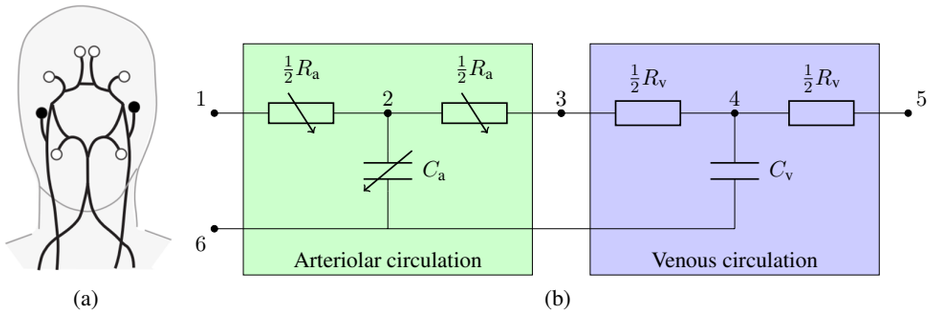

Figure 1: (a) Detail of the arterial network in the head. Black lines represent wave propagation elements. Black circles represent Windkessel elements, white circles the regulation elements. (b) The regulation element based on the work of Spronck *et al.* [7]. The green compartment represents the arteriolar circulation at which regulation is exerted, the blue compartment represents the venous circulation. Node 1 is connected to the upstream vasculature, node 5 to the venous return vessel and node 6 to the extravascular space.

2 METHODS

2.1 Pulse wave propagation model

The pulse wave propagation model is based on theory by Hughes and Lubliner [9], yielding 1-D equations for the conservation of mass and momentum which can be solved for pressure and flow. We assume a Womersley-number dependent velocity profile with an inviscid core and a viscous boundary layer (Bessems *et al.* [10], see also [11]). We use 1-D elements with two nodes, in which we direct nodal flow inwards, leaving only pressures as nodal unknowns (Kroon *et al.* [12]). This ensures pressure continuity and flow conservation at bifurcations without requiring additional coupling equations. Furthermore, it facilitates translation of lumped parameter models into element subroutines.

2.2 Regulation model

To achieve variable cerebral outlet impedances an element subroutine was developed based on the lumped parameter regulation model reported by Spronck *et al.* [7]. The regulation element consists of an arteriolar and a venous compartment, each of which contains a split resistance (modeling viscous friction) and a compliance (modeling vessel distensibility), see Figure 1. Regulation is exerted at the arteriolar compartment. The ordinary differential equations that govern the variable resistance and compliance are incorporated within the finite element subroutine using an easy to implement semi-explicit scheme.

2.3 Implementation, simulation and analysis

Cerebral flows corresponding to pressures measured in healthy volunteers during squatting maneuvres (challenging autoregulation) and visual stimuli (challenging neurovascular coupling) are calculated using our approach of incorporating a semi-explicit ordinary differential equation scheme within the finite element framework. These calculated flows are then compared to those calculated by Spronck *et al.* [7], who used an implicit ordinary differential equation solver from Matlab.

An autoregulatory stimulus is evoked by simulating clamping of the right common carotid artery, causing a drop in perfusion pressure. First, non-regulating baseline conditions are determined by performing a simulation in which the cerebral outlets are coupled to three-component Windkessel

elements. In the subsequent simulation, the cerebral Windkessel elements are replaced by regulation elements. The initial values for the arteriolar and venous resistances and compliance are determined by matching the regulation element's initial impedance with that of its parent Windkessel. Two simulation sets are performed. In one the circle of Willis is complete; in the other the anterior communicating artery (ACoA), which forms an anastomosis between the carotid arteries, is missing.

3 RESULTS AND DISCUSSION

Cerebral flows calculated using the semi-explicit scheme within the finite element method did not vary significantly from those calculated using an implicit Matlab solver (data not shown). Therefore we consider our semi-explicit scheme accurate and stable enough.

The blood flow waveforms resulting from right common carotid clamping are shown in Figure 2 for the ipsilateral middle and anterior cerebral arteries (resp. MCA, ACA) for both simulations. Baseline waveforms are the same irrespective of the geometry of circle of Willis. Pressures are shown in the top plots. Directly after clamping a sudden drop in pressures is seen for both cerebral arteries. The drop is larger when the ACoA is missing (red). Furthermore, a continued drop in pressure is seen for approx. 10 seconds when ACoA is missing (red), whereas the pressure is relatively stable when the circle of Willis is complete (blue). Corresponding flows are shown in the bottom plots. Directly after clamping, a sudden drop in flow is seen for both cerebral arteries, with the larger drop in the case that the ACoA is missing (red). After the sudden drop a recovery towards baseline flows can be observed. The slower recovery in the case that the ACoA is missing (red) is due to the larger drop in pressures and because flow can not be compensated for via the contralateral side. The significant role of the ACoA in pressure equalization and flow recovery can be appreciated from the differences between the red and blue lines.

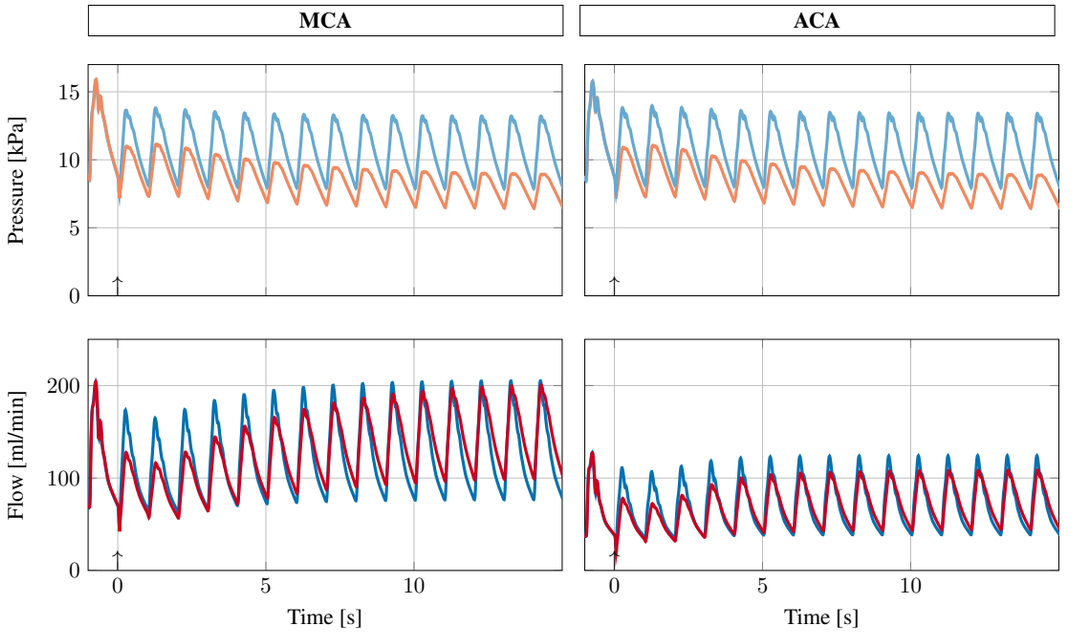

Figure 2: Pressures and flows when simulating clamp placement in the right common carotid artery at 0 seconds (arrow). Top plots: pressure; bottom plots: flow. Left plots: middle cerebral artery (MCA); right plots: anterior cerebral artery (ACA). Blue: simulation set where the circle of Willis is complete; red: simulation set where the anterior communicating artery is missing.

4 CONCLUSIONS

We have successfully implemented a relatively complex lumped parameter model of cerebral blood flow regulation as an element that can be used at multiple cerebral outlets in a distributed parameter pulse wave propagation model. We have shown that we can simulate challenges to the regulation system such as clamp placement. Reversal to baseline flow waveforms after such a stimulus is shown to depend on the geometry of the circle of Willis. Future work will include sensitivity and uncertainty analyses of the model and corroboration of the model predictions using data obtained with transcranial Doppler ultrasonography during supra-aortic bypass surgeries.

REFERENCES

[1] J. Alastruey, K.H. Parker, J. Peiró, S.M. Byrd and S.J. Sherwin, Modelling the circle of Willis to assess the effects of anatomical variations and occlusions on cerebral flows, *Journal of Biomechanics*, 40, 1794–1805, 2007.

[2] P. Reymond, F. Merenda, F. Perren, D. Rüffenacht and N. Stergiopulos, Validation of a one-dimensional model of the systemic arterial tree, *American Journal of Physiology–Heart and Circulation Physiology*, 297, H208–H222, 2009.

[3] G. Mulder, A. Marzo, A.C.B. Bogaerds, S.C. Coley, P. Ronger, D.R. Hose and F.N. van de Vosse, Patient-specific modeling of cerebral blood flow: geometrical variations in a 1D model, *Cardiovascular Engineering and Technology*, 2(4), 334–348, 2011.

[4] M. Ursino and C.A. Lodi, Interaction among autoregulation, CO2 reactivity, and intracranial pressure: a mathematical model, *American journal of physiology–Heart and Circulatory Physiology*, 274(5), H1715–H1728, 1998.

[5] S.J. Payne, A model of the interaction between autoregulation and neural activation in the brain, *Mathematical Biosciences*, 204(1), 260–281, 2006.

[6] B.E Carlson, J.C. Arciero and T.W. Secomb, Theoretical model of blood flow autoregulation: roles of myogenic, shear-dependent and metabolic responses, *American Journal of Physiology–Heart and Circulatory Physiology*, 295(4), H1572–H1579, 2008.

[7] B. Spronck, E.G.H.J. Martens, E.D. Gommer and F.N. van de Vosse, A lumped parameter model fo cerebral blood flwo control combining cerebral autoregulation and neurovascular coupling *American Journal of Physiology–Heart and Circulatory Physiology*, 303(9), H1143–H1153, 2012.

[8] J. Alastruey, S.M. Moore, K.H. Parker, T. David, J. Peiró and S.J. Sherwin, Reducing modelling of blood flow in the cerebral circulation: coupling 1-D, 0-D and cerebral auto-regulation models, *International Journal for Numerical Methods in Fluids*, 56, 1061–1067, 2008.

[9] T.J.R. Hughes and J. Lubliner, On the one-dimensional theory of blood flow in the larger vessels, *Mathematical Biosciences*, 18, 161–170, 1973.

[10] D. Bessems, M.C.M. Rutten and F.N. van de Vosse, A wave propagation model of blodo flow in large vessels using an approximate vleocity profile function, *Journal of Fluid Mechanics*, 580, 145–168, 1973.

[11] F.N. van de Vosse and N. Stergiopulos, Pulse wave propagation in the arterial tree, *Annual Review of Fluid Mechanics*, 43(1), 467–499, 2011.

[12] W. Kroon, W. Huberts, E.M.H. Bosboom and F.N. van de Vosse, A numerical method of reduced complexity for simulating vascular hemodynamics using coupled 0D lumped and 1D wave propagation models, *Computational and Mathematical Methods in Medicine*, 2012:156094, 2012.

3rd International Conference on Computational and Mathematical Biomedical Engineering – CMBE2013
16-18 December 2013, Hong-Kong
P. Nithiarasu and R. Löhner (eds)

Impact of elastic and viscoelastic wall models on wave-propagation in large arteries

Christina Battista*, Mansoor Haider, Mette S. Olufsen*****
Dept of Mathematics, NC State University, Raleigh 26795
*cbattis2@ncsu.edu, **mahaider@ncsu.edu, ***msolufse@ncsu.edu

SUMMARY

This paper illustrates the impact of changing the constitutive equation embedded within 1D fluid dynamics model from elastic to viscoelastic. Four models were investigated, linear and nonlinear elastic, with and without viscoelasticity. Waveforms were compared, in addition to their impact on wave-propagation and reflection. Results show that with a nonlinear viscoelastic model the wave shape and propagation closer resemble recordings from ovine arterial vessels. Simulations were done for an example network consisting of one main vessel with two daughter vessels.

Key Words: *1D arterial blood flow modeling, elastic and viscoelastic wall models*

1 INTRODUCTION

There has been a tremendous rise in the occurrence of cardiovascular diseases such as atherosclerosis and hypertension [1]. Studying the biomechanical properties of arteries can help to better understand how these diseases progress, which may ultimately lead to earlier detection and improved methods of treatment. In this study we couple a generalized viscoelastic wall model with a 1D fluid dynamics model to study the impact of changes in wall properties on arterial blood flow. In particular, we focus on comparing outcomes obtained as the wall model is varied from a simple linear elastic model to a more complex nonlinear viscoelastic model. Results show changes in wave profiles as well as the impact on wave propagation along the network. The main objective is to obtain a model that can be used for prediction of patient specific flow, pressure, and area measurements obtained within the large ovine systemic arteries.

2 METHODS

The one-dimensional model is derived [2] assuming that the fluid is Newtonian, and that the flow is axisymmetric and incompressible. For each vessel, A represents the area, q the volumetric flow, p blood pressure, v viscosity, ρ density, and γ is associated with the velocity profile. Continuity of mass and momentum can be formulated as

$$\frac{\partial A}{\partial t}+\frac{\partial q}{\partial x}=0$$

$$\frac{\partial q}{\partial t}+\left(\frac{\gamma+2}{\gamma+1}\right)\frac{\partial}{\partial x}\left(\frac{q^2}{A}\right)=-\frac{A}{\rho}\frac{\partial p}{\partial x}-2(\gamma+2)\pi\nu\frac{q}{A},$$

where the velocity profile is determined by assuming that

$$u_x(r,x,t)=\frac{\gamma+2}{\gamma}U(x,t)\left(1-\left(\frac{r}{R(x,t)}\right)^{\gamma}\right).$$

Here $A(x,t) = \pi R(x,t)^2$ and the flow rate $Q(x,t) = U(x,t)A(x,t)$. This model is solved within each artery, each of which is connected in a network. At each junction we assume that flow is conserved and that pressure is continuous, i.e., the last point along a parent vessel (subscript p) is connected to the first point along two daughter vessels (subscripts $d1$ and $d2$) giving

$$Q_p(L,t) = Q_{d1}(0,t) + Q_{d2}(0,t)$$

$$p_p(L,t) = p_{d1}(0,t) = p_{d2}(0,t).$$

At the inflow to the network we specify a flow profile. The outflow, representing the effect of the micro-circulation, is modeled using a Windkessel element model specified by

$$p + CR_2\frac{dp}{dt} = (R_1 + R_2)q + CR_1R_2\frac{dq}{dt}.$$

An example model domain is shown in Fig. 1. Length and radius for this domain were set to mimic the ovine descending aorta, with a side branch feeding the abdominal region.

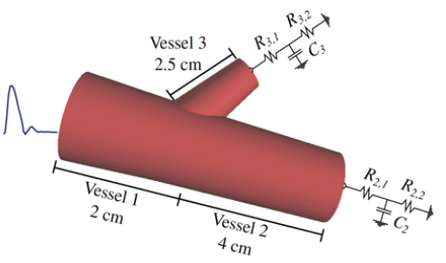

Fig 1. Example model domain used for computations. This network includes three vessels, a parent vessel with two daughters. An inflow waveform [measured] (cm/s) is specified at the inlet. At the outlets we imposed a three-element Windkessel model with two resistors (R_{1i} and R_{2i}) and a capacitor (C_i). At vessel junctions we ensure pressure continuity and flow conservation.

This fluids model is coupled with a viscoelastic wall model formulated using Fung's QLV theory where the elastic response function and the creep function are defined by

$$\epsilon(x,t) = K(0)s^{(e)}[x,p(x,t)] - \int_{t_0}^{t} s^{(e)}[x,p(x,\zeta)]K'(t-\zeta)d\zeta$$

$$\epsilon(x,t) = 1 - \sqrt{\frac{A_0}{A}}.$$

Here ϵ denotes the wall strain, K the creep, and $s^{(e)}[x,p(x,t)]$ the elastic deformation. Depending on the choice of creep and elastic deformation functions (see Table 1) the model can be designed to display either elastic or viscoelastic behavior. A total of four wall models have been investigated. Two models display purely elastic responses and two include viscoelasticity. Elastic models linear and nonlinear (sigmoidal) are obtained by setting $K = 1$ eliminating the integral. For the two viscoelastic models $K = 1 + A_1 \exp(-bt)$, where b denotes the viscoelastic relaxation time and A_1 the amplitude of the response. Again these are distinguished by including either linear or nonlinear elastic deformation.

The 1D model is solved using a stabilized space-time finite element method based on the discontinuous Galerkin method in time (for details see [2]). The numerical scheme is set up to predict pressure and flow and then uses the constitutive viscoelastic wall model to obtain area from pressure. Flow into the vessel is specified, and flow and pressure in the downstream vasculature is accounted for via coupling the 1D domain with a three-element Windkessel model, applied at each outlet as illustrated in Fig 1.

Table 1: Wall models. Left column names the model, the center the creep function, and the right the elastic deformation function. For all models $A_0(x) = \pi R_0(x)$ denotes the unstressed vessel area, E Young's modulus, h wall thickness, $p(x,t)$ pressure, b the relaxation time, A_1 the relaxation gain, p_h the half-width pressure, ξ the sigmoid steepness, and A_m is half the maximum area.

Model	$\boldsymbol{K(t)}$	$\boldsymbol{S^{(e)}[x,p(x,t)]}$
Linear elastic	1	$\frac{R_0(x)}{Eh}p(x,t)$
Nonlinear elastic	1	$1-\sqrt{\frac{A_0(x)\left(p_h^{\xi}+A_m p(x,t)^{\xi}\right)}{A_0(x)p_h^{\xi}+A_m p(x,t)^{\xi}}}$
Kelvin model (linear)	$1 - A_1 \exp(-bt)$	$\frac{R_0(x)}{Eh}p(x,t)$
Nonlinear viscoelastic	$1 - A_1 \exp(-bt)$	$1-\sqrt{\frac{A_0(x)\left(p_h^{\xi}+A_m p(x,t)^{\xi}\right)}{A_0(x)p_h^{\xi}+A_m p(x,t)^{\xi}}}$

3 RESULTS

Preliminary results (see Fig. 2) show that wave shape and amplitude vary significantly with the wall model. The inclusion of viscoelasticity has a dampening effect on the pressure wave, while maintaining flow and area. Moreover, the pressure and flow waveforms becomes more distinct, similar to observations from measurements (not shown). The inclusion of nonlinearity within the elastic model allows more accurate prediction of pressure-area loop (also see [3]). The latter is of particular importance for accurate predictions within the aorta. Moreover, the wave-propagation is impacted, slowing down the wave-propagation speed compared with purely elastic models.

4. CONCLUSIONS

This study has shown that incorporation of viscoelasticity within the arterial wall is important for accurate prediction of flow, pressure and area waveforms, and that the inclusion of nonlinear elastic wall model is of importance in particular to predict deformation within the aorta. These observations are similar to results obtained by other investigators (e.g. [4]), though it is the first study to compare different wall models embedded within a 1D fluid dynamics model. With this improved model, in future studies, we aim to devise patient specific models. However, to do so one important question remains to be addressed: How does the elasticity vary along the vessel? It is well known that vessels become stiffer along their length, e.g., will stiffening obtained by varying $R_0(x)$ be adequate or is it necessary to adjust Young's modulus as well.

ACKNOWLEDGEMENTS

This research was supported in part by NSF via awards NSF/DMS-1122424 and NSF/DMS-0943855 and by NIH under 1P50-GM094503-01A0 sub-award to NCSU.

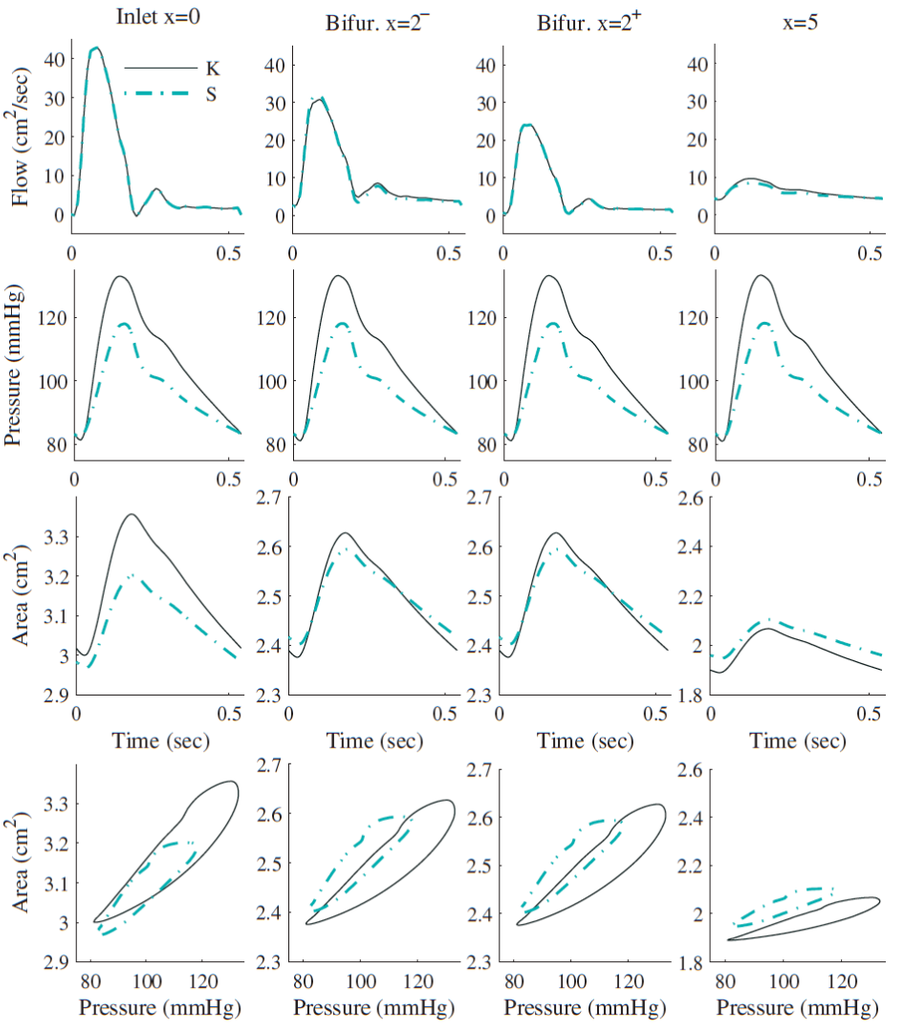

Fig. 2: Blood flow (top row), pressure (2nd row) and area (3rd row) waveforms within the domain shown in Fig. 1. The bottom row shows area pressure loops arising with application of the visco-elastic models. Results with the elastic models (see, e.g. [2]) do not give rise to loops, for these pressure waves are significantly higher.

REFERENCES

[1] V Fuster Epidemic of Cardiovascular Disease and Stroke: The Three Main Challenges, Circ 99, 1132-1137, 1999.

[2] B.N. Steele, D. Valdez-Jasso, M.A. Haider, M.S. Olufsen. Predicting arterial flow and pressure dynamics using a 1D fluid dynamics model with a viscoelastic wall, *SIAM J Appl Math*, 71, 1123-1143, 2011.

[3] D. Valdez-Jasso, D. Bia, Y. Zocalo, R.L. Armentano, M.A. Haider, Olufsen. Linear and nonlinear viscoelastic modelling of aorta and carotid pressure-area dynamics under in vivo and ex vivo conditions, *Ann Biomed Eng,* 29, 1438-1456, 2011.

[4] P. Raymond, F. Merenda, F. Perren, D. Rufenacht, N. Stergiopulos. Validation of a one-dimensional model of the systemic arterial tree, *Am J Physiol*, 297, H208-H222.

3rd International Conference on Computational and Mathematical Biomedical Engineering – CMBE2013
16-18 December 2013, Hong-Kong
P. Nithiarasu and R. Löhner (eds)

On generic and patient specific 1-D models of the systemic arterial tree

P. Reymond, O. Vardoulis, N. Stergiopulos
Laboratory of Hemodynamics and Cardiovascular Technology,
EPFL, BM 5125, Station 17, 1015 Lausanne, Switzerland

SUMMARY

Recent advance in imaging modalities used frequently in clinical routine can provide description of the geometrical and hemodynamical properties of the arterial tree in great detail. The combination of such information with models of blood flow of the arterial tree can provide further information, such as details in pressure and flow waves or details in the local flow field. Such knowledge maybe be critical in understanding the development or state of arterial disease and can help clinicians perform better diagnosis or plan better treatments. In the present review, the state of the art of arterial tree models is presented, focusing on 1-D wave propagation models. Our development of a generic and patient-specific model of the human arterial tree permitting to study pressure and flow waves propagation in patients is presented. The predicted pressure and flow waveforms are in good agreement with the in vivo measurements. We discuss the utility of these models in different clinical application and future development of interest.

Key Words: *arterial hemodynamics, wave propagation, validation of arterial models, heart model, ventricular–vascular coupling*

1. INTRODUCTION

Blood flow phenomena and related hemodynamical forces play an important role in various forms of vascular disease. Pressure wave reflections, for example, play a pivotal role in the development of isolated systolic hypertension. From a clinical standpoint, the assessment of hemodynamical forces within the systemic circulation is still difficult. For instance, in the cerebral circulation, pressure can be measured only invasively and flow, especially in small deep intracranial vessels such as those in the vicinity of the circle of Willis, cannot be measured directly with Doppler ultrasound. This renders modeling of blood flow within the cerebral circulation an attractive alternative and the same may apply to other parts/organs of the systemic circulation. Mathematical models of the arterial tree, when utilized in conjunction with in vivo data can lead to a better understanding of the physiopathology of the cardiovascular system.

In this review article, we describe a 1D model of the circulation, which can be used to predict pressure, and flow waves in generic or patient specific arterial trees. We discuss also the utility of 1D arterial models in various clinical applications and foreseeable future developments of such models.

2. MAIN BODY

We have constructed a complete 1-D model of the arterial tree, which comprises 103 segments and includes a detailed description of all systemic arteries, including the coronaries, a detailed cerebral arterial tree, a heart model and appropriate description of wall viscoelasticity. The approach we followed was to compare the predictions of the generic 1-D model with the average pressure and flow waveforms measured noninvasively in a group of healthy young people (Fig. 1). The underlying hypothesis was that although the generic model would not represent precisely a specific individual it would represent quite well the ‘‘average’’ of the group.

The fluid mechanics equations were solved numerically to obtain pressure and flow throughout the arterial tree. The heart is modeled using the time varying elastance model, providing a versatile and physiologically relevant way to take into account parameters like heart rate, maximum contractility, and changes in preload and atrial pressure. The coronary arteries were modeled assuming a systolic flow impediment proportional to ventricular varying elastance. A nonlinear viscoelastic constitutive law for the arterial wall was considered while distal vessels were terminated with a three-element Windkessel model. We have included all main cerebral artery segments as well as all afferent and efferent arteries in the vicinity of the circle of Willis, a frequent location of cerebral aneurysms. Many extracranial arteries, such as the superficial temporal arteries have also been added, in order to include points where pressure can be measured noninvasively and serve in the validation of the work.

Some data for pressure and flow in major systemic arteries are available, where Doppler measurements for flow velocity are accessible and tonometry (for pressure) is feasible. However, non-invasive measurements of cerebral pressure and flow waves are scarce. Most of the measurements have been performed for extracranial arteries such as the common carotid by Doppler ultrasound and the internal carotid and vertebral artery flow rate by MRI. Few data are available for the efferent vessels of the circle of Willis (anterior, middle and posterior cerebral arteries). For systemic arteries, there is no complete data set for pressure and flow measured at several arterial locations and where arterial properties are also measured or estimated on an individual basis. Hence, 1-D model validation cannot be based on data in the literature. Thus, we performed a more complete set of non-invasive measurements. Flow in the large arteries was quantified with PCMRI, cerebral flow detected with ultrasound Doppler and blood pressure measured with applanation tonometry. Figure 1 shows that the model is able to reproduce well the pressure and flow waveforms characteristics of an average subject.

On a second stage, we proceeded with the construction of a patient-specific model. Measurements of geometry, elasticity, flow and pressure were performed on the same subject. The model predictions were validated with noninvasive measurements of pressure and flow performed on the same person. Model predictions at different arterial locations compared well to measured flow and pressure waves at the same anatomical points. The model predicted pressure and flow waveforms in good agreement with the in vivo measurements with regards to wave shape and features.

Clinical applications and future prospects

Coronary circulation can also be studied with 1-D models and can help understanding the physiological specificity of the coronary circulation [38], when contraction of the myocardium affects coronary perfusion. Many questions remain regarding the physiology and hemodynamics of coronary circulation and numerous models have been proposed. Classical models referred to the systolic extravascular model, waterfall model or intramyocardial pump model and the effect of the contraction can be affected by the elastance and/or pressure of the left ventricle. These different models can be studied with the help of a 1-D wave propagation approach. Pulmonary

circulation can also be studied by the 1-D model to study, for instance, pulmonary hypertension. The interaction between arterial blood flow and cerebrospinal fluid can be also studied with coupled 1-D models of both systems. This interaction seems to play an important role in some cerebrospinal fluid-related pathologies.

Based on a person-specific in vivo measurements, a 1-D model can be used and optimized to find the better fit between measured and simulated pressure and flow waveforms, by adjusting key parameters such as compliance, geometry, and elastance. Estimation of the arterial tree or heart model parameters can be useful to characterize the state of the arterial tree.

Central aortic pressure is a better indicator of cardiac risk than distal peripheral pressure. However, aortic pressure is only available with invasive measurements. Thus, the use of a transfer function between peripheral and central pressure could be a useful clinical tool to help for a better understanding of the cardiac risk in a non-invasive manner. A 1-D wave propagation model is well suited for this task.

In the case of isolated systolic hypertension, pressure load on the heart is affected by the contribution of pressure waves that travel forward and backward (reflected waves) and affect central pulse pressure. In this situation, hemodynamics is governed by global wave phenomena and to a lesser extent by local 3-D flow. Therefore, wave propagation models (1-D models) are the most appropriate.

Arterial tree model may be also utilized to generate large pressure waveform datasets by altering model parameters within physiological range. In studies were processing of various pressure waveforms is required to test methods for the estimation of cardiac output or for the estimation of total systemic compliance by PWV the arterial tree model can play a pivotal role in reducing the need for in vivo data while in the validation zone.

1-D models are also able to provide pressure and flow waveforms in an extended region of the arterial tree, which is useful for diagnostics, treatment planning and for surgical planning. Outcome of bypass surgery predicted by a 1-D wave propagation model with MRI data has been reported. Pulse wave propagation models can be applied to predict the hemodynamic of an arteriovenous fistula in hemodialysis.

3. CONCLUSIONS

We presented the development of a generic arterial tree that predicted pressure and flow at systemic circulation locations with a good agreement as compared to in vivo measurements. A person-specific model was also presented, predicting pressure and flow waveforms with very good accuracy. 1D models have proven to be very useful tools for the better understanding and analysis of the human circulation. Patient-specific models have potential to be used in a clinical environment and could be useful for providing better diagnosis or even better treatment planning in the near future.

REFERENCES

[1] P Reymond, F Merenda, F Perren, D Rufenacht and N Stergiopulos. Validation of a one-dimensional model of the systemic arterial tree, *Am J Physiol Heart Circ Physiol.* 297(1):H208–22, 2009.

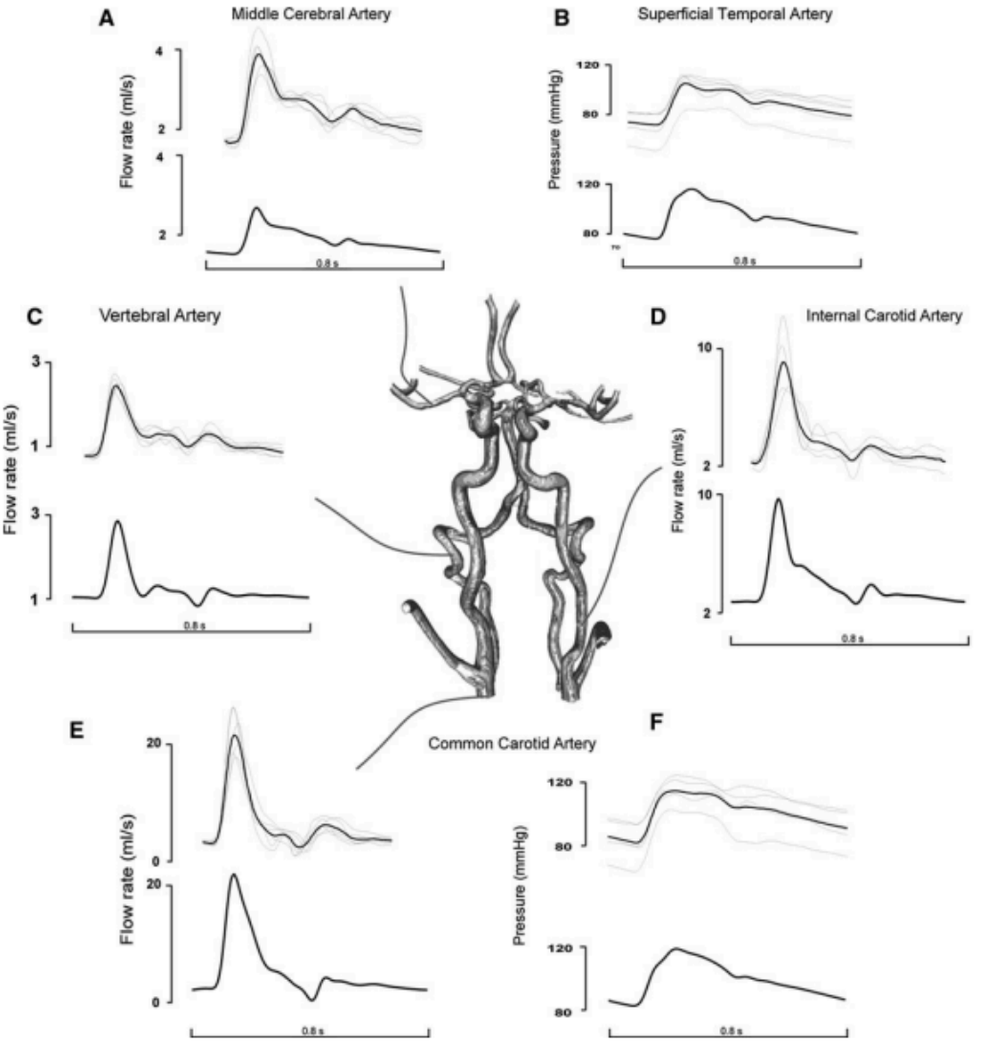

Fig. 1 Taken from [1]. Model results for a generic arterial tree (bottom panels) compared to in vivo measurements (top panels) at various cerebral artery locations. Thick line represents the averaged waveform. Blood flow was measured with color-coded duplex ultrasound (a, c, d, e). Pressure was measured with applanation tonometry in the superficial temporal artery (b) and common carotid (f).

Inverse Problems in Cardiovascular Mathematics

3rd International Conference on Computational and Mathematical Biomedical Engineering - CMBE2013
16-18 December 2013, Hong-Kong
P. Nithiarasu and R. Löhner (Eds.)

Variational estimation of cardiac conductivities

Huanhuan Yang*, Alessandro Veneziani*
*Emory University, 400 Dowman Drive, W401, Atlanta (GA) USA
hyang52@emory.edu, avenez2@emory.edu

SUMMARY

Numerical simulations of cardiac potential are in general significantly sensitive to the parameters of the Bidomain model, the current standard model in electrocardiology. Unfortunately, these parameters - and in particular the cardiac conductivities - are quite problematic to measure *in vivo* and even more in clinical practice. On the other hand, no common agreement has been reached in the literature about cardiac conductivities. In this talk, we consider a data assimilation approach for estimating those parameters. More specifically, we consider the parameters as control variables to minimize the mismatch between the computed and the measured potentials, under the constraint of the Bidomain equations. The functional to be minimized is suitably regularized a lá Tikhonov. We prove the existence of a minimizer and we solve the problem with the BFGS method based on dual equations, showing that this method compares favorably with other methods present in the literature. We provide preliminary numerical results in 2D and 3D, showing the reliability of the approach with different numbers of measurement sites and in presence of noise.

Key Words: *cardiac conductivity, bidomain model, variational data assimilation.*

1 INTRODUCTION

In cardiovascular science, numerical simulations have provided a powerful tool for therapies in heart diseases. Although they are progressively used in clinical practice by integrating mathematical models and data/images, reliability of patient specific simulations is still a crucial issue. Data assimilation in cardiovascular mathematics is therefore an important topic presenting new challenging (inverse) problems. In our project we focus on the assimilation of data and numerical model for the quantification of cardiac conductivities.

The Bidomain model in electrocardiology is a commonly accepted representation of the cardiac potential propagation. The model has been proved to be strongly sensitive to the values of conductivities and in particular to the ratio between the tangential and longitudinal extracellular conductivities [3]. Although the significance of a precise patient specific cardiac conductivity estimation has been recognized since a long time [9], an accurate individual measure of these parameters is extremely difficult for several practical reasons. Experimental estimation has been carried out in different ways by several groups [1, 7, 8], leading to different ranges of possible values with no common agreement on the most accurate ones. On the other hand, computational methods for conductivity estimation have been advocated only in the last few years. Recently, a least-square approach [2] for an estimation of conductivities has been proposed. It refers to 2D synthetic cases and clearly show that the variational estimate may provide accurate results. However, it is computationally expensive and the synthetic data is not achievable in clinic.

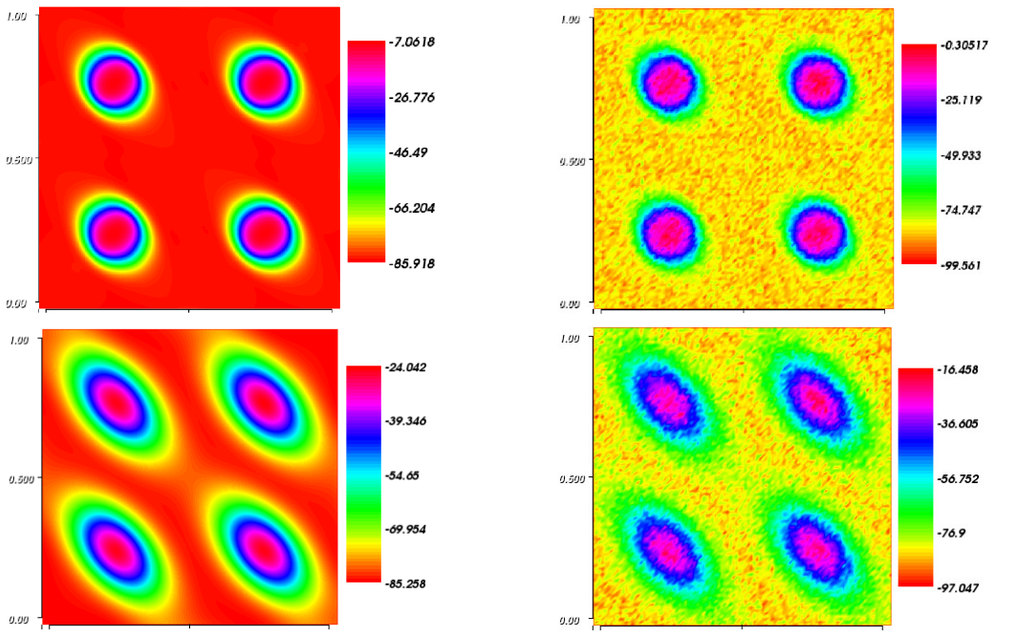

Figure 1: Upperleft: u_{meas} at $t = 2ms$. Lowerleft: u_{meas} at $t = 12ms$. Upperright: u_{meas} at $t = 2ms$ with 15% noise. Lowerright: u_{meas} at $t = 12ms$ with 15% noise

Table 1: On square. The case generated data has much finer mesh size than optimization simulation. $\boldsymbol{\sigma}_{exact} = [2.8, 0.26, 2.2, 1.3], T = 25ms, \Delta t = 0.025ms$, and $dt_{\text{snap}} = 0.5ms$.

noise	0%	10%	15%
$\sigma_{il}\|e_{il}$	2.7504|0.0496	2.72529|0.07471	2.71204|0.08796
$\sigma_{it}\|e_{it}$	0.208004|0.051996	0.210232|0.049768	0.211344|0.048656
$\sigma_{el}\|e_{el}$	2.22046|0.02046	2.23888|0.03888	2.24965|0.04965
$\sigma_{et}\|e_{et}$	1.31297|0.01297	1.32505|0.02505	1.33751|0.03751
Initial $\mathcal{J}$	0.442516	0.45743	0.47792
Final $\mathcal{J}$	0.00161641	0.0187802	0.0403941
Iter. fwd|bwd	18|16	21|18	19|18

2 MAIN BODY

In this talk we present a somehow different numerical approach to be used in 3D problems. We resort to a variational procedure for the estimation of cardiac conductivities from measures of the transmembrane potential available at some sites on the tissue. We provide a rigorous mathematical formulation of the problem based on constrained minimization arguments and a well-posedness analysis, mostly inspired by K. Kunisch and his collaborators on the identification of the optimal stimulus for pace-making [4, 5, 6]. Our numerical procedure is based on the classical Lagrange multiplier approach. Constrained minimization is performed by a gradient-descent method, where the Bidomain equations act as a constraint between the conductivities to be estimated and the cardiac potentials. The gradient of the functional to be minimized is solved by resorting to the adjoint equations of the Bidomain system. In particular, we pursue an Optimize-then-Discretize approach, leading to the solution of a backward in time set of equations.

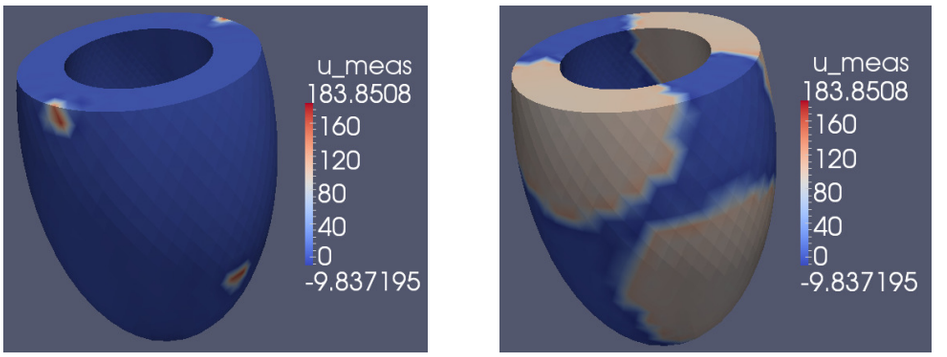

Figure 2: Left: u_{meas} at $t = 1ms$, Right: u_{meas} at $t = 15ms$.

Table 2: On ellipsoid. $T = 20ms$, $\Delta t = 0.1ms$, $\Delta t_{\text{snap}} = 0.5ms$, # sites = 150, noise = 10%.

$\boldsymbol{\sigma}_{exact}$	[2.8,2.2,0.26,1.3]	[2.8,2.2,0.26,1.3]	[3.5,3,0.3,1.8]	[3.5,3,0.3,1.8]
$\boldsymbol{\sigma}_{initial}$	[5, 5, 3, 3]	[2, 2, 1, 1]	[5, 5, 3, 3]	[2, 2, 1, 1]
σ_{il}	2.62885	2.74088	3.4704	3.47661
σ_{el}	2.37449	2.29435	3.12013	3.11378
σ_{it}	0.27818	0.274675	0.306733	0.306189
σ_{et}	1.33207	1.24734	1.6459	1.64325
# fwd|bwd	26|22	17|12	24|22	21|20

Numerical results presented, referring to synthetic test cases, show that the estimation of conductivities can be achieved in presence of noise with a significant reduction of the number of iterations required by the Least Square approach of [2]. A 2D result on a square is reported in Table 1, in which $\boldsymbol{\sigma}$ denotes the conductivity tensor, σ_{il} (σ_{it}) denotes the longitudinal (tangential) intracellular conductivity, while σ_{el} (σ_{et}) is the extracellular counterpart. The corresponding forward solver result is shown in Figure 1. A 3D result on an ellipsoid is also reported in Table 2. Experimental validation is currently carried out in collaboration with Dr. Fenton at Georgia Institute of Technology.

3 CONCLUSIONS

We have investigated a variational data assimilation approach for providing conductivity estimates from potential measurements. We also proved the correct statement of the problem, by showing the existence of a set of parameters minimizing the (regularized) mismatch between numerical results and measurements.

The next steps of the present work will be to perform validation with in vitro experiments and to reduce the computational costs, since the iterated solution of the Bidomain system and its dual in real geometries are fairly demanding. For this reason, we will investigate possible model reduction techniques, to replace in the optimization process with low-dimensional models.

References

[1] L. Clerc. Directional differences of impulse spread in trabecular muscle from mammalian heart. *J Phisiology*, 255:335–346, 1976.

[2] L. S. Graham and D. Kilpatrick. Estimation of the bidomain conductivity parameters of cardiac tissue from extracellular potential distributions initiated by point stimulation. *Annals of Biomedical Engineering*, 38(12):3630–3648, 2010.

[3] P.R. Johnston. A sensitivity study of conductivity values in the passive bidomain equation. *Mathematical biosciences*, 232(2):142–150, 2011.

[4] K. Kunisch and M. Wagner. Optimal control of the bidomain system (i): The monodomain approximation with the rogers-mcculloch model. Technical Report Preprint 03, Institute of Mathematics, 2011.

[5] K. Kunisch and M. Wagner. Optimal control of the bidomain system (ii): Uniqueness and regularity theorems for weak solutions. Technical Report SFB-Report 08, Institute for Mathematics and Scientific Computing, 2011.

[6] K. Kunisch and M. Wagner. Optimal control of the bidomain system (iii): Existence of minimizers and first-order optimality conditions. Technical Report SFB-Report 31, Institute for Mathematics and Scientific Computing, 2011.

[7] D.E. Roberts, L.T. Hersh, and A.M. Scher. Influence of cardiac fiber orientation on wavefront voltage, conduction, velocity and tissue resistivity in the dog. *Circ Res*, 44(5):701–712, 1979.

[8] D.E. Roberts and A.M. Scher. Effect of tissue anisotropy on extracellular potential fields in canine myocardium in situ. *Circ Res*, 50(3):342–351, 1982.

[9] R. Sadleir and C. Henriquez. Estimation of cardiac bidomain parameters from extracellular measurement: two dimensional study. *Annals of biomedical engineering*, 34(8):1289–1303, 2006.

3rd International Conference on Computational and Mathematical Biomedical Engineering - CMBE2013
16-18 December 2013, Hong-Kong
P. Nithiarasu and R. Löhner (Eds.)

Sequential estimation in fluid-structure interaction and identification of arterial wall stiffness: in-vitro validation and in-vivo results

C. Bertoglio[1,7], D. Barber[2], N. Gaddum[3], I. Valverde[3], M. Rutten[4], P. Beerbaum[5]
P. Moireau[6], R. Hose[2], J.-F. Gerbeau[1]
1 REO team, INRIA Paris-Rocquencourt, France
2 Department of Cardiovascular Sciences, University of Sheffield, UK
3 Division of Imaging Sciences and Biomedical Engineering, King's College London, UK
4 Materials Technology Institute, Technical University of Endhoven, The Netherlands
5 Clinic for Paediatric Cardiology and Internal Medicine, Hannover Medical School, Germany
6 M3DISIM team, INRIA Saclay Ile-de-France, France
7 Institute for Computational Mechanics, Technische Universität München, Germany

SUMMARY

The in vivo estimation of arterial stiffness can provide valuable information about the cardiovascular condition of a patient [9]. In clinical practice, the Pulse Wave Velocity [12] gives an estimation of the *average* stiffness of a portion of the arterial network by solving the Moens-Korteweg equation, which assumes a linear solid in an infinite cylindrical domain. Other methods include Vascular Elastography, either based on Ultrasound [5] or Magnetic Resonance (see e.g., [13]), where the models used for estimating arterial stiffness are again based on simplified models.

Recently, in [4] it was proposed an efficient methodology to estimate uncertain parameters (for example Young's modulus or fluid boundary conditions) from measurements of the displacement of the wall in an idealized 3D fluid-structure interaction (FSI) problem. Whereas in [4] validations are only based on synthetic data, we consider in the present work the experimental validation of this method using real data in a fluid-structure interaction context. Hence, this work complements the work of [10] since here we estimate the stiffness parameters and not the boundary conditions.

Key Words: *Fluid-structure interaction, data assimilation, stiffness estimation, medical imaging*

1 METHODS

In order to effectively indentify the stiffness in FSI systems, we use the following "ingredients":

- **Numerical FSI model**: The fluid is described by the Navier-Stokes equations (NSE), in a moving domain in an Arbitrary Lagrangian Eulerian (ALE) formulation, and the structure by the elastodynamic equations, see e.g. [6]. We use a first order stabilized finite element and for the time marching a semi-implicit partitioned FSI-algorithm [7]. The coupling between the solid and the fluid is explicit in the ALE-advection-diffusion step and implicit for the pressure projection step and the Windkessel [3].
- **Sequential Data Assimilation**: We follow a sequential, or *filtering*, approach which modifies the forward dynamics with a correction term proportional to the observation error. More

precisely, we adopt the Reduced-Order Unscented Kalman Filter (ROUKF) [11], inspired from [8]. It does not require any tangent operator and allows to run the estimation with a computational cost of the same order of the forward problem. Moreover, it requires only superficial modifications to the existing solvers.

- **Image registration based segmentation**: the data assimilation process requires segmentations of dynamic image data, which is performed by registration of one reference image to each frame (target image) of the dynamic images using the Sheffield Image Registration Toolkit (ShIRT), for details see [1].

2 IN VITRO VALIDATION

The experimental setup consists of a MR-compatible emulator of the systemic circulation, with a silicon ruber aortic tube, with a elastic strap at the distal end in order to model a coarctation. Pressure measurements were taken at 13 locations between the venous and arterial compliance chambers. Then, MR-acquisitions for extracting the geometry were perfomed, and the images segmented. A non-destructive mechanical test was then performed consisting in placing the tube (without the strap) vertically, filling it with water, and then injecting an additional controlled water volume while measuring the pressure at the bottom. A pressure dependent Young's modulus was then constructued using basic linear solid mechanics theory. We then subdivide the tube's solid volume in 10 regions and estimate simultaneously the Young's modulus for each region. As it can be seen in Figure 1, the estimation algorithm succesfully detects the stiffer regions (first and second, which correspond to the actual placement of the strap), while in the regions where the strap is not presented the stiffness values are close to the one derived from the mechanical test.

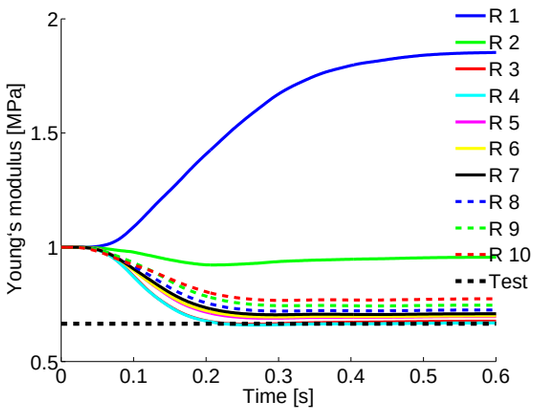

Figure 1: Estimation results for the 10 regions and reference value from the mechanical test.

3 IN VIVO RESULTS

The available clinical data corresponds to a 19 year old male subject with a mild (repaired) coarctation of the descending aorta. A static 3D MR-image was obtained with a 10-seconds untriggered acquisition and a gadolinium contrast agent. A 4D-SSFP sequence was acquired (25 time frames) along the cardiac cycle. Consequently, the 25 surfaces were segmented with the template mesh

obtained from the 3D-Gd. The solid volume was divided into 5 regions (see Figure 2-left) where a Mooney-Rivlin constitutive model with parameters $c_1^j = 3 \cdot 10^5 \cdot 2^{\theta^j}$, $c_2^j = 10^4$ and $\kappa^j = 10^8$ for each region $j = 1, \ldots, 5$, with θ_j being the parameters to estimate. For more details about the FSI-model we refer to [2].

The estimation results are presented in Figure 2. However, the results are not as converged as in the in vitro validation. This is most probably due to modelling errors, since for example external tissue (in particular the superior vena cava and the pulmonary trunk at the ascending aorta) are not taken into account in this case. Another likely cause lies in the low signal-to-noise ratio (SNR), in particular in the coarctation region. Hence, the estimated stiffness parameters evolve and oscillate in time in order to compensate for these modelling and data errors.

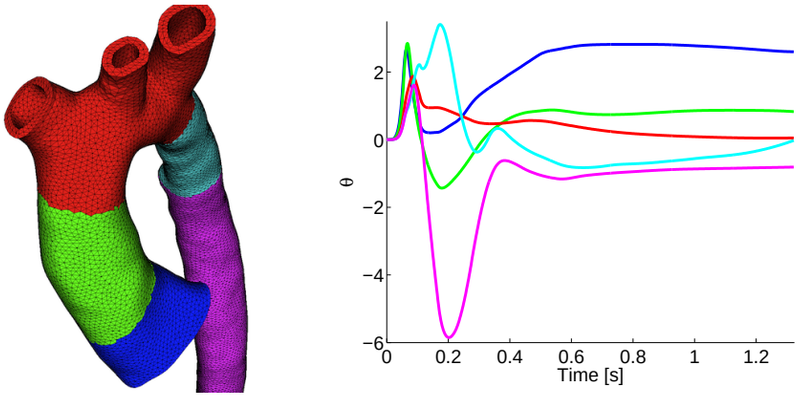

Figure 2: Estimation results for the constitutive parameters θ^j, $j = 1, \ldots, 5$ from clinical data.

4 CONCLUSION

We performed an in vitro validation of the parameter estimation algorithm for coupled fluid-structure systems presented in [4]. For this purpose, we considered a silicon rubber tube emulating the aorta, connected with a mechanical model of the main components of the cardiovascular system. We verified one of the estimated parameters from data coming from an independent non-destructive mechanical test. In addition, we show that we can straightforwardly use the algorithm in a real clinical case, namely for the estimation of the Mooney-Rivlin constitutive parameters in an aorta with repaired coarctation from the 4D-SSFP sequence, obtaining meaningful results for the estimated parameter values.

ACKNOWLEDGEMENT

The research leading to these results has received funding from the European Communitys Seventh Framework Programme (FP7/2007-2013) under grant agreement 224495 (euHeart project). The author also thanks his current affiliation, the Institute for Computational Mechanics at the Technical University of Munich, Germany, for supporting the presentation of these results.

REFERENCES

[1] D.C. Barber, E. Oubel, A.F. Frangi, and D.R. Hose. Efficient computational fluid dynamics mesh generation by image registration. *Medical Image Analysis*, 11(6):648 – 662, 2007.

[2] C. Bertoglio. *Forward and inverse problems in fluid-stucture interaction. Application to hemodynamics*. PhD thesis, Universié Pierre et Marie Curie, Paris, France, 2012.

[3] C. Bertoglio, A. Caiazzo, and M.A. Fernández. Fractional-step schemes for the coupling of distributed and lumped models in hemodynamics. *SIAM J. Sci. Comp.*, 35(3):B551–B575, 2013.

[4] C. Bertoglio, P. Moireau, and J-F. Gerbeau. Sequential parameter estimation in fluid-structure problems. Application to hemodynamics. *Int. J. Numer. Meth. Biomed. Engrg.*, 28:434–455, 2012.

[5] Chris L. de Korte, Hendrik H. G. Hansen, and Anton F. W. van der Steen. Vascular ultrasound for atherosclerosis imaging. *Interface Focus*, 1(4):565–575, 2011.

[6] M.A. Fernández and J-F. Gerbeau. Algorithms for fluid-structure interaction problems. In L. Formaggia, A. Quarteroni, and A. Veneziani, editors, *Cardiovascular Mathematics. Modeling and simulation of the circulatory system*, chapter 9, pages 307–346. Springer Verlag, 2009.

[7] M.A. Fernández, J.F. Gerbeau, and C. Grandmont. A projection semi-implicit scheme for the coupling of an elastic structure with an incompressible fluid. *Int. J. Num. Meth. Engrg.*, 69(4):794–821, 2007.

[8] S. Julier, J. Uhlmann, and H.F. Durrant-Whyte. A new method for the nonlinear transformation of means and covariances in filters and estimators. *Automatic Control, IEEE Transactions on*, 45(3):477–482, 2000.

[9] S. Laurent, J. Cockcroft, L. Van Bortel, P. Boutouyrie, C. Giannattasio, D. Hayoz, B. Pannier, C. Vlachopoulos, I. Wilkinson, and H. Struijker-Boudier. Expert consensus document on arterial stiffness: methodological issues and clinical applications. *European Heart Journal*, 27(21):2588–2605, 2006.

[10] P. Moireau, C. Bertoglio, N. Xiao, C.A. Figueroa, C.A. Taylor, D. Chapelle, and J.-F. Gerbeau. Sequential identification of boundary support parameters in a fluid-structure vascular model using patient image data. *Biomechanics and Modeling in Mechanobiology*, pages 1–22, 2012.

[11] P. Moireau and D. Chapelle. Reduced-order Unscented Kalman Filtering with application to parameter identification in large-dimensional systems. *COCV*, 17:380–405, 2011. doi:10.1051/cocv/2010006.

[12] W.W. Nichols, M.F. O'Rourke, and C. Hartley. *McDonald's blood flow in arteries: theoretical, experimental and clinical principles*, volume 340809418. Hodder Arnold London, 2005.

[13] D.A. Woodrum, A.J. Romano, A. Lerman, U.H. Pandya, D. Brosh, P.J. Rossman, L.O. Lerman, and R.L. Ehman. Vascular wall elasticity measurement by magnetic resonance imaging. *Magnetic Resonance in Medicine*, 56(3):593–600, 2006.

3rd International Conference on Computational and Mathematical Biomedical Engineering - CMBE2013
16-18 December 2013, Hong-Kong
P. Nithiarasu and R. Löhner (Eds.)

Finding cardiac conductivity values: An inverse problem approach

Peter R. Johnston⋆ and Barbara M. Johnston⋆⋆
School of Biomolecular and Physical Sciences and Queensland Micro- and Nanotechnology centre, Griffith University, 170 Kessels Rd, Nathan, Queensland, Australia, 4151
⋆e-mail: P.Johnston@griffith.edu.au, ⋆⋆e-mail: Barbara.Johnston@griffith.edu.au

SUMMARY

Accurate determination of cardiac conductivity values is of paramount importance for detailed simulation of many electrophysiological phenomena. Here we present an approach to determine these values using Tikhonov regularisation applied to potential measurements made on a microneedle array. Results show that it is possible to accurately retrieve most of the required values with measurement noise as high as 10%.

Key Words: *cardiac conductivity, bidomain model, electrophysiology, inverse problem, Tikhonov regularisation*

1 INTRODUCTION

Values for the bidomain electrical conductivities play a significant role in the modelling and simulation of many cardiac related phenomena, for example, activation sequences [1], fibrillation [2], ST segment shifts [3] and defibrillation [4]. To date, work on determining accurate cardiac conductivity values has centred on developing mathematical methods, and, to a lesser extent, experimental techniques, for determining these values. Most of these methods are based on the so–called four electrode technique [5], which uses four collinear equi–spaced electrodes, where current is applied to the outer pair, and measurements are made on the inner pair, of electrodes.

Recently, several alternative methods have been presented for determining the conductivity values. One new experimental technique [6] maps cardiac tissue activation and then obtains the cardiac parameters using a least squares and singular value decomposition approach. A new computational approach [7], although only presently applied to a 2D monodomain, suggests simplifying the problem of retrieving conductivities from transmembrane potential measurements made by microelectrode arrays, by using a novel parallel optimisation algorithm. Johnston et al. [8] demonstrated that a two pass approach, using 'closely' and 'widely' spaced subsets of electrodes (Figure 1(left)) and an inversion technique based on Tikhonov regularisation [9], was able to accurately retrieve four conductivities and fibre rotation from a simulated set of potentials to which noise was added.

Recently, work by Hooks and Trew [10] has confirmed that three unique intracellular electrical conductances can be defined at any point in the ventricular wall and this has added impetus to the search for techniques that will enable six, rather than four, cardiac conductivity values to be determined. As a result, it has been shown recently [11,12] using a three-layered multi–electrode array and a similar mathematical model and inversion technique to that discussed above [8], that it is possible to retrieve all six conductivities as well as fibre rotation. Here we discuss the performance of this method of conductivity value determination in the sense of an inverse problem.

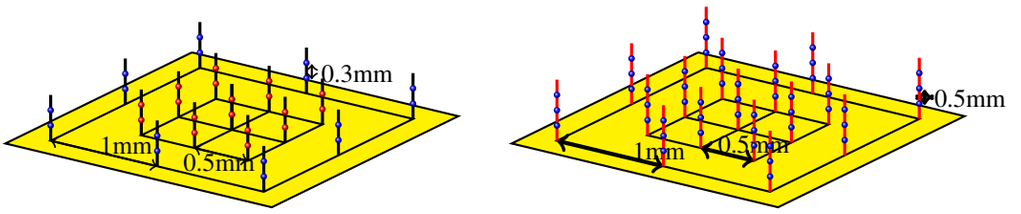

Figure 1: Two–layer (left) and three layer (right) multi–electrode arrays used to retrieve four and six conductivity values (respectively). Subsets of the electrodes are used in a two–pass protocol.

2 METHODS

Mathematically, the bidomain equations governing the electric potential in a slab of cardiac tissue and the adjacent blood mass are given by

$$\nabla \cdot \mathbf{M}_i \nabla \phi_i = \frac{\beta}{R}(\phi_i - \phi_e), \quad \nabla \cdot \mathbf{M}_e \nabla \phi_e = -\frac{\beta}{R}(\phi_i - \phi_e) - I_s, \quad \nabla^2 \phi_b = 0. \tag{1}$$

where ϕ_h ($h = i$, e or b) is the potential, (i=intracellular, e=extracellular, b=blood), I_s is the applied current, β is the surface to volume ratio for the cells and R is membrane resistance. The conductivity tensors, which can be written as $\mathbf{M}_h = \mathbf{A}\mathbf{G}_h\mathbf{A}^T$ ($h = i$ or e) where $\mathbf{A}$ represents the local direction of the fibres and $\mathbf{G}_h$ is a diagonal matrix, containing the longitudinal (g_{hl}), transverse (g_{ht}) and normal tissue conductivities (g_{hn}) along the diagonal, reflect the fact that current can flow along the direction of the fibres (longitudinally) more easily than it can across the sheets of fibres (transversely) or between the sheets (normally).

The boundary conditions necessary to solve the above equations are derived from the assumptions that: the epicardium is insulated; there is continuity of potential and current at the interface between the tissue and the blood; the intracellular space is insulated by the extracellular space; the blood mass is assumed infinite in the positive z direction; and finally, the boundaries of the tissue and blood are insulated.

The model, described by equations (1), shows that the potentials depend on the conductivity parameters in a nonlinear fashion,

$$\mathbf{F}(\mathbf{m}) = \mathbf{\Phi} \tag{2}$$

where $\mathbf{\Phi}$ is the vector of measured potentials, $\mathbf{m} = [g_{il}, g_{it}, g_{in}, g_{el}, g_{et}, g_{en}, \alpha]^T$ (α is the total fibre rotation through the slab) and $\mathbf{F}$ represents the forward model. To obtain $\mathbf{m}$ from equation (2) it is then necessary to minimise the Tikhonov functional

$$\|\mathbf{F}(\mathbf{m}) - \mathbf{\Phi}\|_2^2 + \gamma^2 \|\mathbf{m}\|_2^2 \tag{3}$$

since there will be noise in the measurement vector $\mathbf{\Phi}$. Here γ is the regularisation parameter.

Minimisation of the functionals is performed using the SolvOpt solver [12], which minimises non–linear multivariate functions using a modified Shor's r–algorithm. The constraints applied for the minimisation are that $0 \leq \alpha \leq \pi$ and that the conductivities are positive. The termination criteria used [12] is that the relative error in the functional is less than 10^{-6} for two successive iterations.

For the first pass of the algorithm the Tikhonov functional, from equation (3), to be minimised is

$$f_1 = \sum_{i=0}^{24} [\phi_M(i) - \phi_C(i)]^2 + \gamma_1^2 [g_{il}^2 + g_{it}^2 + g_{in}^2 + g_{el}^2 + g_{et}^2 + g_{en}^2] + \gamma_2^2 \alpha^2 \tag{4}$$

Noise	g_{el}	g_{et}	g_{en}	g_{il}	g_{it}	g_{in}	α
1%	0.5 ± 0.4	0.3 ± 0.4	0.3 ± 0.3	2.2 ± 1.5	2.6 ± 2.3	1.9 ± 1.5	3.0 ± 2.5
2%	0.2 ± 0.5	0.4 ± 0.8	0.4 ± 0.6	1.3 ± 1.6	0.1 ± 3.3	3.6 ± 3.7	2.2 ± 4.6
5%	1.1 ± 0.9	2.3 ± 2.1	1.1 ± 1.6	2.1 ± 3.0	15.7 ± 8.0	1.7 ± 7.3	8.2 ± 7.9
10%	2.0 ± 3.0	0.6 ± 4.1	1.5 ± 3.1	3.0 ± 6.6	9.2 ± 18.6	17.6 ± 14.0	1.4 ± 20.3
20%	3.3 ± 4.1	4.5 ± 5.3	2.3 ± 5.3	25.6 ± 14.5	13.7 ± 28.2	22.9 ± 37.9	29.7 ± 42.5

Table 1: Average percentage relative errors $\pm$ 1 standard deviation for the MacLachlan *et al.* [12] dataset, for various noise levels, where the g_{eh} values are retrieved in the first pass and the g_{ih} and α values are retrieved in the second pass.

where ϕ_M is the difference in measured potential between electrode i and the reference electrode and ϕ_C is similar but for the calculated value at each iteration of the solver. Due to the difference in the magnitudes of the conductivity values and α, two regularisation parameters, $\gamma_1 = 10^{-2}$ and $\gamma_2 = 10^{-5}$ are used. Initial values used are $\alpha = 1$, with the conductivity values all equal to 1×10^{-3}, except for $g_{in} = 1 \times 10^{-4}$.

In the second pass, the mean values for g_{el}, g_{et} and g_{en} from the first pass are held constant and only values for g_{il}, g_{it}, g_{in} and α are retrieved, using starting values from the first pass. The Tikhonov functional to be minimised is now

$$f_2 = \sum_{i=0}^{72} [\phi_M(i) - \phi_C(i)]^2 + \gamma_1^2 [g_{il}^2 + g_{it}^2 + g_{in}^2] + \gamma_2^2 \alpha^2 \tag{5}$$

3 RESULTS

In order to demonstrate the ability of the electrode array and computational algorithm to determine the conductivity values, as well as the total fibre rotation, a forward simulation was performed using the conductivity values mentioned by MacLachlan *et al.* [12]. The "measured" potentials calculated from the forward simulation were then contaminated with varying levels of noise and the two pass Tikhonov regularisation approach was used to recover the original conductivity values. This process was repeated 15 times and the resulting percentage relative errors are given in Table 1. As the described above, the extracellular conductivities were determined from the first pass of the algorithm and the intracellular conductivities and the fibre rotation were determined from the second pass.

From the table it can be seen that the algorithm can obtain the extracellular conductivities more accurately than the intracellular conductivities. Generally, the extracellular conductivities can be recovered to a level of accuracy of about a quarter to a half the size of the added noise. However, the intracellular conductivities can only be recovered to an accuracy of about 2-3 times the added noise.

In the execution of the algorithm it can be seen that the first pass is quite sensitive to the extracellular conductivities, but not to the intracellular conductivities or the fibre rotation. This provides accurate extracellular conductivities for the second pass, which is important because they are held constant there while the algorithm retrieves the intracellular conductivities and fibre rotation. The lack of accuracy in the intracellular starting values for the second pass is not a drawback since the second pass is not particularly sensitive to these starting values. It is worth noting that, although 20% noise appears to be near the limit of the algorithm for retrieving the intracellular conductivities and fibre rotation, it is still able to retrieve the extracellular conductivities quite accurately even for noise levels of 20%.

4 CONCLUSIONS

This paper has presented a two pass approach, based on Tikhonov regularisation, to obtain cardiac conductivity values and fibre rotation from measurements of potential made on a multi–electrode array. It has been shown that, even in the presence of high levels of noise, the conductivities can be obtained to a reasonably high level of accuracy. In particular, of the six conductivity values required, it has been shown that three of these can be retrieved to an accuracy of less than half the added noise in the system.

REFERENCES

[1] Clayton, R. H., Nash, M. P., Bradley, C. P., Panfilov, A. V., Paterson, D. J., and Taggart, P., Experiment-model interaction for analysis of epicardial activation during human ventricular fibrillation with global myocardial ischaemia, *Progress in Biophysics and Molecular Biology*, 107(1):101–111, 2011.

[2] Coronel, R., Wilms-Schopman, F. J. g., De Groot, J. R., Janse, M. J., Van Capelle, F. J. l., and De Bakker, J. M. t., Laplacian electrograms and the interpretation of complex ventricular activation patterns during ventricular fibrillation, *Journal of Cardiovascular Electrophysiology*, 11(10):1119–1128, 2000.

[3] Potse, M., Coronel, R., Falcao, S., LeBlanc, A. R., and Vinet, A., The effect of lesion size and tissue remodeling on ST deviation in partial-thickness ischemia, *Heart Rhythm*, 4(2):200–206, 2007.

[4] Vigmond, E., Vadakkumpadan, F., Gurev, V., Arevalo, H., Deo, M., Plank, G., and Trayanova, N., Towards predictive modelling of the electrophysiology of the heart, *Experimental Physiology*, 94(5):563–577, 2009.

[5] Plonsey, R. and Barr, R. C., The four-electrode resistivity technique as applied to cardiac muscle, *IEEE Transactions on Biomedical Engineering*, 29(7):541–546, 1982.

[6] Graham, L. S. and Kilpatrick, D., Estimation of the bidomain conductivity parameters of cardiac tissue from extracellular potential distributions initiated by point stimulation, *Annals of Biomedical Engineering*, 2010.

[7] Gilboa, E., La Rosa, P., and Nehorai, A., Estimating electrical conductivity tensors of biological tissues using microelectrode arrays, *Annals of Biomedical Engineering*, 40(10):2140–2155, 2012.

[8] Johnston, B. M., Johnston, P. R., and Kilpatrick, D., Analysis of electrode configurations for measuring cardiac tissue conductivities and fibre rotation, *Annals of Biomedical Engineering*, 34(6):986–996, June 2006.

[9] Aster, R. C., Borchers, B., and Thurber, C. H., *Parameter Estimation and Inverse Problems*, Elsevier Academic Press, Burlington, 2005.

[10] Hooks, D. and Trew, M., Construction and validation of a plunge electrode array for three-dimensional determination of conductivity in the heart, *IEEE Transactions on Biomedical Engineering*, 55(2):626–635, 02 2008.

[11] Johnston, B. M., Using a sensitivity study to facilitate the design of a multi-electrode array to measure six cardiac conductivity values, *Mathematical Biosciences*, 244(1):40–46, 2013.

[12] Johnston, B. M. and Johnston, P. R., Multielectrode array and inversion technique for retrieving six conductivities from heart potential measurements, *Medical and Biological Engineering and Computing*, 10.1007/s11517-013-1101-2, 2013

3rd International Conference on Computational and Mathematical Biomedical Engineering – CMBE2013
16-18 December 2013, Hong-Kong
P. Nithiarasu and R. Löhner (Eds.)

Effects of time-varying feedback signals on pressure field in ultrasonic-measurement-integrated simulation of pulsatile blood flow

Kenichi Funamoto* and Toshiyuki Hayase*
*Institute of Fluid Science, Tohoku University, 2-1-1 Katahira, Aoba-ku, Sendai 980-8577, Japan, funamoto@reynolds.ifs.tohoku.ac.jp

SUMMARY

Ultrasonic-measurement-integrated (UMI) simulation, in which feedback signals are applied to a numerical simulation based on differences between ultrasound Doppler measurement and computation, has been proposed to reproduce hemodynamics. In this study, a numerical experiment was conducted to investigate variations of the feedback signals and their effects on the pressure field in the UMI simulation of a three-dimensional pulsatile blood flow. The feedback signals and pressure in the UMI simulation showed time-dependent characteristics. Relatively large feedback signals were applied in the deceleration phase since hemodynamics became rather unstable. The adverse effect of feedback on the pressure field was reduced by the compensation method except for in the early stage of the deceleration phase.

Key Words: *hemodynamics, measurement-integrated simulation, ultrasonic measurement.*

1 INTRODUCTION

Hemodynamic wall shear stresses (WSS) and pressure are the major factors responsible for the development and progression of circulatory diseases. However, existing methodologies of measurement and computation are limited in their ability to obtain accurate and detailed information on hemodynamics. Based on the concept of flow observer [1], the authors have investigated integration of medical imaging and numerical simulation to reproduce hemodynamics and to calculate stresses acting on blood vessels [2]. An ultrasonic-measurement-integrated (UMI) simulation, in which differences between ultrasound Doppler measurement and computation are fed back to the numerical simulation, is one such method (see Fig. 1). In our former studies [2, 3], the efficiency of the UMI simulation was evaluated, and the transient and steady characteristics of the method were revealed. In addition, the effect of the feedback on the pressure field was theoretically examined, and a method of compensation for pressure field was devised [3]. However, variations of feedback signals and their effects on the pressure field in the UMI simulation of unsteady hemodynamics were unknown. In the present study, the relationships between the time-varying parameters, such as velocity error, feedback signal, and pressure, were investigated by a numerical experiment.

2 METHODS

Governing equations of the UMI simulation of blood flow are the Navier-Stokes equations and the pressure equation for incompressible and viscous fluid flow,

$$\rho\left(\frac{\partial \mathbf{u}}{\partial t}+(\mathbf{u}\cdot\nabla)\mathbf{u}\right)=\mu\Delta\mathbf{u}-\nabla p+\mathbf{f}, \tag{1}$$

$$\Delta p=-\nabla\cdot\rho(\mathbf{u}\cdot\nabla)\mathbf{u}+\nabla\cdot\mathbf{f}, \tag{2}$$

where $\mathbf{u} = (u, v, w)$ is the velocity vector, p is the pressure, t is the time, ρ is the density, and μ is the viscosity. $\mathbf{f}$ denotes the feedback signal at each feedback point and is described by the following equation.

$$\mathbf{f}=-K_{\mathrm{v}}^{*}\frac{\Phi_d(\mathbf{u}_{\mathrm{c}}-\mathbf{u}_{\mathrm{s}})}{U}\left(\frac{\rho U^2}{L}\right), \tag{3}$$

where K_{v}* is the feedback gain (nondimensional), U is the characteristic velocity, L is the characteristic length, $\mathbf{u}_{\mathrm{c}}$ and $\mathbf{u}_{\mathrm{s}}$ are velocity vectors of the computational result and the real flow, respectively, and $\mathbf{\Phi}_d$ (d = 1, 2, 3) is a projection function of a three-dimensional vector to the d-dimensional subspace generated by the vectors of the ultrasonic beam directions. Note that the special case with K_{v}* = 0 is an ordinary simulation without feedback. The acquisition of Doppler velocity by projecting a velocity vector in the direction of the ultrasonic beam corresponds to the case of d = 1.

The application of the feedback possibly deteriorates the computational accuracy of the pressure field while improving that of the velocity field when the divergence of the feedback force vector $\mathbf{f}$ is not zero [3]. Hence, pressure deviation, p_{f}, caused by the application of the feedback is estimated by solving the following equation with zero value at the boundaries of the computational domain, and is subtracted from the pressure field p of the convergent result (see Fig. 1):

$$\Delta p_{\mathrm{f}}=\nabla\cdot\mathbf{f}. \tag{4}$$

All parameters were nondimensionalized with the characteristic values, and the above governing equations were solved with an original program based on the SIMPLER method [2].

A numerical experiment was conducted in the same manner as in the former study [2]. Briefly, a three-dimensional configuration of a blood vessel with a thoracic aneurysm was reconstructed from CT slice images of a patient. A synthetic unsteady blood flow inside the aneurysm (Fig. 2(a)) was first defined as the standard solution with realistic unsteady velocity profiles at the upstream and downstream boundaries (see Fig. 2(b)). A UMI simulation was then carried out with simple boundary conditions: an unsteady parallel flow with a uniform velocity profile at the inlet and a free flow condition at the outlet with the same flow rate as the standard solution, considering that the exact boundary conditions of a real blood flow are usually unknown. Concerning the initial condition, a zero velocity field was applied. In the UMI simulation, the feedback signals were applied at all the grid points in the feedback domain M [0.066 m $\le z \le$ 0.106 m, dark gray zone in Fig. 2(a)], assuming the transesophageal ultrasonography of the standard solution with rotation of the probe. The ultrasound probe was assumed to be set at the same height as that of the aneurysm, the point O [(x, y, z) = (0.014 m, 0.000 m, 0.086 m)] in Fig. 2(a). Note that measurement errors such as aliasing in ultrasound Doppler measurement were not considered in this study.

The computational results were evaluated by the space-averaged error norm $\bar{e}_{\Omega}(a, t)$ in a monitoring domain Ω, and the time-space-averaged error norm $\bar{e}_{\Omega T}(a)$ over one cardiac cycle T defined for an arbitrary variable a (velocity vector $\mathbf{u}$, Doppler velocity V, or pressure p).

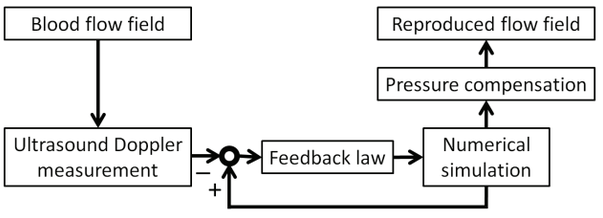

Fig. 1 Block diagram of the ultrasonic-measurement-integrated (UMI) simulation.

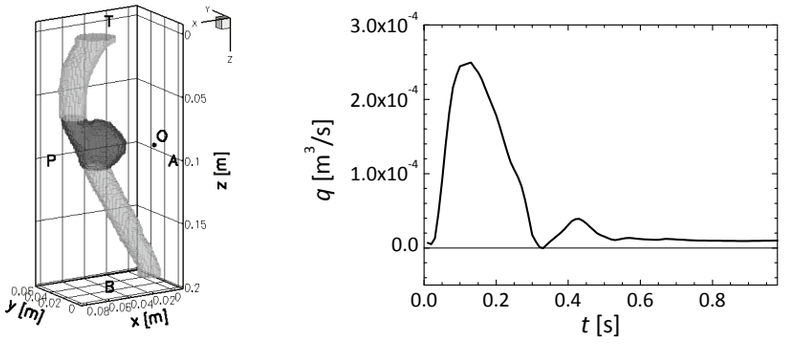

(a) (b)

Fig. 2 Computational conditions: (a) computational domain of a descending aorta with an aneurysm with feedback domain M (dark gray zone) and the origin O of the ultrasonic beam in the UMI simulation, and (b) variation of flow rate.

3 RESULTS AND DISCUSSION

In each computation, a periodic solution was obtained within four cardiac cycles, and it was used in the following evaluation.

The inaccurate boundary conditions introduced error in velocity and pressure in the ordinary simulation without feedback ($K_v^* = 0$). In contrast, in the UMI simulation ($0 < K_v^* \leq 11$), the time-space-averaged error norm of velocity vector $\bar{e}_{M\mathcal{T}}(\mathbf{u})$ in the feedback domain M decreased owing to the feedback. The error norm of pressure $\bar{e}_{M\mathcal{T}}(p)$ was also reduced owing to the improvement of the computational accuracy of velocity field. However, as increasing the feedback gain in the UMI simulation without pressure compensation, the value of $\bar{e}_{M\mathcal{T}}(p)$ gradually increased after taking a minimum value at $K_v^* = 2$. This adverse effect by the application of the feedback was properly eliminated by the pressure compensation method based on Eq. (4); the value of $\bar{e}_{M\mathcal{T}}(p)$ became smaller and monotonically decreased as the feedback gain increased. Although the maximum feedback gain for stable computation in the UMI simulation was $K_v^* = 11$, the value of $K_v^* = 5$ was employed hereafter since the values of both $\bar{e}_{M\mathcal{T}}(\mathbf{u})$ and $\bar{e}_{M\mathcal{T}}(p)$ were almost constant if $K_v^* \geq 5$.

Variations of space-averaged error norms, $\bar{e}_M(V, t)$ and $\bar{e}_M(p, t)$, of Doppler velocity and pressure in the feedback domain showed periodic oscillations, as shown in Figs. 3(a) and (b). In the ordinary simulation (gray lines), the error norms are relatively small in the acceleration phase ($t \leq 0.13$ s) though the flow rate q steeply increases (see Fig. 2(b)). This is because the blood flows as a bulk. In the deceleration phase ($0.13 \text{ s} < t \leq 0.33$ s), blood flow becomes rather unstable, and both error norms of Doppler velocity and pressure increase, showing the peak values at the late stage. Then, in the diastole phase ($0.33 \text{ s} < t \leq 0.98$ s), the error norm of Doppler velocity gradually decreases, and that of pressure also decreases with some deviation. On the other hand, the UMI simulation shows smaller values of $\bar{e}_{M\mathcal{T}}(\mathbf{u})$ and $\bar{e}_{M\mathcal{T}}(p)$ (black lines in Figs. 3(a) and (b)) at each time phase. At the early stage of the deceleration phase ($0.13 \text{ s} < t \leq 0.23$ s), the magnitude of the feedback signal $|\mathbf{f}|$ becomes large so as to reduce the error in Doppler velocity, which increases in this period in the ordinary simulation (Figs. 3(b) and (c)). After that, the error norms of Doppler velocity and pressure, and the magnitude of the feedback signal decrease. The magnitude for pressure compensation $|p_f|$ increases due to the large feedback signals at the early stage of the deceleration phase ($0.13 \text{ s} < t \leq 0.23$ s) as shown in Fig. 3(d), but little effect of the pressure compensation is observed in Fig. 3(b). The advantageous effect of the pressure compensation is observed after the late stage of the deceleration phase ($0.23 \text{ s} < t \leq 0.98$ s). Further investigation is required to improve the pressure field at the early stage of the deceleration phase.

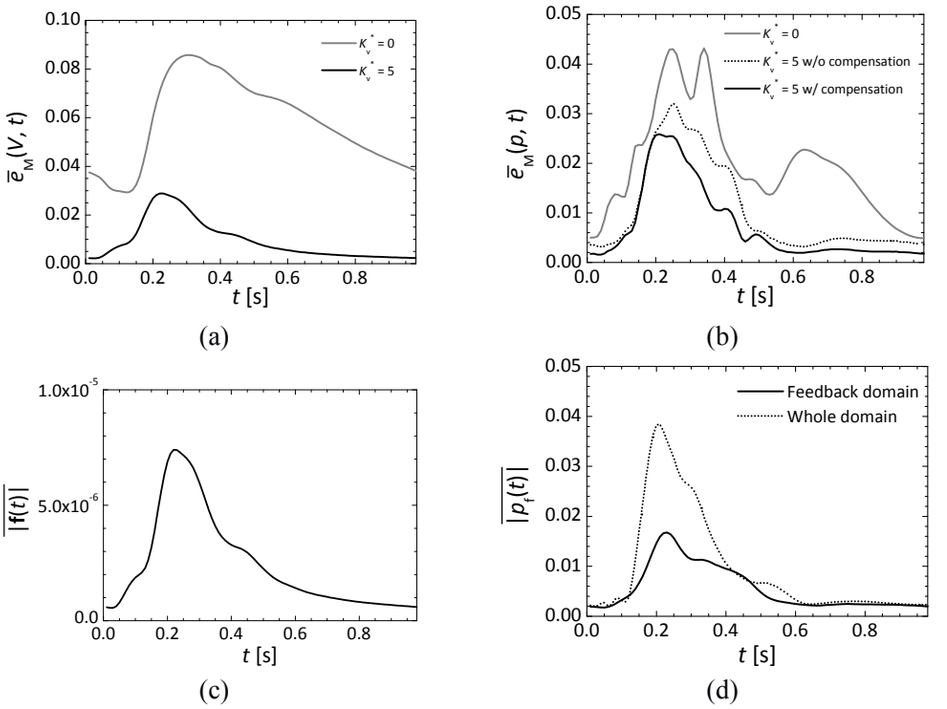

Fig. 3 Variations of space-averaged values: error norms of (a) Doppler velocity and (b) pressure in the feedback domain by the ordinary simulation ($K_v^* = 0$) and the UMI simulation with/without pressure compensation ($K_v^* = 5$), (c) magnitude of feedback signal in the feedback domain, and (d) absolute values of pressure compensation in the feedback domain and in the whole domain.

4 CONCLUSIONS

A numerical experiment revealed variations of feedback signals and their effects on the pressure field in the UMI simulation of a three-dimensional pulsatile blood flow. Relatively large feedback signals were applied in the deceleration phase since hemodynamics became rather unstable. The adverse effect of feedback on the pressure field was reduced by the compensation method except for in the early stage of the deceleration phase.

REFERENCES

[1] T. Hayase and S. Hayashi. State estimator of flow as an integrated computational method with the feedback of online experimental measurement, *Journal of Fluids Engineering,* 119, 814-822, 1997.

[2] K. Funamoto, T. Hayase, Y. Saijo, and T. Yambe. Numerical experiment for ultrasonic-measurement-integrated simulation of three-dimensional unsteady blood flow, *Annals of Biomedical Engineering,* 36, 1383-1397, 2008.

[3] K. Funamoto and T. Hayase. Reproduction of pressure field in ultrasonic-measurement-integrated simulation of blood flow, *International Journal for Numerical Methods in Biomedical Engineering,* 29, 726-740, 2013.

3rd International Conference on Computational and Mathematical Biomedical Engineering – CMBE2013
16-18 December 2013, Hong-Kong
P. Nithiarasu and R. Löhner (eds)

Closed loop baroreflex regulation of blood flow in the cardiovascular system

Andrew Armean Wright[*], Adam Mahdi[**], Mette S. Olufsen[***]
Dept of Mathematics, NC State University, Raleigh 26795
[*]armean.wright@gmail.com, [**]amahdi@ncsu.edu, [*]msolufse@ncsu.edu

SUMMARY

This paper presents a lumped parameter model predicting baroreflex regulation during head-up tilt. Blood flow and pressure are predicted using an electrical circuit analogy. This model is coupled with a control model that regulates heart rate, cardiac contractility, and peripheral resistance in response to changes in blood pressure. The model was applied to predict patient specific measurements of blood pressure and heart rate obtained during head-up tilt. Submitted for MS 3, Inverse Problems in Cardiovascular Mathematics.

Key Words: *1D arterial blood flow modeling, elastic and viscoelastic wall models*

1 INTRODUCTION

A simple change of the body from supine to sitting or standing position requires activation of a series of control mechanisms to maintain homeostasis. Upon postural change, the baroreceptors register a fall in arterial blood pressure and reduced filling of the heart. Activation of the autonomic nervous system then adjusts the heart and vessel properties to increase pressure and pump function of the heart back toward their reference level. This regulation can be disrupted in patients with peripheral and central nervous system diseases. Such patients usually experience dizziness and syncope due to altered function of the autonomic nervous system. These defects are often observed in patients with diabetes, hypertension, and other neurological diseases of which Parkinson's disease is the most dominating.

The autonomic nervous system is complex with many interacting components. This is why analysis of separate elements does not give a satisfactory view of the state of the physiological system. In this study we aim to achieve a better understanding of the control mechanisms and their dynamics via patient specific mathematical modeling where knowledge of the individual elements and their dynamics is integrated. To this end, we are developing a closed loop cardiovascular system level model coupled with a control model that allows us to predict the autonomic nervous system's ability to adjust the heart and vessel properties to maintain blood pressure and pumping function at reference levels. These models are composed of nonlinear differential equations whose solution poses considerable computational challenges. Their application to analysis of clinical data involves computational and conceptual complications due to the inherent noise in the model and data. To ensure high fidelity of our model, we employ methodologies allowing computation of parameter sensitivity, identifiability, and estimation.

2 METHODS

A drop in blood pressure, e.g. in response to head-up tilt, sensed by the arterial baroreceptors located in the aortic arch and carotid sinuses, inhibits firing of afferent baroreceptors. Sensory signals for these receptors are integrated in the nucleus solitary tract from where efferent signals are

transported via sympathetic and parasympathetic chain eventually impacting heart rate, cardiac contractility, and vascular tone. Fig. 1 shows a schematic of physiological pathways.

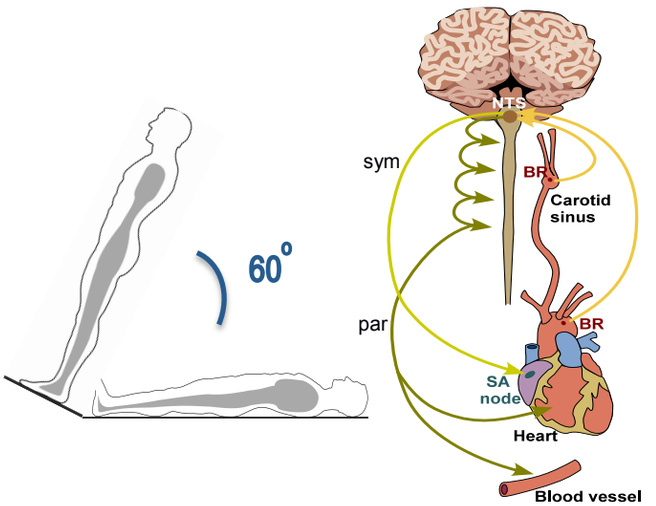

Fig. 1: The baroreflex control loop. A blood pressure drop in response to HUT inhibits afferent firing integrated in the nucleus solitary tract (NTS), from where efferent parasympathetic (par) and sympathetic (sym) signals stimulating heart rate, cardiac contractility, and vascular resistance.

This system can be represented by a lumped parameter model illustrated in Fig. 2. This model includes the arteries and veins in the systemic circulation, as well as the left heart facilitating transport of blood. In addition we have included a neural control model predicting afferent and efferent baroreceptor firing, which modulate heart rate, peripheral resistance, and cardiac contractility. This coupled model was used to predict the response to head-up tilt induced by accounting for gravitational pooling of blood in the lower body.

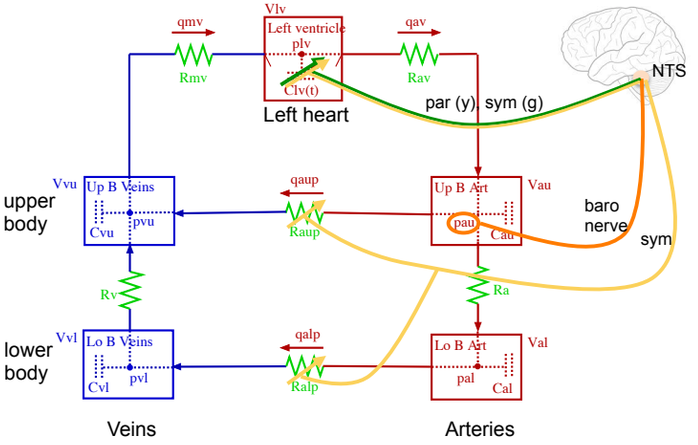

Fig. 2: The baroreflex control loop model. Blood flow and pressure is computed using a compartment model including the left heart as well as systemic arteries and veins in the upper and lower body. Heart rate, cardiac contractility, and peripheral vascular resistance are modulated

Similar to previous studies [1], we use the electrical circuit analogy shown in Fig. 2 to predict blood flow and pressure in the systemic circulation. The model includes four compartments representing arteries and veins in the upper and lower body as well as a compartment representing the heart. For each compartment i, a pressure-volume relation can be defined as

$$V_i - V_{un,i} = C_i(p_i - p_{ext}), \tag{1.1}$$

where V_i (ml) is the compartment volume, $V_{un,i}$ (ml) is the unstressed volume, C_i (ml/mmHg) is the compartment compliance, p_i (mmHg) represents blood pressure, and p_{ext} (mmHg) (assumed constant) is denotes the pressure of the surrounding tissue. Moreover, for each compartment, the change in volume is given by

$$\frac{dV_i}{dt} = q_{in} - q_{out}, \tag{1.2}$$

where q (ml/s) denotes the volumetric flow. Using a linear relationship analogous to Ohm's law the volumetric flow q (ml/s) between compartments can be computed as

$$q = \frac{p_{in} - p_{out}}{R}, \tag{1.3}$$

where p_{in} and p_{out} denote the pressure on either side of the resistor R (mmHg s/ml). A system of differential equations was obtained by differentiating equation (1.1), using (1.2) and (1.3), giving

$$\frac{dp_i}{dt} = C\left(\frac{p_{i-1} - p_i}{R_{i-1}} - \frac{p_i - p_{i+1}}{R_i}\right).$$

For the heart compartment, a differential equation of the form (1.2) is used to describe the change in volume, which is related to pressure via equation (1.1), but described in terms of elastance E=1/C (mmHg/ml) rather than compliance. Pumping is achieved by introducing a variable elastance function of the form

$$E_{lh}(\tilde{t}) = \begin{cases} (E_M - E_m)\left(1 - \cos(\pi\tilde{t} / T_M) + E_m\right)/2, & \tilde{t} \le T_M \\ (E_M - E_m)\left(\left(\cos\left(\pi\left(\tilde{t} - T_M\right)/T_R\right) + 1\right) + E_m\right)/2, & \tilde{t} \le T_M + T_R \\ E_m, & \tilde{t} \le T \end{cases}$$

where $\tilde{t}$ is the time within a cardiac cycle $T = 1/H$; E_M and E_m denote the maximum and minimum elastance, respectively.

Head-up tilt, $\theta = 0..60^o$ at speed v_t is achieved by accounting for pooling of blood in the lower extremities, by adding gravity $\rho g h_{tilt}$ to equations predicting flow between the upper and lower body.

$$q = \frac{\rho g h_{tilt} \sin\left(\theta(t)\right) + p_{in} - p_{out}}{R}, \quad \theta(t) = \frac{\pi}{180}\begin{cases} 0 & t < t_{st} \\ v_t(t - t_{st}) & t_{st} \le t \le t_{st} + t_{ed} \\ 60 & t > t_{st} + t_{ed} \end{cases}$$

As suggested in [2, 3], the baroreflex model uses blood pressure p_{au} as an input to predict baroreflex firing rate f proportional to the difference between the stretch of the arterial wall ϵ_w and the stretch of the baroreceptor cells ϵ.

$$f = \varepsilon_w - \varepsilon, \quad \frac{d\varepsilon}{dt} = -(\alpha + \beta)\varepsilon + \alpha\varepsilon_w, \quad \varepsilon_w = g(p),$$

where ϵ_w is the wall stress, modelled as a nonlinear function of pressure, ϵ is the strain of the baroreceptor cells, and α and β are parameters. A drop in afferent firing rate elicits inhibition of parasympathetic tone T_P, decreasing the acetylcholine concentration C_A, and stimulation of sympathetic tone T_S increasing the noradrenaline concentration C_N. As suggested in [2], these can be modeled using first order kinetic equations of the form

$$\frac{dC_N}{dt} = \frac{-C_N + T_S}{\tau_N}, \quad \frac{dC_A}{dt} = \frac{-C_A + T_P}{\tau_A},$$

$$T_S = T_{SM} - (T_{SM} - T_{Sm})\frac{f^\eta}{(f^\eta + f_S^\eta)}, \quad T_P = T_{Pm} - (T_{PM} - T_{Tm})\frac{f^\xi}{(f^\xi + f_P^\xi)}.$$

Modulation of neurotransmitters increases heart rate, cardiac contractility, and peripheral vascular resistance. Similar to previous work [2] we suggest to compute heart rate h as

$$h = h_0 + dh_{M0}C_N - dh_{0m}C_A - \frac{dh_{Mo}dh_{0m}C_NC_A}{h_0}, \quad dh_{M0} = h_M - h_0, \quad dh_{0m} = h_0 - h_m, \quad (1.4)$$

while we predict cardiac contractility E_m and peripheral vascular resistances R_{aup} and R_{alp} using

$$\frac{d^2X}{dt^2} + \delta\frac{dX}{dt} + \kappa X = \lambda C_i, \quad X = E_m, R_{aup}, R_{alp},$$

where δ, κ, λ are constants that vary depending on the neurotransmitter ($C_i, i = N, A$) in question. This form of the equation was motivated by studying the Bowditch effect proposed by Klabunde [4] and Batzel et al. [5]. It should be noted, that parasympathetic withdrawal is significantly faster than sympathetic stimulation, i.e., timescales for the two responses differ significantly.

3 RESULTS AND CONCLUSIONS

Preliminary results shown in Fig. 3A and B include predictions of arterial blood pressure, using heart rate as an input, and predictions of heart rate using blood pressure as an input. These results were computed for humans (3A) and rats (3B). Future results will be used to discuss how the baroreflex model can be scaled to predict heart rates in humans, and how to incorporate the control model with the cardiovascular model to form a closed model. Preliminary results were obtained using sensitivity analysis and optimization to estimate model parameters that allows patient specific predictions. The advantage of the closed model is that it can easily be adapted to study impacts of disease, e.g., by incorporating disease in equations.

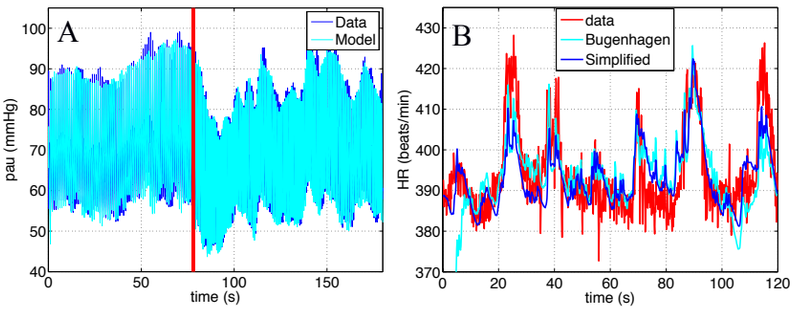

Fig 3: Model predictions of arterial blood pressure using HR as an input (A) and heart rate, using blood pressure as an input (B)

ACKNOWLEDGEMENTS

This research was supported in part by NSF via awards NSF/DMS-1122424 and NSF/DMS-0943855 and by NIH under 1P50-GM094503-01A0 subaward to NCSU.

REFERENCES

[1] N.D. Williams, O. Wind-Willassen, REU Program, J. Mehlsen, J.T. Ottesen, M.S. Olufsen. *Patient specific modeling of head-up tilt*. Math Med Biol, In press, 2013.

[2] A. Mahdi, J.T. Ottesen, M.S. Olufsen. *Qualitative features of a new baroreceptor model*. Proc The 1st international workshop on innovative simulation for healthcare, I-WISH. W. Backfrieder, et al. (eds), Rende (CS), Italy, pp. 75-80, 2012.

[3] A. Mahdi, J. Sturdy, J.T. Ottesen, M.S. Olufsen. *Modeling the afferent dynamics of the baroreex control system,* submitted, 2013.

[4] R. Klabunde. *Physiology and biophysics of the circulation: an introductory text.* Lippincott Williams and Wilkins, Philadelphia, PA, 1972.

[5] J.J. Batzel, F. Kappel, D. Schneditz, and H.T. Tran. *Cardiovascular and respiratory systems: modeling, analysis, and control*. SIAM, Philadelphia, PA, 2007.

3rd International Conference on Computational and Mathematical Biomedical Engineering - CMBE2013
16-18 December 2013, Hong-Kong
P. Nithiarasu and R. Löhner (Eds.)

Boundary control of bidomain equations with state dependent switching source functions in ionic model

Nagaiah Chamakuri[⋆], Christian Engwer[⋆⋆], Karl Kunisch[⋆⋆⋆] and Gernot Plank[⋆⋆⋆⋆]
[⋆] Radon Institute for Computational and Applied Mathematics, Linz, Austria,
nagaiah.chamakuri@ricam.oeaw.ac.at
[⋆⋆] Fachbereich Mathematik und Informatik der Universität Münster, Germany,
christian.engwer@uni-muenster.de
[⋆⋆⋆] Institute of Mathematics and Scientific Computing, University of Graz, Austria,
karl.kunisch@uni-graz.at
[⋆⋆⋆⋆] Institute of Biophysics, Medical University of Graz,Austria, gernot.plank@medunigraz.at

SUMMARY

The bidomain equations are widely accepted as one of the most complete descriptions of the cardiac bioelectric activity at the tissue and organ level. The model consist of a system of elliptic partial differential equations coupled with a non-linear parabolic equation of reaction-diffusion type, where the reaction term, modeling ionic transport is described by a set of ordinary differential equations. In particularly, we use the Fenton-Karma ionic model in our simulation study. In this model, the source functions are discontinuous in state space solution. An approach to compute the derivative of discontinuous source terms is demonstrated for the optimal control of reaction-diffusion systems in cardiac electrophysiology.

The optimal control formulation is presented and a formal derivation of the adjoint equations and the first order optimality conditions, which are the basis for numerical solution are provided. The derivative of discontinuous source functions, due to the Fenton-Karma model, is required to solve the adjoint equations, which poses a lot of computational challenges. The efficient numerical techniques for boundary control of the bidomain model as well as computational techniques to track the derivatives of discontinuous source functions in adjoint equations will be demonstrated, [3]. The numerical realization is described in detail and numerical experiments, which demonstrate the capability of influencing and terminating reentry phenomena, are presented. We employ the parallelization techniques to enhance the solution process of optimality system and a numerical feasibility study in a parallel environment will be shown.

Key Words: *bidomain model, Fenton-Karma ionic model, defibrillation, optimal control, derivatives of Heaviside functions, parallel FEM, NCG algorithm.*

1 INTRODUCTION

The heart is the most important organ in human body because it pumps the blood around the whole body and it carries all the vital materials which help our bodies function. The electrical activation of the heart is highly organized in healthy situations and in diseased case disturbances in the formation and/or propagation of electrical impulses may induce reentrant activation patterns which precipitate its rhythm significantly. The termination of these cardiac arrhythmia is achieved

by applying a strong electrical shock, a process called defibrillation. The link between the high shock strengths required and adverse effects provides the motivation for posing the defibrillation process as an optimization problem where one aims to achieve defibrillation with minimal energy.

The optimal control approach is based on minimizing a properly chosen cost functional $J(v, I_e)$ depending on the extracellular current I_e as input, which must be determined in such a way that wavefronts of transmembrane voltage v are smoothed in an optimal manner, where the transmembrane potential v as one of the state variables, see [3,4]. The optimal control approach to defibrillation is to determine an applied electrical field in such a way that it optimizes a given design objective, which is, in our case, the restoration of a tissue state in which fibrillatory propagation cannot be maintained. This can be achieved by driving the whole tissue to a resting state, or equivalently, to an excited state. The following issues will arise in the current model problem under consideration in the context of solving the optimal control problem. First, the discontinuous source functions appear at the ionic model equations which appear over the complete domain. Secondly, the interface of discontinuous functions will be changing by applying the external stimulus over the computational domain. In this work, we focus on the computational approach to evaluate the derivative of these discontinuous source-functions with respect to the state variable.

2 OPTIMAL CONTROL OF BIDOMAIN EQUATIONS

Let's denote a bounded connected domain by $\Omega \subset \mathbb{R}^2$, with Lipschitz continuous boundary $\partial\Omega$. The space-time domain and its lateral boundary are denoted by $Q = \Omega \times (0, T]$ and $\Sigma = \partial\Omega \times (0, T]$, respectively. The well known bidomain model [8] consist of a linear elliptic partial differential equation and a non-linear parabolic partial differential equation of reaction-diffusion type, where the reaction term is described by a set of ordinary differential equations. In our numerical computations, we considered the Fenton-Karma model, see for more details in [8], to describe the membrane ionic activity. The Fenton-Karma model consists of three ionic currents, $I_{fi}(v, f)$, $I_{si}(v, s)$ and $I_{so}(v)$ which represents the flows of sodium, calcium and potassium. The complete bidomain equations together with the ODE system are expressed as follows.

$$
\begin{aligned}
0 &= \nabla \cdot (\bar{\sigma_i} + \bar{\sigma_e})\nabla u + \nabla \cdot \bar{\sigma_i}\nabla v \quad \text{in } Q && (1)\\
\frac{\partial v}{\partial t} &= \nabla \cdot \bar{\sigma_i}\nabla v + \nabla \cdot \bar{\sigma_i}\nabla u - [I_{fi}(v, f) + I_{si}(v, s) + I_{so}(v) - I_{stim}] \text{ in } Q && (2)\\
I_{fi} &= -f g(v)[v - v_c][1 - v]/\tau_{fi} \quad \text{in } Q && (3)\\
\frac{\partial f}{\partial t} &= [1 - g(v)]\frac{[1 - f]}{\tau_f^-(v)} - \frac{g(v) f}{\tau_f^+} \quad \text{in } Q\,, && (4)\\
I_{si} &= -s\left[1 + \tanh\left[\kappa[v - v_c^{si}]\right]\right]/(2\tau_{si}) \quad \text{in } Q && (5)\\
\frac{\partial s}{\partial t} &= [1 - g(v)]\frac{[1 - s]}{\tau_s^-} - \frac{g(v) s}{\tau_s^+} \quad \text{in } Q\,, && (6)\\
I_{so} &= v[1 - g(v)]/\tau_0 + g(v)/\tau_r \quad \text{in } Q\,, && (7)
\end{aligned}
$$

where $v : Q \to \mathbb{R}$ is the transmembrane voltage, $f, s : Q \to \mathbb{R}$ represents the ionic current variables, $\bar{\sigma_e}, \bar{\sigma_i} : \Omega \to \mathbb{R}^{d\times d}$ are respectively the extra and intracellular conductivity tensors, I_{fi} is the fast inward current, I_{si} is the slow inward current and I_{so} is the slow (ungated) outward current. The initial and boundary conditions are prescribed as

$$
\begin{aligned}
\mathbf{n} \cdot (\sigma_i \nabla v + \sigma_i \nabla u) &= 0 \quad \text{on } \Sigma && (8)\\
\mathbf{n} \cdot \sigma_e \nabla u &= I_e \quad \text{on} \quad \partial\Omega_{12} \times (0, T] && (9)\\
\mathbf{n} \cdot \sigma_e \nabla u &= 0 \quad \text{on } \partial\Omega_3 \times (0, T] && (10)\\
v(x, 0) = v_0\,, \qquad f(x, 0) &= f_0\,, \text{ and } s(x, 0) = s_0 \quad \text{on } \Omega\,, && (11)
\end{aligned}
$$

where $\mathbf{n}$ denotes the outwards normal to the boundary of Ω. Here I_e is the extracellular current density stimulus which acts as control along the boundary $\partial\Omega_{12} = \partial\Omega_1 \cup \partial\Omega_2$, where $\partial\Omega_i$, $i = 1, 2, 3$ are mutually disjoint and satisfy $\partial\Omega_1 \cup \partial\Omega_2 \cup \partial\Omega_3 = \partial\Omega$. For compatibility reasons it is assumed throughout that

$$\int_{\partial\Omega} I_e(t, \cdot)\, d\, s = 0 \tag{12}$$

for almost every $t \in (0, T)$. In the numerical experiments I_e will be only temporally dependent and will be of the form

$$I_e = \hat{I}_e(t)(\chi_{\partial\Omega_1} - \chi_{\partial\Omega_2})\,,$$

where $\chi_{\partial\Omega_i}$ is the characteristic function of the set $\partial\Omega_i$, $i = 1, 2$. Then condition (12) is satisfied if $|\partial\Omega_1| = |\partial\Omega_2|$. The support regions $\partial\Omega_1$ and $\partial\Omega_2$ can be considered to represent a cathode and an anode, respectively.

The following cost functional of tracking type is considered for the termination of reentrant waves.

$$\begin{cases} \min J(v, I_e) = \dfrac{1}{2}\displaystyle\int_0^T \left(\alpha_1 \int_{\Omega_{obs}} |v - v_d|^2\, dx + \alpha_2 \int_{\partial\Omega_{12}} I_e(t)^2\, ds\right) dt \\ \text{subject to (1)-(6),(8)-(11) and } I_e \in U, \end{cases} \tag{13}$$

where $\alpha_1 > 0$, $\alpha_2 > 0$ is the regularization parameter for the control cost, $\Omega_{obs} \subset \Omega$ is the observation domain, $v_d \in L^2(0, T; L^2(\Omega_{obs}))$ and

$$U = \{I_e - \frac{1}{|\partial\Omega_{12}|}\int_{\partial\Omega_{12}} I_e\, ds :\ I_e \in L^2(0, T; L^2(\partial\Omega_{12})), |I_e(t, x)| < R \\ \text{for a.e. } (t, x) \in (0, T) \times \partial\Omega_{12}\}.$$

The set of admissible controls U is a closed, convex and weakly* sequentially compact subset of $L^\infty(0, T; L^2(\partial\Omega_{12}))$. The first order optimality system is obtained by formally setting the partial derivatives of Lagrangian equal to 0. In the process of solving the dual equations the derivative of the ionic currents and right hand side of ODEs w.r.t. the transmembrane voltage are required which are given as follows.

$$\begin{aligned}
(I_{fi})_v &= -\frac{fg}{\tau_{fi}}[-(v - v_c) + (1 - v)] - \frac{f(v - v_c)(1 - v)}{\tau_{fi}} g_v(v) \\
(I_{si})_v &= -\frac{s}{2\tau_{si}}[(1 - tanh^2(\kappa(v - v_c^{si})) \cdot \kappa]\,, \qquad (I_{so})_v = \frac{1 - g}{\tau_0} + \left(\frac{-v}{\tau_0} + \frac{1}{\tau_r}\right) g_v(v) \\
F_v(v, f) &= \frac{-\tau_f^-(v)[(1 - f)g_v(v)] - [1 - g(v)](1 - f)(\tau_f^-(v))_v}{[\tau_f^-(v)]^2} - \frac{f g_v(v)}{\tau_f^+} \\
S_v(v, s) &= -\frac{(1 - s)g_v(v)}{\tau_s^-} - \frac{s g_v(v)}{\tau_s^+}\,, \quad (\tau_f^-(v))_v = -g_v(v)\tau_{v_1}^- + g_v(v)\tau_{v_2}^-
\end{aligned}$$

Here we can clearly see that one needs to evaluate the derivative of state dependent Heaviside function ($g_v(v)$) in many places. It is not directly possible to evaluate the gateaux derivative $\frac{d}{dv}g(v)$, as g is discontinuous, where $v(x) = 0$. Instead of approximating the derivative using some regularization, we have chosen an alternative where not $\frac{d}{dv}g(v(x))$, but $\int_\Omega \frac{d}{dv}g(v(x))dx$ is evaluated. This approach avoids any regularization and allows to directly compute the integral. The integral of Heaviside function can be evaluated as

$$\int_\Omega \frac{dg}{dv} f\, dx = \int_\Gamma \frac{f}{\nabla v \cdot \mathbf{n}_\Gamma} ds\,. \tag{14}$$

where $\mathbf{n}_\Gamma$ denotes the normal vector to Γ, pointing in the direction of ∇v. Here skip the complete details due to space restriction and we refer the reader to [5] mode detailed derivation of functions. To evaluate integrals over the interface we impose a piecewise linear reconstruction of this level set, which is sufficient for first-order representations of the state variable. Using the dune-mc library [6] we compute a polygonal representation of the linearized iso-surface on each cell. An extended marching-cubes algorithm allows the efficient computation of the interface, both in 2D and 3D.

Here we give the brief description of our computational approach to solve the complete optimality system. A piecewise linear finite element method is used for the spatial discretization of the primal and dual equations and their temporal discretization is done by using the linearly implicit Runge-Kutta methods. The solution of the singular linear systems which arise after the full discretization of Eqs (1) and corresponding dual equation are defined up to an additive constant. We impose a zero mean condition to fix this constant. For the numerical realization of this condition we adopted a stabilized saddle point formulation from the work of Bochev and Lehoucq [2]. To solve this linear system we employed a BiCGSTAB method with AMG preconditioner, see [1] for more details on implementation. The complete optimality system is solved by the non-linear conjugate gradient (NCG) by using the Hager-Zhang variant update. A line search procedure based on the Armijo rule with backtracking is used to determine the next update of the solution during the optimization iterations. The numerical results demonstrated the optimal control formulation to the cardiac defibrillation which reduces the total energy by finding optimal pulses when compared to ad-hoc strategies. In this study two electrode configurations were considered and the current injection enters into these electrodes as a Neumann boundary conditions in the extracellular potential model equation.

REFERENCES

[1] P. Bastian, M. Blatt, A. Dedner, C. Engwer, R. Kl ofkorn, R. Kornhuber, M. Ohlberger, and O. Sander. A generic grid interface for parallel and adaptive scientific computing. Part II: implementation and tests in DUNE. *Computing*, 82(2):121138, July 2008.

[2] P. Bochev and R. B. Lehoucq. On the finite element solution of the pure neumann problem. *SIAM Rev.*, 47:5066, January 2005.

[3] N. Chamakuri, K. Kunisch, and G. Plank. On boundary stimulation and optimal boundary control of the bidomain equations. Mathematical Biosciences, 2013.

[4] N. Chamakuri, K. Kunisch, and G. Plank. Optimal control approach to termination of reentry waves in cardiac electrophysiology. *Journal of Mathematical Biology*, pages 130. 10.1007/s00285-012-0557-2.

[5] N. Chamakuri, C. Engwer and K. Kunisch. Boundary control of bidomain equations with state dependent switching source functions in ionic model. *in preparation*.

[6] C. Engwer and A. Ning. Geometric integration over irregular domains with topologic guarantees. *in preparation*.

[7] F. Fenton and A. Karma. Vortex dynamics in three-dimensional continuous myocardium with fiber rotation: Filament instability and fibrillation. *Chaos: An Interdisciplinary Journal of Nonlinear Science*, 8(1):2047, Mar. 1998.

[8] L. Tung. *A bi-domain model for describing ischemic myocardial DC potentials*. PhD thesis, MIT, Cambridge, MA, 1978.

3rd International Conference on Computational and Mathematical Biomedical Engineering - CMBE2013
16-18 December 2013, Hong-Kong
P. Nithiarasu and R. Löhner (Eds.)

Parameters Estimation in Holzapfel-Ogden Law of the Human Left Ventricle using Clinical In-vivo Images

H. Gao*, W. G. Li*, C. Berry, and X. Y. Luo***
*School of Mathematics and Statistics, University of Glasgow, Glasgow, UK
**Institute of Cardiovascular and Medical Science, University of Glasgow, Glasgow, UK
email: hao.gao@glasgow.ac.uk

SUMMARY

One of the central problems in personalized left ventricular (LV) modelling is to identify material parameters for the constitutive laws for myocardium. In this study, by employing a structure-based material model (Holzapfel-Ogden model: H-O), we seek to identify the 8 material parameters by matching the measured LV volume and strain estimated from *in-vivo* cardiac magnetic resonance imaging (CMRI) data. A multi-step optimisation procedure is proposed. Results show that by reformulating the parameter space, it is feasible to determine a set of subject-specific parameters for LV modelling.

Key Words: *Left ventricle, subject-specific parameter, Holzapfel-Ogden Law*

1 INTRODUCTION

Stress and strain have been considered to be important factors in understanding complex heart mechanism. For example, the passive mechanical properties of myocardium play a major role in LV diastolic filling and affect the pumping function. Nonlinear finite element method has been applied to patient-specific modelling of heart functions along with constitutive laws in passive myocardial wall [1, 2, 3]. However, to use such methods, a priori knowledge of the material parameters is essential.

Traditionally, mechanical properties of myocardium can be determined by a series of experimental tests [4] with specimens harvested from a specific LV. This, however, is not possible for human subjects. The alternative is the inverse estimation approach with in-vivo data. Guccione et al[5] estimated parameters for a nonlinear, transversely isotropic four-parameter strain energy function (Guccione's law) a 3D model built from images at the beginning of diastole. They estimated the parameters by minimizing the error between the computed and measured coordinates at end-diastole. Later the material model was extended to estimate passive 3D LV aneurysm and infarct LV models [6]. Nair et al.[7] used a genetic algorithm to estimate 4 parameters of Guccione's law for a rabbit LV model. Recently Xi et al. [8] used reduced-order unscented Kalman filter to optimize the Guccione's law using in-vivo data of a human heart.

Although various studies have demonstrated that it is feasible to inversely estimate material parameters from in-vivo clinical data, most of these focused on using transversely isotropic material models. To our best knowledge, this is the first study in which the parameters are estimated using the orthotropic constitutive law by [10]. In particular, we seek to inversely estimate the material parameters from in-vivo imaging data from a healthy volunteer.

2 METHODOLOGY

2.1 LV model construction

Cardiac magnetic resonance imaging was performed on a healthy volunteer (male, age 28) using a Siemens MAGNETOM Verio (Erlangen, Germany) 3.0 T scanner. The study was approved by the local ethics committee, and written informed consent was obtained before the scan. Cine images are used for functional assessment and LV geometry reconstruction. Custom software written using Matlab is used to extract the endocardial and epicardial boundaries at early diastole, when LV pressure is lowest, see Fig.1(a). Following the manual segmentation, prolate spheroidal coordinates and cubic B-spline are used to fit endocardial and epicardial surfaces, smoothness regularization is imposed to minimize the geometric distortion, and a linear constrain is also imposed on the fitting parameters in order to maintain C^2 continuity at the apex. Fig.1(b) is the unfitted reference LV geometry, Fig.1(c) and (d) show the fitted endocardial and epicardial surfaces. Hexahedral elements are generated using a linear interpolation from endocardial to epicardial surfaces, shown in Fig.1(e). Refer to [11] for more details. A rule-based myocardial fibre generation method [2] is employed to construct the fibre and sheet architecture of the myocardium, shown Fig.1(f). The fibre angle rotates from -60° to 60° from endocardium to epicardium, and the sheet angle rotates from -45° to 45°.

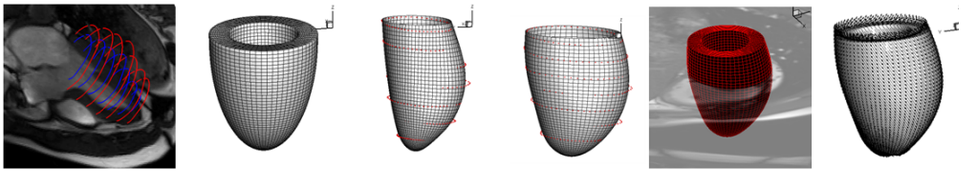

Figure 1: computational LV model. (a) manual segmentation; (b) reference LV mesh described in prolate spheroidal coordinates; (c) fitted endocardial surface, red dots are the original boundary points; (d) fitted epicardial surface, red dots are the original boundary points; (e) fitted LV mesh; (f) rule-based myofiber architecture

2.2 Constitutive law for passive myocardium

The structure-based nonlinear orthotropic constitutive law for passive LV myocardium proposed by Holzapfel and Ogden (H-O model) [10] is

$$\psi = \frac{a}{2b} e^{b(I_1-3)} + \sum_{i=\mathrm{f,s}} \frac{a_i}{2b_i}[e^{b_i(I_{4\mathrm{i}}-1)^2} - 1] + \frac{a_{\mathrm{fs}}}{2b_{\mathrm{fs}}}[e^{b_{\mathrm{fs}}I_{8\mathrm{fs}}^2} - 1] \tag{1}$$

where a, b are the parameters for the matrix response; a_{f}, b_{f} are the parameters for the muscle fibres; a_{s} and b_{s} are for fibre sheet orientation; a_{fs}, b_{fs} represent the shear effects in the fibre-sheet plane. $I_1 = \mathrm{tr}(\mathbf{C})$, where $\mathbf{C} = \mathbf{F}^T\mathbf{F}$, $\mathbf{F}$ is the deformation gradient. $I_{4\mathrm{f}} = \mathbf{f_0} \cdot (\mathbf{C}\mathbf{f_0})$, $I_{4\mathrm{s}} = \mathbf{s_0} \cdot (\mathbf{C}\mathbf{s_0})$, and $I_{8\mathrm{fs}} = \mathbf{f_0} \cdot (\mathbf{C}\mathbf{s_0})$, where $\mathbf{f_0}$ and $\mathbf{s_0}$ are the fibre and sheet orientations in the reference configuration. For a detailed description of H-O model, refer to [10].

2.3 Parameter estimation: inverse problem

End-diastolic LV chamber volume V^{exp} is calculated from corresponding cine images. Four cine short-axis slices from basal to middle LV are selected for extracting strains from early diastole to end of diastole by using a deformable image registration method[12]. Strain is computed for

early of diastole with reference in end of diastole. In each slice, 6 average regional circumferential strain values are obtained. The measurements from in-vivo data are $\varepsilon_i^{\text{exp}}(i = 1...24)$ and V^{exp}. Hence we have a total of 25 data points.

A sensitivity study showed that there exist close correlations among a, b, a_f, b_f, a_s, a_{fs}, b_{fs}, therefore it is impossible to estimate all 8 parameters unambiguously in one step. We therefore adopt a multi-step optimization procedure below.

- **Step 1** The parameters are separated into $a^{\text{group}} = \{a, a_f, a_s, a_{fs}\}$, and $b^{\text{group}} = \{b, b_f, b_s, b_{fs}\}$, each scaled with a control parameter, C_a or C_b,

$$a^{\text{group}} = C_a \times a_0^{\text{group}} \; ; b^{\text{group}} = C_b \times b_0^{\text{group}}. \tag{2}$$

  where a_0^{group} and b_0^{group} are adopted from data fitted to porcine [2]. The objective function to be minimized is

$$O_1 = \sum_{i=1,...,n} (\varepsilon_i - \varepsilon_i^{\text{exp}})^2 + (V - V^{\text{exp}})^2. \tag{3}$$

  Here the LV cavity volume is not normalized, therefore O_1 is volume dominated. By locating the minimized values of O_1, we are able to determine the best values for C_a and C_b in the parameter space.

- **Step 2** a_f, b_f, a_s, and b_s are further refined with the following objective function

$$O_2 = \sum_{i=1,...,n} (\varepsilon_i - \varepsilon_i^{\text{exp}})^2 + (\frac{V - V^{\text{exp}}}{V^{\text{exp}}})^2, \tag{4}$$

  in which a, b, a_{fs} and b_{fs} are the same as in O_1, but O_2 is strain dominated. In order to get accurate information about a_s, b_s, we have to apply extra constrains. For healthy myocardium, the stiffness in the sheet direction should be much less than in the myofiber direction, we impose the following constrains

$$a_f \geq 2a_s \text{ and } b_f \geq 2b_s. \tag{5}$$

- **Step 3** Now a and a_{fs} are optimized again using O_1 but with

$$a = C_3 \times a \text{ and } a_{fs} = C_3 \times a_{fs}, \tag{6}$$

  where C_3 is the scaling factor to be optimized.

The sequential quadratic programming is used in steps 2 &3, which is a gradient based optimization method. In each iteration, a forward nonlinear finite element LV model is solved using ABAQUS. The LV model is applied with a 8mmHg endocardial pressure loading and partially fixed basal plane, following [2]. The simulated circumferential strains from the computational LV model are calculated in the same way as the estimated strains from the CMRI data using a deformable image registration method.

3 RESULTS & DISCUSSION

Table 1 shows the estimated parameters for the healthy volunteer. The initial parameter set fitted for porcine seems to be over stiff for the human subject, this leads to a much smaller end-diastolic LV cavity volume (90.57mL) compared to the measured end-diastolic volume (143mL). After step 1, the end-diastolic volume (145mL) matches well with the measurements, but the simulated strain is slightly lower than the measurements. With step 2, the simulated strain is refined but the LV cavity volume difference increases slightly (150mL). In the final step, the end-diastolic volume (143mL) matches well and strain differences also decrease. Fig.2 shows the strains from 24 regions after each optimization step. After step 3, the simulated regional circumferential strain agree closely with the measurements. The estimated strain data are also slightly smoother than the values recovered from deformable image registration method.

Table 1: Estimated parameters for the healthy volunteer

	$a(kPa)$	b	$a_f(kPa)$	b_f	$a_s(kPa)$	b_s	$a_{fs}(kPa)$	b_{fs}
Initial	0.2362	10.81	20.0370	14.154	3.7245	5.1645	0.4109	11.3
Step 1	0.0472	3.243	4.0074	4.2462	0.7449	1.5494	0.0822	3.39
Step 2	0.0472	3.243	3.1762	4.7435	0.5426	1.5998	0.0822	3.39
Step 3	0.1348	3.243	3.1762	4.7435	0.5426	1.5998	0.2344	3.39

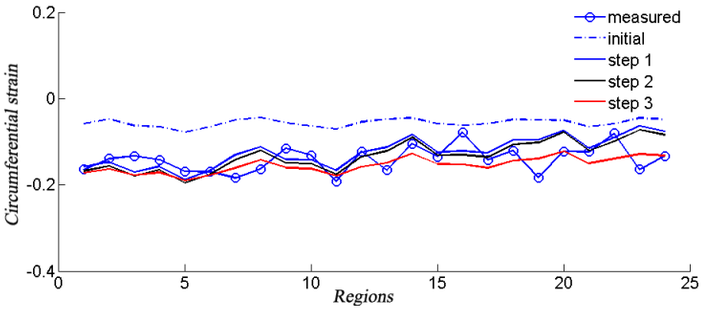

Figure 2: Regional circumferential strain from each optimization step, compared with the measured estimates (line with circle)

4 CONCLUSIONS

We have designed a multi-step optimization procedure to inversely estimate the parameters of the H-O orthotropic material model, using the in-vivo CMRI data from a healthy volunteer. Our initial results show that the estimated parameters are capable of reproducing measured end-diastolic volume and strains.

5 ACKNOWLEDGMENTS

We are grateful for funding provided by the UK EPSRC (EP/I1029990), the British Heart Foundation (PG/11/2/28474), and the Medical Research Scotland.

REFERENCES

[1] J Aguado-Sierra, A Krishnamurthy, et al. Progress in biophysics and molecular biology, 107(1):147–155, 2011.

[2] H Wang, H Gao, XY Luo, et al. International journal for numerical methods in biomedical engineering, 29(1):83–103, 2013.

[3] H Gao, B Griffith, et al. In Functional Imaging and Modeling of the Heart, pages 11–18. Springer, 2013.

[4] S Dokos, B Smaill, Young, et al. American Journal of Physiology-Heart and Circulatory Physiology, 283(6):H2650–H2659, 2002.

[5] JM Guccione, AD McCulloch, and LK Waldman. Journal of biomechanical engineering, 113(1):42–55, 1991.

[6] J Walker, M Ratcliffe, et al. American Journal of Physiology-Heart and Circulatory Physiology, 289(2):H692–H700, 2005.

[7] A Nair, D Taggart, and F Vetter. m. Journal of biomechanics, 40(7):1646–1650, 2007.

[8] J Xi, P Lamata, et al. Journal of the mechanical behavior of biomedical materials, 4(7):1090–1102, 2011.

[9] J Xi, P Lamata, et al. Medical image analysis, 2012.

[10] G Holzapfel and R Ogden. Philosophical Transactions of the Royal Society A: Mathematical, Physical and Engineering Sciences, 367(1902):3445–3475, 2009.

[11] Y Liu, H Wen, et al. American Journal of Physiology-Heart and Circulatory Physiology, 297(3):H1151–H1162, 2009.

[12] A Allan, H Gao, et al. In Engineering in Medicine and Biology Society, EMBC, 2011 Annual International Conference of the IEEE, pages 2650–2653. IEEE, 2011.

Numerical Techniques for Computational Surgery

3rd International Conference on Computational and Mathematical Biomedical Engineering - CMBE2013
16-18 December 2013, Hong-Kong
P. Nithiarasu and R. Löhner (Eds.)

PGD-based efficient thermography inverse analysis

Felipe Bordeu⋆, Francisco Chinesta⋆ and, Elias Cueto⋆⋆
⋆GeM Institute, Ecole Centrale de Nantes, 1 rue de la Noe, BP 92101, F-443OO Nantes, France,
{Felipe.Bordeu;Francisco.Chinesta}@ec-nantes.fr
⋆⋆I3A, University of Zaragoza, Maria de Luna s/n, Zaragoza, Spain, ecueto@unizar.es

SUMMARY

Efficient and robust breast thermography requires adequate resolution and accurate inverse techniques in order to identify and reconstruct the cancer size and location. In this work we are computing the parametric temperature solution related to the position of a cancer of a given size. This solution allows exploring the parametric domain and conclude about the resolution (temperature magnitude, thermal signatures and contrast for the different cancer locations). The second interest of such a solution is the possibility of carrying out fast and accurate inverse analysis in order to reconstruct the breast cancer.

Key Words: *Thermography, Inverse analysis, Model reduction, PGD*

1 INTRODUCTION

Themography allows diagnosis from infrared images of the human body. It has been applied in breast oncology for cancer screening. Promoted by complementary and alternative medicine many years ago its efficiency is quite controversial, with many supporters and also many detractors. It is base on the fact that regions of the body that are more metabolically generate greater heat rates that alter temperature distribution on the breast surface that can be observed in the thermogram (a sort of thermal photo).

A tricky issue in the analysis of thermograms lies in the reconstruction of the cancer from the thermal image. This reconstruction is not easy because the large variability of properties of living tissues, the inherent noise, and also the inherent issues related to inverse techniques (solution unicity, inverse problem illness, etc.). In all cases an efficient diagnosis requires processing very fast the information and for this purpose one must be able of knowing the thermal field for many configurations (cancer size and position) because inverse techniques proceed by modifying the size and location for minimizing the differences between the calculated temperature on the breast surface and the one related to the thermogram.

2 PGD-BASED THERMOGRAPHY ANALYSIS

In breast thermography one should identify the position, shape and size of a cancer from a infrared image, that is from the temperatures measured on the breast surface. A pre-computed solution given such surface temperature for any possible scenario will be of great interest for a fast diagnosis and reconstruction of breast diasses.

For illustrating the procedure we consider the breast occupying a domain Ω. For the sake of simplicity in the description that follows we consider the cancer as a sphere of radius R with $\mathcal{P}$ its center, $\mathcal{B}(R,\mathcal{P})$. The center $\mathcal{P} \in \omega \subset \Omega$, where the distance of points $\mathbf{x} \in \omega$ to the boundary of Ω, $d(\mathbf{x}, \Gamma \equiv \partial\Omega) > R$ that ensures that the cancer remains inside the breast Ω.

A first parametric solution consists of the steady state temperature field for any position of the cancer. If we denote by $\mathbf{y}$ the cartesian coordinates of $\mathcal{P}$, the parametric temperature writes $u(\mathbf{x},\mathbf{y})$ and as it can be noticed it is defined in a space of dimension 6 because $\mathbf{x} \in \Omega \subset \mathcal{R}^3$ and $\mathbf{y} \in \omega \subset \mathcal{R}^3$. Thus $u(\mathbf{x},\mathbf{y}) : \Xi = \Omega \times \omega \rightarrow \mathcal{R}$. Obviously creating a mesh of the 6D domain Ξ is a tricky issue because the excessive number of degrees of freedom potentially involved. The separated representation considered in Proper Generalized Decompositions seems an appealing choice for circumventing the curse of dimensionality.

The separated representation of the temperature field reads:

$$u(\mathbf{x},\mathbf{y}) \approx \sum_{i=1}^{N} X_i(\mathbf{x}) \cdot Y_i(\mathbf{y}) \tag{1}$$

that reveals that the solution of a 6D model will be searched from a sequence of 3D problems, some ones for computing functions $X_i(\mathbf{x})$ and the other for calculating functions $Y_i(\mathbf{y})$. In what follows we are deriving the model and its solution procedure based on the separated representation just introduced.

2.1 Thermal model

The steady state heat equation reads

$$\nabla \cdot (\mathbf{K}(\mathbf{x}) \nabla u) + P(\mathbf{x}) = 0 \tag{2}$$

where $\mathbf{K}(\mathbf{x})$ denotes the conductivity tensor, that in an isotropic medium reduces to $\mathbf{K} = k\mathbf{I}$, with $\mathbf{I}$ the unit matrix. In the previous equation P denotes the thermal power rate that metabolical activity generates. As previously indicated cancers produce higher heat generation rates. We define the characteristic function $\chi(\mathbf{x};\mathbf{y})$ (conductivity at point $\mathbf{x}$ that depends parametrically of the cancer location $\mathbf{y}$) related to the domain occupied by the cancer

$$\chi(\mathbf{x};\mathbf{y}) = \begin{cases} 1 & if\ \mathbf{x} \in \mathcal{B}(R,\mathbf{y}) \\ 0 & if\ \mathbf{x} \in \Omega \backslash \mathcal{B}(R,\mathbf{y}) \end{cases} \tag{3}$$

and from it the conductivity (assumed for the sake of simplicity and without loss of generality isotropic) and the generated heat rate

$$k(\mathbf{x};\mathbf{y}) = k_h + \chi(\mathbf{x};\mathbf{y})\ (k_c - k_h) \tag{4}$$

where k_h is the thermal conductivity of the healthy tissue and k_c the one related to the cancer, and

$$P(\mathbf{x};\mathbf{y}) = P_h + \chi(\mathbf{x};\mathbf{y})\ (P_c - P_h) \tag{5}$$

where P_h and P_c are the generated heat rates of the healthy tissue and the cancer respectively.

We consider the domain boundary $\Gamma = \partial\Omega$ divided in three different parts Γ_R, Γ_N and Γ_D ($\Gamma_R \cup \Gamma_N \cup \Gamma_D = \Gamma$ with null intersections) where Robin, Neumann and Dirichlet boundary conditions apply:

$$-k_s \ (\nabla u \cdot \mathbf{n})_{\mathbf{x}\in\Gamma_R} = h \ (u(\mathbf{x} \in \Gamma_R) - u_a) \tag{6}$$

where u_a denotes the ambient temperature and $\mathbf{n}$ the unit outwards vector defined on the domain boundary,

$$-k_s \ (\nabla u \cdot \mathbf{n})_{\mathbf{x}\in\Gamma_N} = q_g(\mathbf{x}) \tag{7}$$

where q_g is the given heat flux assumed known (it allows par example enforcing null fluxes $q_g = 0$), and

$$u(\mathbf{x} \in \Gamma_D) = u_g(\mathbf{x}) \tag{8}$$

with u_g the given temperature that allows for example prescribing the body temperature.

The standard heat problem weak form consists of finding $u \in \mathcal{H}^1(\Omega)$, with $u(\mathbf{x} \in \Gamma_D) = u_g$ such that

$$\int_\Omega k(\mathbf{x};\mathbf{y}) \ \nabla u^* \cdot \nabla u \ d\mathbf{x} = \int_\Omega u^* \ P(\mathbf{x};\mathbf{y}) \ d\mathbf{x} - \int_{\Gamma_R \cup \Gamma_N} u^* \ k_s \ (\nabla u \cdot \mathbf{n}) \ d\mathbf{x} \tag{9}$$

applies $\forall u^* \in \mathcal{H}^1_0(\Omega)$ with functions in $\mathcal{H}^1_0(\Omega)$ vanishing on Γ_D.

2.2 Separated representation

When the solution is sought in the separated form

$$u(\mathbf{x},\mathbf{y}) \approx \sum_{i=1}^{N} X_i(\mathbf{x}) \cdot Y_i(\mathbf{y}) \tag{10}$$

the weak form must be extended for enforcing the equation in the extended domain $\Xi = \Omega \times \omega$:

$$\int_\omega \int_\Omega k(\mathbf{x};\mathbf{y}) \ \nabla u^* \cdot \nabla u \ d\mathbf{x} \ d\mathbf{y} = \int_\omega \int_\Omega u^* \ P(\mathbf{x};\mathbf{y}) \ d\mathbf{x} \ d\mathbf{y} - \int_\omega \int_{\Gamma_R \cup \Gamma_N} u^* \ k_s \ (\nabla u \cdot \mathbf{n}) \ d\mathbf{x} \ d\mathbf{y} \tag{11}$$

In order to enforce Dirichlet boundary conditions we consider the first mode of the solution $X_1(\mathbf{x}) \cdot Y_1(\mathbf{y}) = u_g(\mathbf{x})$, that implies $Y_1(\mathbf{y}) = 1$. Thus the next modes $X_i(\mathbf{x}) \cdot Y_i(\mathbf{y})$ will be subjected to homogeneous Dirichlet boundary conditions on Γ_D.

If we assume that at present iteration n the solution is known until the order $n-1$, $n > 1$

$$u^{n-1}(\mathbf{x},\mathbf{y}) = \sum_{i=1}^{n-1} X_i(\mathbf{x}) \cdot Y_i(\mathbf{y}) \tag{12}$$

at present iteration we looks for $X_n(\mathbf{x}) \cdot Y_n(\mathbf{y})$

$$u^n(\mathbf{x},\mathbf{y}) = u^{n-1}(\mathbf{x},\mathbf{y}) + X_n(\mathbf{x}) \cdot Y_n(\mathbf{y}) \tag{13}$$

The test function u^* usually considered reads

$$u^*(\mathbf{x},\mathbf{y}) = X_n^*(\mathbf{x}) \cdot Y_n(\mathbf{y}) + X_n(\mathbf{x}) \cdot Y_n^*(\mathbf{y}) \tag{14}$$

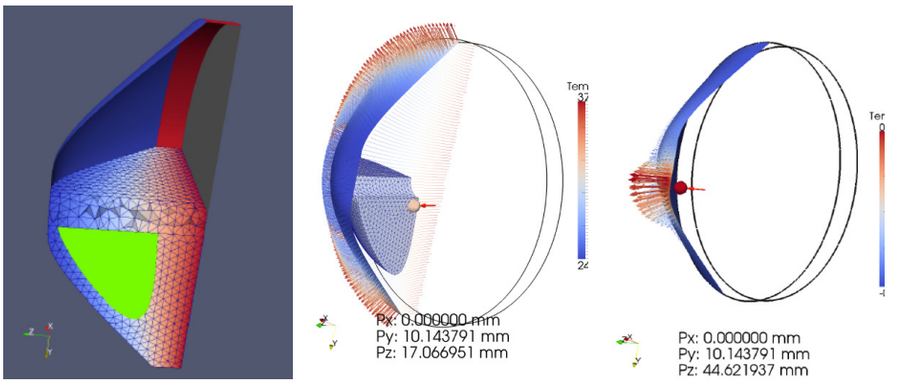

Figure 1: Breast with the region (green) where the center of the cancer can be located (left) and two particularizations of the thermal field (right) for two different locations of the cancer

Introducing (13) and (14) into the extended weak form (11) it results a nonlinear problem (at the present iteration both $X_n(\mathbf{x})$ and $Y_n(\mathbf{y})$ are unknown). Thus, a linearization is compulsory. The simplest strategy lies in considering an alternating direction fixed point schema that considers $Y_n(\mathbf{y})$ known and calculates $X_n(\mathbf{x})$ and from it updates $Y_n(\mathbf{y})$ and so on until reaching convergence.

3 RESULTS

The parametric solution was obtained in the domain depicted in Fig. 1(left) where the center of the sphere representing the cancer can be located in the the green region (ω) by using model parameters and data available. The solution $u(\mathbf{x}, \mathbf{y})$ was calculated and then particularized in real time for two locations of the cancer (Fig. 1)(right). As soon as the cancer is positioned in a particular location, the thermal field and in particular the temperature on the breast surface is instantaneously obtained. As all the possible solutions are available from the parametric solution the possibility of identifying the cancer position "$\mathbf{y}$" in order to minimize the differences between $u(\mathbf{x}; \mathbf{y})$ and $U(\mathbf{x})$, being this one the one associated to the thermography, becomes efficiently feasible. Moreover, such parametric solution allows us for conclude on the technique resolution by analyzing though out the parametric space (cancer location) the magnitude of surface temperatures, signatures and contract.

4 CONCLUSIONS

This work constitutes a first attempt in calculating parametric solutions related to breast cancer, in which the cancer positions is considered as an extra coordinate and then by solving only once the resulting multidimensional problem we have access to the thermal solution for any position of the cancer. Obviously the model can be enriched by introducing other parameters as extra-coordinates (size, shape, generated heat rate, thermal conductivities, etc.). The interested reader can refer to [1] and the references therein for more details on the advanced numerical technique employed.

REFERENCES

[1] F. Chinesta, A. Leygue, F. Bordeu, J.V. Aguado, E. Cueto, D. Gonzalez, I. Alfaro, A. Ammar, A. Huerta. PGD-based computational vademecum for efficient design, optimization and control, *Arch Comput Methods Eng.*, 20, 31-59, 2013.

3rd International Conference on Computational and Mathematical Biomedical Engineering - CMBE2013
16-18 December 2013, Hong-Kong
P. Nithiarasu and R. Löhner (Eds.)

Haptic surgery simulation based on PGD techniques

C. Quesada[⋆], D. González[⋆], I. Alfaro[⋆], E. Cueto[⋆] and F. Chinesta[⋆⋆,†]
[⋆]Aragon Institute of Engineering Research. Universidad de Zaragoza, Spain.
{cquesada,gonzal,iciar,ecueto}@unizar.es
[⋆⋆]Ecole Centrale de Nantes, France.
[†] Institut Universitaire de France.
Fracisco.Chinesta@ec-nantes.fr

SUMMARY

In this paper we present a surgery simulator with haptic feedback able to reproduce complex constitutive equations for soft tissues. It is based on the employ of Proper Generalized Decomposition (PGD) techniques, that allow for a sort of *computational vademecum*, in which a big effort of computing is made off-line in order to be able to only post-process on-line, with the subsequent savings in CPU time.

Key Words: *Surgery simulation, haptic feedback, model order reduction, proper generalized decomposition.*

1 INTRODUCTION

Real-time simulation of endoscopic surgery for the training of surgeons is in general a difficult tasks, due to the huge feedback rates necessary to reach a realistic sensation of touch, estimated to lie between 500 Hz and 1 KHz. Since soft tissues are often modeled under hyperelastic frameworks, this implies to solve between 500 and one thousand times per second a non-linear problem, whose difficulty is well known for any mechanical engineer.

Existing approaches to the problem include mass-spring networks (that do not either reproduce the laws of linear elasticity), the use of mass-lumped explicit finite element solvers (whose stability for large simulation times is often questioned), or the use of supercomputing strategies (parallelization, use of GPUs, etc.) Here, we present an approach based upon the use of reducer-order modeling. In particular, our strategy consist on an intensive off-line simulation procedure that leads to a sort of physics-based meta-model or *computational vademecum* [1]. This vademecum can be then exploited under real-time constraints very efficiently, without the need for actually simulating anything on-line, but rather post-processing.

The main ingredient of this simulator is composed by the off-line construction of the vademecum solution under a Proper Generalized Decomposition (PGD) approach [2], whose structure will be detailed in Section 2 below. Here, we detail how to reach real-time interactive rates for the simulation of solid dynamics, a problem whose solution is dependent on initial and boundary conditions. For details on how to develop a vademecum solution for any load position, see [3].

2 PGD SOLUTION FOR INTERACTIVE SIMULATORS

As mentioned before, one key aspect to develop a realistic surgery simulator is the consideration of realistic constitutive equations (often under the form of hyperelasticity). Another one is to provide with a realistic sense of interactivity. This can be reached by appropriately simulating the dynamics of the problem, even if important dissipations occur. The weak form of the problem of solid dynamics can be formulated as: given $\boldsymbol{f}$, $\boldsymbol{g}$, $\boldsymbol{u}_0$ and $\dot{\boldsymbol{u}}_0$ find $\boldsymbol{u}(t) \in \mathcal{S}_t = \{\boldsymbol{u} | \boldsymbol{u}(\boldsymbol{x},t) = \boldsymbol{g}(\boldsymbol{x},t),\ \boldsymbol{x} \in \Gamma_u,\ \boldsymbol{u} \in \mathcal{H}^1(\Omega)\}$, $t \in [0,T]$ such that for all $\boldsymbol{w} \in \mathcal{V}\{\boldsymbol{u} | \boldsymbol{u}(\boldsymbol{x},t) = \boldsymbol{0},\ \boldsymbol{x} \in \Gamma_u,\ \boldsymbol{u} \in \mathcal{H}^1(\Omega)\}$,

$$
\begin{aligned}
(\boldsymbol{w}, \rho\ddot{\boldsymbol{u}}) + a(\boldsymbol{w},\boldsymbol{u}) &= (\boldsymbol{w},\boldsymbol{f}) + (\boldsymbol{w},\boldsymbol{h})_\Gamma \\
(\boldsymbol{w}, \rho\boldsymbol{u}(0)) &= (\boldsymbol{w}, \rho\boldsymbol{u}_0) \\
(\boldsymbol{w}, \rho\dot{\boldsymbol{u}}(0)) &= (\boldsymbol{w}, \rho\dot{\boldsymbol{u}}_0),
\end{aligned}
$$

The main modification in the standard approach to the problem is to reinterpret the parametric dependence of the problem on its initial conditions $\boldsymbol{u}_0$ and $\dot{\boldsymbol{u}}_0$ as being actually multi-dimensional:

$$
\boldsymbol{u} : \bar{\Omega} \times [0,T] \times \mathcal{I} \times \mathcal{J} \to \mathbb{R}^3,
$$

where $\mathcal{I} = [\boldsymbol{u}_0^-, \boldsymbol{u}_0^+]$ and $\mathcal{J} = [\dot{\boldsymbol{u}}_0^-, \dot{\boldsymbol{u}}_0^+]$ represent the considered intervals of variation of initial boundary conditions, $\boldsymbol{u}_0$ and $\dot{\boldsymbol{u}}_0$. This implies that $\boldsymbol{u}$ is actually defined on a 10-dimensional space. This makes it necessary to define a new (triply-) weak form as:

$$
\begin{aligned}
a(\boldsymbol{w},\boldsymbol{u}) &= \int_{\mathcal{I}}\int_{\mathcal{J}}\int_{\Omega} \boldsymbol{\nabla}^s\boldsymbol{w} : \mathbf{C} : \boldsymbol{\nabla}^s\boldsymbol{u}\ d\Omega d\dot{\boldsymbol{u}}_0 d\boldsymbol{u}_0 \\
(\boldsymbol{w},\boldsymbol{f}) &= \int_{\mathcal{I}}\int_{\mathcal{J}}\int_{\Omega} \boldsymbol{w}\boldsymbol{f}\ d\Omega d\dot{\boldsymbol{u}}_0 d\boldsymbol{u}_0 \\
(\boldsymbol{w},\boldsymbol{h})_\Gamma &= \int_{\mathcal{I}}\int_{\mathcal{J}}\int_{\Gamma_t} \boldsymbol{w}\boldsymbol{h}\ d\Gamma d\dot{\boldsymbol{u}}_0 d\boldsymbol{u}_0.
\end{aligned}
$$

The PGD approximation to the problem assumes a separated representation of the displacement field in the form:

$$
\boldsymbol{u}^h(\boldsymbol{x},t,\boldsymbol{u}_0,\dot{\boldsymbol{u}}_0) = \left[\sum_{i=1}^{N} \boldsymbol{F}_i(\boldsymbol{x}) \circ \boldsymbol{G}_i(\boldsymbol{u}_0) \circ \boldsymbol{H}_i(\dot{\boldsymbol{u}}_0)\right] \circ \boldsymbol{d}(t),
$$

where the nodal coefficients $\boldsymbol{d}(t)$ carry out all the time-dependency of the solution and the symbol "$\circ$" stands for the entry-wise Hadamard or Schur multiplication of vectors.

Functions $\boldsymbol{F}$, $\boldsymbol{G}$ and $\boldsymbol{H}$ will be expressed in terms of low (here, three-) dimensional finite element basis functions. The computation of theses basis is one of the more salient features of PGD, since they are computed on the fly, a priori, without the need to prior computer experiments, typical of POD-based techniques. They are computed by means of a greedy algorithm in which one sum is computed at a time, while one product is computed in a fixed point, alternated directions algorithm. Thus, having an approximation to $\boldsymbol{u}^h$ converged at iteration n, the $(n+1)$-th term is obtained as

$$
\boldsymbol{u}^{n+1}(\boldsymbol{x},t,\boldsymbol{u}_0,\dot{\boldsymbol{u}}_0) = \left[\sum_{i=1}^{n} \boldsymbol{F}_i(\boldsymbol{x}) \circ \boldsymbol{G}_i(\boldsymbol{u}_0) \circ \boldsymbol{H}_i(\dot{\boldsymbol{u}}_0) + \boldsymbol{R}(\boldsymbol{x}) \circ \boldsymbol{S}(\boldsymbol{u}_0) \circ \boldsymbol{T}(\dot{\boldsymbol{u}}_0)\right] \circ \boldsymbol{d}(t).
$$

In this framework, an admissible variation of $\boldsymbol{v}^h$ is computed as

$$
\boldsymbol{w}^h = \boldsymbol{R}^* \circ \boldsymbol{S} \circ \boldsymbol{T} + \boldsymbol{R} \circ \boldsymbol{S}^* \circ \boldsymbol{T} + \boldsymbol{R} \circ \boldsymbol{S} \circ \boldsymbol{T}^*,
$$

where functional dependencies have been omitted for clarity.

If we inject the approximations to $\boldsymbol{u}^h$ and $\boldsymbol{w}^h$ into the weak form of the problem we arrive at a semi-discrete problem that can be approximated in time using your favorite time integrator.

One key aspect in the method developed so far arises when we move to continuous rather than discrete problems. FE discretizations of these problems lead to an impressive number of degrees of freedom if we employ a finite element parametrization of the space of initial conditions. For instance, a mesh composed of, say, one thousand nodes in 3D, will have 3000 degrees of freedom to parametrize the initial displacement condition and other 3000 for the initial velocity one. A problem defined in 6000 dimensions is not feasible, even for PGD methods, due to its computational complexity.

Here a mixed POD-PGD approach is envisaged: based upon the previous solution of similar problems and the use of POD decompositions, a suitable parametrization of the space of initial conditions is obtained. Results for a particular problem will be then projected onto this basis and re-injected into the (off-line, multi-dimensional) obtained PGD solution to advance in time. We thus obtain a sort of response surface or meta-model to be evaluated on-line that takes as input parameters the projection of the previous time step displacement and velocity field onto the reduced basis parametrization of initial conditions for the subsequent time step. A sketch of the proposed method is shown in Fig. 1.

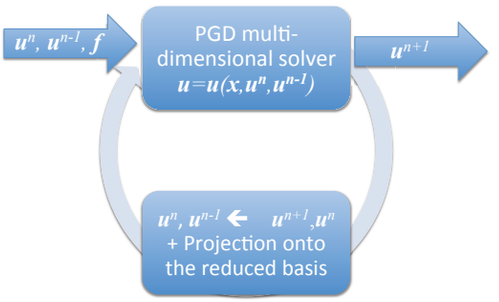

Figure 1: Sketch of the proposed algorithm. A POD basis is employed for the parametrization of the space of initial conditions of the problem (for forward Euler schemes, for instance, this means in practice that the solution deepens on the displacement at time steps n and $n-1$, respectively).

For the problem of liver palpation, Fig. 2 represents the solution as a function of the number of degrees of freedom used to parameterize the space of initial conditions. It can be noticed how the use of an increasing (but still surprisingly reduced) number of degrees of freedom leads to a solution that presents high-frequency oscillations (provoked by the elimination of the higher modes of the solution) but that converges very vastly in amplitude and frequency to the reference one.

3 CONCLUSIONS

The main features of an endoscopic surgery simulator with haptic feedback based on the use of PGD approaches has been presented. It is based upon the construction of what we have called a

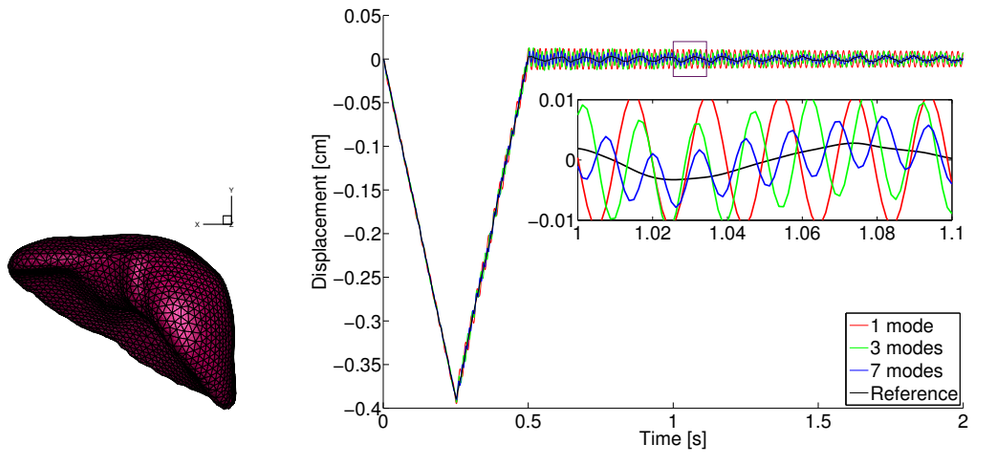

Figure 2: Response of the liver for a peak load. Reference (FE) results, and PGD results with basis composed by 1, 3 and 7 modes.

computational vademecum, i.e., a general, parametric, multidimensional solution to the problem, that is therefore computed off-line, once for life, and that is very efficiently evaluated (rather than simulated) on-line. This has allowed us to obtain very fast solutions (close to 1 KHz, sometimes more), even with the consideration of state-of-the-art constitutive laws for soft tissues under large strain settings.

REFERENCES

[1] F. Chinesta, A. Leygue, F. Bordeu, J.V. Aguado, E. Cueto, D. Gonzalez, I. Alfaro, A. Ammar, A. Huerta. PGD-based computational vademecum for efficient design, optimization and control. *Archives of Computational Methods in Engineering*, 20(1), 31-59, 2013.

[2] S. Niroomandi, D. Gonzalez, I. Alfaro, F. Bordeu, A. Leygue, E. Cueto, F. Chinesta. Real-time simulation of biological soft tissues: a PGD approach. *International Journal for Numerical Methods in Biomedical Engineering*, 29(5), 586-600, 2013.

[3] S. Niroomandi, D. Gonzalez, I. Alfaro, E. Cueto, F. Chinesta. Model order reduction in hyperelasticity: a Proper Generalized Decomposition approach. *International Journal for Numerical Methods in Engineering*, in press, 2013.

3rd International Conference on Computational and Mathematical Biomedical Engineering - CMBE2013
16-18 December 2013, Hong-Kong
P. Nithiarasu and R. Löhner (Eds.)

Real-time numerical simulation of soft tissues

S. Niroomandi*, D. González*, I. Alfaro*, F. Bordeu and E. Cueto***
*Aragón Institute of Engineering Research (I3A). Universidad de Zaragoza.
{siamakn,gonzal,iciar,ecueto}@unizar.es
**GEM UMR CNRS - Ecole Centrale de Nantes. felipe.bordeu@ec-nantes.fr

SUMMARY

In this work we combine a model order reduction technique, like Proper Generalized Decomposition (PGD), with two different numerical methods applied to hyperelastic soft tissues: An explicit treatment and an Asimptotic Numerical Method (ANM). The use of Porper Generalized Decomposition (PGD) techniques, that can be considered as a means of a priori model order reduction, provide us with a meta-model computed in a "off-line" stage. Then in an 'on-line" evaluation stage the results are obtained in real time. The model thus obtained gives a competitive response for this kind of non-linear problems, offering kHz feedback rates, necessary for haptic rendering in surgical simulators.

Key Words: *Real time, model order reduction, proper generalized decomposition (PGD).*

1 INTRODUCTION

Surgical simulators can be classified in five generations. From the first to the fifth one, these virtual descriptions of the patient should include, respectively, accurate representation of the geometry of the organs at a macroscopic level, accurate description of the physical dynamics of the body, accurate descriptions of physiology, microscopic anatomy (at a neurovascular level, for instance) and, finally, biochemical systems. But incorporating this behaviour into virtual reality simulators, due to the impressive computing requirements that they involve, has not been fully accomplished yet.

Many difficulties of very different nature at a macroscopic level appears. The main difficulty comes from the highly non-linear constitutive equations of soft tissues, very often modeled as (possibly visco-) hyperelastic media. These non-linear equations must be solved under real-time constraints, that reach 1kHz of feedback response if we think of haptic devices, or 25 Hz if we need for visual feedback only. Currently, very few surgical training simulators at this level incorporate accurate models for tissue deformation. Some of these are based on the use of explicit finite elements implemented on hardware (Graphic Processing Units, GPU). But in general, explicit algorithms lack of robustness for very long times of simulation. Recently, a growing interest has been paid to investigate Model Order Reduction (MOR) techniques in this framework. Proper Generalized Decomposition (PGD) methods arose recently as a generalization of POD techniques, in which the basis are computed on the fly without no previous snapshot. Instead, the essential field is approximated as a finite sum of separable functions. One key aspect in the rapid development of PGD methods is related to the fact that PGD can be seen as both an efficient technique for high dimensional problems and as an a priori model order reduction technique. This opened the

door to re-interpreting parametric problems as high dimensional ones, just by considering parameters as new dimensions of the state space of the model. In this work we explore the possibilities of PGD methods applied to fast (real time) simulation of hyperelastic solids. It will be shown how a multi-dimensional formulation of the problem, in which the displacement is expressed as to be dependent on both the physical coordinates and the position and orientation of the applied loads (thus, defined in $\mathbb{R}^8$), opens the door to simulations with feedback rates on the order of one kHz. The developed strategy comprises an off-line computation strategy, in which a high-dimensional problem is solved. This solution provides in fact a sort of meta-model or computational vademecum that can be stored in a very compact form. Then, an on-line simulation strategy is developed that solves the meta-model at impressive feedback rates, even on handheld devices. In summary, the aim of this work is to develop the "engine" of a surgical simulator able to be used in medical environments. To do this, we require real-time performance and real-time response means 25 Hz for visual feedback and 500 Hz for haptic feedback.

2 PGD APPLIED TO NON-LINEAR PROBLEMS

The original problem is re-formulated as a high dimensional parametric problem where each parameter is a new coordinate. The PGD method then looks for an effective solution in the form of a finite sum of separable functions, so as to be able to avoid the curse of dimensionality associated to high dimensional problems. In this framework, the displacement field, $\boldsymbol{u}(x, y, z)$, for any load position $\boldsymbol{s}$ and for any force vector orientation and module, $\boldsymbol{t}$, thus rendering a problem defined in ($\mathbb{R}^8$).

For the sake of simplicity, let us assume a load vector $\boldsymbol{t}$ with unit module and oriented in the vertical direction. Now the problem is defined in $\mathbb{R}^5$ ($\boldsymbol{u} = \boldsymbol{u}(\boldsymbol{x}, \boldsymbol{s})$). Let us consider the weak form of the equilibrium equations (balance of linear momentum), and for the sake of simplicity, whitout inertia terms. Under these assumptions, the weak form extended to all possible force vectors applied on the boundary:

$$\int_{\bar{\Gamma}} \int_{\Omega_0} \boldsymbol{S} : \boldsymbol{E}^* d\Omega d\bar{\Gamma} = \int_{\bar{\Gamma}} \int_{\Gamma_{t2}} (\boldsymbol{u}^*)^T \boldsymbol{t} \delta(\boldsymbol{x} - \boldsymbol{s}) d\Gamma d\bar{\Gamma}$$

The PGD approach to the problem is characterized by the construction, in an iterative way, of an approximation to the solution in the form of a finite sum of separable functions. Assume that we have converged to a solution, at iteration n of this procedure,

$$u_j^n(\boldsymbol{x}, \boldsymbol{s}) = \sum_{k=1}^{n} X_j^k(\boldsymbol{x}) \cdot Y_j^k(\boldsymbol{s})$$

We look for an improvement of this approximation, the (n + 1)-th term will look like

$$u_j^{n+1}(\boldsymbol{x}, \boldsymbol{s}) = u_j^n(\boldsymbol{x}, \boldsymbol{s}) + R_j(\boldsymbol{x}) \cdot S_j(\boldsymbol{s})$$

A fixed-point algorithm in which functions R and S are sought iteratively, can be used.

The techniques proposed in this work to solve non-liner problems using PGD approach are presented.

2.1 One possible explicit linearization of the formulation

The Kirchhoff-Saint Venant model is characterized by the energy density functional given by,

$$\Psi = \frac{\lambda}{2}(\text{tr}\boldsymbol{E}) + \mu \boldsymbol{E} : \boldsymbol{E}$$

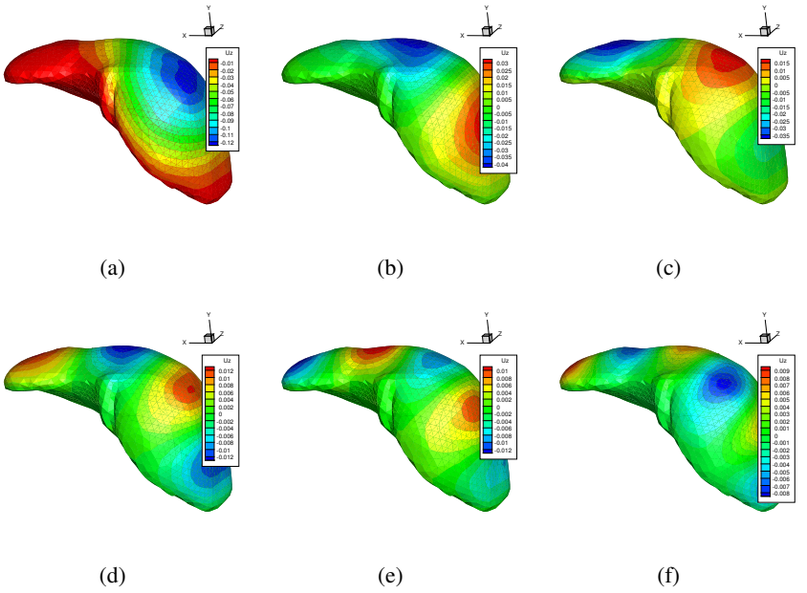

(a) (b) (c)

(d) (e) (f)

Figure 1: Spatial modes

where λ and μ are Lame's constants.The second Piola-Kirchhoff stress tensor can be obtained by

$$\boldsymbol{S}^n = \frac{\partial \Psi}{\partial \boldsymbol{E}} = \mathbf{C} : \boldsymbol{E}^n$$

in which $\mathbf{C}$ is the fourth-order constitutive (elastic) tensor. We assume an incremental application of the load $\Delta \boldsymbol{t}$ provoking $\Delta \boldsymbol{u}(\boldsymbol{x}, \boldsymbol{s})$:

$$\boldsymbol{E}^{t+\Delta t} = \boldsymbol{\nabla}_s \left(\boldsymbol{u}^t + \Delta \boldsymbol{u} \right) + \frac{1}{2} \left(\boldsymbol{\nabla} (\boldsymbol{u}^t + \Delta \boldsymbol{u}) \cdot \boldsymbol{\nabla}^T (\boldsymbol{u}^t + \Delta \boldsymbol{u}) \right).$$

Once substituted into the weak form of the equilibrium equation,

$$\begin{aligned}
&\int_{\bar{\Gamma}} \int_{\Omega(t)} \boldsymbol{E}^* : \mathbf{C} : \boldsymbol{E} d\Omega d\bar{\Gamma} = \\
&= \int_{\bar{\Gamma}} \int_{\Omega(t)} \left(\boldsymbol{\nabla}_s (\Delta \boldsymbol{u}^*) + \boldsymbol{\nabla} (\Delta \boldsymbol{u}^*) \cdot \boldsymbol{\nabla}^T (\boldsymbol{u}^t + \Delta \boldsymbol{u}) \right) : \mathbf{C} \\
&: \left(\boldsymbol{\nabla}_s \left(\boldsymbol{u}^t + \Delta \boldsymbol{u} \right) + \frac{1}{2} \left(\boldsymbol{\nabla} (\boldsymbol{u}^t + \Delta \boldsymbol{u}) \cdot \boldsymbol{\nabla}^T (\boldsymbol{u}^t + \Delta \boldsymbol{u}) \right) \right) d\Omega d\bar{\Gamma}.
\end{aligned}$$

The simplest linearization consists of keeping in the formulation only constant terms and those linear in $\Delta \boldsymbol{u}$. This renders a very simple scheme that has revealed, reasonable convergence properties. The Fig. 1 shows six spatial modes of the solution.

2.2 A combined PGD-ANM approach to hyperelasticity

The Asymptotic Numerical Method (ANM) is based upon expanding the displacement (also the second Piola-Kirchhoff stress tensor $\boldsymbol{S}$ and the load parameter λ) in the neighborhood of each material point in terms of a control parameter "a", prior to their introduction in the weak form of the problem,

$$\left\{ \begin{array}{c} \boldsymbol{u}^{m+1}(a) \\ \boldsymbol{S}^{m+1}(a) \\ \overline{\lambda}^{m+1}(a) \end{array} \right\} = \left\{ \begin{array}{c} \boldsymbol{u}^{m}(a) \\ \boldsymbol{S}^{m}(a) \\ \overline{\lambda}^{m}(a) \end{array} \right\} + \sum_{p=1}^{N} a^p \left\{ \begin{array}{c} \boldsymbol{u}_p \\ \boldsymbol{S}_p \\ \overline{\lambda}_p \end{array} \right\},$$

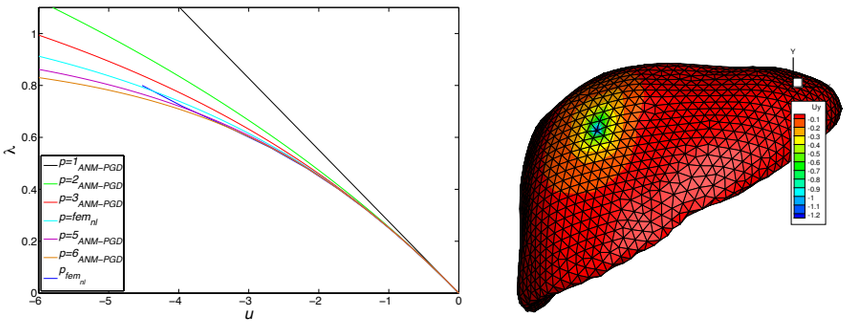

Figure 2: Liver Palpation: Computed solution at different orders of approximation vs. FEM reference solution.

A discretization of the weak form of the problem by using finite elements leads to a sequence of linear problems which at order p, $(p = 1, ..., N)$ in the form

$$\text{Order } p \begin{cases} \boldsymbol{K}_t \boldsymbol{u}_p = \overline{\lambda}_p \boldsymbol{f} + \boldsymbol{f}_p^{nl}(\boldsymbol{u}_i) & i < p \\ \boldsymbol{u}_p^T \boldsymbol{u}_1 + \overline{\lambda}_p \lambda_1 = 0 \end{cases}$$

where K_t denotes the tangent stiffness matrix associated to the problem and common to all the problems at different orders p.

The combination of the PGD approach to parametrized problems (in this case the position of the load is the parameter) and the ANM for a consistent linearization of the weak form of the problem gives rise to a particularly useful formulation. Fig. 2 shows the solution for each value of p of the liver palpation problem.

The displacement field is approximated as a series expansion around the control parameter "a", whereas each term of the series is approximated by a finite sum of functions that only depends of each parameter, $\boldsymbol{X}(\boldsymbol{x}), \boldsymbol{Y}(\boldsymbol{s})$:

$$\boldsymbol{u} = \boldsymbol{u}_0 + \sum_{i_1=1}^{n_1} (\boldsymbol{X}_{i_1} \circ \boldsymbol{Y}_{i_1}) a + \sum_{i_2=1}^{n_2} (\boldsymbol{X}_{i_2} \circ \boldsymbol{Y}_{i_2}) a^2 + ... + \sum_{i_p=1}^{n_p} (\boldsymbol{X}_{i_p} \circ \boldsymbol{Y}_{i_p}) a^p$$

3 CONCLUSIONS

Model order reduction techniques provide a means for accurate solving of state of the art models of non-linear living tissues. In particularity, the Proper Generalized technique (PGD) seems to open new possibilities by constructing physics-based meta-models in a multi-dimensional setting. The combination of the PGD with ANM and the explicit approach to the hyper elasticity problems presented in this work are solved at kHz rates on a laptop with good results of accuracy.

REFERENCES

[1] S. Niroomandi, D. Gonzalez, I. Alfaro, F. Bordeu, A. Leygue, E. Cueto, F. Chinesta. Real-time simulation of biological soft tissues: a PGD approach. International Journal for Numerical Methods in Biomedical Engineering. 29(5), 586-600, 2013.

[2] S. Niroomandi, I. Alfaro, D. Gonzalez, E. Cueto, F. Chinesta. Model order reduction in hyper-elasticity: a Proper Generalized Decomposition approach. International Journal for Numerical Methods in Engineering. DOI: 10.1002/nme.4531, 2013.

3rd International Conference on Computational and Mathematical Biomedical Engineering - CMBE2013
16-18 December 2013, Hong-Kong
P. Nithiarasu and R. Löhner (Eds.)

An implementation of stabilized nearly-incompressible hyperelastic model in interactive speed

Masato Ogata[⋆] **and Takahiro Yamada**[⋆⋆]
[⋆]Mitsubishi Precision Co.,Ltd., 345 Kamimachiya, Kamakura, Japan,ogata@mpcnet.co.jp
[⋆⋆]Graduate School of Environment and Information Sciences, Yokohama National University,
79-7 Tokiwadai Hodogaya Yokohama Japan, tyamada@ynu.ac.jp

SUMMARY

We introduced pressure stabilization into a nearly-incompressible hyperelastic model to improve the computational reliability for tetrahedral elements of the P1-P0 scheme (four nodal points for displacement and one point for pressure). Usually, the finite element method using tetrahedral elements with the P1-P0 scheme does not satisfy the LBB criteria and lacks of numerical reliability. For implementation of the method in interactive speed , it is important to reduce the number of unknowns for the simultaneous equations.

Key Words: *hyperelastic model, deformation, soft tissue, surgical simulator, surgical navigation.*

1 INTRODUCTION

To simulate the deformation of soft tissue , spring model, linear FEM, and Co-Rotated FEM have been used. Many experimental results show that the soft tissue has a nonlinear stress-strain relationship and exhibits nearly incompressibility like rubber, so that these models are not sufficient for precise surgical simulators and navigation systems. We have been studying real-time implementation of the nearly-incompressible hyperelastic model for medical application.

2 NEARLY-INCOMPRESSIBLE HYPERELASTIC MODEL

Mooney-Rivlin model is used to represent the elastic potential energy function of hyperelastic material. Let W^M be the elastic energy density function of the Mooney-Rivlin model. Adding an energy term due to volumetric change and a constraining term to inhibit volumetric change onto W^M, then integrating them over analytical volume Ω_c and boundary ∂S_c yields the potential energy $\tilde{\Phi}_{ptb}$ of the *perturbed Lagrange-multiplier method* [1].

$$\tilde{\Phi}_{ptb} = \int_{\Omega_c} W^M d\Omega + \int \lambda \underbrace{(III_C - 1)}_{W^V} d\Omega + \int_{\Omega_c} \lambda \underbrace{(J-1)}_{W^V} d\Omega - \frac{1}{2}\int_{\Omega_c} \frac{1}{\kappa}\lambda^2 d\Omega + \underbrace{\int_{\partial S_c} R dS + \int_{\Omega_c} B d\Omega}_{\Phi_{ext}} , \quad (1)$$

where, λ indicates the Lagrange multiplier, J is the volume, κ corresponds to the bulk modulus, and $\boldsymbol{R}$ and $\boldsymbol{B}$ are the potential energy due to surface force and the body force. By calculating the

first variant $\delta_u(\tilde{\Phi}_{ptb})$ and $\delta_\lambda(\tilde{\Phi}_{ptb})$ corresponding to displacement $\boldsymbol{u}$ and Lagrange multiplier $\boldsymbol{\lambda}$, we obtain the following equilibrium conditions. Solving the above stationary energy problem is equivalent to solving the following equations.

$$\int_\Omega \left(\frac{\partial W^M}{\partial C_{ij}} + \lambda \frac{\partial W^V}{\partial C_{ij}} \right) \delta C_{ij} d\Omega = \int_{\partial\Omega} \boldsymbol{t} \cdot \delta \boldsymbol{u} dS + \int_\Omega \rho_0 \boldsymbol{g} \cdot \delta \boldsymbol{u} d\Omega \, .$$

$$\int \left[(W^V - \frac{\lambda}{\kappa}) \delta\lambda \right] d\Omega = 0 \, . \tag{2}$$

Here, $\boldsymbol{C}$ is the right Cauchy-Green deformation tensor, $\boldsymbol{t}$ is the surface force, and $\boldsymbol{g}$ is the body force.

3 PRESSURE STABILIZATION

ISSUE OF DISCRETIZATION: Using tetrahedral finite element is suitable for surgical navigation and simulation, because FEM requires solving a large system of simultaneous equations at the final stage. Therefore it is necessary to reduce the number of unknowns for real-time processing. To ensure the numerical result, the interpolation with the tetrahedral finite element has to satisfy LBB condition at least[1][3, 2].

However, discretization using tetrahedral finite element with 13 knowns per element:4/1(P1/P0), does not satisfy LBB condition so that the reliability of numerical solution is low and it causes pressure oscillation. The discretization using tetrahedral finite element which satisfy LBB condition has to use 34 unknowns per element:10/4C (P2/P1) 10 nodal points for displacement and 4 points for pressure. Time for solving simultaneous equation depends on the order of power of two or three of the number of unknowns. For medical application, it is important to reduce the number of the nodal points.

PRESSURE STABILIZATION: Several methods have been proposed for stabilizing the pressure in an incompressible hyperelastic model without increasing the interpolating points[4, 5]. This paper reports applying pressure stabilization to a nearly-incompressible hyperelastic model that is more stable numerically than an incompressible model. The following Eq. (3) is a weak formula of the nearly-incompressible condition that adds a pressure stabilization term.

$$\int_\Omega \delta\lambda \left(W^V - \frac{\lambda}{\kappa} \right) d\Omega - \frac{\beta}{\kappa} \sum\nolimits_e h_e \int_{\partial\omega_e} [\lambda] \, [\delta\lambda] dS = 0, \tag{3}$$

where β is a stabilization coefficient, h_e denotes the dimension of each finite element,and $[\cdot]$ indicates a jump operator.

4 RESULT

PRESSURE STABILIZATION: Figure 1 shows the deformed image and the corresponding pressure with respect to pressure stabilization coefficient β. For the experiment, we used 4/1(P1/P0): a first-order four-nodal interpolation for displacement and one point for pressure, as the shape function and a four-point Gauss integration. We used artery data taken near the kidney consisting of 1101 tetrahedrons with 401 nodal points. The density was $0.5 \times 10^3 kg/m^3$ and $c1 = 0.84 \times 10^5$ Pa, $c2 = 0.84 \times 10^5$ Pa and $\kappa = 4.166667 \times 10^6$ as hyperelastic material properties. With the above condition, we performed the large deformation with boundary condition indicated in Fig. 2(a). As seen in the figure, the positions of the top nodes are fixed, the x positions of the middle nodes are moved 50% of the width (free for y and z directions), and the positions of the bottom nodes are moved 30% of the height in the z direction (free for x and y directions). For $\beta = 0$, the stabilization is being nulled. The pressure is being stabilized by the β value.

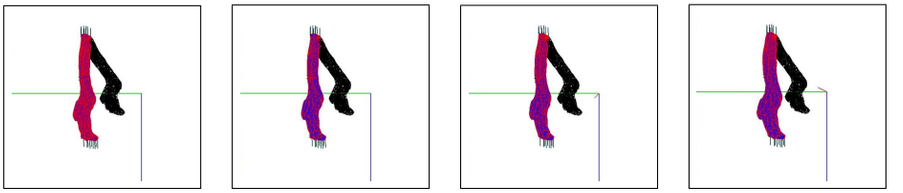

(a) $\beta = 0$ (b) $\beta = 1.0$ (c) $\beta = 100$ (d) $\beta = 1000$

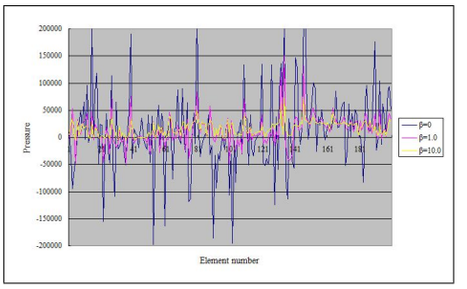

(e) Pressure oscillation: $\beta = 0, 1.0, 10.0$, $\beta = 0$ indicates no stabilization

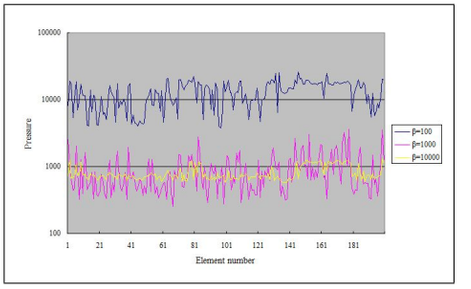

(f) Pressure oscillation: $\beta = 100, 1000, 10000$

Figure 1: Evaluation of implemented pressure stabilized nearly-incompressible hyperelastic model: $\rho = 0.5 \times 10^3 \text{kg/m}^3$; $c_1 = 0.84 \times 10^5$ Pa, $c_2 = 0.84 \times 10^5$ Pa, $\kappa = 4.166667 \times 10^6$.

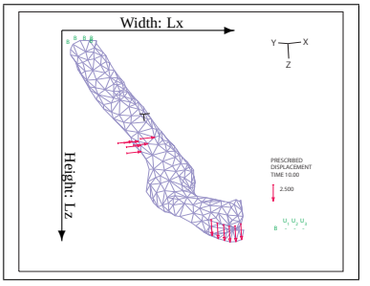

(a) Boundary conditions

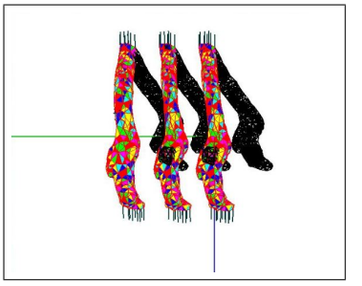

(b) Density is $0.5 \times 10^3 \text{kg/m}^3$.

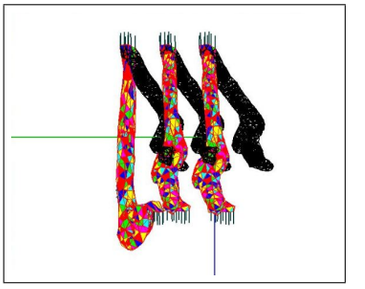

(c) Density is $5 \times 10^3 \text{kg/m}^3$.

Figure 2: Simulation results for each model using artery data. Deformation of PSH, GNL, COR are shown from left to right. The black line drawings are the images from before deformation. Young's modulus is 1Mpa, and Poisson's ratio is 0.49 for linear material. The corresponding material properties are $c_1 + c_2 = 1.67853 \times 10^5$; $c_2 : c_1 = 1 : 1$; $\kappa = 4.166667 \times 10^6$; and $\beta = 100$ for the PSH model.

COMPARISON OF EACH MODEL: We also evaluated the behavior of deformation of each model using the same artery data as mentioned previously. The models are the *stabilized nearly-incompressible hyperelastic model* (abbreviated *PHS*), *geometrically non linear FEM* (*GNL*), *co-rotated FEM* (*COR*), and *linear FEM* (*LN*). It is difficult to adjust the material properties of the hyperelastic model with other models that use linear material properties. We therefore use a conversion to create a similar condition between linear material properties to Mooney-Rivlin

[1]LBB is a necessary and sufficient condition for linear elasticity.

Table 1: The differences of displacement for each model; Density is $\rho = 0.5 \times 10^3 \mathrm{kg/m}^3$.

Node number	$\lvert LN - PSH\rvert / L_{x,y,z} * 100$			$\lvert COR - PSH\rvert / L_{x,y,z} * 100$			$\lvert GNL - PSH\rvert / L_{x,yu,z} * 100$		
	x (%)	y (%)	z (%)	x (%)	y (%)	z (%)	x (%)	y (%)	z (%)
1	0.83	1.67	1.14	0.93	4.82	3.16	1.09	4.68	4.50
100	3.71	19.3	4.05	1.92	0.95	1.15	1.77	0.95	2.27
200	22.7	56.5	7.02	4.73	7.09	0.00	4.27	7.34	0.91
300	14.6	65.6	2.05	0.82	5.89	0.03	0.31	6.62	0.66
400	33.8	96.1	4.84	7.62	5.10	1.21	5.45	4.33	1.14
Average difference(axis)	18.3	43.3	4.41	4.64	4.47	0.88	4.09	4.59	1.43
Average difference	22.0%			3.33%			3.36%		
Maximum difference	96.2%			13.6%			13.4%		

$\beta = 100$ for PSH. PSH is abbreviation of the pressure stabilized nearly-incompressible hyperelastic model.

paremeters; Poisson's ratio and Young's modulus to c_1,c_2 and κ of the Mooney-Rivlin parameters.

The resultant deformations are presented in Fig. 2. Nodal displacement comparisons between the *pressure stabilized nearly-incompressible hyperelastic model* and other models are given in Table 1. The differences are normalized using $L_x, L_y, and L_z$, which are the dimension of the bounding volume of the model before deformation depicted in Fig. 2(a). The average displacement difference is 3.4% and the maximum is 13.4% in the *geometrically nonlinear FEM* case; the average displacement difference is 3.3% and the maximum is 13.6% in the *co-rotated FEM* case; and the average displacement difference is 22% and the maximum is 96% in the *linear FEM* case. For navigation, both *GNL* and *COR* models have more than 13% maximum difference, so neither could be applied for that purpose.

The processing time of *PHS* with personal computer(Intel core i7, 12 cores with 3.2 GHz) is 360ms: 31ms for stiffness matrix generation and 329ms for solving simultaneous equations by conjugate gradient method.

5 CONCLUSION

We report the implementation of the *pressure stabilized nearly-incompressible hyperelastic model*. In addition, we evaluated several deformation models, including the *linear FEM*,the *co-rotated FEM*, the *nonlinear FEM*, and the *pressure stabilized nearly-incompressible hyperelastic model*, for medical application. The experiment identified the relative differences between the models. Unfortunately, mechanical data from surgery is not available, so we cannot complete an absolute evaluation of each model. As future work, we would like to validate the hyperelastic model with real surgery.

REFERENCES

[1] T.Y.P Changl , F. Saleeb and G. Li, Large strain analysis of rubber-like materials based on a perturbed Lagrangian variational principle, Computational Mechanics Vol.8,No.8, pp.221-233, 1991

[2] F. Brezzi, On Existence, uniqueness and approximation of saddle-point problems arising from Lagrangian Multipliers,

[3] M. Bercovier, O. Pironneau, Error estimates for finite element method solution of the Stokes problem in the primitive variables, Num. Math., Vol.33, pp.211-224,1979

[4] O. Klaas, A. Maniatty and M.S. Shephard, A Stabilized Mixed Finite Element Method for Finite Elasticity. Formulation for Linear Displacement and Pressure interpolation, Computer Methods in Applied Mechanics and Engineering, 180, pp.65-79,1999

[5] T. Yamada, R. Miyajima. On Pressure Stabilised Linear Tetrahedron Element for Large Deformation Problems for Incompressible Hyperelasticity. JSCES Proceedings, Vol 17, 2012

BE3rd International Conference on Computational and Mathematical Biomedical Engineering – CMBE2013

16-18 December 2013, Hong-Kong

P. Nithiarasu and R. Löhner (eds)

Computational model for the focused ultrasound ablation of liver tumor in a patient specific geometry

Maxim A. Solovchuk*, Tony W. H. Sheu* and Marc Thiriet**

* Center of Advanced Study in Theoretical Sciences (CASTS), National Taiwan University, No. 1, Sec. 4, Roosevelt Road, Taipei, Taiwan 10617, Republic of China, solovchuk@gmail.com, twhsheu@ntu.edu.tw

** LJLL, University of Paris N 6, Paris, France

SUMMARY

The present study is aimed at predicting liver tumor temperature during a high-intensity focused ultrasound (HIFU) thermal ablation in a patient-specific liver geometry. The model comprises the nonlinear Westervelt equation and bioheat equations in liver and blood vessels. The nonlinear hemodynamic equations are employed with the convected cooling and acoustic streaming effects being taken into account. We found from this three-dimensional three-field coupling study that in large blood vessel both convective cooling and acoustic streaming may change the temperature considerably near blood vessel. More precisely, acoustic streaming velocity magnitude can be several times larger than the blood vessel velocity. The results presented in the current work can be further used to construct a surgical planning platform.

Key Words: *HIFU, liver tumor, blood flow, image-based model.*

1. INTRODUCTION

High intensity focused ultrasound (HIFU) is a therapeutic method for non-invasively ablating benign and malignant tumors [1,2]. The main mechanism of tissue ablation is thermal coagulation. Temperature 56^0C for one second heating can cause irreversible tissue damage [3]. Liver cancer is the second leading cause of death in Asia and is now known as one of the leading causes of death in the world [4].

One primary problem in the thermal ablation therapy of liver tumor is due to a heat sink resulting from the blood flow in large blood vessels. Blood flow cooling reduces the necrosed volume and liver can regenerate. Therefore more energy is necessary for the ablation of tumor close to blood vessel. This can lead to the use of redundant ultrasound power and undesirable damage of healthy tissues. Special care should be taken to avoid destruction of vessel walls by a high temperature. In most of the previous computational studies, liver is considered as a homogeneous tissue, and the

amount of dissipated heat is usually estimated by averaging the effect of blood perfusion over all tissues [5]. Recently, three-dimensional acoustic-thermal-hydrodynamic coupling model has been proposed [6,7]. The model is based on the nonlinear Westervelt equation, bioheat equations for the perfused tissue and blood flow domains. The nonlinear Navier-Stokes equations are employed to describe the flow in large blood vessels. The effect of acoustic streaming is also taken into account in the present HIFU simulation study.

In the present work temperature elevation in liver tumor is considered in a patient specific geometry. The results presented in the current work can be further used to construct a surgical planning platform.

2. RESULTS

The single element HIFU transducer used in this study is spherically focused with an aperture of 12 cm and a focal length of 12 cm, frequency 1 MHz. The solid tumor was assumed to be exposed to a 1.7 s ultrasound. The peak positive and negative pressures are $P_+=7.7$ MPa and $P_-=5.3$ MPa correspondingly. The three-dimensional problem is analyzed using finite-volume method. A detailed description of the solution procedures can be found in our previous articles [6-8]. The present numerical experiments are carried out in a patient specific liver model. A reconstructed surface mesh for the hepatic vein, portal vein and liver is presented in Fig. 1(a). The reconstructed mesh for the liver, solid tumor, hepatic and portal veins is presented in Fig. 1(b).

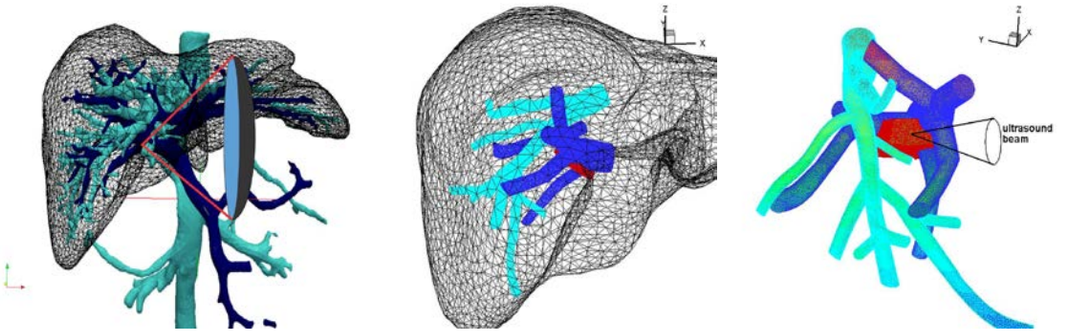

(a) (b) (c)

FIGURE 1: Geometry of the problem. (a) Patient-specific liver geometry reconstructed from MRI image, including hepatic vein (light blue), portal vein (dark blue). (b) Mesh of the liver with a tumor (red), hepatic (light blue) and portal (dark blue) veins. (c) Schematic of the portal vein (dark blue), hepatic vein (light blue), ultrasound beam and tumor (red).

Acoustic streaming is considered as a second order physical effect in the HIFU therapy and it is usually neglected. To investigate the importance of acoustic streaming effect during a thermal therapy, we have plotted in Fig. 2 velocity profiles at different cutting planes in portal venous network with and without acoustic streaming effect. Maximum velocity magnitudes in the portal vein for the cases considered with and without acoustic streaming are 0.26 and 0.09 m/s, respectively. Acoustic streaming increases the velocity magnitude by three times. This will increase the blood flow cooling and decrease the temperature rise [8]. The simulated temperature

contours in tumor and in the portal vein at the cutting plane *z=0.16* are presented in Fig. 3(a) at time *t=1.7* s (end of sonication). Calculation shows that tumor close to blood vessel can be ablated. There is a very sharp temperature gradient near the blood vessel wall. We can see strong asymmetry in the lesion shape due to blood flow cooling. The temperature inside the blood vessel remains almost unchanged except in the boundary layer close to the focal point. Therefore focused ultrasound can be a safe therapy to ablate tumors close to blood vessel wall. However, additional experimental study in vitro and in vivo is necessary. Simulation results can help to optimize an appropriate sonication time, ultrasound power and focal point location.

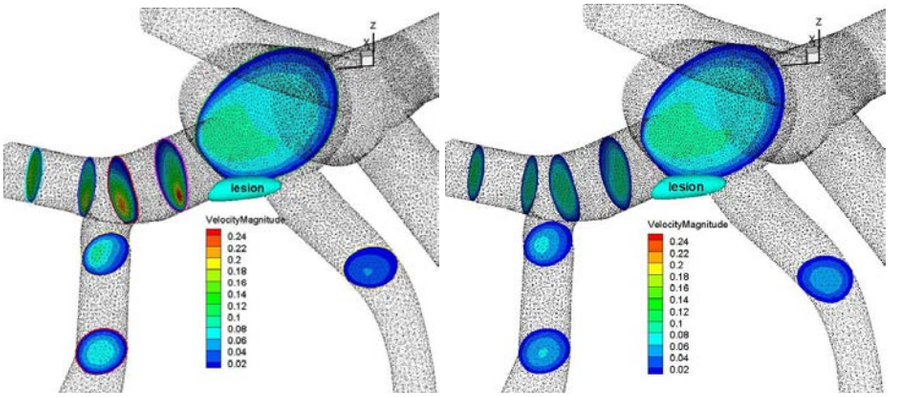

FIGURE 2: Velocity profiles at different cutting planes in portal venous network when acoustic streaming effect is either computed (a) or not (b). Lesion is drawn with light blue. Maximum velocities are 0.26 in (a) and 0.09 m/s in (b).

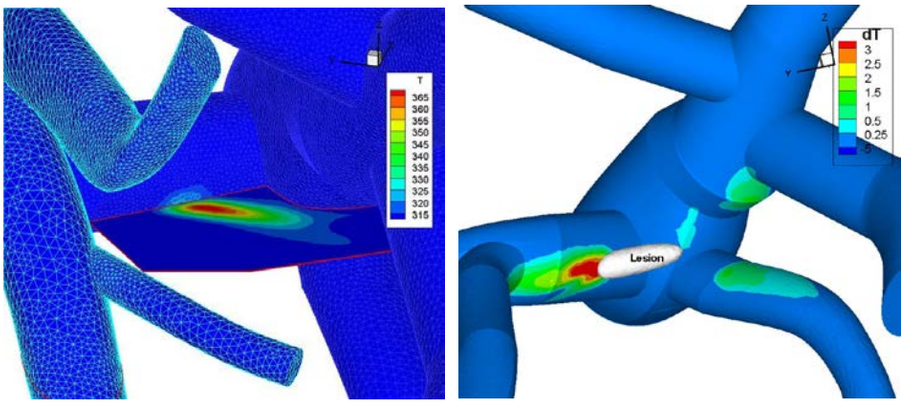

FIGURE 3: (a) Temperature contours in tumor at the selected cutting plane *z=0.16* m, sonication time 1.7 s. (b) Temperature difference on the portal vein wall with and without acoustic streaming, *t=1.7* s. Lesion is drawn with white. The maximum wall temperature difference is 5 K.

Temperature difference on the portal vein wall with and without acoustic streaming is presented in Fig. 3(b). The maximum wall temperature difference is 5 K. This shows the importance of the acoustic streaming effect. The current work is a first step towards the development of HIFU treatment planning platform. This platform can be used to optimize treatment time and applied ultrasound power in order to minimize damage of healthy tissues and to destroy all cancer cells.

3. CONCLUSIONS

The proposed three dimensional physical models for HIFU study was conducted in an image-based liver geometry. During the treatment planning, effect of blood flow cooling is not taken into account usually. In the present work we showed that both blood flow cooling and acoustic streaming effects can significantly affect the treatment and both of them should be taken into account. At high intensities the effect of cooling by acoustic streaming can prevail over convective cooling in large blood vessel. It was shown that tumors closed to the blood vessel wall can be ablated without damaging blood vessel wall. These results can be further used to construct a surgical planning platform for the non-invasive HIFU tumor ablating therapy in real liver geometry from MRI image and can lead in the future to a substantial improvement of the focused ultrasound ablation of liver tumor. The presented model can be used to develop similar planning tools for other organs.

ACKNOWLEDGEMENTS

The authors would like to acknowledge the financial support from the Center of Advanced Study in Theoretical Sciences (CASTS). A patient-specific liver geometry in Fig. 1(a) was provided by IRCAD (France)

REFERENCES

[1] Y. F. Zhou, High intensity focused ultrasound in clinical tumor ablation, *World J. Clin. Oncol.*, 2, 8-27, 2011.

[2] T. A. Leslie and J. E. Kennedy, High intensity focused ultrasound in the treatment of abdominal and gynaecological diseases, *Int. J. Hyperthermia*, 23, 173-182, 2007.

[3] M. A. Solovchuk , T. W. H. Sheu, M. Thiriet, and W. L. Lin, On a computational study for investigating acoustic streaming and heating during focused ultrasound ablation of liver tumor, *J. of Applied Thermal Engineering*, 56(1-2), 62-76, 2013.

[4] J. S. Huang, D. A. Gervais, and P. R. Mueller, Radiofrequency ablation: Review of mechanism, indications, technique, and results, *Chinese J. Radiology*, 26, 119-134, 2001.

[5] H. H. Pennes, Analysis of tissue and arterial blood temperature in the resting human forearm, *J. Appl. Physiol.*, 1, 93-122, 1948.

[6] T. W. H. Sheu, M. A. Solovchuk, A. W. J. Chen, and M. Thiriet, On an acoustics-thermal-fluid coupling model for the prediction of temperature elevation in liver tumor, *Int. J. Heat and Mass Transfer*, 54(17-18), 4117-4126, 2011.

[7] M. A. Solovchuk, T. W. H. Sheu, M. Thiriet, Simulation of nonlinear Westervelt equation for the investigation of acoustic streaming and nonlinear propagation effects, *J. Acoust. Soc. Am.*, 134(5), 2013.

[8] M. A. Solovchuk, T. W. H. Sheu, W. L. Lin, I. Kuo, and M. Thiriet, Simulation study on acoustic streaming and convective cooling in blood vessels during a high-intensity focused ultrasound thermal ablation, *Int. J. Heat and Mass Transfer*, 55(4), 1261-1270, 2012.

3rd International Conference on Computational and Mathematical Biomedical Engineering – CMBE2013
16-18 December 2013, Hong-Kong
P. Nithiarasu and R. Löhner (eds)

Cardiovascular variability and intra-surgical monitoring of autonomic control

Federico Aletti*, Guadalupe Dorantes Mendez*, Nicola Toschi, Filadelfo Coniglione**, Antonio Canichella**, Maria Guerrisi**, Giuseppe Baselli*, Sergio Cerutti*, Mario Dauri**, Manuela Ferrario***

*Dipartimento di Elettronica, Informazione e Bioingegneria, Politecnico di Milano, Piazza Leonardo da Vinci, 32, 20133, Milan, Italy.
E-mail addresses: federico.aletti@polimi.it, lupita.dorantes@gmail.com, giuseppe.baselli@polimi.it, sergio.cerutti@polimi.it, manuela.ferrario@polimi.it
** University of Rome Tor Vergata, Via Montpellier 1, 00133, Rome, Italy.
E-mail addresses: toschi@med.uniroma2.it, filadelfo.coniglione@uniroma2.it, canichella@med.uniroma2.it, guerrisi@med.uniroma2.it, mario.dauri@uniroma2.it

SUMMARY

The analysis of blood pressure waveforms is instrumental in order to garner insight into the performance of the heart, but also into the status of autonomic control of circulation via the investigation of cardiovascular variability and baroreflex function. Combining this information may lead to drastic improvements in the treatment of adverse events during surgery, i.e. in the prevention of intra-operative hypotension, and in the prediction of the effectiveness of fluid therapy. In this paper, we review results that we have obtained in the last few years, by developing new models of cardiovascular variability or refining existing ones, and applying them to high fidelity blood pressure data collected in patients undergoing major surgery.
The baroreflex control of circulation was shown to be impaired by anesthesia and to be affected by mechanical ventilation. This conclusion needs to be further validated in order to take the autonomic status of a patient into consideration for a more efficient, goal directed, personalized delivery of fluid therapy during surgery.

Key Words: *heart rate variability, blood pressure variability, baroreflex, autonomic nervous system, hemodynamic stability, anesthesia*

1. INTRODUCTION

Monitoring of hemodynamic function during surgery requires the use of mathematical modeling techniques to interpret the information conveyed by cardiovascular (CV) measurements, which are routinely available in the operating room (OR). For instance, an intriguing problem for engineers is the development of robust models for the continuous estimation of cardiac output. Such mathematical tools can assist anesthesiologists or intensive and emergency care physicians in the delivery of therapy during crucial maneuvers such as fluid challenges to prevent or contrast hypotension and hypoperfusion.
Beyond the aforementioned development of algorithms to estimate cardiac output from continuous arterial blood pressure (ABP) waveforms collected by monitors in the OR, it is important to assess the status of autonomic control in critical patients, in order to understand the patho-physiological alterations of circulatory function during surgery, and to predict the possible responsiveness to anesthesiological maneuvers aimed at ensuring blood pressure maintenance.

To achieve an insight into autonomic control, one of the most powerful tools is the investigation of heart rate variability (HRV), or more in general cardiovascular variability (CVV) [1,2,3,4]. This can be achieved using both time domain and frequency domain methods applied to the analysis of beat-by-beat and time series of the variability of heart rate (HR) and ABP. Spectral analysis [1,2] has proven to be very effective in the determination of the main features of HR dynamics. System identification of control mechanisms by multivariate analysis of CV signals has aided in shedding light on the causal input-output relationship between CV variables [5-8], and it has contributed to explaining the functioning of the closed loop control of circulation, with a particular emphasis on the mechanism of the baroreflex control of heart rate, vascular resistance, venous volume, and ventricular contractility, through both the sympathetic and parasympathetic branches of the autonomic nervous system (ANS). In order to understand how the ANS responds to therapy, the impairment of baroreflex control of HR and ABP due to anesthesia and surgical maneuvers should be assessed and quantified. However, the little data available in the literature, that point towards an alteration of autonomic control [9-11], do not tackle the problem of determining the specific effects of anesthesia, which should be taken into account first and foremost, because the physiological responsiveness of a subject to volemic alterations and fluid therapy may be attenuated by anesthetization and sedation.
In the following, we will briefly review some of the methodological approaches that we have recently developed for the multivariate analysis of baroreflex control of circulation, and that we have applied to the quantification of baroreflex during surgery.

2. MATHEMATICAL METHODS

The mathematical approaches to the analysis of baroreflex control of circulation that we have applied in our recent papers [7,8,12] are based on the implementation of multivariate models for the prediction of a CV variable (i.e., either HR or systolic blood pressure (SBP), or diastolic blood pressure (DBP), or pulse pressure (PP)) from other CV and respiratory signals.
In our studies, we analyzed ABP recordings from a catheter placed in the aorta of patients undergoing major surgery. The standard pre-processing procedures entail the identification of the SBP and DBP in every cardiac cycle of the recording. Stationary, artifact free segments of data are selected in correspondence of a maneuver of interest for the purpose of the analysis, before and after a major event. For instance, the typical analysis takes into account the epochs before and following the induction of anesthesia, before and after the intubation or before and after the infusion of a bolus that can be classified as a fluid challenge. The length of the selected segments is of three minutes, at least, to allow a robust system identification of the input-output relations between CV variables and the ensuing spectral analysis. For each segment of data, SBP beat-by-beat series are constructed and resampled in the time domain by means of anti-aliasing filtering. The time distance between two consecutive DBP points is used as a metric of heart period (HP) duration, which is assumed to be representative of HR, and the HP time series is derived after resampling in the time domain. Electrocardiographic (ECG) recordings are acquired regularly during surgery, but the quality of the ECG is often limited due to the placement of the electrodes, or for example the use of electrical scalpels, which seriously affect the quality of the ECG signal, due to electrical disturbances.
The alterations of baroreflex control of HR due to anesthesia induction were not systematically studied until our recent study [12], in which a bivariate model of the closed-loop dynamic relationship between SBP and HP was investigated to understand how ANS and baroreflex are affected by anesthesia induction via a bolus of propofol, and by intubation. The gain of the baroreflex (α) was calculated with standard techniques [12] in the frequency domain as well. The focus was on the gain in the low frequency band (LF, $0.04 < f < 0.15$ Hz), since the high frequency band (HF, $0.15 < f < 0.4$ Hz) reflected the disturbance of mechanical ventilation. Our work compared a normotensive (NH) population of patients vs. a chronic hypertensive (CH)

population. ABP was continuously measured in the aorta (sampling frequency=100 Hz) and processed as explained avoce, to obtain time series (sampling frequency=1 Hz) of SBP and HP.

3. RESULTS

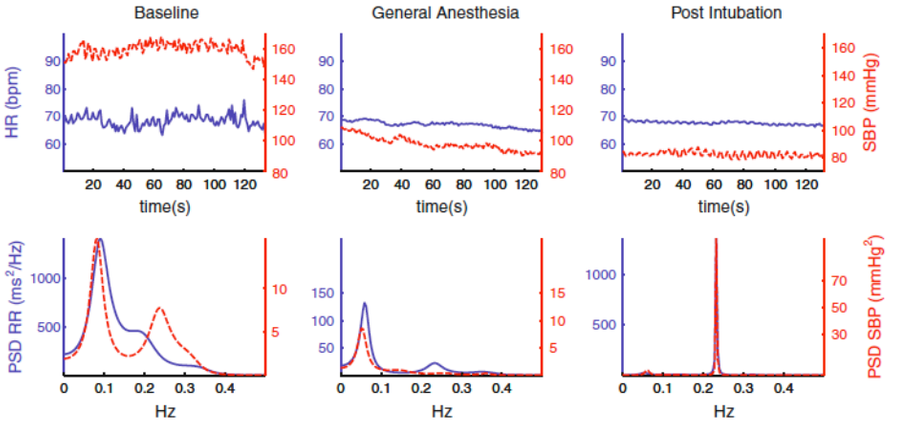

Figure 1 (from Dorantes Mendez et al. 2013 [12]): HR and SBP time series of a patient during baseline, general anesthesia, and post-intubation epochs and corresponding power spectra.

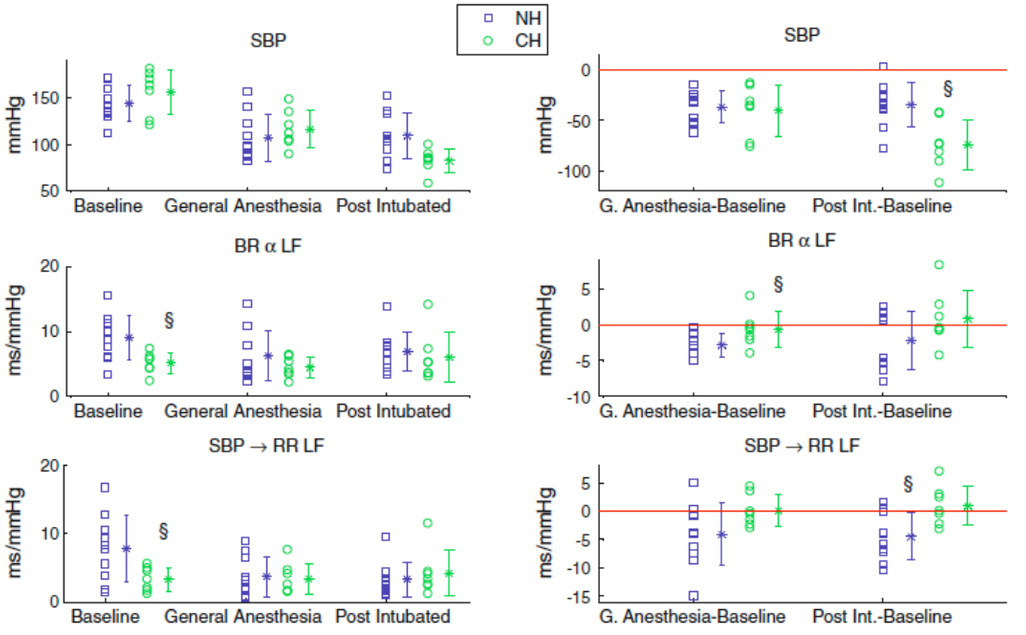

Figure 2 (from Dorantes Mendez et al. 2013 [12]): Left panels: values of SBP and BRS indices (estimated by spectral method, α , and bivariate model, SBP→RR) for each epoch and for each NH patient (squares) and CH patient (circles). Right panels: values of the differences between the indices estimated during general anesthesia induction and during the post intubation epoch with respect to the baseline epoch. The symbol § marks the significant differences between NH and CH (p-value=0.05).

Figure 1 [12] reports a typical example of the time series of HP (indicated as HR in the figure) and SBP, and of the corresponding spectra at baseline, during the preparation of the patient, following the induction the anesthesia via a bolus of propofol, and following intubation and onset of mechanical ventilation. Figure 2 [12] shows the evolution of the baroreflex gain across the same epochs of surgery.

4. CONCLUSIONS

Our studies of the baroreflex during surgery considered the effect of induction of anesthesia and of intubation. For the first time, this analysis was systematically done by a robust mathematical technique that compared different estimates of baroreflex sensitivity. Both the α gain method and the bivariate model showed that propofol anesthesia reduces the baroreflex gain in NH patients, while it has little effect on CH patients. However, these patients are known to be affected by a reduced baroreflex function because of hypertension. Thus, it may be deduced that the effect of anesthesia, similarly to the effect of hypertension, consists in the attenuation or even inhibition of baroreflex control of heart rate. This result needs to be verified in correspondence of major anesthesiological maneuvers, namely fluid infusions, in order to identify the autonomic status of the patient and incorporate this information in the different indices that anesthesiologists consider when determining the responsiveness to therapy. Our early findings are promising, and further work will be devoted to explore the feasibility of integrating hemodynamic monitoring with a continuous probing and tracking of autonomic control of circulation.

Acknowledgments

This work was supported by the ShockOmics project of the European Union (FP7-HEALTH-2013-INNOVATION1-Grant#602706)

REFERENCES

[1] S. Akselrod, D. Gordon, F.A. Ubel, D.C. Shannon, A.C. Berger and R.J. Cohen. Power spectrum analysis of heart rate fluctuation: a quantitative probe of beat-to-beat cardiovascular control, *Science,* 213(4504), 220-2, 1981.

[2] S. Akselrod S, D. Gordon, J.B. Madwed, N.C. Snidman, D.C. Shannon and R.J. Cohen. Hemodynamic regulation: investigation by spectral analysis, *Am. J. Physiol.* 249, H867-75, 1985.

[3] M. Pagani, F. Lombardi, S. Guzzetti, O. Rimoldi, R. Furlan, P. Pizzinelli, G. Sandrone, G. Malfatto, S. Dell'Orto, E. Piccaluga, M. Turiel, G. Baselli, S. Cerutti and A. Malliani. Power spectral analysis of heart rate and arterial pressure variabilities as a marker of sympatho-vagal interaction in man and conscious dog, *Circ. Res.,* 59, 78-93, 1986.

[4] Task Force of the European Society of Cardiology and the North American Society of Pacing and Electrophysiology. Heart rate variability. Standards of measurement, physiological interpretation, and clinical use, *Eur. Heart J.*,17, 354-81, 1996.

[5] R. Mukkamala R and R.J. Cohen. A forward model-based validation of cardiovascular system identification, *Am. J. Physiol. Heart Circ. Physiol.*, 281(6), H2714-30, 2001.

[6] R. Mukkamala R et al. Estimation of arterial ad cardiopulmonary total peripheral resistance baroreflex gain values: validation by chronic arterial baroreceptor denervation, *Am. J. Physiol. Heart Circ. Physiol*., 290(5), H1830-6, 2006.

[7] F. Aletti, T. Bassani, D. Lucini, M. Pagani and G. Baselli. Multivariate decomposition of arterial blood pressure variability for the assessment of arterial control of circulation, *IEEE Trans. Biomed. Eng.* 56(7), 1781-1790, 2009.

[8] F. Aletti, M. Ferrario, D. Xu, D.K. Greaves, J. K. Shoemaker, P. Arbeille, G. Baselli, R.L. Hughson. Short-term variability of blood pressure: effects of lower-body negative pressure and long-duration bed rest, *Am. J. Physiol. Regul. Integr. Comp. Physiol.* 303(1), R77-85, 2012.

[9] Z. Chen, et al. Dynamic assessment of baroreflex control of heart rate during induction of propofol anesthesia using a point process method, *Ann. Biomed. Eng.*, 39(1), 260–76, 2011.

[10] M. Sato, M. Tanaka, S. Umehara, T. Nishikaw. Baroreflex control of heart rate during and after propofol infusion in humans, Br. J. Anaesth., 94, 577–81, 2005.

[11] T. Bassani, V. Magagnin, et al. Testing the involvement of baroreflex during general anesthesia through Granger causality approach, Comput. Biol. Med., 42(3), 306–12, 2012.

[12] G. Dorantes Mendez, et al. Baroreflex sensitivity variations in response to propofol anesthesia: comparison between normotensive and hypertensive patients., J. Clin. Monit. Comput., 27(4), 417-26, 2013.

3rd International Conference on Computational and Mathematical Biomedical Engineering - CMBE2013
16-18 December 2013, Hong-Kong
P. Nithiarasu and R. Löhner (Eds.)

Computational study of CO_2 balance during laparoscopic procedures

Sergey S. Simakov*, Ospan A. Mynbaev*, and Timur M. Gamilov***
*Moscow Institute of Physics and Technology, 141700, Instituski Lane 9, Dolgoprudny, Russia,
simakov@crec.mipt.ru, ospanmynbaev@crec.mipt.ru, gamilov@crec.mipt.ru
**Moscow State University of Medicine & Dentistry, Kremenchugskaya, 3-4-198 121352,
Moscow, Russia

SUMMARY

Two mathematical approaches are proposed for carbon dioxide redistribution modellig due to abdominal CO_2 insufflation during CO_2-pneumoperitoneum. The main objective of this work is studying artificial ventilation parameters during laparoscopic procedure in order to decrease risk for specific patient.

Key Words: *blood flow, laparoscopic procedure, pneumoperitoneum, carbon dioxide balance.*

1 INTRODUCTION

Carbon dioxide (CO_2) is a highly diffusible gas easily soluble in water and blood. CO_2 is rapidly excreted through the lungs therefore it widely applied for medical needs. CO_2-pneumoperitoneum is the leverage to perform laparoscopic surgical manipulations. Potential side-effects of excessive $_2$ insufflated during laparoscopy are vanished in healthy individuals by means of pressure- or/and volume-controlled ventilation.

However, nowadays laparoscopic procedures are widely used by continuously providing new indication areas, involving different type of patients populations, including children, obese individuals and subjects with respiratory, cardiovascular and hematological diseases. Subsequently, CO_2-pneumoperitoneum side-effects could produce potentially harmful consequences particularly in these high risk patients as well as with application of the state of the art technologies in surgical fields, e.g. robotic or telesurgery, when high CO2-pneumoperitoneum pressure used to make properly view for remote surgeons.

A set of mathematical models is proposed for simulating CO_2 balance in organism during CO_2-pneumoperitoneum allowing optimization of artificial ventilation parameters (frequency and tidal volume) as a function from CO_2-pneumoperitoneum pressure and individual features of a particular patient.

2 Mathematical model of CO_2 balance during laparoscopic procedures

Proposed approach deals with excess CO_2 elimination control by optimizing respiratory parameters (respiratory rate and tidal volume) or assess maximum possible time of the CO_2-pneumoperitoneum procedure. This is especially important in the cases of lung diseased patients. It is

also allow CO_2 partial pressure assessment in vital organs (e.g. brain). The model also includes mechanical impact of high CO_2-pneumoperitoneum pressure resulting in partial occlusion of abdominal large vessels that may substantially affect the blood flow and consequently CO_2 transport and excretion.

We using two approaches both based on mass conservation principle. The first mathematical model is derived basing on the ideas of the compartment decomposition of cardiovascular system and mass balance between blood compartments, abdominal cavity and alveolar gases. We divided the whole system to the blood–tissue diffusion region in the abdominal cavity, arterial and venous blood compartments and alveolar gas exchange in the lungs controlled by the respiration rate or artificial ventilation rate. Mass balance is observed for this system resulting in a set of four ODE's. This model combines two approaches developed for tissue–blood CO_2 exchange [1] and CO_2 excretion by lungs [2]. Initially we have developed a rabbit model and validated it by a wide range of available experimental data [3]. After that a human model is established.

The second approach utilizes 1D network dynamical model of closed circulation. The core of the haemodynamic cardiovascular model is the 1D model of incompressible viscous fluid flow through the network of elastic tubes. It is based on the set of mass and momentum balance PDEs augmented with vessel wall elasticity introduced as pressure to cross section area relationship. The vessels are connected with each other at junction nodes and with the heart inlets/outlets through specific boundary conditions. Poiseuille's pressure drop condition, mass balance equation and compatibility condition for the hyperbolic system inside the tube form a system of nonlinear algebraic equations in each junction node. Details on this model can be found in [4,5]. Detailed CO_2 transport is calculated with this model during CO_2-pneumoperitoneum resulting in additional pressure partly occluding abdominal vessels. Important output of this approach is detailed CO_2 partial pressure redistribution especially in vital organs (e.g. brain and coronary circulation).

Both approaches are finally used for artificial ventilation optimization especially for the patients with pathologies (e.g. lung disease).

3 CONCLUSIONS

In accord with our concept, the key driving mechanism of CO_2 redistribution is the increased peritoneal tissue-to-venous and venous-to-arterial CO_2 tension differences resulting in high-pronounced venous CO2 partial pressure with gradually increased arterial CO2 partial pressure values could be the explanation for all systemic disturbances during laparoscopic surgery. Consequently, the intraperitoneal pressure is a determining mechanism of CO_2-pneumoperitoneum-induced local peritoneal and systemic changes during laparoscopic surgery, whereas other factors, such as gas temperature, impaired respiratory and cardiac functions play contributing role in pathophysiology of this phenomenon.

ACKNOWLEDGEMENTS

This work was partially supported by RFBR grants 11-01-00855, 11-01-00971 and Russian President Grant for Young Scientists MK 2719.2012.9.

REFERENCES

[1] G. Gutierrez, A Mathematical Model of Tissue-Blood Carbon Dioxide Exchange During Hypoxia, *American Journal of Respiratory and Critical Care Medicine Home*, 169, 525-533, 2004.

[2] J.H. Stuhmiller and L.M. Stuhmiller, A Mathematical Model of Ventilation Response to inhaled Carbon Monoxide, *Journal of Applied Physiology*, 98, 2033-2044, 2005.

[3] O. Mynbaev, C. Molinas, L. Adamyan, B. Vanacker, and P. Koninckx, Pathogenesis of CO_2 Pneumoperitoneum-Induced Metabolic Hypoxemia in a Rabbit Model, *The Journal of the American Association of Gynecologic Laparoscopists*, 9(3), 306-314, 2002.

[4] S. Simakov and A. Kholodov, Computational study of oxygen concentration in human blood under low frequency disturbances. *Mathematical Models and Computer Simulations*, 1(2), 283-295, 2009.

[5] Y. Vassilevski, S. Simakov, T. Dobroserdova, V. Salamatova, Numerical Issues of modelling Blood Flow in Networks of Vessels with Pathologies, *Russian Journal of Numerical Analysis and Mathematical Modelling*, 26(6), 605-622, 2011.

Multiphysics Modelling & Applications of the Cardiovascular System II

3rd International Conference on Computational and Mathematical Biomedical Engineering - CMBE2013
16-18 December 2013, Hong-Kong
P. Nithiarasu and R. Löhner (Eds.)

Parameter estimation for a 3D Navier-Stokes - 0D coupled system: application to patient-specic haemodynamics

B. Fabrèges*, S. Pant*, I. Vignon-Clementel* and J.-F. Gerbeau*
*INRIA Paris-Rocquencourt, Project-team REO, Building 16 BP 105, 78153 Le Chesnay Cedex FRANCE
B. Fabrèges: benoit.fabreges@inria.fr
S. Pant: sanjay.pant@inria.fr
I. Vignon-Clementel: irene.vignon-clementel@inria.fr
J.-F. Gerbeau: jean-frederic.gerbeau@inria.fr

SUMMARY

In this paper, we present a parameter estimation procedure for a 3D Navier-Stokes problem coupled with a 0D system. The idea is to get a reduced order (0D) model from the 3D model to do the parameter estimation. The estimation is performed on this reduced order model by using the *Unscented Kalman Filter* (UKF). Clinically measured data are taken into account during the parameter estimation and after a first 3D simulation with these parameters, a new iteration of the estimation procedure can be performed by updating the reduced order model according to the 3D results. This process can be repeated and leads to an iterative algorithm. Such a method is applied on a haemodynamics problem: the simulation of the blood flow in the aorta using Windkessel boundary conditions. The 3D results are shown to be in good agreement with the clinical data, showing that the parameters are well estimated.

Key Words: *Parameter estimation, Unscented Kalman Filter, Navier-Stokes, blood flow, Windkessel, Coarctation*

1 INTRODUCTION

The application of computational fluid dynamics (CFD) for analysis and prediction in patient-specific problems has gained considerable interest in the past decade. However, a major issue associated with patient-specific CFD simulations is the adaptation of individual boundary condition parameters for each patient. A common paradigm to estimate such parameters is such that the 3D simulations closely match some set of clinically measured data in the patient. Typical strategies to achieve this include manual tuning and automatic iterative approaches. Manual tuning often requires considerable 0D experience [1] and can become unmanageable if the number of parameters to be estimated is high. Automatic iterative approaches include quasi-Newton methods [2], fixed point algorithms [7], adjoint-based methods [8], and sequential approaches [6].

In this study an iterative sequential parameter estimation procedure is presented. A coupled 3D-0D model is used for haemodynamic analyses and prediction, where certain boundaries of the 3D domain are represented by 0D Windkessels. Hence, a relationship between the flow and the pressure is prescribed at such boundaries. While full 3D-0D models are essential for a detailed analysis of the flow, reduced order models, owing to their computational inexpensiveness, are

employed for parameter estimation. In such reduced order models the 3D domain is abstracted into lower order models (0D or 1D), whose parameters are updated using the results of the full 3D-0D simulations. Such an approach results in relatively fast estimation of parameters, has all the advantages of a sequential estimation approach, and is enhanced from the results of full 3D-0D simulations to improve the reduced order models. In this study, such an estimation procedure is presented and its efficacy is shown on a real-world haemodynamics problem.

2 PARAMETER ESTIMATION PROCEDURE

A 3D simulation of flow in any part of the circulation will typically involve termination of the 3D geometry at certain planes. At such termination points, realistic boundary conditions must be enforced to represent rest of the circulation. Usually, such boundary conditions are represented by Windkessel models or other impedance relationships between the flow and the pressure. A major issue, however, in such boundary conditions is the choice of Windkessel or impedance parameter values. Here, a methodology to estimated these parameter values based on the available clinical measurements/beliefs is proposed.

The estimation of parameters is performed in a representative model, preferably reduced order (for example a lumped parameter, 0D model, or a 1D model), as they are computationally less expensive compared to the full 3D models. For example, under the 3D-0D coupling paradigm proposed here, the 3D part of the flow domain can be represented by a 0D model, and the resulting fully 0D model can be used for parameter estimation. The abstraction of the 3D domain into a 0D model typically involves representing each 3D segment (for eg. an artery) by a combination of electrical analogues such as resistors, inductors, and capacitors. These electrical analogues respectively account for viscous effects, inertial effects, and arterial distensibility.

In order to estimate the parameters in a reduced order model, the use of Unscented Kalman Filter (UKF) [3–6] is proposed. To the UKF, everything that is known, with their respective uncertainties, is prescribed as observations. This includes all the clinically-measured data at various locations and even prior beliefs about flow-splits, flow/pressure waveforms, and mean/min./max. flow/pressure values. Hence, the UKF estimates the parameters such that the all the available information about the solution, with their respective uncertainties, is taken into account. With the estimated parameters a full 3D-0D model can be run and based on the results one can update the 3D abstraction parameters in the reduced order model, for example by using regression analysis. With the revised reduced order model, the parameters can be re-estimated using UKF, and this process can be repeated until convergence or until the computational budget is reached.

3 APPLICATION TO HAEMODYNAMICS

The parameter estimation procedure described above is applied to a patient-specific problem in haemodynamics (c.f. Figure 1). This problem involves prediction of pressure drop across an aortic coarctation. The provided clinical measurements are: the flow and pressure at the inlet, the mean flow rates in the supra-aortic arteries, and the flow rate in the descending aorta. These data were provided in the MICCAI challenge 2013.

For the 3D-0D coupled model, the blood velocity and pressure are modelled by the 3D Navier-Stokes equations and the boundary conditions at the supra-aortic arteries are represented by three-element RCR Windkessels. Moreover, the fluid structure interaction has been taken into account, in a lumped manner, to be able to match the available clinical data. To this effect, a capacitance at the inlet of the aorta, which accounts for aortic distensibility, is added to redistribute the flow.

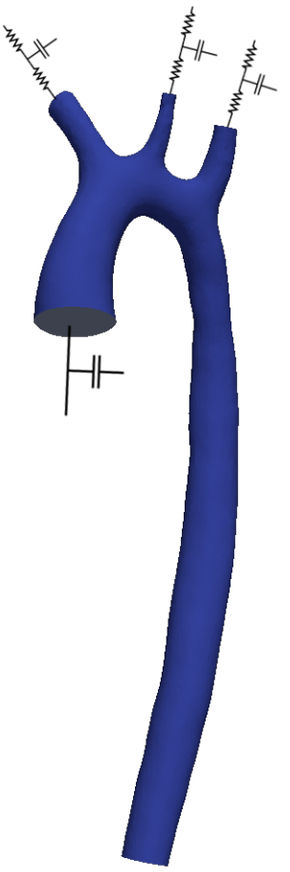

Figure 1: Aorta and the windkessel boundary conditions

With the added capacitance, a fixed mesh is used and only the Navier-Stokes equations are solved, i.e. no special treatment on the 'moving' boundary is needed. The boundary condition at the inlet is thus a two element RC windkessel (with R = 0) and at the descending aorta the measured flow profile is prescribed (see Figure 1). Hence, in this 3D-0D model, there are 10 parameters to be estimated (nine for the three supra-arotic Windkessels, and one for the inlet capacitance). The aforementioned UKF estimation approach estimates these parameters such that the clinical data provided is closely matched. The full 3D-0D model is then run to predict the pressure drop across the coarctation, the clinical quantity of interest.

4 CONCLUSIONS

A generic methodology to perform 3D-0D simulations in haemodynamics is presented where the 0D parameters are estimated to match the measured clinical data using UKF. In the example application presented, the proposed method results in estimation of 0D parameters such that the maximum errors between the clinically measured data and 3D-0D simulations is less than 3% for the flow-rates and less than 6% for the pressures. Hence, it is believed that the parameters are well estimated, and that the proposed method is promising.

REFERENCES

[1] G. Pennati, C. Corsini, D. Cosentino, T.-Y. Hsia, V. Luisi, G. Dubini, and F. Migliavacca, Boundary conditions of patient-specific fluid dynamics modelling of cavopulmonary connections: possible adaptation of pulmonary resistances results in a critical issue for a virtual surgical planning, J. R. Soc. Interface, 1:3, 297-307, 2011.

[2] R.L. Spilker and C.A. Taylor, Tuning multidomain hemodynamic simulations to match physiological measurements, Ann Biomed Eng., 38:8, 2635-2648, 2010.

[3] S. Julier, J. Uhlmann and H.F. Durrant-Whyte, A new approach for filtering nonlinear systems, *in* American Control Conference, 1628-1632, 1995.

[4] D.T. Pham, J. Verron and M.C. Roubeaud, A singular evolutive extended Kalman filter for data assimilation in oceanography, J. Marine Syst., 16:3-4, 323-340, 1998.

[5] P. Moireau and D. Chapelle, Reduced-order Unscented Kalman Filtering with application to parameter identification in large-dimensional systems, ESAIM Contr. Optim. Ca., 17, 380-405, 2011.

[6] C. Bertoglio, P. Moireau and J.-F. Gerbeau, Sequential parameter estimation for fluid–structure problems: Application to hemodynamics, Int. J. Num. Methods in Biomed. Engrg., 28:4, 434-455, 2012.

[7] G. Troianowski, C. A. Taylor, J. Feinstein and I. E. Vignon-Clementel, Three-dimensional simulations in glenn patients: clinically based boundary conditions, hemodynamic results and sensitivity to input data, J. of Biomech. Engrg., 133:11, 111006, 2011.

[8] M. Ismail, W.A. Wall and M.G. Gee, Adoint-Based Inverse Analysis of Windkessel Parameters for Patient-Specific Vascular Models, J. of Comp. Physics, 244, 113-130, 2013.

3rd International Conference on Computational and Mathematical Biomedical Engineering – CMBE2013
16-18 December 2013, Hong-Kong
P. Nithiarasu and R. Löhner (eds)

Complex flow in branching geometries: a modular multiscale coupling that handles backflow

Irene E. Vignon-Clementel*, Mahdi Esmaily Moghadam, Richard Figliola***, Alison L. Marsden****

*INRIA & Université P. et M. Curie 6, France, irene.vignon-clementel@inria.fr
**Mechanical and Aerospace Engineering, University of California San Diego, San Diego, USA, mesmaily@ucsd.edu amarsden@ucsd.edu
***Mechanical Engineering, Clemson University, Clemson, USA, fgliola@clemson.edu

SUMMARY

Flow is simulated in branched geometrical models in a number of engineering applications, including the modeling of blood and air in their larger conduits. In these applications, 3D Navier-Stokes simulations can only be realistically carried in a few branches, while the rest of the circulation represented by reduced models must be taken into account through appropriate coupling conditions. For practical reasons, it is desirable to couple the 3D models and these reduced models in a modular framework. However, such couplings can be numerically challenging. We therefore propose an implicit in time coupling algorithm. A quasi-Newton approach is devised such that the contribution of the reduced model to the 3D domain is taken into account in the tangent matrix of the nonlinear Navier-Stokes solver, without adding a new iteration loop. Different contributions to the tangent matrix are tested. Dirichlet and Neumann couplings are compared. The presence of backflow usually leads to instabilities that are here handled by a boundary stabilization term. These solution methods are tested on typical flow geometries and on realistic cardiovascular and airflow application cases.

Key Words: *Navier-Stokes equations, boundary conditions, finite elements, blood and airflow applications, implicit coupling, stabilization*

1 INTRODUCTION

Flow is simulated in branched geometrical models in a number of engineering applications, including the modeling of blood and air in their larger conduits. In these applications, 3D Navier-Stokes simulations can only be realistically carried in a few branches, while the rest of the circulation must be taken into account through appropriate boundary conditions. 0D electric analog or 1D wave propagation models provide a way to model the rest of the circulation at reduced costs. Such models are matter of research by themselves. It is thus desirable to couple the 3D models and these reduced models in a modular framework.

2 MAIN BODY

Such couplings can however be numerically challenging, especially under physiologically relevant conditions. We therefore proposed in [1] an implicit in time coupling algorithm (Figure

1). Depending on the reduced model, the coupling variables may vary. If flow information is received from the reduced model, it is applied to the 3D model as a Dirichlet boundary condition, and sends back pressure at this outlet to the reduced model at each nonlinear iteration of the Navier-Stokes quasi-Newton solver. If pressure information is received from the reduced model, it is applied to the 3D model as a "Neumann" boundary condition, and sends back flow at this outlet to the reduced model. In fact in this case, a quasi-Newton approach is devised such that the contribution of the reduced model to the 3D domain is taken into account in the tangent matrix of the nonlinear Navier-Stokes solver. This contribution is computed by finite differences. Hence, the framework is more modular than in monolithic approaches (e.g. [2]) that require precise knowledge of the relationship between pressure and flow from the reduced model, and invasive changes in the 3D solver when the reduced model is changed, both of which are difficult for end-users with complex reduced models that are becoming more and more common practice for cardiovascular and pulmonary applications. On the other hand, this iterative approach is a priori more robust than explicit or implicit staggered schemes.
For the Neumann-type coupling, the velocity profile is in general not enforced. Flow at these coupling boundaries is often complex, as a result of the interplay between geometry and flow conditions elsewhere in the 3D domain. Due to this or to physiological flow rate time oscillations, flow reversal can occur at the coupling boundaries that usually rapidly lead to numerical instabilities. Several remedies have been proposed and compared [3] in typical simple geometries as well as patient-specific blood flow simulations (with the monolithic approach in [2] for the boundary conditions). The stabilization approach proved to be the more robust one. This is thus the one that is retained here.

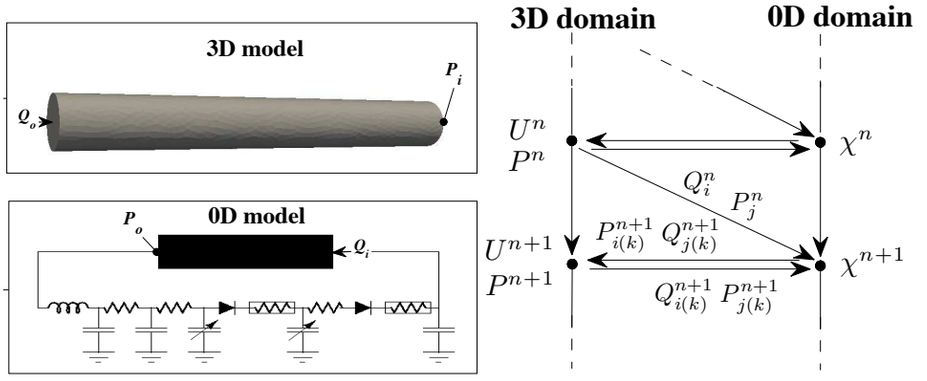

Figure 1: 3D-0D multiscale example. Left: 3D domain (1 inlet i with Neumann coupling, one outlet o with Dirichlet coupling), 0D model (closed loop). Right: implicit coupling algorithm at time step n+1, via Neumann (average normal traction related to the 0D pressure, *P*) or Dirichlet (velocity *U* imposed in the 3D domain, from the flux *Q* in the 0D domain) 3D domain boundary condition at iteration k. χ is the 0D state variable vector.

Results for this multiscale framework first include a comparison of various contributions to the tangent matrix of the reduced model in the 3D-closed loop 0D example shown in Figure 1 (left) but with Neumann couplings at both ends. A static contribution is found the best trade-off to obtain convergence with different meshes and time-steps. Results also show that the Dirichlet coupling case (at both ends) is more robust, but it necessitates the prescription of the velocity profile at the coupling boundaries. Finally, this iterative coupling strategy is successfully tested on realistic cardiovascular and airflow cases [4,5,6]. Such a coupling permits to study the interaction between changes in the 3D domain and the rest of the circulation.

3 CONCLUSIONS

In conclusion, this work provides some insights about issues related to complex flow in branched models of the circulation. Some important points and shortcomings when comparing codes will be presented in this setting [7]. We offer solutions to certain numerical challenges, such as a way to couple the rest of the circulation to the numerical model in a modular, yet robust way, even in the presence of backflow. These solution methods have been tested on typical flow geometries and on realistic cardiovascular and airflow application cases.

REFERENCES

[1] Esmaily-Moghadam M, Vignon-Clementel IE, Figliola R, Marsden AL for the Modeling Congenital Hearts A (2013) A modular numerical method for implicit 0D/3D coupling in cardiovascular finite element simulations. *Journal of Computational Physics* 244:63-79

[2] Vignon-Clementel IE, Figueroa CA, Jansen KE and Taylor CA (2006) Outflow boundary conditions for three-dimensional finite element modeling of blood flow and pressure in arteries. *Computer Methods in Applied Mechanics and Engineering* 195: 3776-3796

[3] Esmaily-Moghadam M, Bazilevs Y, Hsia T-Y, Vignon-Clementel IE, Marsden AL, and Modeling Congenital Hearts Alliance Investigator (2011) A comparison of outlet boundary treatments for prevention of backflow divergence with relevance to blood flow simulations. *Computational Mechanics* 48: 277-291

[4] Esmaily-Moghadam M, Migliavacca F, Vignon-Clementel IE, Hsia T.-Y., Marsden AL, For The Modeling Of Congenital Hearts Alliance Investigator (2012) Optimization of shunt placement for the Norwood surgery using multi-domain modeling. *Journal of Biomechanical Engineering* 134 (5):051002

[5] Oakes J, Marsden AL, Grandmont C, Shadden S, Darquenne C, Vignon-Clementel IE (submitted) Airflow and particle deposition in health and emphysema: from in-vivo to in-silico experiments.

[6] Pant S, Fabrèges B, Gerbeau JF, Vignon-Clementel IE, A multiscale filtering-based parameter estimation for patient-specific coarctation simulations in rest and exercise. *STACOM / MICCAI 2013 (accepted).*

[7] Arbia G, Corsini C, Esmaily-Moghadam M, Marsden AL, Migliavacca F, Pennati G, Hsia T-Y, Vignon-Clementel IE (In Press) Numerical blood flow simulation in surgical corrections: what do we need for an accurate analysis, *J. of Surgical Research*.

3rd International Conference on Computational and Mathematical Biomedical Engineering - CMBE2013
16-18 December 2013, Hong-Kong
P. Nithiarasu and R. Löhner (Eds.)

A combined feedforward and feedback system for simulating neural and local control of coronary resistance and compliance

Christopher J. Arthurs⋆, Kevin Lau⋆ and C. Alberto Figueroa⋆
⋆King's College London, Dept. of Biomedical Engineering, St Thomas' Hospital, London SE1 7EH, christopher.arthurs@kcl.ac.uk, kevin.lau@kcl.ac.uk, alberto.figueroa@kcl.ac.uk

SUMMARY

We present a model of the mechanisms which control coronary resistance and compliance, based upon lumped parameter networks. Metabolic feedback and neural feedforward mechanisms are included, and we investigate the purpose of the physiological small-arterial compliance control.

Key Words: *coronary blood flow, autoregulation, feedback, feedforward.*

1 INTRODUCTION AND BACKGROUND

Physiological coronary blood flow requirements vary greatly. Because the heart is able, depending on the demands of the body, to adjust its output in order to drive aortic flows ranging from approximately 6 l/min to 18 l/min, and because this increase takes place whilst pumping against an increased afterload pressure in the aorta, it must be possible to adjust the power output of the heart accordingly.

An increase in cardiac power output is naturally associated with an increase in myocardial oxygen demand (MVO2). Because the coronary venous oxygen tension is low even under resting conditions, it is difficult for additional oxygen requirements to be satisfied by increasing the proportion of oxygen extracted from the blood. Thus, in order to increase oxygen supply, the coronary blood flow must be increased. Such an increase is facilitated primarily by a reduction in the resistance to flow of the coronary vasculature.

Coronary blood flow control. The mechanisms controlling the flow of blood in the coronary arteries are incompletely understood. Autoregulatory systems control the coronary resistance using mechanisms which are entirely intrinsic to the organ, modulating resistance according to local properties. These mechanisms include the myogenic (blood vessel hoop-stress control), endothelial (control of the flow-induced vessel wall shear stress) and the metabolic (nutrient supply control). Extrinsic neural control of the coronary vascular resistance consists of a neural signal to reduce coronary resistance; this is sent in parallel with the neural commands which increase cardiac output in preparation for exercise [1].

Systems of interest. We focus on the metabolic autoregulatory and the extrinsic neural control systems, as these are important for maintaining the myocardial oxygen supply. The former can be characterised as a feedback system, which means that it must evaluate an error signal which acts as a proxy for discrepancy between MVO2 and the coronary oxygen supply. The extrinsic control can be considered to be feedforward; broadly, it acts to counter the *predicted* O_2 discrepancy which it expects to arise from a given neural command to adjust cardiac work.

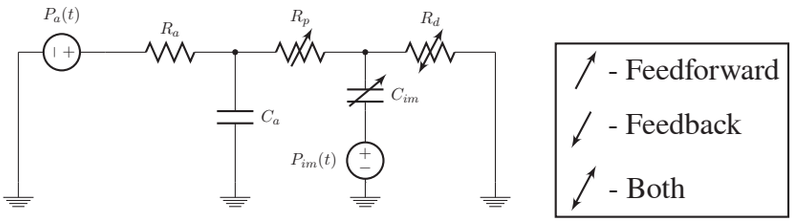

Figure 1: Coronary Windkessel model, used with feedback control of R_p and R_d, and feedforward control of R_p, R_d and C_{im}. P_a and P_{im} are the aortic and intramyocardial pressures, respectively.

The purpose of the present work is to develop a combined model of the metabolic and feedforward coronary flow control systems. We use a lumped-parameter network (LPN) approach, investigating performance during MVO2 changes due to exercise. Our final goal is to use the developed LPN models to create realistic boundary conditions at the coronary outlets of a 3D Navier-Stokes model of blood flow in the aorta and associated large arteries.

Pre-existing work and understanding. Previous work on this topic includes a mass-balance model of feedforward and feedback control [1]. This work demonstrated that feedforward improves the speed and accuracy of the flow response to changes in MVO2, and that a delay in the feedforward resistance control improved the stability of the response, but did not employ equivalent electric circuits, a heart model, a 3D domain, or compliance control. A LPN model, employed as a boundary condition for a 3D domain has been used to simulate the response to light exercise [2]; however, this model is not based upon a requirement to minimise some error signal and so does not represent true feedback control. To our knowledge, no such model has yet included the feedforward control of the microvascular compliance, which has been identified as being physiological and likely important; current understanding is that reducing the compliance reduces wasteful flow oscillations which fill and empty the compliance on each cardiac cycle [3].

2 MODELS AND EXPERIMENTS

Control equations. Consider the LPN circuits shown in Figs. 1 and 2. Write S_d, S_p for the reciprocals of the distal and proximal coronary resistances R_d and R_p respectively, and let $\bar{P}_a$ be the mean aortic pressure, k^d_{ff} and k^d_{fb} the feedforward and feedback gains for R_d, k^p_{ff} the feedforward gain for R_p, Q_a the flow from the aorta into the coronaries, γ the blood oxygen volume proportion, τ the error integration duration, and $MVO2$ the myocardial oxygen demand. We postulate that control of the resistances can be modelled by the differential equations

$$\bar{P}_a \frac{dS_d}{dt} = k^d_{fb}\left[\int_{t-\tau}^{t} MVO2(s) - \gamma Q_a(s)\, ds\right] / \tau + \gamma^{-1} k^d_{ff} \frac{dMVO2}{dt}, \quad (1)$$

$$\bar{P}_a \frac{dS_p}{dt} = \gamma^{-1} k^p_{ff} \frac{dMVO2}{dt}. \quad (2)$$

We investigate the impact of intramyocardial compliance control by adjusting C_{im} manually.

The case for compliance control. The case for controlling the coronary resistance in exercise is clear; the case for compliance control is less so. Since it is known that in the larger blood vessels [3], having diameters in the range 100-250 μm, experience a resistance-increasing sympathetic vasoconstriction during exercise that can be considered part of the feedforward system, we included this in our model. This component is of interest on its own, as it causes a small increase in resistance at precisely the time when an increase in coronary flow is required. While the overall resistance of

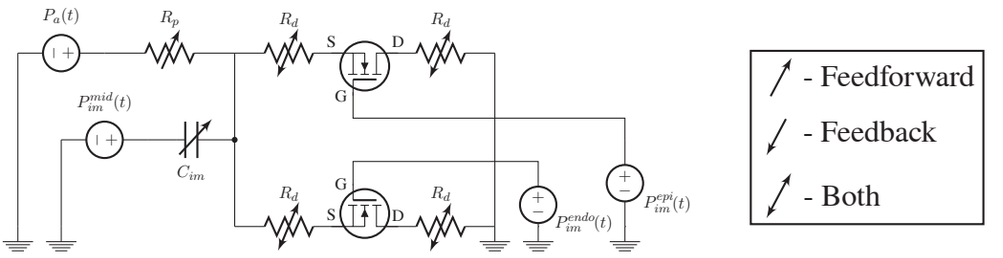

Figure 2: Coronary collapse field effect transistor (FET) model, used with feedback control of R_d, and feedforward control of R_p, R_d and C_{im}. P_{im}^{endo}, P_{im}^{mid} and P_{im}^{epi} are the intramyocardial pressures in the subendocardial, mid-myocardial and subepicardial layers, respectively. P_a is the aortic pressure.

the coronary tree still falls, the magnitude of the fall is attenuated by this vasoconstriction in the small arteries. This apparent paradox is interesting; it has been proposed that this vasoconstriction serves to decrease the compliance of the small arteries in order to reduce non-nutritive filling and emptying of the capacitance during the systole-diastole cycle, and that this preserves subendocardial flow during exercise [3]. The following experiments allow us to investigate this phenomenon further.

First experiment. We begin by testing our control system by coupling the circuit shown in Fig. 1 to a LPN heart model. By computing the pressure-volume area for the left ventricle (LV), we make an estimate of the amount of energy expended by the LV on each cycle; from this we compute the per-cycle LV MVO2. The feedback system (the integral term in Equation (1)) then adjusts the resistance in order to match MVO2 with the coronary oxygen supply. We then increase the demands on the heart by placing it in an exercise state and observe the behaviour of the coronary flow as it adjusts to meet the new demands. This experiment allows us to investigate the function and importance of the three coronary flow control components that we have included: metabolic feedback resistance, neural feedforward resistance, and neural feedforward compliance control.

Second experiment. Retaining the resistance control mechanisms of Equations (1) and (2), we investigate subendocardial flow during exercise using the coronary LPN model shown in Fig. 2. This model includes field effect transistors (FETs) which represent the vasculature in two different layers of the myocardium: the subendocardium and the subepicardium. Each layer is subject to different magnitudes of extravascular compression during systole; this is represented by using differing scalings of the LV pressure and myocardial elastance for the FET gate voltages, accurately affecting flow through them [4]. This model is intended to investigate the hypothesis that flow to the subendocardium is improved by the reduction in compliance associated with the feedforward control system.

Third experiment. We couple the model shown in Fig. 1 at the coronary outlets of a 3D model of the human aorta, and use this to simulate exercise. This requires us to estimate the proportion of the total required oxygen supply that each coronary outlet needs to provide, and with minimum resistance limits set for the coronary vasculature, allows us to observe potential local ischemia.

Results. In Experiment 1, we observe that the reduction in compliance may serve to control or dampen oscillations in coronary blood flow which, in our models, occur on the time-scale of the time-delay contained within the feedback system when the feedback gain is large. This is shown in Fig. 3. Because coronary flow should have the fastest possible response time to changes in MVO2, a large gain is desirable, but as is typical of feedback control systems, the gain cannot become too large without causing oscillations in the response. Thus, any mechanism which allows the use of a larger gain by damping oscillations would be beneficial for coronary flow control.

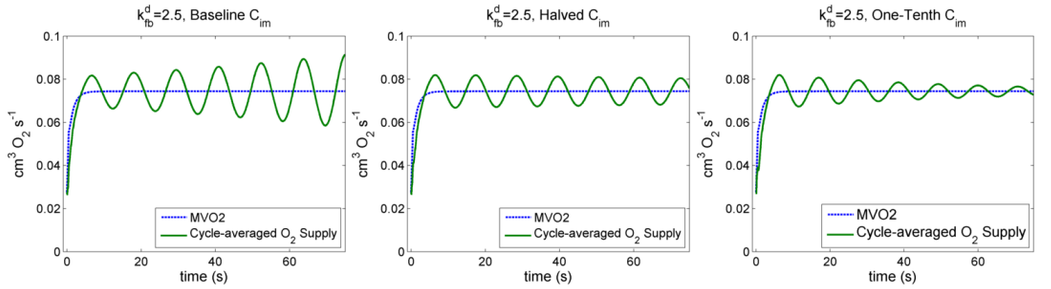

Figure 3: The effect of compliance on the feedback oscillations in myocardial oxygen supply (LPN of Fig. 1). Reducing the compliance damps the oscillations caused by the feedback.

In Experiment 2, we have observed the same oscillation-damping nature of the feedforward compliance control, and have seen that reducing the compliance also increases the flow to the subendocardium (i.e. through the endocardial FET). An improvement in subendocardial flow of around 10% was observed when the compliance was reduced to one-tenth of its baseline value, with smaller improvements associated with smaller reductions in compliance.

Results for Experiment 3 are in preparation.

3 CONCLUSIONS

We have presented a new model of the control of coronary blood flow in response to changing cardiac work. Combining feedforward and feedback control for a LPN model of the coronary vasculature, we have successfully simulated coronary flow in response to increased MVO2. We have produced evidence that the role of compliance reduction may be one of damping longer-term oscillations in order to allow a larger feedback gain and thus a faster response to changes in MVO2.

The results of simulations using a 3D domain and boundary conditions generated using our LPNs will allow us to assess the usefulness of our model for simulating myocardial ischemia during exercise, coronary steal, and synergies with other control systems such as the baroreflexes.

We gratefully acknowledge support from the European Research Council under the European Union's Seventh Framework Programme (FP/2007-2013) / ERC Grant Agreement n. 307532, and the United Kingdom Department of Health via the National Institute for Health Research (NIHR) comprehensive Biomedical Research Centre award to Guy's & St Thomas' NHS Foundation Trust in partnership with King's College London and King's College Hospital NHS Foundation Trust.

REFERENCES

[1] JK Miyashiro and EO Feigl. A model of combined feedforward and feedback control of coronary blood flow. *American Journal of Physiology-Heart and Circulatory Physiology*, 268(2):H895–H908, 1995.

[2] HJ Kim, KE Jansen, and CA Taylor. Incorporating autoregulatory mechanisms of the cardiovascular system in three-dimensional finite element models of arterial blood flow. *Annals of biomedical engineering*, 38(7):2314–2330, 2010.

[3] Eric O Feigl. Neural control of coronary blood flow. *Journal of vascular research*, 35(2):85–92, 1998.

[4] Tahseen Ejaz, Tadashi Takemae, Yukio Kosugi, Shinchi Okubo, and Minora Hongo. Simulation study of coronary circulation using electronic circuit model for the coronary vessel. In *Engineering in Medicine and Biology Society, 1997. Proceedings of the 19th Annual International Conference of the IEEE*, volume 1, pages 231–234. IEEE, 1997.

3rd International Conference on Computational and Mathematical Biomedical Engineering – CMBE2013
16-18 December 2013, Hong-Kong
P. Nithiarasu and R. Löhner (eds)

Numerical investigation of the effects of the cerebrovascular and neck circulations on multi-scale simulation

Marie Oshima*, Takashi Maeda, Fuyou Liang***, and Shu Takagi******
*Institute of Industrial Science, The University of Tokyo, 4-6-1 Komaba, Meguro-ku, Tokyo 153-8505, Japan, marie@iis.u-tokyo.ac.jp
** Tokyo Metro, Co. Ltd., 3-19-6 Uneno Taito-ku, Tokyo,110-8614, Japan
*** School of Naval Architecture, Ocean & Civil Engineering, Shanghai Jiao Tong University, 800 Dongchuan RD. Minhang District, Shanghai, China, fuyouliang@sjtu.edu.cn
**** Department of Mechanical Engineering, The University of Tokyo, 7-3-1, Hongo Bunkyo-ku, Tokyo, 113-8654, Japan, takagi@mech.t.u-tokyo.ac.jp

SUMMARY

A vascular disease such as arterial stenosis caused by atherosclerosis affects the flow and pressure distributions locally and also globally throughout the entire circulatory system. In the present study, the multi-scale simulation has been developed to examine the hemodynamics in the localized area taking account of the entire circulatory system. Since the present paper focuses on the atherosclerosis in the common carotid artery, the cerebrovascular and the neck circulations have an influence on the blood flow dynamics of the region of interest. The arterial network model of the cerebrovascular and neck circulations has been designed for the 1D simulation based on Liang's 1D (one dimensional) -0D (zero dimensional) simulation models and has been implemented on the multi-scale simulation program of 3D (three dimensional) simulation combined with 1D-0D simulation developed by the authors. In order to examine its effects on the flow rate on the bifurcation segment of the common carotid artery, the numerical results are compared between the cases without and with the present network model.

Key Words: *Multi-Scale Simulation, Circulatory System, Network Model of the Cerebrovascular and Neck circulations*

1 INTRODUCTION

Arterial stenosis is a serious cardiovascular disease and sometimes leads to cerebral ischemic or a stroke due to a large pressure drop and an abrupt decrease in the flow rate in the stenotic artery. It affects not only hemodynamics in a localized stenotic region but also it thorough the peripheral areas to the entire circulatory system. The objective of the paper is to develop a computational method to examine the hemodynamics locally as well as globally in the circulatory system. The authors has been developing a multi-scale method such that the 3D simulation developed by the authors [1] is combined with the 1D-0D simulation F. Y. Liang, *et al* [2, 3].

The region of the interest in this paper is a segment of the common carotid artery (CCA) bifurcating into the internal carotid artery (ICA) and the external carotid artery (ECA) like one of

preferential locations of atherosclerosis. In the previous study [4], the distributions and the wave forms of flow rates in ICA and ECA showed some differences from physiological conditions. It is known that the cerebrovascular and neck circulations have a big influence on the hemodynamics in CCA region. Thus, the network model of the cerebrovascular and neck circulations is developed and is implemented on the 1D simulation model. The simulation is conducted to the simulation of CCA segment and the results are compared to investigate the effects of the cerebrovascular and neck circulations on the region of the interest.

2 NUMERICAL METHOD

In this study, the boundary conditions of the 3D flow simulation are given by the 1D-0D simulation of the circulatory system as described schematically in Figure 1. The simulation method of each domain is described in the following sessions.

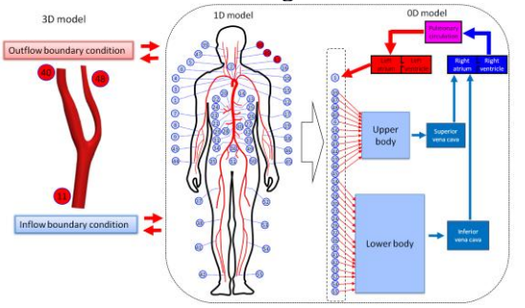

Figure 1. Schematic illustration of 3D-1D-0D multi-scale simulation

2.1 The 3D simulation method

The 3D simulation is conducted to a patient-specific model, which is constructed from the medical images. In the 3D simulation, blood vessel assumed to be rigid. Since blood is incompressible Newtonian fluid, the governing equations consist of the continuity and Navier-stokes equations as follows:

$$\nabla \cdot u = 0 \tag{1}$$

$$\frac{\partial u}{\partial t} + (u \cdot \nabla)u = -\frac{P}{\rho} + \frac{\mu}{\rho}\nabla^2 u \tag{2}$$

where u and P are the velocity and the pressure and ρ and μ are the density and the viscosity coefficient, respectively.

The governing equations are discretized using the finite volume method with the 2nd order central difference scheme(CDS). The advection term is descretized using the mixing scheme such as 95 % of CDS and 5% of the first upwind difference scheme(UDS). The velocity and pressure are solved by the SMAC method with the Euler Implicit method.

2.1 The 1D simulation method

The 1D simulation is applied to a total of 83 arteries which consists of 55 arteries based on Liang model [2] and newly added 27 arteries of cerebrovascular and neck circulations. The governing equations of the 1D simulation can be obtained by integrating the continuity and Navier-Stokes equations over an artery cross-section:

$$\frac{\partial A}{\partial t} + \frac{\partial Q}{\partial z} = 0 \tag{3}$$

$$\frac{\partial Q}{\partial t}+\frac{\partial}{\partial z}\left(\frac{Q^2}{A}\right)+\frac{A}{\rho}\frac{\partial P}{\partial z}+8\pi\frac{\mu}{\rho}\frac{Q}{A}=0 \qquad (4)$$

where A and Q are the cross-sectional area and the flow rate. In addition, the pressure-area relationship is applied to equations (3) and (4):

$$P-P_0=\frac{Eh_0}{r_0\left(1-\sigma^2\right)}\left(\sqrt{\frac{A}{A_0}}-1\right) \qquad (5)$$

where E, h, r, and s represent the Young's modulus, the wall thickness and arterial radius, and the Poisson ratio. The subscript 0 means a value at the reference state. Since the artery is an incompressible material, the Poisson ratio in the paper is taken to be 0.5. The Lax-Wendroff method is used to solve equations (3)-(4).

2.3 The 0D simulation method

The 0D simulation is applied to the peripheral vascular network, which consists of arteries smaller than one used for the 1D simulations, capillaries, venous system, and heart. The 0-D simulation is given by lumped parameter models as follows:

$$C\frac{dP_i}{dt}+Q_{i+1}-Q_i=0 \qquad (6)$$

$$L\frac{dQ_{i+1}}{dt}=-\left(P_{i+1}-P_i\right)-RQ_{i+1} \qquad (7)$$

Where C, L, and R represent the compliance. the inductance, and the resistance of the blood vessel. The 4th order Runge-Kutta method is used to solve equations (6) and (7).

3 CEREBROCASULCAR AND NECK CIRCULATIONS MODEL

The arterial network model of cerebrovascular and neck circulations consist of 27 arteries as summarized in Figure 2. The geometry and physical properties of the present network model use static data based on reference [3].

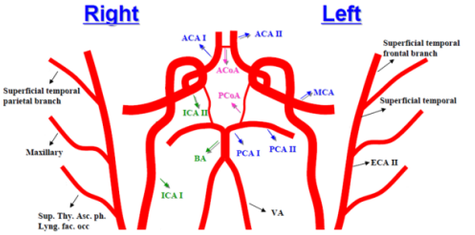

Figure 2. Arterial network model of cerebrovascular and neck circulations

4 NUMERICAL RESULTS

The present arterial network model of cerebrovascular and neck circulations is implemented on the multi-scale (3D-1D-0D) simulation. In this study, the simulation is performed for the left carotid artery of a 66 year-old male patient. The patient-specific model is constructed from a total 160 slices of CT images. One CT image has 512 x 512 pixels with resolution of 0.468 mm/pixel and the distance between slices is 0.5 mm. The hybrid of tetra-prism mesh is used for the analysis.

The effects of the present model are compared in Figure 3. Since the flow rate into CCA varies due to 1D-0D simulation, the flow rate in each artery is normalized by the flow rate of CCA.

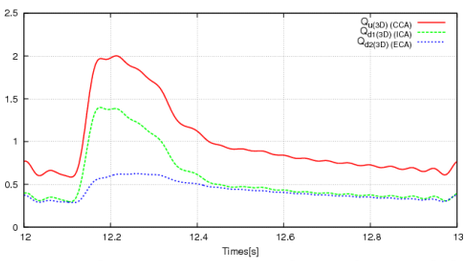

(a) circulatory system without the model

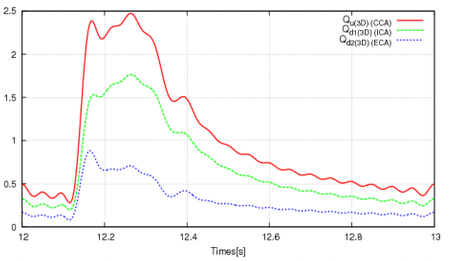

(b) circulatory system with the model

Figure 2. Comparison of flow rates between cases without and with the model

The averaged flow rate over one cardiac cycle between ICA and ECA are 58 % for ICA and 42 % for ECA without the model while they become 70 % for ICA and 30% for ECA with the model. The flow rate of ECA in the present model is reduced comparing to one without the model. The further investigation is required to examine the effects of model on the flow distribution. However, the profile of wave form of ECA in the case with the model is becoming similar to those of CCA and ICA comparing to those in the case without the model.

5 CONCLUSIONS

The arterial network model of cerebrovascular and neck circulations has been designed and has implemented on the multi-scale simulation. The simulation was conducted for 3D simulation of a 66 year-old patient combined with 1D-0D simulation. The numerical results of the flow distribution and the wave form of flow rate in each artery were compared. The results showed that the model reduced the averaged flow rate in ECA while the transient wave form of ECA became similar to that of CCA and ICA.

REFERENCES

[1] M. Oshima, R. Torii, S. Tokuda, S. Yamada, and A. Koizumi. Patient-specific modeling and multi-scale blood simulation for computational hemodynamic study on the human cerebrovascular system, *Current Pharmaceutical Biotechnology*, PMID:22335478 , 2012.

[2] F. Y. Liang, S. Takagi, R. Himeno, H. Liu. *Multi-scale modelling of the human cardiovascular system with applications to aortic valvular and arterial stenosis*, Medical Biol. Eng. Comput., 47, 743-755, 2009.

[3] F. Y. Liang, K. Fukasaku, H. Liu, S. Takagi. A computational model study of the influence of the anatomy of the circle of willis on cerebral hyperperfusion following carotid artery surgery, *BioMedical Engineering on Line*,10:84, 2011.

[4] M.Oshima, Y. Sat, F. Y. Liang, S.Takagi. Multi-scale Simulation of Cerebral Blood Flow with 3D-1D-0D Coupling model, *2nd International Workshop on Advanced Computational Mechanics*, 111, 2010.

3rd International Conference on Computational and Mathematical Biomedical Engineering - CMBE2013
16-18 December 2013, Hong-Kong
P. Nithiarasu and R. Löhner (Eds.)

Transport processes & chemical reactions in large arteries

E. Boileau, I. Sazonov, P. Nithiarasu
College of Engineering, Swansea University, Swansea, U.K., SA2 8PP
e.boileau@swansea.ac.uk

SUMMARY

Transport of chemical species in anatomical geometries have been modelled using many different simplifying assumptions, depending on the availability of experimental data. In recent years, an increasing number of computational studies have dealt with mass transfer, with the aim of correlating disturbed flow patterns and the onset of arterial disease. Our understanding of the impact of transport on flow control mechanisms will not only rely on realistic hæmodynamics of blood flow and chemical species, but also on an accurate characterisation of the biomechanical and biochemical processes involved. We present herein a comparative study of different model formulations, in order to better characterise some of the processes involved in the pathways to endothelial dysfunction.

Key Words: *endothelium, wall shear stress (WSS), chemical reaction, mass transport*

1 INTRODUCTION

The endothelium consists of a single layer of cells that cover the inner surface of blood vessels. In addition to providing a non-thrombogenic surface and a semi-selective barrier between the lumen and the surrounding tissue, it plays a critical role in the local regulation of blood flow, and hence the control of blood pressure. In the surface boundary layer, blood flow affects cellular responses by modifying the interactions between blood-borne agonists and endothelial receptors, and these signal transduction pathways can be altered by mass transport phenomena and reaction kinetics.

In healthy vessels, an increase in blood vessel diameter normally results in lower vascular resistance, and vice versa. The progressive impairment of this endothelial dilator function is known as endothelial dysfunction, and it has been shown to predict long-term development of arterial disease [1]. In recent years, a number of computational studies have dealt with mass transfer in anatomical geometries, with the aim of characterising the influence of disturbed flow on arterial disease [2,3]. We consider herein the effects of direct, wall shear stress (WSS)-mediated, and indirect receptor-ligand interactions in a generic transport model.

1.1 Signalling in the blood vessel wall

In the last few years, the role of purinergic signalling in the cardiovascular system has been a subject of increasing interest [4], although few computational studies have succeeded in obtaining meaningful results, from a physiological point of view [5]. The release of the nucleotide adenosine-5' triphosphate (ATP) by endothelial cells, via WSS-dependent mechanisms, is thought to play an important role in endothelium-mediated vasodilation. Its influence on regional blood

flow is also seen through the effects of its end-products, such as adenosine diphosphate (ADP). Simulations performed on image-based patient-specific geometries had revealed that existing paradigms may not be adequate to model the kinetics of ATP at the endothelium [5]. In particular, variations in mass transfer are seen to be highly dependent on the model formulation and the values of the parameters, suggesting that the ATP source term is a critical component of the model. In addition, chemical kinetics can be influenced by the local concentration, and our results also suggest that geometry may affect the pattern of catalytic reactions, with potential implications for endothelium-mediated regulatory mechanisms.

2 MODEL FOR TRANSPORT & CHEMICAL REACTIONS

The model for mass transport requires the solution of the continuity and momentum equations. Plasma concentrations of ATP and ADP are obtained by successively solving the conservation of species equation:

$$\frac{\partial[n]}{\partial t} + (\mathbf{u} \cdot \nabla)[n] = D_n \nabla^2[n]$$

where D_n is the corresponding diffusion coefficient for n = ATP, ADP. The Reynolds number is relatively small, in comparison with a very large Peclet number, of the order of 10^6, based on D_{ATP}. Mass transport is highly convection dominated, and variations of the concentration field near the boundary impose severe restrictions either on the spatial discretisation or on the accuracy of the computational method.

2.1 Heterogeneous reactions

Rates of heterogeneous biochemical reactions such as receptor desensitisation during cellular transduction or enzyme catalysed reactions are often almost linear for relatively small concentration of substrate, but levels out as the concentration increases. This phenomenon is usually represented by a Hill-type equation, following Michaelis-Menten kinetics. The reaction rate is approximately 1^{st} order, and the reactive surface boundary condition, representing the hydrolysis of ATP/ADP and ATP-derived ADP at the endothelium, is expressed as:

$$D_n \frac{\partial[n]}{\partial \mathbf{n}} = \frac{V_{max,n}[n]}{K_n} - S_n$$

where $\mathbf{n}$ is the vector normal to the arterial wall, $V_{max,n}$ is the maximum enzyme reaction velocity and K_n is the Michaelis-Menten constant for species n. Flow-mediated ATP release is included as a separate source term S_{ATP}, which depends on WSS. Two different WSS-dependent source terms for ATP production have been considered for comparison. The boundary condition for ADP is determined by substituting the term corresponding to the rate of production of ATP-derived ADP:

$$S_{ADP} = \frac{V_{max,ATP}[ATP]}{K_{ATP}}$$

The inlet Danckwert's boundary condition, typical of reactive flows, is usually replaced by a uniform concentration (Dirichlet boundary condition). A number of simplifying assumptions are made, depending on the model formulation, and whether blood-wall coupling is considered.

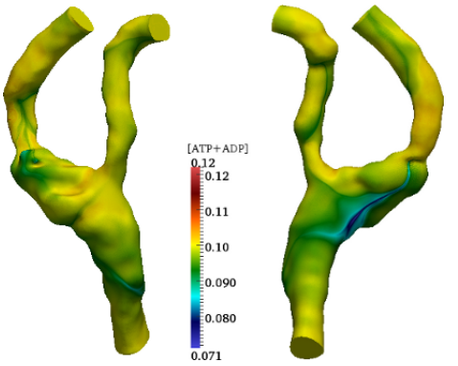

Figure 1: Combined nucleotide surface concentration at one instant during the cardiac cycle, for one specific geometry. Over the cardiac cycle, the combined surface concentration is affected by the geometry, with potential implications for endothelium-mediated regulatory mechanisms.

3 RESULTS & FUTURE WORK

We investigate the dependence of the surface concentration of nucleotides (especially [ATP]) on the instantaneous WSS, the rate of mass transfer, both spatially and temporally, as represented by the Sherwood number, and the influence of geometry. Lumenal and surface concentration of species are obtained for different patient-specific geometries (Figure 1). Production and degradation at the endothelium is affected by numerous flow features. These local variations may either provide a mechanism for rapid coordination of cell activity and signalling, or constitute a pathological change in the local cellular environment, as influenced by transport processes.

We investigate the possibility of coupling local transport phenomena at the endothelium with models describing intra- and inter-cellular calcium ion oscillations in endothelial and smooth muscle cells, as a first step in the study of vasomotion.

REFERENCES

[1] J.P.J. Halcox, A.E. Donald, E. Ellins, D.R. Witte, M.J. Shipley, E.J. Brunner, M.G. Marmot, J.E. Deanfield, Endothelial function predicts progression of carotid intima-media thickness, *Circ.*, 119, 1005-12, 2009.

[2] C.R. Ethier, Computational modeling of mass transfer and links to atherosclerosis, *Annals Biomed. Eng.*, 30, 461-471, 2002.

[3] K. Perktold, M. Prosi, P. Zunino, Mathematical models of mass transfer in the vascular walls, in L. Formaggia, A. Quarteroni, A. Veneziani (Eds.) *Cardiovascular Mathematics. Modeling and simulation of the circulatory system.*, Vol. **1**, Springer-Verlag, 2009.

[4] A.W. Lohman, M. Billaud, B.E. Isakson, Mechanisms of ATP release and signalling in the blood vessel wall, *Cardiovasc. Res.*, 95, 269-80, 2012.

[5] E. Boileau, R.L.T. Bevan, I. Sazonov, M.I. Rees, P. Nithiarasu, Flow-induced ATP release in a patient-specific arterial geometries – a comparative study of computational models, *Int. J. Numer. Meth. Biomed. Engng.*, 2013.

3rd International Conference on Computational and Mathematical Biomedical Engineering – CMBE2013

16-18 December 2013, Hong-Kong

P. Nithiarasu and R. Löhner (Eds.)

A viscoelastic fluid-structure interaction model for carotid arteries under pulsatile flow

Zhongjie Wang*, Xiao Yun Xu**

*Department of Chemical Engineering, Imperial College London, South Kensington Campus, SW7 2AZ, zhongjie.wang09@imperial.ac.uk

** Department of Chemical Engineering, Imperial College London, South Kensington Campus, SW7 2AZ, yun.xu@imperial.ac.uk

SUMMARY

A fluid-structure interaction model incorporating viscoelastic wall behaviour has been developed and applied to an idealised carotid artery under pulsatile flow. The shear and bulk moduli of the arterial wall are described by Prony series, where the parameters can be derived from in vivo measurements. The aim of this study is to develop a fully-coupled numerical model for pulsatile flow in human arteries with viscoelastic wall behaviour in order to predict both longitudinal and radial displacements. Comparisons are made between the numerical and analytical solutions for wall displacements and our results demonstrate that the coupled model is capable of predicting the viscoelastic behaviour of carotid arteries. Comparisons between the elastic and viscoelastic wall models suggest that the effect of viscoelasticity and longitudinal wall motion cannot be neglected when analysing carotid wall mechanics.

Key Words: *Viscoelastic model, pulsatile flow, numerical analysis, Prony series, longitudinal motion.*

1 INTRODUCTION

Human carotid arteries exhibit viscoelastic behaviour characterized by hysteresis of the pressure-diameter relation and longitudinal wall motion [1]. It is known that the mechanical properties of arteries change with the progress of arterial diseases, such as atherosclerosis, and the main alterations of physical properties of large arteries are reflected through changes in diameter and stiffness. Therefore, increased arterial stiffness has been used as a marker for assessment of vascular diseases. However, stiffness does not represent all the mechanical alterations, since arterial walls also exhibit viscous behaviour [2]. Ultrasound techniques have been widely used to measure vessel wall displacements, as well as pressure and diameter waveforms. A considerable phase lag between blood pulsation and arterial movement has been found on ultrasound data, from which viscoelastic properties can be derived [3]. This study is aimed at the development of a fully coupled numerical model for viscoelastic behaviour of human arteries under pulsatile flow. A better understanding of mechanical properties of carotid arteries may help in early diagnosis and prevention of carotid diseases.

2 METHODOLOGY

An idealized model of the common carotid artery is adopted first in order to compare the numerical and analytical solutions for validation purpose [4]. The model has a diameter of 6.1 mm, a length of 10 diameters, and a uniform wall thickness of 0.61 mm. It consists of two domains, the fluid (blood) domain and the vessel wall. Blood flow is governed by the Navier-Stokes equations, and the blood is assumed to be incompressible and Newtonian with a dynamic viscosity of 4 mPa.s and a density of 1050 kg/m3. The arterial wall is modelled as an incompressible, homogenous, isotropic, and viscoelastic material. Since it has been found that nonlinear stiffening of carotid artery is negligible [1], a linear viscoelastic material model is employed, where Prony series are used to describe the shear and bulk moduli, as shown in equations (1) and (2).

$$E'_{(\omega)} = E_e + \sum_{i=1}^{m} \frac{\omega^2 \rho_i^2 E_i}{\omega^2 \rho_i^2 + 1} \qquad (1) \qquad E''_{(\omega)} = \sum_{i=1}^{m} \frac{\omega \rho E_i}{\omega^2 \rho_i^2 + 1} \qquad (2)$$

Here $E'_{(\omega)}$, $E''_{(\omega)}$ (the real and imaginary parts of complex material functions), E_e (the equilibrium modulus) and ω (the dynamic frequency) are all positive constants. Values for ρ_i (relaxation time) and E_i (relaxation strengths) are determined by data fitting using the nonlinear least-squares method in Matlab. The above equations can be readily used in our FSI simulations. The flow and wall equations are solved in a coupled manner by two-way coupling of Ansys and Fluent. The following boundary conditions are applied for the fluid domain: at the model inlet, time-dependent axial velocity profiles obtained from Womersley solution are imposed; whereas a pressure waveform derived from the analytical model are imposed at the outlet. For the vessel

wall, two types of boundary conditions are tested as described below in the next section. The computational mesh consisting of 41250 elements in the vessel wall and 240813 elements in the fluid domain and a coupled time step of 0.01 second is used.

3 RESULTS

Most computational models of arterial wall focus on radial displacements only. Recent in vivo ultrasound studies have demonstrated that there is a considerable longitudinal movement driven by the pulsatile blood flow and pressure waves on the inner layers of the arterial wall, and the magnitude of longitudinal displacement is as large as that of radial displacement. To investigate the longitudinal displacement of human carotid arteries with viscoelastic property, two types of tethering are tested: (i) fixed ends, or (ii) allowing for longitudinal motion by connecting the inlet and outlet to a viscoelastic foundation. Preliminary results obtained from the viscoelastic model with fixed ends are shown in Figure 1. It can be observed that there is a phase lag of 0.02s between the predicted radial displacement and the input pulsatile pressure waveform. This agrees well with the corresponding analytical solution [4].

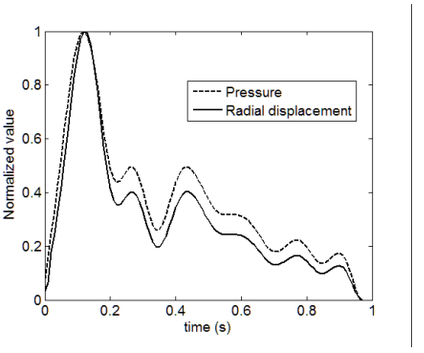

Figure 1 Pressure waveform and predicted radial displacement with fixed ends

Using the second type of boundary condition, the predicted longitudinal displacement and the corresponding pressure waveform are shown in Figure 2. The maximum longitudinal displacement is 1 mm, which is comparable to the radial displacement.

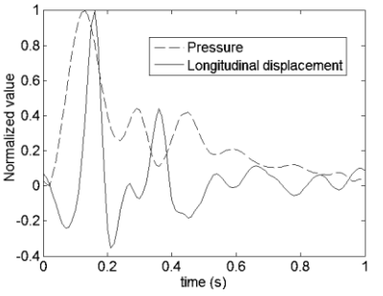

Figure 2 Predicted longitudinal displacement from the viscoelastic model with non-fixed ends

4 CONCLUSIONS

This paper presents a FSI model of carotid arteries with viscoelastic wall behaviour. Our results show that the numerical model can be used to predict the pressure-diameter hysteresis under physiological conditions. The phase lag between pressure and radial displacement obtained from the numerical model is comparable to that of the analytical solution. On the other hand, the hysteresis between pressure and longitudinal displacement can also be predicted by applying suitable boundary conditions at the ends.

REFERENCES

[1] D. Valdez-Jasso, D. Bia, Y. Zocalo, R.L. Armentano, M.A. Haider and M.S. Olufsen. Linear and nonlinear viscoelastic modeling of aorta and carotid pressure-area dynamics under in vivo and ex vivo conditions, Ann Biomed Eng, 39, 1438-56, 2011.

[2] R.L. Armentano, J.L. Megnien, A. Simon, F. Bellenfant, J. Barra and J. Levenson. Effects of hypertension on viscoelasticity of carotid and femoral arteries in humans, Hypertension, 26, 48-54, 1995.

[3] H. Hasegawa and H. Kanai. Measurement of elastic moduli of the arterial wall at multiple frequencies by remote actuation for assessment of viscoelasticity, Japanese Journal of Applied Physics Part 1-Regular Papers Short Notes & Review Papers, 43, 3197-3203, 2004.

[4] R.K. Wairriner, K.W. Johnston, R.S. Cobbold. A viscoelastic model of arterial wall motion in pulsatile flow: implications for Doppler ultrasound clutter assessment, Physiol. Meas, 29, 157-179, 2008.

Towards Clinically Relevant Computational Vascular Mechanics

3rd International Conference on Computational and Mathematical Biomedical Engineering – CMBE2013

16-18 December 2013, Hong-Kong

P. Nithiarasu and R. Löhner (eds)

Patient-specific simulation of stent-graft deployment within an abdominal aortic aneurysm

David PERRIN*, Pierre BADEL*, Stéphane AVRIL*, Jean-Noël ALBERTINI, Laurent ORGEAS***, Christian GEINDREAU***, Aurélien DUMENIL****, Cemil GOKSU******

* Ecole Nationale Supérieure des Mines de Saint-Etienne, CIS-EMSE, CNRS:UMR5307, LGF, F-42023 Saint Etienne, France, {perrin ; badel ; avril}@emse.fr

** CHU Hôpital Nord Saint-Etienne, Department of CardioVascular Surgery, Saint-Etienne F-42055, France, j.noel.albertini@chu-st-etienne.fr

*** CNRS / Université de Grenoble (Grenoble-INP / UJF), Laboratoire Sols-Solides-Structures-Risques (3SR Lab), BP 53, 38 041 Grenoble cedex 9, France,{laurent.orgeas ; christian.geindreau}@3sr-grenoble.fr

**** Therenva, 35000 Rennes, France, {aurelien.dumenil ; cemil.goksu}@therenva.fr

SUMMARY

In this study, finite element analysis is used to simulate the surgical deployment procedure of a bifurcated stent-graft on a real patient's arterial geometry. The stent-graft is modeled using realistic constitutive properties for both the stent and most importantly for the graft. The arterial geometry is obtained from pre-operative imaging exam. The obtained results are in good agreement with the post-operative imaging data. As the whole computational time was reduced to less than 2 hours, this study constitutes an essential step towards predictive planning simulations of aneurysmal endovascular surgery.

Key Words: *stent-graft, endovascular treatment, FE analysis.*

1 INTRODUCTION

Endovascular aneurysm repair (EVAR) is a widely and increasingly used technique to treat abdominal aortic aneurysms (AAAs) owing to several assets related to the minimally invasive approach. However, to date, the durability of stent-graft (SG) treatments remains the principal issue of EVAR. Secondary interventions after 5 years are required in up to 22% of cases due to endoleaks, stenosis or thrombosis of the SG or failure of the SG's constituents; also, in tortuous AAAs, a lack of SG flexibility was associated with the above-mentioned complications [1]. These facts clearly emphasize the need to predict, as soon as the surgical planning, the mechanical response of SGs in a given geometry. In pursuit of this goal, FE analyses can be used for predicting the deployment of stent-grafts, hence the initial success or failure of the procedure.

In the literature, the expansion of bare stents has been the object of intensive research and many numerical studies [2]. However, the deployment of SG – widely used in the treatment of aortic aneurysms – has been the object of very few studies [3,4]. And yet, the presence of the textile component onto which the stents are sutured is a key aspect which drastically influences the behavior of the SG and requires proper modeling. Provided that the mechanical properties of each constituent are cautiously calibrated, numerical simulations of the deformation of SGs [5] has the potential to provide important indications to aid a surgeon: guiding the surgeon in choosing the right dimensions for the stent-graft, especially lengths, in patient-specific aneurysm models and anticipating (i) potential short-term complications such as stent-graft kinks or inadequate apposition onto the arterial wall, (ii) potential long-term complications such as stent rupture or fabric tear. In short, introducing the appropriate SG models into simulations of the deployment would be very useful in surgical planning.

The goal of the present study was, thus, to develop a model able to simulate the positioning of a bifurcated SG in a given patient-specific AAA, under static conditions. Significant effort was made to build a clinically-relevant and very cost-efficient simulation model within the perspective of using it as a tool to help clinicians in surgical planning.

2 METHODS

Geometry and properties. The geometry of the pathological aorta, including the abdominal aorta and the iliac arteries, was obtained from the pre-operative CT scan of the considered patient, followed by segmentation of the lumen and 3-node shell meshing of the wall using the surgery-oriented EndoSize® software (Therenva, France). The stent-graft which was implanted in this patient was modeled as a multi-component structure including the textile graft onto which the

metallic stents are sewn. The graft was modeled with 4-node shell elements and the stents with 2-node beam elements tied to the textile.

Since only the *in vivo* tangent behavior is considered, the artery's constitutive model was assumed as orthotropic elastic with Young's moduli of 1 and 0.5 MPa in circumferential and longitudinal directions. One important aspect for the simulation was the proper characterization and modeling of the in-plane and bending behaviors of the textile due to their significant impact on the simulation results (kinks and fabric wrinkles). A realistic orthotropic constitutive model was set up based on in-house experimental characterization [5]. The simulation strategy (presented below) restraining the stents to their elastic response, a linear elastic model was assigned to these components (Young's modulus E = 40 GPa, and Poisson's ratio $\upsilon = 0.46$).

Simulation strategy. To make the simulation as efficient as possible within the perspective of being clinically tractable and relevant, the main focus of this work was dedicated to reducing the computational cost to obtain a relevant final deployed state of the SG. Hence, the numerous actual steps of the deployment procedure were simplified in two steps. In the first step, the SG is initially surrounded by a "virtual" shell containing the SG to be deployed, and contact between the shell and the SG is activated (see Fig. 1a). Then mesh morphing of this shell onto the actual arterial geometry is achieved by prescribing displacements to all the nodes of the shell (Fig. 1b). Stresses in the SG result from this step as the SG diameter is oversized of about 15% with regard to the proximal neck of the aorta. Then, in the second step, the shell has initially the shape of the original artery before SG implantation. After assigning the elastic properties of the artery to the shell and prescribing proper boundary conditions, the mechanical equilibrium between the SG and the artery is computed, hence the final geometry after SG implantation *in vivo* (Fig. 1c).

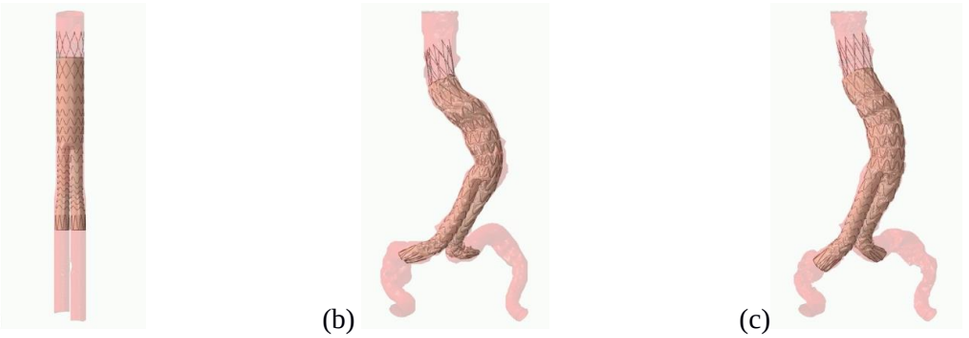

(a) (b) (c)

Fig. 1. (a) initial configuration of the model; (b) result of morphing onto the arterial geometry (step 1); (c) result of mechanical equilibrium (step 2).

3 RESULTS AND DISCUSSION

Figure 1 presents the initial geometry, the result of step 1 (morphing onto the patient's arterial geometry) and those of step 2 (mechanical equilibrium). Wrinkles are reproduced in a realistic manner. Figure 2 shows a comparison with post-operative geometry obtained from CT-scan images. The qualitative agreement is very encouraging. Some discrepancies can be noticed in

iliac portions, which is likely due to boundary conditions in this region where the internal iliac arteries may locally constrain the artery (not considered yet). In addition, part of these differences may be due to the length of the iliac SG limbs and the overlap between the limbs and the main body of the SG which are not known.

Validation of the approach on a cohort of real cases is on-going. The results reported constitute the first step towards predictive planning simulations of aneurysmal endovascular surgery.

Fig. 2. Qualitative comparison of the computed SG geometry (in red) to the real SG geometry (in green) obtained from post-operative CT-scan.

Acknowledgements

This work is a part of a thesis granted by the Region Rhône-Alpes.

REFERENCES

[1] M.A. Bartoli, B. Thevenin, et al. Secondary procedures after infrarenal abdominal aortic aneurysms endovascular repair with second-generation endografts, *Annals of Vascular Surgery*, 26, 166-174, 2012.

[2] S. Morlacchi and F. Migliavacca. Modeling Stented Coronary Arteries: Where We are, Where to Go, *Annals of Biomedical Engineering*, 41, 1428-1444, 2012.

[3] S. De Bock, F. Iannaccone, et al. Virtual evaluation of stent graft deployment: A validated modeling and simulation study, *Journal of the Mechanical Behavior of Biomedical Materials*, 13, 129-139, 2012.

[4] A. Prasad, N. Xiao, et al. A computational framework for investigating the positional stability of aortic endografts, *Biomechanics and Modeling in Mechanobiology*, 1, 1-19, 2012.

[5] N. Demanget, P. Latil, et al. Severe Bending of Two Aortic Stent- Grafts: An Experimental and Numerical Mechanical Analysis, *Annals of Biomedical Engineering*, 40, 2674–86, 2012.

3rd International Conference on Computational and Mathematical Biomedical Engineering – CMBE2013
16-18 December 2013, Hong-Kong
P. Nithiarasu and R. Löhner (eds)

Acoustic localisation of coronary artery stenosis: wave propagation in soft tissue mimicking gels.

H Thomas Banks*, Malcolm J Birch, Mark P Brewin**, Steve E Greenwald***, Shuhua Hu*, Zack R Kenz*, Carola Kruse****, Simon Shaw****, John R Whiteman****.**

* CRSC Department of Mathematics, North Carolina State University, Raleigh NC, USA, htbanks@ncsu.edu, shu3@ncsu.edu, zrkenz@ncsu.edu
**Clinical Physics, Barts Health NHS Trust, London, UK, m.j.birch@qmul.ac.uk, m.p.brewin@qmul.ac.uk
***Blizard Institute, Barts and The London School of Medicine and Dentistry, Queen Mary, University of London, UK. s.e.greenwald@qmul.ac.uk
****BICOM, Institute of Computational Mathematics, Brunel University, UK, Carola.Kruse@brunel.ac.uk, Simon.Shaw@brunel.ac.uk, John.Whiteman@brunel.ac.uk

SUMMARY

Plaque in coronary arteries produces turbulent flow downstream and time-varying wall shear stresses. These produce low amplitude acoustic shear waves which propagate through the chest and can be measured by skin sensors. We report here preliminary measurements of 2-D forced oscillations, induced within the gel by an electro mechanical vibrator or by turbulent flow. In the vibrator experiments, we have found that axial movements within the gel of as little as 20 μm give rise to predominantly axial movements at the surface, typically of 25 – 50% of this amplitude, with a time delay that is consistent with previously determined phase velocity measurements in the same material. In the steady flow experiments shearing movements at the gel surface were seen at flow rates above 50 ml min^{-1} (estimated Reynolds number 500 – 2500) with frequencies in the range 125 – 1000Hz. For all flow rates the peak amplitude was seen at frequencies around and 240Hz. These data provide input for direct and inverse solver software (being developed concurrently and described in a companion presentation) to simulate the response of the gel to the shear waves. This mathematical loop makes it possible to characterise the source given the signal and to compare material data with predicted values.

This work is supported by the Engineering and Physical Sciences Research Council. Grants: EP/H011072/1 & EP/H011285/1.

Key Words: *Coronary artery disease, Acoustic shear waves, Experimental measurement, Viscoelasticity, Computational modelling.*

1 INTRODUCTION

Plaque developing in a coronary artery produces turbulent flow downstream and time varying wall shear stresses. These give rise to low amplitude acoustic waves which propagate through the chest and can, in principle be measured by skin sensors. The stenotic signal is composed of

pressure, p-, and shear, s-, waves at frequencies no more than 2 kHz but above those normally associated with healthy heart sounds. In soft tissue the wavelength and speed of the p-waves is too great to provide useful information at the chest wall about the location of their origin. However, the s-wave propagation velocity of about 50 to 90 m/s is an order of magnitude less. For disturbances at less than 2 kHz, s-waves will have wavelengths of about 3 to 9 cm, although they will undergo greater attenuation than p-waves on their propagation to the chest wall [1]. Therefore detection of these s-waves at the chest surface should, in principle, allow greater precision in locating their source.

The objectives of this project are to simulate the propagation of shear waves induced by an arterial stenosis both experimentally in chest phantoms composed of the appropriate tissue mimicking materials and computationally by software approximations to the underlying partial differential equations. The overall aim is to produce a stand alone system suitable for screening and or diagnosis of coronary artery disease.

We report here measurements of shearing oscillations and flow-induced turbulence in soft tissue-mimicking gels which provide input to the numerical model of soft tissue behaviour described elsewhere.

2 METHODS

Cylindrical specimens of 3% agarose gel were cast around an axial rod and bead connected to an electromechanical vibrator (figure 1), to generate shear-waves of known characteristics and location (frequency 250-750 Hz, amplitude 10-50 μm). Displacement of the bead was monitored with a laser transducer (AR700, Schmitt Industries, Oregon, USA) interfaced to a real time data capture system (CRIO type 9024, National Instruments, Newbury, UK), sampling at 17kHz. and displayed in real time by LabView software (version 11.0.1, National Instruments, Newbury, UK). Circumferential and axial displacement at the gel surface were mapped optically by tracking the movement of carborundum micro-particles on the surface through a long focus microscope connected to a high speed camera (MotionBLITZ EoSens Mini1, Mikrotron GmbH, Unterschleissheim, Germany) running at frame rates of 3000 – 5000 frames per second. Particles were tracked by custom written software running under a Zeiss KS400 image analysis system.

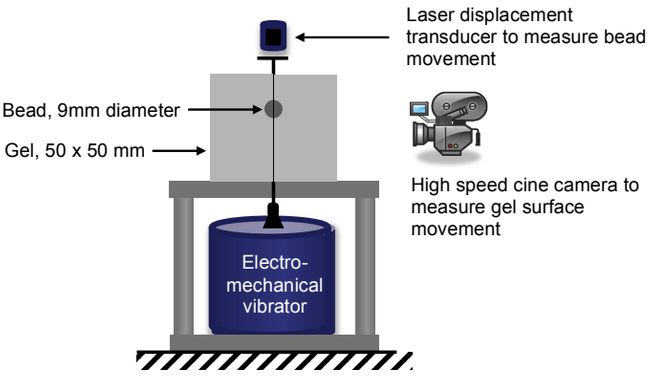

Figure 1. Forced vibration rig. Gels cast with bead in various positions. Laser measures bead movement; camera attached to long-focus microscope measures surface movement. Axial positions of bead and camera are variable.

In the flow study (figure 2) a silicone rubber tube (i.d. 4.5mm, to mimic a coronary artery) containing a stenosis was embedded in a cuboidal gel phantom (200m x 45mm x 25mm) at depths of 10 or 20 mm below the gel surface, the lateral displacement of which was mapped by a piezo-electric accelerometer placed on the gel surface directly above the tube at different points along the length of the gel block. Stenoses of 50 and 90% diameter reduction were tested. Steady flow was produced from a reservoir giving a constant pressure head, connected to the stenosed tube and measured with a cannulating ultrasonic flow probe (T403, Transonic Systems, Europe B.V., Maastricht The Netherlands). After passing through the tube the circulating fluid (40% by volume, glycerol in water, viscosity 4.0 cp, i.e. close to that of blood) drained into a collecting vessel and was pumped back to the reservoir. The presence of turbulence was verified by visualising the flow with a duplex ultrasound scanner.

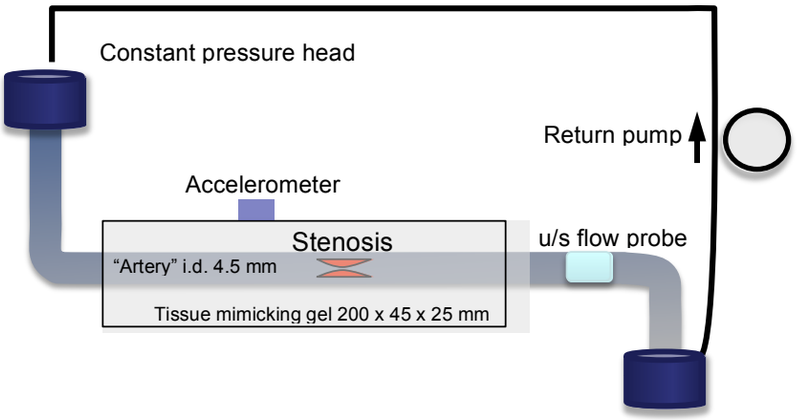

Figure 2. Steady flow rig. Tube embedded at a depth of 10 or 20 mm (typical depth below chest surface of left anterior descending coronary artery). Accelerometer placed at various positions on the gel surface to map shearing strains.

3 RESULTS

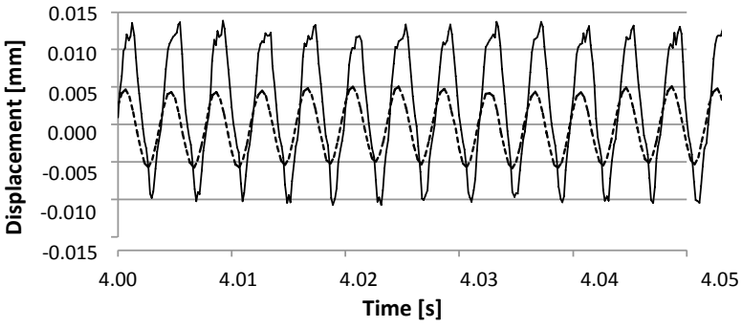

Figure 3. Bead movement parallel to the long axis of the cylindrical gel specimen (solid line) and gel surface movement in the same direction (broken line). In this plot, the bead is positioned 10mm above the base of the gel and the camera is imaging the surface at the same axial position. Vibrator frequency 250 Hz.

Figure 3 is a typical plot of the bead and corresponding gel movement. The mean amplitude of the surface movement is half that of the gel surface corresponding to an attenuation of 27 m^{-1} and the phase lag between them is 260°, giving a wave speed of 8.6 ms^{-1}. More detailed mapping of the strain field at the gel's surface is in progress.

Measurements of the gel surface movements due to turbulent flow in the embedded stenosed tube are summarised in figure 4a, which shows the variation with frequency of the acceleration power in the plane of the gel surface relative to 1 mW. Differences from the zero flow spectrum (thick black line) can be seen at mean flow rates greater than 50 ml min^{-1}. At all flow rates the maximum signal occurred at frequencies in the range 230 – 250 Hz. Figure 4b shows the amplitude at 240 Hz for each flow rate relative to the zero flow condition. The shaded area indicates the flow rates for which the critical Reynolds number for a stenosis was exceeded, showing that turbulent flow can be detected in this set up, even with a stenosis of a severity insufficient to cause clinical symptoms.

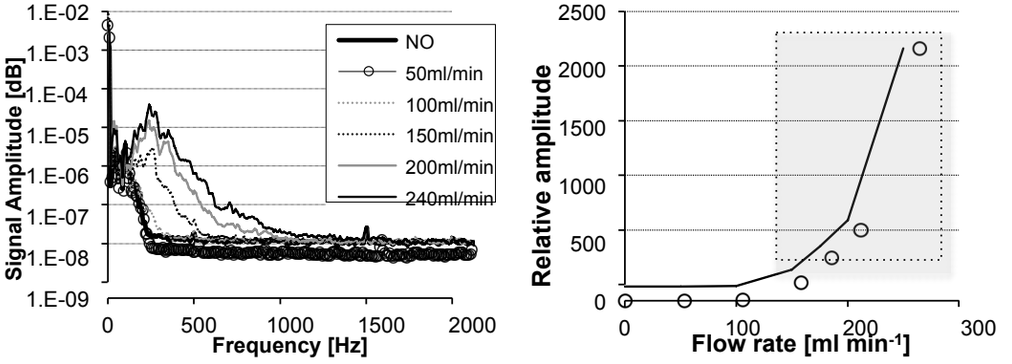

Figure 4a. Fourier transform of accelerometer signal due to flow of 40% glycerol water solution through a 50% stenosis in a tube 20 mm below the accelerometer at the gel surface. Figure 4a shows amplitude at 240 Hz relative to no flow signal for various flow rates. Points within the shaded area are flow rates at which the critical Reynolds number for stenotic flow was exceeded.

3 CONCLUSIONS

Early results of the computations agree well with the forced oscillation data and are able to predict the location of the shear wave source [2]. The next steps will compare computational results with experimental data from progressively more realistic representations of the chest containing one or more stenosed tubes carrying pulsatile flow, aiming ultimately to produce a device suitable for clinical use. We envisage this to consist of an array of stick-on displacement sensors, the signals from which will serve as input to the inverse solver software, thus producing a stand alone system suitable for screening and or diagnosis of coronary artery disease.

REFERENCES

[1] Catheline, S., F. Wu, and M. Fink. "A solution to diffraction biases in sonoelasticity: The acoustic impulse technique." *Journal of Acoustical Society of America.* 105.5, 2941-2950. 1999.

[2] Banks HT, Hu S, Kenz ZR, Kruse C, Shaw S, Whiteman JR, et al. "Material parameter estimation and hypothesis testing on a 1D viscoelastic stenosis model: Methodology." *Journal of Inverse and III-posed Problems.* 21, 25 - 57. 2013

3rd International Conference on Computational and Mathematical Biomedical Engineering – CMBE2013

16-18 December 2013, Hong-Kong

P. Nithiarasu and R. Löhner (eds)

Numerical simulations of coronary bioresorbable vascular scaffolds

Boyi Yang*, Bill Gogas, Tiziano Passerini*, Alessandro Veneziani*, Habib Samady**

* Department of Mathematics and Computer Science, Emory University, Atlanta, GA, USA

** Andreas Gruentzig Cardiovascular Center, Emory University, School of Medicine, Atlanta, GA, USA

SUMMARY

In order to validate the advantages and investigate the potential risks of coronary bioresorbable scaffolds (BVS), we simulate blood flow around the struts of realistic bioresorbable stents to evaluate possible biomechanical effects of the struts size in comparison with metallic ones.

Key Words: *coronary bioresorbable scaffold, drug eluting stent, restenosis, blood flow, wall shear stress, finite element method, Navier-Stokes equations.*

1. INTRODUCTION

The invention of coronary BVS opens a new era for the cardiovascular intervention technology[1]. The self-dissolving and drug-eluting features of BVS provide a number of long-term benefits for the patients; however, we speculate that their higher thickness at post implantation stage might cause excessive disturbance in blood flow, which could lead to potential risks of stent thrombosis and restenosis[2]. We take advantage of advanced computational fluid dynamics simulations to investigate the flow patterns and wall shear stress (WSS) of the scaffolded segments of the vessel at different stages of absorption. It is worth reminding that these kinds of stents are not yet approved by the Food and Drug Administration in the US.

2. CFD FOR BVS

The utilization of computational modeling techniques to virtually assess the performance of deployed coronary stents has been proven to be an important tool to predict their mechanical behavior over time[3] and these numerical simulations provide the preliminary “proof of concept”

for new technologies to further qualify for clinical application. Herein we develop a series of 3D simulations to test the hypothesis that the change of hemodynamic conditions over time due to the bioresorption process has beneficial impact on the flow dependent vascular responses.
Blood was assumed to behave as a Newtonian fluid. Flow velocity and pressure in the coronary artery were computed by numerically solving the unsteady Navier-Stokes equations. The spatial discretization of the Navier-Stokes equations was based on the Finite Element Method (FEM). In particular, a piecewise linear approximation was adopted for pressure and piecewise quadratic for velocity. The numerical solver used is based on LifeV (www.lifev.org).
The geometry of the scaffold was carefully constructed based on the design of Abbott's Absorb BVS, a clinically tested stent model (see Figure 1). In the post-implantation stage (stage 1), we assumed that the BVS is in its full shape and half-embedded into the vessel. For the follow-up stage(stage 2), we reduce the thickness of the stent uniformly and the radius of the lumen to a proper extent in order to mimic bioresorption and neointimal hyperplasia respectively. In order to yield more comprehensive results, for each stage we simulate several cases, starting from one straight vessel and moving to curved vessels with different curvatures. The geometry volume was discretized as an unstructured mesh of tetrahedral elements. Mesh generation was a delicate step, in finding the trade-off between accuracy and computational costs. As a matter of fact, since we are mostly interested in the solution close to the vessel wall and struts, we generated proper mesh "boundary layers". Consequently, the meshing process was split into two steps: The neighborhood of the vessel wall and struts was finely meshed; then the rest of the lumen was filled with slightly coarser mesh to achieve computing efficiency.
The results from our simulations provide much information about the blood flow patterns of the scaffolded vessel segment, especially local hemodynamic conditions around the BVS struts. Stage 1 results demonstrated some blood flow disturbance around the struts, but not at a critical level to cause flow separation behind struts (see Figure 2: A, B). In addition, the WSS has a dramatic change from top surface of the strut to the side surfaces. However, in stage 2 the flow disturbance has significant reduction (see Figure 2: C, D), and the WSS has much less fluctuations along the surface of each strut (see Figure 3). Comparison with metallic stents with a similar design will be presented.

3. CONCLUSIONS

These simulation results support the conjecture that BVS have a competitive advantage in the clinical application since blood flow resumes to its normal condition in the early stages of the stent dissolution process. On the other hand, open problems and challenges remain to be faced when simulating stents in a patient-specific scenario. As an extension of this work, we will address our companion project dealing with the integration of OCT images and angiographies to reconstruct individual coronaries with deployed stents.

Acknowledgments: The contribution of Don Giddens, Luke Timmins, Dave Molony at the Department of Biomedical Engineering at GA Tech during many useful discussions is gratefully acknowledged.

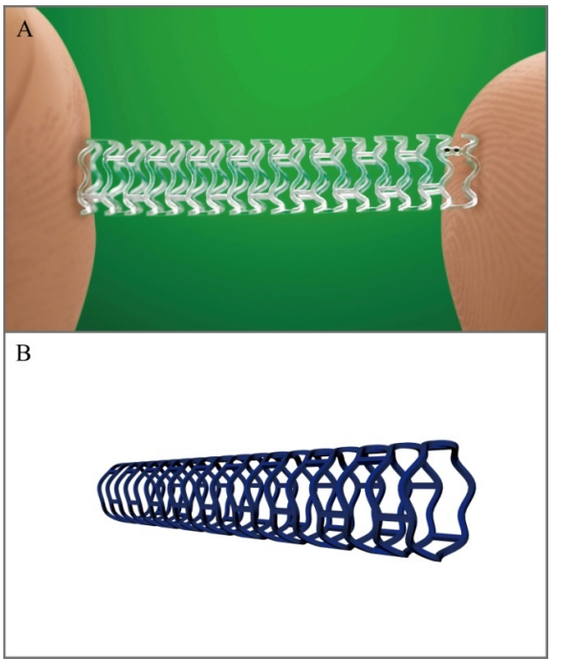

Figure 1: BVS Geometry Constructed for CFD Simulations. Panel A: A Real Photo of Abott Absorb BVS (Abbott Vascular, SC, Calif.). Panel B: The BVS Geometry we constructed for CFD simulations.

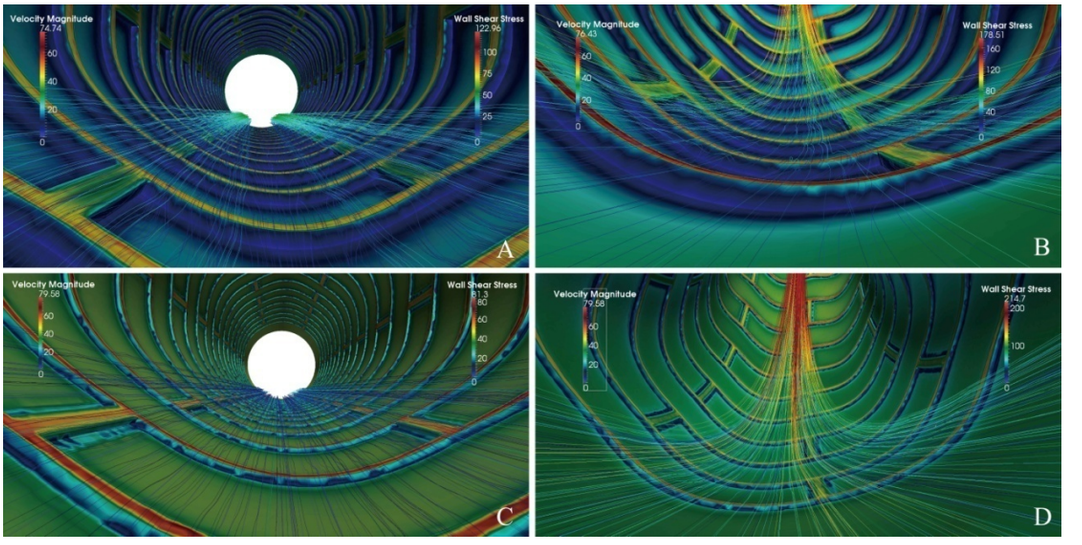

Figure 2: Comparison of Streamlines and Wall Shear Stress between Stage 1 and 2. Panel A: Stage 1 Straight Vessel. Panel B: Stage 1 Curved Vessel. Panel C: Stage 2 Straight Vessel. Panel D: Stage 2 Curved Vessel.

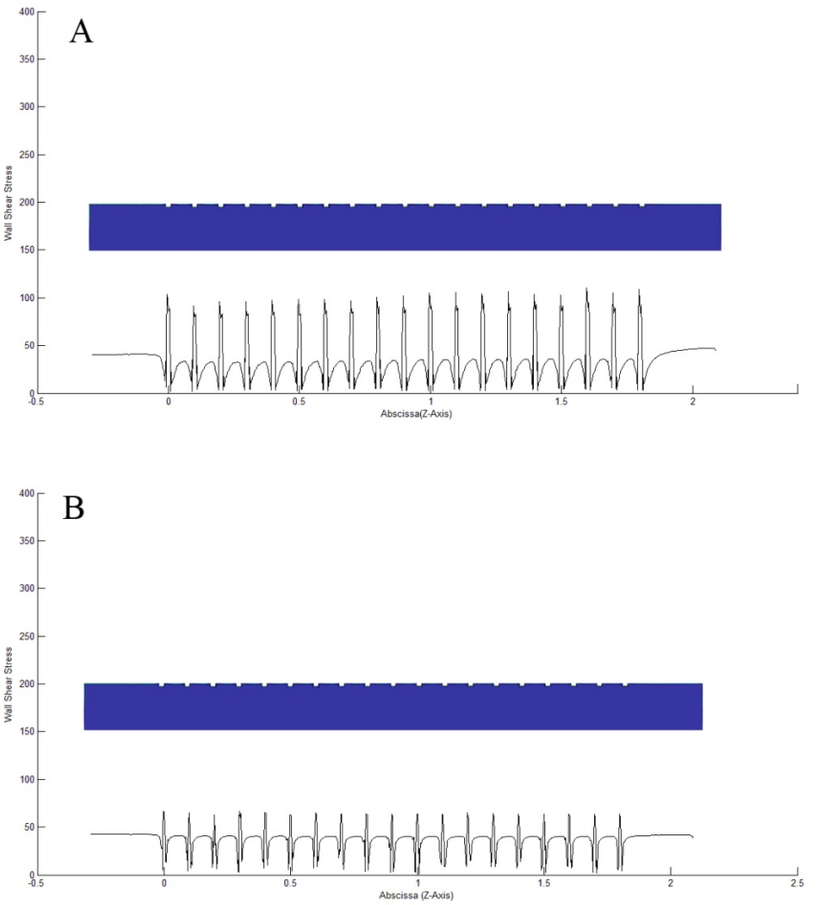

Figure 3: Plot of the Wall Shear Stress vs. axial distance on the top and both sides of the struts. Panel A: Stage 1 WSS Plot. Panel B: Stage 2 WSS Plot.

REFERENCES

[1] Wykrzykowska JJ, Onuma Y, Serruys PW. Vascular restoration therapy: the fourth revolution in interventional cardiology and the ultimate "rosy" prophecy. EuroIntervention. 2009 Dec 15;5 Suppl F:F7-8.

[2] Sarno G, Lagerqvist B, Frobert O, et al. Lower risk of stent thrombosis and restenosis with unrestricted use of 'new-generation' drug-eluting stents: a report from the nationwide Swedish Coronary Angiography and Angioplasty Registry (SCAAR). Eur Heart J. 2012 Mar;33(5):606-13.

[3] L. Formaggia, A. Quarteroni, A. Veneziani (eds.), Cardiovasucular Mathematics, Springer, Milan, 2009

3rd International Conference on Computational and Mathematical Biomedical Engineering - CMBE2013
16-18 December 2013, Hong-Kong
P. Nithiarasu and R. Löhner (Eds.)

Efficient Uncertainty Quantification in Patient Specific Vascular Material Models

Michael W. Gee⋆, Jonas Biehler⋆⋆ and Wolfgang A. Wall⋆⋆
⋆Technische Universität München, Mechanics & High Performance Computing Group,
Boltzmannstr 15, 85748 Garching, Germany, gee@tum.de
⋆⋆Technische Universität München, Institute for Computational Mechanics, Boltzmannstr 15,
85748 Garching, Germany, {biehler,wall}@lnm.mw.tum.de

SUMMARY

Computational Mechanics meanwhile plays a prominent role in the patient specific analysis and modeling of the human vascular system and its diseases. Though classical mechanical concepts of course hold, they are challenged by quite a few aspects when applied to problems that incorporate living tissue material and in vivo patient specific geometries. Among these one of the most important is the uncertainty and variability in material properties that can not be assessed easily in a patient specific, predictive (that is, non-invasive) setting.

Therefore, retrospectively obtained population averaged mean material properties are commonly employed in conjunction with patient specific geometries to build deterministic mechanical models of a vascular system of interest to address a specific question at hand. Such models very often neglect the large variability of material behavior between patients and, more importantly, the spatial variability of material behavior within one patient that can strongly influence the outcome of computational models.

While such a deterministic setting might serve well in qualitative assessments of patient specific characteristics, a sensitivity analysis with respect to assumed model parameters and a rigorous uncertainty quantification with respect to spatially variable model parameters are a must when truly predictive and clinically relevant statements shall be derived from computational models.

In this presentation, we present an uncertainty quantification framework based on a Bayesian framework [1] suitable to be applied to large scale nonlinear solid mechanics models with uncertain material behavior. We utilize rupture risk assessment of abdominal aortic aneurysms as a model problem to demonstrate applicability of such a UQ approach to large scale nonlinear problems and difficulties as well as computational performance issues that arise in this context.

Key Words: *uncertainty quantification, abdominal aortic aneurysm, rupture risk assessment*

1 Model Problem

Samples of abdominal aortic aneurysms (AAA) where tested using uniaxial tensile tests as described in [2], see Figure 1. A hyperelastic material model introduced in [3]

$$\Psi\left(I_1, J, \mathbf{x}, \boldsymbol{\xi}\right) = \alpha(\bar{I}_1 - 3) + \beta\left(\mathbf{x}, \boldsymbol{\xi}\right)(\bar{I}_1 - 3)^2 + \frac{\kappa}{\eta^2}(\eta \ln J + J^{-\eta} - 1)\,, \tag{1}$$

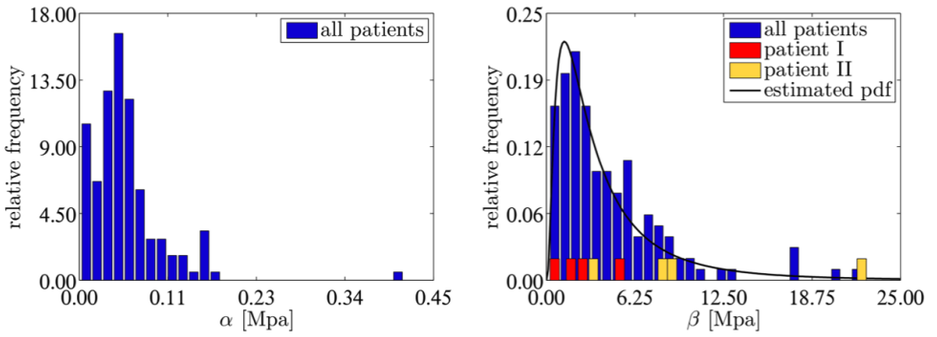

Figure 1: Relative frequency of material parameters α and β from uniaxial tensile tests of aneurysmatic aortic wall [2]. Black line is fitted probability density function as given in (2). Two patients are highlighted in red and yellow to demonstrate inter- and inner-patient variability of β between individual test samples.

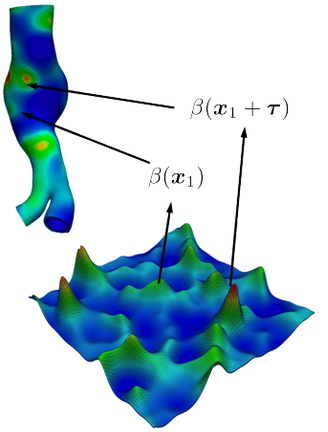

Figure 2: Correlation of material property β depending on the distance $\boldsymbol{\tau}$. One exemplary realization of a random field $\beta\left(\mathbf{x}, \boldsymbol{\xi}, d\right)$.

is utilized to describe the near-incompressible nonlinear elastic behavior of the sample tested. Therein, exemplarily, the material parameter $\beta\left(\mathbf{x}, \boldsymbol{\xi}\right)$ is a 3D random field with marginal probability density function

$$\rho_\beta(x) = \frac{1}{x\sigma\sqrt{2\pi}} e^{-\frac{(\ln x - \nu)^2}{2\sigma^2}} \quad , \quad \mu = 1.0857 \quad , \quad \sigma = 0.9205 \; . \tag{2}$$

Its autocorrelation function is

$$R(\boldsymbol{\tau}) = \sigma_\beta^2 \, e^{-(|\boldsymbol{\tau}|/d)^2}, \tag{3}$$

that describes correlation between material parameters $\beta\left(\mathbf{x}\right)$ and $\beta\left(\mathbf{x} + \boldsymbol{\tau}\right)$, see also the illustrative Figure 2. Therein, the correlation length d determines the wavelength of correlation between material parameters β at two distant points $\mathbf{x}$ and $\mathbf{x} + \boldsymbol{\tau}$.

2 Methods

Here, we follow a 2-level sampling strategy proposed in [1]. Therein, sampling of the quantities of interest (e.g. peak stress and strain, peak strain energy) is performed on a coarse version of the

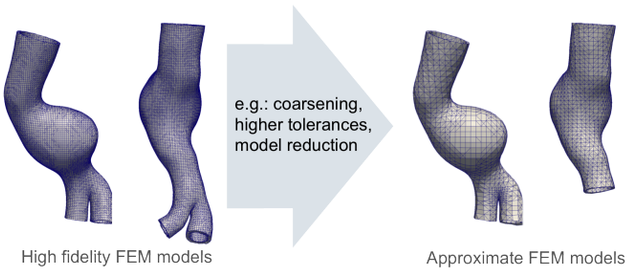

Figure 3: High fidelity discretizations of two abdominal aortic aneurysms (left) and their coarse representations (right) that involve coarser discretization and model reduction.

problem at hand, see Figure 3. The coarse representation of the problem at hand can be obtained by e.g. coarsening the discretization, obtaining only an approximate solution or by model reduction techniques. No a priori relationship between the coarse and the high fidelity model of the problem at hand needs to be established. Instead, a *probabilistic* link $p(y|x)$ between the high fidelity model (where one realization is expensive to compute on) and its coarse representation (that is computationally very cheap to evaluate) is build using a Bayesian regression

$$\pi_y(y) = \int p(y|x)\pi_x(x)dx \ , \tag{4}$$

where π_y and π_x are the distributions of the stochastic variable of interest on the coarse and fine model x and y, respectively. The conditional probability $p(y|x)$ is then assessed via

$$p(y|x) \approx p(y|x, \boldsymbol{\theta}, \sigma) = \frac{1}{\sqrt{2\pi\sigma^2}} \exp\left\{-\frac{(y - f(x, \boldsymbol{\theta}))^2}{2\sigma^2}\right\} \ , \tag{5}$$

where $f(x, \boldsymbol{\theta})$ is a Bayesian regression model. That is, a few selected training realizations on both, the high fidelity and the coarse model are evaluated to determine the posterior for the correlation of the high fidelity to the coarse model of the problem.

$$\pi(\boldsymbol{\theta}) = \frac{p((x_{1:n}, y_{1:n})|\boldsymbol{\theta})}{p(x_{1:n}, y_{1:n})} \propto p((x_{1:n}, y_{1:n})|\boldsymbol{\theta})\, p(\boldsymbol{\theta}) \ , \tag{6}$$

and pairs $(x_{1:n}, y_{1:n})$ are the training realizations evaluated on both models. For details on the 2-level regression model, we refer to [1].

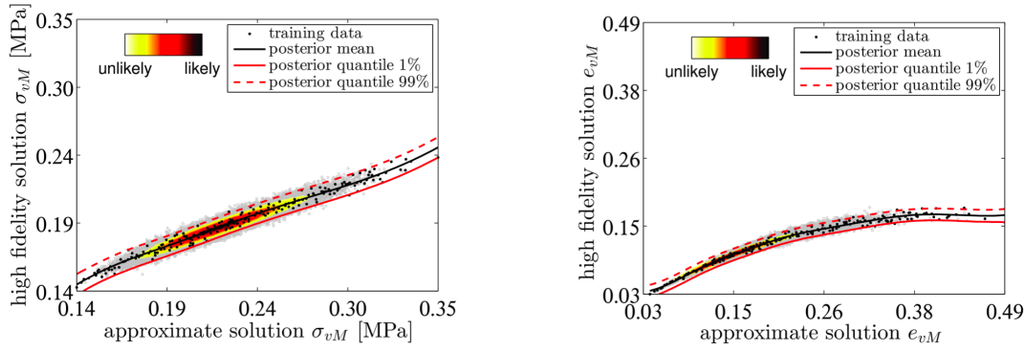

Figure 4: Regression model correlating the approximate solution of peak stress (left) and peak strain (right). Horizontal axis are values from sampling on the coarse model, vertical axis are a selected few training realizations (black dots) also evaluated on the high fidelity model. Grey dots are samples on both the fine and the coarse model for comparison.

3 Examples

The right AAA in Figure 3 is utilized to demonstrate properties of the proposed UQ methodology. Figure 4 shows the training (black dots) and correlation of the regression model (lines) in Eqs. (4) through (6). Even without establishing an a priori relationship between the coarse and fine model, very good correlation exist between the coarse and fine model problem which than can be exploited to perform sampling on the coarse problem only. Figure 5 provides distributions of stress (left) and strain (right) at a given location. For comparison, naive Monte Carlo sampling has been performed on the high fidelity model as well.

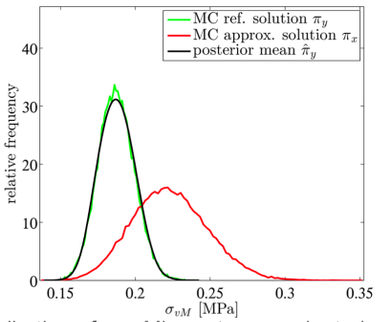

Distribution of von Mises stress evaluated at the center of the dorsal surface of the aneurysm sac.

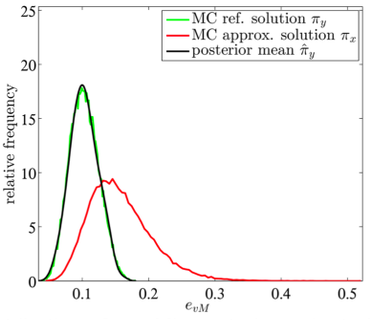

Distribution of von Mises strain evaluated at the center of the ventral surface of the aneurysm sac.

Figure 5: Distributions of stress (left) and strain (right) at a given fixed location of the model AAA. Red curve is sampling on the (cheap) coarse model. Black curve is posterior mean on the high fidelity model obtained from the regression model in Figure 4. Green curve is naive MC sampling on the high fidelity model for comparison.

One can observe that the 2-level regression model recovers the naive MC solution very well. The computational cost though has been reduced by up to a factor of 40 compared to naive MC sampling since sampling on the coarse model is significantly more efficient and only a few training samples ($n < 200$) had to be evaluated on both models.

Exploiting modern parallel HPC capabilities and the intrinsic parallelity of sampling based approaches, the method proposed here allows for a full uncertainty quantification for unknown material distributions in large scale nonlinear forward models within the clinically relevant time frame of one day.

References

[1] Koutsourelakis P. Accurate uncertainty quantification using inaccurate models. SIAM Journal of Scientific Computing, 2009, 31(5), 3274–3300.

[2] Maier A, Gee MW, Reeps C, Pongratz J, Eckstein HH, Wall WA. A Comparison of Diameter, Wall Stress, and Rupture Potential Index for Abdominal Aortic Aneurysm Rupture Risk Prediction. Annals of Biomedical Engineering, 2010, 38(10), 31243134.

[3] Raghavan M, Vorp D. Toward a biomechanical tool to evaluate rupture potential of abdominal aortic aneurysm: identification of a finite strain constitutive model and evaluation of its applicability, Journal of Biomechanics 2000, 33(4), 475–482.

3rd International Conference on Computational and Mathematical Biomedical Engineering - CMBE2013
16-18 December 2013, Hong-Kong
P. Nithiarasu and R. Löhner (Eds.)

Identification of material parameters for nonlinear elasticity: Toward solution of the inverse elasticity problem based on image similarity

Sebastian Kehl*, Wolfgang A. Wall and Michael W. Gee***
*Technische Universität München, Mechanics and High Performance Computing Group,
Boltzmannstraße 15, 85747 Garching bei München, kehl@lnm.mw.tum.de, gee@tum.de
**Technische Universität München, Institute for Computational Mechanics,
Boltzmannstraße 15, 85747 Garching bei München, Germany, wall@lnm.mw.tum.de

SUMMARY

In the setting of cardiovascular applications medical imaging techniques play a key role in providing information on in-vivo states. Information on displacement or strain, to be used as reference solution in standard identification algorithms, is implicitly included in these images. Thus image processing techniques such as image registration have to be applied to extract the desired information from the images. Due to the inverse nature of the image registration problem, measurements obtained from image registration are subject to regularization strategies. Consequently this will affect the final best fit estimation of the parameter identification based on these measurements. To obviate this drawback, an extended approach is deployed by directly integrating image based measures of similarity into a parameter identification framework.

Key Words: *parameter identification, image registration, nonlinear elasticity, abdominal aortic aneurysm.*

1 MOTIVATION

Advances in computational methods steadily increase the applicability and practical relevance of computational models. With respect to clinical application patient specific computational models become increasingly powerful tools to predict outcome and development of diseases or to allow for better planing and development of (surgical) interventions, see e.g. [1]. Such models incorporate complex 3-dimensional geometries, finite deformation kinematics and nonlinear constitutive properties. Despite these sophisticated means, material parameters are often based on population averaged mean values and are furthermore assumed to be of spatial homogeneity. Especially for soft living human tissue the latter assumption does not generally hold. Incorporation of spatially accurate representations of material parameters is therefore of high importance to further advance computational methods toward application in a clinical setting.

Although not being directly measurable in-vivo, material parameters can be accurately estimated by means of inverse analysis procedures, which often rely on non-invasively available information. In the case of cardiovascular applications, this information is conveniently obtained from medical imaging techniques, such as CT, MRT or Ultrasound. Since usually inverse algorithms for parameter identification utilize some measure of displacement or strain as reference solution, image processing techniques are utilized to extract the desired information from image data. This often includes image registration, which itself constitutes an inverse problem. To render the image registration well-posed regularization techniques are introduced, which are not specifically

fit to the subsequent parameter identification, thus resulting in a deterioration of the final best fit material parameters.

As a remedy, we propose a new embedded registration and inverse analysis approach inspired by Miga [2], where results are not disturbed by artificial regularization effects during the image registration step. Instead of splitting the identification process into image registration and the subsequent inverse computation (sequential registration based approach), we directly utilize an image based measure of similarity in the objective function to be minimized directly by the inverse algorithm (integrative image based approach). In contrast to [2], we propose to apply an intensity based measure of image similarity and to control regularity of the solution directly in the objective function.

2 METHODS

To highlight the general applicability, we utilize an unspecific representation of the weak form $\mathcal{F}(\mathbf{v}, \mathbf{u}, \mathbf{p})$ of nonlinear elasticity to define a forward model, where displacements $\mathbf{u}$, virtual displacement $\mathbf{v}$ and material parameters $\mathbf{p}$ are introduced (see e.g. [6] for a detailed description). A total Lagrangian formulation is used to represent quantities.

The inverse problem is formulated by means of an enriched objective function $\mathcal{I}$, as e.g in [5], as the sum of similarity measure $\mathcal{S}$, regularization $\mathcal{R}$ on the material parameters and the forward model $\mathcal{F}$ as

$$\mathcal{I}(\mathbf{v}, \mathbf{u}, \mathbf{p}) = \mathcal{S}(\mathbf{u}(\mathbf{p})) + \alpha\mathcal{R}(\mathbf{p}) + \mathcal{F}(\mathbf{v}, \mathbf{u}, \mathbf{p}). \tag{1}$$

Now, a transition of the measure of similarity $\mathcal{S}$ is performed, such that the standard least square error $\mathcal{S}_d$ of deviation between measured displacements $\hat{\mathbf{u}}$ and computed displacements $\mathbf{u}$ is replaced by an image based measure. In here we propose to apply the so called "*sum of squared differences*"(SSD) $\mathcal{S}_I$ as an intensity-based measure of similarity between images [3].

$$\mathcal{S}_d = \frac{1}{2}\left|\left|\mathbf{u} - \hat{\mathbf{u}}\right|\right|^2 \qquad \rightarrow \qquad \mathcal{S}_I = \frac{1}{2}\left|\left|S - T \circ \varphi(\mathbf{u})\right|\right|^2, \tag{2}$$

where the source image S is introduced as image representation of the undeformed computational model, and the target image T represents the reference state to be approached. Due to the total Lagrangian formulation, the computational evaluation of the SSD-measure necessitates the back propagation of the target image T according to the current solution $\mathbf{u}(\mathbf{p})$. The function $\varphi(\mathbf{u})$ accounts for the mapping between model space and image space.

With the Gateaux-derivative of both, the SSD-measure $\mathrm{d}_u\mathcal{S}$ and the forward model $\mathrm{d}_u\mathcal{F}(\mathbf{v}, \mathbf{u}, \mathbf{p})$, $\mathbf{v}$ can be chosen as the solution of the adjoint problem

$$\mathrm{d}_u\mathcal{F}(\mathbf{v}, \mathbf{u}, \mathbf{p}) = -\mathrm{d}_u\mathcal{S}, \tag{3}$$

such that the gradient $\partial\mathcal{S}/\partial\mathbf{p}$ can be evaluated efficiently. Based on this gradient the BFGS Quasi-Newton method (see e.g [4]) is applied to find the best-fit set of parameters $\mathbf{p}^*$.

3 SEQUENTIAL VS. INTEGRATIVE INVERSE ANALYSIS

To demonstrate the misfit of estimated parameters when image registration is involved as an intermediate step to obtain displacement measurements, we apply the two approaches depicted in (2)

to a simplified linear forward model. We assume the Poisson problem on a rectangular domain $\Omega \subset \mathbb{R}^2$

$$\begin{aligned} \mu \Delta u &= b \qquad \text{in } \Omega \\ u &= 0 \qquad \text{on } \partial\Omega \end{aligned} \tag{4}$$

to model the deflection u of a thin membrane with unknown material parameter μ under constant load b. Except for the simplification in the forward model we apply the procedure introduced above. A Thikonov regularization on the vector of material parameters is applied in the objective function (1). With the exact solution being a circular occlusion of increased material stiffness (see Fig. 2a), we have constructed grayscale images of the deflected and non-deflected membrane (see Fig. 1a and Fig. 1b). These images are then used to generate measurements of displacement

(a) Non-deflected membrane S (b) Deflected membrane T

Figure 1: Cut views of the 3-dimensional images of the deflected and non-deflected membrane

via non-parametric diffusion regularized image registration. The standard displacement based measure of similarity $\mathcal{S}_d$ (sequential registration based approach) is then used to estimate μ. Furthermore the images of the deflected membrane T and the non-deflected membrane S are directly used in the SSD-measure $\mathcal{S}_I$ (integrative image based approach).

The results of the two approaches are given in Figure 2b and Figure 2c for different weights of the regularization $\mathcal{R}$. BFGS-iterations were terminated for $||\partial\mathcal{I}/\partial\mathbf{p}|| < 1.0e^{-6}$. For a decreasing

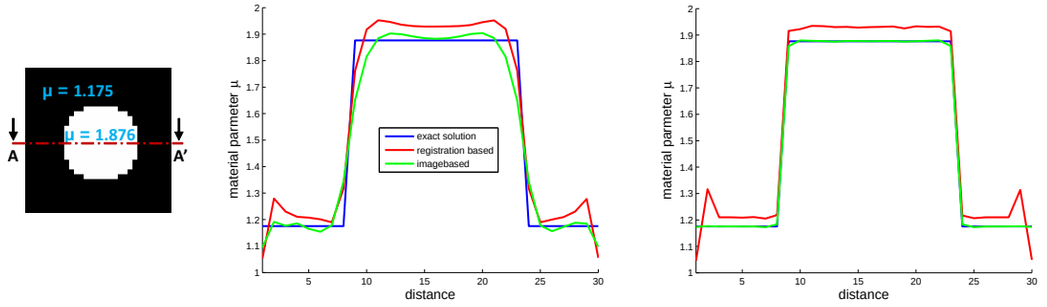

(a) Circular region of increased stiffness (b) Estimation of μ along section AA' with $\alpha = 1.0e^{-2}$ (c) Estimation of μ along section AA' with $\alpha = 1.0e^{-4}$

Figure 2: Identification of material parameters for the 2D poisson equation

weight α of the regularization $\mathcal{R}$ the exact solution (blue line in Fig. 2b and Fig. 2c) is more and more recovered by the direct image based approach (green line), whereas the registration based approach retains a constant offset (red line), due to the not physically motivated regularization in the image registration step.

4 CONCLUSION

The presented example shows that with the image based approach the error introduced by the registration can be omitted. Although using the same forward model for data generation as well as data inversion does not allow for a general evaluation of an inverse algorithm, in this case it is suitable to highlight the potential of the image based integrative inverse analysis method. Especially in cardiovascular applications, with information being conveniently available as image data, the proposed method appears as the obvious strategy and will generally outperform registration based procedures. The error revealed by using a simplified model, will be even more pronounced when strong material nonlinearities, finite deformations, growth & remodelling, and discontinuities from, e.g sliding contact are involved. In this presentation we will provide a full overview of the integrative image based inverse analysis method and will apply it to sophisticated nonlinear models of the human aorta and abdominal aortic aneurysms.

REFERENCES

[1] A. Maier, M. W. Gee, C. Reeps, J. Pongratz, H.-H. Eckstein, and W. A. Wall. A comparison of diameter, wall stress, and rupture potential index for abdominal aortic aneurysm rupture risk prediction. *Annals of biomedical engineering*, 38(10):3124–3134, 2010.

[2] M. I. Miga. A new approach to elastography using mutual information and finite elements. *Physics in Medicine and Biology*, 48(4):467, 2003.

[3] J. Modersitzki. *Numerical Methods for Image Registration (Numerical Mathematics and Scientific Computation)*. Oxford University Press, 2004.

[4] J. Nocedal and S. J. Wright. *Numerical optimization*, volume 2. Springer New York, 1999.

[5] A. A. Oberai, N. H. Gokhale, and G. R. Feijoo. Solution of inverse problems in elasticity imaging using the adjoint method. *Inverse Problems*, 19(2):297, 2003.

[6] O. C. Zienkiewicz and R. L. Taylor. *The finite element method for solid and structural mechanics*. Butterworth-Heinemann, 2005.

3rd International Conference on Computational and Mathematical Biomedical Engineering - CMBE2013
16-18 December 2013, Hong-Kong
P. Nithiarasu and R. Löhner (Eds.)

Shear-induced migration of red blood cells in the abdominal aorta and the carotid bifurcation: considerations on oxygen transport

J. Biasetti*, P. G. Spazzini and T. C. Gasser***
*Dept. of Solid Mechanics, KTH Royal Institute of Technology, Stockholm, Sweden,
biasetti@kth.se, tg@hallf.kth.se
**Mechanics Division, National Institute of Metrological Research (INRiM), Turin, Italy,
p.spazzini@inrim.it

SUMMARY

Shear-induced migration of red blood cells (RBCs) affects many important biological functions, oxygen availability among them. Its magnitude has not been properly assessed in large vessels, motivating the present study of the shear-induced migration of RBCs in the abdominal aorta and the carotid artery. Phillips' model was applied to model the shear-induced migration of RBCs in patient-specific geometries. Marked migration has been observed in regions prone to atherosclerosis, namely the outer wall of the iliac arteries and the outer wall of the carotid sinus. Lowering of wall hematocrit is postulated to induce a decrease in oxyhemoglobin availability, hence contributing to local hypoxia and possibly to atherosclerosis.

Key Words: *shear-induced migration, red blood cell, oxygen transport, hemoglobin, abdominal aorta, abdominal aortic aneurysm, carotid bifurcation.*

1 INTRODUCTION

Blood is a biphasic fluid composed of a fluid phase (plasma) and a solid phase constituted of blood cells such as red blood cells (RBCs), white blood cells (WBCs) and platelets (PLTs). Experimental evidence shows that flowing suspensions of rigid and deformable particles exhibit particle migration [1] from regions of higher shear rate to region of lower shear rate. RBCs also show this behavior and their migration to the center of micro and small vessels (μm to mm size) has been well established, both numerically [2] and experimentally [3].
RBCs distribution influences blood viscosity, and therefore the velocity profile, and also a series of biological activities such as oxygen distribution in the lumen [4]. Arterial wall hypoxia has been proposed to be a contributing factor to atherosclerosis [5]. Assessment of the adimensional wall-oxygen consumption rate, the Da number, and of the adimensional mass transport coefficient, the Sh number, led to postulate that oxygen supply to the arterial wall is fluid-limited [5], hence underlying the importance of mass transport from and to the wall. Disregarding the presence of hemoglobin, and therefore its possible lowering in concentration due to RBCs migration, causes a drastic decrease in oxygen transport to the wall [4]. Therefore, given the importance of RBCs distribution, the present study aims at evaluating RBCs distribution as a results of shear-induced migration in four patient-specific geometries: a normal aorta, a fusiform abdominal aortic aneurysm (AAA), a normal carotid bifurcation and a stenotic carotid bifurcation, and to discuss possible effects on oxygen transport.

2 METHODS and RESULTS

Four patient-specific geometries were investigated: a normal aorta, a fusiform AAA, a normal carotid bifurcation and a stenotic carotid bifurcation. The patient-specific geometries were reconstructed from computer tomography angiography (CT-A) scans acquired at Karolinska University Hospital, Stockholm. Blood was modeled as a non-Newtonian fluid with viscosity function of shear rate and hematocrit (volume fraction of RBCs) using the Quemada viscosity model [6]. Shear-induced migration of RBCs was modeled with the extension of Phillips' model [7] to the case of solid and fluid phases with different densities developed in [8]. Computations were performed using the commercial software COMSOL Multiphysics. Reasonable physiological boundary conditions taken from literature were applied at inlet and outlets [9, 10, 11]. Additionally, for all cases, a no viscous stress condition, $\boldsymbol{\tau}\mathbf{n} = \mathbf{0}$, was applied at the outlets. The no-slip boundary condition, $\mathbf{u}_w = 0$, was applied at the walls. An inlet fixed solid phase volume fraction of $\phi = 0.45$, representing a normal hematocrit value, was set for all cases. The outlet proved to be a region prone to oscillations of the volume fraction of the solid phase, forcing to impose a fixed volume fraction value of $\phi = 0.45$. At the lumen wall a no flux condition, $-\mathbf{n} \cdot \phi_d \mathbf{u}_d = 0$, was applied. The fluid phase was discretized with Lagrange P_2P_1 elements, i.e. Lagrange elements with quadratic interpolation for the velocity field and linear interpolation for the pressure field, while Lagrange linear elements were used for volume fraction of the solid phase. The Galerkin method was used to discretize the equations with anisotropic diffusion. The Generalized-α method [12] was used as time-advancing algorithm. An adaptive time stepping approach was employed to ensure a proper resolution of the transient flow field.
Simulations show the significant role played by secondary flow in the RBCs migration process. In regions of marked curvature like the CCA, the ICA sinus, the iliac arteries, and for this particular case also the abdominal aorta secondary flows convecting RBCs from the inner curvature wall to the outer curvature wall are present, see Figures 1 and 2. Shear-induced migration of RBCs lowers the wall hematocrit value by moving RBCs towards the core flow while secondary flows enhance or dampen the migration. In the stenosis, instead, the drastic reduction in hematocrit is due to the strong shear layer formed in the narrowed passage area, hence due to pure shear-induced migration.

3 CONCLUSIONS

RBCs are the main oxygen carrier, transporting it as oxyhemoglobin molecules; oxygen availability to the underlying vessel wall is linked to wall hematocrit values [4]. In this work the shear-induced migration of RBCs in the abdominal aorta and in the carotid artery has been investigated using Phillips' model [41]. The presented results show the importance of secondary flow in the RBCs migration process. In regions of marked curvature like the CCA, the ICA sinus, the iliac arteries, and for this particular case also the abdominal aorta secondary flows convecting RBCs from the inner curvature wall to the outer curvature wall are present, where the initial migration away from the wall is caused by the shear-induced motion. A correlation emerged between RBCs migration and regions prone to atherosclerosis, namely the iliac arteries, the external wall of the ICA sinus and the carotid stenosis. The decreased wall hematocrit leads to a reduced oxyhemoglobin availability in the near wall region and this decrease can result, following [4], in a decrease of the oxygen Sh number and a worsening of the hypoxic conditions. The present results are in line with published results showing that secondary flow were able to convect oxygen diffused in plasma away from the outer wall [14].

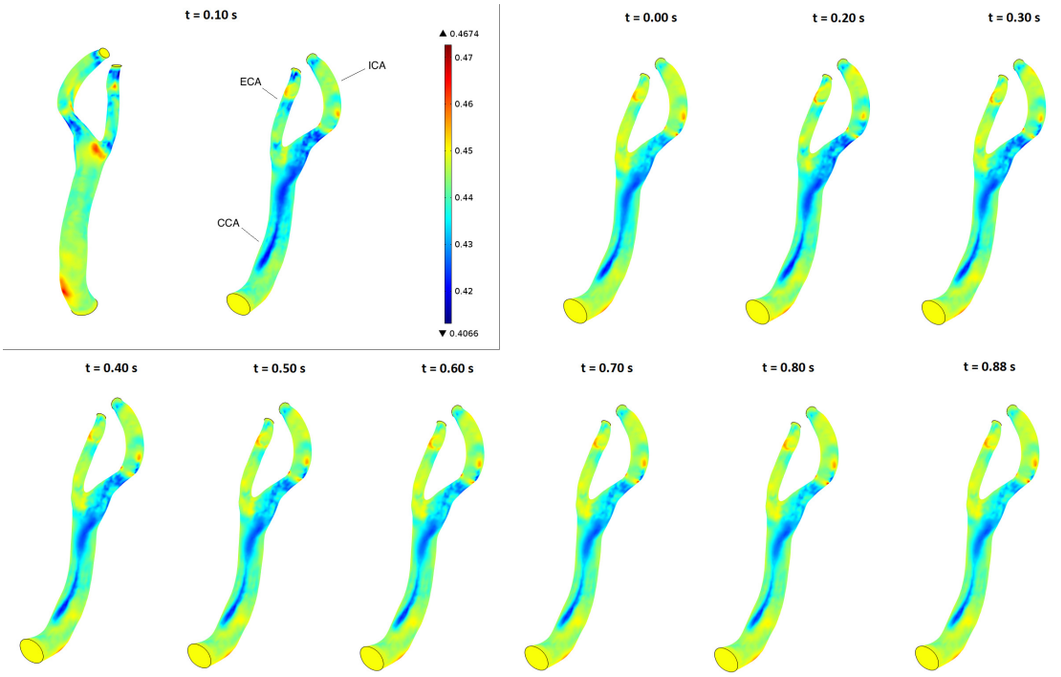

Figure 1: Wall hematocrit in the patient-specific normal carotid bifurcation during the cardiac cycle, internal wall view. Inset: internal and external wall view at t = 0.30 s. RBCs' migration is clearly observed at the outer wall, the inner curvature wall, of the ICA sinus and on the inner curvature wall of the CCA.

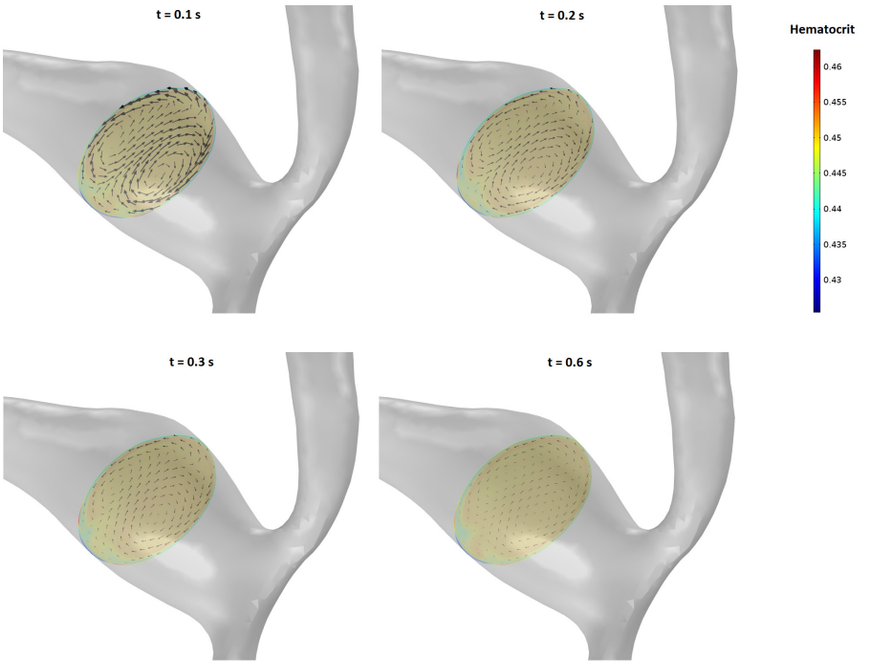

Figure 2: In-plane velocity vectors on a plane normal to the centerline in the carotid sinus of the stenotic carotid bifurcation at four time steps during the cardiac cycle, plane contours colour-coded with the hematocrit value. Secondary flow is seen in all the four times, and is present throughout the cardiac cycle (not shown).

REFERENCES

[1] J. R. Abbott, N. Tetlow, A. L. Graham, S. A. Altobelli, E. Fukushima, L. A. Mondy and T. A. Stephens. Experimental observations of particle migration in concentrated suspensions: Couette flow. *J. Rheol.*, 35:773–794, 1991.

[2] P. Bagchi. Mesoscale simulation of blood flow in small vessels. *Biophysical Journal*, 92:1858–1877, 2007.

[3] P. A. M. M. Aarts, S. T. van den Broek, G. W. Prins, G. D. C. Kuiken, J. J. Sixma and R. M. Heethaar. Blood platelets are concentrated near the wall and red blood cells, in the center in flowing blood. *Arterioscler. Thromb. Vasc. Biol.*, 8:819–824, 1988.

[4] J. A. Moore and C. R. Ethier. Oxygen mass transfer calculations in large arteries. *Journal of Biomechanical Engineering*, 119:469-475, 1997.

[5] J. M. Tarbell. Mass transport in arteries and the localization of atherosclerosis. *Annu. Rev. Biomed. Eng.*, 5:79–118, 2003 (doi:10.1146/annurev.bioeng.5.040202.121529).

[6] D. Quemada. Rheology of concentrated disperse systems II. A model for non-Newtonian shear viscosity in steady flows. *Rheol. Acta*, 17:632–642, 1978.

[7] R. J. Phillips, R. C. Armstrong, R. A. Brown, A. L. Graham and J. R. Abbott. A constitutive equation for concentrated suspensions that accounts for shear-induced particle migration. *Phys. Fluids A*, 4:30–40, 1991.

[8] R. Rao, L. Mondy, A. Sun and S. Altobelli. A numerical and experimental study of batch sedimentation and viscous resuspension. *International Journal for Numerical Methods in Fluids*, 39:465–483, 2001.

[9] C. Mills, I. Gabe, J. Gault, D. Mason, J. Ross, E. Braunwald et al. Pressure-flow relationships and vascular impedance in man. *Cardiovasc. Res.*, 4:405-417, 1970.

[10] A. S. Les, S. C. Shadden, C. A. Figueroa, J. M. Park, M. M. Tedesco, R. J. Herfkens, R. L. Dalman and C. A. Taylor. Quantification of hemodynamics in abdominal aortic aneurysms during rest and exercise using magnetic resonance imaging and computational fluid dynamics. *Ann. Biomed. Eng.*, 38:1288–1313, 2010.

[11] S.-W. Lee, L. Antiga, J. D. Spence and D. A. Steinman. Geometry of the carotid bifurcation predicts its exposure to disturbed flow. *Stroke*, 39:2341-2347, 2008.

[12] K.E. Jansen, C.H. Whiting, and G.M. Hulbert. A generalized-α method for integrating the filtered Navier-Stokes equations with a stabilized finite element method. *Comput. Meth. Appl. Mech. Eng.*, 190:305–319, 2000.

[13] P. Deuflhard. A modified Newton method for the solution of ill-conditioned systems of nonlinear equations with application to multiple shooting. *Numerische Mathematik*, 22:289–315, 1974.

[14] S. Tada and J. M. Tarbell. Oxygen mass transport in a compliant carotid bifurcation model. *Annals of Biomedical Engineering*, 34:9,13891399, 2006 (doi:10.1007/s10439-006-9155-z).

3rd International Conference on Computational and Mathematical Biomedical Engineering – CMBE2013

16-18 December 2013, Hong-Kong

P. Nithiarasu and R. Löhner (eds)

Physical and numerical aspects of vascular remolding with application to Abdominal Aortic Aneurysms

T.Christian Gasser* and Giampaolo Martufi*,**

*KTH Solid Mechanics, Royal Institute of Technology (KTH), Stockholm, Sweden
**Department of Civil Engineering, University of Calgary, Canada

SUMMARY

The formation of an Abdominal Aortic Aneurysms (AAA), i.e. the progressive dilatation of the infrarenal aorta, is the most common aortic pathology that requires clinical attention. Computational biomechanical models have been suggested to study AAAs and to assist the clinical decision making process. Despite that quasi-static simulations have been successfully launched, AAA models require significant further development to realistically predict the development of this disease. Specifically, the inherent property of vascular tissue to adapt to mechanical and biochemical environments remains a challenging modeling task. This presentation applies our recently proposed collagen turn-over model to study aneurysm expansion. To this end a multi-scale constitutive description is integrated in a Finite Element environment and coupled to adaptive time stepping. The outlined approach leads to a stable numerical analysis that predicts basic features of the mechanical and histological properties of the AAA wall.

Key Words: *vascular tissue, remodeling, constitutive description, aneurysm.*

1 INTRODUCTION

Mechanical stress and deformation influence vascular cell physiology and play a key role in explaining the origin and progression of vascular pathology. Consequently, biomechanical research might help to better understand and more effectively treat vascular diseases. Specifically, the formation of an Abdominal Aortic Aneurysms (AAA), i.e. the progressive dilatation of the infrarenal aorta based on proteolytic degradation of elastin and collagen in the wall, is the most common aortic pathology that requires clinical attention. If untreated AAAs enlarge and eventually rupture, which often leads to death. The recommended aortic aneurysm management is ultrasound surveillance until the aortic diameter reaches 5-5.5cm when repair, either open or

endovascular (EVAR), is offered. However, clinical studies showed also that a biomechanical rupture risk assessment could improve this intervention criterion [2,4,7].

Biomechanical simulations have to face many challenges [9], and one critical part is reconstructing patient-specific geometries from available medical modalities, like Computer Tomography-Angiography (CT-A). In addition vascular tissue is highly deformable, anisotropic, non-linear and inelastic. Despite that some phenomenological models successful capture the macroscopic mechanical properties of vascular tissue, they cannot allocate stress to the different histological constituents in the vascular wall. In contrast, histomechanical constitutive models [3,5,6] overcome this limitation, and address micro-structural components individually. Most importantly, they naturally provide an interface to incorporate evolution equations for extracellular matrix (ECM) proteins and cells. Specifically, rate equations for elastin, collagen and vascular SMCs were used to account for the remodeling properties of the vascular wall [5]. Motivated by the aneurysmatic loss of elastin and SMC, it was demonstrated that irreversible AAA growth can successfully be modeled by the exclusive turnover of collagen [8].

2 MAIN BODY

Multi-scale constitutive description. A histo-mechanical constitutive model for vascular tissue is used, where collagen fibers are assembled by proteoglycan (PG) cross-linked collagen fibrils (CFPG-complex) and reinforce an otherwise isotropic matrix material, see Figure 1 (left). Each collagen fiber is assembled by a bundle of collagen fibrils mutually interconnected by PG-bridges that provide interfibrilar load transition. The fiber's referential direction is denoted by the unit direction vector $\boldsymbol{M}$ and multiplicative kinematics account for the straightening and stretching of collagen fibrils [8]. Finally, an orientation density function ρ captures the spatial organization of collagen fibers in the tissue [6].

Mechanical stimulus. We assumed that fibroblast cells sense the state of strain and continuously produce and degrade collagen fibrils towards achieving a homeostatic collagen stretch λ_{ph}. Specifically, the turnover of collagen fibrils is mediated by a mechanical stimulus $\xi(\boldsymbol{M}) = \lambda(M)/\lambda_{\mathrm{ph}} \rightarrow 1$ [8]. Hence, for $\xi > 1$, the existing collagen is stretched too much, such that in total more collagen is required along the direction $\boldsymbol{M}$ in order to reach homeostasis. Equivalently, for $\xi < 1$, the collagen turnover needs to slow down to reach homeostasis through a net loss of collagen.

Turnover of collagen. Collagen fibers are dynamically deposited and removed in the current configuration [8]. Specifically, it is assumed that collagen degrades isotropic according to $\dot{\rho} = \eta\rho$, where η defines the time-scale of the degradation process and ρ is the total collagen density. This relation is independent from the orientation $\boldsymbol{M}$ and the local strain, such that degrading collagen is purely time-based. In contrast, for a particular direction $\boldsymbol{M}$, the production of collagen fibrils is related to the stimulus $\xi(\boldsymbol{M})$ and reads $\dot{\rho}(\boldsymbol{M}) = \min[\eta\rho\xi(\boldsymbol{M});\ \dot{\rho}_{\max}]$. Here, $\dot{\rho}_{\max}$ denotes the maximum collagen production rate that reflects that fibroblasts can only produce a certain amount of collagen in time.

Finite Element implementation. The model has been implemented into FEAP (University of California at Berkeley, US) at the Gauss-point level of a Q1P0 mixed finite element formulation. A micro-sphere approach was followed, and the integration over the unit sphere was carried out by spherical *L*-designs, which allowed the exact spherical integration of polynoms of degree *L* with $N = (L + 1)2$ integration points. An adaptive time stepping algorithm was used, which related the size of the time increment to the maximum of the collagen increment, i.e. to $\max[\Delta\rho]$ of the whole computational domain.

Patient-specific geometry acquisition and parameter estimation. Patient-specific AAA geometry was extracted from Computer CT-A using A4clinics Research Edition (VASCOPS GmbH, Austria) based on an operator insensitive segmentation with deformable models [1], see Figure 1 (right). Constitutive model parameter were either estimated from the literature or extracted from our patient follow-up data [10]. Here, patients with small AAAs were followed up with CT-A for in average one year, and the expansion of the aneurysm was measured at planes perpendicular to the luminal center line.

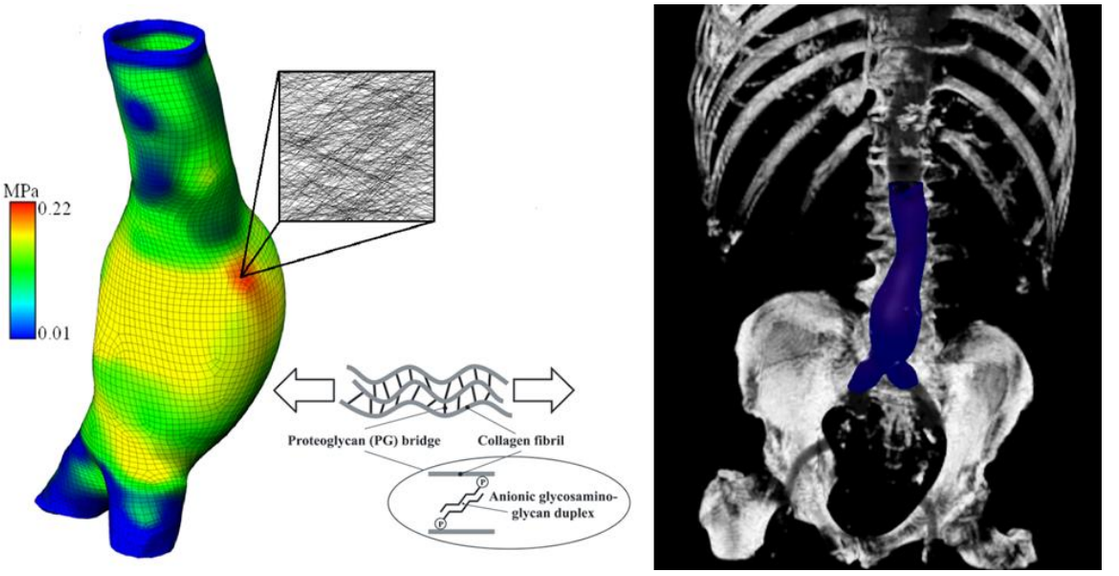

Figure 1: Multi-scale constitutive description of the Abdominal Aortic Aneurysm wall (left) and operator-insensitive reconstruction of a patient-specific AAA geometry from clinical image data (right).

3 CONCLUSIONS

A multidisciplinary approach is central to the development of a meaningful vascular simulation model. Robust and physiologically relevant constitutive models, where specifically the inherent property of vascular tissue to adapt to mechanical and biochemical environments is appropriately addressed, are mandatory for many applications. We proposed a multi-scale histomechanical AAA wall model that is able to

link the macroscopic mechanical strain with collagen turnover at the tissue's cellular level, and vice versa. The model could be successfully calibrated to match the growth of small AAAs, which were followed-up for one year. However, a rigorous validation against experimental data would be crucial to further explore the model's descriptive and predictive capabilities. Most important from a clinical perspective; it needs to be established whether or not the proposed active wall model can improve the AAA rupture risk assessment by replacing currently applied passive wall models.

REFERENCES

[1] M. Auer and T.C. Gasser, Automatic reconstruction and finite element generation of abdominal aortic aneurysms, IEEE Trans. Med. Imag. 29, 1022-1028, 2010.

[2] M. F. Fillinger, M. L. Raghavanand S. P. Marra, J-L-Cronenwett, and F. E. Kennedy. In vivo analysis of mechanical wall stress and Abdominal Aortic Aneurysm rupture risk. J. Vasc. Surg., 36, 589-597, 2002.

[3] T.C. Gasser, S. Gallinetti, X. Xing, C. Forsell, J. Swedenborg, and J. Roy. Spatial orientation of collagen fibers in the Abdominal Aortic Aneurysm's wall and its relation to wall mechanics. Acta Biomat. 8, 3091-3103, 2012.

[4] T.C. Gasser, M. Auer, F. Labruto, J. Swedenborg and J. Roy. Biomechanical rupture risk assessment of abdominal aortic Aneurysms. Model complexity versus predictability of Finite Element Simulations, Europ. J. Vasc. Endovasc. Surg. 40, 176-185, 2010.

[5] J.D. Humphrey and K.R. Rajagopal. A constrained mixture model for growth and remodeling of soft tissues. Math. Models Methods Appl. Sci. 12, 407, 2002.

[6] Y. Lanir. Constitutive equations for fibrous connective tissues. J. Biomech. 16, 1-12, 1983.

[7] A. Maier, M.W. Gee, C. Reeps, J. Pongratz, H.H. Eckstein, W.A. Wall. A comparison of diameter, wall stress, and rupture potential index for abdominal aortic aneurysm rupture risk prediction. Ann. Biomed. Eng. 38, 3124-3134, 2010.

[8] G. Martufi and T.C. Gasser. Turnover of fibrillar collagen in soft biological tissue with application to the expansion of abdominal aortic aneurysms. J. R. Soc. Interface, 9, 3366–3377, 2012.

[9] G. Martufi and T. C. Gasser. Review: The role of biomechanical modeling in the rupture risk assessment for abdominal aortic aneurysms. ASME J. Biomech. Eng. 135, 021010. doi: 10.1115/1.4023254, 2013.

[10] G. Martufi, J. Roy, J. Swedenborg, N. Sakalihasan, G. Panuccio, and T. C. Gasser. Multidimensional growth measurements of abdominal aortic aneurysms. J. Vasc. Surg. 58, 748-55. 2013.

Modelling of Pulse Wave Propagation in the Arterial Tree II

3rd International Conference on Computational and Mathematical Biomedical Engineering - CMBE2013
16-18 December 2013, Hong-Kong
P. Nithiarasu and R. Löhner (Eds.)

Including gravitational stress in a blood pressure wave propagation model for cardiovascular space physiology

C. Leguy[⋆,⋆⋆], J. Keijsers[⋆,§], W. Huberts[†], A. Narracott[‡], J. Rittweger[⋆] and F. van de Vosse[§]
[⋆] German Aerospace Center (DLR), Cologne, Germany, carole.leguy@dlr.de
[⋆⋆] Simon Fraser University, Vancvouer, Canada
[§] Eindhoven University of Technology, Eindhoven, The Netherlands
[†] Maastricht university, Maastricht, The Netherlands
[‡] University of Sheffield, Sheffield, UK

SUMMARY

Human factors remain an important issue for long term space flight. In particular, a better understanding of the response of the cardiovascular system to changes in orthostatic stress is crucial for the development of better countermeasures for astronauts. The goal of this study is to better characterize blood fluid shift during orthostatic stress using 1D pulse propagation model that will includes the effects of gravity on the arterial and venous system. Effects of gravity and vein collapsible properties were implemented in a 1D pulse wave propagation model. For single artery/vein model, we have shown that the model is able to simulate hydrostatic pressure and qualitatively reproduce increased arterial blood volume flow after a muscle contraction that is an influential phenomenon in orthostatic tolerance via increased venous return. To go forwards to a qualitative estimate of in vivo data, a model of the full circulation has to be considered and peripheral vascular regulation has to be implemented. We aim at a better represention of physiological responses and provide new information about the relative importance of the different phenomena involved in fluid shift towards the lower body.

Key Words: *wave propagation model, venous system, hydrostatic pressure, muscle pump.*

1 INTRODUCTION

Human body limitations will be the most important issues for long term space missions. Cardiovascular deconditioning (the adaptation of the cardiovascular system to less a demanding environment) is one of the most important adaptations to space. Astronauts follow physical training to reduce cardiovascular deconditioning. However, they can still suffer from orthostatic intolerance when landing. To improve countermeasure programs, a better understanding of the response of the cardiovascular system to changes in hydrostatic pressure is crucial. In particular, a better understanding of fluid redistribution and blood pooling to the lower limbs is essential.

Orthostatic stress to the cardiovascular system can be generated with ground facilities either with Lower Body Negative Pressure (LBNP), tilt table, short arm human centrifuge or parabolic flight. Most physiological measurements that can be performed non-invasively during orthostatic stress tests are arterial parameters as blood pressure and ultrasound that can be used to assess arterial blood flow velocity and wall distension. To obtain quantitative data from the venous system is more laborious because of its lower pressure and blood flow velocity. This hampers the assessment

and analysis of the fluid shift towards the venous system and motivates a modeling approach. Finite element models as 1D wave propagation would allow simulating the entire arterial and venous system while keeping low computational time and flexibility. Using a comprehensive physiological data-set under orthostatic stress as input, a 1D wave propagation system would allow going beyond measured parameters and better characterizing fluid shift toward the lower body especially within the venous system. The goal of this reseach project is to better characterise blood fluid shift during orthostatic stress by combining hemodynamics parameters during orthostatic stress and a 1D pulse wave propagation model that will include the effects of gravity on the arterial and venous system.

2 PHYSIOLOGICAL BACKGROUND

Cardiovascular responses to orthostatic stress have been studied under 45 mmHg LBNP and 70 degrees Head Up Tilt (HUT) [1]. Muscle pump effect that is an influential phenomenon in orthostatic tolerance via increased venous return and tissue blood perfusion was used to study venous refilling after they have been emptied by the action of the calf muscle. The in vivo data demonstrates that muscle pump effect and sudden changes in gravitational stress dramatically increases the perfusion of the lower limb femoral artery with an initial blood volume flow (BVF) increased by 6 folds in average and characteristic half-time decay in the order of 5 seconds. It can be assumed that the increased BVF within the arterial side is generated by an increase in the pressure difference across the capillary bed after HUT and LBNP whereas hyperhemia vasodilation may increase further BVF after muscle contraction. Unfortunately, these data do not allow determining the relative importance of the venous valves, perfusion pressure (arterial/venous) and vascular bed resistance. However wave propagation system can be used to further characterized blood fluid shift by simulated hemodynamical conditions within the venous system.

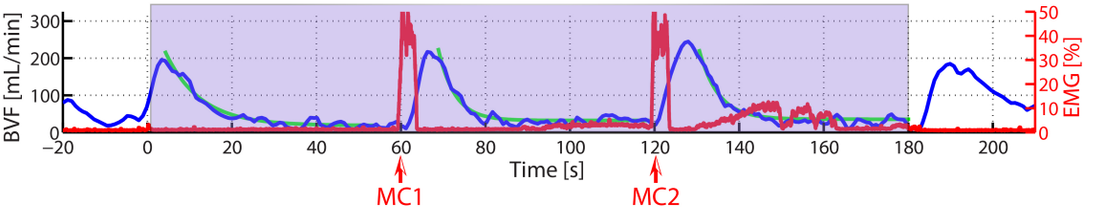

Figure 1: Blood volume flow in the femoral artery after a 70 degree haed up tilt (grey area) and Muscle Contraction (MC1 and MC2). EMG of the calf muscle is represented in red [1].

3 METHODS

After applying orthostatic stress, blood volume flow in the femoral artery is strongly increased due to the increased perfusion pressure between the arterial and venous system. The increase is due to the hydrostatic component immediately generated on the arterial side in the legs whereas closing the venous valves will reduce pressure in the venous side. To simulate the former physiological response both gravity, an appropriate pressure-volume relationship of the veins and the venous valves need to are implemented.

A 1D wave propagation model based on Bessems *et al* [2,3] is used, and gravitational acceleration

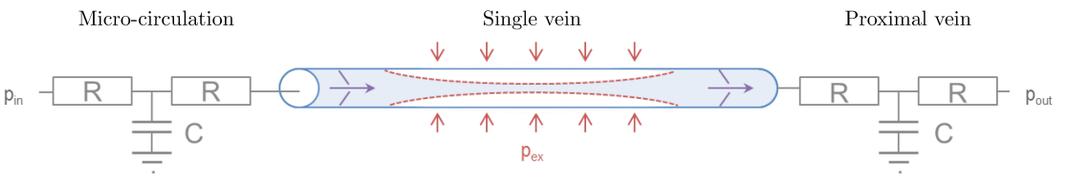

Figure 2: Schematic representation of the 1D finite element model.

term is added to the momentum balance equation such that

$$\frac{\rho}{A}\frac{\partial q}{\partial t} + \frac{\rho}{A}\frac{\partial}{\partial z}\frac{q^2}{A} + \frac{\partial p}{\partial z} = \frac{2}{a}\tau_\omega + \rho g \tag{1}$$

with ρ the blood density, A the vessel cross-sectional area, q the blood volume flow, z the longitudinal coordinate and g the gravity.

A non-linear relationship is used to define vein's constitutive low that takes into account their collapsibility properties.

Based on the collapsible tube model proposed by Shapiro *et al* [4] and the arctangent model of Langewouters *et al* [5] , the following formulations are used for cross-sectional area and compliance:

$$A(p_{tr}) = A_m\left(\frac{1}{2} + \frac{1}{\pi}\tan^{-1}\left(\frac{p_{tr}-p_0}{p_1}\right)\right) \text{ and } \mathrm{C(p_{tr})} = \frac{\mathrm{A_m}/\pi \mathrm{p_1}}{1+\left(\frac{\mathrm{p_{tr}}-\mathrm{p_0}}{\mathrm{p1}}\right)^2}, \tag{2}$$

where A_m is the maximum cross-sectional area, p_{tr} is the transmural pressure, p_0 is the transition point and p_1 determines the slope of the transition from collapsed to open. p_0 is set to zero and p_1 is varied to test the model.

The effects of muscle contraction are simulated by increasing external pressure p_{ex} up to 50 kPa. Finally, venous valves are implemented using a high resistive element. First, a model with a single artery and vein was implemented, see Figure 2. The effects of venous valves are simulated during a 70 degree Head Up Tilt (HUT) and muscle contraction.

4 RESULTS

Currently, the full model is able to simulate the effect of gravitational stress for the entire arterial system. When simulating a 70 degree head up tilt, a linear hydrostatic pressure gradient is found. These pressure changes induce variations in cross-sectional area, with a 14% increase in the femoral artery and a decrease of 5% in the common carotid artery.

The effects of venous valves and muscle contraction were simulated for a single artery and vein configuration. It is shown that the presence of valves, by preventing backflow, increases the outflow induced by the muscle contraction by 30%. This emptying of the vein during the contraction phase induced an extra blood volume flow coming from the arterial system (as measured in the former in vivo study) of 40 and 44 ml for a supine and tilted position, respectively.

5 CONCLUSION

The goal of this study is to better characterize blood fluid shift under orthostatic stress using in vivo data and 1D wave propagation model. Hydrostatic pressure has been simulated in a 1D wave

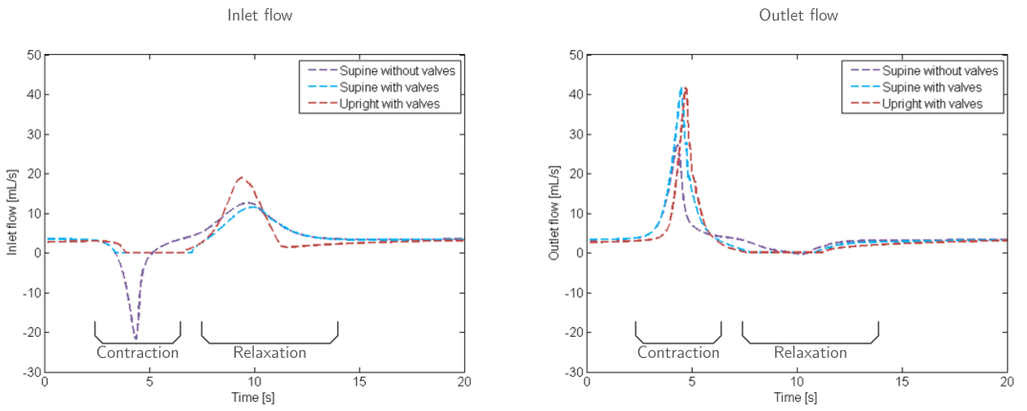

Figure 3: Inlet and outlet blood volume flow during and after muscle contraction.

propagation system of systemic arteries and corresponds to in vivo assessments. A collapsible tube model low and valves elements have been used for a single vein. Muscle contraction was simulated by increasing external pressure. Increase in venous outflow (venous return) during contraction and increased arterial inflow (refilling of the vein) during the relaxation phase have been simulated. We have shown that the model is able to quantitatively reproduce in vivo arterial BVF response after muscle contraction. However, the obtained blood volume flow increase is lower than the one measured in vivo. This discrepancy should come from the fact that our model does not take into account the full hydrostatic column that is present in the lower legs. An integration of the venous model to a systemic representation is needed; it will additionally allow simulating the effect of tilting and LBNP. Furthermore, as in vivo data suggest, vasodilation of the capillary bed after muscle contraction plays an important role in the large blood volume flow increase. Thus regulatory mechanism of the capillary bed vascular should be implemented. This future development should allow to better represent in vivo obtained measurements and provide new information about the relative importance of the different physiological phenomena in fluid shift towards the lower body. In the future, the validity of the former model will be further tested against in vivo data provided during short arm centrifuge and parabolic flight experiments that will provide an extended range of physiological-responses while human performance is pushed to the limit during space physiology studies.

REFERENCES

[1] C.A.D. Leguy, L.E.J. Beck, J. Kummel, J. Zange, B. Ganse, J. Rittweger and A.P. Blaber, Assessment of muscle pump dynamics under orthostatic stress in the lower limbs, 19^{th} *Human in space symposium*, Cologne, Germany, July 2013.

[2] D. Bessems, M.C.M. Rutten, F.N. van de Vosse, *A Wave Propagation Model of Blood Flow in Large Vessels Using an Approximate Velocity Profile Function*, J. Fluid Mech., Vol. **580**, 145-168, 2007.

[3] W. Huberts, A. Bode, J.W. Kroon, R.N. Planken, J.H.M. Tordoir, F.N. van de Vosse, E.M.H. Bosboom, *A pulse wave propagation model to support decision-making in vascular access planningg in the clinic*, Med. Eng. Phys., Vol. **34**, 233-248, 2012.

[4] A. Shapiro *Steady Flow in Collapsible Tubes*, J Biomech Eng, Vol. **99(3)**, 126-147, 1977.

[5] G.J. Langewouters, K.H. Wesseling, W.J.A. Goedhard, *The pressure dependent dynamic elasticity of 35 thoracic and 16 abdominal human aortas in vitro described by a five component model*, J Biomech, Vol. **18(8)**, 613-620, 1985.

3rd International Conference on Computational and Mathematical Biomedical Engineering - CMBE2013
16-18 December 2013, Hong-Kong
P. Nithiarasu and R. Löhner (Eds.)

Assessment of statistical variability in material parameters for 1D wave propagation in arterial networks

V. Eck*, J. Feinberg, H.P. Langtangen**, L.R. Hellevik***
*Division of Biomechanics, Department of Structural Engineering, NTNU, Trondheim, Norway
**Simula Research Laboratory, Fornebu, Norway

SUMMARY

In this paper we aim at assessing the impact of statistical variability in model parameters in 1D wave propagation simulations of arterial networks. Utilizing a stochastic collocation method together with a deterministic wave propagation model, we focus in particular on the impact of statistical variation in model parameters on forward and backward propagation waves in the ascending aorta. Results of pressure waves in the ascending aorta are presented with confidence intervals for the diastolic and systolic pressures for both total pressure and the forward propagating pressure.

Key Words: *Blood flow, 1D modeling, wave propagation, systolic hypertension, stochastic collocation method, sensitivity analysis, stochastic model parameters.*

1 INTRODUCTION

The research of arterial wave propagation modeling, initiated by Lambert [1], has evolved to a rather mature and established state as summarized by van de Vosse and Stergiopulos in [2]. Currently, 1D network models for arterial wave propagation have been argued to provide a means to diagnose disorders (see e.g. [3–12]) and to predict the outcome of medical interventions, and has thus the potential of serving as an integral part of a decision making tool for vascular interventions. Such 1D network models provide valuable physiological insight in patient specific modalities (morphometric rendering of the arterial network) in addition to serving as physiological boundary conditions for 3D CFD/FSI models [11, 13–19]. Further, a distributed approach is much less computational demanding than e.g. a 3D fluid-structure interaction approach, which is yet not feasible for larger vascular networks.

However, despite their potentials to predict useful clinical parameters, distributed models have so far mostly been used for research as analytical tools, as they provide realistic results for simulating a variety of physiological and pathological conditions. However, the distributed models have not yet been incorporated into clinical practice. This may in part be attributed to the large number of material parameters which must be mapped onto a complex geometrical representation of the vascular network, required to construct a patient specific model.

Further, the issue on data uncertainty and how patient specific a distributed 1D model has to be, has received little attention. One might improve the usefulness of distributed models if one could prove, by means of a sensitivity analysis, that many parameters could be "off the shelf" average values, and only a limited number of parameters need to be patient specific. Recently, some focus has been devoted to sensitivity analyses of the predicted variables with respect to variations in the model parameters. Most approaches have resorted to conventional sensitivity analysis and

Monte Carlo simulations [20–22], whereas others have used the computationally more efficient high-order stochastic collocation method based on the generalized polynomial chaos expansion [23, 24]. The former focused mostly on a small synthetic vascular network (with two generations of bifurcations), while the latter investigated a relatively complete arterial network with potential physiological and pathological implications.

In this work we present an assessment of statistical variation in material parameters in a distributed model of pressure and wave propagation in arterial networks, focusing on the impact of the forward and backward propagating waves.

2 METHODS AND RESULTS

We have previously developed a flexible 1D network model [25, 26], which has the fluid dynamical modalities as may be found in [13, 14] (Womersley number corrections for convective and frictional terms), a numerical scheme which is second order in time and space (MacCormack), and flexible non-reflective, Riemann-invariant boundary conditions which are similar to, but more generic than those found in [6, 7, 27]. The code has a very flexible network setup which supports a wide range of formats for network representation (CSV, XML) which are compatible with e.g. archTK which is another network simulators tailored for simulation of simulations of the hemodynamics in the arm [28].

We demonstrate how a MacCormack-discretization (explicit and second order in time and space) of the governing equations, combined with a stochastic collocation method, can successfully simulate the statistical variability in this type of hyperbolic equations.

We have validated our implementation with a simulation of a single bifurcation, which has been published by others previously [23] with a somewhat different approach. Results from a material parameter sensitivity analysis of the wave dynamics, in particular reflected waves (i.e. backward propagating), for a multiple bifurcating network will be presented. Typical results from such sensitivity analyses are shown in figure 1.

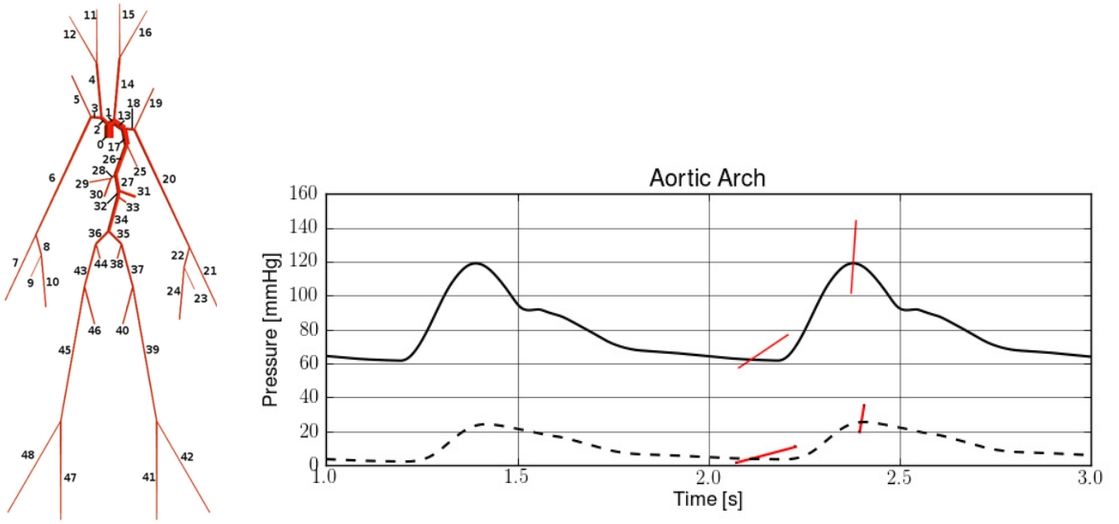

Figure 1: Left: vascular network of the arterial tree consisting of 49 vessels. Right: pressure waves in the ascending aorta with confidence intervals (solid red lines) for diastolic an systolic pressure; straight line: total pressure, dashed line: forward propagation pressure.

The results in figure 1 are calculated with absorbing boundary conditions for all terminating vessels, causing a non-physiological diastolic decay in the ascending aortic pressure. Simulations with lumped model boundary conditions at the terminating vessels will be presented at the conference.

3 CONCLUSIONS

In conclusion, we assess the impact of statistical variation in material parameters on wave dynamics ,e.g., reflected waves, in arterial systems. Particularly the reflected waves in the ascending aorta show not negligable changes in timing and amplitude ue to changed network model parameters down the tree. The effect of the parameter changes may be related to certain pathologies e.g. systolic hypertension.

REFERENCES

[1] J.W. Lambert. On the nonlinearities of fluid flow in nonrigid tubes. *Journal of the Franklin Institute*, 266(2):83–102, 1958. cited By (since 1996) 6.

[2] Frans N. van de Vosse and Nikos Stergiopulos. Pulse wave propagation in the arterial tree. *Annual Review of Fluid Mechanics*, 43(1):467–499, 2011. doi: 10.1146/annurev-fluid-122109-160730.

[3] Yunlong Huo and Ghassan S. Kassab. A hybrid one-dimensional/Womersley model of pulsatile blood flow in the entire coronary arterial tree. *Am J Physiol Heart Circ Physiol*, 292(6):H2623–2633, 2007. doi: 10.1152/ajpheart.00987.2006.

[4] J.J. Wang and K.H. Parker. Wave propagation in a model of the arterial circulation. *Journal of biomechanics*, 37(4):457–470, 2004.

[5] J Wan, B Steele, SA Spicer, S Strohband, GR Feijóo, TJ Hughes, and CA Taylor. A one-dimensional finite element method for simulation-based medical planning for cardiovascular disease. *Comput Methods Biomech Biomed Engin*, 5(3):195–206, Jun 2002.

[6] S Sherwin, V Franke, J Peiró, and K Parker. One-dimensional modelling of vascular network in space-time variables. *Journal of Engineering Mathematics*, pages 217–233, 2003.

[7] Luca Formaggia, Daniele Lamponi, and Alfino Quarteroni. One-dimensional models for blood flow in arteries. *Journal of Engineering Mathematics*, 47:251–276, 2003.

[8] Luca Formaggia, F Nobile, Alfino Quarteroni, and A Veneziani. Multiscale modelling of the circulatory system: a preliminary analysis. *Comput Visual Sci*, pages 75–83, 1999.

[9] MS Olufsen. Structured tree outflow condition for blood flow in larger systemic arteries. *ajp*, 45(1): H257–H268, 1999.

[10] N. Stergiopulos, D.F. Young, and T.R. Rogge. Computer simulation of arterial flow with applications to arterial and aortic stenoses. *J of biomechanics*, 25(12):1477–1488, 1992.

[11] RL Spilker, JA Feinstein, DW Parker, VM Reddy, and CA Taylor. Morphometry-based impedance boundary conditions for patient-specific modeling of blood flow in pulmonary arteries. *Ann Biomed Eng*, 35(4):546–559, Apr 2007.

[12] Thusitha Mabotuwana, Leo Cheng, and Andrew Pullan. A model of blood flow in the mesenteric arterial system. *BioMedical Engineering OnLine*, 6(1):17, 2007. ISSN 1475-925X. doi: 10.1186/1475-925X-6-17.

[13] David Bessems, Marcel Rutten, and Frans van de Vosse. A wave propagation model of blood flow in large vessels using an approximate velocity profile function. *J Fluid Mech*, 580:145–168, 2007.

[14] David Bessems. *On the propagation of pressure and flow waves through the patient specific arterial system*. PhD thesis, TU Eindhoven, September 2007.

[15] Karim Azer and Charles S. Peskin. A one-dimensional model of blood flow in arteries with friction and convection based on the womersley velocity profile. *Cardiovascular Engineering*, 7(2):51–73, 2007.

[16] Brooke N. Steele, Mette S. Olufsen, and Charles A. Taylor. Fractal network model for simulating abdominal and lower extremity blood flow during resting and exercise conditions. *Computer Methods in Biomechanics and Biomedical Engineering*, 10(1):39–51, Feb 2007.

[17] I. Vignon and C.A. Taylor. Outflow boundary conditions for one-dimensional finite element modeling of blood flow and pressure waves in arteries. *Wave motion*, 39:361–374, 2004.

[18] P.J. Blanco, J.S. Leiva, R.A. Feijóo, and G.C. Buscaglia. Black-box decomposition approach for computational hemodynamics: One-dimensional models. *Computer Methods in Applied Mechanics and Engineering*, 200(13-16):1389 – 1405, 2011. ISSN 0045-7825. doi: DOI:10.1016/j.cma.2010.12.006.

[19] P.J. Blanco, M.R. Pivello, S.A. Urquiza, and R.A. Feijóo. On the potentialities of 3d–1d coupled models in hemodynamics simulations. *Journal of biomechanics*, 42(7):919–930, May 2009.

[20] W. Huberts, C. de Jonge, W.P.M. van der Linden, M.A. Inda, J.H.M. Tordoir, F.N. van de Vosse, and E.M.H. Bosboom. A sensitivity analysis of a personalized pulse wave propagation model for arteriovenous fistula surgery. part a: Identification of most influential model parameters. *Medical Engineering & Physics*, 35(6):810 – 826, 2013. ISSN 1350-4533. doi: http://dx.doi.org/10.1016/j.medengphy.2012.08.013. URL http://www.sciencedirect.com/science/article/pii/S1350453312002408.

[21] C. A. D. Leguy, E. M. H. Bosboom, H. Gelderblom, A. P. G. Hoeks, and F. N. van de Vosse. Estimation of distributed arterial mechanical properties using a wave propagation model in a reverse way. *Medical Engineering & Physics*, 32(9):957–967, 11 2010. doi: http://dx.doi.org/10.1016/j.medengphy.2010.06.010. URL http://www.sciencedirect.com/science/article/pii/S1350453310001372.

[22] C.A.D. Leguy, E.M.H. Bosboom, A.S.Z. Belloum, A.P.G. Hoeks, and F.N. van de Vosse. Global sensitivity analysis of a wave propagation model for arm arteries. *Medical Engineering & Physics*, 33(8):1008 – 1016, 2011. ISSN 1350-4533. doi: http://dx.doi.org/10.1016/j.medengphy.2011.04.003. URL http://www.sciencedirect.com/science/article/pii/S1350453311000841.

[23] Dongbin Xiu and Spencer J. Sherwin. Parametric uncertainty analysis of pulse wave propagation in a model of a human arterial network. *Journal of Computational Physics*, 226(2):1385 – 1407, 2007. ISSN 0021-9991. doi: http://dx.doi.org/10.1016/j.jcp.2007.05.020. URL http://www.sciencedirect.com/science/article/pii/S0021999107002392.

[24] Peng Chen, Alfio Quarteroni, and Gianluigi Rozza. Simulation-based uncertainty quantification of human arterial network hemodynamics. *Int j numer method biomed eng*, 29(6):698–721, Jun 2013. ISSN 2040-7947 (Electronic). doi: 10.1002/cnm.2554.

[25] P.R. Leinan. *Biomechanical modeling of fetal veins. The umbilical vein and ductus venosus bifurcation*. PhD thesis, Norwegian University of Science and Technology:, Trondheim, 2012.

[26] Leif Hellevik, J. Vierendeels, T. Kiserud, N. Stergiopulos, F. Irgens, E. Dick, K. Riemslagh, and P. Verdonck. An assessment of ductus venosus tapering and wave transmission from the fetal heart. *Biomechanics and Modeling in Mechanobiology*, 8:509–517, 2009. ISSN 1617-7959. 10.1007/s10237-009-0155-4.

[27] Luca Formaggia, Daniele Lamponi, Massimiliano Tuveri, and Alessandro Veneziani. Numerical modeling of 1d arterial networks coupled with a lumped parameters description of the heart. *Comput Methods Biomech Biomed Engin*, 9(5):273–288, Oct 2006. ISSN 1025-5842 (Print); 1025-5842 (Linking). doi: 10.1080/10255840600857767.

[28] W Huberts, A S Bode, W Kroon, R N Planken, J H M Tordoir, F N van de Vosse, and E M H Bosboom. A pulse wave propagation model to support decision-making in vascular access planning in the clinic. *Med Eng Phys*, 34(2):233–248, Mar 2012. ISSN 1873-4030 (Electronic); 1350-4533 (Linking). doi: 10.1016/j.medengphy.2011.07.015.

3rd International Conference on Computational and Mathematical Biomedical Engineering – CMBE2013
16-18 December 2013, Hong-Kong
P. Nithiarasu and R. Löhner (Eds.)

Numerical Analysis of Blood Flow in the Dysplastic Circle of Willis Using One-dimensional Patient-Specific Model

Xunjie YU, Changjin JI, Ying HE*, and Junyuan CHEN
Department of Modern Mechanics, University of Science and Technology of China,
Mail Box 4, Hefei, 230027, China
*Email: yhe@ustc.edu.cn

SUMMARY

In this work, aiming at studying the impact of anatomical variations in the circle of Willis on the capacity of collateral blood supply, a computational scheme for constructing the patient-specific one-dimensional geometric models has been developed based on computerized tomography images. The lengths and diameters for different structures of circle of Willis (CoW) are extracted. Blood flow in the circle of Willis is modeled using one dimensional equations derived from axisymmetric Navier-Stokes equations for flow in elastic and compliant vessels.

Two frequently observed anatomical variations of the CoW (ACA, A1 aplasia and ACA,A1 hypoplasia) have been simulated. The results are compared with those of the complete and well-balanced CoW. The simulated results about the role of ACoA in the blood regulation are in agreement with the available data. However, the result of our patient-specific models show that the ACoA outward hypertrophic remodeling can compensate the blood flow in the contralateral side well, which is different from that obtained by the previous average anatomical geometric models.

Keywords: *The circle of Willis; Patient-specific modeling; Anatomical variation; Outward hypertrophic remodeling; 1D modeling*

1 INTRODUCTION

As the most important collateral pathways in the brain, the circle of Willis plays a critical role in adequately perfusing the brain. For the past decades, extensive modeling work of hemodynamics in CoW has been conducted. Ferrandez et al [1] carried out 2D simulation of blood flow in CoW with integration of a new active boundary condition to study the influence of blood autoregulation. They concluded that a missing or dysfunction of right A1 segment of anterior cerebral artery is the worst case from the view of outflow balance. Long et al. [2] performed 3D numerical studies of blood flow for exploring the relationship between different CoW configurations and stenosis severities of CCA. It is revealed that when the stenosis is not greater than 86%, the additional pathways are able to raise the ipsilateral MCA pressure considerably without reducing the flow perfusion.

Recently, Jou et al [3] demonstrated that cross-flow exists at every AcoA through investigation of different configurations of CoW with aneurysms. It is shown that after formation of the AcoA aneurysm, mean cross-flow appears to decrease by 22% with patent PcoAs and by 37% with occluded PCoAs. They further pointed that there exists some interactions between the geometry of AcoA and cerebral aneurysms. Xu et el [4] concluded from their numerical work as well that when the aneurysm is formed and grows, WSS and flow velocity gradually decreases, which suggests that A1 dysplasia/hypoplasia is potential risk in the formation of AcoA.

1D modeling is an effective method to study the effects of anatomical variations and occlusions on cerebral blood flows. In the work of Liang et al. [5] and Alastruey et al.[6] different

topological structures of CoW were employed to investigate the regulation mechanism of cerebral blood flow.

Currently, 1D modeling for CoW is mostly based on average anatomical data. Aiming at confirming the conclusion that a missing or dysfunctional A1 segment of ACA can lead to long-term blood flow reduction through efferent vessel, 1D numerical modeling using patient-specific structures of the CoW was conducted.

2 METHODS

Numerous papers discuss one-dimensional model for blood flow and pressure. We employed equations derived by Olufsen [7]. Predicting blood flow in a compliant vessel requires three governing equations, including mass, momentum, and state equations. They may be respectively defined as:

$$\frac{\partial A}{\partial t}+\frac{\partial q}{\partial x}=0 \tag{1}$$

$$\frac{\partial q}{\partial t}+\frac{\partial}{\partial x}\left(\frac{q^2}{A}\right)+\frac{A}{\rho}\frac{\partial P}{\partial x}=-\frac{2\pi\nu r}{\delta}\frac{q}{A}. \tag{2}$$

$$P(x,t)-P_0=\frac{4}{3}\frac{Eh}{r_0}\left(1-\sqrt{\frac{A_0}{A}}\right). \tag{3}$$

Where A is the cross-sectional area, q is the flow rate, P is the pressure, E is Young's modulus, h is the wall thickness, ν is kinematic viscosity, and δ is the boundary layer thickness. Three types of boundary conditions including inflow, outflow and bifurcation condition were established. The flow rate of the upper ascending aorta was applied as the inflow condition. At the bifurcations, the boundary conditions were represented by the conservation of mass flux and total pressure. The outflow condition is determined by Windkessel model, which is given by

$$\frac{\partial P}{\partial t}=R_1\frac{\partial q}{\partial t}-\frac{p}{R_2C}+\frac{q(R_1+R_2)}{R_2C} \tag{4}$$

where the total resistance $R_T=R_1+R_2$ and the total compliance C of vascular bed are obtained from the structured tree model of smaller arteries. Provided that the radii at the roots and terminals in smaller arterial trees are known, the geometry of the structured tree can be determined by the principal of minimum work. The root impedance is determined by the method of Olufsen [7]. The total resistance R_t for the truncated artery is assumed to be equal to the root impedance *Z(0,0)* of the structured smaller arterial tree and R_1 is assumed to be equal to $0.2R_T$. On the other hand, the total compliance of the smaller arterial tree is given by the sum of the compliances of the smaller arterial segments.

Three sets of patient-specific data have been obtained at the 1st affliated hospital of Anhui Medical Univeristy. The 3D geometries of CoW have been reconstructed from high-resolution CT images using Simpleware software package as shown in Fig.1. The daimeters of vessel segments were measured directly in the 3D models by Simpleware.

In order to get the lengths of vessels for 1D model, a scheme was developed to acquire the skeleton of CoW. The vessel regions in every slice were firstly extracted by threshold segmentation method . Subsequently, thinning filter of Simpleware was applied to the images interatively to get the barycenters of vessel regions. Since there are different braching directions for CoW, some barycenters of vessel regions may not represent those of vessel cross sections, especially in the vicinities of braching areas. The barycenters in these regions were re-searched manually as shown in the circle of Fig. 2a. After the barycenters of vessel cross sections along the flow directions were obtained (Fig. 2b), the adjacent points for every barycenter were identified by scanning the 3×3×3 cubic region. The skeleton of CoW was thus obtained by connnecting the adjacent points (Fig. 2c). The length measurements can be acquired along the centerline of every segment. Currently, the thinning process is not totally automatic, it may be improved by using a

robust approach for decomposing the biomedical geometries into tips, segments, and junctions, such as that proposed by Jiao et al. [8]. TIn the 1D model, 33 arterial segments were taken into consideration (Fig. 3), where the data for the arterial network of CoW were from the image measurements.

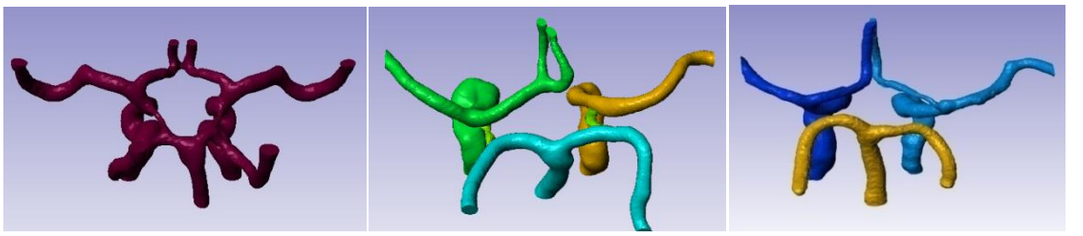

Fig. 1 3D models of CoW reconstruced from cerebral CT data
(a. Complete b. A1 aplasia,c. A1 hypoplasia)

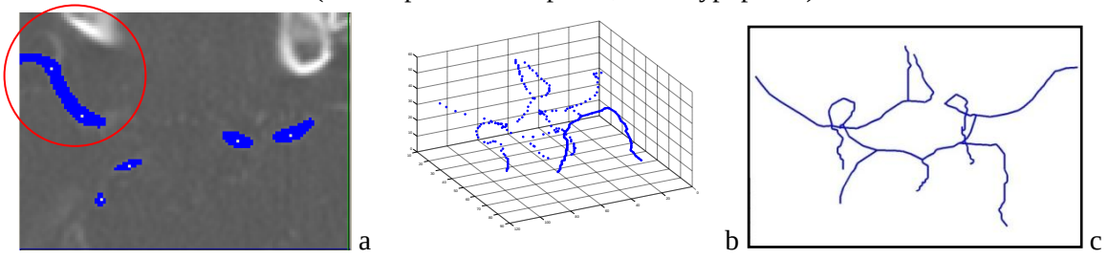

Fig. 2 a. Barycenters in the vessel regions of one slicing image
b. Coordinates of the barycenters extracted from the image data
c. Skeleton of the patient-specific CoW by connecting the adjacent points in Fig.2 b

3 RESULTS

Fig. 4 shows the blood flow waveforms in different vessels of complete CoW. It is seen that the flow rates from the left and right efferent arteries have not significant differences (Fig. 4a) and there is almost no flow passing through AcoA(Fig. 4b).

For comparison, The flow rates in the CoW with A1 aplasia were simulated when the radius of AcoA was changed from 0 to 1 mm. Fig. 5a illustrates the variation of the mean flow rate in AcoA with the change of its diameter. It is flound that when the radius is less than 0.3 mm or larger than 0.8 mm, the increasing of flow rate with radius is slow, but when the radius of AcoA is larger than 0.3 mm, the mean flow rate increases considerably. Fig. 5b and Fig. 5c give the flow rate of left and right ACA when the diameter of AcoA equals to 0.4 and 0.8 mm respectively. It can be seen that the flow rate in R. ACA is slightly lower when the radius of AcoA is 0.4 mm. If the radius of AcoA becomes 0.8 mm, the flow rates in the two sides have become almost the same. In the patient-specific model with A1 aplasia, the calibre of AcoA has been enlarged more than 0.8 mm to adequately compensate the reduction of flow in R. ACA. Hence, it is implied that even in the structure with A1 aplasia, the collateral capacity can be enhanced through the remodeling of AcoA.

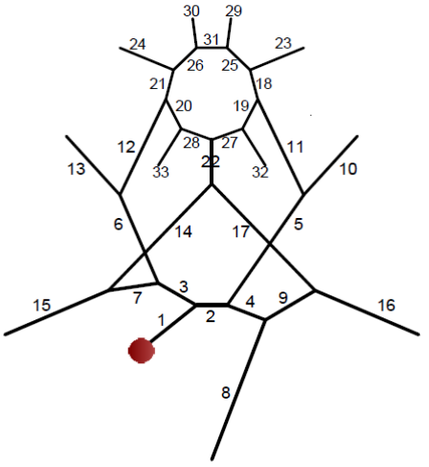

Fig. 3 1D Model of the Simulated Arterial Network

4 CONCLUSIONS

In this work, a computational scheme for constructing the patient-specific geometric models has been developed based on CT images and one-dimensional numerical analysis has been carried out. The simulated results for the CoW with A1 aplasia show that the ACoA outward hypertrophic remodeling can compensate the blood flow in the contralateral side well, which is different from that obtained by the previous average anatomical geometric models.

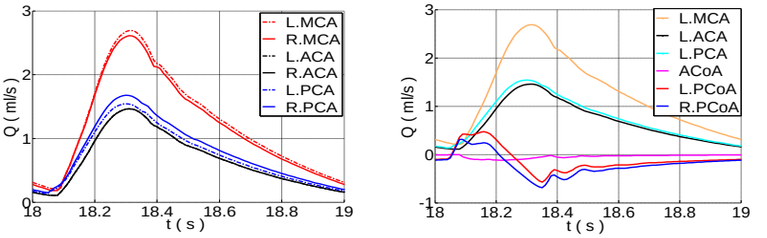

Fig. 4 Simulated flow waveforms in efferent arteries and communicating arteries for the complete CoW

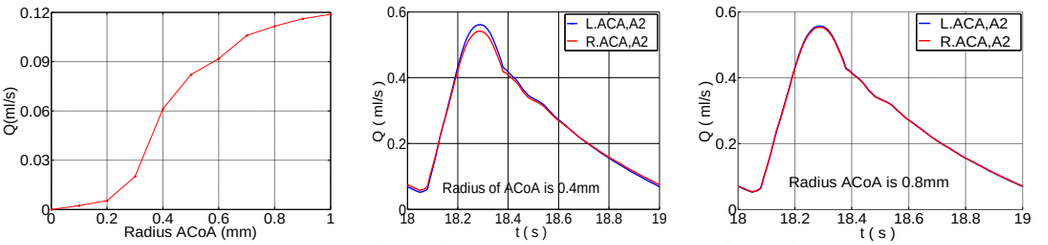

Fig. 6 (a) Mean flow rate in AcoA for different AcoA radius. (b) and (c) Flow waveforms in ACA, A2 segment while the radii of AcoA are 0.4 mm (b) and 0.8 mm (c) respectively

REFERENCES

[1] Ferrandez, A, David, T.， Brown， MD , Numerical Models of Auto-regulation and blood flow in the cerebral circulation *Comp. Meth. Biomech. Biomed. Eng.* , 5, 7-20, 2002,

[2] Long, Q., Luppi, L., Konig CS, Rinaldo,V., Das, SK, Study of the collateral capacity of the circle of Willis of patients with severe carotid artery stenosisby 3D computational modeling, *J. Biomech.*, 41, 2735-2742, 2008,

[3] Jou, LD, Lee, DH, Mawad, MZ, Cross-flow at the anterior communicating artery and implication in cerebral aneurysm formation, *J. Biomech.*, 43, 2189-2195, 2010,

[4] Xu, LY, Zhang Z., Wang H, Yu YQ, Contribution of the hemodynamics of A1 dysplasia or hypoplasia to anterior commnucating artery aneurysms: a three-dimensional numerical study, *J. Comput. Ass. Tomo.*, 36, 421-426, 2012,

[5] Alastuey, J, Parker, KH, Peiro J, Byrd, SM, Sherwin, SJ, Modeling of the circle of Willis to assess the effects of anatomical variations and occlusions on cerebral flows. *J. Bomech.*, 40, 1794-1805, 2007.

[6] Liang, FY, Fukasaku, K, Liu H., and Takagi S., A computational model study of the influence of the anatomy of the circle of Willis on cerebral hyperperfusion following carotid artery surgery . *BioMed. Eng. Online*, 10:84, 2011.

[7] Jiao XM, Einstein DR, Dyedov, V, Carson JP, Automatic identification and truncation of boundary outlets in complex imaging-derived biomedical geometries, *Med. Biol. Eng. Comp.*, 47, 989-999, 2009.

[8] Olufsen, M, Structured tree outflow condition for blood flow in larger systemic arteries, *Am. J. Physiol. Heart Circ. Physiol.*, 276, 257-268, 1999.

Standard Session IV

3rd International Conference on Computational and Mathematical Biomedical Engineering - CMBE2013
16-18 December 2013, Hong-Kong
P. Nithiarasu and R. Löhner (Eds.)

Large scale simulations in an extensive human upper respiratory tract.

A.M. Gambaruto*, H. Calmet*, A. Bates, R. Cetto**, H. Owen*, D.J. Doorly**, G. Houzeaux*, M. Vázquez***

*Computer Applications in Science & Engineering (CASE), Nexus I - Campus Nord UPC, Calle Jordi Girona 2, 2a. Planta, 08034 Barcelona, Spain, Email: hadrien.calmet@bsc.es; guillaume.houzeaux@bsc.es; raul.delacruz@bsc.es; mariano.vazquez@bsc.es

**Department of Aeronautics, Imperial College London, South Kensington Campus, London SW7 2AZ, UK, Email: a.bates11@imperial.ac.uk; raul.cetto10@imperial.ac.uk; d.doorly@imperial.ac.uk

SUMMARY

The respiratory tract is anatomically complex and effects a large number of physiological functions at a broad range of flow conditions. This study aims to provide high temporal and spatial resolution data for an extensive geometric domain of a healthy individual, spanning from the face exterior to the primary lung bifurcations. The adiabatic, incompressible, Newtonian Navier-Stokes equations are solved using the finite element method. Flow structures and description of the flow field are used to analyse the respiratory functions.

Key Words: *upper respiratory tract, extensive domain, high performance computing, form and function.*

1 INTRODUCTION

Numerical simulations of the human physiological system have permitted many aspects of the physiological state of an individual to be investigated. These simulations provide a deeper understanding of the highly intricate and optimised design that nature has endowed through evolutionary adaptation. In this work the upper human respiratory tract of a healthy individual is studied, as shown in Fig. 1. Specifically, different respiratory flow patterns are analysed to observe different functional aspects of the flow passages.

The upper respiratory tract is responsible for conditioning inspired air, hence prepare it for entering the lungs by adjusting the temperature and humidity, while also filtering the air to remove suspended particles such as dust. On expiration some of the temperature and humidity is recaptured by the nasal lining to reduce losses, and evacuation of deposited particles also occurs. Furthermore the nasal cavity is unique in that it contains the olfactory sensors.

In order to carry out these functions in a short time and for a large volume of air (typical breathing is approximately 10,000 l/day and 12-15 breaths/min, hence 0.5 l tidal-volume), in a short distance (in the order of 10cm for humans, and 1cm for smaller creatures such as mice), the anatomy of the airways, and especially the nasal cavity, is very complex. Furthermore the function of the upper respiratory tract must maintain it's efficiency despite the considerable variability of flow pattern: from a sniff or during exercise to a restful breathing cycle.

Appropriate stimulation and analysis of the computed results must address the mechanisms and performance of these functions, during different respiratory cycles.

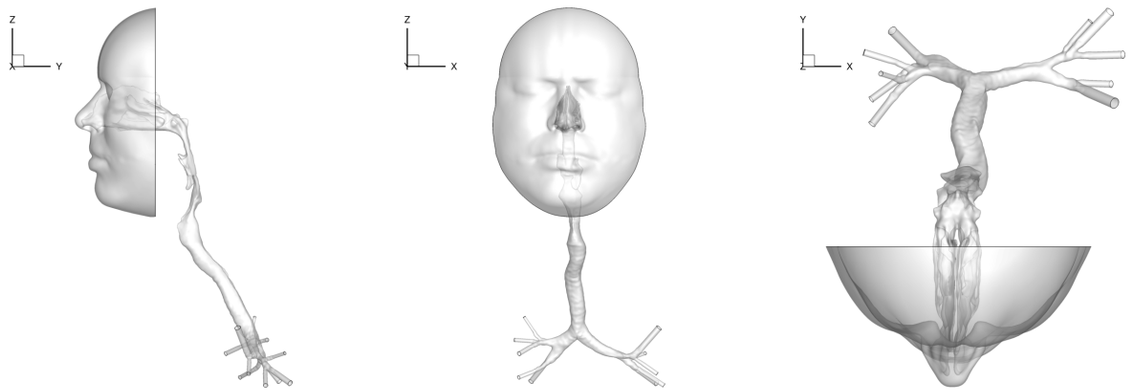

Figure 1: Sagittal, coronal and axial views of the computational domain. Note that the sinuses have been removed.

2 METHODS

The current work presents features of how the upper respiratory tract of a healthy individual functions, through use of finely resolved numerical simulations. The finite element computational method is employed to solve the incompressible, Newtonian Navier-Stokes equations. Simulations of particle transport and deposition and other measures of clinical relevance are presented, together with a detailed analysis of the fluid mechanics. The resolution is fine enough to account for the smallest flow features and provide information regarding turbulence intensity and modelling, that will be of interest for more practical numerical simulations on a coarser mesh. The simulations are performed on fine spatial (350M elements) and temporal (10^{-6} s) resolutions, taking advantage of supercomputing facilities. Some preliminary results are shown in Fig. 2.

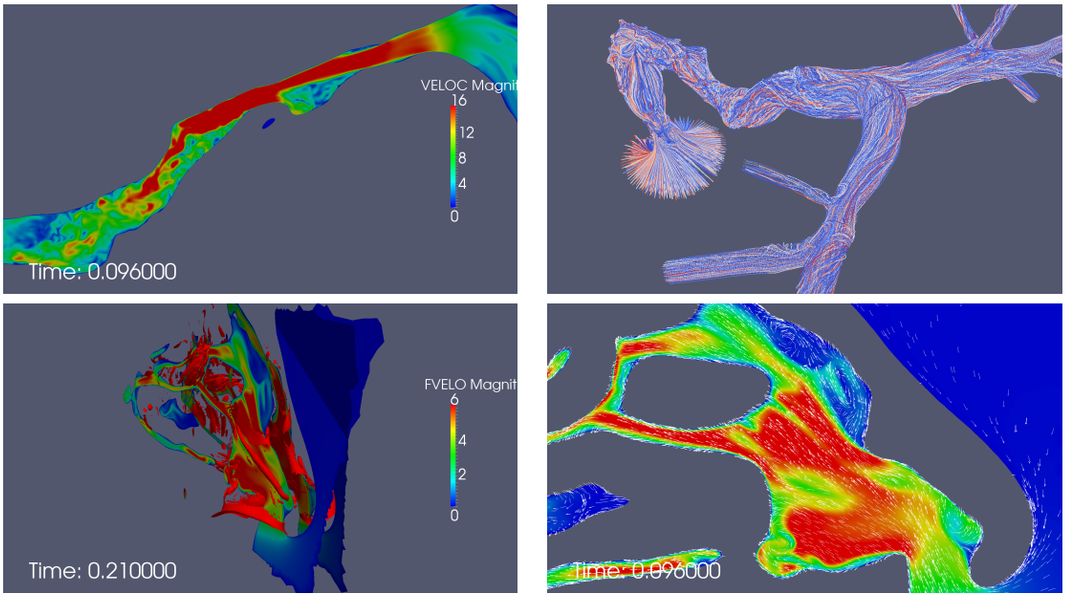

Figure 2: Simulation of upper respiratory tract of a healthy subject. Sectional cuts with velocity magnitude, particle traces, Q iso-surfaces.

3 CONCLUSIONS

Numerical simulations can provide a wealth of information for patient specific studies, which are not possible from in-vivo or experimental works alone. An anatomically accurate reconstruction of a healthy subject is used in order to probe and visualise the complex and interacting flow structures, and bring physiological relevance to the measures found. Results regarding turbulent flow structures is presented in order to validate future works with a reduced, and more feasible, mesh resolution. The results presented are unique, in that they include fine spatial and temporal resolutions, for an extensive computational domain of a healthy subject.

REFERENCES

[1] C.E. Rennie , K.A. Gouder, D.J. Taylor, N.S Tolley, R.C. Schroter, D.J. Doorly. Nasal inspiratory flow: at rest and sniffing, *International Forum of Allergy & Rhinology*, 1(2):128-135, (2011). J. Mynard and P. Nithiarasu, A one dimensional arterial blood flow model incorporating ventricular pressure, aortic valve and regional coronary flow using the locally conservative Galerkin (LCG) method, *Communications in Numerical Methods in Engineering*, 24, 367-417, 2008.

[2] D.J. Doorly, D.J. Taylor, A.M. Gambaruto, R.C. Schroter, N. Tolley. Nasal architecture: form and flow. *Phil. Trans. R. Soc. A*, 366(1879):3225-3246, (2008).

[3] A.M. Gambaruto, D.J. Taylor, D.J. Doorly. Decomposition and description of the nasal cavity form, *Ann Biomed Eng*, 40:1142-1159, (2012).

3rd International Conference on Computational and Mathematical Biomedical Engineering - CMBE2013
16-18 December 2013, Hong-Kong
P. Nithiarasu and R. Löhner (Eds.)

An immersed boundary method for patient-specific modelling of flow and aerosol deposition in the respiratory airways

Laura Nicolaou⋆ and Tamer A. Zaki⋆
⋆Department of Mechanical Engineering, Imperial College London, Exhibition Road, London SW7 2AZ, UK, laura.nicolaou-fernandez03@imperial.ac.uk and t.zaki@imperial.ac.uk

SUMMARY

An immersed boundary (IB) method for patient-specific modelling of flow in the respiratory airways is presented. No-slip conditions are enforced via momentum forcing and mass conservation at immersed boundaries is satisfied via a mass source term developed for moving walls. An iterative scheme to compute the forcing term implicitly reduces the errors at the boundary and enhances stability. In addition, the mass source term accurately accounts for airway movement during breathing, and reduces the spurious force oscillations which typically arise in IB simulations of moving body problems. The method is developed for use in a generalised curvilinear system, which is particularly useful in bioflow problems involving complex geometries. Flow in realistic extrathoracic airways is examined with this method.

Key Words: *immersed boundary, moving boundaries, curvilinear, respiratory airways.*

1 INTRODUCTION

Understanding the flow dynamics in the respiratory system is important in determining the efficiency of aerosolized drug delivery and the toxicity of airborne pollutants. Accurate and efficient prediction poses a challenge due to the complexity of the flow in the airways and the complexity of the airway geometries. Due to the bifurcating nature of the lung and the effect of the breathing cycle on the flow, patterns in the respiratory airways are complex even during quiet breathing. The flow remains turbulent in the mouth and throat and the larger airways, before extensive branching increases the total cross-sectional area and therefore reduces the gas velocity through each airway, causing laminarisation. In most of the tracheobronchial tree, the flow is intermittently turbulent with eddies forming at the branching points. Accurate solution of the flow field therefore motivates the use of direct numerical simulations (DNS) in order to resolve all the scales in the flow. Due to the high grid resolution requirements, it is desirable to adopt an efficient computational strategy. To this end, an immersed boundary method for curvilinear coordinates is developed, which allows the use of structured grids to model the complex patient-specific airways. Use of structured grids greatly simplifies the task of grid generation, particularly for moving airway boundaries and circumvents the need for remeshing at every time step which leads to more efficient computational algorithms. Compared to a Cartesian grid, curvilinear grids can further improve efficiency by minimising the number of grid points outside the fluid domain, can have a more natural alignment with the streamlines which is desirable for the accuracy of the solution, and can provide a better wall-normal resolution.

2 NUMERICAL METHOD AND RESULTS

The no-slip condition at the immersed boundary (i.e. the airway walls) is applied via a direct forcing approach, which consists in adding a momentum forcing term, $\boldsymbol{f}$, on the boundary and outside the lung geometry. The forcing ensures that the velocity at the airway walls satisfies the boundary conditions. A mass source/sink, q, is applied to cells containing the immersed boundary in order to ensure mass conservation. The equations are discretized on a staggered curvilinear grid using a finite volume scheme, following the method described in [1]. Time integration is performed using a second-order fractional step method. The diffusive terms are treated implicitly

using the Crank-Nicolson scheme and the non-linear convective terms are treated explicitly using an Adams-Bashforth scheme. The discretized equations are given by

$$\frac{\hat{\boldsymbol{u}} - \boldsymbol{u}^{n-1}}{\Delta t} = -\left(\gamma N(\boldsymbol{u}^{n-1}) + \delta N(\boldsymbol{u}^{n-2})\right) - \nabla p^{n-1} + \frac{1}{Re}\left(\alpha L(\hat{\boldsymbol{u}}) + \beta L(\boldsymbol{u}^{n-1})\right) + \boldsymbol{f}^n \quad (1)$$

$$\nabla^2 \phi^n = \frac{1}{\Delta t}\left(\nabla \cdot \hat{\boldsymbol{u}} - q^n\right) \quad (2)$$

$$\boldsymbol{u}^n = \hat{\boldsymbol{u}} - \Delta t \nabla \phi^n \quad (3)$$

$$p^n = p^{n-1} + \phi^n \quad (4)$$

where $N(\boldsymbol{u})$ are the convective terms, $L(\boldsymbol{u})$ are the implicit diffusive terms and $(\alpha, \beta, \gamma, \theta)$ are weighting coefficients which depend on the numerical scheme adopted. In our case, $\alpha = 3/2$, $\beta = -1/2$ for the Adams-Bashforth scheme and $\gamma = \theta = 1/2$ for the Crank-Nicolson scheme.

2.1 Momentum forcing term

The accuracy and stability of direct forcing methods used in conjunction with the fractional step algorithm depend on the computation of the forcing term. In the semi-implicit fractional step method, the velocities and forcing terms are coupled through the implicit diffusive terms. Kim et al. [2] proposed a solution which consisted in provisionally advancing the velocity field explicitly in order to compute the forcing term and then adding it to the semi-implicit momentum equations. However, this scheme introduces errors near the immersed boundary as the velocities are advanced implicitly but the forcing term is calculated explicitly. The error due to the explicit treatment of the diffusive terms in the calculation of $\boldsymbol{f}^n$ can render the scheme unstable in two scenarios: (i) the low-Reynolds-number flow in the terminal bronchioles; (ii) the turbulent flow in the extrathoracic airways where near-wall resolution can render the viscous stability constraint more restrictive.

The solution proposed herein consists in splitting the intermediate velocity equation into two steps,

$$\frac{\tilde{\boldsymbol{u}} - \boldsymbol{u}^{n-1}}{\Delta t} = \frac{1}{Re}\left(\alpha L(\tilde{\boldsymbol{u}}) + \beta L(\boldsymbol{u}^{n-1})\right) - G p^{n-1} - \gamma N(\boldsymbol{u}^{n-1}) - \theta N(\boldsymbol{u}^{n-2}) + \boldsymbol{f}^{n-1} \quad (5)$$

$$\frac{\hat{\boldsymbol{u}} - \tilde{\boldsymbol{u}}}{\Delta t} = \frac{\alpha}{Re}\left(L(\hat{\boldsymbol{u}}) - L(\tilde{\boldsymbol{u}})\right) + \boldsymbol{\delta f}^n, \quad (6)$$

which fully recovers Eq. 1. In the first step, an approximation, $\tilde{\boldsymbol{u}}$, of the intermediate velocity is determined. This velocity field does not satisfy the exact boundary conditions at the immersed boundary since the forcing applied is evaluated from the previous time step. In the second step, the forcing is updated and the no-slip constraint at the immersed boundary is satisfied. The exact expression for $\boldsymbol{\delta f}^n$ is obtained from Eq. 6 by applying the no-slip constraint at the immersed boundary ($\hat{\boldsymbol{u}} = \boldsymbol{u}^n_{IB}$ at IB points):

$$\boldsymbol{\delta f}^n = \frac{\boldsymbol{u}^n_{IB} - \tilde{\boldsymbol{u}}}{\Delta t} - \frac{\alpha}{Re}\left(L(\hat{\boldsymbol{u}}) - L(\tilde{\boldsymbol{u}})\right). \quad (7)$$

Since the diffusive term, $L(\hat{\boldsymbol{u}})$, in Eq. 7 is unknown, an iterative method is required to solve for $\hat{\boldsymbol{u}}$ and $\boldsymbol{\delta f}^n$ implicitly. The first term in the forcing (Eq. 7) drives the velocity at the boundary to the target value (i.e. it enforces the no-slip boundary constraint) while the second term ensures that the diffusive term at the boundary and, hence, the velocities $\hat{\boldsymbol{u}}$ at surrounding non-IB points are correct. Compared to the explicit forcing method, the implicit approach remains stable up to approximately 2.5 times larger Δt. The second-order accuracy of the scheme in both space and time is demonstrated in fig. 1 using the standard decaying vortex test case [2].

2.2 Mass source term for moving boundaries

Application of IB methods to moving boundary problems can lead to spurious force oscillations (SFOs) due to the violation of local mass conservation [3,4]. In the present method, an extension of the mass source term by Kim et al. [2] for use with moving boundaries is proposed in order to

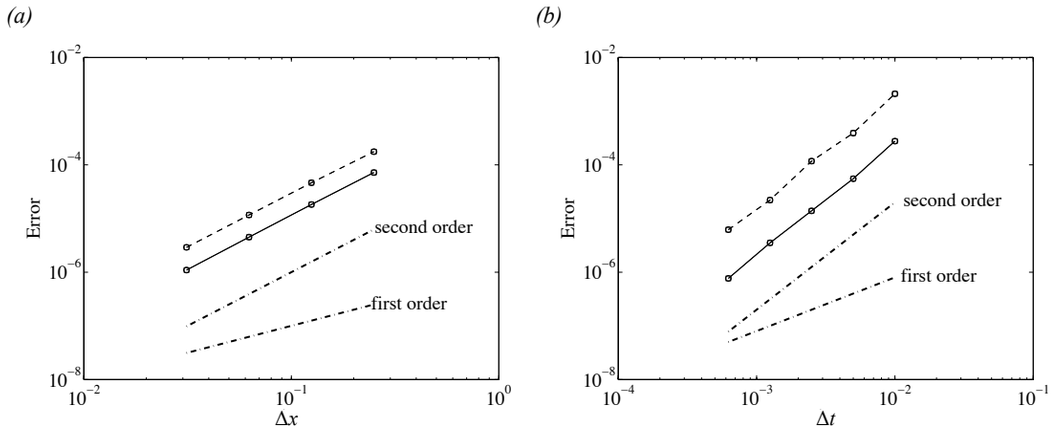

Figure 1: L_2 (——) and L_∞ (- - -) norms for the u ($\square$) and v ($\circ$) velocities versus (a) grid spacing, and (b) time step for decaying vortex problem at $Re = 500$.

satisfy mass conservation near the boundary and suppress SFOs. The present mass source term is designed to enforce local and global mass conservation and is given by

$$q^n = \frac{1}{\Delta V}\left(\sum_{i=1}^{6} \beta_s \hat{\boldsymbol{u}} \cdot \boldsymbol{n} \Delta S_i + \boldsymbol{u}_\Gamma^n \cdot \boldsymbol{n}_\Gamma \Delta_\Gamma\right), \tag{8}$$

where ΔV is the cell volume, ΔS_i is the area of each cell face, $\boldsymbol{n}$ is the unit normal vector outward at each cell face and β_s is the fraction of the cell face inside the solid. The quantities u_Γ, n_Γ and Δ_Γ are the surface velocity, the surface outward unit normal vector (pointing towards the fluid), and the area of the boundary within the cell, respectively.

The first term on the right-hand-side of Eq. 8 mimics the cut-cell/virtual cell-merging technique [3] without requiring construction of new polyhedral cells. It ensures that the continuity equation is satisfied for the fraction of the cell inside the fluid by excluding the contribution from outside the lung geometry. Since two neighbouring cells which share a common face have the same value of the surface flux, but with opposite signs, the global contribution of this term vanishes [2]. The second term in Eq. 8 is an addition to the original mass source term, and ensures that the continuity equation is satisfied when the boundary is moving by including the flux at the boundary. Figure 2 demonstrates the ability of the proposed mass source term to suppress spurious force oscillations in a moving body problem.

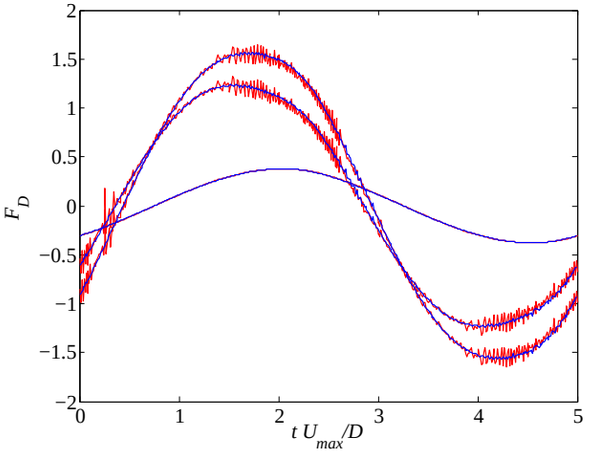

Figure 2: Temporal evolution of drag force on an oscillating cylinder at $Re_{\max} = 100$: —, momentum forcing without a mass source; —, momentum forcing with a mass source.

2.3 Flow in the extrathoracic airways

The new IB method has been applied to perform the first set of fully-resolved simulations of the flow in realistic extrathoracic airways [5]. Through realistic geometric representation of the airways and detailed flow fields, the effect of geometric variation on the mean flow as well as the

turbulent fluctuations has been studied. Comparison of the main flow features with PIV measurements in the same geometries [6] shows good agreement with our numerical predictions. Figure 3 shows the grid, flow field and deposition pattern in one of these geometries. The velocity profiles in the mouth are highly skewed towards the inner wall due to the airway curvature. The flow accelerates at the back of the mouth due to the restriction in cross-sectional area, developing a pharyngeal jet which impinges onto the posterior wall. Due to the bend in the airway, the flow shifts towards the outer wall, separating from the inner wall and leading to a recirculation region (fig. 3b). The maximum kinetic energy occurs in the upper pharynx near the jet (fig. 3c). The flow field has a large effect on the particle deposition as can be observed in fig. 3d. A deposition hot-spot is observed at the posterior wall of the upper pharynx where particles deposit via impaction due to the pharyngeal jet. The method is currently being applied to the intrathoracic airways, taking into account the airway movement during the breathing cycle.

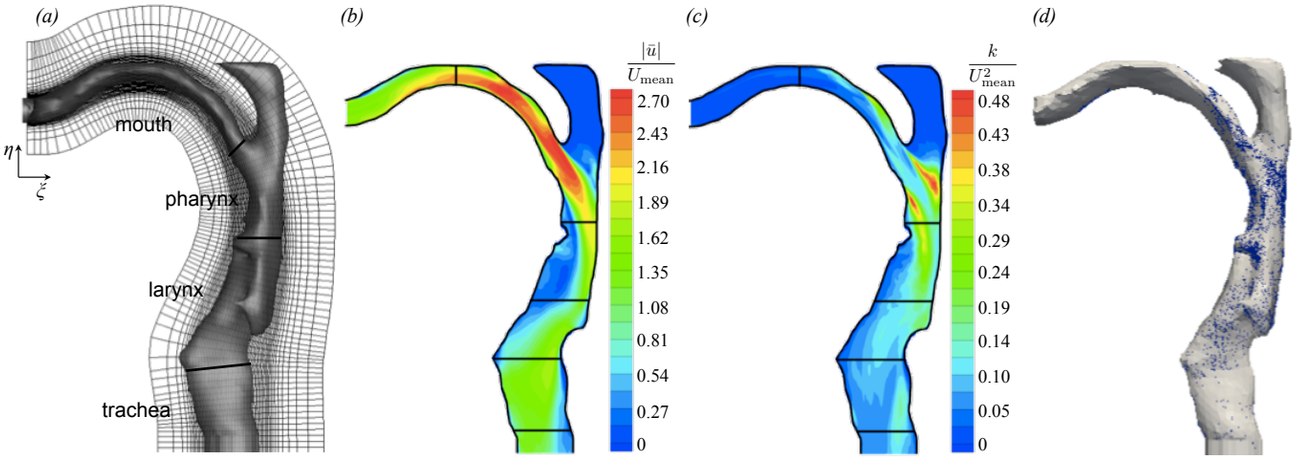

Figure 3: Flow in realistic extrathoracic airways. (a) Airway geometry and curvilinear grid (every eighth grid line in ξ and η is plotted); (b) mean velocity magnitude; (c) mean turbulent kinetic energy; (d) particle deposition.

3 CONCLUSIONS

An immersed boundary method for patient-specific simulations of flow in the respiratory airways has been presented. The implicit iterative scheme decreases the errors at the boundary and enhances stability. The method can also be applied in generalized curvilinear coordinates for efficient modelling of the complex airway geometries. Finally, the new mass source term improves local mass conservation at moving geometry walls and suppresses spurious force oscillations. The method has been applied for detailed simulations of the turbulent flow in realistic extrathoracic airways.

REFERENCES

[1] M. Rosenfeld, D. Kwak, M. Vinokur, A fractional step solution method for the unsteady incompressible Navier-Stokes equation in generalized coordinate systems, *J Comput Phys*, 94, 102–137, 1991.

[2] J. Kim, D. Kim, H. Choi, An immersed-boundary finite-volume method for simulations of flow in complex geometries, *J Comput Phys*, 171, 132–150, 2001.

[3] J. H. Seo, R. Mittal, A sharp-interface immersed boundary method with improved mass conservation and reduced spurious pressure oscillations, *J Comput Phys*, 230, 7347–7363, 2011.

[4] J. Lee, J. Kim, H. Choi, K.-S. Yang, Sources of spurious force oscillations from an immersed boundary method for moving-body problems, *J Comput Phys*, 230, 2677–2695, 2011.

[5] L. Nicolaou, T. A. Zaki, Direct numerical simulations of flow in realistic mouth-throat geometries, *J Aerosol Sci*, 57, 71–87, 2013.

[6] A. Heenan, W. Finlay, B. Grgic, A. Pollard, P. Burnell, An investigation of the relationship between the flow field and regional deposition in realistic extra-thoracic airways, *J Aerosol Sci*, 35, 1013–1023, 2004.

3rd International Conference on Computational and Mathematical Biomedical Engineering – CMBE2013
16-18 December 2013, Hong-Kong
P. Nithiarasu and R. Löhner (eds)

Flow pattern comparison between LES Simulation and Reynolds-Average Navier-Stokes modeling for flow in realistic upper airway models with obstructive sleep apnea

M.Z. Lu*, Y. Liu*, and J.Y. Ye**
*Department of Mechanical Engineering, The Hong Kong Polytechnic University, Hong Kong, mingzhen.lu@connect.polyu.hk
**Tongren Hospital, Capital Medical University, Beijing, China

SUMMARY

The realistic upper airway models with obstructive sleep apnea were constructed by the CT-images. Both models before and after surgery were simulated by the CFD techniques with unsteady Large Eddy Simulation (LES) and unsteady Reynolds-Average Navier-Stokes (RANS) with two-equation turbulent models: k-ε, standard k-ω, and k-ω Shear Stress Transport (SST). Among all the approaches, k-ω SST model resulted in the best agreement with the results of validated LES results on the axial velocity distributions downstream of the minimum cross-sectional area, where is characterized by flow separation and large radial velocity gradients across the developed shear layers. The largest discrepancies in axial velocity distributions on the anterior side was found between the LES and k-ε results.

Key Words: *OSA, RANS, LES, Upper airway.*

1. INTRODUCTION

Obstructive sleep apnea (OSA) is a common disorder characterized by partial or complete narrowing of the pharyngeal airway during sleep [1], resulting in repetitive airflow cessation, blood oxygen desaturation and sleep disruption [2]. However, the pathogenesis of this disorder has not been fully understood yet, it is necessary to further understand the pathophysilogy with OSA for treatment planning. Using experimental techniques to investigate the detailed airflow in the upper airway is expensive and difficult. Recently, because of the non-invasive nature, the Computational Fluid Dynamics (CFD) technology has been utilized to characterize the flow features in the upper airway.

Several researchers have used CFD with different turbulent models, including steady Reynold-Averaged Navier-Stokes (RANS) model (i.e. k-ε, standard k-ω, and k-ω Shear Stress Transport (SST)), one-equation Spalart-Allmaras model and unsteady Large Eddy Simulation (LES) model, to analyze the flow characteristics through the airway models [3,4]. Steady RANS (k-ε and k-ω) model and unsteady LES prediction of the flow in the upper airway has been compared by Mihaescau et al. [3]. They found the expensive LES model could be well captured the flow separation regions downstream of the constricted area and the k-ω results were closer to the LES results. Then Mylavarapu et al. validate theirs result with experimental data [4]. To test their

conclusion, we compare the unsteady RANS (k-ε, standard k-ω, and k-ω Shear Stress Transport (SST)) and LES results with a realistic upper airway model of OSA for before and after surgery.

2. METHODS

Two 3D models that are reconstructed from the CT images are built on a severe OSA subject for both pre- and post- surgery [5].

Four different CFD turbulent models with Fluent (ANSYS 12) framework were investigated. We attempt to study the inspiratory process with tidal volume 700 ml and the breathing frequency 12 cycles per minute following a sinusoid. The airflow is assumed as incompressible flow due to the very low Mach number. Second-order finite-volume schemes was employed for discretization the flow governing equations on the computational domain. While the time-integration was performed using second-order implicit discretization and the coupling between the pressure and the velocity field was implemented through the SIMPLE algorithm. The initial velocity is 1.256 m/s according to the nostril area. The pressure boundary condition in the outlet is set as zero. No-slip boundary condition is applied at the surface of the whole airway and the time step is set as 0.001s. The WALE sub-grid scale (SGS) model is employed in the LES calculations.
The cell quantity in the computational model is about 3,400,000 for both two models. A refined mesh has been employed near the larynx; these numbers are determined by using different meshes, from coarse to progressively finer meshes, and the numerical results of velocity are mesh-convergent to within a prescribed tolerance (~0.2%).

3. RESULTS

The axial velocity distribution during inspiration along a sagittal-plane through the upper airway model in Fig. 1. indicates that all turbulent models can capture a jet-like axial velocity increasing from the minimum cross-sectional area because of the sudden narrowed airway near the soft-palate before surgery. The discrepancies were mainly found in the axial velocity distributions downstream of the minimum cross-sectional area. In this regions, before the surgery, LES results can capture four vortexes (Fig. 2d), which are considered as a important factor in the airway occlusion in the anterior side [6]. Only two vortexes can be found for the k-ω results (Fig. 2b-c) and just one for k-ε results (Fig. 2a). Meanwhile, the LES results illustrated a longer increasing region along the posterior side of the sagittal plane (Fig. 1d). After the surgery, due to the flow improvement, the differences were emerged in the anterior side: all of the four models can capture a large vortex downstream of the minimum cross-sectional area as illustrated in Fig. 2e-h. The k-ω SST seems more closer to the LES result at the anterior side downstream the minimum cross-sectional area(Fig. 1g-h).

Figure 3 shows the axial velocity contour at two cross-sectional planes. The maximum axial velocity can be seen by all the four turbulent models at the minimum cross-sectional area (near the retropalatal pharynx). For the downstream plane, the reversed flow can be identified and the flow patterns obtained by the RANS models are different from that by LES simulation (Fig. 3a-d). However, for the results after surgery, though the k-ε results are clearly different from those by k-ω and LES simulations (Fig. 3e-h), the pattern by k-ω is similar to that of LES simulation.

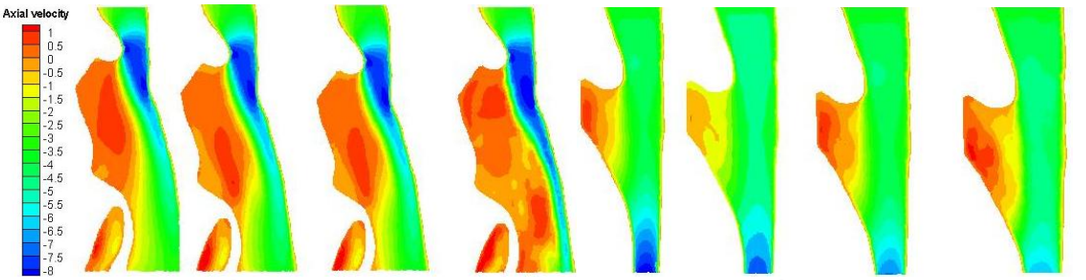

Fig. 1. Axial velocity distribution (m/s) in the sagittal plane: (a) RANS (k-ε) solution before treatment; (b) RANS (standard k-ω) solution before treatment; (c) RANS (k-ω SST) solution before treatment; (d) LES solution before treatment; (e) RANS (k-ε) solution after treatment; (f) RANS (standard k-ω) solution after treatment; (g) RANS (k-ω SST) solution after treatment; (h) LES solution after treatment.

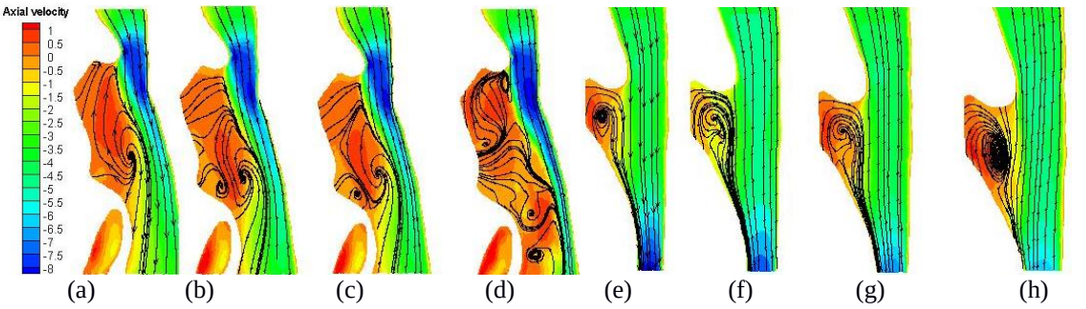

Fig. 2. Axial velocity streamlines distribution (m/s) in the sagittal: (a) RANS (k-ε) solution before treatment; (b) RANS (standard k-ω) solution before treatment; (c) RANS (k-ω SST) solution before treatment; (d) LES solution before treatment; (e) RANS (k-ε) solution after treatment; (f) RANS (standard k-ω) solution after treatment; (g) RANS (k-ω SST) solution after treatment; (h) LES solution after treatment.

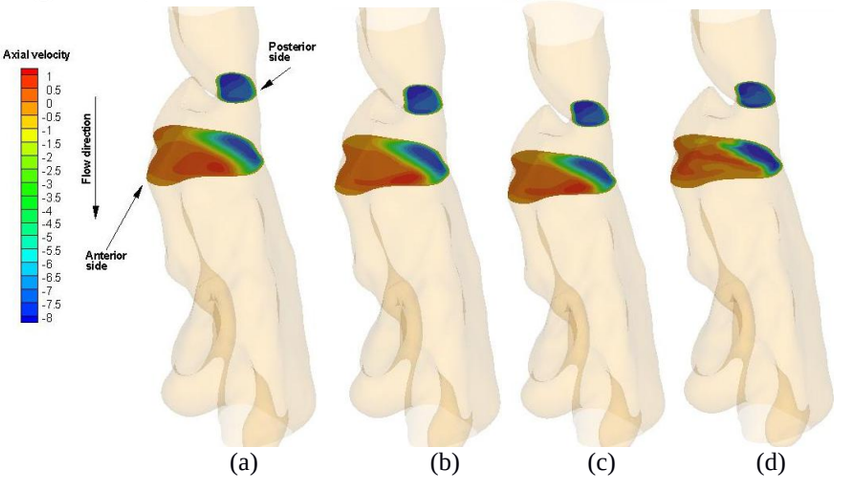

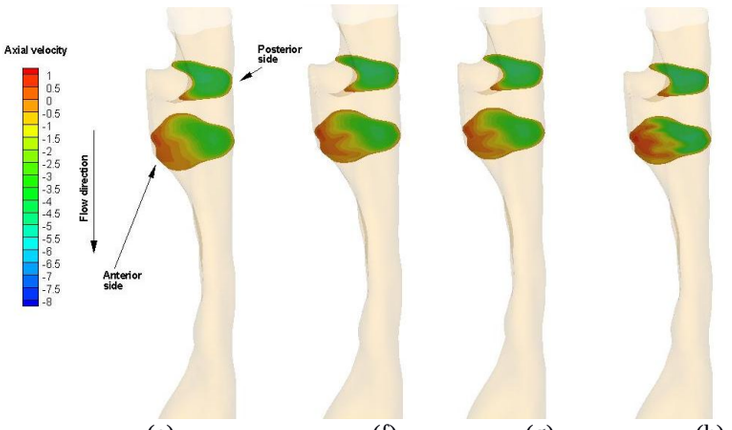

(e) (f) (g) (h)

Fig. 3. Axial velocity distribution (m/s) of the minimum cross-sectional plane (higher) and its downstream cross-sectional plane (below): (a) RANS (k-ε) solution before treatment; (b) RANS (standard k-ω) solution before treatment; (c) RANS (k-ω SST) solution before treatment; (d) LES solution before treatment; (e) RANS (k-ε) solution after treatment; (f) RANS (standard k-ω) solution after treatment; (g) RANS (k-ω SST) solution after treatment; (h) LES solution after treatment.

4. CONCLUSIONS

In the past years, many researchers have used the CFD to understand the airflow features in the upper airway with OSA. However due to the complexity of the geometry model, the prediction accuracy is a challenge for this technique. Although LES has been validated for the airflow prediction, other turbulent models may contribute to the airway flow behavior. According to our study before, the region downstream the minimum cross-sectional area is a key region, due to the seperation flows there may stimulate the mechanoreceptors and then affect the surgical outcome of OSA [6]. For the comparion of different CFD models, it is believed that unsteady k-ω SST results were closer to LES in the axial velocity distribution downstream the minimum cross-sectional area.

REFERENCES

[1] M. Mihaescu, G. Mylavaraou, E.J. Gutmark and N.B. Powell. Large Eddy Simulation of the pharyngeal airflow associated with Obstructive Sleep Apnea Syndrome at pre and post-sugical treatment, *Journal of Biomechanics*, 44, 2221-2228, 2011.

[2] C. Guilleminault, A. Tilkian and W.C. Dement. The sleep apnea syndromes, *Annual Review of Medicine*, 27 (1), 465-484, 1976.

[3] M. Mihaescu, S. Murugappan, M. Kalra, S. Khosla and E. Gutmark. Large Eddy Simulation and Reynolds-Averaged Navier-Stockes modeling of flow in a realistic pharyngeal airway model: An investigation of obstruction sleep apnea, *Journal of Biomechanics*, 41, 2279-2288, 2008.

[4] G. Mylavarapu, S. Murugappan, M. Mihaescu, M. Kalra, S. Khosla and E. Gutmark. Validation of computational fluid dynamics methodology used for human upper airway flow simulations, *Journal of Biomechanics*, 42, 1553-1559, 2009.

[5] H.Y. Luo and Y. Liu. Modeling the Bifurcating Flow in an CT-Scanned Human Lung Airway. *Journal of Biomechanics*, 41, 2681-2688, 2008.

[6] Y. Liu, J.Y. Ye, Z.G. Liu, L.X. Huang, H.Y. Luo and Y.R. Li. Flow oscillation-A measure to predict the surgery outcome for obstructed sleep apnea (OSA) subject, *Journal of Biomechanics*, 45, 2284-2288, 2012.

Poster Abstracts

3rd International Conference on Computational and Mathematical Biomedical Engineering - CMBE2013
16-18 December 2013, Hong-Kong
P. Nithiarasu and R. Löhner (Eds.)

Efficient Reconstruction of Coronary Vessels from 2D Angiography

Dongbin Chen*, Jingjing Deng*, Xianghua Xie*, Perumal Nithiarasu, and Dave Smith*****
*Department of Computer Science, Swansea University, United Kingdom
**College of Engineering, Swansea University, United Kingdom
***Cardiac Unit, Morriston Hospital, Swansea, United Kingdom

SUMMARY

The recovery of three-dimensional (3D) object information from biplane CT angiographic images is still a challenge in application of modelling coronary vessel trees. The proposed method of 3D reconstruction is obtained from the two-dimensional (2D) corresponding feature points by using triangulation projection based on the rotated mechanical angles of the CT angiographic machine. Those 2D feature points are on the centrelines of vessels. This research also includes how to extract the interested coronary vessels from CT angiographic images and how to represent those vessels as a group of connected 2D points that are on centrelines of them. One of the contributions in the paper is that we developed automatic searching algorithm to obtain the 2D corresponding points from a pair of biplane skeleton images under the two constraints of epipolar lines and corresponding bifurcations. We apply the Lucas-Kanade optical flow algorithm to register the corresponding bifurcations from an image sequence for the application of the proposed searching algorithm. The 3D reconstruction applies the readings of rotated mechanical angles and isocentre of the CT angiographic machine (Siemens Axiom) to establish the biplane image relationships of rotation and translation, and then projects the 2D centrelines of coronary vessels onto 3D world coordinates. Another contribution of the paper is that we apply the back projection algorithm to project the 3D points onto 2D image planes for evaluating the accuracy of the 3D reconstruction. The proposed method has been tested on patient data.

Key Words: *3D reconstruction, biplane angiographic image, coronary vessel.*

1 INTRODUCTION

Coronary vessel disease is one of the main causes of death in the world. The technique of coronary angiography is the conventional method to diagnose coronary disease. The research on 3D modelling of coronary vessels from CT biplane angiographic images has been carried out for many years, e.g. [5, 6, 4]. Many researchers have developed different methods to establish accurate 3D model of coronary vessels from biplane CT angiographic images, e.g. [3, 11]. However, the recovery of 3D object information from biplane CT angiographic images is still a challenge in application to 3D modelling coronary vessels. The main task of 3D reconstruction from biplane angiographic images is to produce a 3D model of coronary vessels with accurate geometrical information. The centrelines of coronary vessels used to reconstruct 3D model are helpful in accurate estimation of geometrical information of the coronary vessels since they can reduce the error of 3D reconstruction which may be caused by, for instance, the deformation of coronary vessels along the cardiac cycle [11]. Skeleton image algorithms can be used to extract the centrelines of vessels [1]. A medial axis extraction algorithm [10] has also shown to be useful to produce centrelines of coronary vessels from the vessel segmentation results since it is effective to identify clearly the medial axis of vessels without complex pruning processes.

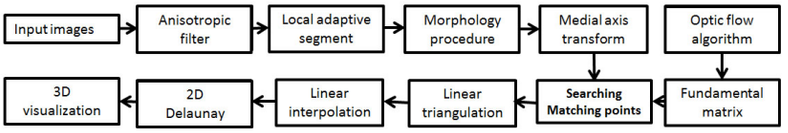

Figure 1: The procedure of the proposed 3D reconstruction.

In this paper, we present a method of 3D reconstruction based on triangulation projection, combined with output from the mechanical rotations and imaging information of the CT machine. One of the contributions in the paper is the development of an automatic searching algorithm that can find the corresponding points from a pair of biplane skeleton images based on the constraints of epipolar lines and two neighbour bifurcations. Anther contribution is that we use the Lucas-Kanade optical flow algorithm to search the corresponding bifurcations from an image sequence for the application of the proposed searching algorithm. Moreover, a new procedure of morphological operations was designed for the application. We developed the back projection algorithm from 3D to 2D for evaluating the accuracy of the proposed 3D reconstruction.

2 IMAGING INFORMATION

A Siemens Axiom CT biplane angiographic machine was used to capture the patient data. The gantry motions are characterised by the angle values of CRA/CAU (Cranial/Caudal) and LAO/RAO (Left/Right Anterior Oblique). Each pair of biplane images has the fixed cardiac phase in a pair of angiographic sequences. The corresponding image distance (SD) between the x-ray source and the image intensifier, patient distance (SP) between the X-ray and the patient position, field of view (FOV) and two gantry orientations were automatically recorded and stored with each image file. All of the captured sequences have the imaging resolution of 512×512 pixels with the pixel size of 0.27799 mm.

3 CENTRELINE EXTRACTION

The whole procedure of 3D reconstruction is illustrated in Figure 1. A number of low level image processing algorithms are involved, including anisotropic diffusion, improved local adaptive thresholding algorithm, morphological process, and medial axis extraction. First we apply anisotropic diffusion to remove image noise. This selected approach [9] is a modification of the linear diffusion. We apply four neighbour directions (up, down, left and right) to calculate the anisotropic diffusion of angiographic images. Next, we segment the images based on local adaptive thresholding. This algorithm produces good segmentation for images with uneven illumination distribution. The thresholding algorithm in [2] uses the local mean and the standard deviation of each pixel to compute local threshold. We add local curvature measurement as another constraint to compute the local threshold. Noise in images is assumed to correspond to high curvature. We also remove redundant boundaries at the beginning of calculation as prior knowledge. The, morphological operations are carried out to connect the segments. We apply the dilate operation five times with the 3×3 window first and then use erosion operation three times with the same window size. Finally, we apply close operation two times with the same window size. This morphology procedure not only connects some broken segment areas but also removes small segment areas. The centrelines of vessels are then obtained by using the medial axis extraction algorithm detailed in [10]. In the stage, we not only remove redundant pixels from the segment result but also produce a clean and complete vascular tree for 3D reconstruction. The Figure 2(b) shows an example of the skeletons of vessels resulted from the medial axis extraction.

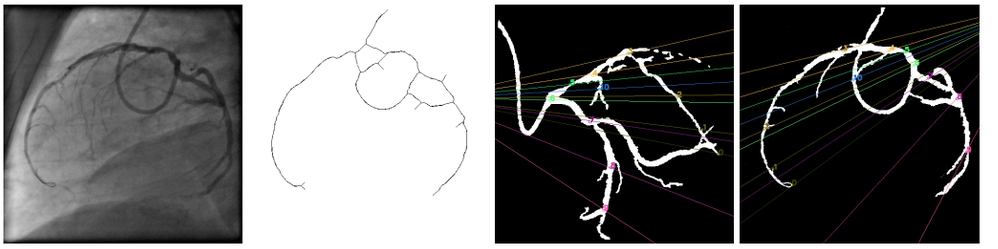

Figure 2: (a) the original image; (b) the skeleton result; (c) and (d) a pair of segmentation results that are labelled the corresponding epipolar lines and bifurcations

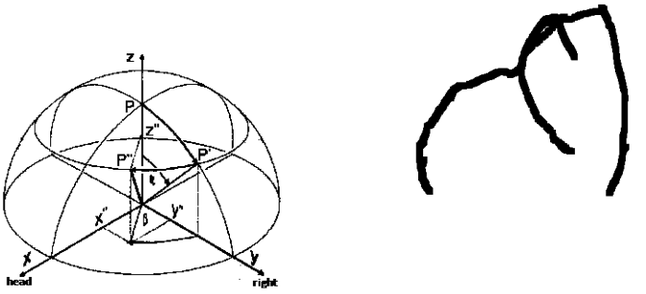

Figure 3: (a) the biplane coordinate; (b) the 3D reconstruction on a view angle.

4 3D RECONSTRUCTION

Here, present an algorithm for searching corresponding points from a pair of biplane skeleton images. We use epipolar lines and two-neighbour bifurcations as the searching constraints. We selected bifurcations manually on the first pair of biplane images. We then applied the Lucas-Kanade optical flow algorithm [8] to determine those bifurcations on their neighbour frames from the biplane sequences. After obtaining those bifurcations from a pair of biplane images, we use the eight-point algorithm [7] to calculate the fundamental matrix of the pair of images. The fundamental matrix is applied to produce epipolar lines on the pair of images. Under the above two constraints, the proposed searching algorithm can find the corresponding points robustly from a pair of biplane skeleton images. Figures 2(c) and 2(d) shows a pair of segmentation results that are labelled with the corresponding epipolar lines and bifurcations.

For reconstructing the centrelines in 3D, we utilise the triangulation projection algorithm, which is based on the output from the CT angiographic machine. First, we define the 3D coordinate in world space to be $P = [X, Y, Z, 1]$ and its corresponding image coordinates to be $p_{1,2} = [u_{1,2}, v_{1,2}, 1]$, which denotes CRA/CAU view and RAO/LAO view respectively. Second, we use the cone camera model and define the camera matrix, A_1 and A_2, relating to the biplane images respectively as, $A = \begin{bmatrix} SD & 0 & C_{\mathrm{x}} \\ 0 & SD & C_{\mathrm{y}} \\ 0 & 0 & 1 \end{bmatrix}$ where SD is the distance from X-ray source to image intensifier, and (C_x, C_y) denote the principal point of the camera, which can be computed through either camera calibration or the imaging centre point as the estimated value. We obtain the image scalars, defined as S_1 and S_2, the ratio between SP and SD from the corresponding image files. From the perspective projection and the linear transformation from 3D world coordinate system to 3D camera coordinate system. They can be formulated as follows:

$$\begin{aligned} S_1 \times [u_1, v_1, 1]^T &= A_1 \times [R_1|T_1] \times [X, Y, Z, 1]^T \\ S_2 \times [u_2, v_2, 1]^T &= A_2 \times [R_2|T_2] \times [X, Y, Z, 1]^T \end{aligned} \tag{1}$$

where the matrices $[R|T]$ are established by the rotation matrix and translation vector of CRA/CAU

view and RAO/LAO view respectively. That is, we use the readings of the gantry rotations of the CT machine to compute $[R|T]_2$, which is corresponding to $[R|T]_1$ as the original orientation and the original point of the world coordinate. We define (α_1, β_1) and (α_2, β_2) to denote the readings of LAO/RAO, and CRAN/CAUD gantrys rotations respectively. The solutions of rotation matrix R_2 and translation T_2 vector in the equation (2) can be derived by

$$\begin{aligned} R_2 &= R_x(\alpha_2) \times R_y(\beta_2) \times R_y(\alpha_1) \times R_x(\beta_1) \\ T_2 &= R_2 \times [0, 0, I_{so}]^T + [0, 0, I_{so}]^T \end{aligned} \tag{2}$$

where I_{so} denotes the isocentre distance of the gantry system obtained from the CT machines specification, and R_x and R_y in a right-hand coordinate shown on the Figure 3(a) can be described below:

$$R_x(\phi) = \begin{bmatrix} 1 & 0 & 0 \\ 0 & cos\phi & -sin\phi \\ 0 & sin\phi & cos\phi \end{bmatrix} \qquad R_y(\phi) = \begin{bmatrix} cos\phi & 0 & -sin\phi \\ 0 & 1 & 0 \\ sin\phi & 0 & cos\phi \end{bmatrix} \tag{3}$$

Linear triangulation method is used:

$$\begin{bmatrix} (a_1^i - u_i \times a_3^i)^T \times R_i \\ (a_2^i - v_i \times a_3^i)^T \times R_i \end{bmatrix} \times P^T = \begin{bmatrix} (u_i \times a_3^i - a_1^i)^T \times T_i \\ (v_i \times a_3^i - a_2^i)^T \times T_i \end{bmatrix} \tag{4}$$

where the a_j^i is the j^{th} row of the camera matrix A_i. An example result is shown in Figure 3. We applied the back projection algorithm from 3D to 2D to test the accuracy of the 3D reconstruction. We obtained the average error of 4.169 pixels for the example shown here.

REFERENCES

[1] Bernard, T., Manzanera, A.: Improved low complexity fully parallel thinning algorithm. In: Image Analysis and Processing. pp. 215–220 (1999)

[2] Bradley, D., Roth, G.: Adaptive thresholding using the integral image. Journal of Graphics, GPU, and Game Tools 12(2), 13–21 (2007)

[3] Chen, S., Carroll, J.: 3-d reconstruction of coronary arterial tree to optimize angiographic visualization. IEEE Trans. Medical Imaging 19(4), 318–336 (2000)

[4] Essa, E., Xie, X., Sazonov, I., Nithiarasu, P.: Automatic ivus media-adventitia border extraction using double interface graph cut segmentation. In: IEEE ICIP. pp. 69–72 (2011)

[5] Essa, E., Xie, X., Sazonov, I., Nithiarasu, P., Smith, D.: Shape prior model for media-adventitia border segmentation in ivus using graph cut. In: MICCAI Workshop on Medical Computer Vision. pp. 114–123 (2012)

[6] Jones, J.L., Essa, E., Xie, X., Smith, D.: Interactive segmentation of media-adventitia border in ivus. In: Computer Analysis of Images and Patterns. pp. 466–474 (2013)

[7] Longues-Higgins, H.C.: The reconstruction of a scene from two projectionsconfigurations that defeat the eight-point algorithm. In: Artificial Intelligence Applications. pp. 173–177 (1984)

[8] Lucas, B., Kanade, T., et al.: An iterative image registration technique with an application to stereo vision. In: Artificial Intelligence (1981)

[9] Perona, P., Malik, J.: Scale-space and edge detection using anisotropic diffusion. IEEE Trans. PAMI 12(7), 629–639 (1990)

[10] Qiu, T., Yan, Y., Lu, G.: A medial axis extraction algorithm for the processing of combustion flame images. In: Image and Graphics. pp. 182–186 (2011)

[11] Shechter, G., Devernay, F., Coste-Manière, È., McVeigh, E., et al.: Temporal tracking of 3d coronary arteries in projection angiograms. In: Medical Imaging. vol. 4684 (2002)

3rd International Conference on Computational and Mathematical Biomedical Engineering – CMBE2013
16-18 December 2013, Hong-Kong
P. Nithiarasu and R. Löhner (eds)

Non-Singular Method of Fundamental Solutions for Biomedical Stokes Flow Problems

Eva Sincich* and Božidar Šarler**

*University of Nova Gorica, Vipavska 13, SI-5000 Nova Gorica, Slovenia, eva.sincich@ung.si

**University of Nova Gorica, Vipavska, 13, SI-5000 Nova Gorica, Slovenia & Institute of Metals and Technology, Lepi pot 11, SI-1000, Ljubljana, Slovenia & COBIK, Velika pot 22, SI-5250 Solkan Slovenia, bozidar.sarler@ung.si

SUMMARY

The purpose of the present paper is development of a Non-singular Method of Fundamental Solutions (NMFS) for Stokes flow problems, widely applicable in biomedical engineering. The NMFS is based on the classical Method of Fundamental Solutions (MFS) with regularization of the singularities. The Stokes problem is decomposed into three coupled Laplace problems. The solution is structured by collocating the pressure and the velocity field boundary conditions by the Laplace fundamental solution. The regularization is achieved by replacement of the concentrated point sources by distributed sources over the disks around the singularity of fundamental solution. The NMFS solution is compared to MFS solution and analytical solution (a.s.) in case of simple 2D duct flow. The described developments represent a first use of NMFS for Stokes problems. The method requires the discretization on the boundary only and is easily applicable in 3D, thus representing an ideal candidate for solving complex biomedical engineering free and moving boundary flow problems in the future.

Key Words: *non-singular method of fundamental solutions, Stokes decomposition, blood flow.*

1. INTRODUCTION

The modeling of vascular systems with its contained blood represents a complex multiscale and multiphysics fluid-structure interaction problem. The blood rheology is depending on the scale considered. For example, the particulate flow has to be considered when taking into account the interactions of the blood cells on the micro level, and the non-Newtonian turbulent flow has to be considered on the macro level. For an exhaustive treatment of these topics as well as biomedical motivations we refer to [1,2,3] and the references therein. Due to the complexity of the spectra of the problems appearing in vascular systems, there is a substantial need to apply novel numerical methods to related problems. For this purpose, the method of fundamental solutions (MFS) [4] appears to be an ideal candidate, since it is a meshless boundary collocation technique, particularly suitable for tracking moving and free boundary problems. The method has similar

coding complexity in 2 or 3D. The main drawback of the method represents the fact that it is straightforwardly suitable only for problems with known fundamental solution, and that when using singular fundamental solution, there is a need to include an artificial boundary, positioned outside the physical boundary in order to make the collocation possible. The optimal location of the artificial boundary is a delicate issue. In general, it can be observed that if the artificial boundary is too close to the physical one, then the accuracy of the problem is poor. On the other hand, if the artificial boundary is too far then the problem becomes ill-posed. Recent advances of the method for fluid [5], porous media flow with moving boundaries [6] and for solid mechanics [7], which involve regularization of the singularities, permit to omit the artificial boundary. We shall refer to the latter as the non-singular method of fundamental solutions (NMFS) and demonstrate its use for a class of vascular systems that reduce to a simple Stokes flow. One of the simplest related examples is that of a straight, uniform rigid duct with a steady rate of a laminar liquid flowing through it. In order to demonstrate the NMFS for such problems, we use the regularized Laplace fundamental solution, as suggested by Liu [8], combined with the decomposition of the 2D Stokes problem into three Laplacian problems [9]. First, we intend to describe briefly the underlying mathematical formulation of our method in a quite general framework. Second, we will show the applicability of our novel technique by considering the flow in a duct.

2. GOVERNING EQUATIONS

Let Ω be a connected two-dimensional domain with boundary Γ. We consider Cartesian coordinate system with base vectors $\mathbf{i}_x$ and $\mathbf{i}_y$ and coordinates x and y.The velocity field $\mathbf{q} = u\mathbf{i}_x + v\mathbf{i}_y$ is solution of the following Stokes equation (1.a) and satisfies the incompressibility condition (1.b)

$$\mu\Delta\mathbf{q}(x,y) = \nabla P(x,y) \text{ in } \Omega, \quad \nabla\cdot\mathbf{q} = 0 \text{ in } \Omega, \tag{1.a, 1.b}$$

with μ representing the viscosity and P the pressure. Moreover, arguing as in [9] one can prove that (1.a) and (1.b) are equivalent to

$$\Delta f(x,y) = 0\ \Delta g(x,y) = 0,\ \Delta P(x,y) = 0 \text{ in } \Omega,\ \partial_x u + \partial_y v = 0 \text{ in } \partial\Omega \tag{2.a, 2.b, 2.c, 2.d}$$

provided the components u and v of the velocity vector $\mathbf{q}$ satisfy

$$\mu u(x,y) = f(x,y) + \frac{x}{2}P(x,y),\ \mu v(x,y) = g(x,y) + \frac{y}{2}P(x,y) \text{ in } \Omega. \tag{3.a, 3.b}$$

In this paper, for simplicity, we assume that the two components (u,v) of the velocity field satisfy the Dirichlet conditions on the boundary $\partial\Omega$

$$u = \bar{u} \text{ in } \partial\Omega,\ v = \bar{v} \text{ in } \partial\Omega \tag{4.a, 4.b}$$

where $\bar{u}$ and $\bar{v}$ are two given sufficiently smooth functions. Extension to other types of boundary conditions is straightforward.

2. SOLUTION PROCEDURE AND NUMERICAL EXAMPLE

The underlying idea of both the methods employed in the present paper, namely the MFS and NMFS, consists in representing the three harmonic functions f, g, and P, appearing in (2.a-c) as a linear combination of N global approximating functions with unknown coefficients, determined through collocation with the boundary conditions. We take the form ϕ of the approximation functions for MFS (fundamental solution of Laplace equation (5.a)) and $\tilde{\phi}$ for NMFS (desingularized fundamental solution (5.b))

$$\phi(\mathbf{p},\mathbf{s}) = \frac{1}{2\pi}\log(|\mathbf{p}-\mathbf{s}|^{-1}),\ \tilde{\phi}(\mathbf{p},\mathbf{s}) = \begin{cases} \phi(\mathbf{p},\mathbf{s}); & \mathbf{p} \neq \mathbf{s} \\ \dfrac{1}{\pi R^2}\displaystyle\int_{A(\mathbf{s},R)} \phi(\mathbf{p},\mathbf{s})\,dA = \frac{1}{2\pi}\log\left(\frac{1}{R}\right)+\frac{1}{4\pi}; & \mathbf{p} = \mathbf{s} \end{cases} \tag{5.a, 5.b}$$

where $\mathbf{p}$ denote points on the physical boundary, and $\mathbf{s}$ denote the source points lying on the artificial boundary in case of MFS and on the physical boundary in case of NMFS. $A(\mathbf{s},R)$ represents a circular disk with radius R centered at $\mathbf{s}$. We consider N source points $\mathbf{s}_j$, $j=1,\ldots,N$ and N collocation points $\mathbf{p}_i$, $i=1,\ldots,N$ and we discretize the problem by representing f, g, and P as

$$f(\mathbf{p}_i) = \sum_{j=1}^{N} a_j \phi(\mathbf{p}_i,\mathbf{s}_j),\ g(\mathbf{p}_i) = \sum_{j=1}^{N} b_j \phi(\mathbf{p}_i,\mathbf{s}_j),\ P(\mathbf{p}_i) = \sum_{j=1}^{N} c_j \phi(\mathbf{p}_i,\mathbf{s}_j) \tag{6.a, 6.b, 6.c}$$

where ϕ has to be replaced with $\tilde{\phi}$ when dealing with the NMFS method. We then plug the above choices into (3.a-b), (2.d) and (4.a, 4.b). Respectively, we reformulate our boundary value problem (1.a, 1.b, 4.a-b) to the solution of a linear system of $3N$ algebraic equations $\mathbf{A}\mathbf{x}=\mathbf{b}$ where the $3N\times 3N$ full matrix $\mathbf{A}$ has to be meant as a discretization of the inherent partial differential equation, the $3N\times 1$ vector $\mathbf{x}$ collects the unknown coefficients a_j, b_j, c_j in (6.a-c) and the $3N\times 1$ vector $\mathbf{b}$ contains the given information of the Dirichlet boundary condition (6.a, 6.b). We solve the Stokes problem (1.a) and (1.b) in a rectangular domain $\Omega = (-x_0, x_0)\times(-y_0, y_0);\ x_0 = 2,\ y_0 = 0.5$, for laminar flow between two plates. The following a.s. [9] is considered $u(x,y) = \frac{1}{2\mu}(y^2 - y_0^2)\partial_x P;\ \mu = 1, \partial_x P = 6$, $v(x,y) = 0$,

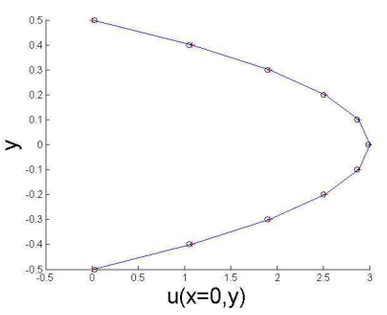

Fig.1a. The profile of *u* at *x=0* along *y* axis.

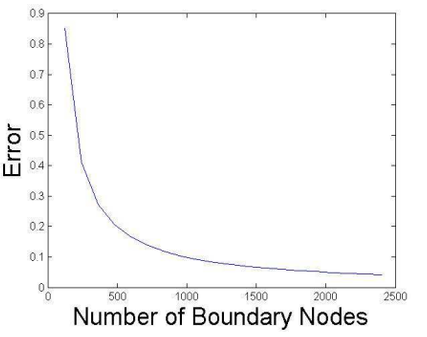

Fig.1b. Error as a function of the discretization.

where the Dirichlet boundary conditions in (4.a) and (4.b) are derived directly from the a.s. We solve the problem with MFS and NMFS. We use 1200 equidistant boundary nodes picking the source points at a distance 0.0417 from the physical boundary in MFS method. On the other hand the numerical solution computed with the NMFS has been obtained with the same number of boundary nodes and by choosing R in (6.b) equal to 0.0033. In Fig. 1.a the first component of velocity field along $x = 0$ is presented (+:MFS, o:MMFS, -:a.s.). Moreover, in Fig. 1.b we show the error computed as the Euclidean norm of the difference between the a.s. and the MMFS solution, measured along the profile $x = 0$ in 11 equidistant points on the interval $[-y_0, y_0]$.

3. CONCLUSIONS

The Laplace decomposition technique combined with NMFS is for the first time applied for solving a simple Stokes problem where both components of fluid velocity are specified on the boundary of the solution domain. The accuracy and efficiency of the new method is validated by considering a simple test example arising in steady flow problems. Moreover, we show that the NMFS solution converges to the a.s. with the increasing number of the nodes. The future extensions of the presented work will be focused on flow in axisymmetry and 3D, as well as free and moving boundary problems. The developed method, with its boundary only character of discretization, can potentially be used in effective simulation of a broad spectrum of involved biomedical problems. Indeed, even though we are aware that for a general computational haemodynamics problems the non-linear convective term of the Navier Stokes equation cannot be dropped out, we believe that the adopted linear model could find application in the study of small scale problems, such as the blood flow in capillars.

ACKNOWLEDGEMENT: This work was performed within the Creative Core Program (AHA-MOMENT) contract no. 3330-13-5000031, sponsoderd by RS-MIZS (Slovenia) and European Regional Fund (EU), and project Local Meshless Kernel Techniques for Liquid-Solid Processes, supported by the Research Grants Council of Hong Kong, project No. CityU 101112.

REFERENCES

[1] M. Epstein, *The Elements of Continuum Biomechanics*, Wiley-VCH, 2012.
[2] W.R. Milnor, *Hemodynamics. Second edition*, William and Wilkins, 1989.
[3] L. Formaggia, A. Quarteroni, A. Veneziani, *Cardiovascular mathematics – Modelling and simulation of the circulatory system*, Springer, 2009.
[4] C.S. Chen, A. Karageorghis, Y.S. Smyrlis, *The method of fundamental solutions - a meshless method*, Dynamic publishers, 2008.
[5] B. Šarler, Solution of potential flow problems by the modified method of fundamental solutions: formulations with single layer and the double layer potential fundamental solutions. *Engineering Analysis with Boundary Elements*, 12, 1374-1382, 2009.
[6] M. Perne, F., B. Šarler, F. Gabrovšek, Calculating transport of water from a conduit to the porus matrix by boundary distributed source method, *Engineering Analysis with Boundary Elements*, 36, 1649-1659, 2012.
[7] Q.G. Liu, B. Šarler, Non-Singular method of fundamental solutions for two-dimensional isotropic elasticity problems, *CMES: Computer Modeling in Engineering and Sciences*, 91, 235-266, 2013.
[8] Y.J. Liu, A new boundary meshfree method with distributed sources. *Engineering Analysis with Boundary Elements*, 34, 914-919, 2010.
[9] A. E. Curteanu, L. Elliot, D.B. Ingham, D. Lesnic, *Engineering Analysis with Boundary Elements*, 31, 501-513, 2007.

3rd International Conference on Computational and Mathematical Biomedical Engineering – CMBE2013

16-18 December 2013, Hong-Kong

P. Nithiarasu and R. Löhner (Eds.)

Simulation of arterial hypertension and progressive arteriosclerosis with a 0-D multipurpose cardiovascular model

Michael Broomé*,,***, Elira Maksuti*,**
Anders Waldenström*,**and Anna Bjällmark*,*****

* Department of Medical Engineering, School of Technology and Health, KTH Royal Institute of Technology, Stockholm, Sweden. broom@kth.se

** Department of Physiology and Pharmacology, Karolinska Institutet, Stockholm, Sweden

*** ECMO Department, Karolinska University Hospital, Stockholm, Sweden

**** Department of Public Health and Clinical Medicine, Umeå University, Umeå, Sweden

***** Department of Molecular Medicine and Surgery, Karolinska Institute, Stockholm, Sweden

SUMMARY

The effects of systemic vascular resistance and progressive stiffening/arteriosclerosis in the vascular tree on arterial blood pressure is explored in a 0D cardiovascular simulation model. Pulse pressure is both sensitive and specific for increases in stiffness and mean arterial pressure both sensitive and specific for changes in vascular resistance.
Key Words: *0D vascular model, arterial hypertension, arteriosclerosis.*

1 INTRODUCTION

Arterial hypertension is a major cause of cardiovascular disease in western society [1]. Primary hypertension in middle-aged people is characterized by increase in both systolic (SAP) and diastolic (DAP) arterial blood pressure with discrete symptoms [1, 2]. In more advanced age, isolated systolic hypertension is a more common disease manifestation [3-6]. Increased SAP and pulse pressure (PP=SAP-DAP) are more strongly associated with morbidity than DAP [5]. In epidemiological cardiovascular research, blood pressures (SAP, DAP, PP) are often studied as risk factors for cardiovascular events (eg. stroke and myocardial infarction), assumed to be statistically independent of the studied outcome [7]. This is problematic since SAP and PP are both associated with arteriosclerosis, closely related to the studied outcome. Furthermore DAP often decreases in arteriosclerosis, although in an earlier stage being a pathogenic factor [8]. A different approach could be to consider the first stage of hypertensive disease as an increase in systemic vascular resistance characterized by an increase in mean arterial pressure (MAP), then in a later stage developing to systolic hypertension and increase in PP as a sign of increase in

vascular stiffness and progressive arteriosclerosis [9]. This approach may better separate cause and effect, questioning the current assumptions of statistical independence between the risk factor and outcome. The aim of this study was to investigate if a 0D vascular simulation model can be used to predict which blood pressure measurement is best capable of showing the underlying vascular pathology in hypertension.

2 MAIN BODY

We have developed a closed-loop real-time multi-purpose 0D lumped parameter cardio-vascular model with cardiac function determined by separate time-varying elastance functions representing all four chambers, septal interactions, pericardium and 27 vascular segments [10]. Vascular resistance ***R*** (eq.1), blood inertia ***I*** (eq.2), vascular elastance ***E*** (eq.3), wall resistance ***Ω*** (eq.4) and pressure ***p*** (eq.5) are based on physical dimensions of the vessels and non-linear physical relations as described below. Eq.1-3 are based on Poiseuille flow in a single tube with radius ***r***, length ***l*** and thickness ***h*** scaled to ***n*** tubes in parallel. Eq.4 characterizes the viscoelastic tube properties and eq.5 the non-linear pressure-radius relation of each vessel due to progressive wall stiffening with vessel expansion [11].

$$R = \frac{8 \cdot \eta \cdot l}{\pi \cdot r^4 \cdot n} \qquad \textit{Equation 1.}$$

$$I = \frac{\rho \cdot l}{\pi \cdot r^2 \cdot n} \qquad \textit{Equation 2.}$$

$$\mathrm{E} = \frac{Y_{inc} \cdot h}{2 \cdot \pi \cdot r^3 \cdot l \cdot n} \qquad \textit{Equation 3.}$$

$$\Omega = \lambda \cdot \sqrt{I \cdot E} \qquad \textit{Equation 4.}$$

$$p(r) = P_0 \cdot e^{\frac{\pi \cdot l \cdot \left(r^2 - r_0^2\right)}{\varphi}} \qquad \textit{Equation 5.}$$

P_0	Normal mean vascular pressure	r_0	Vessel radius at normal mean pressure
η	Blood viscosity	Y_{inc}	Young's modulus
λ	Vascular wall resistance scaling factor	φ	Vascular wall stiffness constant

Increased vascular stiffness is simulated by a stepwise (+1000 mmHg) increase of tissue Youngs modulus (Y_{inc}) from 2000 to 8000 mmHg in all vascular segments, whereas stepwise decrease in radius (r_0) of systemic arterioli by 2.5% is used to simulate an increase in systemic vascular resistance by approximatively 10% for each step up to a 50%

increase (figure 1). Pressure curves are simulated in normal physiology (Fig 2a), with a stiffness increase from 3000 to 6000 mmHg (Fig 2b), with a decrease in systemic arterioli radius by 15% (Fig 2c) and with both changes concomitantly (Fig 2d). Heart rate and cardiac input parameters were unchanged. Autonomic reflexes and adaptive remodeling are not taken into account.

Data shows a clear relation between stiffness and pulse pressure, as well as between systemic vascular resistance and mean arterial pressure (Figure 1). Pressure curve shapes (Figure 2) are similar to those measured in normal and hypertensive patients [12].

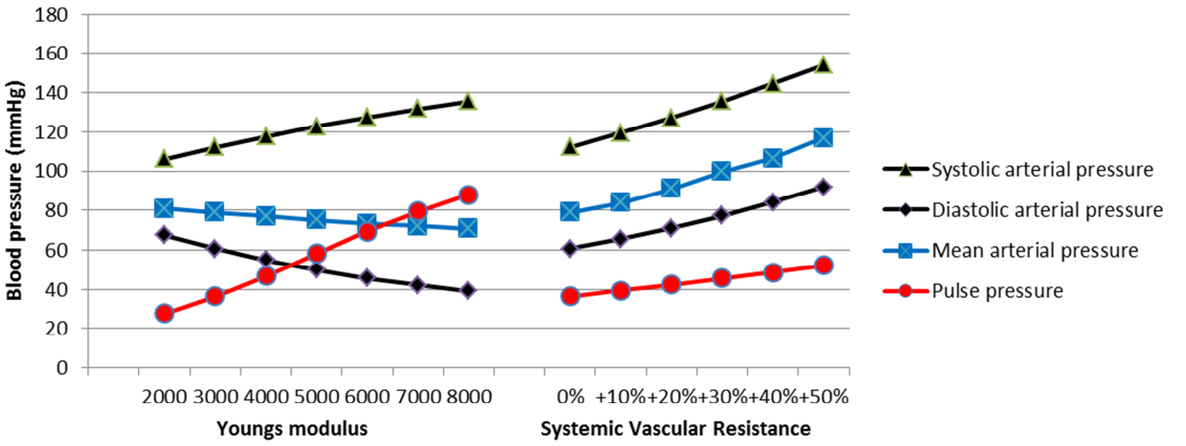

Figure 1. Arterial systolic, diastolic, mean and pulse pressure during stepwise increase in vascular stiffness with unchanged baseline vascular resistance (left) and stepwise increase in systemic vascular resistance with unchanged baseline stiffness (right).

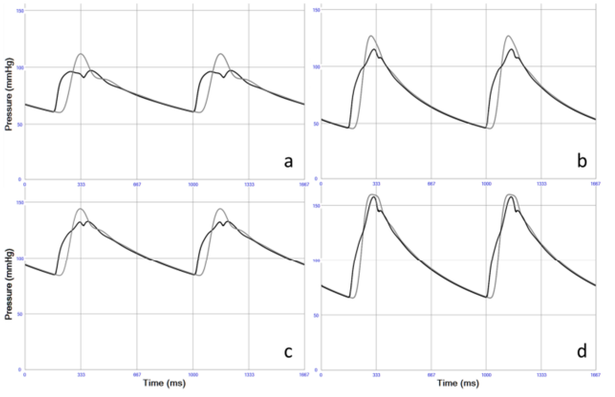

Figure 2 abcd. Blood pressure in ascending aorta (black) and a peripheral artery (gray) in a/ normal (Y_{inc}=3000 mmHg), b/ increased (Y_{inc}=6000 mmHg) vascular stiffness, c/ increased vascular resistance (systemic arterioli radius -15%) and d/ both increased stiffness and resistance.

3 CONCLUSIONS

We conclude that the hemodynamic physiological effects of arterial hypertension and progressive stiffening/arteriosclerosis of the vascular tree can be adequately described in a 0D cardiovascular simulation model. We also conclude that systolic pressure is

sensitive both for increases in resistance and stiffness, but cannot differentiate the two. Diastolic pressure increases with increased resistance, but decreases with increased stiffness and is therefore difficult to interpret in the individual patient. Pulse pressure is both sensitive and specific for increases in stiffness and mean arterial pressure both sensitive and specific for changes in vascular resistance. Based on this simulation study we propose that measuring/registering mean arterial pressure (as a surrogate marker for vascular resistance) and pulse pressure (as a surrogate marker for vascular stiffness) is more adequate than only measuring systolic and diastolic pressure.

REFERENCES

1. Chobanian, A.V., et al., *Seventh report of the Joint National Committee on Prevention, Detection, Evaluation, and Treatment of High Blood Pressure.* Hypertension, 2003. **42**(6): p. 1206-52.
2. Burt, V.L., et al., *Prevalence of hypertension in the US adult population. Results from the Third National Health and Nutrition Examination Survey, 1988-1991.* Hypertension, 1995. **25**(3): p. 305-13.
3. Mitchell, G.F., et al., *Changes in arterial stiffness and wave reflection with advancing age in healthy men and women: the Framingham Heart Study.* Hypertension, 2004. **43**(6): p. 1239-45.
4. Kocemba, J., et al., *Isolated systolic hypertension: pathophysiology, consequences and therapeutic benefits.* Journal of human hypertension, 1998. **12**(9): p. 621-6.
5. White, W.B., *Systolic versus diastolic blood pressure versus pulse pressure.* Current cardiology reports, 2002. **4**(6): p. 463-7.
6. Williams, B., L.H. Lindholm, and P. Sever, *Systolic pressure is all that matters.* Lancet, 2008. **371**(9631): p. 2219-21.
7. Strandberg, T.E. and K. Pitkala, *What is the most important component of blood pressure: systolic, diastolic or pulse pressure?* Current Opinion in Nephrology and Hypertension, 2003. **12**(3): p. 293-7.
8. Hayoz, D. and H.R. Brunner, *Remodelling of conduit arteries in hypertension: special emphasis on the mechanical and metabolic consequences of vascular hypertrophy.* Blood pressure. Supplement, 1997. **2**: p. 39-42.
9. Stergiopulos, N. and N. Westerhof, *Determinants of pulse pressure.* Hypertension, 1998. **32**(3): p. 556-559.
10. Broomé, M., et al., *Closed-loop real-time simulation model of hemodynamics and oxygen transport in the cardiovascular system.* Biomedical Engineering Online, 2013. **12**(1): p. 69.
11. Danpinid, A., et al., *In vivo characterization of the aortic wall stress-strain relationship.* Ultrasonics, 2010. **50**(7): p. 654-65.
12. Safar, M.E. and A. Benetos, *The shape of the blood pressure curve and genetic hypertension.* Trends in cardiovascular medicine, 1995. **5**(3): p. 96-102.

``

3rd International Conference on Computational and Mathematical Biomedical Engineering – CMBE2013

16-18 December 2013, Hong-Kong

P. Nithiarasu and R. Löhner (eds)

Prediction of the Optimal Timing of LVAD Therapy in terms of Ventricular Unloading: Simulation Study

Ki Moo Lim*

*Dept. of Medical IT Convergence Engineering, Kumoh National Institute of Technology, Republic of Korea, kmlim@kumoh.ac.kr

SUMMARY

It is important to begin left ventricular assist device (LVAD) treatment at appropriate time for heart failure patients who expect cardiac recovery after the therapy. In order to predict the optimal timing of LVAD implantation, we predicted pumping efficacy of LVAD according to the severity of heart failure theoretically. We used LVAD-implanted cardiovascular system model which consist of 8 Windkessel compartments for the simulation study. The time-varying compliance theory was used to simulate ventricular pumping function in the model. The ventricular systolic dysfunction was implemented by increasing the end-systolic ventricular compliance. Using the mathematical model, we predicted cardiac responses such as left ventricular peak pressure, cardiac output, ejection fraction, and stroke work according to the severity of ventricular systolic dysfunction under the treatments of continuous and pulsatile LVAD. Left ventricular peak pressure, which indicates the ventricular loading condition, decreased maximally at the 1st level heart-failure under pulsatile LVAD therapy and 2nd level heart-failure under continuous LVAD therapy. We conclude that optimal timing for pulsatile LVAD treatment is 1st level heart-failure and for continuous LVAD treatment is 2nd level heart-failure when considering LVAD treatment as "bridge to recovery".

``

Key Words: *ventricular assist device, time-varying compliance, cardiac output, ejection fraction, heart-failure.*

1. INTRODUCTION

Left ventricular assist device (LVAD) is a mechanical circulatory device that is used to partially or completely replace the function of a failing heart. It is very important to determine appropriate timing of LVAD therapy for a specific patient. Particularly, for the patient who expects cardiac recovery after several years of LVAD therapy, it should be determined with consideration of LVAD efficacy for ventricular unloading. However, it has been determined by the empirical no-how of clinical doctor without any clear standard criteria. Animal experiments or clinical studies could provide appropriate criteria for determining the timing of LVAD therapy. However, it will not be easy due to the high economical and time cost. We previously compared the function of continuous and pulsatile LVADs and predicted hemodynamic responses according to the cannulation types of LVAD by using mathematical model of human cardiovascular system. Therefore, as an alternative way to experimental study, we predict cardiovascular response according to the severity of heart failure and determine the optimal timing for LVAD therapy in terms of ventricular unloading by using numerical method.

2. MAIN BODY

We modified previously developed lumped model of the cardiovascular system and integrated it with LVAD function [1, 2]. The model was formulated with regard to an electric analog model, consisting of elements such as resistors, capacitors, and diodes. By mapping hemodynamic parameters into the electric elements, flow resistance to the electric resistors, vessel compliance to the capacitors, and the function of cardiac valves to the diodes, this model calculates the blood pressure and flow rate for each component of the body. Fig. 1 shows a schematic diagram of the cardiovascular system model. The LVAD function was modeled as a flow generator with a mean flow rate of 75 mL/s, which is enough pumping flow for 100% assistance. In order to apply a generalized waveform of continuous and pulsatile LVADs to the model, we used a constant flow rate for continuous LVAD and a harmonic profile of flow rate for pulsatile LVAD.

We modeled voluntary pumping of ventricle by applying time-varying compliance of ventricle. In order to model various contractile heart-failures, we varied end-systolic compliance with five levels. Fig. 2 shows the time-varying compliance of normal and failed ventricle with five different severities.

``

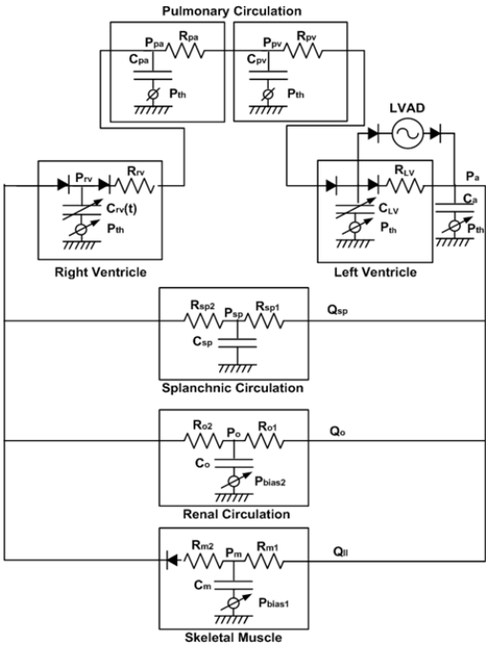

Fig. 1 Schematic of the LVAD-implanted cardiovascular system model consisting of eight compartments. R, flow resistance; C, vascular compliance. See Lim et al. [1] for detailed parameter information.

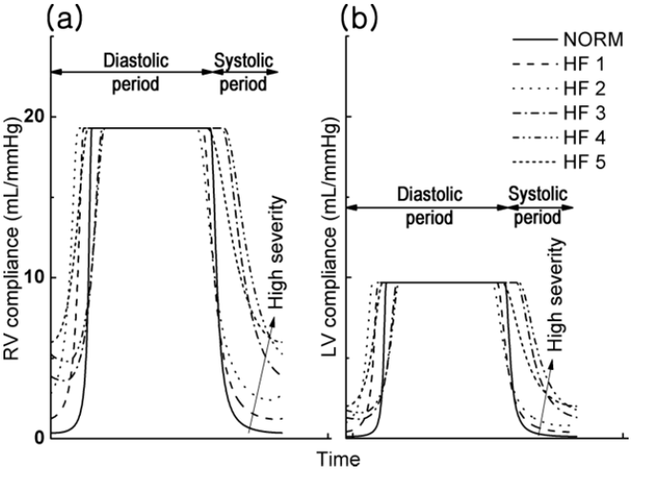

Fig. 2 Time-varying compliances of left (a) and right ventricles according to the severity of systolic dysfunction.

3. CONCLUSIONS

Fig. 3 shows the pressure-volume diagram of left ventricle according to the severity of heart-failure.

``

Fig. 3(a) is the result under heart-failure without LVAD therapy, Fig. 3(b) is the results under heart-failure with continuous LVAD therapy, and Fig. 3(c) is the result under pulsatile LVAD therapy. The internal area, which means the stroke work, of the pressure-volume loop decreased according to the severity of heart-failure under all the conditions. It shifted right under the condition of no LVAD therapy and shifted left under the condition of pulsatile LVAD therapy. The stroke work was decreased most significantly at the severity 2 in the case of continuous LVAD therapy and at the severity 1 in the case of pulsatile LVAD therapy. These results will be useful when considering the timing of pulsatile and continuous LVAD implantations clinically.

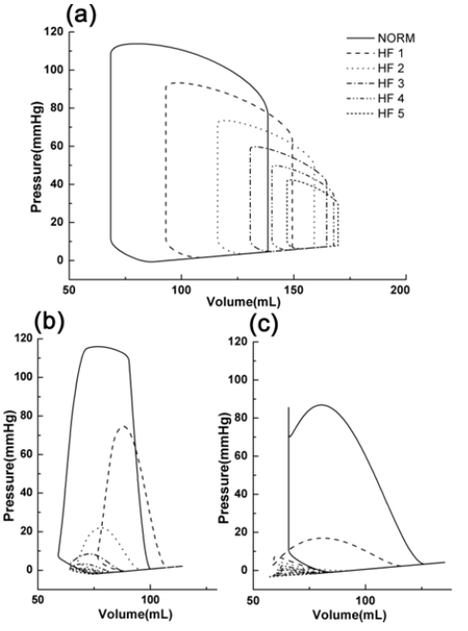

Fig. 3 Pressure-volume loops under normal and various heart-failure conditions from severity 1 (HF 1) to severity 5 (HF 5). (a) No LVAD treatment; (b) CLVAD treatment; (c) PLVAD treatment.

REFERENCES

1. Y. Shi, T. Korakianitis, and C. Bowles, Numerical simulation of cardiovascular dynamics with different types of VAD assistance. J Biomech, 40(13): 2919-33. 2007.
2. K.M. Lim, I.S. Kim, S.W. Choi, B.G. Min, Y.S. Won, H.Y. Kim, and E.B. Shim, Computational analysis of the effect of the type of LVAD flow on coronary perfusion and ventricular afterload. J Physiol Sci, 59(4): 307-16. 2009.

3rd International Conference on Computational and Mathematical Biomedical Engineering – CMBE2013

16-18 December 2013, Hong-Kong

P. Nithiarasu and R. Löhner (eds)

Influence of the side branch diameter on the endovascular treatment of intracranial aneurysms located near a bifurcation

Abraham Y. S. Tang*, H. N. Chan*, Anderson C. O. Tsang, Gilberto K. K. Leung**, K. M. Leung*** and K. W. Chow***

*Department of Mechanical Engineering, The University of Hong Kong, Pokfulam, Hong Kong, abmtang@hku.hk

**Division of Neurosurgery, Department of Surgery, Li Ka Shing Faculty of Medicine, The University of Hong Kong, Queen Mary Hospital, Pokfulam, Hong Kong

***Department of Neurosurgery, Kwong Wah Hospital, Waterloo Road, Hong Kong

SUMMARY

Intracranial aneurysm is the dilatation of the cerebral artery which constitutes life-threatening pathological condition. Upon aneurysm rupture, dangerous subarachnoid hemorrhage associated with high mortality can be resulted. Endovascular stenting, a minimally invasive surgery, can treat the aneurysm and reduce the rupture risk. Aneurysms are commonly located near the arterial bifurcation. The diameter of the side branch vessel is believed to play a crucial role in the treatment efficacy. Computational fluid dynamics (CFD) analysis is performed and several hemodynamic factors are determined. The reduction in volume flow rate into the aneurysm subsequent to treatment is highly related to the side branch diameter. The flow alternation in the side branch vessel due to stenting is also important. This quantitative study can definitely assist clinicians in therapeutic discussion making and treatment planning.

Key Words: *intracranial aneurysm, endovascular stent, side branch, computational fluid dynamics.*

1. INTRODUCTION

Intracranial aneurysm, a local dilatation of the cerebral artery, is a serious brain disorder. The incidence rate of intracranial aneurysm is about 5% in the population. Aneurysms are commonly located near the bifurcation point of the blood vessels [1]. The weakened aneurysm wall may rupture, leading to massive internal bleeding inside the subarachnoid space. Severe hemorrhage stroke associated with high mortality and morbidity rate can be caused.

A minimally traumatic surgical procedure is endovascular stenting, where a flow diverting is deployed to cover the aneurysm neck, thereby reducing the blood flow into the aneurysm. The stent might, however, cover the side branch vessel nearby as well, possibly leading to insufficient blood supply to the downstream tissues and organs, thus causing tissue ischemia. In addition, surgeons might deploy a second stent at the same location to reduce the effective porosity as well. This might drastically alter the flow in the side branch and eventually becomes occluded [2].

Computational fluid dynamics (CFD) is an increasingly sophisticated tool to determine the hemodynamics in medical engineering [3]. In this study, the effect of various side branch diameters has been tested by computational simulations. The single stent and double stent placement are also compared with the pre-operation situation. Several hemodynamic parameters including the intra-aneurysmal pressure and the volume flow rates are determined.

2. METHODOLOGY

An idealized Y-shaped model is employed throughout the study, with the aneurysm located near the bifurcation point of the artery (Fig. 1). The diameters of the parent artery and distal parent vessel are 4 mm and 3 mm respectively. The critical dimensions of the aneurysm are the height, dome and the neck size, which would take on values of 15 mm, 15 mm and 5 mm respectively. The aspect ratio, which is defined as the aneurysm height-to-neck ratio, is 3.0. In this study, the side branch diameter (denoted as “d”) would vary from 1.0 mm to 3.0 mm.

Considering the post-stenting condition, the metallic stent is a mesh device which covers both the aneurysm and the side branch (Fig. 1), with porosity roughly equals 66%. The double stent placement, however, would have a porosity about 35%.

Computational fluid dynamics analysis is performed by the software Fluent 6.3.26 (ANSYS, Canonsburg, Pennsylvania, USA). Tetrahedral elements are utilized in the mesh. Pulsatile velocity profile and time-dependent pressure waveform (122/82 mmHg) are prescribed at the inlet and outlets respectively. Non-slip boundary conditions are applied to all the walls. Newtonian blood is assumed, with density and viscosity being 1060 kg m^{-3} and 0.0035 kg m^{-1} s^{-1}.

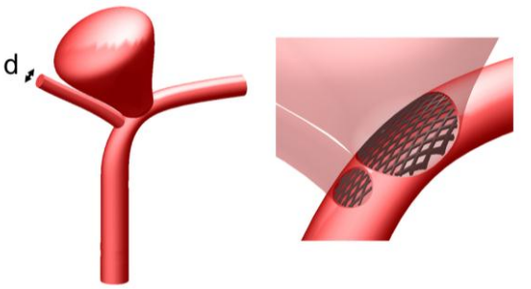

Fig. 1 Numerical model utilized in the CFD study. (Left) The diameter of the side branch diameter (denoted as "d") would vary from 1.0 mm to 3.0 mm. (Right) The post-stenting condition of the intracranial aneurysm.

3. RESULTS AND DISCUSSIONS

The maximum intra-aneurysmal pressure is important since this could be related to the rupture risk of the aneurysm. Considering the d = 3.0 mm case, this pressure would increase by 0.2 mmHg and 0.4 mmHg after the single and double stent placement. However, for d = 1.0 mm case, the pressure would decrease by 0.6 mmHg for both single and double stent placement. Consequently, the stenting efficacy for large side branch diameter is minimal.

Another crucial parameter is the volume flow rate entering the aneurysm. Figure 2 indicates that when the side branch diameter is large, the reduction of the flow rate into aneurysm due to stenting is small. A large side branch diameter would therefore provide an unfavourable environment for the treatment.

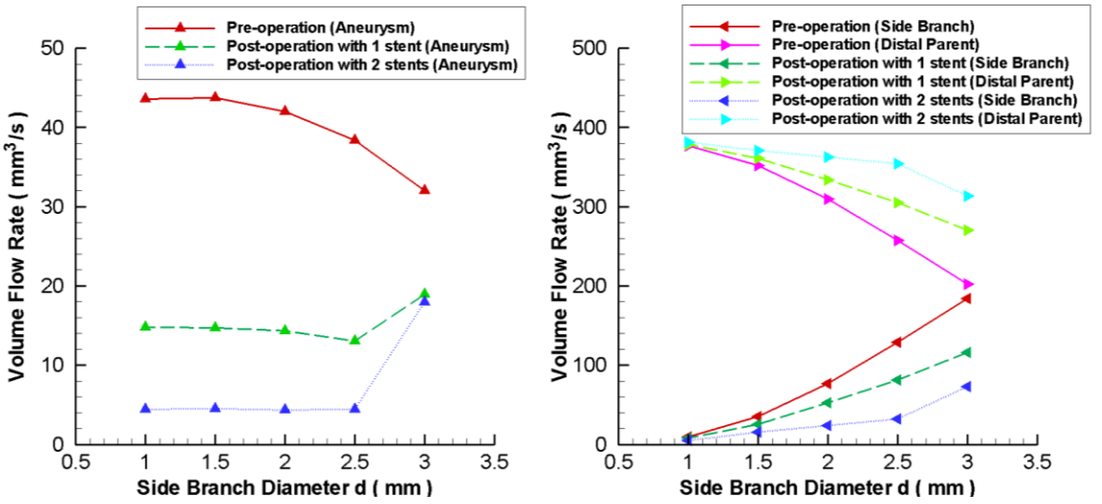

Fig. 2 (Left) Volume flow rate entering the aneurysm (Right) Volume flow rate in the side branch vessel and distal parent vessel.

Moreover, the alternation of the flow inside the side branch vessel is also determined. After stenting, the flow in a large / small side branch will be drastically / slightly altered. Consequently, a small side branch diameter can provide a more desirable hemodynamic environment for the treatment, as flow reduction in aneurysm is maximized while the flow in the side branch vessel is preserved for downstream tissues.

4. CONCLUSIONS

In conclusions, vascular diseases are dangerous and deserve careful investigation. In this study, computational simulations are performed to study the side branch diameter effect on the treatment efficacy of intracranial aneurysm. Based on the results, a small side branch diameter is more desirable for stenting, which can lead to large flow reduction in aneurysm without drastically altering the flow in the side branch. Moreover, a double stent can enhance the flow reduction into aneurysm, but would cause significant flow change in the side branch vessel, thus leading to undesirable consequences. In terms of future work, patient specific models would be utilized to validate the present results. This analysis can certainly provide useful information to clinicians for treatment planning and decision making.

REFERENCES

[1] D.M. Sforza, C.M. Putman and J.R. Cebral. Hemodynamics of cerebral aneurysms, *Annual Review of Fluid Mechanics*, 41, 91-107, 2009.

[2] A.Y.S. Tang, H.N. Chan, A.C.O. Tsang, G.K.K. Leung, K.M. Leung, A.C.H. Yu and K.W. Chow. The effects of stent porosity on the endovascular treatment of intracranial aneurysms located near a bifurcation, *Journal of Biomedical Science and Engineering*, 6, 812-822, 2013.

[3] A.Y.S. Tang, S.K. Lai, K.M. Leung, G.K.K. Leung and K.W. Chow. Influence of the aspect ratio on the endovascular treatment of intracranial aneurysms: a computational investigation, *Journal of Biomedical Science and Engineering*, 5, 422-431, 2012.

3rd International Conference on Computational and Mathematical Biomedical Engineering – CMBE2013

16-18 December 2013, Hong-Kong

P. Nithiarasu and R. Löhner Eds

Comparisons of image-based computational flow dynamics in giant and small intracrenial aneurysms

Chubin. Ou*, Jiaqi. Wang, Wei. Huang***, John Ching-kwong. Kwok**** and Matthew M.F. Yuen*****

*Department of mechanical engineering, Hong Kong University of Science and Technology, Clear Water Bay, Kowloon, Hong Kong, cou@ust.hk

**Department of mechanical engineering, Hong Kong University of Science and Technology, Clear Water Bay, Kowloon, Hong Kong, jwangaq@ust.hk

***Department of mechanical engineering, Hong Kong University of Science and Technology, Clear Water Bay, Kowloon, Hong Kong, mewhuang@ust.hk

****Division of biomedical engineering, Hong Kong University of Science and Technology; Department of neurosurgery, Kwong Wah Hospital, Kowloon, Hong Kong, jckkwok@ha.org.hk

*****Department of mechanical engineering and division of biomedical engineering, Hong Kong University of Science and Technology, Clear Water Bay, Kowloon, Hong Kong, meymf@ust.hk

SUMMARY

Intracranial aneurysm is a localized bulging of the arterial wall in human brain. Mechanical factors such as wall shear stress, oscillatory, and dynamics of blood flow play crucial roles in the formation, progression and rupture of intracranial aneurysms. However, the mechanical parameters of interest are difficult to measure *in vivo*. Our objective was to demonstrate an approach that computational fluid dynamics (CFD) combined with three-dimensional (3D) digital subtraction angiogram (DSA) to provide such mechanical information in a patient-specific manner. The DSA images from two patients, one with a giant aneurysm and other one with a small aneurysm, were obtained for analysis. It was found that there were different patterns of flow dynamics in the giant and small aneurysms. More investigations are needed for better understanding the aneurysm growth and rupture.

Key words: *blood flow, wall shear stress, aneurysm, growth*

1 INTRODUCTION

Intracranial aneurysm is a localized bulging of the arterial wall in human brain. It presents in 2-5% of the populations worldwide [1]. Most aneurysms remain unruptured and safe. In the case of rupture, it causes bleeding, which leads to subarachnoid haemorrhage, stroke, coma or even death. Mechanical factors play crucial roles in the the formation, progression and rupture of intracranial aneurysms. However, it is difficult to measure wall shear stress, oscillatory, and dynamics of blood flow in human subjects. Computational fluid dynamics (CFD) has been used to study and analyse the flow field inside aneurysms. Our objective was to demonstrate an approach that computational fluid dynamics (CFD) combined with three-dimensional (3D) digital subtraction angiogram (DSA) to provide such mechanical information in a patient-specific manner.

2 METHODOLOGY

A 63-year-old woman presented with symptoms due to a giant unruptured ophthalmic internal carotid artery (ICA) aneurysm. A 47-year-old woman presented with symptoms due to a small unruptured left cavernous segment ICA aneurysm. Both patients were examined by a biplane 3D DSA machine, which provided high resolution volumetric image data. Sections of the artery with the aneurysms are reconstructed into 3D geometry. The geometry will be smoothed by using the Laplacian algorithm and then be meshed for CFD analysis.

The governing equation for the blood flow inside the aneurysm is given by the Navier Stokes equation:

$$\rho\left(\frac{\partial v}{\partial t} + v \cdot \nabla v\right) = -\nabla p + \nabla T + f \quad (1)$$

Where ρ is the density of the fluid, which in the case of blood, is assumed to be a constant of 1066kg/m^3 as an incompressible fluid. v, p, T and f refers to the velocity vector, pressure viscous stress tensor and body force respectively.

The flow is assumed to be incompressible and laminar. To account for the shear-thinning effect of blood, Bird Carreau Non-Newtonian Model [2] is used to describe the relationship between shear strain rate $\dot{\gamma}$ and viscosity μ as as below:

$$\mu = \mu_\infty + \frac{(\mu_0 - \mu_\infty)}{(1+(\lambda\dot{\gamma})^2)^{(1-n)/2}} \quad (2)$$

Pulsatile volume flow rate is prescribed at the inlet and pressure is prescribed at the outlet. The pulsatile waveform is adapted from Watton et al [3] and approximated using Fourier series. Due to the lack of data on the viscoelasticity of patients' vascular wall, the wall is assumed to be rigid with no-slip condition applied. The flow field inside the aneurysm is simulated for three cardiac cycles with a time step of 0.01s to confirm numerical stability.

3 RESULTS

The nonlinear equations are solved by CFX using second-order upwind scheme and finite volume method. The result is then imported into Tecplot for analysis. Time averaged wall shear stress (WSS), wall shear stress gradient (WSSG), oscillatory shear index (OSI) flow streamline and vorticity level are studied and compared between the giant aneurysm case and the small aneurysm case. It is found that high speed flow enters the distal end of the neck in the giant aneurysm, which produced high wall shear stress on the aneurysm sac wall on that side. However, in the small aneurysm, both blood flow speed and wall shear stress were less than normal adjacent vessel. Higher vorticity level was found in the giant aneurysm while lower in the small one.

4 CONCLUSIONS

We demonstrated an image-based CFD analysis approach to provide key hemodynamic information for prospective studies of aneurysm growth and rupture in both giant and small intracranial aneurysms. Such detailed information may be useful for the surgical management, endovascular planning, and treatment of intracranial aneurysms. More investigations are needed for better understanding the aneurysm growth and rupture.

REFERENCES

[1] J.C. Lasheras. The biomechanics of arterial aneurysms. *Annu.Rev.Fluid Mech.*, 39, 293-319, 2007.

[2] R.B. Bird and P.J. Carreau. A nonlinear viscoelastic model for polymer solutions and melts—I. *Chemical Engineering Science*, 23, 427-434, 1968.

[3] Watton PN, Selimovic A, Raberger NB, Huang P, Holzapfel GA, Ventikos Y. Modelling evolution and the evolving mechanical environment of saccular cerebral aneurysms. Biomech Model Mechanobiol (2011) 10:109-132

3rd International Conference on Computational and Mathematical Biomedical Engineering – CMBE2013

16-18 December 2013, Hong-Kong

P. Nithiarasu and R. Löhner (eds)

Changes in residual strain and residual stress of rat's abdominal aorta in response to danshen extract

Hui Han*, Yi Wah Mak*, David C. C. Lam and Wei Huang*****

*Department of Health Technology and Informatics, Hong Kong Polytechnic University, Hung Hom, Kowloon, Hong Kong

**Department of Mechanical and Aerospace Engineering, Hong Kong University of Science and Technology, Clear Water Bay, Kowloon, Hong Kong

*** Department of Mechanical and Aerospace Engineering, Hong Kong University of Science and Technology, Clear Water Bay, Kowloon, Hong Kong, mewhuang@ust.hk

SUMMARY

Danshen, the dried root of Salvia miltiorrhiza and a traditional Chinese herb, has been applied for the reduction of hypertension. Our objective was to study the anti-hypertensive effect of danshen extract on residual strain and residual stress at the zero-stress state of rat's abdominal aorta. The approach by monitoring the changes of opening angles and residual strains of blood vessel at zero-stress state was applied to study the effects of aqueous extract of danshen. In addition, the rat's abdominal aortas were prepared for the measurement of the incremental Young's modulus in circumferential direction. The residual stress distribution in the abdominal aorta was estimated on the Hooke's law. Our results demonstrated that the zero-stress state of rat's abdominal aorta was affected by danshen extract. The present work provides a new approach to study the anti-hypertension effect and mechanism of danshen extract. More *in vivo* and *in vitro* studies are needed.

Key Words: *zero-stress state, elastic Young's modulus, Chinese herbal medicine*

1 INTRODUCTION

Hypertension affects millions of people in the world. Danshen, among other Chinese herbs, has been used traditionally for the treatment of hypertension in Chinese. Different anti-hypertensive molecular mechanisms of aqueous extract of danshen have been studied [1, 2]. The viscoelastic properties of blood vessel contribute to the vascular biology and tissue remodelling in hypertension. However, how danshen affects the mechanical properties of blood vessel is not clear.

To study the mechanical properties of a blood vessel, one has to know the zero-stress state of the vessel wall. The zero-stress state of a blood vessel is very different from the *in vivo* state and the no-load state of the vessel. In a living subject, the blood vessels are constantly subjected to blood pressure, blood flow, and mechanical stresses. After dissecting from the body, a blood vessel specimen is cut into small rings and placed on a Petri dish; the arterial small rings are at no-load state. At no-load state, the internal pressure, external pressure, and longitudinal stress in a short ring-shaped segment are all zero; however, there are residual stress and residual strain in the wall of the segment. When such a ring is cut radially to release the residual stress in the wall, it usually opens up into a sector. When the sector configuration does not change further, the vessel wall is at the zero-stress state. The zero-stress state can be characterized by residual strain, residual stress, and opening angle, which is the angle subtended between two radii, with origin located at the midpoint, and tips at the outer edges of the endothelium. The zero-stress state of a blood vessel is the basic configuration of blood vessel affected solely by intrinsic parameters [3, 4]. The residual strain and residual stress in aorta of hypertensive rats were changed rapidly and significantly [5, 6]. In the present study, we evaluated the effect of aqueous abstract of danshen on the residual strain and residual stress at the zero-stress state of rat's abdominal aorta.

2 MATERIALS AND METHODS

Sprague Dawley rats, male, around 350g, were used. Rat was anesthetized with an intraperitoneal injection of pentobarbital sodium (50 mg/kg body weight). After a bolus of normal saline with 1000 U/kg body weight of heparin (1000 U/ml) was injected, the blood in cardiovascular system was washed out by vascular perfusion of 0.1 M physiological saline buffer (PBS) for 5 min under a perfusion pressure of 80 mm Hg in the left ventricle and a draining pressure of 0 mm Hg at the right atrium. Then the abdominal aorta, located below the renal arteries and above the bifurcation of left and right ileal arteries, was isolated from surrounding tissues for dissection. The reason for choosing this piece of aorta was because it does not have side branch and has uniform diameter.

After dissecting from the abdominal aorta, the aortic specimens were cut into small rings with about 1-mm height; and the rings were placed on the small wells filled with Krebs solution bubbled with a gas of 95% O_2-5% CO_2 at 37°C. The arterial small rings were at no-load state. By cutting radially to release the residual stress in the wall, the vessel ring opened up into a sector quickly; at 20 min after cutting, the sector's configuration would not change and was defined as the zero-stress state of a blood vessel. Danshen extract prepared with methanol was added in the Krebs solution (danshen concentration: 1 mg/ml). Additionally, other sets of samples were tested in a solution of 10^{-5} Mol/L Norepinephrine in Krebs solution as positive control or a Krebs solution as negative control, respectively. During the experiment, the temperature of Krebs solution in the heating box was kept at 37°C with a temperature control system consisted of a stirring hot plate (Cole-Parmer, Vernon Hill, Illinois, USA) and an ANC 675 Thermal Controller (Yeou Jenq Electric Co., Taiwan). The changes of the aorta's zero-stress state after adding danshen extract, Norepinephrine solution or Krebs solution were monitored by taking photos routinely for analysis to determine the opening angle and residual strain [7].

For constitutive equations of soft tissue involving finite strain, Green's strain is used [3]. In circumferential direction, Green's strain, ε, is related to the circumferential stretch ratio λ by the equation:

$$\varepsilon = \left(\lambda^2 - 1\right)/2 . \tag{1}$$

The circumferential stretch ratios for the inner wall, λ_{iw}, and the outer wall, λ_{ow}, are

$$\lambda_{iw} = l_{iw}^{no-load} / l_{iw}^{zero-stress}, \text{ and } \quad \lambda_{ow} = l_{ow}^{no-load} / l_{ow}^{zero-stress}, \tag{2}$$

where $l_{iw}^{no-load}$ is the circumferential length of inner wall at no-load state and $l_{iw}^{zero-stress}$ is the circumferential length of inner wall at zero-stress state. Similarly, $l_{ow}^{no-load}$ is the circumferential length of the outer wall at no-load state and $l_{ow}^{zero-stress}$ is circumferential length of the outer wall at zero-stress state.

From the difference of the vessel geometry between the no-loaded state and the zero-stress state, the strains in the inner wall, ε_{iw}, and outer wall, ε_{ow}, of the blood vessel were computed by

$$\varepsilon_{iw} = \left(\lambda_{iw}^2 - 1\right)/2, \quad \varepsilon_{ow} = \left(\lambda_{ow}^2 - 1\right)/2 . \tag{3}$$

$\varepsilon_{i\omega}$ and $\varepsilon_{o\omega}$ are the residual strains in the inner wall and outer wall, respectively.

Additionally, other sets of abdominal aorta, located below the renal arteries and above the bifurcation of left and right ileal arteries, were prepared for measuring the elastic Young's modulus of rat's abdominal aorta with a built testing device and established procedures [8]. The

residual stress was then estimated by the multiplication of the residual strains by the circumferential elastic Young's modulus of rat's abdominal aorta based on the Hooke's law.

3 CONCLUSIONS

We presented an approach to study the anti-hypertensive effects of danshen extract by monitoring the changes of opening angles and residual strains, and estimating the residual stress at the zero-stress state of blood vessel. The new approach may help us understanding the effects of danshen on the mechanical properties of blood vessels and how the elastic properties of blood vessel contribute to vascular biology and tissue remodeling in hypertension. More *in vivo* and *in vitro* studies are needed to study the anti-hypertension effect and molecular mechanism of danshen on the tissue remodeling and zero-stress state of blood vessels.

REFERENCES

[1] D.D. Kim, F. A. Sánchez, R. G. Durán, T. Kanetaka, W. N. Durán. Endothelial nitric oxide synthase is a molecular vascular target for the Chinese herb Danshen in hypertension. *Am J Physiol* 292, H2131-2137, 2007.

[2] J. Wang, J., Q. Jiang, L. Wan, K. Yang, Y. Zhang, Y. Chen, E. Wang, N. Lai, L. Zhao, H. Jiang, Y. Sun, N. Zhong, P. Ran, and W. Lu. Sodium Tanshinone IIA Sulfonate Inhibits Canonical Transient Receptor Potential Expression in Pulmonary Arterial Smooth Muscle from Pulmonary Hypertensive Rats. *Am J Respir Cell Mol Biol.* 48, 125-134, 2013.

[3] Y. C. Fung. *Biodynamics: Circulation*. Springer-Verlag, 1984. 2nd ed., 1996.

[4] R.N. Vaishnav and J. Vossoughi. Estimation of residual strains in aortic segments. *Biomedical Engineering, II, Recent Developments*, edited by C.W. Hall. New York: Pergamon, pp. 330–333, 1983.

[5] S.Q. Liu and Y.C. Fung. Relationship between hypertension, hypertrophy, and opening angle of zero-stress state of arteries following aortic constriction. *J. Biomech. Eng.* 111, 325-335, 1989.

[6] T. Matsumoto and K. Hayashi. Stress and Strain Distribution in Hypertensive and Normotensive Rat Aorta Considering Residual Strain. *J. Biomech. Eng.* 118, 62-74, 1996.

[7] H. Han, D. C. C. Lam, and W. Huang. Effect of danshen on the zero-stress state of rat's abdominal aorta. *Molecular and Cellular Biomechanics*, 9, 295-307, 2012.

[8] W. Huang, W., D. Delgado-West, J. Wu, and Y. C. Fung. Tissue remodeling of rat pulmonary artery in hypoxic breathing: II. Course of Change of Mechanical Properties. *Annals of Biomedical Engineering*, 29, 552-562, 2001.

3rd International Conference on Computational and Mathematical Biomedical Engineering – CMBE2013

16-18 December 2013, Hong-Kong

P. Nithiarasu and R. Löhner (Eds)

Hemodynamic investigation of flow diverter angle at the aneurysm neck

Kaavya Karunanithi*, Chang J. Lee*, Winston Chong and Yi Qian***

*Australian School of Advanced Medicine, Macquarie University, Sydney, Australia

kaavya.karunanithi@mq.edu.au

chang-joon.lee@mq.edu.au

yi.qian@mq.edu.au

**Monash Medical Center, Melbourne, Australia

wkwinston.chong@gmail.com

SUMMARY

Flow diverters are currently the treatment of choice for intracranial aneurysms. However, there is a significant rate of failure that has been associated with this much favored procedure. Our study aims to investigate how the deployed flow diverter‘s angle of curvature across the aneurysm neck affects its hemodynamics and its occlusion rate. We aim to optimize the desired angle of curvature needed to achieve maximum occlusion thereby increasing its success rate. The clinical implication brought forth by this study includes determination of radial stent deployment force by surgeons to attain the required flow diverter angle at the aneurysm’s neck for its success.

Key Words: *Flow diverter angle, volume flow reduction, energy loss, aneurysm neck.*

1 INTRODUCTION

Flow Diverter (FD) stents have provided a new method of endovascular reconstruction for large and complex aneurysms. FD stents are designed to treat the aneurysm without coiling by using a fine mesh to divert flow away from the aneurysm sac, reduce flow into the aneurysm and promote progressive thrombosis [1, 2]. Various large scale, multi-center studies have been conducted to investigate short, mid and long term success rate of flow diverter treatment of cerebral

aneurysms. Although vascular reconstruction is achieved in most of the cases, reported failure rates including technical, clinical adverse events and delayed aneurysm rupture range from 1.5% to 6 % [3, 4]. This study aims at understanding how the angle of deployment of flow diverter across the aneurysm neck affects its hemodynamics using Computational Flow Dynamics (CFD). Optimized deployment techniques can be then developed by clinicians to attain the desired angle of curvature.

2 METHOD

An optimum flow diverter angle at the aneurysm neck enables its occlusion. This is accomplished by reducing the volume of blood flowing into the aneurysm. 4 cases of flow diverter-aneurysm geometry were assembled using Creo Elements Direct Modeling Express 4.0. The flow diverter angle across the neck was fixed at 0◦ (Case1), 35◦ (Case2) and 70◦ (Case3) for 3 cases. A no stent case was included as control (Case4). The patient aneurysm geometry is an Internal Carotid Artery (ICA) aneurysm having a neck width of 4.1mm. The SILK flow diverter (Balt Extrusions) was modeled using Pro Schools Edition 4.0. Meshing was done using ICEM (Ansys, Pennsylvania) and solved in Ansys CFX 13.0.

3 RESULTS AND CONCLUSIONS

The Volume Flow Reduction percentage (VFR %) and Energy Loss (EL %) was calculated for each case. High EL and VFR% are indicators of aneurysm occlusion and thereby its success [5, 6]. The results showed that flow diverter angle across the neck significantly alter the hemodynamics inside the aneurysm. The results showed that for the curved stent cases (Case 2 and Case3), the volume flow reduction ranged from 88% to 93%. A difference of more than 50% flow reduction was observed in the curved stent cases than the straight flow diverter geometry, whose volume flow reduction was just above 41%. Higher EL% is observed with an increasing angle of curvature. The Energy loss for Case 2 and 3 was calculated as 51% and 58% whereas the same for Case 1 was 40%. The study warrants further investigation of the effect of flow diverter deployment angle on aneurysm hemodynamics. It confirms the crucial role played by flow diverter positioning for successful treatment of cerebral aneurysms.

REFERENCES

[1] James V Byrne, I. S. Flow Diverters in the Management of Intracranial Aneurysms: A Review, *EJMINT* Original Article, 2012.

[2] Lubicz, B., Collignon, L., Raphaeli, G., Pruvo, J.-P., Bruneau, M., De Witte, O., & Leclerc, X. Flow-Diverter Stent for the Endovascular Treatment of Intracranial Aneurysms, *Stroke*, 41(10), 2247-2253, 2010.

[3] Berge, J., Biondi, A., Machi, P., Brunel, H., Pierot, L., Gabrillargues, J., Bonafe, A. Flow-diverter silk stent for the treatment of intracranial aneurysms: 1-year follow-up in a multicenter study. [Clinical Trial Multicenter Study], *AJNR Am J Neuroradiol*, 33(6), 1150-1155, 2012

[4] Park, H. K., Horowitz, M., Jungreis, C., Genevro, J., Koebbe, C., Levy, E., & Kassam, A. Periprocedural morbidity and mortality associated with endovascular treatment of intracranial aneurysms, *AJNR Am J Neuroradiol*, 26(3), 506-514, 2005.

[5] Zhang, Y., Chong, W., & Qian, Y. Investigation of intracranial aneurysm hemodynamics following flow diverter stent treatment, *Medical Engineering & Physics*, 35(5), 608-615, 2013.

[6] Takao, H., Murayama, Y., Otsuka, S., Qian, Y., Mohamed, A., Masuda, S., Abe, T. Hemodynamic Differences between Unruptured and Ruptured Intracranial Aneurysms during Observation, *Stroke*, 43(5), 1436-1439, 2012.

[7] Ma, D., Dargush, G. F., Natarajan, S. K., Levy, E. I., Siddiqui, A. H., & Meng, H. Computer modeling of deployment and mechanical expansion of neurovascular flow diverter in patient-specific intracranial aneurysms, *Journal of Biomechanics*, 45(13), 2256-2263, 2012.

3rd International Conference on Computational and Mathematical Biomedical Engineering – CMBE2013
16-18 December 2013, Hong-Kong
P. Nithiarasu and R. Löhner (eds)

Image-based hair counting for hair care diagnosis system

Huang-Chia Shih and Bo-Syun Lin
Human-Computer Interaction Multimedia Lab.
Department of Electrical Engineering, Yuan Ze University, Taiwan

SUMMARY

Recently years, many researches focus on the field of medical image processing, meanwhile, commercial software products have been developed to apply for clinical usages such as the computed tomography (CT) imaging, cardiovascular imaging, ultrasound imaging, X-ray imaging. Unfortunately, the product of hair care diagnosis is short of robustness and efficiency. To cope with this, we aim to develop a practical hair counting algorithm for understanding the hair health condition such as the thickness, density, and length information. This clinical analysis system performs the scalp condition and therapy suggestion for doctors and patients. In the experiments, the proposed hair counting algorithm outperforms in accuracy. It shows that our system is robust to the curls, oily, and dandruff-cohere situations.

Key Words: *hair counting; hair follicle pathology analysis; follicle diagnosis; hair scalp diagnosis; hair healthy recommendation system.*

1. INTRODUCTION

With the development of the digital image processing technology, the computer-aid diagnosis and treatment is capable of dealing with the computed tomography (CT) image, positron emission tomography (PET), and the chest X-ray image.

Nowadays, because the rapid climate change, air pollution, and acid rain problem, scalp care is a concerning subject to the general public. People desire to quantitatively assess the healthy condition of the cranial hair such as the density, diameter, and length. Many hair properties enable doctor to make the decision of therapy more accurate. For scalp image analysis, there are few patents and literatures focused on the treatment of follicular [1], [2]. Unfortunately, it still short of a robust system to deal with hair and scalp image analysis.

The main contribution of this paper is the proposal of a novel approach that computes the precise number of hair, which overcomes four major difficulties. First, the oily and wet hair produces the bright spot on the middle part of the hair. Before counting the number of hairs, we need to eliminate the bright spot to avoid the hair-breaking situation. Second, the bending or curling hair will deduce the line detection faults. When the hair is not a straight line, the conventional line detection algorithm is unavailable. Third, the ambiguous situations were occurred when two or more than two hairs crossover and occluded each other. It has become more difficult to locate the hair accurately. Finally, because the scalp image is very tiny and hided, it easily results in the feature of scalp being blurred and missing. It is frequently occurs when the lighting condition is insufficient or over-exposure.

2. METHOD

Fig. 1 illustrates the flow diagram of the proposed approach, which includes three modules: 1) Preprocessing, 2) Multi-scale line detection, and 3) Hair labeling and counting.

In the preprocessing module, it applies the contrast adjustment to the original input image. We also use the morphological algorithm [3] to solve the bright spot problem. In the multi-scale line detection module, a modified Hough transform algorithm [4] is used to detect every hair and filter out regions without hair or tiny line segment. Finally, the hair labeling and counting is employed to determine the number of hairs and the scalp health condition.

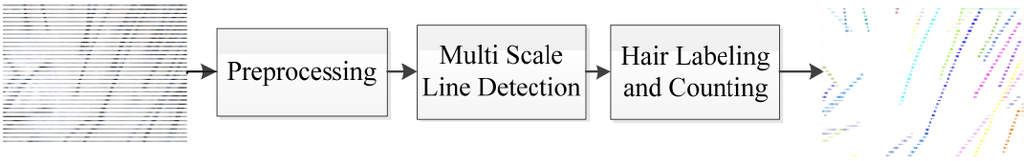

Fig. 1 System flowchart

2.1 Preprocessing

In practice, the color of hair is darker than skin color tone. In order to simplify the system, we use the black hair as the test image. Nevertheless, the hairs with the other color are remain valid using the simply color transformation method. As long as the contrast between the color of hair and skin color tone is maximized, most of noises of the test image can be effectively depressed. However, there are still some difficulties unable to eliminate completely using the fundamental image processing algorithms. For instance, the hair with the hole suffers from oily spot reflection. With the conventional region growing method, it produces many false merges between two individual hairs. In this paper, we apply the morphological-based processing to deal with the oily spot removal, which enables to reduce the hole appears in the middle of hair efficiently.

2.2 Multi-scale Line Detection (MSLD)

Based on our observation, the amount of hair segments are lost if the general Hough transform (HT) applied. Therefore, we proposed the multi-scale approach to avoid this problem. HT is applied for three different resolutions images which are 1024*768, 512*384, and 256*192 in this study. Each scale undergoes different treatment, such as adjustment towards the threshold of the Hough transform and the sensitive minimum length of the line segment. Finally, we rescale three vectored line images as size of 1024*768, and apply the OR operator. As a result, taking the advantage of the multi-scale line segments is increasing the counting accuracy.

As shown in Fig. 2, single scale is unable to cover all of the length and curvature hairs. For example, when the hairs are crossover, parallel with overlapping each other, as well as the curvature of the hair exceeded the tolerance of HT line detection. In Fig. 2(a), the situation of unfound and mislabeled hair is presented. In Fig. 2(b), test image combined from different scales, and compensates for the disadvantages of single scale.

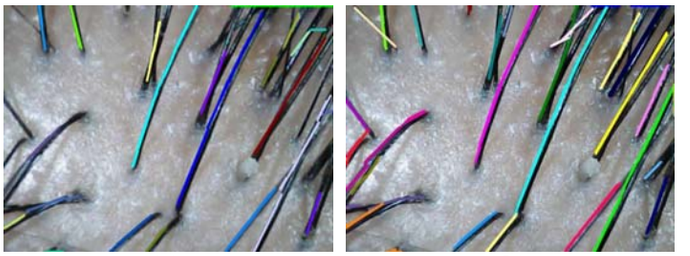

(a) (b)

Fig. 2 Comparison of single scale and multi-scale line extraction, which the color denotes the labeling, (a) result image of single scale, (b) result image of multi-scale.

2.3 Hair Labeling and Counting

Based on the MSLD method, a great number of line segments can be extracted. All lines with different length depend on the curvature of the hair and the direction of the hair flow. In this study, we aim to count the number of hair precisely. Generally speaking, the hairs will not go straight all the time. Based on the conventional Hough line detection, the curling hair can be extracted as many pieces of straight lines. However, these lines unable to represent truly amount of hairs. Using the non-linear polynomial line fitting is the one of the solutions, but it is high computational cost. Therefore, we treat hair counting problem as clustering and labeling problem. The line segments can be mutually correlated. Assume that each of hair with a unique labeling, and each of line segments treated as the object. Hence, we adopt with the orientation and distance similarity approach to identify individual hair.

3. RESULTS

To evaluate our system, the UPMOST (UPG622) electron microscope is used as the capturing device, user can manually adjust focus and light source. For the dataset total of 40 images are captured at the resolution of 1024*768.

First of all, all captured images are separated in to two dataset, images with adjusted light source are classified to dataset 1, and images without light source are classified to dataset 2.

Table. 1 Analysis and comparisons of experimental results

		Precision	**Recall**
Dataset1	Using morphological opening & multi-scale	94.98%	83.50%
	Without morphological opening & multi-scale	92.77%	74.79%
	Using morphological opening only	93.04%	80.67%
	Using multi-scale only	93.20%	77.42%
Dataset2	Using morphological opening & multi-scale	98.05%	85.56%
	Without morphological opening & multi-scale	96.52%	75.14%
	Using morphological opening only	97.09%	78.43%
	Using multi-scale only	95.95%	77.93%

In this experiment, the preprocess step is performed to the input image, then convert it to a thinning image, and adjusted them into three different scales. Then apply HT to each scale for

identifying line segments. Table 1 shows that the results after applying the morphological opening & MSLD method. It reaches 98.05% and 94.93% in precision rate, and 83.50% and 85.56% in recall rate, respectively. It also indicates that performance is significant better than the other strategies, and recall rate is also higher than other results. Finally, the labeling algorithm is applied to detect each individual hair as shown in Fig. 3. In this paper, the thinning process is used to find line segments. However, due to image quality and thinning procedure, it result unidentified hair.

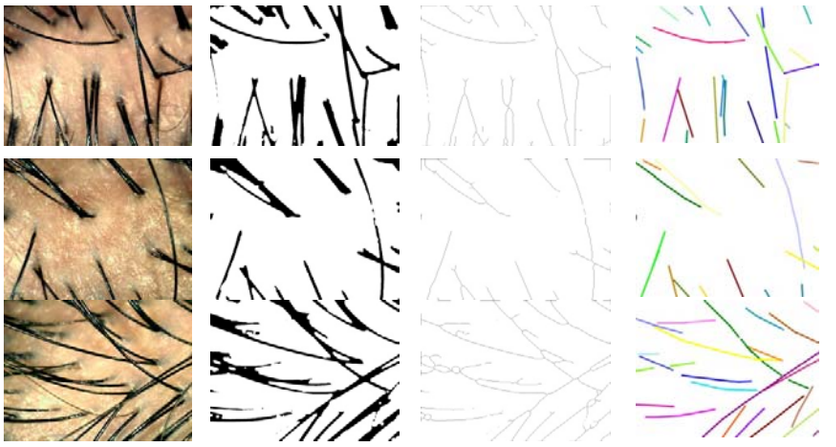

(a) (b) (c) (d)

Fig. 3 result images, (a) original image, (b) binarized image with morphological opening, (c) Thinning image, (d) detected hairs with labelings. (the pixels with the same color denotes the same hair)

4. CONCLUSIONS

This study aimed to achieve automated hair counting and how to perform effective hair counting and labeling algorithm. During the preprocessing step, we overcome the problem of bright spots, and applied for thinning process and Hough transform. We proposed the multi-scale approach to avoid the piece-wised problem for conventional Hough transform. The results outperformed the traditional line detection algorithm.

REFERENCES

[1] S. Amornsiripanitch. Total Quality of hair parameters measuring method, *United states Patent, pub. No. US 6,389,150B1*, May 14, 2002.

[2] P. Vallotton and N. Thomas. Automated body hair counting and length measurement, *Skin Research and Technology*, 14, 493-497, 2008.

[3] R.C. Gonzalez, and R.E. Woods. *Digital Image processing*, Prentice Hall, 2010.

[4] A. Jain. *Fundamentals of Digital Image Processing*, Prentice-Hall, 1989.

3rd International Conference on Computational and Mathematical Biomedical Engineering – CMBE2013
16-18 December 2013, Hong-Kong
P. Nithiarasu and R. Löhner (eds)

Biomechanisms of Impact-Resistance in Woodpecker's Ocular

Lizhen Wang[*,], Xiaoyu Liu[*,**],Yikun Ni[*,**] and Yubo Fan[*,**]**

*Key Laboratory for Biomechanics and Mechanobiology of Ministry of Education, School of Biological Science and Medical Engineering, Beihang University, 100191 Beijing, China
**International Joint Research Center of Aerospace Biotechnology and Medical Engineering,Ministry of Science and Technology of China,100191, Beijing, China
Email: yubofan@buaa.edu.cn

SUMMARY

Shaken baby syndrome (SBS) usually occurs in children when they subjected to high decelerations, which could result in vision loss and so on. However, woodpecker has no retinal haemorrhages at a high deceleration of 1000g during pecking. It must have special features to attenuate repetative impact force to sustain rapid pecking without ocular injury. In this study, the biomechanical analysis of kinematics parameters and orientation of ocular within the orbit during impact was investigated using finite element (FE) method.

Key Words: *woodpecker, ocular, resistance, retinal detachment*

1. INTRODUCTION

Eye disorders such as retinal hemorrhages were usually associated with shaken baby syndrome (SBS), which could lead to vision loss and blindness [1]. Retinal haemorrhages in SBS were thought to be the result of acceleration-deceleration induced shearing forces when the vitreous moves within the globe and the globe moves within the orbit [2]. However, woodpecker has no retinal haemorrhages at a high deceleration of 1000g during pecking [3]. Woodpecker was a naturally occurring model resistant to impact injuries those encountered in SBS. It must has special features to attenuate repetative impact force to sustain rapid pecking without ocular injury. Therefore, we focused on investigating the kinematics parameters and connections between orbital rim and sclera during impact using the finite element (FE) approach.

2. MAIN BODY

A numerical model of eye model with fat tissue and orbit was created according to the anatomy structure (Fig. 1). Retina model was incorporated into the current eye model with breakable bond contact attached to the supporting tissue. To validate the numerical eye model, six matched simulations were conducted to compare the eye model of Virginia Tech-Wake Forest University (VT-WFU). Different conditions were loaded with an duration of 5 ms based on the data in our previous study [4]. Parametric analysis was done by changing the kinematics parameters and orientation of ocular within the orbit to evaluate the biomechanics effects on ocular displacement and strain during impact. Significant positive correlation was found between the eye model and the VT-WFU eye model (R=0.91 for peak stress, R=0.93 for peak strain and R=0.89 for peak deflection). Stress waves and negative pressure contribute to the detachment [4]. Stress wave propagation in the retina leads to its break. It was stated that the orientation of ocular within the orbit has an obvious influence for woodpecker. By comparing the FE predicted strain of retina, it

reduced 15.6% and 28.6% compared to human. It was found that peak strains induced different location of retina for human, on the contrary, no difference for woodpecker when eye subjected to deceleration in different direction during impact.

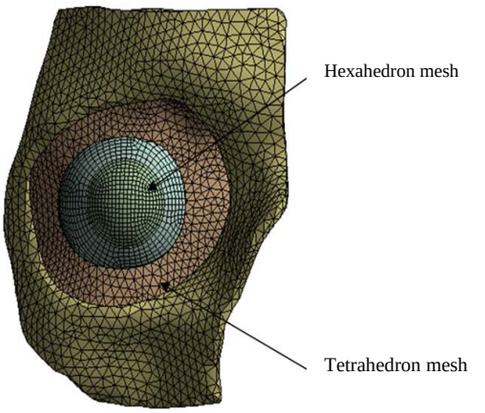

Fig. 1: Finite element model of woodpecker's eye including eyeball and extraocular tissues

3. CONCLUSIONS

The understanding of the mechanism of resisting ocular injury of woodpecker eye was provided. The effects of the direction of movement and the connection of orbital rim and sclera on the retina and vitreous strain distribution were obvious. In addition, the orientation of the ocular within the orbit had been minimized the Green Lagrange strain on the retina, which reduced the probability of impact injury

REFERENCES

[1] Morad Y, et al. American Journal of Ophthalmology, 134: 354-359, 2002.
[2] Duhaime AC, et al. New England Journal of Medicine, 338:1822-1829, 1998.
[3] Wang L, et al. Plos One, 6:e26490, 2011.
[4] Nagarajan R, et al. Journal of AAPOS,13: 364-369, 2009

3rd International Conference on Computational and Mathematical Biomedical Engineering – CMBE2013
16-18 December 2013, Hong-Kong
P. Nithiarasu and R. Löhner (eds)

The Mechanical Competition between Teeth of Black Carp and Mollusk Shells

C. He*, W. Zhou, H. Wang**, S. Shi*, and H. Yao***
*Department of Mechanical Engineering, the Hong Kong Polytechnic University, Hung Hom, Kowloon, Hong Kong SAR, P. R. China, mmhyao@polyu.edu.hk
**Institute of Applied Mechanics, Zhejiang University, Hangzhou 310027, P. R. China

SUMMARY

This work has explained the mechanism that why the pharyngeal teeth of black carp can crush the mollusk shells easily while the mechanical properties are similar for both biomaterials

Key Words: *biomechanics, biomineralized material, pharyngeal teeth.*

1. INTRODUCTION

There are a great number of researches focusing bio-armors (exoskeletons) such as shells of snails[1], crabs[2] and lobsters[3], which have been proved to exhibit high toughness and high strength. However, in nature, there is a species of fish called Mylopharyngodon piceus or black carp, which is one of four Chinese domestic fishes inhabiting in East China. Unlike other three which live on grass, phytoplankton or zooplankton, the black carp mainly feeds on shelled mollusks. Does such unique diet imply that the pharyngeal teeth of black carp, its major masticatory apparatus, are superior to the mollusk shells in mechanical properties?

2. MAIN BODY

Mollusks such as snail and mussels adopt hard shells to protect their vulnerable bodies. Recent studies on biomaterials have revealed that these shells especially the nacre layers exhibit excellent mechanical properties, inspiring a number of biomimetic endeavours. Nevertheless, in nature, there is a species of fish called *Mylopharyngodon piceus* or black carp, whose main diet is exactly snails and mussels. Does such unique diet imply that the pharyngeal teeth of black carp, its major masticatory apparatus, are superior to the mollusk shells in mechanical properties? In this work, structural and mechanical characterizations are conducted on the pharyngeal teeth of black carp, showing that enameloid, the outermost layer of black carp teeth, possesses similar elastic modulus and hardness in comparison to those of the pond snail shells. To shed light on the mechanics underlying the capability of pharyngeal teeth to crush mollusk shells, parametric studies on the geometry of the shells are conducted by means of finite element method. It is found that whether a mollusk shell is crushable or not, for given pharyngeal teeth, depends on the radius (R) and thickness (t) of the shell. A predation map (*Fig. 1*) for black carp teeth is constructed by delimiting the t–R plane into three phasic regions corresponding to three possible consequences of the mechanical competition between pharyngeal teeth and shells.

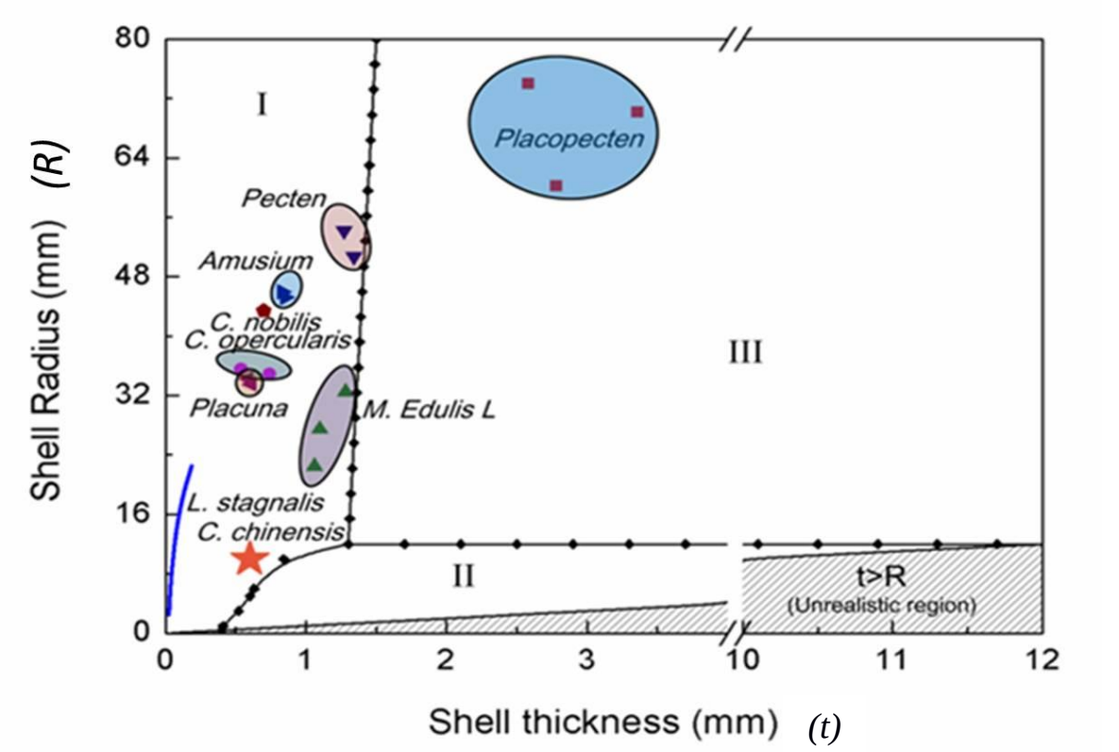

Fig. 1. Locations of shells of mollusk species in the predation map of black carp. While Placopecten, Pecten, Amusium, C. nobilis, C. opercularis, Placuna, and M. Edulis L are marine species, L. stagnalis and C. chinensis are freshwater dwellers.

3. CONCLUSIONS

It is concluded that whether a mollusk shell is crushable for given pharyngeal teeth or not depends on the radius (R) and the thickness (t) of the shell. It is interesting to notice that all randomly-selected freshwater shells fall in the crushable regime (Regime I) of the predation map (see the right figure) for black carp while the seashells do not necessarily. This feature of black carp teeth can be speculated as a result of evolution in response to its freshwater diet. Our results not only shed light on the mechanism of pharyngeal teeth crushing shells but also may serve as a significant guideline for the design of new protective or invasive structural materials.

REFERENCES

[1] H. Yao, M. Dao, T. Imholt, J. Huang, K. Wheller, A. Bonilla, S. Suresh, C. Ortiz, Protection mechanisms of the iron-plated armor of a deep-sea hydrothermal vent gastropod, *Proc. Natl. Acad. Sci.* USA 2010, 19, 987.

[2] P. Y. Chen, A. Y. M. Lin, J. McKittrick, M. A. Meyers, Structure and mechanical properties of crab exoskeletons, *Acta Biomater*. 2008, 4, 587.

[3] P. Romano, H. Fabritius, D. Raabe, The exoskeleton of the lobster Homarus americanus as an example of a smart anisotropic biological material, *Acta Biomater.* 2007, 3, 301.

3rd International Conference on Computational and Mathematical Biomedical Engineering - CMBE2013
16-18 December 2013, Hong-Kong
P. Nithiarasu and R. Löhner (Eds.)

A quasi-analytical method for calculating junction pressure losses in 1D vascular network models: Validation with high-resolution CFD

Kristian Valen-Sendstad[⋆], Jonathan P. Mynard[⋆†]

[⋆]Biomedical Simulation Laboratory, Department of Mechanical and Industrial Engineering, University of Toronto, Toronto ON, Canada;

[†]Heart Research Group, Murdoch Childrens Research Institute, Parkville VIC, Australia;

kvs@mie.utoronto.ca; jonathan.mynard@mcri.edu.au

SUMMARY

In 1D blood flow models, pressure losses at vessel junctions are often neglected but may be important in some settings. We validated a quasi-analytical method of estimating these pressure losses using high resolution CFD with Reynolds numbers spanning laminar and transitional regimes relevant to blood flows. The method is accurate and may be easily applied in 1D blood flow models.

Key Words: *arterial, venous, bifurcation, pressure loss, one-dimensional modelling.*

1 INTRODUCTION

One-dimensional (1D) modelling is increasingly being used to study vascular haemodynamics. In these models, a 1D form of the Navier-Stokes equations is solved in individual segments and vascular networks are formed by connecting segments at junctions with two coupling conditions:

$$\sum Q_{\text{in}} = \sum Q_{\text{out}}, \quad P_i + \tfrac{1}{2}\rho U_i^2 = P_j + \tfrac{1}{2}\rho U_j^2 + P_{\text{loss}} \tag{1}$$

where Q, P, U and ρ are flow (into or out of the junction), pressure, velocity and blood density. The second condition specifies mechanical energy conservation between two branches i and j, with P_{loss} representing the pressure losses caused by disturbed flow and recirculation zones in the vicinity of the junction. These 'minor' losses are usually neglected in 1D modelling studies, with continuity of static pressure ($P_i = P_j$) or total pressure ($P_{\text{loss}} = 0$) often assumed. However, there are a number of situations where P_{loss} may be significant; e.g. venous junctions where static pressure is low and velocity is high, in vascular bypass operations or in dialysis patients who are given an arterio-venous fistula. Existing methods for estimating P_{loss} have only been validated against experiments that used Reynolds numbers (Re) greatly exceeding Re in blood vessels. In the current study, we validated a quasi-analytical approach for estimating P_{loss} using high resolution 3D computational fluid dynamics (CFD) over a physiological range of Re. This paper focuses on converging flow which is relevant to the aforementioned (patho)physiological situations.

2 MAIN BODY

2.1 Three-dimensional simulations

For laminar and turbulent incompressible Newtonian flow, the Navier–Stokes equations read

$$\frac{\partial \vec{u}}{\partial t} + \vec{u} \cdot \nabla \vec{u} = \nu \nabla^2 \vec{u} - \frac{1}{\rho} \nabla p + \vec{f}, \qquad \nabla \cdot \vec{u} = 0. \tag{2}$$

Here $\vec{u}$ is the velocity vector, ν is kinematic viscosity, p is pressure, and $\vec{f}$ represents body forces. Let $t_n \in \mathbb{R}^+$ denote a discrete point in time. The velocity $\vec{u}_{n-1} = \vec{u}(\mathrm{x}, t_{n-1})$ is known, and the solution to $\vec{u}_n = \vec{u}(\mathrm{x}, t_n)$ is sought. This is done using an Incremental Pressure Correction solver as proposed by Goda [3], and consists of the following steps:

$$\frac{\vec{u}_I - \vec{u}_{n-1}}{\Delta t} = -B(\tilde{\vec{u}}, \bar{\vec{u}}) + \nu \nabla^2 \vec{u}_{n-\alpha} - \nabla p_{n-1/2} + f_{n-\alpha}, \qquad \nabla \cdot \vec{u}_{n-\alpha} = 0, \tag{3}$$

where the subscript I means *intermediate* and $\vec{u}_{n-\alpha} = (1-\alpha)\vec{u}_n + \alpha \vec{u}_{n-1}$, $\alpha \in [0,1]$. For the convective term we have chosen the implicit second-order accurate Adams-Bashforth scheme,

$$B(\tilde{\vec{u}}, \bar{\vec{u}}) = B\left(\frac{3}{2}\vec{u}_{n-1} - \frac{1}{2}\vec{u}_{n-2}, \vec{u}_{n-\alpha}\right). \tag{4}$$

For the viscous term we have chosen a second order accurate Crank–Nicholson discretization ($\alpha = \frac{1}{2}$). For the flow field to be divergence free at the next time step, the pressure is projected on to a divergence free velocity field by solving

$$\nabla^2 \Phi = -\frac{1}{\Delta t} \nabla \cdot \vec{u}_I. \tag{5}$$

where $\Phi = p_{n-1/2} - p_{n-3/2}$. The updated velocity and pressure can then be updated by

$$\vec{u}_n = \vec{u}_I - \Delta t \nabla \Phi, \qquad p_{n-1/2} = p_{n-3/2} + \Phi. \tag{6}$$

These particular choices have been made to ensure that the numerical scheme is minimally dissipative and energy preserving. Due to the range of geometries and *Re* in our study, the flow can become unstable and exhibit transitional shear layer instabilities. In an attempt to resolve the various scales of the flows, the time step was chosen to fulfil the Courant–Friedrichs–Lewy condition, hence avoiding artificial numerical viscosity. Convergence tests showed a difference in pressure drop, which is the primary focus of the study, of less than 1% for the two finest meshes. The final meshes consisted of 2–3 million linear elements. The solver was implemented in FEniCS (http://fenicsproject.org) and has been extensively verified for biomedical flows, cf. [4,6]. Steady velocity with a power law profile (mainly flat with a boundary layer) was imposed at the inlets and zero pressure was prescribed at the outlet.

2.2 Pressure loss approximation in a 1D model

The method for estimating P_{loss} is based on that described by Bassett et al [1] for simulating gas dynamics in engine pipes. The derivation employed a control volume analysis [1], with pressure

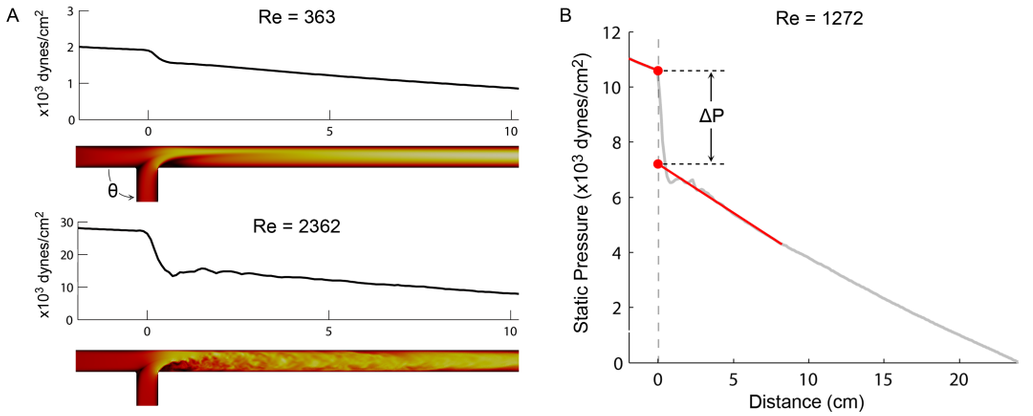

Figure 1: (A) Simulated velocity fields for steady converging flow at the lowest and highest *Re* tested (full branch lengths not shown), with plots of static pressure along the main duct. (B) Method of calculating ΔP, used to compare 1D and 3D results in Fig. 2.

losses calculated between a 'datum' branch (i.e. the supplier branch with the largest Q_{in}) and all 'collector' branches (i.e. those with flow exiting the junction). However, we found this method led to non-physiological discontinuities in the solution for pulsatile flow if maximal supplier flow switched between different branches. We therefore extended the model by defining a 'pseudo-datum' branch, an imaginary equivalent branch containing all junction inflow, with the following flow (Q_{dat}) and cross-sectional mean velocity (U_{dat}):

$$Q_{\text{dat}} = \sum_{j \in S} Q_j, \qquad U_{\text{dat}} = \left[\sum_{j \in S} U_j Q_j \cos\left(\tfrac{1}{2}\theta_j\right) \right] / Q_{\text{dat}} \tag{7}$$

Here S is the set of supplier branches, the cosine term approximates the redirection of the flow jet, and θ_j is the angle shown in Fig. 1. The corresponding angle of the pseudo-datum branch is calculated via the flow-weighted expression:

$$\theta_{\text{dat}} = \left[\sum_{j \in S} Q_j \theta_j \right] / Q_{\text{dat}} \tag{8}$$

Defining $\lambda = U_{\text{out}}/U_{\text{dat}}$, P_{loss} can then be approximated from the control volume analysis [1] as

$$P_{\text{loss}} = \tfrac{1}{2}\rho U_{\text{dat}}^2 \left(1 + \lambda^2 - 2\lambda \cos\left[\tfrac{3}{4}\theta_{\text{dat}}\right]\right) \tag{9}$$

Use of Eq. 9 in a 1D model was validated against 3D simulations of converging flow in a T-junction by comparing the static pressure drop (ΔP) between supplier and collector branches at the junction. Fig. 1A shows the velocity fields at two *Re* (defined according to flow in the outlet branch). For the 3D data, ΔP was calculated by linearly extrapolating pressure to the junction centre-point as described by Gardel [3] and illustrated in Fig. 1B. The 1D governing equations and solution method have been described in [5].

Fig. 2 compares ΔP from 3D simulations and three 1D approaches (Loss, Total, Static) over a range of *Re*, inlet flow ratios and side branch angles. Excellent agreement was found between 3D data and the 1D simulations employing Eq. 9 ('Loss' in Fig. 2). By contrast, ΔP was generally underestimated by assuming continuity of total or static pressure, with errors in the range 0 to 11,000 dynes/cm^2 (i.e. 0 to 8 mmHg).

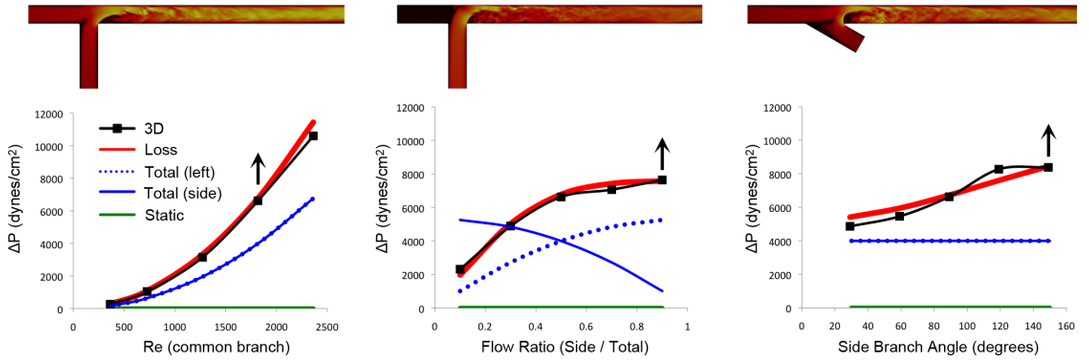

Figure 2: Relation of static pressure drop (ΔP) to outlet Re, flow ratio and side branch angle from 3D simulations and 1D simulations employing Eq. 9 ('Loss') or continuity of static or total pressure. Note: ΔP was similar for left-right and side-right flow paths for 3D and 1D (Loss, Static) simulations, thus only one line is shown (average ΔP); conversely, solid and dotted lines are shown separately for the side-right and left-right flow paths in the case of total pressure continuity.

3 CONCLUSIONS

A quasi-analytical expression for approximating pressure losses in vascular junctions was validated against high resolution CFD. This method is accurate over the full range of physiological Re that span laminar and transitional regimes, including flows exhibiting substantial instabilities.

Acknowledgments KVS is supported by a Postdoctoral Research Fellowship from the Government of Canada. JPM is supported by a CJ Martin Early Career Research Fellowship from the National Health and Medical Research Council of Australia. Computations were performed on the GPC supercomputer at the SciNet HPC Consortium.

REFERENCES

[1] M. D. Bassett, R. J. Pearson, N. P. Fleming, and D. E. Winterbone. A multi-pipe junction model for one-dimensional gas-dynamic simulations. SAE Trans, 112, 565-583, 2003.

[2] A. Gardel, Les pertes de charge dans les écoulements au traverse de branchments en té, Bull Technique de la Suisse Romande, 83, 123-130, 1957.

[3] K. Goda. A multistep technique with implicit difference schemes for calculating two-or three-dimensional cavity flows. J Comput Phys, 30, 76-95, 1979.

[4] A. Logg, K.-A. Mardal, G. N. Wells et al. Automated Solution of Differential Equations by the Finite Element Method, Springer, Ch. 22 (Simulation of transitional flows), 2012.

[5] J. P. Mynard and P. Nithiarasu. A 1D arterial blood flow model incorporating ventricular pressure, aortic valve and regional coronary flow using the locally conservative Galerkin (LCG) method. Comm Num Meth Eng, 24, 367-417, 2008.

[6] K. Valen-Sendstad, K. A. Mardal, and D. A. Steinman. High-resolution computational fluid dynamics detects high-frequency velocity fluctuations in bifurcation, but not sidewall, aneurysms of the middle cerebral artery. J Biomech, 46, 402-407, 2012.

3rd International Conference on Computational and Mathematical Biomedical Engineering - CMBE2013
16-18 December 2013, Hong-Kong
P. Nithiarasu and R. Löhner (Eds.)

Noninvasive quantification of fractional flow reserve: an approach based on one-dimensional pressure-flow analysis

E. Boileau, P. Nithiarasu
College of Engineering, Swansea University, Swansea, U.K., SA2 8PP
e.boileau@swansea.ac.uk

SUMMARY

We present preliminary results of an approach based on one-dimensional pressure-flow analysis to determine noninvasively the functional severity of coronary stenoses using the concept of myocardial fractional flow reserve (FFR). Recent studies have shown that estimation of FFR from computed tomography coronary angiography (CTCA) scans can be a useful guide in clinical decision-making for revascularization of specific lesions.

Key Words: *Fractional flow reserve (FFR), coronary stenosis, one-dimensional systemic and coronary models*

1 INTRODUCTION

At present, FFR appears as one of the most accurate index to assess the functional severity of coronary stenoses [1], and to determine whether angiographically equivocal stenoses can be responsible for myocardial ischæmia. It is the only reliable diagnostic method to ascertain the appropriateness of percutaneous coronary intervention (PCI) and, to date, has shown to significantly improve event-free survival [2]. FFR is performed invasively in the catheterization laboratory and represents the fraction of the normal maximal coronary blood flow that is achieved in the presence of a stenotic artery. It can be derived from the ratio of the mean hyperemic distal intracoronary pressure to the mean arterial pressure measured by the coronary catheter. It is generally agreed that lesions at greater risk of causing cardiac death or acute myocardial infarction (AMI) are those identified by an FFR < 0.75. On the contrary, revascularization of a functionally nonsignificant stenosis is considered to be of no benefit for the patient [2].

1.1 Noninvasive assessment of CAD

Noninvasive assessment of coronary artery disease (CAD) can be made using a variety of imaging modalities. In particular, computed tomography coronary angiography (CTCA) has been shown to provide a relatively high diagnostic accuracy for the detection of coronary stenoses, compared with invasive coronary angiography [3]. At the same time, other studies have shown that anatomical assessment of the hæmodynamic significance of coronary stenoses, as determined by visual and quantitative CTCA, does not always correlate well with the functional assessment of FFR [4]. This is particularly true in patients with intermediate severity lesions. Estimation of FFR from CTCA data (FFR_{CT}) can provide a noninvasive method for identifying ischæmia-causing stenosis in patients with suspected or known CAD. The diagnostic performance of this new method relies

on the accurate calculation of coronary flow and pressure from acquired CTCA scans, using computational fluid dynamics (CFD), and requires the construction of a realistic physiological model. Calculation of FFR_{CT} appears as a novel noninvasive technique with a potentially high diagnostic performance, compared with CTCA alone, for the detection of functionally significant coronary stenoses [5,6].

2 ESTIMATION OF FFR FROM CTCA

Computation of FFR_{CT} has been performed so far in a number of studies using three-dimensional (3D) models of the coronary tree and ventricular myocardium [5,6]. Since coronary flow and pressure are unknown *a priori*, the 3D model requires the coupling of lumped parameter models. These models need to be tuned so that both the cardiac output and the mean aortic pressure are 'matched with' the data obtained from allometric scaling laws and the patient's measured brachial artery pressure, respectively. Relevant boundaries of a 3D model typically include the aortic root, and the outlet boundaries of the ascending aorta and the coronary arteries. In addition to being limited by artifacts from CTCA, and the robustness of the segmentation algorithms, the overall accuracy of the results depend on an appropriate treatment of the defective boundary data. This process requires approximately 6 hours per case [6].

Although an approach based on one-dimensional (1D) modelling will not result in a complete spatial distribution of FFR_{CT}, as in a 3D model of the coronary tree, it would nevertheless present some advantage over the later in evaluating the significance of specific coronary stenoses, as identified by CTCA scans. 1D modelling of the systemic circulation has been carried out extensively in recent years, for gaining a better understanding of pressure-flow propagation, and can provide useful information at a reasonable computational cost. Predictions from such models exhibit many of the features of the systemic and coronary arteries, suggesting that they could be used as suitable tools in clinical decision-making.

2.1 1D model of transient pulsatile blood flow in compliant vessels

The one-dimensional governing equations are described by the system:

$$\frac{\partial \mathbf{U}}{\partial t} + \frac{\partial \mathbf{F}}{\partial x} = \mathbf{S}$$

$$\mathbf{U} = \begin{bmatrix} A \\ u \end{bmatrix} \quad \mathbf{F} = \begin{bmatrix} Au \\ \frac{u^2}{2} + \frac{p}{\rho} \end{bmatrix} \quad \mathbf{S} = \begin{bmatrix} 0 \\ \frac{-8\pi\mu}{\rho} \frac{u}{A} \end{bmatrix}$$

where $\mathbf{U}$ is the vector of primitive variables, $\mathbf{F}$ is the flux vector, $\mathbf{S}$ is the source vector term, μ is the blood viscosity and ρ its density. The system is closed by the pressure-area relationship:

$$p = p_{ext} + \beta \left(\sqrt{A} - \sqrt{A_0} \right), \quad \beta = \frac{\sqrt{\pi} h E}{A_0 (1 - \sigma^2)}$$

under the assumption of a thin homogeneous elastic wall, and where p_{ext} is the external pressure from the tissue, A_0 is the cross-sectional area at zero transmural pressure, h is the vessel wall thickness, E is the Young's modulus and σ is the Poisson ratio.

The human arterial network that we use is based on the improved model presented in [7,8]. The new coronary model includes all major branches up to the third generation, ending with subendocardial vessels of varying length to account for the micro-circulation. A time-varying external pressure proportional to the ventricular pressure is applied to the distal part of the equivalent

subendocardial vessels. To account for the ventriculo-vascular coupling, the aortic valve operates as a variable reflection coefficient with respect to backward-running aortic waves, and as a variable transmission coefficient with respect to forward-running ventricular waves. The model also includes an afterload-corrected ventricular pressure. Different ventricular input pressures, constructed from experimental data, are considered.

3 RESULTS & FUTURE WORK

Preliminary results are presented, using the baseline model for the arterial network, for varying degree of stenosis in the left coronary artery. Interestingly, FFR is independent of changes in heart rate and systemic blood pressure and is not altered by conditions known to increase the base-line myocardial flow [1].

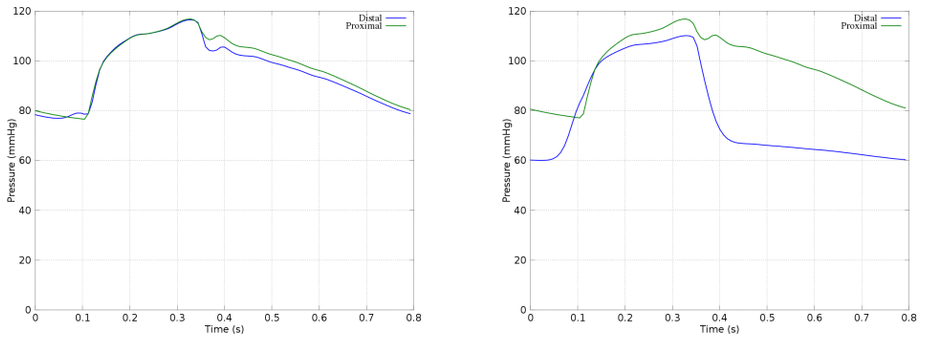

(a) 70% stenosis, FFR = 0.95

(b) 90% stenosis, FFR = 0.73

Figure 1: Mean pressure proximal and distal of a stenosis of varying degree of severity in the left coronary artery. FFR is calculated as the ratio of the mean distal intracoronary pressure to the mean aortic pressure.

The numerical simulations presented do not currently include a model of hyperemic blood flow, to account for the effect of adenosine on reducing the peripheral resistance of the microcirculation downstream. In addition, a stenosis element will be considered, to account for viscous losses, stenosis length and curvature. Future work will focus towards the validation of a comprehensive 1D model of the coronary tree, that should provide accurate estimates of FFR_{CT}, in a fraction of the time required by the current 3D models.

REFERENCES

[1] N.H.J. Pijls, B. de Bruyne, K. Peels, P.H. van der Voort, H.J.R.M. Bonnier, J. Bartunek, J.J. Koolen, Measurements of fractional flow reserve to assess the functional severity of coronary artery stenoses, *N. Engl. J. Med.*, 334, 1703-8, 1996.

[2] N.H.J. Pijls, P. van Schaardenburgh, G. Manoharan, E. Boersma, J-W. Bech, M. van't Veer, F. Bär, J. Hoorntje, J. Koolen, W. Wijns, B. de Bruyne, Percutaneous coronary intervention of functionally nonsignificant stenosis: 5-year follow up of the DEFER study, *J. Am. Coll. Cardiol.*, 49, 2105-11, 2007.

[3] M.J. Budoff, D. Dowe, J.G. Jollis, M. Gitter, J. Sutherland, E. Halamert, M. Scherer, R. Bellinger, A. Martin, R. Benton, A. Delago, J.K. Min, Diagnostic performance of 64-multidetector row coronary computed tomographic angiography for evaluation of coronary artery stenosis in individuals without known coronary artery disease. Results from the prospective multicenter ACCURACY (Assessment by Coronary Computed Tomographic Angiography of Individuals Undergoing Invasive Coronary Angiography) trial, *J. Am. Coll. Cardiol.*, 52, 1724-32, 2008.

[4] W.B. Meijboom, C.A.G. van Mieghem, N. van Pelt, A. Weustink, F. Pugliese, N.R. Mollet, E. Boersma, E. Regar, R.J. van Geuns, P.J. de Jaegere, P.W. Serruys, G.P. Krestin, P.J. de Feyter, Comprehensive assessment of coronary artery stenoses. Computed tomography coronary angiography versus conventional coronary angiography and correlation with fractional flow reserve in patients with stable angina, *J. Am. Coll. Cardiol.*, 52, 636-43, 2008.

[5] B-K. Koo, A. Erglis, J-H. Doh, D.V. Daniels, S. Jegere, H-S. Kim, A. Dunning, T. DeFrance, A. Lansky, J. Leipsic, J.K. Min, Diagnosis of ischemia-causing coronary stenoses by noninvasive fractional flow reserve computed from coronary computed tomographic angiograms. Results from the prospective Mmlticenter DISCOVER-FLOW (Diagnosis of Ischemia-Causing Stenoses Obtained Via Noninvasive Fractional Flow Reserve) study, *J. Am. Coll. Cardiol.*, 58, 1989-97, 2011.

[6] J.K. Min, J. Leipsic, M.J. Pencina, D.S. Berman, B-K. Koo, C. van Mieghem, A. Erglis, F.Y. Lin, A.M. Dunning, P. Apruzzese,M.J. Budoff, J.H. Cole, F.A. Jaffer, M.B. Leon, J. Malpeso, G.B.J. Mancini, S-J. Park, R.S. Schwartz, L.J. Shaw, L. Mauri, Diagnostic accuracy of fractional flow reserve from anatomic CT angiography, *JAMA*, 308, 1237-65, 2012.

[7] J. Mynard, P. Nithiarasu, A one dimensional arterial blood flow model incorporating ventricular pressure, aortic valve and regional coronary flow using the locally conservative Galerkin (LCG) method, *Communications in Numerical Methods in Engineering*, 24, 367-417, 2008.

[8] K. Low, R. van Loon, I. Sazonov, R.L.T. Bevan, P. Nithiarasu, An improved baseline model for a human arterial network to study the impact of aneurysms on pressure-flow waveforms, *Int. J. Numer. Meth. Biomed. Engng.* 28, 12241246, 2012.